Local moment phases in quantum impurity problems

Adam Philip Tucker
University College, Oxford

A thesis submitted for the degree of
Doctor of Philosophy
at the University of Oxford, Trinity 2014

Local moment phases in quantum impurity problems

Adam Philip Tucker
University College, Oxford

A thesis submitted for the degree of Doctor of Philosophy
at the University of Oxford, Trinity 2014

Abstract

This thesis considers quantum impurity models that exhibit a quantum phase transition (QPT) between a Fermi liquid strong coupling (SC) phase, and a doubly-degenerate non-Fermi liquid local moment (LM) phase. We focus on what can be said from exact analytic arguments about the LM phase of these models, where the system is characterized by an SU(2) spin degree of freedom in the entire system.

Conventional perturbation theory about the non-interacting limit does not hold in the non-Fermi liquid LM phase. We circumvent this problem by reformulating the perturbation theory using a so-called 'two self-energy' (TSE) description, where the two self-energies may be expressed as functional derivatives of the Luttinger-Ward functional.

One particular paradigmatic model that possesses a QPT between SC and LM phases is the pseudogap Anderson impurity model (PAIM). We use infinite-order perturbation theory in the interaction, U, to self-consistently deduce the exact low-energy forms of both the self-energies and propagators in each of the distinct phases of the model. We analyse the behaviour of the model approaching the QPT from each phase, focusing on the scaling of the zero-field single-particle dynamics using both analytical arguments and detailed numerical renormalization group (NRG) calculations.

We also apply two 'conserving' approximations to the PAIM. First, second-order self-consistent perturbation theory and second, the fluctuation exchange approximation (FLEX). Within the FLEX approximation we develop a numerical algorithm capable of self-consistently and coherently describing the QPT coming from both distinct phases.

Finally, we consider a range of static spin susceptibilities that each probe the underlying QPT in response to coupling to a magnetic field.

Acknowledgements

I would first like to thank my supervisor, Prof. David Logan, who has certainly taught me a lot about physics. I would also like to thank Dr. Martin Galpin, who has provided me with a lot of help and support in tackling this DPhil in a mentoring role.

Fred Jayatilaka, Phil Derry and Andrew Mitchell have also helped to break up the monotony of the PTCL, primarily by making the office a fun place to be. Other members of the Logan group I would particularly like to thank are Chris Wright and Sam Wilson-Fletcher.

My friends in Oxford should also get a mention. Firstly, Teresa, my beloved girlfriend who has helped me stay on track. Secondly, I would like to thank the 9 Warwick street lads, Greg 'red trousers get the ladies' Wyatt, Lyle 'let's run a marathon together with no training' Murray and Anthony 'skinny jeans' Bradley, who provided a great ambience in which to live in over the years. Others who should be noted are Lucy 'the flake' Ambrose, Ben 'DJ BJ' Barnett, Jess 'furrowed brow' Liley, Claudia 'doesn't like my shower music' Herresthal, Jenny 'the lab-rat' Rouka, Susan 'the archetypal Rhodes scholar' Humphrey, Alun 'where are the lads?' Biffin, and last but not least Joanna 'captain of the boats' Green.

I would like to thank my parents, who, together with my brother, Ross, who have done so much for me. I certainly would not be the person I am today without their constant support and guidance.

Finally, I would like to dedicate this thesis to my grandmother who recently passed away after losing a long battle with cancer.

Contents

1 Introduction **1**

1.1 The Anderson impurity model and the Kondo effect 1

1.2 Impurity models that exhibit a quantum phase transition 5

1.3 Aims and methods 8

1.4 Outline 9

2 Many-body theory **11**

2.1 Propagators 11

2.1.1 Properties of $D_{ii;\sigma}(\omega)$ 14

2.1.2 The Hilbert transform 14

2.1.3 Other propagators 15

2.2 Feynman diagrams for the exact propagator 15

2.2.1 Adiabatic switching on 16

2.2.2 Perturbation series 17

2.2.3 The Dyson equation 19

2.3 Propagators for the Anderson impurity model 21

2.3.1 Non-interacting limit 23

2.3.2 Atomic limit 23

2.3.3 The interacting Anderson model 25

2.3.4 The self-energy and the skeleton expansion 25

2.4 Fermi liquid theory 26

2.4.1 Luttinger-Ward functional 27

2.4.2 For the metallic Anderson model 28

2.4.3 General points 29

3 Local moment phases **31**

3.1 Local quantities 32

3.1.1 Behaviour of the local magnetization, $m(h)$ 34

3.1.2 Local propagators 36

3.1.3 Local self-energies 39

3.1.4 Zero field 40

3.2 Excess Quantities . . . 44
3.2.1 Excess density of states . . . 44
3.2.2 Excess charge and magnetization . . . 45
3.3 Phase shifts and the Friedel-Luttinger sum rule . . . 46
3.4 Luttinger Integrals . . . 49
3.4.1 Generalization of Luttinger's argument . . . 52
3.4.2 The Friedel sum rule . . . 53
3.5 Conventional single self-energy at zero field in an LM phase . . . 54
3.6 Exact deductions for the atomic limit . . . 55
3.6.1 Luttinger integral for the singly-occupied regime . . . 58

4 Pseudogap AIM: exact results **61**

4.1 Preliminaries . . . 61
4.1.1 Hybridization function . . . 63
4.1.2 Particle hole transformations . . . 64
4.2 Non-interacting limit . . . 65
4.3 Friedel sum rules . . . 66
4.3.1 SC phase: $U < U_c$ . . . 66
4.3.2 LM phase: $U > U_c$ . . . 67
4.4 The Luttinger integral, I_L . . . 69
4.4.1 General ph asymmetry . . . 70
4.4.2 Particle-hole symmetry . . . 72
4.5 Low-ω behaviour: LM phase . . . 73
4.5.1 Particle-hole asymmetry . . . 74
4.5.2 Particle-hole symmetry . . . 77
4.6 Luttinger self-consistency . . . 79
4.6.1 First-order contribution . . . 80
4.6.2 Second-order diagram . . . 81
4.6.3 Low-ω behaviour of the second-order diagram . . . 82
4.6.4 Infinite-order perturbation theory . . . 83
4.6.5 Self-consistency for the PAIM . . . 88
4.6.6 Phases of the PAIM . . . 91
4.6.7 Self-consistency in the atomic limit . . . 92
4.7 Low-ω behaviour: SC phase . . . 93
4.7.1 ASC phase: $x \neq 0$ . . . 93
4.7.2 SSC phase: $x = 0$ . . . 95
4.8 Scaling arguments as the QCP is approached . . . 96
4.9 Quantum critical point . . . 98
4.9.1 Scaling behaviour as the QCP is approached . . . 99

4.9.2 Numerical results for the SC and LM scaling functions 104
4.10 Finite field 110
4.10.1 Global field 110
4.10.2 Local field 111
4.11 Infinite-order Luttinger self-consistency 117
4.12 Concluding remarks 119

5 Self-consistent second-order perturbation theory **121**
5.1 Diagrams 122
5.2 Low-ω asymptotics 125
5.2.1 SSC phase 125
5.2.2 LM phase: General PH symmetry/asymmetry 127
5.2.3 ASC phase 128
5.2.4 Single self-energy in the LM phase 128
5.3 Second-order numerical procedure 130
5.3.1 Algorithm 130
5.3.2 Technical details 131
5.4 Numerical results 131
5.4.1 Particle-hole symmetry 131
5.4.2 General particle-hole asymmetry: $x \neq 0$ 137
5.4.3 Excess charges and Luttinger integrals 142
5.5 Concluding remarks 143

6 Fluctuation exchange approximation **145**
6.1 Preliminaries 145
6.2 Diagrams 146
6.2.1 Self-energies 146
6.2.2 Propagators 150
6.3 Implementing the approximation 151
6.3.1 Polarization propagators 151
6.3.2 Stability criteria 153
6.3.3 General algorithm 154
6.4 Phase diagram at ph symmetry 156
6.5 Analytic results in the symmetric strong coupling phase 157
6.5.1 Symmetries of the propagators 157
6.5.2 Low-ω behaviour of the self-energy, $\Sigma'(\omega)$ 159
6.5.3 Low-ω behaviour of the self-energy, $\Sigma''(\omega)$ 163
6.6 Analytic results for the QCP at ph symmetry 163
6.6.1 Low-ω behaviour 164

6.6.2 Determining the coefficient, $\alpha_{sc}(r)$ . . . 166
6.6.3 QCP plateau value . . . 167
6.7 Numerics in the SSC phase . . . 168
6.7.1 Flow equation . . . 168
6.7.2 Algorithm specifics . . . 169
6.7.3 Numerical results for the low-energy scale . . . 170
6.7.4 Results for the dynamics . . . 171
6.8 Local moment phase at ph symmetry . . . 173
6.8.1 Luttinger self-consistency . . . 174
6.8.2 Low-$\tilde{\omega}$ scaling behaviour . . . 180
6.8.3 LM phase numerical procedure . . . 182
6.8.4 Methodology . . . 183
6.8.5 Numerical results for the static quantities . . . 185
6.8.6 Numerical results for the dynamics . . . 187
6.9 Asymmetric strong coupling phase . . . 189
6.9.1 Low-$\tilde{\omega}$ scaling behaviour . . . 190
6.9.2 Approaching the QCP . . . 193
6.9.3 Algorithm specifics . . . 195
6.9.4 Numerical results in the ASC phase . . . 197
6.10 Local moment phase for general particle-hole asymmetry . . . 198
6.10.1 Low-$\tilde{\omega}$ scaling behaviour . . . 198
6.10.2 Numerical implementation and algorithm . . . 199
6.10.3 Numerical results . . . 199
6.11 Finite field effects . . . 201
6.12 Excess quantities . . . 204
6.13 Concluding remarks . . . 204

7 Spin susceptibilities 207

7.1 Local moment phase: susceptibilities at zero temperature . . . 208
7.1.1 Spin susceptibility and local moment formation . . . 208
7.1.2 Condition for the QCP . . . 216
7.1.3 Local charge susceptibility . . . 219
7.2 Local moment phase susceptibilities: $h = 0$, $T \to 0$ . . . 222
7.2.1 Global uniform field . . . 223
7.2.2 Conduction band susceptibility . . . 226
7.3 Local field: Susceptibilities from correlation functions . . . 226
7.4 Verification from NRG . . . 230
7.4.1 Alternative calculation from NRG . . . 234
7.4.2 Excess spin susceptibility . . . 235

7.5 Concluding remarks . . . 235

8 Summary **237**

A Phase shifts and Luttinger integrals **243**

A.1 Relating the phase shift to the renormalized level . . . 243

A.2 Relating the phase shift to the spectral function . . . 245

A.3 Discontinuous phase shift: PAIM ph symmetry . . . 246

A.3.1 SC phase . . . 246

A.3.2 LM phase . . . 247

A.4 LM phase: Luttinger integral pole contribution . . . 247

B Symmetries of the Hamiltonian **251**

B.1 Particle-hole transforms . . . 251

B.2 Physical properties . . . 253

B.3 A and B propagators . . . 255

B.4 Reversing the field . . . 255

C Numerical renormalization group **257**

C.1 Linear-chain Hamiltonian . . . 258

C.2 Logarithmic discretization . . . 259

C.3 Iterative diagonalisation . . . 261

C.4 Fixed points . . . 261

C.5 Calculation of the dynamics . . . 262

C.5.1 Anders-Schiller basis set . . . 262

C.5.2 Full density matrix approach . . . 263

C.5.3 Spectral broadening . . . 264

C.6 Self-energies . . . 264

D Free energies and hyperscaling **265**

D.1 Free energy . . . 265

D.1.1 Results . . . 266

D.2 Homogeneous functions . . . 269

D.3 Hyperscaling . . . 272

D.3.1 LM phase . . . 272

D.3.2 SC phase . . . 274

D.3.3 $U = U_c$ . . . 275

D.3.4 Hyperscaling relations . . . 275

E Free spins **277**

Bibliography **281**

Acronym	Description
AIM	Anderson impurity model
ASC	asymmetric strong coupling
AQCP	asymmetric quantum critical point
FDM	full density matrix
FL	Fermi liquid
FLEX	fluctuation exchange approximation
GAIM	gapped Anderson impurity model
LM	local moment
LMA	local moment approach
NFL	non-Fermi liquid
NIL	non-interacting limit
NRG	numerical renormalization group
PAIM	pseudogap Anderson impurity model
QCP	quantum critical point
QPT	quantum phase transition
SC	strong coupling
SQCP	symmetric quantum critical point
SSC	symmetric strong coupling
SSE	single self-energy
TSE	two self-energy

Table 1: Glossary of acronyms used in this thesis.

List of Figures

1.1 Schematic representation of the metallic Anderson impurity model. . 2
1.2 Pictorial representation of the Kondo effect. 4
1.3 Schematic representation of the pseudogap Anderson impurity model. 6
1.4 Schematic of critical behaviour as a function of U, T and h. 7

2.1 Diagrammatic perturbation expansion for the interacting propagator. 19
2.2 Diagrammatic representation of the Dyson equation. 20
2.3 Diagrammatic perturbation series for the self-energy. 25
2.4 The skeleton expansion for the self-energy. 26
2.5 Diagrammatic perturbation series for the Luttinger Ward functional. 27

3.1 The zero temperature local magnetization, $m(h)$, plotted versus field, h, and the interaction strength, U. 35
3.2 The spectral function, $\pi|\omega|^r D_\sigma(\omega, h)$, plotted versus ω for the PAIM. 38
3.3 Second-order diagrammatic contributions to Φ_{LW} and the self-energy. 52
3.4 First-order diagrammatic contribution to the self-energy. 56
3.5 Pictorial representation of the atomic limit singly occupied regime. . 57
3.6 The atomic limit Luttinger Integral, I_L, plotted as a function of U and $x = \varepsilon + \frac{U}{2}$. 60

4.1 Table denoting the zero-temperature low-ω dependence of the spectral function, $\pi D(\omega)$, in each phase of the PAIM. 62
4.2 NRG calculations: The renormalized levels in each phase phase plotted versus U. 68
4.3 NRG calculations: The local moment, $|\tilde{\mu}|$, and the local charge, $n(0)$, are plotted versus U. 69
4.4 NRG calculations: PAIM phase diagram in the (U, x) plane for $r = 0.4$. 69
4.5 NRG calculations: The Luttinger integral, I_L, plotted as a function of U across the phase boundary away from ph symmetry. 71
4.6 NRG calculations: The Luttinger integral, I_L, plotted as a function of U across the phase boundary at ph symmetry. 72

4.7 NRG calculations: $\pi(1+\beta^2(r))\Sigma^I(\omega)D(\omega)$ is plotted versus ω showing the LM phase pinning condition. 78
4.8 Time-ordered Goldstone contributions to the second-order Feynman diagram. 82
4.9 Time-ordered Goldstone contributions to a third-order Feynman diagram. 84
4.10 Representation of a particular third-order Goldstone time-ordered diagram. 85
4.11 A seventh-order Goldstone time-ordered diagram. 87
4.12 Table summarizing the self-consistent solutions found from the order-by-order diagrammatic analysis of Section 4.6. 91
4.13 Schematic phase diagram in the (r, U) plane for $x = \varepsilon + \frac{U}{2} = 0$. . . . 95
4.14 NRG calculations: Scaling spectra, $|\tilde{\omega}|^r \Psi^I_\alpha(\tilde{\omega}) = \pi\Gamma_0|\omega|^r D(\omega)$, plotted versus $\tilde{\omega} = \omega/\omega_*$ in both phases. 97
4.15 NRG calculations: Critical point spectral coefficients, $C(r)$, plotted as a function of r. 102
4.16 NRG calculations: Single and two self-energy scaling curves plotted as entire functions of $\tilde{\omega}$ for a fixed band exponent, $r = 0.45$. 104
4.17 NRG calculations: Scaling spectra, $\pi\Gamma_0|\omega|^r D(\omega) \equiv |\tilde{\omega}|^r \Psi^I_\alpha(\tilde{\omega})$, plotted versus $\tilde{\omega}$ for $r = 0.45$. 105
4.18 NRG calculations: The spectral function, $\pi\Gamma_0|\omega|^r D(\omega)$, plotted versus ω for a fixed asymmetry and band exponent, $r = 0.6$, approaching the QCP coming from both unique phases. 107
4.19 NRG calculations: The spectra, $\pi\Gamma_0|\omega|^r D(\omega)$, plotted versus ω approaching the QCP coming from both phases for $r = 0.35$ at ph symmetry. 108
4.20 NRG calculations: The spectra, $\pi\Gamma_0|\omega|^r D(\omega)$, plotted versus ω, approaching the QCP coming from both phases for $r = 0.35$ and $x = -1$. 109
4.21 NRG calculations: The spectral function, $\pi\Gamma_0|\omega|^r D_\downarrow(\omega, h = h')$, plotted versus ω for $h = h'$, $r = 0.35$, and $x < 0$. 113
4.22 Schematic phase diagram in the (U, h) plane. 113
4.23 NRG calculations: The field dependent renormalized levels, $\varepsilon^*_\sigma(h)$, plotted versus field for the ph asymmetric model with $r = 0.35$. . . . 114
4.24 NRG calculations: The local magnetization, $m(h)$, plotted versus h in the ASC phase. 115
4.25 NRG calculations: The local magnetization, $m(h)$, plotted versus U for a range of fields across the QCP. 116
4.26 NRG calculations: The zero-field two self-energies, $\Sigma_{A\sigma}(\omega, 0)$, plotted versus ω in the LM phase. 118

4.27 NRG calculations: The self-energies, $\Sigma_\sigma(\omega, h)$, plotted versus ω for a range of fields. 119

5.1 Diagrammatic first and second-order skeleton contributions to the self-energy. 123
5.2 The local moment, $|\tilde{\mu}|$, versus U/π at ph symmetry, shown at both first and second-order levels of approximation. 131
5.3 Phase diagram for ph symmetry, shown at the levels of first and second-order approximations, together with NRG. 132
5.4 Second-order results for the low-energy scales as the QCP is approached from each phase. 133
5.5 Second-order results for the modified spectral function, $F(\omega)$, plotted as a function of ω in the LM phase. 135
5.6 Second-order results for the modified spectral function, $F(\omega)$, plotted as a function of ω in the SSC phase. 136
5.7 The TSEs, $\Sigma^{I(2)}_{A\sigma}(\omega)$, plotted versus ω in the LM phase at ph symmetry. 136
5.8 Second-order results for the local charge, $\bar{n}$, and local moment, $|\tilde{\mu}|$, plotted versus U/π for different asymmetries. 137
5.9 Phase diagram in the (U, x) plane shown for both first and second-order perturbation theories. 138
5.10 Second-order renormalized levels in each phase plotted versus U/π. . 139
5.11 The second-order self-energies plotted versus ω in each phase. 141
5.12 The modified spectral function, $F(\omega)$, in the ASC phase plotted versus ω. 142
5.13 The modified spectral function, $F(\omega)$, in the ph asymmetric LM phase plotted versus ω. 143

6.1 Diagrammatic representation of the FLEX approximation to the skeleton expansion. 146
6.2 Ladder summations for the polarization propagators in the transverse-spin and particle-particle channels. 148
6.3 Infinite resummation of diagrams to form the three polarization propagators in the FLEX approximation to the self-energy. 149
6.4 Time-ordered (Goldstone) contributions to $\Sigma^{PH}_{A\downarrow}(t)$ and $\Sigma^{PP}_{A\downarrow}(t)$. . . . 150
6.5 Ph symmetric phase diagram in the (r, U) plane. Results are shown for first and second-order perturbation theories, FLEX and NRG. . . 156
6.6 The self-energy coefficient, $a_{ssc}(r)$, plotted versus r. 161
6.7 QCP spectrum plateau values, $1 - K(r)$, plotted versus r, calculated from both FLEX and NRG. 167

6.8 FLEX results: The SSC low-energy scale, ω_m, plotted versus U/π as the QCP is approached. 170
6.9 FLEX results: The modified spectral function, $F(\omega)$, in the SSC phase plotted versus ω. 172
6.10 FLEX results: The imaginary part of the polarization propagator, $\mathrm{Im}\Pi(\omega)$, plotted versus ω as the QCP is approached from the SSC phase. 172
6.11 FLEX results: The self-energy scaling function, $|\omega|^{-r}\Sigma^I(\omega)$ plotted versus $\tilde{\omega}$ in the SSC phase. 173
6.12 FLEX results: The SSC phase modified spectral function, $F(\omega)$, plotted versus ω from both FLEX and NRG. 174
6.13 FLEX results: The local moment, $|\tilde{\mu}|$, plotted versus U/π as the FLEX algorithm is iterated. 184
6.14 FLEX results: The local moments, $|\tilde{\mu}|$ and $|\mu_0|$, plotted versus U/π at ph symmetry. 185
6.15 FLEX results: The renormalized levels plotted versus U/π as the QCP is approached at ph symmetry. 186
6.16 The local moment, $|\tilde{\mu}|$, plotted as a function of U/π from FLEX, UHF and NRG. 187
6.17 FLEX results: The modified spectral function, $F(\omega)$, plotted versus ω, as the QCP is approached from both phases. 187
6.18 FLEX results: LM phase self-energy scaling functions, $|\omega|^{-r}\Sigma^I_{A\sigma}(\omega)$, plotted versus $\tilde{\omega}$. 188
6.19 The modified spectral function, $F(\omega)$, plotted versus ω deep in the LM phase from FLEX, NRG and second-order perturbation theory. . 189
6.20 FLEX results: The ASC phase low-energy scale, ω_m, plotted versus the renormalized level, $|\varepsilon^*|$. 192
6.21 FLEX results: Phase diagram in the (U, x) plane for the asymmetric model. 196
6.22 FLEX results: The renormalized level, ε^*, is plotted versus U/π in the ASC phase. 196
6.23 FLEX results: The self-energy scaling function, $|\omega|^{-r}\Sigma^I(\omega)$, is plotted versus $\tilde{\omega}$ in the ASC phase. 197
6.24 FLEX results: The low-energy scale, ω_*, is plotted versus U/π as the QCP is approached from each phase. 200
6.25 FLEX results: The spectral function, $\pi\Gamma_0|\omega|^r D(\omega)$, plotted versus ω in the ph asymmetric LM phase. 201
6.26 FLEX results: The transverse spin polarization propagator, $\mathrm{Im}\Pi^{+-}(\omega, h)$, plotted versus ω for different local fields. 202

6.27 FLEX results: The local magnetization, $m(h)$, and the renormalized levels, $\varepsilon^*_\sigma(h)$, plotted versus U/π, for different local fields. 203

7.1 Schematic showing the local magnetization, $m(h)$, as a function of field in the LM phase. Both the $T = 0$ and $T > 0$ cases are shown. . 209
7.2 Diagrammatic representation of the self-energy, expressed in terms of the skeleton expansion. 212
7.3 Diagrammatic form of the Bethe-Salpeter equation for the reducible vertex function. 214
7.4 NRG results showing the local susceptibility, χ_s, as a function of U/π as the SQCP is approached from both phases. 219
7.5 NRG results showing the local susceptibility, χ_s, as a function of U/π as the AQCP is approached from both phases. 220
7.6 NRG results showing the local charge susceptibility, χ_c, as a function of U/π as the AQCP is approached from both phases. 222
7.7 NRG results showing the correlation functions, $\langle \hat{s}_z^2 \rangle$ and $\langle \hat{s}_z \hat{S}_z \rangle$, plotted versus U/π. 233
7.8 NRG results showing the local magnetization, $m(h)$, at a fixed field, h, and a range of different temperatures. 234

C.1 Diagram showing logarithmic discretization of the pseudogap conduction band. 259
C.2 Schematic of the NRG linear chain Hamiltonian. 260
C.3 Zero-field pseudogap AIM RG flows and fixed points in the $(U/\Gamma, x/\Gamma)$ plane. 262
C.4 Schematic of the Anders-Schiller basis set. 263

D.1 Schematic showing the QPT in the $(|U - U_c|, h, T)$ plane. 273

E.1 The magnetization, $m(h, T)$, shown as a function of h, both at $T = 0$ and $T > 0$, for the case of an ensemble of free spins. 278

CHAPTER 1

Introduction

The behaviour of strongly correlated electron systems has fascinated both theorists and experimentalists in condensed matter physics for the past 60 years. In these systems, interactions between particles are too large to neglect; the implementation of simple perturbative techniques is often insufficient. Moreover, by virtue of the fact that these systems often contain a macroscopically-large number of particles, they are very challenging to solve and a number of physically motivated approximations are often needed to obtain a physical understanding of the underlying behaviour. In some cases, the physics that arises is completely driven by interactions, leading to 'collective' emergent behaviour, completely distinct from the corresponding non-interacting system [1]. Notable examples of strongly-correlated electron systems include high-temperature superconductors [2,3], heavy Fermions [4], as well as those exhibiting the fractional quantum hall effect [5], and the 'Kondo effect' [2,6], which we discuss below.

1.1 The Anderson impurity model and the Kondo effect

In this thesis we study the Anderson impurity model (AIM) [7], originally proposed in order to describe the physics of magnetic impurities in solids at low temperature, but more recently found to apply to so-called quantum dot devices [8, 9]. The Anderson model has been extensively studied over the past 50 years [2], and its underlying behaviour has been mostly understood. The basic model, in which the impurity couples to a metallic conduction band, is known to possess a single non-magnetic ground-state for all parameters [10–12]; however more complex variants exhibit a quantum (zero temperature) phase transition between two distinct phases. In this thesis it is models of this type that we consider, focusing on the rich behaviour that arises as a consequence of quantum criticality. Before proceeding however, we first give a brief historical summary of how the original Anderson model came about,

and specifically why it is of interest to theorists and experimentalists alike.

In the 1930s, experimentalists probing the electrical properties of gold wires embedded with magnetic impurities [13], noticed two striking phenomena that could not be explained by existing theory. First, experimentalists observed a Curie-Weiss term in the impurity magnetic susceptibility, indicating the apparent formation of local magnetic moments in the samples; it was not clear how these moments could form in presence of a metallic host of delocalized electrons. Second, was the observation of a minimum in the electrical resistivity of the materials at low temperature, an effect that became more prominent with the concentration of the impurities. Anderson proposed his model in order to capture the behaviour of the former effect, although it soon became apparent that both phenomena were connected.

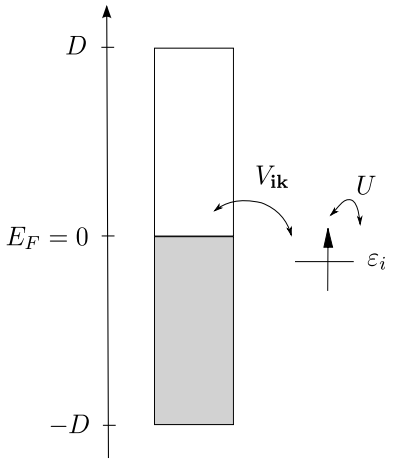


Figure 1.1: Schematic of the Anderson impurity model coupled to a conduction band with a metallic (flat band) density of states.

The single-impurity[1] Anderson model Hamiltonian in second-quantized notation is given by

$$\hat{H} = \sum_{\mathbf{k}\,\sigma} \epsilon_{\mathbf{k}} \hat{n}_{\mathbf{k}\sigma} + \sum_{\sigma} \epsilon_i \hat{n}_{\sigma} + U \hat{n}_{\uparrow} \hat{n}_{\downarrow} + \sum_{\mathbf{k}\,\sigma} (V_{i\mathbf{k}} c^{\dagger}_{i\sigma} c_{\mathbf{k}\sigma} + \text{h.c.}), \tag{1.1}$$

and also shown schematically in Fig. 1.1. The spin $\sigma = \uparrow, \downarrow$, and we set the chemical potential, $\mu = 0$. As shown in Fig. 1.1, the model simply describes a single electron level with energy, ε_i, and repulsion energy, U, coupled via matrix elements, $V_{i\mathbf{k}}$, to a conduction band of non-interacting delocalized electron states. The first term in eq. (1.1) describes the electrons in the conduction band, with bandwidth $2D$. The energies of such states are represented by $\varepsilon_{\mathbf{k}}$, while $\hat{n}_{\mathbf{k}\sigma} = c^{\dagger}_{\mathbf{k}\sigma} c_{\mathbf{k}\sigma}$; $c^{\dagger}_{\mathbf{k}\sigma}$ and $c_{\mathbf{k}\sigma}$ are creation and annihilation operators (i.e. $c^{\dagger}_{\mathbf{k}\sigma}$ creates an electron in the conduction

[1] It is assumed within the model that the impurities within a solid are dilute, such that inter-impurity interactions are neglected. Thus only one impurity is accounted for in the Anderson model Hamiltonian, eq. (1.1).

band with spin σ and wavevector $\mathbf{k}$). The second and third terms describe the electrons on the impurity single level, where $\hat{n}_\sigma = c^\dagger_{i\sigma} c_{i\sigma}$ counts the number of electrons on the impurity with spin σ. The third term embodies the interactions between electrons on the impurity, where U is the on-site Coulomb repulsion energy, such that for large-U double occupancy is disfavoured. The last term in the Hamiltonian describes the coupling between the single impurity level and the conduction band; where the magnitude of $V_{i\mathbf{k}}$ defines the strength of the coupling [2].

Anderson originally applied an unrestricted Hartee-Fock (UHF) mean-field treatment [7] to the model and consequently concluded it possesses a phase transition between non-magnetic and magnetic ground-states as a function of the interaction strength U.[2] However, this was later shown [10–12] to be fundamentally incorrect: the model possesses a non-magnetic ground-state at zero temperature for all parameters.

Significant progress was made in 1964 when Kondo [14] was able to successfully predict the resistivity minimum found in experiments [13, 15] for the first time. Kondo studied a simpler system - the s-d model[3] which contains a single spin-$\frac{1}{2}$ (the impurity) coupled antiferromagnetically (via a coupling 'J') to a metallic conduction band. The Anderson model shown in Fig. 1.1 can in fact be shown to map directly onto the s-d model in the regime where the impurity level is singly occupied via a so-called Schrieffer-Wolff transformation [17]. By applying third-order perturbation theory in the coupling-J to the s-d model, Kondo derived the following expression for the electrical resistivity at low temperature:

$$R(T) = a + bT^5 - c \ln\left(\frac{k_B T}{D}\right), \tag{1.2}$$

where a, b and c are positive coefficients, and D is once again the half-bandwidth of the conduction band. The first term comes about from electrons scattering off the impurity spins; whereas the second term arises from electron-phonon scattering processes. It is the third term which was the major result of Kondo's work, diverging as $T \to 0$. Together, the second and the third terms in eq. (1.2) thus result in a low-temperature minimum in $R(T)$. Whilst this result explains the presence of the minimum found in experimental results, it does not explain the underlying physics as the temperature ultimately vanishes, eq. (1.2) predicting an unphysical divergence in $R(T)$ as $T \to 0$. This issue became aptly known as the "Kondo problem", a conundrum not solved until the 1970s.

In 1970 it was Anderson who made the first steps to solving the Kondo problem [18]. He treated the s-d model with a perturbative (to second-order in J)

[2] A magnetic ground-state involves a spin-degree of freedom arising in the entire system.

[3] The s-d model was originally proposed by Zener, [16]; however this model later become known as the Kondo model by virtue of Kondo's success in describing its underlying behaviour.

renormalization group technique known as poor-man's scaling (PMS). Essentially the idea of this approach was to progressively eliminate high-energy excitations to the conduction band edges by renormalizing both the antiferromagnetic coupling, J, and the conduction bandwidth, D. The result was that in the limit $T \to 0$, the coupling $J \to \infty$, such that the spin-$\frac{1}{2}$ 'locks up' into a many-body singlet state. However, since PMS is inherently perturbative in J, the technique ultimately breaks down at low-temperature, and therefore cannot be trusted in this regime. A non-perturbative technique was clearly needed to describe the low-temperature physics of the s-d model (and hence the Anderson model) and solve the Kondo problem.

The ultimate solution came in 1975 when Wilson, building on the scaling ideas of Anderson's PMS, developed the numerical renormalization group (NRG) technique [10]. The NRG was able to solve the s-d model, taking into account all energy scales and hence correctly capturing the $T \to 0$ limit non-perturbatively. The essential idea was to logarithmically discretize the conduction band, such that all energy scales of the problem were equally well sampled. In consequence, the NRG predicted that the impurity spin-$\frac{1}{2}$ degree of freedom is fully quenched (screened) by the conduction band states. Thus, the resulting $T = 0$ ground-state of the entire system is a non-magnetic many-body singlet. This truly many-body phenomenon, as illustrated pictorially in Fig. 1.2, became known as the 'Kondo effect'.

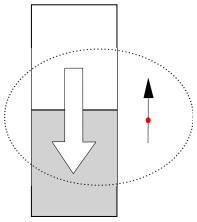


Figure 1.2: A pictorial representation of the Kondo effect. All of the delocalized conduction band states, as depicted by the large white arrow, act to screen the impurity spin degree of freedom for $T < T_K$, such that the system 'locks up' into a global singlet state.

Later, the NRG was applied equally well to the single-impurity Anderson model [11, 12], also predicting that the system has a non-magnetic 'singlet' ground-state for all U at $T = 0$. Furthermore, there were two other important results obtained from the NRG. First, is the existence of a low-energy scale, $k_B T_K$, found to be exponentially small in the interaction strength, U. For $T \ll T_K$, the Kondo effect occurs, and the system 'flows' to its zero temperature ground-state. Moreover, since $k_B T_K$ is the only low-energy scale in the problem, for $T \ll T_K$ and any combination of 'bare' parameters (ε_i, U) of the Hamiltonian, eq. (1.1), physical thermodynamic quantities scale in terms of T/T_K. For example, the impurity contribution to the entropy, $S_{\rm imp}(T) \overset{T \ll T_K}{\sim} F(T/T_K)$, where $F(x)$ is a *universal* function.

The second important deduction from NRG is that, as also argued by Nozières

[19], the low-temperature ($T \ll T_K$) behaviour of the Kondo effect is consistent with Landau's Fermi liquid theory [20, 21].

The Bethe ansatz technique was later applied to both the s-d (Kondo) and Anderson models [22, 23], solving them exactly within an analytical framework. Many approximate techniques have also been applied to the AIM. Firstly, diagrammatic perturbation theory in the interaction, U, was extensively examined in a series of important papers by Yosida and Yamada [24–27]. However, despite its virtues for small U, it failed to capture the large-U limit where local moment formation and the Kondo effect are crucial to the underlying physics. Many large-N techniques have also been applied to the AIM [2], such as slave boson mean-field theory, the non-crossing approximation and the $1/N$ expansion. However, none are able to capture the full behaviour of the AIM on all energy scales. Finally, the local moment approach [28–30] (LMA), a diagrammatic technique involving the resummation of certain classes of Feynman diagrams, has been very successful in correctly capturing the single-particle dynamics of the model.

1.2 Impurity models that exhibit a quantum phase transition

The simple Anderson model (with a single impurity level coupled to a metallic conduction band), as well as the Kondo (s-d) model are not the only models that exhibit Kondo physics. There are many variants and extensions of the basic Anderson model that have also been studied; in some cases the model has a Fermi liquid ground-state where the (conventional) Kondo effect is prevalent, and in other cases the model exhibits underlying non-Fermi liquid behaviour. Examples of these type of models include an array of multi-impurity and multi-band cases, including the two-channel Kondo model originally proposed by Nozières and Blandin [31, 32]. Furthermore, two other variants on the AIM that exhibit non-Fermi liquid behaviour at $T = 0$, are the so-called 'gapped' and 'pseudogap' (softgap) Anderson models. For much of this thesis we focus on the latter and therefore here we provide a summary of previous work.

Although the Hamiltonian for this model has exactly the same form as eq. (1.1), the conduction band density of states is no longer flat. Instead, as is shown pictorially in Fig. 1.3, the density of states has a power-law dependence given by

$$\rho_b(\omega) = \rho_0 |\omega|^r \theta(D - |\omega|), \tag{1.3}$$

with ρ_0 a constant, and the exponent $r > 0$, such that it vanishes at the Fermi level (the $r = 0$ case corresponding to the usual metallic AIM). The step function simply cuts the power law dependence off at the half bandwidth, D.

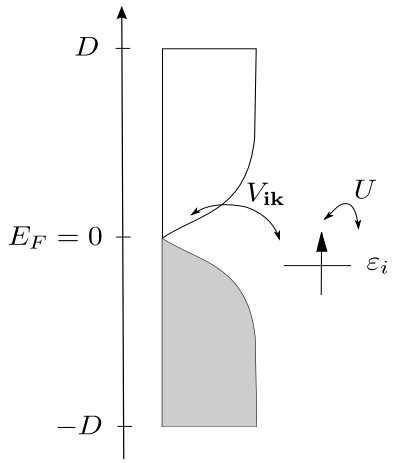


Figure 1.3: Schematic of the Anderson impurity model coupled to a conduction band with a 'pseudogap' density of states.

The pseudogap Kondo model,[4] obtained via a simple Schrieffer-Wolff transformation [17] from the PAIM (in the singly occupied regime where $\varepsilon_i < 0$, $\varepsilon_i + U > 0$), was first studied by Withoff and Fradkin in 1990 [33]. They applied Anderson's poor man's scaling [18] to the problem and concluded that, since there is a depletion of band states around the Fermi level, for any finite band exponent, r, a doubly degenerate non-Fermi liquid local moment (LM) phase tends to be stabilized relative to a Fermi liquid phase where the Kondo effect persists. For the PAIM the consequence of this is that at some finite critical $U = U_c(r)$, there is a quantum critical point (QCP) between the two distinct phases at zero temperature. For $U < U_c(r)$, the Kondo singlet strong coupling (SC) phase is the ground-state; in contrast for $U > U_c(r)$, the LM phase, in which the spin degree of freedom on the impurity is not quenched, becomes the ground-state. The zero-temperature Kondo scale, ω_K, finite in the SC phase, vanishes at a finite U for any finite r via

$$\omega_K \propto |1 - \tfrac{U}{U_c}|^{\frac{1}{r}}, \qquad \text{with } U_c(r) \overset{r\to 0}{\propto} \tfrac{1}{r}. \tag{1.4}$$

Moreover for $U \to U_c^+(r)$, such that the QCP is approached from the LM phase, there is an equivalent low-energy scale, which we denote ω_L (with the same dependence on U/U_c as eq. (1.4)). Furthermore, just as for the metallic Kondo effect discussed above, physical properties of the system (such as the local impurity propagator $G(\omega)$) exhibit scaling in terms of ω/ω_* (where $\omega_* = \omega_K$ or ω_L) as the QCP is approached for $U \to U_c^{\pm}(r)$ [34–37]. Uniquely at the QCP where $U = U_c$, the system is scale free and as a result exhibits non-trivial *interacting* behaviour. Thus, much of the literature has focused on the unique properties of the QCP.

[4] Equivalent to the Kondo (s-d) model described above, but with a pseudogap density of states.

The system has been extensively studied both at the particle-hole (ph) symmetric point (where $x = \varepsilon_i + U/2 = 0$), and the more general case (where $x \neq 0$). NRG studies [35–43], notably ref [43], have allowed the thermodynamic properties of the system to be fully elucidated. As we discuss further in Chapter 4, one important result of ref [43] is that there are 2 distinct quantum critical points (QCPs), each governing the critical behaviour for a particular r range. Furthermore, it is known from considering a scaling ansatz for the singular part of the free-energy [37] (as detailed in Appendix D) that both QCP are only pristine identically at $T = 0$ and $h = 0$, where $h = \frac{1}{2}g\mu_B B$ is an applied magnetic field.[5] In other words for any finite T or h, the QCP is strictly destroyed and smoothed into a crossover region. The essential underlying physics is depicted in Fig. 1.4.

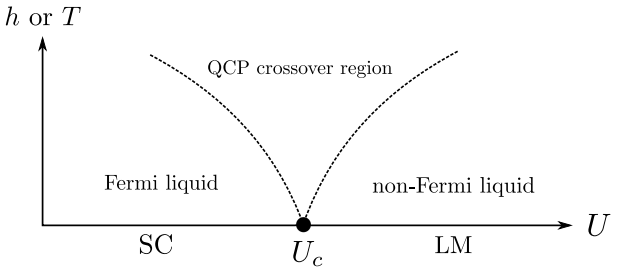


Figure 1.4: Schematic of the critical behaviour as a function of U, T and h. The QCP only occurs at both zero-field and zero-temperature, and $U = U_c$ separating a Fermi liquid SC phase where the Kondo effect persists and a doubly degenerate non-Fermi liquid LM phase where the impurity spin degree of freedom is incompletely quenched. The dotted lines denote the low-energy scale coming from either phase, and thus defining a continuous QCP crossover region for finite T or h.

As for the metallic case, the single-particle dynamics have been broadly examined using NRG [35,39,41] and within the local moment approach (LMA) [34,41,44,45]. In Chapter 4 we give a full discussion of the important results of these studies, and therefore do not consider them any further here. Perturbative renormalization group techniques [46–49] in the spirit of Anderson's PMS [18] have been applied to the model with much success, in some cases capturing the exact behaviour consistent with NRG.

The PAIM is not the only model to exhibit a quantum phase transition between LM and SC phases. As alluded to above, another model that displays this behaviour is the gapped AIM. For this model the single impurity level is coupled to a conduction band with a hard gap around the Fermi level.[6] The consequence is that at ph symmetry (where $x = \varepsilon_i + U/2 = 0$) the depletion of band states around the Fermi level destroys the Kondo effect, and hence the Fermi liquid phase, for any U [50–52].

[5] The field may be applied either globally to the entire system, or locally to only the impurity level.

[6] The density of states is given by $\rho_b(\omega) = \rho_0\theta(|\omega| - \delta)$ with 2δ the size of the gap.

Away from ph symmetry the situation is more complex, NRG calculations [50] find that it is possible for the Kondo effect to exist, but only below a critical gap, $\delta < \delta_c$. These results are backed up by results from the local moment approach [51], the exact self-consistent calculations of ref [52], as well as a further more recent NRG study [53].

In more recent years there have been NRG studies of impurity models coupled to both fermionic and bosonic baths. The Bose-Fermi Kondo [54, 55] and Anderson models [56, 57] have both been found to exhibit quantum phase transitions between a LM and SC phase, and thus also feature in the class of models that we study in this thesis.

1.3 Aims and methods

The principal aim of this thesis is to examine the *exact* properties of non-Fermi liquid local moment phases that arise in both the pseudogap and gapped single impurity models, as well as the other more complicated models mentioned above. The first way in which we look to achieve this aim is by considering the general diagrammatics that provide the foundation of many-body theory.

In a series of seminal papers [58–61] Luttinger and coworkers fully derived the diagrammatic framework that underpins many-body theory, by considering a general system of fermions with local two-particle interaction terms. In fact, since the Anderson model Hamiltonian also contains an interaction term of this form, it may be shown that Luttinger's original analysis applies equally well to the quantum impurity systems that we consider in this thesis. As we examine further later on, one of the essential results of these papers is that in a Fermi liquid phase the free energy of an interacting system of fermions may be written as a *functional* of the exact single-particle propagator, G_σ (where $\sigma = \uparrow, \downarrow$), and thus may be described diagrammatically in terms of the Luttinger-Ward functional, $\Phi_{LW} \equiv \Phi[G_\uparrow, G_\downarrow]$ (where $[\ldots]$ denotes a functional). The interaction self-energy, Σ_σ [62, 63], which may be thought of physically as the energy of a single σ-spin particle's interactions as it travels through the many-body system, is then obtained via a functional derivative of Φ_{LW} with respect to the *exact* single-particle propagator, i.e. $\Sigma_\sigma = \delta\Phi_{LW}/\delta G_\sigma$. The self-energy is thus also a functional of the exact propagator, $\Sigma_\sigma \equiv \Sigma[G_\uparrow, G_\downarrow]$ and may be constructed diagrammatically in terms of the so-called 'skeleton expansion', a fundamental concept that we explicitly return to in the discussion of Chapter 2.

In this thesis we aim to use the exact diagrammatic arguments of Luttinger and Ward [59], but within a so-called 'two self-energy' (TSE) framework to describe the underlying non-Fermi liquid behaviour of LM phases. This TSE description underlies the local moment approach (LMA), a non-perturbative approximate technique based

on the resummation of certain Feynman diagrams to infinite order in U.[7] As alluded to above, the LMA has been instrumental to our understanding of the single-particle dynamics of the metallic [28–30], pseudogap [34, 41, 45, 64, 65] and gapped Anderson impurity models [51]. The TSE description, inherent within the LMA, allows the existence of broken-symmetry in both the LM and SC phases. For the PAIM, the idea of using unrestricted Hartree-Fock (UHF) propagators as the basis Green functions, along with the concept of "symmetry restoration" in a SC phase, allowed the LMA to correctly describe the QCP for $U \to U_c^{\pm}(r)$.

Furthermore, within many-body theory, the exact propagator, G_σ, can be written in terms of the interaction self-energy, Σ_σ, via the Dyson equation [62]. As stated above, from the arguments of Luttinger and Ward, in a Fermi liquid phase $\Sigma_\sigma \equiv \Sigma[G_\uparrow, G_\downarrow]$ is a functional of the propagator and expressed diagrammatically via the skeleton expansion. Thus, the Dyson equation and the skeleton expansion in principal provide a *self-consistency* condition for the determination of the exact propagator, G_σ. There are a number of physically motivated approximations based on this self-consistency condition that conserve quantities such as particle number, energy and momentum [66, 67], and are automatically consistent with the exact Friedel sum rule, originally derived by Langreth for the AIM [68].

The second fundamental aim of this thesis is to apply the fluctuation exchange approximation (FLEX), one such 'conserving approximation', to the pseudogap AIM. FLEX was first developed by Bickers et al [69–71] for the Hubbard model and other similar lattice models. It has also been successfully applied to the metallic AIM at zero temperature by White [72], and also at finite temperature by Chen *et al.* [73]. The class of Feynman diagrams included in the FLEX approximation is essentially the same as the diagrams included in the LMA, but with a crucial difference. Within FLEX the self-energy is a functional of the propagator via the skeleton expansion, and thus the system must be iterated to full self-consistency for the fully-interacting G_σ. In this thesis we implement FLEX within a TSE description in order to accurately describe the LM phase of the model.

1.4 Outline

Having discussed the necessary preliminaries in this introduction, we conclude by providing an outline of the rest of this thesis. In Chapter 2 we provide a basic introduction to the standard many-body techniques that we use in the chapters that follow.

In Chapter 3 we introduce the framework needed to describe in detail the un-

[7] The LMA approximation essentially involves the diagrams of the random phase approximation (RPA) [62], but crucially broken symmetry solutions are permitted such that the diagrams may be summed in a meaningful way.

derlying physics of LM phases. Since the ground state of these phases is doubly-degenerate, it is crucially not perturbatively connected to the non-interacting limit of the model, and therefore a non-Fermi liquid. Thus, the standard many-body diagrammatic techniques, as laid out in Chapter 2, do not apply in a conventional sense. However, we show that by introducing a symmetry breaking magnetic field, h, the conventional diagrammatic methods hold equally well. The limit that the field vanishes is then taken carefully such that the zero-field LM phase is described ingeniously within a two-self-energy (TSE) description.

In Chapter 4 we apply the TSE framework to the pseudogap AIM in order to obtain a number of *new* exact results about the LM phase. We proceed to consider the dynamic behaviour of the local propagator, G_σ, and specifically its low-ω behaviour in each phase of the PAIM (both at ph symmetry and more generally). By adapting Luttinger's original diagrammatic order by order analysis [60], we obtain *exact* low-ω results for the local self-energies in both SC and LM phases. We proceed to then consider the universal scaling of the single-particle propagator as the quantum critical point is approached from either phase.

In the second half of this thesis we focus on applying approximate diagrammatic treatments to the pseudogap AIM. In Chapter 5 we apply self-consistent second-order perturbation theory in U to the model. The skeleton expansion (as mentioned above - a diagrammatic series involving the full interacting propagator) is truncated at second-order level, and in consequence the self-consistent propagator is determined numerically. In the procedure we allow for the possibility that broken-symmetry solutions can exist. The system may then converge to either a broken-symmetry LM phase solution within a TSE description, or a Fermi liquid SC solution within a conventional perturbative formulation.

In Chapter 6, we take the self-consistency procedure of Chapter 5 much further by including an infinite-order (in U) subset of diagrams - appropriate to the FLEX approximation discussed above - in the skeleton expansion for the self-energy. Once again, by allowing for the possibility of self-consistent solutions we aim to capture the underlying behaviour in each distinct phase and the non-trivial interacting nature of the QCP between them. Numerical results for the single-particle propagator are obtained and a comparison is given with numerically exact NRG results. Finally as a result of the fact that FLEX is a conserving approximation, we show that many of the exact relations derived in Chapter 4, are satisfied in each phase of the model.

In Chapter 7 we return to consider some further exact relations for LM phases in general. We examine an array of static spin susceptibilities that probe the zero-field phase transition. Specifically focusing on the LM phase we find that the limits $T \to 0$ and $h \to 0^{\pm}$ do not commute. We thus deal with each distinct limiting process separately.

Finally in Chapter 8, we summarize the important results of each chapter.

CHAPTER 2

Many-body theory

In this chapter we outline the theoretical framework that we use in the rest of this thesis. Initially we introduce the single-particle propagator (Green function), the quantity of paramount importance in many-body theory. We discuss its physical properties and show how it is related to the excitation energies of the many-body system, before considering its representation as a perturbation expansion in terms of Feynman diagrams. In addition, we consider how the local impurity propagator may be specifically calculated for the Anderson impurity model, explicitly discussing two important soluble limits before moving on to the *interacting* many-body case. We formally introduce the local interaction self-energy from the so-called Dyson equation and show how it may be represented in terms of a perturbation expansion involving the single-particle propagator. We conclude the chapter with a discussion of the basic results of Landau's Fermi liquid theory [2] and its specific implications for the AIM, before considering the Luttinger-Ward functional, Φ_{LW} [59]. For a more detailed analysis of the standard many-body techniques discussed in this chapter we refer the reader to refs [62, 63].

2.1 Propagators

The time-ordered (causal) single-particle propagator (Green function) is defined by the following correlation function

$$G^t_{ij;\sigma}(t) \equiv G_{ij;\sigma}(t) = -i\langle \Psi_0^N | \hat{T}[\hat{c}_{i\sigma}(t)\hat{c}^\dagger_{j\sigma}(0)] | \Psi_0^N \rangle \tag{2.1}$$

where the superscript 't' denotes time-ordered, and $\hat{T}$ is the Wick time-ordering operator given by

$$\begin{aligned} \hat{T}[\hat{c}_{i\sigma}(t)\hat{c}^\dagger_{j\sigma}(0)] = \hat{c}_{i\sigma}(t)\hat{c}^\dagger_{j\sigma}(0) \quad & \text{for } \; t > 0, \\ -\hat{c}^\dagger_{j\sigma}(0)\hat{c}_{i\sigma}(t) \quad & \text{for } \; t \leq 0. \end{aligned} \tag{2.2}$$

with the $(-)$ sign coming from swapping two Fermionic operators. $|\Psi_N^0\rangle$ is the exact interacting ground state of the full N-body system at zero temperature. $\hat{c}_{i\sigma}^\dagger(t)$ and $\hat{c}_{i\sigma}(t)$ are creation and annihilation operators in the Heisenberg representation[1] on site i at time t. By virtue of the time-ordering in eq. (2.2), eq. (2.1) may be split into two components

$$G_{ij;\sigma}(t) = G_{ij;\sigma}^+(t) + G_{ij;\sigma}^-(t) \tag{2.3}$$

where $G_{ij;\sigma}(t) = G_{ij;\sigma}^+(t)$ for $t > 0$ and $G_{ij;\sigma}(t) = G_{ij;\sigma}^-(t)$ for $t \leq 0$. Physically, the so-called 'retarded' function, $G_{ij;\sigma}^+(t)$, describes the propagation of a σ-spin electron added to the system at site j at $t = 0$, and destroyed at $t > 0$ at site i. Similarly, the 'advanced' function, $G_{ij;\sigma}^-(t)$, describes the propagation of a σ spin hole added to the system at $t < 0$ and removed at time $t = 0$ from site i. Choosing the retarded function, $G_{ij;\sigma}^+(t)$, it is convenient to work with the frequency representation of the correlators, given via the Fourier transform

$$G_{ij;\sigma}^+(\omega) = \int_{-\infty}^{\infty} \mathrm{d}t \mathrm{e}^{i(\omega+i\eta)t} G_{ij;\sigma}^+(t) \tag{2.4a}$$

$$= -i \int_0^{\infty} \mathrm{d}t \mathrm{e}^{i(\omega+i\eta)t} \langle \Psi_0^N | \hat{c}_{i\sigma}(t) \hat{c}_{j\sigma}^\dagger(0) | \Psi_0^N \rangle \tag{2.4b}$$

where eq. (2.1) (for $t > 0$) has been inserted into the first line to obtain the second line and $\eta = 0^+$ is a positive infinitesimal to ensure convergence of the integral. From eq. (2.4b), it may be shown [62] by writing the operator $\hat{c}_{i\sigma}(t) = \mathrm{e}^{-i\hat{H}t} \hat{c}_{i\sigma} \mathrm{e}^{-i\hat{H}t}$, inserting a complete set of states $\hat{1} = \sum_n |\Psi_n^{N+1}\rangle\langle\Psi_n^{N+1}|$, and performing the integration, that the frequency representation is given by

$$G_{ij;\sigma}^+(\omega) = \sum_n \frac{\langle \Psi_0^N | \hat{c}_{i\sigma} | \Psi_n^{N+1} \rangle \langle \Psi_n^{N+1} | \hat{c}_{j\sigma}^\dagger | \Psi_0^N \rangle}{\omega - \mu - [E_n^{N+1} - E_0^{N+1}] + i\eta} \tag{2.5}$$

where the energies, E_n^N, are eigenvalues of the full Hamiltonian: $\hat{H}|\Psi_n^N\rangle = E_n^N |\Psi_n^N\rangle$. The chemical potential, μ, is given by

$$\mu(N) = \left(\frac{\partial E}{\partial N} \right)_V = E_0^{N+1} - E_0^N \tag{2.6}$$

with V the volume of the system. In the limit that the number of particles and volume of the system $N \to \infty$, $V \to \infty$ (such that N/V goes to a constant), it is shown that $\mu(N) = \mu(N-1) \equiv \mu$ to within a vanishing correction $O(N^{-1})$.

[1] In the Heisenberg formulation of quantum mechanics, the operators are time dependent given via $\hat{X}(t) = \mathrm{e}^{-i\hat{H}t} \hat{X} \mathrm{e}^{i\hat{H}t}$. By contrast, the many-body states, $|\Psi_n^N\rangle$, are time-independent. [62]

Similarly, via an analogous argument, the advanced function may be expressed as

$$G^{-}_{ij;\sigma}(\omega) = \sum_{n} \frac{|\langle \Psi^{N}_{0}|\hat{c}^{\dagger}_{j\sigma}|\Psi^{N-1}_{n}\rangle\langle \Psi^{N-1}_{n}|\hat{c}_{i\sigma}|\Psi^{N}_{0}\rangle}{\omega - \mu + [E^{N-1}_{n} - E^{N-1}_{0}] - i\eta}. \tag{2.7}$$

The forms of eqs. (2.5, 2.7) are known as the Lehmann (spectral) representation of the propagator. The Lehmann representation is important because it tells us how the propagator relates to the single-particle excitations of the many-body system, as we shall now see. By virtue of the fact that the energy difference, $[E^{N+1}_{n} - E^{N}_{0}] > 0$, the retarded function, $G^{+}_{ij;\sigma}(\omega)$, only has positive weight for $\omega > \mu$, and by the same argument $G^{-}_{ij;\sigma}(\omega)$ only has weight for $\omega < \mu$.[2] On inspection of eq. (2.5), we see that the retarded function, $G^{+}_{ij;\sigma}(\omega)$, has poles in the lower half of the complex plane just off of the real axis, and thus is analytic for the entire the upper half plane (and vice-versa for $G^{-}_{ij;\sigma}(\omega)$). In the limit that $|\omega| \to \infty$ both retarded and advanced functions decay to zero [62]. As a consequence of this it is readily shown that the real and imaginary parts are related via a (one-sided) Hilbert transform of the form

$$G^{\pm}_{ij;\sigma}(\omega) = \frac{1}{\pi}\int_{-\infty}^{\infty} \mathrm{d}\omega' \frac{\mathrm{sgn}(\omega')\mathrm{Im}G^{\pm}_{ij;\sigma}(\omega')}{\omega' - \omega - i\,\mathrm{sgn}(\omega')\eta} = \int_{-\infty}^{\infty} \mathrm{d}\omega' \frac{D^{\pm}_{ij;\sigma}(\omega')}{\omega - \omega' + i\,\mathrm{sgn}(\omega')\eta}, \tag{2.8}$$

such that we define the spectral functions, $D^{\pm}_{ij;\sigma}(\omega)$, in terms of the imaginary part of the propagator via

$$D^{\pm}_{ij;\sigma}(\omega) = -\frac{1}{\pi}\,\mathrm{sgn}(\omega)\mathrm{Im}G^{\pm}_{ij;\sigma}(\omega), \tag{2.9}$$

with the full spectrum, $D_{ij;\sigma}(\omega) = D^{+}_{ij;\sigma}(\omega) + D^{-}_{ij;\sigma}(\omega) = -\frac{1}{\pi}\,\mathrm{sgn}(\omega)\mathrm{Im}G_{ij;\sigma}(\omega)$. For the site diagonal case where $i = j$, the spectral functions are represented by the delta functions

$$D^{+}_{ii;\sigma}(\omega) = \sum_{n} |\langle \Psi^{N+1}_{n}|\hat{c}^{\dagger}_{i\sigma}|\Psi^{N}_{0}\rangle|^{2}\delta(\omega - [E^{N+1}_{n} - E^{N+1}_{0}]), \tag{2.10a}$$

$$D^{-}_{ii;\sigma}(\omega) = \sum_{n} |\langle \Psi^{N-1}_{n}|\hat{c}_{i\sigma}|\Psi^{N}_{0}\rangle|^{2}\delta(\omega + [E^{N-1}_{n} - E^{N-1}_{0}]). \tag{2.10b}$$

Hence, $D_{ii;\sigma}(\omega) \geq 0$ for all ω. $D_{ii;\sigma}(\omega)$ contains poles at all of the excitation energies of the N-body system with respect to adding and removing a single particle. Thus $D_{ii;\sigma}(\omega)$ is the principal quantity of interest when considering the dynamics of a many-body system. As the number of particles $N \to \infty$, the spectrum becomes continuous as the spacing between energy levels vanishes.

[2] For convenience we choose to set the origin of energy to the chemical potential, $\mu = 0$ in the rest of this thesis.

2.1.1 Properties of $D_{ii;\sigma}(\omega)$

We may obtain two important sum-rules from integrating $D_{ii\sigma}(\omega)$ which will be useful in the rest of this thesis. Firstly, on integrating the spectral function $D_{ii;\sigma}(\omega)$ over all frequency it is possible to show that it is normalized to unity. By using the delta functions forms of eq. (2.10) and integrating we find

$$\begin{aligned}\int_{-\infty}^{\infty} \mathrm{d}\omega\ D_{ii;\sigma}(\omega) &= \sum_n |\langle\Psi_0^N|\hat{c}_{i\sigma}^\dagger|\Psi_n^{N+1}\rangle|^2 + \sum_n |\langle\Psi_n^{N-1}|\hat{c}_{i\sigma}|\Psi_0^N\rangle|^2 \\ &= \langle\Psi_0^N|\hat{c}_{i\sigma}^\dagger\hat{c}_{i\sigma} + \hat{c}_{i\sigma}\hat{c}_{i\sigma}^\dagger|\Psi_0^N\rangle = 1. \end{aligned} \tag{2.11}$$

where we have used the fact that the anticommutator between the Fermionic operators is unity: $\{\hat{c}_{i\sigma}^\dagger, \hat{c}_{i\sigma}\} = 1$. Similarly, by integrating the spectral function up to the chemical potential, $\mu = 0$, we obtain

$$\begin{aligned}\int_{-\infty}^{0} \mathrm{d}\omega\ D_{ii;\sigma}(\omega) &= \sum_n |\langle\Psi_n^{N-1}|\hat{c}_{i\sigma}|\Psi_0^N\rangle|^2 \\ &= \langle\Psi_0^N|\hat{c}_{i\sigma}^\dagger\hat{c}_{i\sigma}|\Psi_0^N\rangle = \langle\Psi_0^N|\hat{n}_{i\sigma}|\Psi_0^N\rangle = \langle\hat{n}_{i\sigma}\rangle. \end{aligned} \tag{2.12}$$

where $\langle\hat{n}_{i\sigma}\rangle$ is the expectation value of the local charge on the level-i; it gives the mean number of σ-spin electrons on site-i in the N-particle ground state.

2.1.2 The Hilbert transform

Taking eq. (2.8), and expressing $G_{ii;\sigma}(\omega) = G_{ii;\sigma}^{+}(\omega) + G_{ii;\sigma}^{-}(\omega)$, the full propagator is expressed in terms $D_{ii;\sigma}(\omega')$ via the integral

$$G_{ii;\sigma}(\omega) = \int_{-\infty}^{\infty} \mathrm{d}\omega' \frac{D_{ii;\sigma}(\omega')}{\omega - \omega' + i\eta\,\mathrm{sgn}(\omega')}. \tag{2.13}$$

Using the relation $(x+i\eta)^{-1} = \mathrm{P}(\frac{1}{x}) - i\pi\delta(x)$, where P denotes the Cauchy principal value, the real part of the propagator is thus given by

$$\mathrm{Re}G_{ii;\sigma}(\omega) \equiv G_{ii;\sigma}^{R}(\omega) = \mathrm{P}\int_{-\infty}^{\infty} \mathrm{d}\omega' \left(\frac{D_{ii;\sigma}(\omega')}{\omega - \omega'}\right). \tag{2.14}$$

Hence, if one has knowledge of the spectral function, $D_{ii;\sigma}(\omega')$, of the system, then by virtue of the underlying analyticity of the propagator, the corresponding real part is easily obtained via eq. (2.14). In the results that follow we make extensive use of this relation explicitly in order to calculate $\mathrm{Re}G_{ii;\sigma}(\omega)$

2.1.3 Other propagators

We also make use of two other types of single-particle propagator. For convenience in Chapters 3-4 we explicitly make use of the retarded function[3] defined by

$$G^r_{ij;\sigma}(t) = -i\theta(t)\langle\Psi^N_0|\{\hat{c}_{i\sigma}(t), \hat{c}^\dagger_{j\sigma}(0)\}|\Psi^N_0\rangle, \tag{2.15}$$

where $\{\hat{A}, \hat{B}\}$ is the usual anticommutator, and the 'r' superscript denotes the retarded function. From similiar arguments to those used above, the Lehmann representation of the retarded function is given by

$$G^r_{ij;\sigma}(\omega) = \sum_n \frac{\langle\Psi^N_0|\hat{c}_{i\sigma}|\Psi^{N+1}_n\rangle\langle\Psi^{N+1}_n|\hat{c}^\dagger_{j\sigma}|\Psi^N_0\rangle}{\omega - [E^{N+1}_n - E^{N+1}_0] + i\eta} + \sum_n \frac{\langle\Psi^N_0|\hat{c}^\dagger_{j\sigma}|\Psi^{N-1}_n\rangle\langle\Psi^{N-1}_n|\hat{c}_{i\sigma}|\Psi^N_0\rangle}{\omega + [E^{N-1}_n - E^{N-1}_0] + i\eta}, \tag{2.16}$$

and therefore in contrast to the time-ordered function considered above, is analytic in the upper half plane for all ω. Splitting this function into real and imaginary parts we obtain

$$G^r_{ij;\sigma}(\omega) = G^R_{ij;\sigma}(\omega) - i\pi D_{ij;\sigma}(\omega), \tag{2.17}$$

such that both $D_{ij;\sigma}(\omega)$ and $G^R_{ij;\sigma}(\omega)$ are common to both $G^r_{ij;\sigma}(\omega)$ and $G^t_{ij;\sigma}(\omega)$ (the time-ordered function: $G^t_{ij;\sigma}(\omega) = G^R_{ij;\sigma}(\omega) - i\pi\,\mathrm{sgn}(\omega)D_{ij;\sigma}(\omega)$). Thus the Hilbert transform relation eq. (2.14) still holds.

The other type of Green function that we use in this thesis is the imaginary-time Matsubara function, $G(\tau)$, (with $\tau = it$) [62] convenient for use for the finite-temperature calculations of Chapter 7. However, for reasons of brevity we do not explicitly refer to it any further here. As we shall see, it is the time-ordered functions, $G^t_{ij;\sigma}(\omega)$, which feature in the $(T = 0)$ diagrammatic techniques used below.

2.2 Feynman diagrams for the exact propagator

As stated above, the Lehmann representation of the time-ordered propagator given by eqs. (2.5, 2.7) allows us to relate the Green function to the excitation energies of the overall many-body system. However, crucially what the Lehmann representation does not do, is prescribe a way of calculating the interacting many-body Green function. Here we give a brief summary for how the full Green function, $G^t_{ij;\sigma}(\omega)$, can be calculated from a perturbation series involving the corresponding non-interacting propagator.[4] For a complete discussion of the perturbation expan-

[3] This retarded function should not be confused with the retarded function of eq. (2.5).

[4] As we shall see in Section 2.3, the non-interacting propagator can be obtained exactly by other means.

sion for the propagator we refer the reader to Chapter 3 of ref [62], or Appendices B-E of ref [63].

2.2.1 Adiabatic switching on

The essential idea that underpins any diagrammatic treatment, is that the eigenstates of the full interacting Hamiltonian can be obtained from the eigenstates of the non-interacting system as interactions are switched on infinitely slowly, or *adiabatically*. In order to achieve this we introduce a time-dependent Hamiltonian of the form

$$\hat{H} = \hat{H}_0 + \mathrm{e}^{-\epsilon|t|}\hat{H}_I, \tag{2.18}$$

where $\hat{H}_0$ is the Hamiltonian of the non-interacting system, $\hat{H}_I$ is the interaction Hamiltonian and ϵ is a small positive constant. For very large times, such that we take the limit $t \to \pm\infty$, the exponential function means that the full Hamiltonian simply reduces to the non-interacting limit, $\hat{H}_0$. In contrast, for $t = 0$, the Hamiltonian takes its full interacting value, $\hat{H} = \hat{H}_0 + \hat{H}_I$. As we shall see, the limit $\epsilon \to 0^+$ is taken at the end of the calculation, such that the perturbation, $\hat{H}_I$, is turned on and off infinitely slowly. It is important that any physical result, stemming from the form of eq. (2.18), is independent of the specific value that ϵ takes (provided $\varepsilon \to 0^+$).

For the argument that follows it is necessary to work within the *interaction* picture of quantum mechanics [62]. Provided the state vector, $|\Psi_S^N(t)\rangle$, is a solution to the time-dependent Schrodinger equation, $i\hbar\partial|\Psi_S^N(t)\rangle/\partial t = \hat{H}|\Psi_S^N(t)\rangle$, then it readily shown from standard arguments that the corresponding state, $|\Psi_I^N(t)\rangle$ within the interaction representation is given by

$$|\Psi_I^N(t)\rangle = \mathrm{e}^{i\hat{H}_0 t/\hbar}|\Psi_S^N(t)\rangle. \tag{2.19}$$

The operators must also be transformed into the interaction picture. A time-dependent operator, $\hat{A}_I(t)$ in the interaction representation is given in terms of the time independent Schrodinger operator, $\hat{A}_S$, by

$$\hat{A}_I(t) = \mathrm{e}^{i\hat{H}_0 t/\hbar}\hat{A}_S\mathrm{e}^{-i\hat{H}_0 t/\hbar}. \tag{2.20}$$

It may then be shown [62], that the state vector in the interaction picture may be evolved in time from t_0 to t via

$$|\Psi_I^N(t)\rangle = \hat{U}_\epsilon(t, t_0)|\Psi_I^N(t_0)\rangle, \tag{2.21}$$

where $\hat{U}_\epsilon(t, t_0)$ is a time-evolution operator given by

$$\hat{U}_\epsilon(t, t_0) = \sum_{n=0}^{\infty} \left(\frac{-i}{\bar{h}}\right)^n \frac{1}{n!} \int_{t_0}^{t} \mathrm{d}\tau_1 \ldots \int_{t_0}^{t} \mathrm{d}\tau_n \mathrm{e}^{-\epsilon(|\tau_1|+\ldots+|\tau_n|)} \hat{T}[\hat{H}_I(\tau_1) \ldots H_I(\tau_n)], \tag{2.22}$$

explicitly dependent on ϵ. In analogy with eq. (2.2), $\hat{T}$ is the Wick time-ordering operator that places operators chronologically from right to left. Specifically, we consider evolving the interacting state, $|\Psi_I^N(t)\rangle$ at $t = 0$ from an initial state, $|\Psi_I^N(t)\rangle = |\Phi_0^N\rangle$ at $t = -\infty$, such that $|\Phi_0^N\rangle$ is an eigenstate of the non-interacting Hamiltonian, $\hat{H}_0$:

$$\hat{H}_0|\Phi_0^N\rangle = E_0|\Phi_0^N\rangle. \tag{2.23}$$

By inserting $t = 0$, $t_0 = -\infty$ into eq. (2.21), the interacting ground state (we drop the explicit I subscript in the following discussion for simplicity) is given in terms of the time-evolution operator by

$$|\Psi_0^N\rangle = \hat{U}_\epsilon(0, -\infty)|\Phi_0^N\rangle, \tag{2.24}$$

which thus expresses an exact eigenstate of the overall Hamiltonian, $\hat{H}$, in terms of the non-interacting eigenstate of $\hat{H}_0$ (given by eq. (2.23)). The question we now must ask is what happens in the limit that $\epsilon \to 0$? The solution is provided by the Gell-Mann Low theorem, which we now consider.

2.2.2 Perturbation series

The Gell-Mann Low theorem [62, 74] may be used to generate the eigenstate of the full interacting system from the eigenstates of the non-interacting system in the limit $\epsilon \to 0^+$. For a detailed discussion of how the Gell-Mann Low theorem may be proven we refer the reader to ref [62]. The key result is that if

$$\lim_{\epsilon \to 0} \frac{\hat{U}_\epsilon(0, -\infty)|\Phi_0^N\rangle}{\langle\Phi_0^N|\hat{U}_\epsilon(0, -\infty)|\Phi_0^N\rangle} \equiv \frac{|\Psi_0^N\rangle}{\langle\Phi_0^N|\Psi_0^N\rangle} \tag{2.25}$$

exists to all orders in perturbation theory, then it is an eigenstate of the full interacting Hamiltonian,

$$\hat{H}\frac{|\Psi_0^N\rangle}{\langle\Phi_0^N|\Psi_0^N\rangle} = E\frac{|\Psi_0^N\rangle}{\langle\Phi_0^N|\Psi_0^N\rangle}. \tag{2.26}$$

The eigenstate $|\Psi_0^N\rangle$ is generated *adiabatically* from $|\Phi_0^N\rangle$ via eq. (2.24) when interactions are switched on. There are two salient points that we emphasize to

the reader before proceeding. Firstly, the non-interacting ground-state, $|\Phi_0^N\rangle$, must be non-degenerate for the Gell-Mann Low theorem to hold.[5] Secondly, whilst the Gell-Mann Low theorem asserts that $|\Phi_0^N\rangle$ is an eigenstate of the interacting system, it may not be the true ground state. The theorem relies on the fact that the overlap $\langle\Phi_0|\Psi_0\rangle \neq 0$ and thus $|\Psi_0\rangle$ must be of the same underlying symmetry as $|\Phi_0\rangle$. In other words, it is possible that the true interacting ground-state is not adiabatically connected to the non-interacting limit, as is the case for any non-Fermi liquid phase.

By inserting eq. (2.26) for the many-body eigenstate into eq. (2.1) it is possible to show that the (time-ordered) single-particle propagator is expressed as

$$G_{ij;\sigma}(t) = -i\sum_{n=0}^{\infty}\left(\frac{-i}{\hbar}\right)^n \frac{1}{n!}\int_{-\infty}^{\infty} \mathrm{d}\tau_1 \ldots \int_{-\infty}^{\infty} \mathrm{d}\tau_n \times \frac{\langle\Phi_0^N|\hat{T}[\hat{H}_I(\tau_1)\ldots H_I(\tau_n)\hat{c}_{i\sigma}(t)\hat{c}^{\dagger}_{j\sigma}(0)]|\Phi_0^N\rangle}{\langle\Phi_0^N|\hat{S}|\Phi_0^N\rangle}, \quad (2.27)$$

where $\hat{S} = \hat{U}_{\epsilon}(\infty,-\infty)$, and the operators $\hat{c}^{\dagger}_{j\sigma}(t) = \mathrm{e}^{-i\hat{H}_0 t}\hat{c}^{\dagger}_{j\sigma}\mathrm{e}^{i\hat{H}_0 t}$, $\hat{c}_{i\sigma}(t) = \mathrm{e}^{-i\hat{H}_0 t}\hat{c}_{i\sigma}\mathrm{e}^{i\hat{H}_0 t}$ have been transformed to the interaction picture. Eq. (2.27) allows the systematic calculation of any *nth*-order (in the interaction part of the Hamiltonian, $\hat{H}_I$) contribution to $G_{ij;\sigma}(t)$. By virtue of the fact that the interaction part of the Hamiltonian, $\hat{H}_I(\tau_i)$, involves products of creation and annihilation operators, $\hat{c}^{\dagger}_{j\sigma}(\tau_i)$ or $\hat{c}_{i\sigma}(\tau_i)$, the matrix elements in the integrand of eq. (2.27) involve many time-ordered products of these operators.

Whilst it may be possible to simply calculate the first few orders of terms in the perturbation series, eq. (2.27), evaluating matrix elements involving time-ordered products quickly becomes lengthy and arduous. Fortunately there is a method that allows the form of eq. (2.27) to be greatly simplified, especially for higher order terms. Wick's theorem [62, 75] allows matrix elements of time ordered products of operators to be written solely as products of two-fermion matrix elements of the form $\langle\Phi_0^N|\hat{T}[\hat{c}_{i\sigma}(t_2)\hat{c}^{\dagger}_{j\sigma}(t_1)]|\Phi_0^N\rangle$. This means to any order in the interaction, $\hat{H}_I$, the integrand of eq. (2.27) may be written in terms of the non-interacting zeroth-order propagator, given by $G^0_{ij;\sigma}(t) \equiv g_{ij;\sigma}(t) = \langle\Phi_0^N|\hat{T}[\hat{c}_{i\sigma}(t)\hat{c}^{\dagger}_{j\sigma}(0)]|\Phi_0^N\rangle$. In consequence, Wick's theorem allows the full propagator, $G_{ij;\sigma}(t)$, to be given in solely in terms of $g_{ij;\sigma}(t)$ and the interaction strength (which we denote as U).

We now discuss the most significant advantage of using Wick's theorem to reduce the matrix elements in eq. (2.27) to the products of two-Fermion terms. Each term in the perturbation series for the interacting propagator, $G_{ij;\sigma}(t)$ may be represented graphically in terms of a Feynman diagram. There is a one-to-one correspondence between the form of the diagrams and the structure of the perturbation series in

[5] A point that we return to in Chapter 3 when we explicitly consider a diagrammatic treatment in a doubly degenerate LM phase.

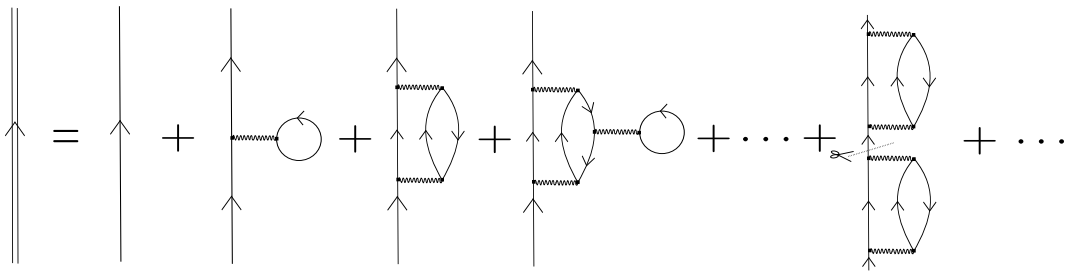


Figure 2.1: The perturbation expansion of the interacting propagator, G (double line), in terms of the non-interacting propagator, g, (single lines). Wiggly lines denote the interaction strength, U.

eq. (2.27). In order to construct all *nth*-order contributions to $G_{ij;\sigma}(t)$, one must simply draw all topologically distinct diagrams of that order, and then convert them to the underlying equations. The rules for converting diagrams to their mathematical form are well known [63], and may be used to construct any diagram for $G_{ij;\sigma}(t)$ in terms of its constituent $g_{ij;\sigma}(t)$ and U. Fig. 2.1 shows the interacting propagator, $G_{ij;\sigma}(t)$, denoted by a double line, in terms of the non-interacting propagators, $g_{ij;\sigma}(t)$, single lines, and interaction strength, U, wiggly lines.

For reasons of brevity we do not discuss the diagrammatic rules any further here. Once again, we refer the reader to refs [62, 63] for further information.

2.2.3 The Dyson equation

In order to proceed, the diagrammatic perturbation expansion of eq. (2.27) may be written in a particular compact and more useful form. From the perturbative series of Fig. 2.1 it may be shown that the interacting Green function may be expressed in terms of a matrix equation [62][6]

$$\mathbf{G}_\sigma(\omega) = \mathbf{g}_\sigma(\omega) + \mathbf{g}_\sigma(\omega)\mathbf{T}_\sigma(\omega)\mathbf{g}_\sigma(\omega) \tag{2.28}$$

where $\mathbf{G}_\sigma(\omega)$, $\mathbf{g}_\sigma(\omega)$, are matrices describing the interacting and non-interacting Green functions respectively ($G_{ij;\sigma}(\omega)$ is the $ijth$ element of $\mathbf{G}_\sigma(\omega)$ etc..). $\mathbf{T}_\sigma(\omega)$ is the so-called '*reducible* (improper) self-energy' matrix, and involves all diagrams sandwiched between two propagator lines. In other words, contributions to $\mathbf{T}_\sigma(\omega)$ contain all interaction terms such that for $U = 0$, $\mathbf{T}_\sigma(\omega) = 0$, and eq. (2.28) simply gives the non-interacting function. Furthermore, eq. (2.28) may be written in an even more convenient form, which proves more useful for further study. $\mathbf{T}_\sigma(\omega)$ may be expressed in terms of both reducible and irreducible terms. If in a contribution to $\mathbf{T}_\sigma(\omega)$ a single propagator line may be cut to yield two further contributions to

[6] We also choose to Fourier transform all quantities to the frequency domain, where the perturbation expansion holds equally well.

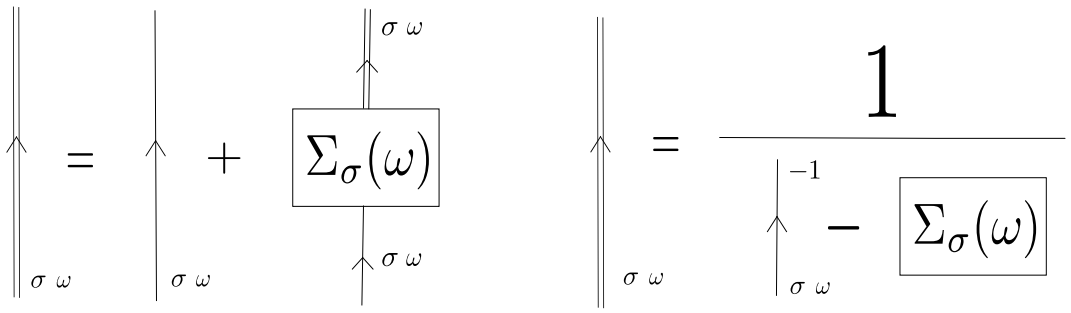


Figure 2.2:]
The Dyson equation for the interacting Green function, $\mathbf{G}_\sigma(\omega)$ (double line), in terms of the non-interacting Green function, $\mathbf{g}_\sigma(\omega)$ (single line), and the self-energy, $\mathbf{\Sigma}_\sigma(\omega)$. Left: In open form. Right: In closed form.

$\mathbf{T}_\sigma(\omega)$, then the process is deemed reducible. It may be shown by iteration [62] that reducible terms can be excluded from further consideration in the self-energy - we may replace $\mathbf{T}_\sigma(\omega)\mathbf{g}_\sigma(\omega)$ with $\mathbf{\Sigma}_\sigma(\omega)\mathbf{G}_\sigma(\omega)$, such that $\mathbf{\Sigma}_\sigma(\omega)$ defines the irreducible (proper) self-energy matrix, involving only irreducible terms. All of the diagrams on the RHS of Fig. 2.1 are contributions to $\mathbf{g}_\sigma(\omega)\mathbf{\Sigma}_\sigma(\omega)\mathbf{g}_\sigma(\omega)$ apart from the last diagram, where the scissors show how by cutting a propagator line it may be reduced. The resulting equation (in open form) for $\mathbf{G}_\sigma(\omega)$, as shown in Fig. 2.2, is given by

$$\mathbf{G}_\sigma(\omega) = \mathbf{g}_\sigma(\omega) + \mathbf{g}_\sigma(\omega)\mathbf{\Sigma}_\sigma(\omega)\mathbf{G}_\sigma(\omega), \tag{2.29}$$

known as the Dyson equation [62].

For the single-impurity problems discussed in this thesis,[7] interactions only occur on the impurity, and as such the matrix equation reduces to the simple diagonal form $G_{ii;\sigma}(\omega) = g_{ii;\sigma}(\omega) + g_{ii;\sigma}(\omega)\Sigma_{ii;\sigma}(\omega)G_{ii;\sigma}(\omega)$, where the 'i' subscript denotes the impurity level. In Fig. 2.2, $G_{ii;\sigma}(\omega)$, again denoted by a double line is expressed as an open equation on the LHS. By iteration of this equation, the perturbation expansion shown in Fig. 2.1 can be verified explicitly, by considering all possible irreducible contributions for $\Sigma_{ii;\sigma}(\omega)$. The RHS shows the Dyson equation in closed form for the interacting propagator in terms of $g_{ii;\sigma}(\omega)$ and $\Sigma_{ii;\sigma}(\omega)$.

Physically the self-energy, $\Sigma_{ii;\sigma}(\omega)$, can be thought of as containing all possible interactions between a single σ-spin particle and the many-body interacting system. Just as for the propagator, $G_{ii;\sigma}(\omega)$, there are an equivalent set of rules for constructing all possible diagrams for $\Sigma_{ii;\sigma}(\omega)$ [60, 63].

Before proceeding, we comment on the structure of the diagrammatic perturbation expansion shown in Fig. 2.1. Whilst the diagrams simply correspond to the basic mathematical terms in eq. (2.27), and therefore are not equivalent to real phys-

[7] For multi-impurity problems the matrix form of eq. (2.29) is necessary.

ical processes, it is sometimes instructive to think of them as such. In attempting to develop intelligent approximations for $\mathbf{G}_\sigma(\omega)$, the appearance of the perturbation series allows us some feel for which diagrams may be important to include in order to capture the underlying physics.

2.3 Propagators for the Anderson impurity model

The diagrammatic perturbation theory discussed in the last section can be applied to the single-level Anderson impurity model that we discuss in the rest of this thesis. However, even if the full interacting propagator $G_{ii;\sigma}(\omega)$ is determined as a perturbation expansion in terms of the non-interacting Green function, $g_{ii;\sigma}(\omega)$, we must first determine $g_{ii;\sigma}(\omega)$ in some other distinct way. The so-called 'equations of motion' (EOM) methods allow us to determine the *exact* Green function in two important limits, one of which is the non-interacting limit where $U = 0$, the other is the atomic limit in which the impurity level is completely decoupled from the band.

As stated in Chapter 1, the Hamiltonian for the single-impurity Anderson model is given by

$$\hat{H} = \sum_{\mathbf{k}\,\sigma}(\epsilon_{\mathbf{k}} - \sigma h)\hat{n}_{\mathbf{k}\sigma} + \sum_{\sigma}(\epsilon_i - \sigma h)\hat{n}_{i\sigma} + U\hat{n}_{i\uparrow}\hat{n}_{i\downarrow} + \sum_{\mathbf{k}\,\sigma}(V_{i\mathbf{k}}c^\dagger_{i\sigma}c_{\mathbf{k}\sigma} + \text{h.c.}), \quad (2.30)$$

where we have also included a specific term $\hat{H}_{\text{field}} = -2h\hat{S}_z$, where $\hat{S}_z = \frac{1}{2}\sum_\sigma \sigma[\hat{n}_{i\sigma} + \sum_{\mathbf{k}}\hat{n}_{\mathbf{k}\sigma}]$ is the spin z-component in the system, which describes the coupling to a magnetic field $h = \frac{1}{2}g\mu_B B$ (applied globally to the entire system - both to the impurity level and also the conduction band states). The explicit $(-)$ sign simply ensures that $\uparrow$ spins are favoured in energy over $\downarrow$ spins.

Differentiation of eq. (2.1) with respect to t gives

$$\frac{\mathrm{d}}{\mathrm{d}t}G_{ij;\sigma}(t) = \frac{\mathrm{d}}{\mathrm{d}t}\Big[- i\theta(t)\langle\hat{c}_{i\sigma}(t)\hat{c}^\dagger_{j\sigma}(0)\rangle + i\theta(-t)\langle\hat{c}^\dagger_{j\sigma}(0)\hat{c}_{i\sigma}(t)\rangle\Big] \quad (2.31a)$$

$$= -i\delta(t)\langle\{\hat{c}_{i\sigma}(t), \hat{c}_{j\sigma}(0)\}\rangle - i\langle\hat{T}[[\hat{c}_{i\sigma}(t), \hat{H}], \hat{c}^\dagger_{j\sigma}(0)]\rangle \quad (2.31b)$$

where $[\hat{A}, \hat{B}] = \hat{A}\hat{B} - \hat{B}\hat{A}$. Upon Fourier transformation to the frequency domain, eq. (2.31b) simply becomes

$$(\omega^+)G_{ij;\sigma}(\omega, h) = \langle\{\hat{c}_{i\sigma}, \hat{c}_{j\sigma}\}\rangle + \langle\langle[\hat{c}_{i\sigma}, \hat{H}]; \hat{c}^\dagger_{j\sigma}\rangle\rangle_\omega, \quad (2.32)$$

where we include the explicit h-dependence in the propagator, $\omega^+ = \omega + i\eta\,\mathrm{sgn}(\omega)$, and $\langle\langle\hat{A}; \hat{B}\rangle\rangle_\omega$ simply denotes the Fourier transform of $\langle\hat{T}[\hat{A}, \hat{B}]\rangle$. We now evaluate the commutator $[\hat{c}_{i\sigma}, \hat{H}]$ with the Anderson impurity model Hamiltonian given by

eq. (1.1). Setting $i = j$, such that i represents the single-impurity level, we obtain

$$(\omega^+ - \varepsilon_{i\sigma})G_{ii;\sigma}(\omega, h) = 1 + \sum_{\mathbf{k}} V_{i\mathbf{k}} G_{\mathbf{k}i;\sigma}(\omega, h) + F_{ii;\sigma}(\omega, h) \tag{2.33}$$

where $\varepsilon_{i\sigma} = \varepsilon_i - \sigma h$ and $F_{ii;\sigma}(\omega, h) = U\langle\langle \hat{n}_{i-\sigma}\hat{c}_{i\sigma}; \hat{c}^\dagger_{i\sigma}\rangle\rangle_\omega \equiv \langle\langle [\hat{c}_{i\sigma}, \hat{H}_I]; \hat{c}^\dagger_{i\sigma}\rangle\rangle_\omega$ (with $\hat{H}_I = U\hat{n}_{i\uparrow}\hat{n}_{i\downarrow}$). In contrast, if either of the indices i or j are set to the delocalized band states we obtain

$$(\omega^+ - \varepsilon_{\mathbf{k}\sigma})G_{\mathbf{k}i;\sigma}(\omega, h) = V_{\mathbf{k}i} G_{ii;\sigma}(\omega, h) \tag{2.34a}$$

$$(\omega^+ - \varepsilon_{\mathbf{k}'\sigma})G_{i\mathbf{k}';\sigma}(\omega, h) = V_{i\mathbf{k}'} G_{ii;\sigma}(\omega, h) \tag{2.34b}$$

$$(\omega^+ - \varepsilon_{\mathbf{k}\sigma})G_{\mathbf{k}\mathbf{k}';\sigma}(\omega, h) = \delta_{\mathbf{k}\mathbf{k}'} + V_{i\mathbf{k}'} G_{i\mathbf{k};\sigma}(\omega, h) \tag{2.34c}$$

By inserting eq. (2.34a) into eq. (2.33) for $G_{\mathbf{k}i;\sigma}(\omega)$ we find

$$(\omega^+ - \varepsilon_{i\sigma})G_{ii;\sigma}(\omega, h) = 1 + \sum_{\mathbf{k}} \frac{V_{i\mathbf{k}} V_{\mathbf{k}i}}{\omega^+ - \varepsilon_{\mathbf{k}\sigma}} G_{ii;\sigma}(\omega, h) + F_{ii;\sigma}(\omega, h). \tag{2.35}$$

Rearranging this equation gives the form

$$G_{ii;\sigma}(\omega, h) = [\omega^+ - \varepsilon_{i\sigma} - \Gamma_{ii;\sigma}(\omega, h) - [F_{ii;\sigma}(\omega, h)/G_{ii;\sigma}(\omega, h)]]^{-1}. \tag{2.36}$$

$\Gamma_{ii;\sigma}(\omega, h)$ is the *hybridization function* that couples the impurity single-level to the conduction band states, given by

$$\Gamma_\sigma(\omega, h) = V^2 \sum_{\mathbf{k}} \frac{1}{\omega^+ - \varepsilon_{\mathbf{k}\sigma}} \tag{2.37a}$$

$$= V^2 \sum_{\mathbf{k}} \left[\mathrm{P}\left(\frac{1}{\omega - \varepsilon_{\mathbf{k}\sigma}} \right) - i\pi \,\mathrm{sgn}(\omega)\delta(\omega - \varepsilon_{\mathbf{k}\sigma}) \right] \tag{2.37b}$$

$$= \Gamma^R_\sigma(\omega, h) - i\,\mathrm{sgn}(\omega)\Gamma^I_\sigma(\omega, h). \tag{2.37c}$$

where we have once again used $[x + i\eta]^{-1} = \mathrm{P}(x^{-1}) - i\pi\delta(x)$ to express the real and imaginary parts. We assume uniform band-impurity coupling strength, $V_{i\mathbf{k}} = V_{\mathbf{k}i} = V$ and in the interest of brevity we drop the explicit ii subscripts hereafter (and replace ε_i with ε). Eq. (2.37b) simply relates the density of states of the conduction band given by

$$\rho_b(\omega, h) = \sum_{\mathbf{k}} \delta(\omega - \varepsilon_{\mathbf{k}\sigma}), \tag{2.38}$$

to $\Gamma^I_\sigma(\omega, h) = \pi V^2 \rho_b(\omega, h)$. Thus $\Gamma^I_\sigma(\omega, h)$ 'controls' the type of conduction band that the impurity level is coupled to. For the AIM, the conduction band density of states is generally of the form, $\rho_b(\omega, h) = \rho_0\theta(D - |\omega|)|\omega + \sigma h|^r$ and so we set the

hybrizidation to

$$\Gamma^I_\sigma(\omega, h) = \Gamma_0|\omega + \sigma h|^r, \tag{2.39}$$

with $\Gamma_0 = \pi\rho_0 V^2$ the hybridization strength. We consider the infinite bandwidth limit of the conduction band, such that $D \to \infty$. If the band exponent $r = 0$, then $\Gamma^I_\sigma(\omega, h) = \Gamma_0$, the hybridization function is ω-independent and the impurity is coupled to a metallic flat band. In contrast, for $r \to \infty$, the conduction band vanishes completely. For $0 < r < \infty$, the single level is coupled to a band with a vanishing power-law density of states around the Fermi level, known as the pseudogap Anderson model.

As we shall see, eq. (2.36) involving the ratio $F(\omega, h)/G(\omega, h)$ is the general form of the Anderson model local propagator, and will be important in what is to follow. However, we first consider the simple non-interacting limit where $U = 0$, and the model is exactly soluble.

2.3.1 Non-interacting limit

For $U = 0$, eq. (2.36) simply becomes

$$G^0_\sigma(\omega, h) \equiv g_\sigma(\omega, h) = [\omega^+ - \varepsilon_\sigma - \Gamma_\sigma(\omega, h)]^{-1}, \tag{2.40}$$

which is now in closed form. For coupling to a metallic host, the spectral function, $d_\sigma(\omega, h) = -\frac{1}{\pi}\,\mathrm{sgn}(\omega)\mathrm{Im}g_\sigma(\omega, h)$, becomes a simple Lorentzian centred on $\omega = \varepsilon_\sigma$, with broadening equivalent to Γ_0

$$\pi d_\sigma(\omega, h) = \frac{\Gamma_0}{[\omega - \varepsilon_\sigma]^2 + [\Gamma_0]^2}. \tag{2.41}$$

In the case of $\varepsilon_\sigma = \varepsilon - \sigma h = 0$, $\pi\Gamma_0 d_\sigma(\omega) \to 1$ as $\omega/\Gamma_0 \to 0$, (which occurs at $h = 0$ and the specific case of particle-hole symmetry where $x = \varepsilon + \frac{U}{2} = 0$) this is the well known spectral pinning condition in the non-interacting limit [2].

2.3.2 Atomic limit

The other distinct limit of the AIM that requires special consideration and may be solved exactly by applying EOM methods is the limit where the band coupling strength, $V = 0$. The local interaction strength by contrast is non-zero, $U \neq 0$; eq. (2.36) becomes

$$(\omega^+ - \varepsilon_\sigma)G_\sigma(\omega, h) = 1 + F_\sigma(\omega, h). \tag{2.42}$$

It is then possible to repeat the EOM procedure to find $F_\sigma(\omega, h) \equiv \langle\langle \hat{n}_{-\sigma}\hat{c}_\sigma; \hat{c}_\sigma^\dagger\rangle\rangle_\omega$ in the absence of coupling to the host band. In this limit it is straightforward to show

$$(\omega^+ - \varepsilon_\sigma - U)F_\sigma(\omega, h) = \langle \hat{n}_{-\sigma}\rangle, \tag{2.43}$$

and hence is expressed in closed form. By inserting eq. (2.43) in to eq. (2.42), the exact atomic limit Green function in closed form then becomes

$$G_\sigma(\omega, h) = G_\sigma^{AL}(\omega, h) = \frac{1 - \langle \hat{n}_{-\sigma}\rangle}{\omega^+ - \varepsilon_\sigma} + \frac{\langle \hat{n}_{-\sigma}\rangle}{\omega^+ - \varepsilon_\sigma - U}. \tag{2.44}$$

As such, the corresponding spectral function, $D_\sigma^{AL}(\omega, h) = -\frac{1}{\pi}\,\mathrm{sgn}(\omega) G_\sigma^{AL}(\omega, h)$ becomes

$$D_\sigma^{AL}(\omega, h) = [1 - \langle \hat{n}_{-\sigma}\rangle]\delta(\omega - \varepsilon_\sigma) + \langle \hat{n}_{-\sigma}\rangle\delta(\omega - \varepsilon_\sigma - U). \tag{2.45}$$

In consequence of this simple discrete pole form, the local σ-spin charge, given via eq. (2.12), takes on integer values in the atomic limit

$$\langle \hat{n}_\sigma\rangle = \int_{-\infty}^{0} \mathrm{d}\omega\; D_\sigma^{AL}(\omega, h) \; = [1 - \langle \hat{n}_{-\sigma}\rangle]\theta(-\varepsilon_\sigma) + \langle \hat{n}_{-\sigma}\rangle\theta(-[\varepsilon_\sigma + U]). \tag{2.46}$$

There are 3 obvious cases to consider. Firstly, when $\varepsilon_\sigma > 0$, then $\langle \hat{n}_\uparrow\rangle$, $\langle \hat{n}_\downarrow\rangle$=0 and $D_\sigma^{AL}(\omega)$ reduces to a single pole for all U

$$D_\sigma^{AL}(\omega, h) = \delta(\omega - \varepsilon_\sigma). \tag{2.47}$$

The decoupled impurity has zero occupancy as the level, ε_σ lies above the Fermi level.

The second distinct case arises when $\varepsilon_\sigma < 0$, and $\varepsilon_\sigma + U < 0$, then both $\langle \hat{n}_{i\uparrow}\rangle$, $\langle \hat{n}_{i\downarrow}\rangle$=1. Now the impurity level lies far enough below the Fermi level that it is doubly occupied, with one electron of each spin type. The spectrum becomes a single pole positioned at $\omega = \varepsilon_\sigma + U$

$$D_\sigma^{AL}(\omega, h) = \delta(\omega - \varepsilon_\sigma - U). \tag{2.48}$$

The last case is when $\varepsilon_\sigma < 0$, but $\varepsilon_\sigma + U > 0$. In this regime, the impurity level is singly occupied, and $\langle \hat{n}_\uparrow\rangle = \langle \hat{n}_\downarrow\rangle = \frac{1}{2}$. The impurity level could equally have spin up or down with equal probability, and the ground-state is doubly degenerate. The spectrum contains poles positioned at $\omega = \varepsilon_\sigma + U, \varepsilon_\sigma$ given by

$$D_\sigma^{AL}(\omega, h) = \frac{1}{2}[\delta(\omega - \varepsilon_\sigma - U) + \delta(\omega - \varepsilon_\sigma)]. \tag{2.49}$$

A point to notice here is that the form of the NIL spectral function given via eq. (2.41) is a Lorentzian centred on $\omega = \varepsilon_\sigma$ with width Γ_0. The effect of coupling to the conduction band is to simply broaden the atomic limit pole given by eq. (2.47). However, in the full interacting case, when both interactions (finite U) and coupling to the band (finite V) are considered, the spectrum for the full interacting system is no longer a simple Lorentzian, as we shall see below.

Later in this thesis (Section 3.6) we will once again consider the case of the atomic limit as the most simple example of a system that contains both non-degenerate and doubly degenerate ground-states.

2.3.3 The interacting Anderson model

We now move to discuss the interacting Anderson model with the on-site local interaction, U, included. The Dyson equation, eq. (2.29), gives the propagator in terms of the local interaction self-energy $\Sigma_\sigma(\omega) \equiv \Sigma_{ii;\sigma}(\omega, h)$ and the zeroth-order non-interacting Green function $g_\sigma(\omega, h)$, given via eq. (2.40)

$$G_\sigma(\omega, h) = [g_\sigma^{-1}(\omega, h) - \Sigma_\sigma(\omega, h)]^{-1}, \tag{2.50a}$$

$$= [\omega^+ - \varepsilon_\sigma - \Gamma_\sigma(\omega, h) - \Sigma_\sigma(\omega, h)]^{-1}. \tag{2.50b}$$

On comparison with eq. (2.36), obtained via equations of motion, we see that $\Sigma_\sigma(\omega, h) = F_\sigma(\omega, h)/G_\sigma(\omega, h)$. This is a fact that shall be utilized later in this thesis when calculating exact numerical results.

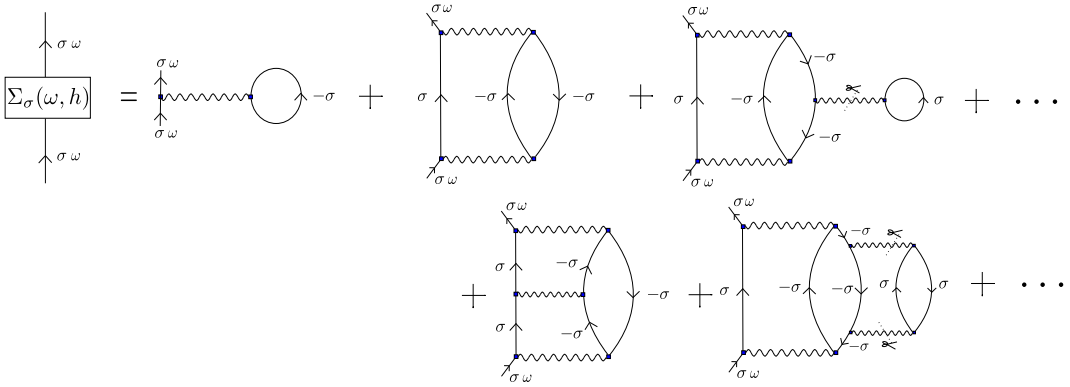


Figure 2.3: The first few terms in the perturbation expansion for $\Sigma_\sigma(\omega, h)$ in terms of $g_\sigma(\omega, h)$, $g_{-\sigma}(\omega, h)$ and U. All frequencies and spins are conserved at each vertex.

2.3.4 The self-energy and the skeleton expansion

As we have seen, the exact form of the non-interacting Green function may be easily calculated in terms of the 'bare' level energy, ε_σ, and the hybridization function,

$\Gamma_\sigma(\omega, h)$. The interaction self-energy, $\Sigma_\sigma(\omega, h)$ can then be calculated via a diagrammatic perturbation expansion [62]. Fig. 2.3 shows the first few diagrams in the perturbation series for $\Sigma_\sigma(\omega, h)$. The single lines once again represent the non-interacting propagator, $g_\sigma(\omega, h)$; the wiggly lines represent the interaction strength, U, which for the single-impurity Anderson model can only occur between $\uparrow$ and $\downarrow$ spin electrons.

In fact, the irreducible self-energy, $\Sigma_\sigma(\omega, h)$ can be written in a more convenient form, that will prove useful to us later in this thesis. There is a certain class of diagrams, known as 'skeleton diagrams' [62, 63], which contain no self-energy insertions on the individual propagator lines. A self-energy insertion is any diagram which could itself make an individual contribution to $\Sigma_\sigma(\omega, h)$. For example, the 3rd and 5th diagrams shown in Fig. 2.3 are not skeleton diagrams as interaction lines may be cut to detach self-energy insertions (shown by the scissors). All diagrams for $\Sigma_\sigma(\omega, h)$ can then be obtained from the skeleton diagrams by inserting the full propagators, $G_\sigma(\omega, h)$, on the individual lines. Fig. 2.4 shows the first few skeleton diagrams for $\Sigma_\sigma(\omega, h)$ in terms of both $G_\sigma(\omega, h)$ and $G_{-\sigma}(\omega, h)$. The reason that we have rewritten the perturbation expansion for $\Sigma_\sigma(\omega, h)$ in this way will now become clear. As we shall see in the next section, expressing $\Sigma_\sigma(\omega, h)$ in this way is equivalent to writing it as a *functional* of the full interacting propagator, $\Sigma_\sigma(\omega, h) \equiv \Sigma[\{G_{\sigma'}\}]$ (with $\sigma' = \uparrow$ or $\downarrow$).

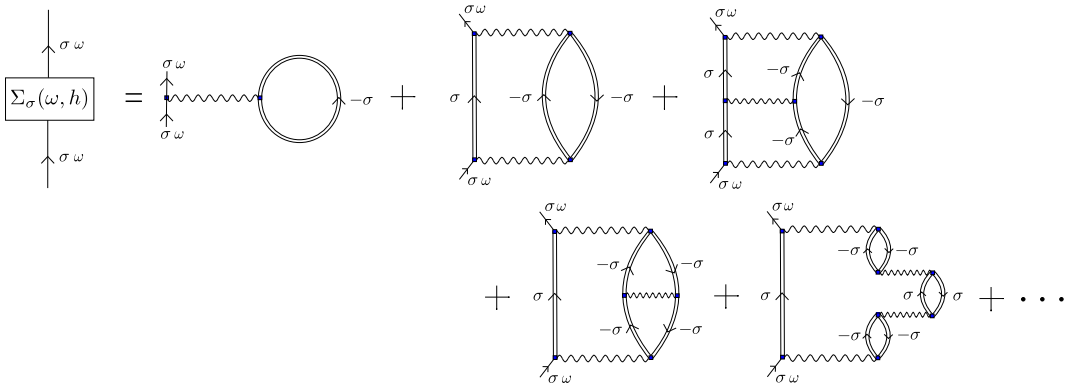


Figure 2.4: The skeleton expansion for $\Sigma_\sigma(\omega, h)$ up to 4th-order. All double lines denote full interacting propagators, $G_\sigma(\omega, h)$, whilst wiggly lines denote the interaction strength, "U". All frequencies and spins are conserved at each vertex.

2.4 Fermi liquid theory

In a series of seminal papers, Luttinger and coworkers developed the underlying diagrammatic arguments for a full microscopic derivation of Landau's Fermi liquid

theory[8] [58–61,76,77]. In this section we briefly sketch the key ideas, and specifically how they apply to the Anderson impurity model.

2.4.1 Luttinger-Ward functional

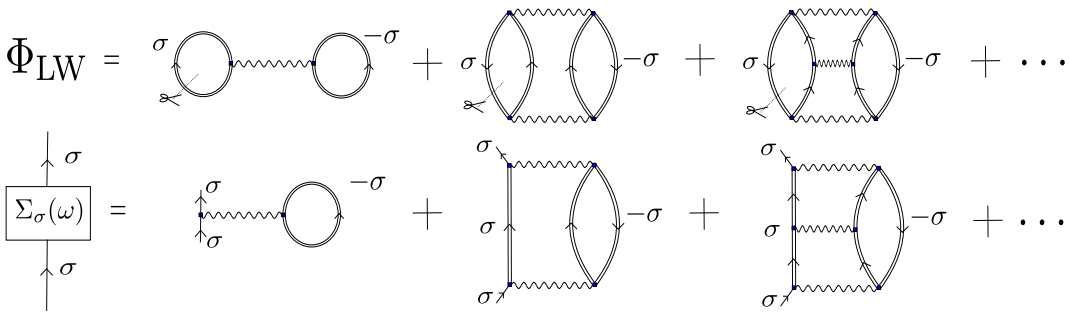


Figure 2.5: Top: The first few closed linked skeleton diagrams for the Luttinger-Ward functional, Φ_{LW}. Bottom: The first few terms of the skeleton expansion for the self-energy, $\Sigma_\sigma(\omega, h) = \delta\Phi_{LW}/\delta G_\sigma(\omega, h)$.

The Luttinger-Ward functional [59], $\Phi_{LW} \equiv \Phi[\{G_{\sigma'}\}]$ (where $[\ldots]$ as before denotes a functional and $\{G_{\sigma'}\}$ denotes the set $(G_\uparrow, G_\downarrow)$), is a very important quantity that allows the thermodynamic potential (the state function for the grand canonical ensemble) of the system, $\Omega \equiv \Omega[\{G_{\sigma'}\}]$, to be expressed in terms of the single-particle propagator, $G_\sigma \equiv G_\sigma(\omega, h)$. This result is significant because in principal it allows the thermodynamic properties (embodied by Ω) of the system to be determined in terms of the dynamic (ω-dependent) propagator, $G_\sigma(\omega, h)$. Furthermore, Luttinger and Ward showed [59] that $\Phi[\{G_{\sigma'}\}]$ is simply made up of a perturbation series of all 'closed-linked' skeleton diagrams involving the interacting propagator, $G_\sigma(\omega, h)$.[9]

Whilst the skeleton expansion for the self-energy (as shown in Fig. 2.4) involved diagrams with one line entering and one line leaving, diagrams for Φ_{LW} may be obtained by simply closing the equivalent self-energy diagram (as shown in Fig. 2.5). In addition, the *exact* self-energy, $\Sigma_\sigma(\omega, h)$, may be obtained via the functional derivative of $\Phi[\{G_{\sigma'}\}]$ with respect to one of the σ-propagator lines, $G_\sigma(\omega, h)$, i.e.

$$\Sigma_\sigma(\omega, h) \equiv \Sigma[\{G_{\sigma'}\}] = \frac{\delta\Phi[\{G_{\sigma'}\}]}{\delta G_\sigma}. \tag{2.51}$$

Thus, functional differentiation is equivalent to cutting a single propagator line in the perturbation expansion for Φ_{LW}, yielding a contribution to $\Sigma_\sigma(\omega, h)$ (as shown by the scissors in Fig. 2.5).

[8] Landau had originally developed a phenomenological approach for explaining the low-temperature properties of liquid helium ^{3}He [2].

[9] As before, a skeleton diagram is a diagram that contains no self-energy insertions on any individual propagator line.

The form of the Dyson equation, eq. (2.50), allows the full interacting Green function, $G_\sigma(\omega, h)$ to be determined in terms of the irreducible self-energy, $\Sigma_\sigma(\omega, h)$. Furthermore, $\Sigma_\sigma(\omega, h)$ may be obtained via the functional derivative of the Luttinger Ward functional, eq. (2.51), and hence is expressed via the skeleton expansion in terms of the full propagators as shown in Fig. 2.5. In consequence, these two equations provide a *self-consistency* condition for the determination of both the propagator and self-energy. In principal, if all possible skeleton diagrams were to be included in the expansion for $\Sigma_\sigma(\omega, h)$, then it would be possible to determine the full propagator *exactly*. Obviously, this is impossible in practice, but physically relevant approximations may be made by truncation of the skeleton expansion to only include specific diagrams. Later in this thesis we make full use of the self-consistency equations alluded to here.

2.4.2 For the metallic Anderson model

The key results of Luttinger *et al.*'s diagrammatic analysis of Fermi liquid theory are the following four proofs that hold to all orders in the interaction U (see ref [2] for further details):

$$\Sigma^t_\sigma(\omega, h) \equiv \Sigma_\sigma(\omega, h) = \Sigma^R_\sigma(\omega, h) - i\,\mathrm{sgn}(\omega)\Sigma^I_\sigma(\omega, h) \quad \text{with} \quad \Sigma^I_\sigma(\omega, h) \geq 0 \tag{2.52a}$$

$$\Sigma^I_\sigma(\omega = 0, h) = 0 \tag{2.52b}$$

$$\Sigma^I_\sigma(\omega, h) \propto \omega^2 \ \text{ as } \ \omega \to 0 \tag{2.52c}$$

$$I_{L_\sigma}(h) = \mathrm{Im}\int_{-\infty}^{0} \frac{\partial \Sigma^r_\sigma(\omega, h)}{\partial \omega} G^r_\sigma(\omega, h) = 0 \tag{2.52d}$$

where the 't' superscript denotes the time-ordered function, together with the retarded function, $\Sigma^r_\sigma(\omega, h) = \Sigma^R_\sigma(\omega, h) - i\Sigma^I_\sigma(\omega, h)$. Luttinger's original Hamiltonian involved fermions with short ranged two-body interactions. However, it may be shown by a simple canonical transformation that the quantum impurity models studied here can be transformed into the same basic model that Luttinger considered.

With these results in mind, we may express the low-ω form of the local impurity self-energy as a simple Taylor expansion

$$\Sigma_\sigma(\omega, h) \overset{\omega\to 0}{\sim} \left[\Sigma^R_\sigma(0, h) + \omega\left(\frac{\partial \Sigma^R_\sigma(\omega, h)}{\partial \omega}\right)_{\omega=0} + \ldots\right] - i\,\mathrm{sgn}(\omega)O(\omega^2). \tag{2.53}$$

Inserting this into the Dyson equation, eq. (2.50) for the interacting propagator, we find:

$$G_\sigma(\omega, h) \overset{\omega\to 0}{\sim} [\omega/Z - \varepsilon^*_\sigma(h) + i\,\mathrm{sgn}(\omega)\Gamma_0]^{-1}. \tag{2.54}$$

The quantity, Z, is the 'quasiparticle weight' given by

$$Z = \left[1 - \left(\frac{\partial \Sigma^R_\sigma(\omega, h)}{\partial \omega}\right)_{\omega=0}\right]^{-1}, \tag{2.55}$$

such that $Z = 1$ in the non-interacting limit and $\varepsilon^*_\sigma(h) = \varepsilon - \sigma h + \Sigma^R_\sigma(\omega = 0, h)$ is the renormalized level energy (the bare level energy plus corrections from interactions). The propagator therefore becomes

$$G_\sigma(\omega, h) \overset{\omega \to 0}{\sim} Z\tilde{g}_\sigma(\omega, h), \quad \text{where} \tag{2.56a}$$

$$\tilde{g}(\omega, h) = [\omega^+ - Z\varepsilon^*_\sigma(h) + iZ\,\mathrm{sgn}(\omega)\Gamma_0]^{-1}, \tag{2.56b}$$

such that eq. (2.56b) has the same form as the non-interacting Green function given by eq. (2.40), but with the bare level energy, $\varepsilon_\sigma(h)$, replaced by a renormalized level, $Z\varepsilon^*_\sigma(h)$, and the bare hybridization strength, Γ_0, replaced by $Z\Gamma_0$. Thus, the low-ω asymptotics of the interacting propagator, $G_\sigma(\omega, h)$, in a Fermi liquid phase are precisely the same as the NIL Green function, $g_\sigma(\omega, h)$, but with bare parameters replaced by their renormalized counterparts. As we shall see, the underlying signature of a Fermi liquid phase is that the low-ω behaviour of the propagator has the same fundamental form as the non-interacting propagator. (Generally the condition for this behaviour to occur, and not just for the metallic AIM considered here, is that $\Sigma^I_\sigma(\omega, h)$ vanishes more rapidly than $\Gamma^I_\sigma(\omega, h)$ as $\omega \to 0$, i.e. $\Sigma^I_\sigma(\omega, h) \propto |\omega|^\lambda$ with $\lambda > r$.)

In Chapter 3 we explicitly consider Luttinger's diagrammatic argument for the vanishing of the Luttinger integral, $I_{L_\sigma}(h)$, given by eq. (2.52d), in the context of a 'two self-energy description'. Subsequently, in Chapter 4, we generalize Luttinger's results, eqs. (2.52b-2.52d), to the case of the pseudogap Anderson model, in both its Fermi liquid and non-Fermi liquid phases.

2.4.3 General points

Before we proceed to the next chapter, we make some general points about Fermi liquid phases.

A Fermi liquid may be thought of as a phase where *the low-lying excitations of the interacting system are in one-to one correspondence with the excitations of the non-interacting limit* [2]. The effect of interactions is to dress a bare electron to form a weakly-interacting quasiparticle. Furthermore, a non-interacting system (at $T = 0$) is characterized by having a sharp Fermi surface - i.e. electronic states below the Fermi level are filled and states above are empty. By virtue of the fact that within a Fermi liquid description the quasiparticles behave like weakly-interacting particles, the system also exhibits a sharp Fermi surface, but with the bare electrons

replaced by quasiparticles.

In other words, for a Fermi liquid the ground-state of the interacting model is *adiabatically* connected to the ground-state of the non-interacting limit. As interactions are slowly switched off, the ground-state of the non-interacting system is continuously accessed from the interacting system. In consequence, as discussed in Section 2.2.1, the Gell-Man Low theorem holds and the perturbation expansion of eq. (2.27) is valid to all orders in the interaction, U.

In the next chapter, we consider non-Fermi liquid *doubly degenerate* local moment (LM) phases, which occur in many impurity models, but are crucially not adiabatically connected to the non-interacting limit. The diagrammatic many-body perturbation theory outlined here does not apply in the conventional sense (a perturbation expansion about the NIL is simply invalid). However, as we shall see it is possible to describe these degenerate phases using the diagrammatics explained in this chapter within a *two self-energy* (TSE) description.

CHAPTER 3

Local moment phases

As discussed previously, the Anderson impurity model (AIM) coupled to a metallic conduction band behaves as a Fermi liquid for all values of the interaction strength 'U'. The interacting many-body ground state of the system is perturbatively connected to the non-interacting limit, as described in Section 2.4. Thus, diagrammatic perturbation theory in U can be undertaken and the skeleton expansion expressing the local self-energy as a functional derivative of $\Phi_{LW} \equiv \Phi[\{G_{\sigma'}\}]$ holds to all orders. However, this metallic model is certainly non-trivial, for large U, the Kondo effect occurs in which the low-energy scale, T_K, vanishes exponentially. The impurity spin degree of freedom is completely quenched at low temperature and the ground-state is a genuine many-body singlet (as shown pictorially in Fig. 1.2).

We remind the reader that in contrast to the basic metallic case, many variants of the Anderson model exhibit a zero temperature *local* quantum phase transition (QPT) to a phase in which the local spin degree of freedom is not screened by the band. At $T = 0$ there is a transition between a Fermi liquid phase (in which the Kondo effect persists), adiabatically connected to the NIL, and a distinct non-Fermi liquid (NFL) phase where the perturbation expansion of eq. (2.27) is crucially not valid. For single level models, examples of this type of system include the pseudogap AIM [33, 42, 43, 46, 78–81], and the gapped AIM [50–53, 82], as well as models with couplings to bosonic degrees of freedom [54–57, 83–85]. For multi-impurity models, the possible examples are vast, including impurity models for double [86–90] and triple [91–95] quantum dot devices. In all of these models the non-Fermi liquid phase is 'common' (as shown in Fig. 1.4) in that it takes up a significant portion of parameter space, and does not require fine tuning of parameters. Furthermore, we emphasize that the non-Fermi liquid LM phases considered in this chapter possess a *globally* doubly-degenerate ground-state, containing an SU(2) spin degree of freedom in the *entire* system.

In this chapter we set to put the machinery in place in order to describe doubly

degenerate local moment (LM) phases within a two self-energy (TSE) description. We initially consider the zero-temperature *local* static charge, $n(h)$, and magnetization, $m(h)$, and in particular their field-dependence in a LM phase. In contrast to the SC phase where $m(h)$ is continuous across $h = 0$, we show that in a LM phase $\lim_{h\to 0^{\pm}}[m(h)]$ is non-vanishing, and thus a suitable *order parameter* for the transition. Furthermore, the behaviour of $m(h)$ has a strong bearing on the underlying forms of the local single-particle propagators, $G_{\sigma}(\omega, h)$, particularly at zero-field. By virtue of the fact that the ground-state is doubly-degenerate, we show that a description of the zero-field propagator requires consideration of two distinct self-energies which reflect the fundamental *broken-symmetry* nature of the phase. The conventional self-energy that arises from the Dyson equation, eq. (2.50), in standard many-body theory, which we refer to as the 'single-self-energy' (SSE), may then be obtained by direct consideration of the TSEs.

After considering the local quantities mentioned above, we move to discuss the 'excess' charge and magnetization. In quantum impurity physics an excess quantity is defined as the expectation value of that quantity for the entire system (the conduction band plus the impurity level), minus the expectation value for the system in the absence of the impurity. We find that both the excess charge, $n_{\rm imp}(h)$ and magnetization, $m_{\rm imp}(h)$, have precisely the same structure as their purely local counterparts. Moreover, in Section 3.3 we derive a distinct Friedel-Luttinger sum rule [96] in *each* phase, relating the scattering phase shift to a relevant excess charge and a Luttinger integral, $I_{L_{\sigma}}(h)$. Furthermore, in Section 3.4 we generalize Luttinger and Ward's [59] original argument for the vanishing of the Luttinger integral, $I_{L_{\sigma}}(h)$, to the LM phase (where we define it in terms of broken-symmetry propagators). To conclude the chapter we specifically analyse the simple *exactly soluble* case of the atomic limit (previously discussed in Section 2.3), where we find that in its singly occupied regime the TSE description is applicable.

Before proceeding we make one further comment. The two self-energy (TSE) description discussed in this chapter underlies the 'local moment approach' (LMA) [28,29,34,45,51,64,65]. In that context the approach was approximate, arising, in the first instance, from the use of mean-field propagators. However, we emphasize that here in its current guise the TSE framework is *exact*, free from any approximation.

3.1 Local quantities

In examining both distinct (LM and SC) phases, and the principal differences between them, we choose to initially focus on the zero-temperature local impurity charge, $n(h)$, and magnetization, $m(h)$. Specifically, we concentrate on their underlying dependence in response to a magnetic field, $h = \frac{1}{2}g\mu_B B$. As stated in Section 2.3 with reference to the AIM Hamiltonian, eq. (2.30), the field, h, may be

applied either locally - i.e. just to the impurity level, (such that $\hat{H}_{\rm field} = -2h\hat{s}_{\rm z} = -2h(\frac{1}{2}[\hat{n}_{\uparrow} - \hat{n}_{\downarrow}])$, where $\hat{s}_{\rm z}$ is a local operator that measures the z-component of spin solely on the impurity level), or globally - to both the impurity plus the conduction band states (such that $\hat{H}_{\rm field} = -2h\hat{S}_{\rm z} = -2h[\hat{s}_{\rm z} + \hat{s}_{\rm z}^{bath}]$, with the conduction band operator given by $\hat{s}_{\rm z}^{bath} = \frac{1}{2}\sum_{\mathbf{k}}[\hat{n}_{\mathbf{k}\uparrow} - \hat{n}_{\mathbf{k}\downarrow}]$). Initially it is unimportant to the discussion whether the field is applied locally or globally and therefore we do not specify which at this stage.

The local impurity magnetization, $m(h)$, and local charge, $n(h)$, are defined by

$$m(h) = \sum_{\sigma} \sigma n_{\sigma}(h), \tag{3.1a}$$

$$n(h) = \sum_{\sigma} n_{\sigma}(h), \tag{3.1b}$$

where as usual the convention is $\sigma = \pm 1$ for $\uparrow$ / $\downarrow$ spins, and $n_{\sigma}(h) = \langle \hat{n}_{\sigma} \rangle$, is the expectation value of the local charge on the impurity level[1]. As shown in Section 2.1.1 via eq. (2.12), the local charge may be obtained simply in terms of an integral over the single-particle spectrum, $D_{\sigma}(\omega)$:

$$n_{\sigma}(h) \equiv \langle \hat{n}_{\sigma} \rangle = \int_{-\infty}^{0} {\rm d}\omega \; D_{\sigma}(\omega, h) = -\frac{1}{\pi}{\rm Im}\int_{-\infty}^{0} {\rm d}\omega \; G_{\sigma}^{r}(\omega, h), \tag{3.2}$$

where we have used eq. (2.17) to express $D_{\sigma}(\omega, h)$ in terms of the retarded impurity propagator, $G_{\sigma}^{r}(\omega, h)$. In the following arguments of this chapter we refer explicitly to the retarded propagator in all cases such that we drop the explicit 'r' label and hence $G_{\sigma}^{r}(\omega, h) \equiv G_{\sigma}(\omega, h)$. Furthermore, putting eq. (3.2) into eqs. (3.1a-3.1b), the local magnetization and the local charge may be written simply as

$$m(h) = \int_{-\infty}^{0} {\rm d}\omega \; [D_{\uparrow}(\omega, h) - D_{\downarrow}(\omega, h)], \tag{3.3a}$$

$$n(h) = \int_{-\infty}^{0} {\rm d}\omega \; [D_{\uparrow}(\omega, h) + D_{\downarrow}(\omega, h)]. \tag{3.3b}$$

The local propagator is given via the Dyson equation, eq. (2.50), in terms of the hybridization function, $\Gamma_{\sigma}(\omega, h)$ and the local self-energy, $\Sigma_{\sigma}(\omega, h)$

$$G_{\sigma}(\omega, h) = [\omega^{+} - \varepsilon + \sigma h - \Gamma_{\sigma}(\omega, h) - \Sigma_{\sigma}(\omega, h)]^{-1}, \tag{3.4}$$

with $\omega^{+} = \omega + i\eta$ and $\eta = 0^{+}$. Here we note that if the magnetic field h is applied solely to the impurity level, then the hybridization function, given by eq. (2.37), is independent of both h and σ, i.e. $\Gamma_{\sigma}(\omega, h) \equiv \Gamma(\omega)$. For convenience we once again

[1]The local magnetization is then given from eq. (3.1a) in terms of the z-component of the spin on the impurity site: $m(h) = 2\langle \hat{s}_{\rm z} \rangle = [n_{\uparrow}(h) - n_{\downarrow}(h)]$.

adopt the notation of the last chapter, setting $\varepsilon_\sigma = \varepsilon - \sigma h$, such that $\uparrow$ spins are favoured in energy over $\downarrow$ spins. With this convention it may be seen by considering eqs. (3.3-3.4), that the induced local magnetization is in the same direction as the applied field, i.e.

$$\mathrm{sgn}(h) = \mathrm{sgn}(m(h)). \tag{3.5}$$

By considering eq. (2.30), it follows that by changing the sign of the applied magnetic field $h \to -h$ and also swapping $\uparrow$ and $\downarrow$ spins, the Hamiltonian is invariant (we refer the reader to Appendix B for a full discussion of transformations of the Hamiltonian). From this symmetry it follows that

$$G_\sigma(\omega, h) = G_{-\sigma}(\omega, -h). \tag{3.6}$$

Hence by inserting this equation into eq. (3.2), from eqs. (3.1a-3.1b) we find $m(h)$ is odd, and $n(h)$ even in h, i.e.

$$m(h) = -m(-h), \tag{3.7a}$$
$$n(h) = n(-h). \tag{3.7b}$$

3.1.1 Behaviour of the local magnetization, $m(h)$

The preceding discussion is entirely general and holds regardless of the nature of the zero-field phase (LM or SC). What differentiates the two phases is the field behaviour of the local magnetization, $m(h)$. In a SC phase, $m(h)$ vanishes continuously as the field h is reduced towards zero. By contrast, in a LM phase as $h \to 0^+$, the system possesses a finite *permanent* zero-field local moment with magnitude $m(h = 0^+) = |\tilde{\mu}|$. The left of Fig. 3.1 shows a schematic representation of the behaviour of the local magnetization as a function of h in a doubly degenerate LM phase. The low-field behaviour of $m(h)$ is essentially the same as for the simple case of a free spin (as explicitly detailed in Appendix E), i.e. on application of even the tiniest field in some arbitrary direction, a magnetization is induced along the field direction, c.f. eq. (3.5). We refer to an 'A' type state for $h \to 0^+$, and a 'B' type state for $h \to 0^-$, such that the local magnetization becomes

$$m(h \to 0^+) = +|\tilde{\mu}|, \tag{3.8a}$$
$$m(h \to 0^-) = -|\tilde{\mu}|, \tag{3.8b}$$

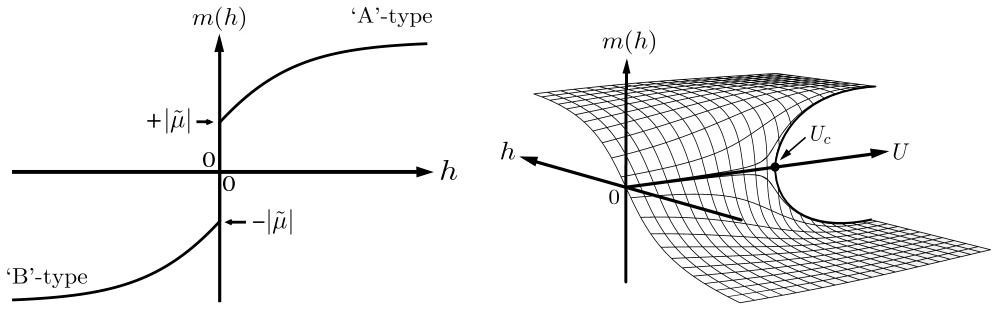


Figure 3.1: Left: The zero temperature local magnetization, $m(h)$, as a function of h in a doubly degenerate local moment (LM) phase. Right: 3D representation of the magnetization, $m(h)$ as a function of the interaction strength U and the field-h. For $U < U_c$, the system is in a Fermi liquid SC phase, $m(h = 0) = m(h \to 0) = 0$. By contrast, for $U > U_c$, the local magnetization, $m(h)$ is discontinuous across $h = 0$ in a LM phase, $m(h \to \pm 0) \to \pm|\tilde{\mu}|$. The critical $U = U_c$ is the point at which local moments start to form.

respectively. Thus, the local magnetization is discontinuous across $h = 0$ as shown in Fig. 3.1. In contrast, identically at $h = 0$, $m(h = 0) = 0$, reflecting the fact that the permanent local moment has equal probability of being up or down. Before proceeding, we emphasize that in contrast to the simple free-spin case, the LM phase local magnetization, $m(h)$, is not fully saturated on application of an infinitesimal field, but reaches a value $|\tilde{\mu}|$ which lies in the interval $[0, 1]$.

The *permanent* local moment, $|\tilde{\mu}| = m(h = 0^+) \equiv -m(h = 0^-)$, is thus a good candidate for an order parameter for the quantum phase transition between the two distinct phases. In a LM phase for $U > U_c$ it is finite, but vanishes in a SC phase where $m(h \to 0^{\pm}) = 0$. Making the reasonable assumption that as the transition is approached for $U \to U_c^+$, $m(h = 0^+) = |\tilde{\mu}|$ vanishes continuously (a hypothesis that may be verified explicitly on a model-by-model basis). The right panel of Fig. 3.1 shows a three-dimensional schematic representation of $m(h)$ plotted versus both U and h; showing the vanishing of $|\tilde{\mu}|$ as $U \to U_c^+$.

The local moment, $|\tilde{\mu}|$, is well known to be the order parameter within an unrestricted Hartree Fock (UHF) mean-field approach [62]. However, as discussed in the introduction, due to its crude nature, in which all dynamical contributions to $\Sigma_\sigma(\omega)$ are neglected, UHF is known to overestimate the propensity for local moment formation. For example, mean-field theory applied to the metallic AIM by Anderson is known to falsely predict a QPT to a LM phase for large U [7]. Furthermore, we accentuate the point that the deductions we make in this chapter are *exact*, and hence have nothing to do with mean-field theory. Moreover, when a QPT genuinely does occur between a SC and LM phase, the order parameter for the transition is certainly the local moment, $|\tilde{\mu}|$. In the literature this has been found from NRG calculations for the pseudogap AIM [37,42], and also the Bose-Fermi Anderson model [55,57,65],

together with the pseudogap Anderson-Holstein model [83]. However, we stress that whilst $m(h \to 0^+)$ has been calculated numerically and quoted as the order parameter for the transition, the underlying theory for precisely why this behaviour occurs has been somewhat overlooked.

A further point is as follows. As shown in Fig. 3.1, the magnetization, $m(h)$, is of course non-zero for any non-zero h, whether $U < U_c$ or $U > U_c$. This reflects the fact that the quantum phase transition is destroyed on application of any finite-field (as indicated by the schematic shown in Fig. 1.4). Physically, this field-dependence means that for $U > U_c$, the ground-state of the system is no longer doubly-degenerate. One of the components (A or B) of the zero-field ground-state has been 'picked out' according to whether $h > 0$, $h < 0$. Once again, this behaviour is directly analogous to the free-spin case of Appendix E, but with the pure $|\uparrow\rangle$, $|\downarrow\rangle$ states replaced with the (many-body) A and B states.

3.1.2 Local propagators

The underlying field-dependence of the local magnetization, described above makes a significant impact on the structure of the local propagators, which in turn from eqs. (3.2-3.3) determine $m(h)$. As stated above, in a LM phase for $h > 0$, such that the 'A' state is picked out of the doubly degenerate ground-state, we denote the propagator $G_\sigma(\omega, h) \equiv G_{A\sigma}(\omega, |h|)$. The broken symmetry propagator $G_{A\sigma}(\omega, |h|)$ reflects the LM state correponding to $m(h) > 0$ for all $h \geq 0$ (with $m(h = 0^+) = +|\tilde{\mu}|$). In contrast if $h < 0$, the 'B' state is picked out; the propagator $G_\sigma(\omega, h) \equiv G_{B\sigma}(\omega, -|h|)$ refers to $m(h) < 0$ for all $h \leq 0$ (with $m(h = 0^-) = -|\tilde{\mu}|$). Thus, in consequence of eq. (3.6), the following symmetry between the 'A' and 'B' propagators holds

$$G_{A\sigma}(\omega, |h|) = G_{B-\sigma}(\omega, -|h|). \tag{3.9}$$

The (field) notation that we use for the broken-symmetry Green functions underlines the point that the 'A' state is accessed only for $h \geq 0$ and the 'B' state for $h \leq 0$. In other words, the full propagator can be expressed in the form

$$G_\sigma(\omega, h) = \theta(h) G_{A\sigma}(\omega, |h|) + \theta(-h) G_{B\sigma}(\omega, -|h|) \tag{3.10}$$

where $\theta(x)$ is the heaviside step function: $\theta(x) = 1$, for $x > 0$; $\theta(x) = 0$, for $x < 0$, and $\theta(0) = \frac{1}{2}$. Thus, in direct parallel to the behaviour of $m(h)$ (shown in Fig. 3.1), $G_\sigma(\omega, h)$ is discontinuous across $h = 0$, i.e. $G_\sigma(\omega, 0^+) = G_{A\sigma}(\omega, 0)$ and $G_\sigma(\omega, 0^-) = G_{B\sigma}(\omega, 0)$, where in a LM phase (from eq. (3.3a)) the presence of a permanent local moment means that $G_{A\sigma}(\omega, 0)$ and $G_{B\sigma}(\omega, 0)$ are not the same for

all ω. In contrast, identically at zero-field, eq. (3.10) simply gives

$$G_\sigma(\omega,0) = \tfrac{1}{2}[G_{A\sigma}(\omega,0) + G_{B\sigma}(\omega,0)], \tag{3.11a}$$
$$= \tfrac{1}{2}[G_{B-\sigma}(\omega,0) + G_{A-\sigma}(\omega,0)], \tag{3.11b}$$
$$= G_{-\sigma}(\omega,0), \tag{3.11c}$$

once again reflecting that in a LM phase the ground-state is globally doubly degenerate. Furthermore, eq. (3.11) also shows, by virtue of the symmetry (eq. (3.9)) $G_{A\sigma}(\omega,|h|) = G_{B-\sigma}(\omega,-|h|)$, that the full Green function at zero-field is rotationally invariant, i.e. $G_\sigma(\omega,0) = G_{-\sigma}(\omega,0) = G(\omega,h=0)$ is independent of spin-σ. This property simply reflects the overall spin symmetry of the Hamiltonian precisely at $h = 0$.

Local broken-symmetry spectral functions

As the ω-dependence of $G_\sigma(\omega,h)$ is discontinuous across $h = 0$ in a LM phase, the same must also be true for the local impurity single-particle spectrum, $D_\sigma(\omega,h) = -\frac{1}{\pi}\mathrm{Im}G_\sigma(\omega,h)$ (for the retarded functions considered here). In particular, we label the spectral functions by

$$D_\sigma(\omega,0^+) = D_{A\sigma}(\omega,0), \tag{3.12a}$$
$$D_\sigma(\omega,0^-) = D_{B\sigma}(\omega,0). \tag{3.12b}$$

From eq. (3.11) the spin-independent zero-field function $D_\sigma(\omega,0) = D_{-\sigma}(\omega,0) = D(\omega,0)$ is written as

$$D_\sigma(\omega,0) = \tfrac{1}{2}[D_{A\sigma}(\omega,0) + D_{B\sigma}(\omega,0)]. \tag{3.13}$$

Thus, on the application of even an infinitesimal field, $h = 0^\pm$, the ω dependence of the spectral function, $D_\sigma(\omega,h)$, changes abruptly. This has been found for the underscreened spin-1 phase arising in two-level quantum dot systems [96,97]. Moreover, Fig. 3.2 shows numerical NRG calculations for the pseudogap AIM. Both $\pi|\omega|^r D_{A\sigma}(\omega,0) \equiv \pi|\omega|^r D_\sigma(\omega,0^+)$, and $\pi|\omega|^r D_\sigma(\omega,0)$ are shown (where r is the pseudogap band exponent).[2] There is a significant redistribution of weight in the high-energy Hubbard satellites of the spectrum on the application of a tiny field.[3]

We now return to eq. (3.2) for $n_\sigma(h)$. By inserting eq. (3.10) into eq. (3.2) for

[2] We consider the pseudogap AIM explicitly in Chapter 4. For now the model specifics are unimportant to the discussion.

[3] At zero-field, Hubbard satellite bands occur in the spectrum, $D_\sigma(\omega,0)$, at large energies: $\omega = \varepsilon$, $\varepsilon + U$ as a result of the single-particle atomic limit processes discussed in Section 2.3.2. The delta functions of eq. (2.45) are broadened by coupling to the conduction band with finite width $\sim O(\Gamma_0)$ (c.f. eq. (2.41) in the NIL).

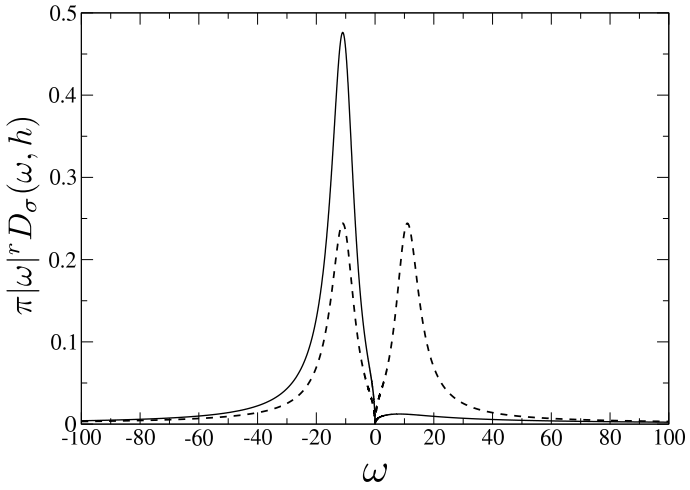


Figure 3.2: The spectral function, $\pi|\omega|^r D_\sigma(\omega,h)$, plotted versus ω for the pseudogap AIM for $r = 0.35$, $x = \varepsilon + \frac{U}{2} = 0$, and $U/\pi = 10$. The dashed line shows $\pi|\omega|^r D_\sigma(\omega, h = 0)$, whereas the solid line shows $\pi|\omega|^r D_\sigma(\omega, h = 0^+) \equiv \pi|\omega|^r D_{A\sigma}(\omega, h = 0)$. We have taken the unit of energy to be $\Gamma_0^{1/(1-r)} \equiv 1$, such that $\omega \equiv \omega/\Gamma_0^{1/(1-r)}$ and $\pi|\omega|^r D_\sigma(\omega,h) \equiv \pi\Gamma_0|\omega|^r D_\sigma(\omega,h)$ are dimensionless.

$G_\sigma(\omega,h)$, $n_\sigma(h)$ simply takes the form

$$n_\sigma(h) = \theta(h) n_{A\sigma}(|h|) + \theta(-h) n_{B\sigma}(-|h|), \tag{3.14}$$

with $n_{A\sigma}(|h|) = -\frac{1}{\pi}\mathrm{Im}\int_{-\infty}^{0} \mathrm{d}\omega\, G_{A\sigma}(\omega,|h|)$, (and similarly for $n_{B\sigma}(-|h|)$), such that from eq. (3.9)

$$n_{A-\sigma}(|h|) = n_{B\sigma}(-|h|). \tag{3.15}$$

The local charge, $n(h) = \sum_\sigma n_\sigma(h)$ follows using eqs. (3.14-3.15) as

$$n(h) = [\theta(h) + \theta(-h)] \sum_\sigma n_{A\sigma}(|h|) = n_{A\sigma}(|h|), \tag{3.16}$$

and therefore $n(h) = n(-h)$ is *continuous* across $h = 0$, not showing any abrupt behaviour. The corresponding 'A' state magnetization is similarly defined as

$$m_A(|h|) = \sum_\sigma \sigma n_{A\sigma}(|h|), \tag{3.17}$$

such that $m_A(|h|) > 0$ for $h \geq 0$ and $U > U_c$, with

$$m_A(0) = +|\tilde{\mu}| \tag{3.18}$$

the permanent local moment; and also $m_B(-|h|) = \sum_\sigma \sigma n_{B\sigma}(-|h|)$, such that

$m_B(-|h|) = -m_A(|h|) = -|\tilde{\mu}|$ from eq. (3.15). From eqs. (3.1a, 3.14, 3.17), the local magnetization, $m(h)$ is given in terms of $m_A(|h|)$ by

$$m(h) = [\theta(h) - \theta(-h)]m_A(|h|). \tag{3.19}$$

This form recovers the symmetries of eqs. (3.7-3.8) and the field-dependence shown on the left panel of Fig. 3.1. Eq. (3.19) shows in particular that $m(h)$ is determined in a LM phase for any field in terms of the broken symmetry propagators by

$$m_A(|h|) = -\frac{1}{\pi}\mathrm{Im}\sum_\sigma \sigma \int_{-\infty}^{0} \mathrm{d}\omega\, G_{A\sigma}(\omega, |h|), \tag{3.20a}$$

$$= \int_{-\infty}^{0} \mathrm{d}\omega\, [D_{A\uparrow}(\omega, |h|) - D_{A\downarrow}(\omega, |h|)], \tag{3.20b}$$

with $D_{A\sigma}(\omega, |h|) = -\frac{1}{\pi}\mathrm{Im}G_{A\sigma}(\omega, |h|)$.

Hereafter, for any field we choose to only work solely with A-type propagators. The B-type propagators can be eliminated from further consideration by using eq. (3.9) in eq. (3.10):

$$G_\sigma(\omega, h) = \theta(h)G_{A\sigma}(\omega, |h|) + \theta(-h)G_{A-\sigma}(\omega, |h|), \tag{3.21}$$

and hence the local charge, eq. (3.16) is given by

$$n_\sigma(h) = \theta(h)n_{A\sigma}(|h|) + \theta(-h)n_{A-\sigma}(|h|). \tag{3.22}$$

3.1.3 Local self-energies

For any field, $h \geq 0$, the broken-symmetry propagator for the 'A' state, $G_{A\sigma}(\omega, |h|)$, may be written from a Dyson equation (in analogy with eq. (3.4)) in terms of its corresponding self-energy, $\Sigma_{A\sigma}(\omega, |h|)$. It is given by

$$G_{A\sigma}(\omega, |h|) = [\omega^+ - \varepsilon_\sigma - \Gamma_\sigma(\omega, h) - \Sigma_{A\sigma}(\omega, |h|)]^{-1}, \tag{3.23}$$

where, as discussed in Section 2.3.4, $\Sigma_{A\sigma}(\omega, |h|) = \Sigma[\{G_{A\sigma'}\}]$ (with $\sigma' =\uparrow$ or $\downarrow$), is a *functional* of the time-ordered, $G_{A\uparrow}$, $G_{A\downarrow}$, and given diagrammatically by the skeleton expansion [59] shown in Fig. 2.4. Thus, the Dyson equation, eq. (3.23), allows the determination of $G_{A\sigma}(\omega, |h|)$ for a given, $\Sigma_{A\sigma}(\omega, |h|)$. In turn, the skeleton expansion, $\Sigma[\{G_{A\sigma'}\}]$, then allows the determination of $\Sigma_{A\sigma}(\omega, |h|)$ for a given $G_{A\sigma}(\omega, |h|)$. As alluded to above, the two equations (the Dyson equation and the skeleton expansion) in principle provide a self-consistency condition for the determination of the *exact* propagator, $G_{A\sigma}(\omega, |h|)$ and the *exact* self-energy, $\Sigma_{A\sigma}(\omega, |h|)$, if all possible Feynman diagrams are included.

For any finite-field $h > 0$, eq. (3.10) gives $G_\sigma(\omega, h) = G_{A\sigma}(\omega, |h|)$. By virtue of the fact that the propagators are the same, so too are the associated self-energies on comparing eqs. (3.4) and (3.23): $\Sigma_\sigma(\omega, h) \equiv \Sigma_{A\sigma}(\omega, |h|)$ (or equivalently $\Sigma[\{G_{\sigma'}\}] = \Sigma[\{G_{A\sigma'}\}]$). As mentioned above, for any $h \neq 0$, the ground-state of the system in a LM phase is no longer doubly degenerate, the magnetic field selecting (or 'picking out') either the A or B components. Even though the QPT is strictly destroyed on application of any finite field, it is appropriate to keep the explicit 'A' label in $G_{A\sigma}(\omega, |h|)$ or $\Sigma_{A\sigma}(\omega, |h|)$ for $U > U_c$; in acknowledgment that the total Green function, $G_\sigma(\omega, h)$, is discontinuous across $h = 0$ and to indicate that as $h \to 0^+$ the system possesses a permanent local moment, $m(h \to 0^+) = m_A(0) = |\tilde{\mu}|$.

3.1.4 Zero field

We now consider the zero-field limit, which is quite subtle. Setting $h = 0$ in eq. (3.10) gives the full propagator as an average of the two broken symmetry propagators (c.f. eq. (3.11))

$$G_\sigma(\omega, 0) = \tfrac{1}{2}[G_{A\sigma}(\omega, 0) + G_{A-\sigma}(\omega, 0)]. \tag{3.24}$$

Lehmann representation

In fact the precise zero-field form of eq. (3.24) may be obtained by direct consideration of the Lehmann representation of the propagator both identically at $h = 0$ and $h \to 0^\pm$. The (retarded) local impurity propagator at finite-temperature is given by [62, 63]

$$\mathcal{G}_\sigma(t, h) = -i\theta(t)\tfrac{1}{Z}\mathrm{Tr}(\mathrm{e}^{-\beta\hat{H}}\{\hat{c}_\sigma(t), \hat{c}_\sigma^\dagger(0)\}), \tag{3.25}$$

where $\mathrm{Tr}(\ldots) = \sum_n \langle\Psi_n|\ldots|\Psi_n\rangle$ and the partition function $Z = \mathrm{Tr}(\mathrm{e}^{-\beta\hat{H}})$ with $\beta = 1/T$. Upon Fourier transformation, eq. (2.4a), a simple argument (involving many of the same steps as Section 2.1), shows that the Lehmann representation of this quantity is given by

$$\mathcal{G}_\sigma(\omega, h) = \frac{1}{\sum_n \mathrm{e}^{-\beta[E_n - E_0]}} \sum_{n,m} \mathrm{e}^{-\beta[E_n - E_0]} \frac{(1 + \mathrm{e}^{-\beta[E_m - E_n]})|\langle n|\hat{c}_\sigma|m\rangle|^2}{\omega + i\eta - [E_m - E_n]}, \tag{3.26}$$

where $|n\rangle \equiv |\Psi_n\rangle$, such that $\hat{H}|n\rangle = E_n|n\rangle$ and therefore E_0 is the ground-state energy. Taking the $T \to 0$ limit (i.e. $\beta \to \infty$) on this equation, such that $\mathcal{G}_\sigma(\omega, h) \to$

$G_\sigma(\omega, h)$, we obtain[4]

$$G_\sigma(\omega,h) = \frac{1}{g_0} \sum_{\substack{\alpha\in\{A,B\} \\ m\notin\{A,B\}}} \left(\frac{|\langle m|\hat{c}_\sigma^\dagger|\alpha\rangle|^2}{\omega^+ - [E_m - E_0]} + \frac{|\langle m|\hat{c}_\sigma|\alpha\rangle|^2}{\omega^+ + [E_m - E_0]} \right) + \frac{2}{g_0} \sum_{\substack{\alpha\in\{A,B\} \\ \beta\in\{A,B\}}} \frac{|\langle\alpha|\hat{c}_\sigma|\beta\rangle|^2}{\omega + i\eta}, \tag{3.27}$$

where g_0 is the ground-state degeneracy, and α (and β) run over the degenerate states of the ground-state, i.e. the state $|\alpha\rangle$ has energy $E_\alpha \equiv E_0$. Thus, the first term in eq. (3.27) involves excitations above the ground-state manifold (with $E_m \neq E_0$), whereas the second term involves (zero-energy - $E_A = E_B = E_0$) excitations between the degenerate states of the ground-state.

In a LM phase (at zero-temperature and precisely at $h = 0$) there is an 'unquenched' SU(2) spin degree of freedom in the entire system. As a consequence, the A and B (degenerate) states are eigenstates of the overall z-component of spin operator $\hat{S}_\mathrm{z} = \hat{s}_\mathrm{z} + \sum_\mathbf{k} \hat{s}_\mathbf{kz}$, with eigenvalues of $\pm\frac{1}{2}$ respectively. The purely *local* operator, $\hat{c}_\sigma$, only changes the ground-state expectation value, $\langle\hat{S}_\mathrm{z}\rangle$, by a $\frac{1}{2}$. Since the A and B ground-states differ in $\langle\hat{S}_\mathrm{z}\rangle$ by 1, the matrix elements, $\langle\alpha|\hat{c}_\sigma|\beta\rangle$ (where $\alpha, \beta \in \{A, B\}$), must vanish.[5] Hence, for the LM phase where $g_0 = 2$, the second term in eq. (3.27) vanishes. The first term becomes

$$G_\sigma(\omega, h=0) = \frac{1}{2} \sum_{\substack{\alpha\in\{A,B\} \\ m\notin\{A,B\}}} \left(\frac{|\langle m|\hat{c}_\sigma^\dagger|\alpha\rangle|^2}{\omega^+ - [E_m - E_0]} + \frac{|\langle m|\hat{c}_\sigma|\alpha\rangle|^2}{\omega^+ + [E_m - E_0]} \right), \tag{3.28}$$

Alternatively, if $h = 0^+$, the ground-state degeneracy is lifted ($g_0 = 1$) and the 'A' state is picked out of the ground-state manifold. Eq. (3.27) then reduces to

$$G_\sigma(\omega, 0^+) \equiv G_{A\sigma}(\omega, 0) = \sum_{m\notin\{A,B\}} \left(\frac{|\langle m|\hat{c}_\sigma^\dagger|A\rangle|^2}{\omega^+ - [E_m - E_0]} + \frac{|\langle m|\hat{c}_\sigma|A\rangle|^2}{\omega^+ + [E_m - E_0]} \right), \tag{3.29}$$

and likewise obtaining a similar relation on taking $h \to 0^-$ for the 'B' propagator, $G_\sigma(\omega, 0^-) \equiv G_{B\sigma}(\omega, 0)$. Thus, on comparison of eq. (3.28) with eq. (3.29), we see that eq. (3.24) is indeed satisfied at zero-field.

Another important point should be made here before we proceed. The fact that the two equations, eq. (3.28) and eq. (3.29), are distinct reflects the order of limits that have been taken in order to obtain them. In the first instance to obtain eq. (3.28) from the finite-temperature propagator, eq. (3.26), we explicitly

[4] Assuming the degenerate ground-state is separated from the excited states by a finite energy gap.

[5] Since $[\hat{c}_\sigma, \hat{S}_\mathrm{z}] = \frac{\sigma}{2}\hat{c}_\sigma$, the matrix element $\sigma\langle A|\hat{c}_\sigma|A\rangle = 2[\langle A|\hat{c}_\sigma\hat{S}_\mathrm{z}|A\rangle - \langle A|\hat{S}_\mathrm{z}\hat{c}_\sigma|A\rangle]$. Allowing $\hat{S}_\mathrm{z}$ to act on the states, it immediately follows that $\langle A|\hat{c}_\sigma|A\rangle = 0$. Similar arguments show that the matrix elements $\langle B|\hat{c}_\sigma|B\rangle$, $\langle A|\hat{c}_\sigma|B\rangle$, $\langle B|\hat{c}_\sigma|A\rangle$ also vanish.

take the limit $h \to 0^+$ *before* $T \to 0$, such that we continuously access the doubly-degenerate LM phase propagator, $G_\sigma(\omega, h = 0)$ (with $m(h = 0) = 0$). By contrast to obtain eq. (3.29), we consider taking the opposite order of limits, i.e. $T \to 0$ *before* $h \to 0^+$, thus generating the 'A' state propagator, $G_{A\sigma}(\omega, 0)$ (with $m_A(0) = +|\tilde{\mu}|$). In consequence, the limits $T \to 0$ and $h \to 0^\pm$ fundamentally *do not commute* in a LM phase. (This underlying behaviour is analogous to what happens for a free-spin (see Appendix E).) By contrast, in a SC phase where the ground-state is non-degenerate, it is not difficult to see from the structure of the above equations, that we obtain the same form for $G_\sigma(\omega, h)$ regardless of the order of limits taken.

Zero-field self-energies

The full interacting (spin-independent) propagator at zero-field, $G_\sigma(\omega, 0) = G(\omega, 0)$, is expressed via eq. (3.24), in terms of the so-called *two-self-energy* (TSE) description. Each of the broken-symmetry propagators, $G_{A\sigma}(\omega, 0)$, $G_{A-\sigma}(\omega, 0) \equiv G_{B\sigma}(\omega, 0)$, are written in terms of two distinct self energies $\Sigma_{A\sigma}(\omega, 0)$, $\Sigma_{A-\sigma}(\omega, 0) \equiv \Sigma_{B\sigma}(\omega, 0)$ via their Dyson equations, eq. (3.23). However, $G_\sigma(\omega, 0)$ itself may be expressed via its own unique Dyson equation in terms of a single self-energy (SSE), $\Sigma_\sigma(\omega, 0)$[6]. The exact relation between the SSE, $\Sigma(\omega, 0) \equiv \Sigma_\sigma(\omega, 0)$ $(= \Sigma_{-\sigma}(\omega, 0))$ and the TSEs, $\Sigma_{A\sigma}(\omega, 0)$, $\Sigma_{A-\sigma}(\omega, 0)$, may be obtained by inserting the three distinct Dyson equations into eq. (3.24). We find

$$\Sigma(\omega, 0) = \tfrac{1}{2}[\Sigma_{A\sigma}(\omega, 0) + \Sigma_{A-\sigma}(\omega, 0)] + \frac{[\frac{1}{2}(\Sigma_{A\sigma}(\omega, 0) - \Sigma_{A-\sigma}(\omega, 0))]^2}{g^{-1}(\omega, 0) - \frac{1}{2}[\Sigma_{A\sigma}(\omega, 0) + \Sigma_{A-\sigma}(\omega, 0)]}, \tag{3.30}$$

where $g^{-1}(\omega, 0) = [\omega^+ - \varepsilon - \Gamma(\omega)]$, is the non-interacting Green function, and the hybridization function, $\Gamma(\omega) = \Gamma_\sigma(\omega, 0)$ at zero-field.

It is the self-energies, $\Sigma_{A\uparrow}$, $\Sigma_{A\downarrow}$, whether at finite, or zero field that are determined from the diagrammatic perturbation theory laid out in Chapter 2. The self-energy, $\Sigma_{A\sigma}(\omega, 0) \equiv \Sigma[G_{A\uparrow}, G_{A\downarrow}]$ is a functional of the propagators and may be obtained via the skeleton expansion. In a LM phase, the single self-energy, $\Sigma_\sigma(\omega, 0) = \Sigma(\omega, 0)$, is then calculated subsequently via eq. (3.30) from the known TSEs, $\Sigma_{A\sigma}(\omega, h)$, and therefore is a derivative quantity.

Calculating the self-energies

As alluded to above, it is the SSE, $\Sigma_\sigma(\omega, 0)$, that is usually calculated at zero-field, even in a LM phase. As stated in Section 2.3, for any field (including $h = 0$), $\Sigma_\sigma(\omega, h)$ is directly computable via the ratio $F_\sigma(\omega, h)/G_\sigma(\omega, h)$ [98] from numerically exact

[6]This is the quantity that is usually referred to as just 'the self-energy', and may be calculated directly from the exact numerics of NRG [98].

NRG calculations ($F_\sigma(\omega,h) = \langle\langle[\hat{c}_\sigma, \hat{H}_I]; c_\sigma^\dagger\rangle\rangle$, with $\hat{H}_I$ the interaction part of the Hamiltonian).[7] By including explicit A labels at finite field, the 'A' type self-energy is obtained by the ratio

$$\Sigma_\sigma(\omega,h) \equiv \Sigma_{A\sigma}(\omega,|h|) = \frac{F_{A\sigma}(\omega,|h|)}{G_{A\sigma}(\omega,|h|)}. \tag{3.31a}$$

In a LM phase the full-interacting propagator, $G_\sigma(\omega,0)$, may be expressed as a simple average of the broken-symmetry functions via eq. (3.24). Similarly, we assume that the correlator, $F_\sigma(\omega,0) = \frac{1}{2}[F_{A\sigma}(\omega,0) + F_{A-\sigma}(\omega,0)]$ (with $F_{A-\sigma}(\omega,|h|) = F_{B\sigma}(\omega,|h|)$). Hence, we may express the single self-energy as

$$\Sigma_\sigma = \frac{F_\sigma}{G_\sigma} = \frac{\frac{1}{2}[F_{A\sigma} + F_{A-\sigma}]}{\frac{1}{2}[G_{A\sigma} + G_{A-\sigma}]}, \tag{3.31b}$$

$$= \frac{\frac{1}{2}[G_{A\sigma} + G_{A-\sigma}][\Sigma_{A\sigma} + \Sigma_{A-\sigma}] + \frac{1}{2}[G_{A\sigma} - G_{A-\sigma}][\Sigma_{A\sigma} - \Sigma_{A-\sigma}]}{G_{A\sigma} + G_{A-\sigma}}, \tag{3.31c}$$

$$= \tfrac{1}{2}(\Sigma_{A\sigma} + \Sigma_{A-\sigma}) + \tfrac{1}{2}\left[\frac{G_{A\sigma} - G_{A-\sigma}}{G_{A\sigma} + G_{A-\sigma}}\right](\Sigma_{A\sigma} - \Sigma_{A-\sigma}). \tag{3.31d}$$

(We have suppressed the arguments here for simplicity: all functions are at $(\omega, h = 0)$.) The term in square brackets may be written as

$$\left[\frac{G_{A\sigma} - G_{A-\sigma}}{G_{A\sigma} + G_{A-\sigma}}\right] = \left[\frac{G_{A-\sigma}^{-1} - G_{A\sigma}^{-1}}{G_{A\sigma}^{-1} + G_{A-\sigma}^{-1}}\right] = \left[\frac{\frac{1}{2}[\Sigma_{A\sigma} - \Sigma_{A-\sigma}]}{g^{-1} + \frac{1}{2}[\Sigma_{A\sigma} + \Sigma_{A-\sigma}]}\right] \tag{3.31e}$$

where on obtaining eq. (3.31c), we have used eq. (3.31a) and $G_{A\sigma}$, $G_{A-\sigma}$ have been expressed in terms of their corresponding Dyson equations to yield eq. (3.31e). The non-interacting propagator is given simply by $g^{-1} \equiv g^{-1}(\omega,0) = [\omega^+ - \varepsilon - \Gamma(\omega)]$. On substitution of eq. (3.31e) into eq. (3.31d), the relation, eq. (3.30), for the single-self-energy, $\Sigma_\sigma(\omega,0)$, in terms of the TSEs is directly obtained (and everything is consistent).

Using NRG, both the $F_{\alpha\sigma}(\omega,h)$, $G_{\alpha\sigma}(\omega,h)$ $[\alpha = A,B]$ correlation functions can be calculated for a given temperature, T. Thus, by first taking the $T \to 0$ limit, followed by the $h \to 0^\pm$ limit, the zero-field 'A' or 'B' functions can be 'picked out' and the $F_{\alpha\sigma}(\omega,0)$, $G_{\alpha\sigma}(\omega,0)$ obtained (with $\alpha = A,B$). In contrast, the $h \to 0^\pm$ limit can be taken before the $T \to 0$ limit. This second process yields the usual zero-field (spin-independent) correlators, $G_\sigma(\omega,0)$ and $F_\sigma(\omega,0)$. The resulting self-energies in both cases can then be calculated via $\Sigma_\sigma = F_\sigma/G_\sigma$. For the pseudogap AIM, which NRG results are presented for in the next chapter, we have calculated both the TSEs and SSEs in this way and have confirmed that both eqs. (3.30, 3.31b) hold.

[7] For the specifics of the NRG procedure we refer the reader to Appendix C.

To conclude this section, we make the following salient point. The focus here has naturally been on the doubly-degenerate LM phase. However, all of the above equations apply equally to the Fermi liquid SC phase if the A and B labels are simply dropped, and the local moment $|\tilde{\mu}| = 0$. In the SC phase the single and two self-energies become coincident and the local magnetization $m(h)$ is continuous across $h = 0$.

3.2 Excess Quantities

3.2.1 Excess density of states

Having discussed the local properties of the system, we now look to establish the *excess* quantities. An 'excess' quantity is defined as the difference in a particular physical property of the *entire* system calculated with and without the impurity present.

The excess density of states is defined by

$$\Delta\rho_{\mathrm{imp},\sigma}(\omega, h) = \rho_\sigma(\omega, h) - \rho_{0,\sigma}(\omega, h). \tag{3.32}$$

As one would expect, $\rho_\sigma(\omega, h)$, simply involves a contribution from both the impurity Green function, $G_\sigma(\omega, h)$ and the conduction band Green function $G_{\mathbf{kk};\sigma}(\omega, h)$

$$\rho_\sigma(\omega, h) = -\frac{1}{\pi}\mathrm{Im}\bigg[\sum_{\mathbf{k}} G_{\mathbf{kk};\sigma}(\omega, h) + G_\sigma(\omega, h)\bigg]. \tag{3.33}$$

In contrast, the density of states of the system in the absence of the impurity is just the purely diagonal function

$$\rho_{0,\sigma}(\omega, h) = -\frac{1}{\pi}\mathrm{Im}\sum_{\mathbf{k}} \frac{1}{\omega^+ - \epsilon_{\mathbf{k}\sigma}} = \delta(\omega - \epsilon_{\mathbf{k}\sigma}), \tag{3.34}$$

with $\epsilon_{\mathbf{k}\sigma} = \epsilon_{\mathbf{k}} - \sigma h$ (where h is a uniform global field in this instance). From the equations of motion methods discussed in Chapter 2, we use eq. (2.34) in order to express $G_{\mathbf{kk};\sigma}(\omega, h)$ in terms of the impurity propagator

$$G_{\mathbf{kk};\sigma}(\omega, h) = \sum_{\mathbf{k}} \frac{1}{\omega^+ - \epsilon_{\mathbf{k}\sigma}} + \sum_{\mathbf{k}\sigma} \frac{|V_{i\mathbf{k}}|^2}{(\omega^+ - \epsilon_{\mathbf{k}\sigma})^2} G_\sigma(\omega, h). \tag{3.35}$$

Inserting this equation into eq. (3.33), and then expressing the excess density of

states via eq. (3.32), we may relate it to the single-particle propagator via

$$\Delta\rho_{\mathrm{imp},\sigma}(\omega,h) = -\frac{1}{\pi}\mathrm{Im}\left[1+\sum_{\mathbf{k}}\frac{|V_{i\mathbf{k}}|^2}{(\omega^+-\epsilon_{\mathbf{k}})^2}\right]G_\sigma(\omega,h) \tag{3.36a}$$

$$= -\frac{1}{\pi}\mathrm{Im}\left[1-\frac{\partial\Gamma_\sigma(\omega,h)}{\partial\omega}\right]G_\sigma(\omega,h) \tag{3.36b}$$

where we have used the definition of the hybridization function, eq. (2.37). For the infinitely wide 'flat band' model, where the impurity is coupled to a metallic conduction band, $\Gamma_\sigma(\omega,h)=\Gamma_0=\rho_0\pi V^2$, and therefore the derivative $\partial\Gamma_\sigma(\omega,h)/\partial\omega=0$. In this case $\Delta\rho_{\mathrm{imp},\sigma}(\omega,h)$ just reduces to the local impurity spectrum, $D_\sigma(\omega,h) = -\frac{1}{\pi}\mathrm{Im}G_\sigma(\omega,h)$, such that the local and excess quantities are coincident.

3.2.2 Excess charge and magnetization

The excess charge, $n_{\mathrm{imp},\sigma}(h)$ is defined as the difference in the number of σ-spin electrons in the entire system with and without the impurity present. It is given in familiar notation as

$$n_{\mathrm{imp},\sigma}(h) = \langle\sum_{\mathbf{k}}\hat{n}_{\mathbf{k}\sigma}+\hat{n}_\sigma\rangle - \langle\sum_{\mathbf{k}}\hat{n}_{\mathbf{k}\sigma}\rangle_0, \tag{3.37}$$

where $\langle\ldots\rangle_0$ denotes the average over the ground state in the absence of the impurity. It is easily shown from an analogous argument to that leading to eq. (2.12), that the excess charge, $n_{\mathrm{imp},\sigma}(h)$, is obtained by integrating the excess density of states up to the Fermi level [2, 99]

$$n_{\mathrm{imp},\sigma}(h) = \int_{-\infty}^{0}\mathrm{d}\omega\ \Delta\rho_{\mathrm{imp},\sigma}(\omega,h). \tag{3.38}$$

The corresponding *excess* charge and magnetization are then simply given by (c.f. eq. (3.3))

$$n_{\mathrm{imp}}(h) = \sum_\sigma n_{\mathrm{imp},\sigma}(h), \tag{3.39a}$$

$$m_{\mathrm{imp}}(h) = \sum_\sigma \sigma n_{\mathrm{imp},\sigma}(h), \tag{3.39b}$$

respectively. In a LM phase the full Green function is given in terms of the broken symmetry propagators by eq. (3.10). By inserting this form into eq. (3.36b), we find that $\Delta\rho_{\mathrm{imp},\sigma}(\omega,h)$ has exactly the same structure as the local propagators

$$\Delta\rho_{\mathrm{imp},\sigma}(\omega,h) = \theta(h)\Delta\rho_{\mathrm{imp},A\sigma}(\omega,|h|)+\theta(-h)\Delta\rho_{\mathrm{imp},B\sigma}(\omega,-|h|), \tag{3.40}$$

where $\Delta\rho_{\mathrm{imp},\alpha\sigma}(\omega,|h|) = (1-\partial\Gamma_\sigma(\omega,h)/\partial\omega)G_{\alpha\sigma}(\omega,|h|)$, $[\alpha = A,B]$. By using the symmetry of eq. (3.9) we obtain

$$\Delta\rho_{\mathrm{imp},B\sigma}(\omega,-|h|) = \Delta\rho_{\mathrm{imp},A-\sigma}(\omega,|h|), \tag{3.41}$$

such that once again, only the 'A' functions ever need to be considered. The 'excess' quantities thus have exactly the same form as for their purely local counterparts discussed in the last section, as we now summarize. Together eqs. (3.38, 3.40, 3.41) imply that the excess charge can also be written in the form

$$n_{\mathrm{imp},\sigma}(h) = \theta(h)n_{\mathrm{imp},A\sigma}(|h|) + \theta(-h)n_{\mathrm{imp},A-\sigma}(-|h|). \tag{3.42}$$

Using eq. (3.42), the total excess charge, eq. (3.39), can then be expressed solely in terms of the A-type excess charge

$$n_{\mathrm{imp}}(h) = \sum_\sigma n_{\mathrm{imp},\sigma}(h) = \sum_\sigma n_{\mathrm{imp},A\sigma}(|h|) = n_{\mathrm{imp}}(-h), \tag{3.43}$$

which is also shown to be an even function of h. The excess magnetization by contrast is given by

$$m_{\mathrm{imp}}(h) = \sum_\sigma \sigma\, n_{\mathrm{imp},\sigma}(h) = [\theta(h)-\theta(-h)]m_{\mathrm{imp},A}(|h|) = -m_{\mathrm{imp}}(-h), \tag{3.44}$$

and therefore, in analogy with $m(h)$, is both an odd function of h and discontinuous across $h=0$. $m_{\mathrm{imp},A}(|h|)$ may also be expressed in terms of the corresponding excess density of states by

$$m_{\mathrm{imp},A}(|h|) = \sum_\sigma \sigma n_{\mathrm{imp},A\sigma}(|h|) = \sum_\sigma \sigma \int_{-\infty}^{0} \mathrm{d}\omega\ \Delta\rho_{\mathrm{imp},A\sigma}(\omega,|h|). \tag{3.45}$$

As stated above, if the conduction band that the single-impurity is coupled to is purely metallic with a flat density of states, such that $\Gamma^I_\sigma(\omega) = \Gamma_0$, then the local and excess quantities are coincident. However, for a general ω-dependent host density of states this is generally not the case, as we shall see in the next chapter explicitly for the pseudogap AIM.

3.3 Phase shifts and the Friedel-Luttinger sum rule

In this section we consider the so-called Friedel-Luttinger sum rule [96], which in conventional Fermi liquid theory [2] relates the static scattering phase shift, $\delta_\sigma(h)$ to the excess charge, $n_{\mathrm{imp};\sigma}(h)$ (discussed above) and a 'Luttinger integral', denoted as $I_{L_\sigma}(h)$, of the form of eq. (2.52d). In this section we derive a Friedel-Luttinger sum

rule, not only for the well known [2] Fermi liquid case (with $U < U_c$), but also for the non-Fermi liquid LM phase (with $U > U_c$). As we shall see below, by considering a phase shift, $\delta_{A\sigma}(|h|)$, in terms of the broken-symmetry propagators, $G_{A\sigma}(\omega, |h|)$, we obtain analogs of the usual Fermi liquid relations, but for $U > U_c$. In addition, we also show (with the help of Appendix A) that the phase shifts, $\delta_\sigma(h)$, $\delta_{A\sigma}(|h|)$, may be determined in terms of the so-called renormalized levels, which embody the interaction induced renormalization of the bare level energy, ε.

The (s-wave) scattering phase shift is defined for any-h in terms of the argument of the Green function, $G_\sigma(\omega, h)$ [2], i.e.

$$\begin{aligned}\delta_\sigma(h) = [\delta_\sigma(\omega,h)]_{\omega=-\infty}^{\omega=0} &= [\arg(G_\sigma(\omega,h))]_{-\infty}^{0} \\ &= [\mathrm{Im}\ln G_\sigma(\omega,h)]_{-\infty}^{0} = \mathrm{Im}\ln G_\sigma(0,h) + \pi \end{aligned} \tag{3.46}$$

where $\mathrm{Im}\ln G_\sigma(-\infty, h) = -\pi$ follows from eq. (2.50)[8]. Equivalently we may write $\delta_\sigma(h)$ as

$$\delta_\sigma(h) = \int_{-\infty}^{0} \mathrm{d}\omega \frac{\partial \delta_\sigma(\omega,h)}{\partial\omega} = \mathrm{Im}\int_{-\infty}^{0} \mathrm{d}\omega \frac{\partial}{\partial\omega}\ln G_\sigma(\omega,h). \tag{3.47}$$

Where on differentiating eq. (3.23) with respect to ω we obtain

$$\frac{\partial}{\partial\omega}\ln G_\sigma(\omega,h) = -G_\sigma(\omega,h)\left[1 - \frac{\partial\Gamma_\sigma(\omega,h)}{\partial\omega} - \frac{\partial\Sigma_\sigma(\omega,h)}{\partial\omega}\right]. \tag{3.48}$$

Inserting this equation into eq. (3.47), the phase shift becomes

$$\begin{aligned}\delta_\sigma(h) &= -\mathrm{Im}\int_{-\infty}^{0} \mathrm{d}\omega\ G_\sigma(\omega,h)\left[1 - \frac{\partial\Gamma_\sigma(\omega,h)}{\partial\omega}\right] && \text{(3.49a)} \\ &\qquad + \mathrm{Im}\int_{-\infty}^{0} \mathrm{d}\omega\ G_\sigma(\omega,h)\frac{\partial\Sigma_\sigma(\omega,h)}{\partial\omega} \\ &= \pi n_{\mathrm{imp};\sigma}(h) + I_{L_\sigma}(h) && \text{(3.49b)}\end{aligned}$$

where we have used eq. (3.36b) to recognise that the integrand of the first integral is $\pi \times \Delta\rho_{\mathrm{imp};\sigma}(\omega, h)$ and in consequence use eq. (3.38) to express it in terms of the excess charge, $n_{\mathrm{imp},\sigma}(h)$. The so-called Luttinger integral is defined from eq. (3.49) (c.f. eq. (2.52d)) as

$$I_{L_\sigma}(h) = I_{L_{-\sigma}}(-h) = \mathrm{Im}\int_{-\infty}^{0} \mathrm{d}\omega\ G_\sigma(\omega,h)\ \frac{\partial\Sigma_\sigma(\omega,h)}{\partial\omega}. \tag{3.50}$$

We remind the reader that all functions here are retarded, such that the hybridiza-

[8]The definition we use for the phase shift is shifted by π from the common definition: $\delta_\sigma(h) = \mathrm{Im}\ln G_\sigma(0,h)$. For details of why we do this, we refer the reader to Appendix A.

tion function and self-energy have the same form as the propagator, $G_\sigma(\omega, h) = G^R_\sigma(\omega, h) - i\pi D_\sigma(\omega, h)$, i.e.

$$\Gamma_\sigma(\omega, h) = \Gamma^R_\sigma(\omega, h) - i\Gamma^I_\sigma(\omega, h), \tag{3.51a}$$

$$\Sigma_\sigma(\omega, h) = \Sigma^R_{A\sigma}(\omega, h) - i\Sigma^I_\sigma(\omega, h), \tag{3.51b}$$

with $D_\sigma(\omega, h)$, $\Gamma_I(\omega, h)$, $\Sigma^I_\sigma(\omega, h) \geq 0$ for all ω. By direct consideration of eq. (3.46), the scattering phase shift $\delta_\sigma(h)$ may also be related (by a straightforward calculation detailed in Appendix A) to the impurity renormalized level, $\varepsilon^*_\sigma(h)$, via

$$\delta_\sigma(h) = \pi n_{\mathrm{imp};\sigma}(h) + I_{L_\sigma}(h) = \frac{\pi}{2} - \tan^{-1}\left[\frac{\varepsilon^*_\sigma(h)}{\eta + \Gamma^I_\sigma(0, h) + \Sigma^I_\sigma(0, h)}\right] \tag{3.52}$$

where the $\tan^{-1}(\alpha)$ is defined in the interval $[-\frac{\pi}{2}, \frac{\pi}{2}]$. The renormalized level, $\varepsilon^*_\sigma(h)$ is given by

$$\varepsilon^*_\sigma(h) = \varepsilon - \sigma h + \Gamma^R_\sigma(0, h) + \Sigma^R_\sigma(0, h). \tag{3.53}$$

As discussed in Section 2.4, in a Fermi liquid SC phase (such that at zero-field and $U < U_c$), the perturbation expansion shown in Fig. 2.1 holds to all orders in the interaction, U. It is then the time-ordered self-energy $\Sigma^t_\sigma(\omega, h) = \Sigma^R_\sigma(\omega, h) - i\,\mathrm{sgn}(\omega)\Sigma^I_\sigma(\omega, h)$, that is obtained from functional differentiation of the Luttinger-Ward functional, Φ_{LW}, via eq. (2.51). By contrast, in a LM phase for $U > U_c$ precisely at $h = 0$, the system in a (SSE) conventional framework is fundamentally not perturbatively connected to the non-interacting limit. Hence the SSE, $\Sigma_\sigma(\omega, 0)$, is not expressible in terms of a functional derivative of Φ_{LW}. However, we may proceed in direct analogue to eqs. (3.46-3.50) to derive similar expressions for a static phase shift, $\delta_{A\sigma}(|h|)$, defined in terms of the broken-symmetry propagators, $G_{A\sigma}(\omega, |h|)$, eq. (3.23). The 'A' type phase shift is then written as

$$\delta_{A\sigma}(|h|) \equiv \delta_{B-\sigma}(-|h|) = \pi n_{\mathrm{imp};A\sigma}(|h|) + I_{L_{A\sigma}}(|h|) \tag{3.54}$$

where $n_{\mathrm{imp};A\sigma}$ is the excess charge on the 'A' type state as defined above and obtained from eq. (3.38) with $\Delta\rho_{\mathrm{imp};\sigma}(\omega, h)$ replaced by $\Delta\rho_{\mathrm{imp};A\sigma}(\omega, |h|)$. Moreover, $I_{L_{A\sigma}}(|h|)$ is a Luttinger integral, given by

$$I_{L_{A\sigma}}(|h|) = I_{L_{B-\sigma}}(-|h|) = \mathrm{Im}\int_{-\infty}^{0} \mathrm{d}\omega\; G_{A\sigma}(\omega, |h|)\,\frac{\partial\Sigma_{A\sigma}(\omega, |h|)}{\partial\omega}. \tag{3.55}$$

The equivalent (broken-symmetry) relation to eq. (3.52) is expressed as

$$\delta_{A\sigma}(|h|) = \frac{\pi}{2} - \tan^{-1}\left[\frac{\varepsilon^*_{A\sigma}(h)}{\eta + \Gamma^I_\sigma(0, h) + \Sigma^I_{A\sigma}(0, |h|)}\right] \tag{3.56}$$

with the 'A' type renormalized level being expressed in terms of $\Sigma_{A\sigma}(0,|h|)$ via

$$\varepsilon^*_{A\sigma}(|h|) = \varepsilon - \sigma|h| + \Gamma^R_\sigma(0,|h|) + \Sigma^R_{A\sigma}(0,|h|). \tag{3.57}$$

where on dropping the A-subscripts we re-obtain the SC phase results above. We emphasize that for $U > U_c$, the zero-field LM phase is separated from the SC phase by a quantum critical point (QCP) at $U = U_c$ (as shown in Fig. 1.4). However, the key point is that in a LM phase, it is the self-energy, $\Sigma^t_{A\sigma}(\omega,|h|)$ that is a functional of the (broken-symmetry) propagators given as the functional derivative of the LW functional, i.e. $\Sigma^t_{A\sigma}(\omega,|h|) = \Sigma[\{G^t_{A\sigma'}\}] = \delta\Phi_{LW}/\delta G^t_{A\sigma}(\omega,|h|)$. Moreover, for $U > U_c$, Φ_{LW} is precisely the same functional of $\{G^t_{A\sigma}\}$, as it is of $\{G^t_\sigma\}$ for $U < U_c$.

As is shown explicitly in Appendix A, the static phase shifts also determine the local impurity spectrum at $\omega = 0$. For the broken-symmetry functions we obtain

$$\pi[\Gamma^I_\sigma(0,|h|) + \Sigma^I_{A\sigma}(0,|h|)]D_{A\sigma}(0,|h|) = \sin^2(\delta_{A\sigma}(|h|)) \tag{3.58}$$

for $U > U_c$, and likewise for $U < U_c$ on dropping the explicit 'A' labels. This equation applies to the generic case where $\delta_{A\sigma}(\omega,|h|)$ is continuous across the Fermi level. If by contrast it is discontinuous across $\omega = 0$, of the form $\delta_{A\sigma}(\omega,|h|) \overset{\omega\to 0^\pm}{\sim} \delta_{A\sigma}(|h|) \pm \Delta$, then (see Appendix A) eq. (3.58) generalizes to

$$\lim_{\omega\to 0^\pm} \left(\pi[\Gamma^I_\sigma(\omega,|h|) + \Sigma^I_{A\sigma}(\omega,|h|)]D_{A\sigma}(\omega,|h|)\right) = \sin^2(\delta_{A\sigma}(|h|) \pm \Delta). \tag{3.59}$$

In practice this case is only relevant to the ph symmetric PAIM at $h = 0$, as we shall see in the next chapter.

3.4 Luttinger Integrals

We now explicitly consider the Luttinger integrals appearing in the analysis of the phase shift above (eq. (3.50) for $U < U_c$ and eq. (3.55) for $U > U_c$). Here we briefly sketch the general argument [59] for the vanishing of the Luttinger integral, $I_{L_{A\sigma}}(h)$, for any phase where the self-energy can be expressed in terms of the skeleton expansion as a functional of the propagators. Obviously this applies to Fermi liquid phases, explicitly considered by Luttinger, where the perturbation expansion for the propagator (eq. (2.27)) is valid about the non-interacting limit (and the 'A' subscript may be dropped). Here we show that it also holds for a LM phase ($U > U_c$) within a TSE description.

As a simple example we firstly consider the second-order closed linked skeleton diagram contribution to the Luttinger-Ward functional (in terms of A-type broken symmetry propagators - valid for $h \geq 0$), $\Phi_{LW} \equiv \Phi_{LW}[\{G^t_{A\sigma}\}]$, shown in Fig. 3.3.

From the diagrammatic rules laid out in ref [63], the second-order contribution to Φ_{LW} can be expressed as (where we neglect real-numerical factors that are unimportant for the discussion that follows)

$$\Phi^{(2)}_{LW}[\{G_{A\sigma'}\}] \propto \int \ldots \int_{-\infty}^{+\infty} \prod_{i=1}^{4} \mathrm{d}\omega_i G_{A\sigma}(\omega_1) G_{A\sigma}(\omega_2) G_{A-\sigma}(\omega_3) G_{A-\sigma}(\omega_4) \qquad (3.60)$$
$$\times [\theta(\omega_1)\theta(-\omega_2)\theta(\omega_3)\theta(-\omega_4)] \times \delta(\omega_1 + \omega_3 - [\omega_2 + \omega_4]).$$

where the propagators appearing are time-ordered functions, $G_{A\sigma}(\omega) \equiv G^{t}_{A\sigma}(\omega, |h|)$, and we suppress the explicit field-dependence (although the analysis holds generally for both $h = 0$ and $h \neq 0$). Within eq. (3.60), a step function $\theta(\omega_i)$ is associated with every ascending (particle) line and a $\theta(-\omega_i)$ with descending (hole) lines, such that particles (holes) lie above (below) the Fermi level. The delta function constraint reflects the fact that all frequencies must be conserved at each vertex of a diagram, i.e. at every vertex there is an associated factor $\delta(\omega_{in} - \omega_{out})$. Finally, all internal frequencies are integrated over such that, Φ_{LW} is independent of ω.

As a consequence of the fact that in general Φ_{LW} is a functional of the propagators obtained by the expansion shown in Fig. 2.5, we may consider a variation $\delta\Phi_{LW}$, coming from a variation of the σ-spin propagators, $\delta G_{A\sigma}(\omega)$

$$\delta\Phi_{LW} = \int_{-\infty}^{\infty} \frac{\mathrm{d}\omega}{2\pi} \frac{\delta\Phi_{LW}}{\delta G_{A\sigma}(\omega)} \delta G_{A\sigma}(\omega), \qquad (3.61)$$

which is just the chain rule for functional differentiation. Moreover, a variation in a σ-spin propagator, $\delta G_{A\sigma}(\omega_i)$, may be obtained by shifting its internal frequency from $\omega_i \to \omega_i + \delta\omega$:

$$\delta G_{A\sigma}(\omega_i) = [G_{A\sigma}(\omega_i + \delta\omega) - G_{A\sigma}(\omega_i)] \equiv \delta\omega(\partial G_{A\sigma}(\omega_i)/\partial\omega_i) \qquad (3.62)$$

Inserting this equation into eq. (3.61), we obtain

$$\delta\Phi_{LW} = \left[\int_{-\infty}^{\infty} \frac{\mathrm{d}\omega}{2\pi} \frac{\delta\Phi_{LW}}{\delta G_{A\sigma}(\omega)} \frac{\partial G_{A\sigma}(\omega)}{\partial\omega} \right] \delta\omega, \qquad (3.63)$$

for arbitrary $\delta\omega$.

Now specifically returning to the second-order diagram given by eq. (3.60), we consider a variation in the internal frequencies $\omega_i \to \omega_i + \delta\omega$ of the σ-spin propagators

(here $i = 1, 2$):

$$\Phi^{(2)}_{LW} + \delta\Phi^{(2)}_{LW} \propto \int \ldots \int_{-\infty}^{\infty} \prod_{i=1}^{4} \mathrm{d}\omega_i G_{A\sigma}(\omega_1 + \delta\omega) G_{A\sigma}(\omega_2 + \delta\omega) G_{A-\sigma}(\omega_3) G_{A-\sigma}(\omega_4) \times [\theta(\omega_1 + \delta\omega)\theta(-[\omega_2 + \delta\omega])\theta(\omega_3)\theta(-\omega_4)] \times \delta(\omega_1 + \omega_3 - [\omega_2 + \omega_4]) \tag{3.64}$$

where $\delta\Phi^{(2)}_{LW}$ is the additional contribution to the second-order diagram coming from the frequency shifts in the propagators. Since frequency (and spin) are conserved at each vertex in the diagram, the delta function constraint remains unchanged by this uniform frequency shift. Thus on making the simple variable change $\omega_i + \delta\omega = \omega'_i$ for both $i = 1, 2$, we find

$$\Phi^{(2)}_{LW} + \delta\Phi^{(2)}_{LW} \propto \int \ldots \int_{-\infty}^{\infty} \mathrm{d}\omega'_1 \, \mathrm{d}\omega'_2 \, \mathrm{d}\omega_3 \, \mathrm{d}\omega_4 G_{A\sigma}(\omega'_1) G_{A\sigma}(\omega'_2) G_{A-\sigma}(\omega_3) G_{A-\sigma}(\omega_4) \times [\theta(\omega'_1)\theta(-\omega'_2)\theta(\omega_3)\theta(-\omega_4)] \times \delta(\omega'_1 + \omega_3 - [\omega'_2 + \omega_4]). \tag{3.65}$$

By comparing eqs. eq. (3.60) and eq. (3.65) we may immediately see that there is no change in $\Phi^{(2)}_{LW}$ i.e. $\delta\Phi^{(2)}_{LW} = 0$ for *any* arbitrary frequency shift-$\delta\omega$ of the σ-spin propagators. Thus, at second-order level, eq. (3.63) becomes

$$\delta\Phi^{(2)}_{LW} = 0 = \left[\int_{-\infty}^{\infty} \frac{\mathrm{d}\omega}{2\pi} \frac{\delta\Phi_{LW}}{\delta G_{A\sigma}(\omega)} \frac{\partial G_{A\sigma}(\omega)}{\partial\omega} \right] \delta\omega, \tag{3.66}$$

and hence the term in brackets vanishes since we consider any arbitrary $\delta\omega$ shift in the propagators. We return to this important point below. However first we show at second-order level that the functional derivative of Φ_{LW} with respect to a σ-spin propagator is equivalent to the self-energy, $\Sigma_{A\sigma}(\omega)$.

Returning to eq. (3.64), using eq. (3.62) to express $G_{A\sigma}(\omega_i + \delta\omega) = [G_{A\sigma}(\omega_i) + \delta G_{A\sigma}(\omega_i)]$ for $i = 1, 2$, and multiplying out we find

$$\delta\Phi^{(2)}_{LW} \propto \int_{-\infty}^{\infty} \mathrm{d}\omega_1 \;\; \delta G_{A\sigma}(\omega_1) \Bigg[\int \ldots \int_{-\infty}^{\infty} \prod_{i=2}^{4} \mathrm{d}\omega_i \; G_{A\sigma}(\omega_2) G_{A-\sigma}(\omega_3) G_{A-\sigma}(\omega_4) [\theta(-\omega_2)\theta(\omega_3)\theta(-\omega_4) + \theta(\omega_2)\theta(-\omega_3)\theta(\omega_4)] \times \delta(\omega_1 + \omega_3 - [\omega_2 + \omega_4]) \Bigg], \tag{3.67}$$

such that the linear terms in $\delta G_{A\sigma}(\omega_i)$ make a contribution to $\delta\Phi^{(2)}_{LW}$ (we neglect the higher-order term involving $\delta G_{A\sigma}(\omega_1)\delta G_{A\sigma}(\omega_2)$).

The term in brackets is a contribution to the second-order skeleton diagram for the self-energy, $\Sigma^{(2)}_{A\sigma}(\omega)$, which may be verified by direct consideration of the

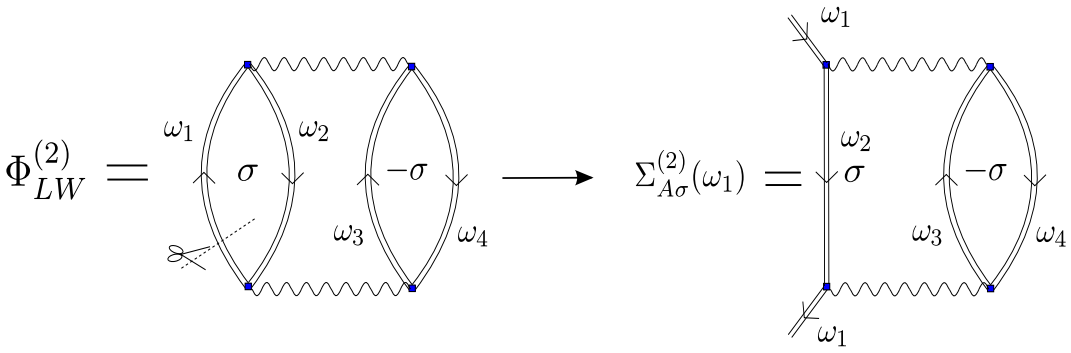


Figure 3.3: Left: A closed linked second-order skeleton contribution to the Luttinger-Ward functional, Φ_{LW}. Frequency and spin are conserved at each vertex. Right: Second-order skeleton contribution to the self energy, obtained by functional differentiation wrt one of the propagators. This is equivalent to cutting an internal propagator line in the contribution to Φ_{LW}. The double lines represent $G_{A\sigma}(\omega, |h|)$ for $U > U_c$ and $G_\sigma(\omega, h)$ for $U < U_c$.

diagrammatic rules [63]. On comparison of eq. (3.67) with eq. (3.61), we see that the self-energy can be expressed as the functional derivative of the Luttinger-Ward functional:

$$\Sigma^{(2)}_{A\sigma}(\omega) = \frac{\delta \Phi^{(2)}_{LW}}{\delta G_{A\sigma}(\omega)}. \tag{3.68}$$

As previously discussed in Section 2.4, the process of functional differentiation is equivalent to cutting a propagator line. This process is shown in Fig. 3.3 specifically for the second-order skeleton diagram by the pair of scissors. Thus, by inserting eq. (3.68) into eq. (3.66) we simply obtain

$$\left[\int_{-\infty}^{\infty} \frac{\mathrm{d}\omega}{2\pi} \, \Sigma^{(2)}_{A\sigma}(\omega) \frac{\partial G_{A\sigma}(\omega)}{\partial \omega} \right] = 0. \tag{3.69}$$

which is the main result that we seek.

The argument to obtain eq. (3.69) does not rely on anything in particular about the second-order diagram specifically considered above (and shown in Fig. 3.3). In fact, due to the conservation of frequency and spin at the vertices of *any* closed linked skeleton diagram for Φ_{LW}, any frequency shift of the σ (or equivalently -σ) propagators leaves Φ_{LW} unaffected (and hence $\delta\Phi_{LW} = 0$). Thus, eq. (3.69) holds to all orders of the interaction strength U, which is the result originally obtained by Luttinger when considering Fermi liquid phases [59].

3.4.1 Generalization of Luttinger's argument

Using standard arguments from complex analysis, relying on the fact that all propagators and self-energies are analytic functions of frequency everywhere except the

real axis, a straightforward, if lengthy, calculation shows that

$$\int_{-\infty}^{\infty} \frac{\mathrm{d}\omega}{2\pi i}\, \Sigma_{A\sigma}(\omega)\frac{\partial G_{A\sigma}(\omega)}{\partial \omega} = \frac{1}{\pi}\Sigma^I_{A\sigma}(0)G^R_{A\sigma}(0) + \mathrm{Im}\int_{-\infty}^{0} \frac{\mathrm{d}\omega}{\pi} G^r_{A\sigma}(\omega)\frac{\partial \Sigma^r_{A\sigma}(\omega)}{\partial \omega}, \tag{3.70}$$

where the second term on the RHS is the Luttinger integral, $I_{L_{A\sigma}}/\pi$, that appears in eq. (3.55) from the phase shift analysis described above. Moreover, by virtue of the fact that the integral on the LHS vanishes via Luttinger's argument, eq. (3.69), $I_{L_{A\sigma}}(|h|)$ is simply given by

$$I_{L_{A\sigma}}(|h|) = I_{L_{B-\sigma}}(-|h|) = -\Sigma^I_{A\sigma}(0)G^R_{A\sigma}(0). \tag{3.71}$$

As we shall see, for all cases considered hereafter (the one exception is the SC phase of the PAIM at ph symmetry) $\Sigma^I_{A\sigma}(\omega)$ vanishes at the Fermi level and hence

$$I_{L_\sigma}(h) = I_{L_{A\sigma}}(|h|) = I_{L_{B-\sigma}}(-|h|) = 0 \tag{3.72}$$

for both SC Fermi liquid phases (on dropping the 'A' labels) and LM non-Fermi liquid phases, and holds for all fields, including $h = 0$. We reiterate that this result is obtained as a consequence of the fact that in a LM phase at zero-field the TSEs, $\Sigma_{A\sigma}(\omega, 0)$, are expressed in skeleton form. In other words, $\Sigma_{A\sigma}(\omega, 0)$, is the same functional of $G_{A\uparrow}(\omega, 0)$, $G_{A\downarrow}(\omega, 0)$ that $\Sigma_\sigma(\omega, h)$ is of $G_\uparrow(\omega, h), G_\downarrow(\omega, h)$ in a Fermi liquid phase.[9]

3.4.2 The Friedel sum rule

In the previous section we showed that each of the Luttinger integrals, $I_{L_{A\sigma}}(|h|)$ (in a LM phase) and $I_{L_\sigma}(h)$ (in a SC phase) vanish. In consequence, the Friedel-Luttinger sum rules, eqs. (3.52, 3.56), which relate the scattering phase shifts, $\delta_\sigma(h)$, $\delta_{A\sigma}(|h|)$ to the renormalized levels reduce to

$$n_{\mathrm{imp};A\sigma}(|h|) = \frac{1}{2} - \frac{1}{\pi}\tan^{-1}\left[\frac{\varepsilon^*_{A\sigma}(|h|)}{\eta + \Gamma^I_\sigma(0, |h|)}\right] : \text{LM phase}, \tag{3.73a}$$

$$n_{\mathrm{imp};\sigma}(h) = \frac{1}{2} - \frac{1}{\pi}\tan^{-1}\left[\frac{\varepsilon^*_\sigma(h)}{\eta + \Gamma^I_\sigma(0, h)}\right] : \text{SC phase}. \tag{3.73b}$$

These equations, well known for the Fermi liquid SC phase [2,68], relate the excess charge, $n_{\mathrm{imp};A\sigma}(|h|)$ (or $n_{\mathrm{imp};\sigma}(h)$) to the renormalized levels, $\varepsilon^*_{A\sigma}(|h|)$ (or $\varepsilon^*_\sigma(h)$). They allow us to deduce a number of *exact* relations about both the LM and SC phases in the chapters that follow. Firstly however, we consider the LM phase at

[9] The first-order 'static' diagram (see Fig. 3.4) does not make a contribution to $I_{L_{A\sigma}}(|h|)$. Since this diagram makes an ω-independent contribution to $\Sigma_{A\sigma}(\omega, |h|)$, its derivative vanishes in the integrand of eq. (3.55).

zero-field explicitly in a terms of a single self-energy description.

3.5 Conventional single self-energy at zero field in an LM phase

The preceding analysis of the Luttinger integrals and phase shifts is entirely general, holding in a SC phase (where $U < U_c$) within a conventional SSE description, and in a LM phase (where $U > U_c$) within a TSE description. However, in this section we change tact, looking at the LM phase from a different perspective. We define a phase shift, δ, (spin-independent for $h = 0$) in terms of a SSE description. (We reiterate that in a LM phase the spin independent SSE, $\Sigma(\omega, 0) \equiv \Sigma_\sigma(\omega, 0)$, is distinct from the TSEs, $\Sigma_{A\uparrow}(\omega, 0)$, $\Sigma_{A\downarrow}(\omega, 0)$, and given in terms of them via eq. (3.30).)

In analogy with eq. (3.49), the phase shift is given by

$$\delta = \pi n_{\mathrm{imp},\sigma}(0) + I_L = \tfrac{\pi}{2} n_{\mathrm{imp}}(0) + I_L \tag{3.74}$$

where $n_{\mathrm{imp},\sigma}(0) = \frac{1}{2} n_{\mathrm{imp}}(0)$, as $n_{\mathrm{imp}}(0)$ is σ-independent for $h = 0$. The corresponding Luttinger integral is given by

$$I_L = \mathrm{Im} \int_{-\infty}^{0} \mathrm{d}\omega \, \frac{\partial \Sigma(\omega, 0)}{\partial \omega} G_\sigma(\omega, 0), \tag{3.75}$$

where $\Sigma(\omega, 0)$ is the SSE, and $G_\sigma(\omega, 0) = \frac{1}{2}[G_{A\sigma}(\omega, 0) + G_{A-\sigma}(\omega, 0)]$ (eq. (3.24)), the full rotationally-invariant Green function, $G_\sigma(\omega, 0) = G(\omega, 0)$. By dropping the 'A' and σ labels in eq. (3.56), δ may also be written in terms of a spin-independent renormalized level, $\varepsilon^*(0)$

$$\delta = \frac{\pi}{2} - \tan^{-1}\left[\frac{\varepsilon^*(0)}{\eta + \Gamma^I(0,0) + \Sigma^I(0,0)}\right], \tag{3.76}$$

where $\varepsilon^*(0) = \varepsilon + \Gamma^R(0,0) + \Sigma^R(0,0)$, and $\Gamma(\omega, 0) \equiv \Gamma_\sigma(\omega, 0)$ is naturally independent of spin at zero-field. The single-particle spectrum may once again be related (c.f. eq. (3.58)) to the phase shift by

$$\pi[\Gamma^I_\sigma(0,0) + \Sigma^I(0,0)] D_\sigma(0,0) = \sin^2(\delta) \tag{3.77a}$$

or if $\delta(\omega) = \mathrm{Im} \ln G(\omega, 0)$ is discontinuous across $\omega = 0$

$$\lim_{\omega \to 0^\pm} \pi[\Gamma^I_\sigma(\omega,0) + \Sigma^I(\omega,0)] D_\sigma(\omega,0) = \sin^2(\delta \pm \Delta). \tag{3.77b}$$

We also note that since eq. (3.13) gives $D(\omega, 0) = \frac{1}{2}[D_{A\sigma}(\omega, 0) + D_{A-\sigma}(\omega, 0)]$,

eqs. (3.58, 3.59) give the relation

$$\sin^2(\delta) = \tfrac{1}{2}[\sin^2(\delta_{A\sigma}(0)) + \sin^2(\delta_{A-\sigma}(0))], \tag{3.78}$$

for the generic case where $\delta(\omega)$ is continuous across $\omega = 0$, and we assume that both the SSE and TSEs vanish at the Fermi level, $\Sigma^I(0) = \Sigma^I_{A\sigma}(0) = 0$ (which as we shall see, is what we find in all cases in a LM phase).

Before we proceed we make some comments about the results of this section. Eqs. (3.74-3.77a) are the direct analogs of their counterparts in the SC phase given in Section 3.3, expressed in terms of the SSE. However, we emphasize that the diagrammatic arguments given in Section 3.4 for the vanishing of the Luttinger integrals, I_{L_σ} (SC phase) and $I_{L_{A\sigma}}$ (LM phase), do not hold in a LM phase for I_L (eq. (3.75)). This is because the argument relied on the fact that the self-energies, $\Sigma_\sigma(\omega, h)$ (SC phase) and $\Sigma_{A\sigma}(\omega, |h|)$ (LM phase) are expressible in skeleton form as functional derivatives of the Luttinger-Ward functional, Φ_{LW}, with respect to the appropriate propagator (G_σ or $G_{A\sigma}$). We reiterate that the SSE, $\Sigma(\omega)$, at zero-field in a LM phase is *not* expressible in terms of such a functional derivative of Φ_{LW} and hence the Luttinger integral, I_L (eq. (3.75)) cannot be argued to vanish and must be determined by other means. In the next chapter we consider I_L explicitly for the pseudogap Anderson model. However, to conclude this present chapter we return to the simple case of the atomic limit (as discussed in Section 2.3) and specifically consider what values I_L can take in each regime.

3.6 Exact deductions for the atomic limit

We revisit the zero-field atomic limit of the AIM where the hopping $V = 0$, and hence the Hamiltonian simply describes a single-correlated level

$$\hat{H}_{AL} = \sum_\sigma \varepsilon \hat{n}_\sigma + U \hat{n}_\uparrow \hat{n}_\downarrow \tag{3.79}$$

where $\hat{n}_\sigma = \hat{c}^\dagger_\sigma \hat{c}_\sigma$ as usual. The *exact* Green function follows in closed form from the equations of motion methods [2] described in Section 2.3.2

$$G^{AL}_\sigma(\omega, 0) = \frac{1 - n_{-\sigma}(0)}{\omega^+ - \varepsilon} + \frac{n_{-\sigma}(0)}{\omega^+ - \varepsilon - U}, \tag{3.80}$$

where $G^{AL}_\sigma(\omega, 0)$ is independent of spin-σ for $h = 0$. In the ground-state, the mean occupancy of the level, $n_\sigma(0)$, may easily be determined from the spectral function, $D^{AL}_\sigma(\omega, 0)$ via eq. (3.2).

As previously discussed, there are three distinct regimes: Firstly where $-\varepsilon > U$, the ground-state is doubly-occupied with $n_\uparrow(0) = n_\downarrow(0) = 1$. Secondly is the case

where $\varepsilon > 0$ and the impurity level is empty, i.e. $n_\uparrow(0) = n_\downarrow(0) = 0$. Thirdly, where $\varepsilon < 0$, but $U > -\varepsilon$, the ground state is a singly-occupied impurity, with $n_\uparrow(0) = n_\downarrow(0) = \frac{1}{2}$. For $\varepsilon < 0$, the simple level crossing 'phase transition' between the singly and doubly-occupied regimes thus occurs at $U = U_c = -\varepsilon$.

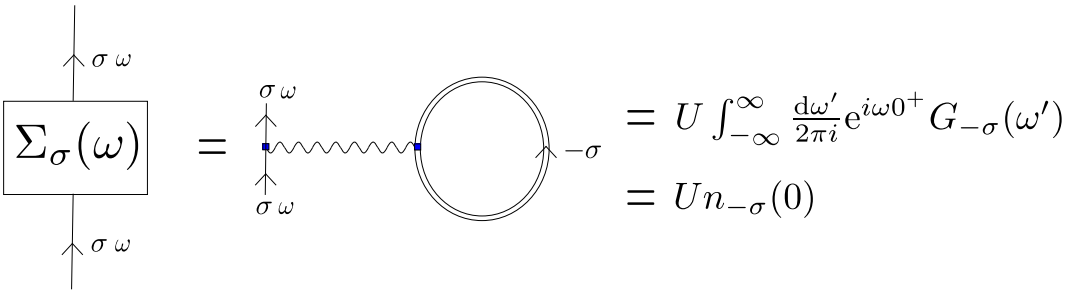


Figure 3.4: The self-energy, $\Sigma_\sigma(\omega)$ expressed at the level of first-order self-consistent perturbation theory (otherwise known as mean-field unrestricted Hartree-Fock (UHF)). As we explicitly show in Section 4.6.7, in the atomic limit the only diagram which contributes to the skeleton expansion for $\Sigma_\sigma(\omega)$ is the ω-independent bubble-diagram. From the Feynman diagram rules [63], the self-energy is expressed in terms of an integral over the (time-ordered) propagator, $G^t_{-\sigma}(\omega)$. It is readily shown by Fourier transform that the diagram is equivalent to $Un_{-\sigma}(0)$, with $n_{-\sigma}(0)$ calculable via eq. (3.2).

In the doubly-occupied regime the propagator is given from eq. (3.80) simply by $G^{AL}_\sigma(\omega, 0) = [\omega^+ - \varepsilon - U]^{-1}$, i.e. it is of the form $G^{AL}_\sigma(\omega, 0) = [\omega^+ - \varepsilon - \Sigma_\sigma(\omega, 0)]^{-1}$ with the self-energy simply given by $\Sigma_\sigma(\omega, 0) = U$. As we shall see in the next chapter, it may be shown by a simple diagrammatic argument that *all* dynamical skeleton diagram contributions (diagrams above first-order) vanish in the atomic limit. The *exact* self-energy may thus obtained by undertaking simple first-order self-consistent perturbation theory, where the bubble diagram (as shown in Fig. 3.4) $\Sigma_\sigma(\omega, 0) = Un_{-\sigma}(0)$. A second point to note is that the doubly-occupied state is a Fermi liquid, by virtue of the fact that if interactions are continuously switched off (i.e. $U \to 0$), $\Sigma_\sigma(\omega, 0) = U \to 0$, we are simply left with the non-interacting propagator $G_\sigma(\omega, 0) = g(\omega) = [\omega^+ - \varepsilon]^{-1}$ — The doubly-occupied state is thus *adiabatically* connected to the non-interacting limit (and hence a Fermi liquid). A final point is that since $\Sigma_\sigma(\omega, 0) = U$ is independent of ω, its derivative with respect to ω vanishes and hence the Luttinger integral, eq. (3.50), $I_{L_\sigma}(0) = 0$, as indeed the general Luttinger arguments of Section 3.4 indicate for a Fermi liquid phase.

For the empty regime where $\varepsilon > 0$, the Green function is just the non-interacting propagator, $G_\sigma(\omega, 0) = [\omega^+ - \varepsilon]^{-1}$ and hence $\Sigma_\sigma(\omega, 0) = 0$ for any U. Once again the system is trivially connected to the non-interacting limit and is thus a Fermi liquid with $I_{L_\sigma} = 0$.

For the singly-occupied (LM) regime the behaviour is more subtle and thus requires a two self-energy description to fully elucidate the underlying physics. From

eq. (3.80), with $n_{-\sigma}(0) = \frac{1}{2}$ we obtain

$$G_\sigma^{AL}(\omega, 0) = \frac{1}{2}\left[\frac{1}{\omega^+ - \varepsilon} + \frac{1}{\omega^+ - \varepsilon - U}\right]. \tag{3.81}$$

which is of the form of eq. (3.11) with

$$G_{A\uparrow}(\omega) = G_{B\downarrow}(\omega) = [\omega^+ - \varepsilon]^{-1}, \tag{3.82a}$$

$$G_{A\downarrow}(\omega) = G_{B\uparrow}(\omega) = [\omega^+ - \varepsilon - U]^{-1}. \tag{3.82b}$$

As discussed previously, the degenerate 'A' and 'B' states in a local moment phase

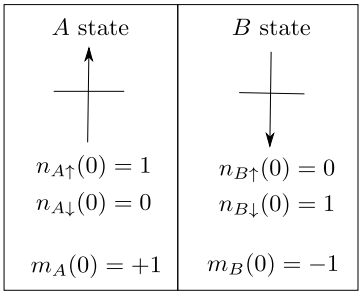


Figure 3.5: Schematic illustrating the two degenerate states of the singly-occupied LM regime as discussed in the text.

may be 'picked out' by applying an infinitesimal magnetic field, $h = 0^{\pm}$. For the A state, the local charge, $n_\sigma(0^+) = n_{A\sigma}(0)$, whereas for the B state, $n_\sigma(0^-) = n_{B\sigma}(0) \equiv n_{A-\sigma}(0)$. As shown in Fig. 3.5 the physical picture in the atomic limit is very clear. The A state corresponds to the impurity occupied with an $\uparrow$ spin, with local charges, $n_{A\uparrow}(0) = 1$, $n_{A\downarrow}(0) = 0$ and hence the local magnetization $m_A(0) = n_{A\uparrow}(0) - n_{A\downarrow}(0) = +1$ is fully saturated. By contrast, the B state corresponds to the impurity level occupied by a $\downarrow$ spin, with $n_{B\uparrow}(0) = 0$, $n_{B\downarrow}(0) = 1$ and hence $m_B(0) \equiv -m_A(0) = -1$. The charge, $n_\sigma(0)$ within a conventional (single-self-energy) approach is given by

$$n_\sigma(0) = \tfrac{1}{2}[n_{A\sigma}(0) + n_{B\sigma}(0)] = \tfrac{1}{2}, \tag{3.83}$$

for both $\sigma = \uparrow, \downarrow$, and hence the total charge is simply $n(0) = 2n_\sigma(0)$.

The atomic limit propagators given in eq. (3.82) have excitation energies that correspond to adding and removing electrons from A and B states. For example $G_{A\uparrow}$ corresponds to removing an $\uparrow$-electron from the $\uparrow$-occupied level, whereas $G_{B\uparrow}$ corresponds to adding an $\uparrow$-electron to the $\downarrow$-occupied level. Each propagator in eq. (3.82) has the form of eq. (3.23), i.e. $G_{A\sigma}(\omega, 0) = [\omega^+ - \varepsilon - \Sigma_{A\sigma}(\omega, 0)]^{-1}$ and hence the TSEs: $\Sigma_{A\uparrow}(\omega, 0) \equiv \Sigma_{B\downarrow}(\omega, 0) = 0$ and $\Sigma_{A\downarrow}(\omega, 0) \equiv \Sigma_{B\uparrow}(\omega, 0) = U$. Therefore,

as we previously discussed for the SSE, $\Sigma_\sigma(\omega,0)$, in the doubly-occupied regime, the TSEs in the singly-occupied regime are obtained via first-order self-consistent perturbation theory and hence are of the form $\Sigma_{A\sigma}(\omega,0) = Un_{A-\sigma}(0)$.

A further point to note here is that conventional 'bare' perturbation theory in U (from the non-interacting ground-state) does not recover the singly-occupied regime discussed here. For $\varepsilon < 0$, the local charge in the NIL is $\langle \hat{n}_{-\sigma}\rangle_{U=0} = 1$, whereas by contrast in the LM phase (singly-occupied regime) for any $U > 0$, $\langle \hat{n}_{-\sigma}\rangle_U \equiv n_{-\sigma}(0) = \frac{1}{2}$. Thus, there is a discontinuous change in $n_{-\sigma}(0)$ for any $U > 0$, and therefore the LM regime is crucially not perturbatively connected to the NIL and hence not a Fermi liquid.

A final point is that since the TSEs $\Sigma_{A\uparrow}(\omega,0)$, $\Sigma_{A\downarrow}(\omega,0)$ are ω-independent, once again the corresponding Luttinger integrals, $I_{L_{A\sigma}}$ given by eq. (3.50) trivially vanish. This result is the same as eq. (3.72) given by the general diagrammatic arguments of Luttinger [59].

3.6.1 Luttinger integral for the singly-occupied regime

The considerations of the previous section for the LM regime focused on the TSEs, $\Sigma_{A\sigma}(\omega,0)$. However, we may equally well consider the spin-independent SSE, $\Sigma(\omega) \equiv \Sigma_\sigma(\omega,0)$, obtained by inserting the TSEs, $\Sigma_{A\uparrow}(\omega,0) = 0$ and $\Sigma_{A\downarrow}(\omega,0) = U$ into eq. (3.30):

$$\Sigma(\omega) = \tfrac{1}{2}U + \frac{\frac{1}{4}U^2}{\omega^+ - \varepsilon - \frac{1}{2}U}. \tag{3.84}$$

where we have also used $G^0(\omega) = g(\omega) = [\omega^+ - \varepsilon]^{-1}$, and $\omega^+ = \omega + i\eta$. The form of eq. (3.84) is totally distinct from the ω-independent TSEs. The SSE is in general both ω-dependent and involves all orders in the interaction strength U.[10] Moreover, the $O(U)$ term highlights the fact that the LM (singly occupied) regime is not perturbatively connected to the NIL. As discussed above, by virtue of the fact that for $\varepsilon < 0$, $\langle \hat{n}_{-\sigma}\rangle_{U=0} = 1$, the leading $U/2$ term in eq. (3.84) is not equal to $U\langle \hat{n}_{-\sigma}\rangle_{U=0}$ of leading-order perturbation theory.

Finally, as a consequence of the fact that the exact forms of both the SSE $\Sigma(\omega)$, eq. (3.84), and the propagator $G(\omega) \equiv G_\sigma(\omega,0)$, eq. (3.81), are known, we may calculate the zero-field Luttinger integral I_L - given by eq. (3.75). Thus, in this section we explicitly calculate I_L in the singly-occupied LM regime.

[10] The exception is the ph symmetric limit, where $\varepsilon = -\frac{U}{2}$. In this particular case eq. (3.84) reduces to $\Sigma(\omega) = \frac{1}{2}U + \frac{1}{4}U^2/\omega^+$; thus the self-energy only involves powers up to U^2 and second-order perturbation theory is exact.

Splitting the SSE, eq. (3.84), into real and imaginary parts we find

$$\Sigma^R(\omega) = \tfrac{1}{2}U + \tfrac{1}{4}U^2 \ \mathrm{P}\left(\frac{1}{\omega - x}\right), \tag{3.85a}$$

$$\Sigma^I(\omega) = \tfrac{1}{4}U^2\pi\delta(\omega - x) \tag{3.85b}$$

where the P denotes the Cauchy principal value, and $x = \varepsilon + \frac{U}{2}$. The parameter, x, defines how close the system is to particle-hole symmetry, (with $x = 0$ corresponding to the ph symmetric point where $\varepsilon = -\frac{U}{2}$ - for a full discussion of ph transformations - we refer the reader to Appendix B). In order to calculate I_L, we need to differentiate each part. The derivatives trivially follow as

$$\frac{\partial\Sigma^R(\omega)}{\partial\omega} = -\frac{\frac{1}{4}U^2}{(\omega - x)^2}, \qquad \frac{\partial\Sigma^I(\omega)}{\partial\omega} = \tfrac{1}{4}U^2\pi\delta'(\omega - x) \tag{3.85c}$$

where $\delta'(x)$ is the derivative of a delta function; we shall see later that this can be evaluated provided it exists under an integral sign. By expressing the retarded functions $G^r(\omega) = [G^R(\omega) - i\pi D(\omega)]$ and $\Sigma(\omega) = [\Sigma^R(\omega) - i\Sigma^I(\omega)]$, the Luttinger integral, I_L, given by eq. (3.75) can be written as the sum of two terms

$$I_L = -\int_{-\infty}^{0}\Big[\frac{\partial\Sigma^R(\omega)}{\partial\omega}\pi D(\omega) + \frac{\partial\Sigma^I(\omega)}{\partial\omega}G^R(\omega)\Big]\,\mathrm{d}\omega \tag{3.86}$$

$D(\omega)$ and $G^R(\omega)$ are given from eq. (3.81) as

$$D(\omega) = \tfrac{1}{2}[\delta(\omega - x - \tfrac{1}{2}U) + \delta(\omega - x + \tfrac{1}{2}U)] \tag{3.87a}$$

$$G^R(\omega) = \tfrac{1}{2}(\mathrm{P}[\omega - x - \tfrac{1}{2}U]^{-1} + \mathrm{P}[\omega - x + \tfrac{1}{2}U]^{-1}) \tag{3.87b}$$

Now we consider the first term in the integral, eq. (3.86), by inserting eq. (3.87a) and eq. (3.85c)

$$I_L^{(1)} = \frac{\pi}{2}\int_{-\infty}^{0}\mathrm{d}\omega\frac{\frac{1}{4}U^2}{(\omega - x)^2} \times [\delta(\omega - x - \tfrac{1}{2}U) + \delta(\omega - x + \tfrac{1}{2}U)], \tag{3.88a}$$

which on integrating becomes

$$I_L^{(1)} = \frac{\pi}{2}[\theta(-x - \tfrac{1}{2}U) + \theta(-x + \tfrac{1}{2}U)] = \frac{\pi}{2} \tag{3.88b}$$

where to obtain the last equality we recognise $x = \varepsilon + \frac{U}{2}$ and $\varepsilon < 0$, $\varepsilon + U > 0$ for the singly-occupied regime we consider here.

Next we turn to the second term in the integral, I_L, eq. (3.86), whilst inputting

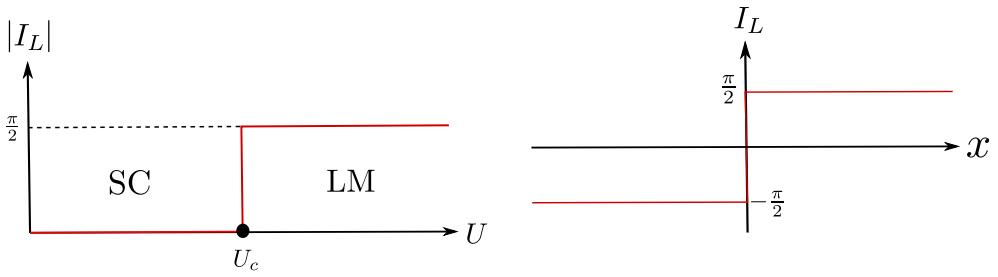


Figure 3.6: Schematic illustrating the dependence of the Luttinger integral, I_L (given by eq. (3.86)) in the atomic limit. Left shows $|I_L|$ plotted versus U for a generic $x = \varepsilon + \frac{U}{2} \neq 0$. As discussed in the text $I_L = 0$ for the SC Fermi liquid phase where the impurity is either empty of doubly occupied. In the LM phase where the impurity is singly-occupied, $|I_L| = \frac{\pi}{2}$ in accordance with eq. (3.90). $U_c = -\varepsilon$ (between the singly and doubly occupied regimes) is denoted by the black circle. The right panel shows the x-dependence of I_L in the singly-occupied regime given by eq. (3.90).

eqs.(3.87b, 3.85c) for $G^R(\omega)$ and $\partial\Sigma^I(\omega)/\partial\omega$ respectively:

$$I_L^{(2)} = -\frac{\pi}{2}\int_{-\infty}^{0} \mathrm{d}\omega \tfrac{1}{4}U^2\delta'(\omega - x) \times \left[\mathrm{P}\Big(\frac{1}{\omega - x - \frac{1}{2}U}\Big) + \mathrm{P}\Big(\frac{1}{\omega - x + \frac{1}{2}U}\Big)\right] \quad (3.89a)$$

By performing a parts integration on this term, the delta function derivative term can be eliminated, i.e.

$$\int_{-\infty}^{0} \mathrm{d}y\ \delta'(y-a)f(y) = [\delta(y-a)f(y)]_{-\infty}^{0} - \int_{-\infty}^{0} \mathrm{d}y\ \delta(y-a)f'(y). \quad (3.89b)$$

The first term on the RHS of eq. (3.89b) vanishes and we are left with

$$I_L^{(2)} = -\frac{\pi}{2}\int_{-\infty}^{0} \mathrm{d}\omega \tfrac{1}{4}U^2\delta(\omega - x)\left[\frac{1}{[\omega - x - \frac{1}{2}U]^2} + \frac{1}{[\omega - x + \frac{1}{2}U]^2}\right] \quad (3.89c)$$

which can now be evaluated to give

$$I_L^{(2)} = -\pi\theta(-x) \quad (3.89d)$$

Thus putting eqs.eq. (3.88b) and eq. (3.89d) together for I_L we obtain

$$I_L = [1 - 2\theta(-x)]\frac{\pi}{2} = [\theta(x) - \theta(-x)]\frac{\pi}{2} \quad (3.90)$$

such that for $x \neq 0$, $|I_L| = \frac{\pi}{2}$, and by symmetry we conclude that for $x = 0$, $I_L = 0$. Both the U and x dependence of I_L are shown in Fig. 3.6.

The Luttinger integral, I_L is thus generically non-zero in a LM phase, obtained here in the context of the simple atomic limit. In the next chapter we explicitly consider the pseudogap AIM, applying the two-self-energy framework that we have developed in this chapter to a genuinely many-body system.

CHAPTER 4

Pseudogap AIM: exact results

4.1 Preliminaries

The zero-field pseudogap Anderson impurity model (PAIM) is a paradigm for a system that contains a quantum phase transition separating a SC phase (adiabatically connected to the NIL and hence a Fermi liquid), and a doubly degenerate LM (non-Fermi liquid) phase. In this chapter we apply the perturbative framework developed in the last chapter to both phases of the model in order to obtain a number of important *exact* results, with particular emphasis paid to the LM phase where the TSEs $\Sigma_{A\sigma}(\omega, 0)$ and the SSE $\Sigma_\sigma(\omega, 0) \equiv \Sigma(\omega)$ are fundamentally distinct. Before proceeding however, we give a brief discussion of the important properties of the PAIM and what has already been considered in the literature [33, 34, 37, 43–46, 48, 100].

As discussed in the introduction, the PAIM (or the related pseudogap Kondo model[1]) in which the impurity is coupled to a conduction band with density of states, $\rho_b(\omega) = \rho_0|\omega|^r$ (for $r > 0$) has been extensively studied in the literature. Most notably an NRG study [43] was able to fully describe the thermodynamic properties in each of the phases, both at particle-hole symmetry, where $\varepsilon = -\frac{U}{2}$ ($x = \varepsilon + \frac{U}{2} = 0$) and the more general asymmetric case. It is well known [38, 43, 78] that the strong coupling phase at particle-hole symmetry, which we denote as the "symmetric strong coupling" (SSC) phase, has distinct physical properties from the "asymmetric strong coupling" (ASC) phase found away from ph symmetry.[2] Moreover, each of the SSC and ASC phases correspond to different *stable* NRG fixed points, for a full discussion of the NRG 'flows' and 'fixed points' we refer the reader to ref [43] (although we give a brief description in Section C.4). The LM

[1] Just as for the metallic AIM, the pseudogap Kondo model is obtained from the PAIM by a Schrieffer-Wolff transformation [2, 17]. However there are regimes of the PAIM where charge fluctuations occur that cannot be accessed from the corresponding Kondo model.

[2] There are actually a pair of ASC phases, one for each $x > 0$ or $x < 0$, related to each other by a ph transformation - see Appendix B for details.

phase by contrast is found to be described by the same NRG fixed point regardless of the initial ph symmetry [78].

QCP behaviour

Much of the emphasis in the literature has naturally focused on the properties of the unique (local) quantum critical point (QCP) [37, 43, 46, 48] that separates the two phases. It is well known from a scaling analysis [37] and also NRG calculations [37, 41] that the QCP both at ph symmetry and for general asymmetry is *interacting* in nature. Moreover, as we shall discuss further in Section 4.8, there are two distinct critical points. Specifically at ph symmetry the model only exhibits a phase transition for $0 < r < \frac{1}{2}$, characterized by a single critical point (which we denote the "symmetric quantum critical point" (SQCP)) for $0 < r < \frac{1}{2}$. For $r \geq \frac{1}{2}$ by contrast, the LM phase is the ground-state of the symmetric model for all U. For the generic $x \neq 0$ model the transition is more subtle. A QPT arises for all $r < 1$: For $0 < r \leq r_* \simeq \frac{3}{8}$, the critical point is the same as for the ph symmetric case (i.e. the SQCP). For $r > r_*$, the QCP is characterized by an asymmetric critical point, we denote AQCP, distinct from the SQCP.[3]

	SSC	ASC	LM	SQCP	AQCP
$\lim_{\omega\to 0} \pi D(\omega) \sim$	$C_{ssc}(r)\lvert\omega\rvert^{-r}$	$C_{asc}(r)\lvert\omega\rvert^{r}$	$C_{LM}(r)\lvert\omega\rvert^{r}$	$C_{s}(r)\lvert\omega\rvert^{-r}$	$C_{a}(r)\lvert\omega\rvert^{-r}$

Figure 4.1: Table denoting the $T = 0$ low-ω dependence of the spectral function $\pi D(\omega) = -\mathrm{Im}G^r(\omega)$ in each of the phases of the PAIM and precisely at each of the quantum critical points.

Behaviour of the dynamics

The $T = 0$ single-particle dynamics of the PAIM in both phases and as the QCP is approached from either side, $U \to U_c^{\pm}$ have also been comprehensively studied. The low-ω asymptotic behaviour of the single-particle spectrum, $D(\omega)$, in both phases (and at the QCP) are well known from both numerically-exact NRG calculations [35, 39, 41], the local moment approach (LMA) [34, 45, 64] and perturbative renormalization group [46, 48, 49]. The low-ω results for $D(\omega) \equiv D_\sigma(\omega, h = 0)$ are summarized in Fig. 4.1. As we shall explain below, the low-ω dependencies in both the SSC and ASC phases have precisely the same low-ω forms as the corresponding

[3] 1) Within an NRG context [43], each of the SQCP and AQCP are described by different *critical* fixed points. 2) As for the ASC stable fixed points described above, there are actually a pair of AQCP fixed points, one for each of $x > 0$ and $x < 0$, related by a simple ph transformation. We refer the reader to Appendix C, Section C.4 for more details about the NRG fixed points.

non-interacting spectral functions, $d(\omega, x = 0)$, $d(\omega, x \neq 0)$. This behaviour highlights the Fermi liquid nature of each SC phase, the interacting ground-state being adiabatically connected to the ground-state of the NIL. In contrast, in the LM phase $\pi D(\omega) \sim C_{LM}(r)|\omega|^r$ for any x, and may be shown to be fundamentally distinct from the NIL, underlining the inherent non-Fermi liquid behaviour of the phase. Finally, as we shall see in Section 4.9, each of QCPs have spectral functions with leading low-ω behaviour completely renormalized from the non-interacting limit.

Summary

In Section 4.3 we apply the Friedel sum rules, derived in Chapter 3, to both phases of the PAIM and obtain new exact results for the excess charge and magnetization in the LM phase. We then proceed to discuss the relevant Luttinger integrals, in each phase and find that whilst $I_L \equiv I_{L_\sigma}$ vanishes in the Fermi liquid phase, $|I_L| = \frac{\pi}{2}$ in a LM phase. In the next part of the chapter we consider the low-ω behaviour of the relevant self-energies and propagators. In Section 4.6, we use Luttinger's original diagrammatic arguments [60] to obtain exact results for the low-ω forms of the self-energies, self-consistently, to all orders in the interaction, U. We apply these self-consistent results to all phases of the PAIM.

In Sections (4.8-4.9) we use general scaling arguments, together with NRG, to show that the QCP is coherently described coming from both phases; within the TSE description in the LM and also the 'usual' single-self energy (SSE) description in the SC phase. We conclude the chapter with a discussion of the subtle physics that arises within the PAIM at finite-field, once again focusing on what can be said from exact analytic arguments. We supplement the analytic arguments with exact numerical calculations from the full-density matrix (FDM) formulation of NRG [101, 102]. For more details of this procedure, we refer the reader to Appendix C.

4.1.1 Hybridization function

As mentioned in Section 2.3, for the pseudogap model, the (retarded) hybridization function $\Gamma_\sigma(\omega, h) = \Gamma^R_\sigma(\omega, h) - i\Gamma^I_\sigma(\omega, h)$ is given by [39, 64]

$$\Gamma^I_\sigma(\omega, h) = \Gamma_0|\omega + \sigma h|^r, \qquad \Gamma^R_\sigma(\omega, h) = -\operatorname{sgn}(\omega + \sigma h)\Gamma_0\beta(r)|\omega + \sigma h|^r, \quad (4.1a)$$

where $\beta(r) = \tan(\frac{\pi r}{2})$ and $\Gamma_0 = \pi\rho_0 V^2$. The $r = 0$ case of course corresponds to the metallic flat band model with a constant host density of states, such that $\Gamma(\omega) = \Gamma_0$. Here we take the limit of infinite bandwidth, $D \to \infty$, and a band exponent r in the range $0 < r < 1$.

As discussed in Section 3.1, a magnetic field h may either be applied locally (solely to the impurity level) or globally to the impurity plus the conduction band

states. In this chapter we concentrate solely on the local case, such that the hybridization function becomes completely independent of both h and σ. eq. (4.1) thus simply reduces to[4]

$$\Gamma^I_\sigma(\omega,0)=\Gamma^I(\omega)=\Gamma_0|\omega|^r, \qquad \Gamma^R_\sigma(\omega,0)=\Gamma^R(\omega)=-\operatorname{sgn}(\omega)\beta(r)\Gamma^I(\omega). \quad (4.1b)$$

4.1.2 Particle hole transformations

In this section we briefly state some important symmetries that we make explicit use of below. If all particles are swapped for holes and all spins exchanged, then the specific operators in the Hamiltonian, eq. (2.30), undergo the transformation

$$c^\dagger_\sigma \leftrightarrow c_{-\sigma}, \qquad c^\dagger_{\mathbf{k}\sigma} \leftrightarrow -c_{-\mathbf{k}-\sigma}. \quad (4.2)$$

The AIM Hamiltonian may be labeled by $x=\varepsilon+\frac{U}{2}$, $\hat{H}\equiv\hat{H}(x)$. It is readily shown (as explained in Appendix B) that under this simple canonical transformation the Hamiltonian remains unchanged, i.e. $\hat{H}(x)\equiv\hat{H}(-x)$. The upshot for the (time-ordered) propagators are that the following symmetry arises

$$G^t_{A\sigma}(\omega;x,|h|)=-G^t_{A-\sigma}(-\omega;-x,|h|), \quad (4.3a)$$

($G^r_{A\sigma}(\omega;x,|h|)=-[G^r_{A-\sigma}(-\omega;-x,|h|)]^*$) for the retarded (superscript- r) functions. As a result, the spectral functions, $D_{A\sigma}(\omega;x,|h|)=-\frac{1}{\pi}\operatorname{sgn}(\omega)\mathrm{Im}G^t_{A\sigma}(\omega;x,|h|)$ (or equivalently $D_{A\sigma}(\omega;x,|h|)=-\frac{1}{\pi}\mathrm{Im}G^r_{A\sigma}(\omega;x,|h|)$) are related by

$$D_{A\sigma}(\omega;x,|h|)=D_{A-\sigma}(-\omega;-x,|h|). \quad (4.3b)$$

In addition, as a direct consequence of eq. (4.3a), the (time-ordered) self-energies are related by

$$\Sigma_{A\sigma}(\omega;x,|h|)=U-\Sigma_{A-\sigma}(-\omega;-x,|h|), \quad (4.3c)$$

c.f. eq. (B.22), such that it follows that $\Sigma^I_{A\sigma}(\omega;x,|h|)=-\Sigma^I_{A-\sigma}(-\omega;-x,|h|)$. As a consequence of these self-energy relations, the renormalized levels have the symmetry

$$\begin{aligned}\varepsilon^*_{A\sigma}(x,|h|)&=\varepsilon-\sigma|h|+\Sigma_{A\sigma}(0;x,|h|)=x-\tfrac{U}{2}-\sigma|h|+\Sigma_{A\sigma}(0;x,|h|)\\&=-[-x-\tfrac{U}{2}+\sigma|h|+\Sigma_{A-\sigma}(-x,|h|)]=-\varepsilon^*_{A-\sigma}(-x,|h|). \quad (4.3d)\end{aligned}$$

[4] $\Gamma^I(\omega)$ may be rewritten as $\Gamma^I(\omega)=\Gamma_0^{1/(1-r)}[|\omega|/\Gamma_0^{1/(1-r)}]^r$, such that $[|\omega|/\Gamma_0^{1/(1-r)}]^r$ is dimensionless and $\Gamma_0^{1/(1-r)}$ is the natural unit of energy for the problem. In this chapter when plotting numerical results we rescale all parameters in terms of this quantity.

In a SC phase, appropriate for $U < U_c$, the explicit A labels may be dropped in all of these equations; thus eq. (4.3a) reduces to $G_\sigma(\omega; x, h) = -G_{-\sigma}(-\omega; -x, h)$. In consequence, only $x \geq 0$ or $x \leq 0$ needs to be considered explicitly - in the rest of this thesis we focus on the $x \leq 0$ case. Precisely at the ph symmetric point where $x = \varepsilon + \frac{U}{2} = 0$ all of the above symmetries reduce to useful relations that we exploit below.

4.2 Non-interacting limit

Before proceeding to discuss the full interacting model we briefly consider some of the properties of the non-interacting limit of the PAIM. For a full review of the behaviour zero-field non-interacting limit of the PAIM we refer the reader to ref [100]. Here we state the key results for the spectral functions for this exactly soluble limit, such that we may later make reference to them. From the Dyson equation, eq. (2.50), the NIL single-particle propagator is given by

$$g(\omega) = [\omega^+ - \varepsilon - \Gamma(\omega)]^{-1} \tag{4.4a}$$

$$= [(\omega - \varepsilon + \mathrm{sgn}(\omega)\Gamma_0\beta(r)\Gamma_0|\omega|^r) - i(\eta + \Gamma_0|\omega|^r)]^{-1} \tag{4.4b}$$

$$\pi d(\omega) = -\,\mathrm{Im} g(\omega) = \frac{\Gamma_0|\omega|^r + \eta}{[\omega - \varepsilon + \mathrm{sgn}(\omega)\Gamma_0\beta(r)|\omega|^r]^2 + [\Gamma_0|\omega|^r + \eta]^2}, \tag{4.4c}$$

completely spin independent at $h = 0$. For the ph symmetric point where $x = \varepsilon + \frac{U}{2} = 0$, the low-$\omega$ behaviour of $d(\omega)$ then becomes

$$\pi\Gamma_0 d(\omega) \overset{\omega\to 0}{\sim} \frac{|\omega|^{-r}}{1 + \beta^2(r)} = \cos^2(\tfrac{\pi}{2}r)|\omega|^{-r} \tag{4.5a}$$

where for $0 < r < 1$, the hybridization function terms vanish slower than the ω term in the denominator of eq. (4.4c). From eq. (4.5a) we obtain the pinning condition for the modified spectral function $F(\omega)$ [100]

$$F(\omega) = \pi\Gamma_0|\omega|^r[1 + \beta^2(r)]d(\omega) \overset{\omega\to 0}{\sim} 1 \tag{4.5b}$$

which for the $r = 0$ metallic case reduces to the well known result [2], i.e. $F(\omega) = \pi\Gamma_0\, d(\omega) \overset{\omega\to 0}{\sim} 1$.

By contrast, away from ph symmetry the value of $\varepsilon = x \neq 0$ and therefore the low-ω form of eq. (4.4c) simply becomes

$$\pi d(\omega, x \neq 0) \overset{\omega\to 0}{\sim} \frac{\Gamma_0|\omega|^r}{\varepsilon^2}, \tag{4.6}$$

vanishing at the Fermi level. Thus the low-ω forms of $d(\omega)$ at ph symmetry, eq. (4.5a), and for the more general model, eq. (4.6), are fundamentally distinct.

In summary, for $x = 0$, the level energy, ε vanishes and hence the spectral function diverges as $\propto |\omega|^{-r}$. For all other finite values of ε, $d(\omega)$ simply vanishes via eq. (4.6).

4.3 Friedel sum rules

We now move to describe the fully interacting case of the pseudogap AIM, paying particular attention to each distinct phase of the model. We first apply the Friedel sum rules, eqs. (3.73a-3.73b) derived in the last chapter to both the SC and LM phases of the PAIM.

4.3.1 SC phase: $U < U_c$

The zero-field hybridization function vanishes at the Fermi level, i.e. $\Gamma(0) = 0$. Therefore the Friedel sum rule applicable to the SC phase is given from eq. (3.73b) by

$$n_{\mathrm{imp},\sigma}(0) = \frac{1}{2} - \frac{1}{\pi}\tan^{-1}\left[\frac{\varepsilon^*(0)}{\eta}\right], \tag{4.7}$$

where $\eta = 0^+$ as usual. At $h = 0$, the propagators in a SC phases are spin-independent, and as a consequence, $n_{\mathrm{imp},\sigma}(0) = \frac{1}{2}n_{\mathrm{imp}}(0)$. The zero-field excess magnetization then follows as, $m_{\mathrm{imp}}(0) = [n_{\mathrm{imp}\uparrow}(0) - n_{\mathrm{imp}\downarrow}(0)] = 0$, and the renormalized level, $\varepsilon^*_\sigma(h = 0)$, is also independent of spin given by $\varepsilon^*(0) = \varepsilon + \Sigma^R_\sigma(0, 0)$. Thus, there are 3 distinct possibilities arising from the form of eq. (4.7):

1. If $\varepsilon^*(0) < 0$, such that it lies below the Fermi level, then $n_{\mathrm{imp}}(0) = 2$.

2. If $\varepsilon^*(0) > 0$, then $n_{\mathrm{imp}}(0) = 0$.

3. If $\varepsilon^*(0) = 0$, then $n_{\mathrm{imp}}(0) = 1$.

Thus, the change in the number of electrons due to the addition of the impurity is integral, as one might expect from a physical perspective.[5] For the SC phase, these results are well known [34]. Under a particle-hole transformation ($x \to -x$) (as explained in Appendix B), it turns out that $n_{\mathrm{imp}}(0) \leftrightarrow 2 - n_{\mathrm{imp}}(0)$. The cases (1), (2), therefore correspond to the general asymmetric model, with $n_{\mathrm{imp}}(0) = 0, 2$, characteristic of the asymmetric SC (ASC) phase for $x > 0$ and $x < 0$ respectively. In contrast, case (3) corresponds to the ph symmetric model, where $x = \varepsilon + \frac{U}{2} = 0$, $n_{\mathrm{imp}}(0) = 1$, is characteristic of the symmetric SC (SSC) phase.

[5] By contrast, for the $r = 0$ metallic case where $\Gamma_I(\omega) = \Gamma_0$, the excess charge (equivalent to the local charge, $n(h)$) varies continuously as a function of U.

4.3.2 LM phase: $U > U_c$

In the LM phase, the Friedel sum rule, eq. (3.73a) gives

$$n_{\mathrm{imp},A\sigma}(0) = \frac{1}{2} - \frac{1}{\pi}\tan^{-1}\left[\frac{\varepsilon^*_{A\sigma}(0)}{\eta}\right], \tag{4.8}$$

with $\varepsilon^*_{A\sigma}(0) = \varepsilon + \Sigma_{A\sigma}(0,0)$. We want to determine the *excess* charge and magnetizations that are given by $n_{\mathrm{imp}}(0) = \sum_\sigma n_{\mathrm{imp},A\sigma}(0)$ (eq. (3.43)), and $m_{\mathrm{imp},A}(0) = \sum_\sigma \sigma n_{\mathrm{imp},A\sigma}(0)$ (eq. (3.45)), respectively. The excess magnetization, $m_{\mathrm{imp},A}(0)$ is the analogue of the local magnetization, $m_A(0) = +|\tilde{\mu}| > 0$ (eq. (3.8)), which is in general non-vanishing in a LM phase. Physically, it is natural that the excess and local magnetizations lie in the same direction, such that $\mathrm{sgn}(m_{\mathrm{imp},A}(0)) = \mathrm{sgn}(m_A(0))$. In order for this condition to be fulfilled eq. (4.8) is satisfied only if renormalized levels are sign definite, i.e.

$$\varepsilon^*_{A\uparrow}(0) < 0 \quad \varepsilon^*_{A\downarrow}(0) > 0, \tag{4.9}$$

corresponding to

$$n_{\mathrm{imp},A\uparrow}(0) = 1 \quad n_{\mathrm{imp},A\downarrow}(0) = 0, \tag{4.10}$$

and hence

$$n_{\mathrm{imp}}(0) = 1 \quad m_{\mathrm{imp},A}(0) = 1 \tag{4.11}$$

Thus, from eq. (3.44), $m_{\mathrm{imp}}(h) = \mathrm{sgn}(h)\, m_{\mathrm{imp},A}(|h|)$, such that identically at zero-field $m_{\mathrm{imp}}(0) = 0$, but as $h \to 0^{\pm}$, $m_{\mathrm{imp},A}(0^{\pm}) = \pm 1$, which we refer to as a 'fully-saturated' excess moment.

In Fig. 4.2 we show the zero-field renormalized levels, $\varepsilon^*_\sigma(0)$ in the ASC phase and $\varepsilon^*_{A\uparrow}(0), \varepsilon^*_{A\downarrow}(0)$ in the LM phase as a function of U, calculated from FDM-NRG for a typical $r = 0.35$ and $x = -1$. The numerical calculations thus explicitly confirm the *exact* deductions of eqs. (4.7-4.11). We have also calculated each of the excess charges ($n_{\mathrm{imp};\sigma}(0)$ for the SC phase (both the SSC and ASC) and $n_{\mathrm{imp};A\sigma}(0)$ for the LM phase) by an integral over the appropriate excess density of states, eq. (3.38). The results of these numerical calculations indeed confirm the deductions from the Friedel sum rules above.

In contrast to the SC phase, where $n_{\mathrm{imp}}(0) = 1$ uniquely at $x = 0$, we have shown that $n_{\mathrm{imp}}(0) = 1$ for the *entire* LM phase, regardless of ph symmetry (i.e. for any x). These exact results are obtained as a direct consequence of the argument of Section 3.4 in which we showed that $I_{L_{A\sigma}} = 0$ (the Luttinger integral eq. (3.50) defined in terms of the TSEs and the broken symmetry propagators) for a LM phase. The fact

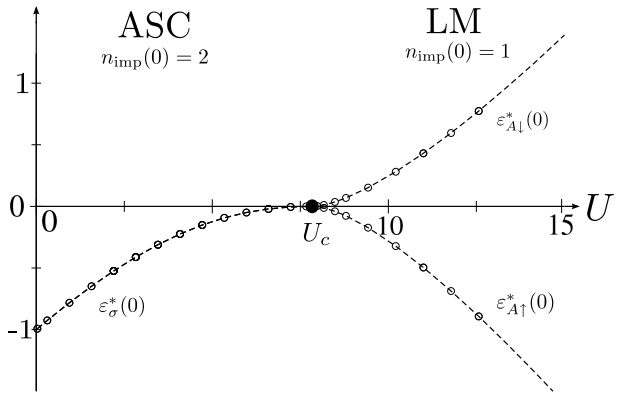


Figure 4.2: The renormalized levels in each phase phase plotted versus U (where we take $\Gamma_0^{1/(1-r)} \equiv 1$ as the unit of energy.) The critical point is denoted with $U = U_c$ where all renormalized levels vanish.

that $n_{\rm imp}(0) = 1$ in a LM phase was conjectured within the local moment approach (LMA) [34], however we emphasize that in the present context the result, eq. (4.11) is *exact*.

Another result of the above analysis that should be noted is that on crossing the transition, $U = U_c$ (as shown in Fig. 4.2), the excess magnetization, $m_{{\rm imp};A}(0)$, changes discontinuously. The change in the excess magnetization, given by $\delta m_{{\rm imp};A}(0)$ $= m_{{\rm imp};A}(U = U_c^+) - m_{{\rm imp};A}(U = U_c^-) = \pm 1$. Therefore on traversing the transition into the LM phase, the system suddenly gains an additional fully saturated moment, $m_{{\rm imp},A}(0) = 1$. By contrast, the local moment, $m_A(0) = +|\tilde{\mu}|$, the appropriate order parameter for the transition, increases continuously from zero on increasing U above U_c, and only saturates to unity for $[U/U_c] \gg 1$. The physical picture is clear, on moving across the transition into the LM phase, an additional *fully-saturated* moment condenses in the system, but at $U = U_c$ has precisely no weight on the impurity itself. Moreover, as U is increased above U_c, the fraction of the moment localized on the impurity itself, the local moment - $|\tilde{\mu}|$ evolves continuously, fully saturating as $(U/U_c) \to \infty$.

The LHS of Fig. 4.3 shows both $m_A(0) \equiv |\tilde{\mu}|$ and $m_{{\rm imp},A}(0)$ calculated for the PAIM from FDM-NRG for a typical r $(= 0.4)$ and $x = -0.4$, thus confirming the results of the above discussion. The RHS shows the local charge, $n(0) = n_\sigma(0) + n_{-\sigma}(0)$, which shows no critical behaviour and is completely continuous across $U = U_c$. Fig. 4.4 shows the PAIM phase diagram in the (U, x) plane for $r = 0.4$. The various $n_{\rm imp}$'s for each of the SC and LM phases are indicated, as determined in the discussion above.

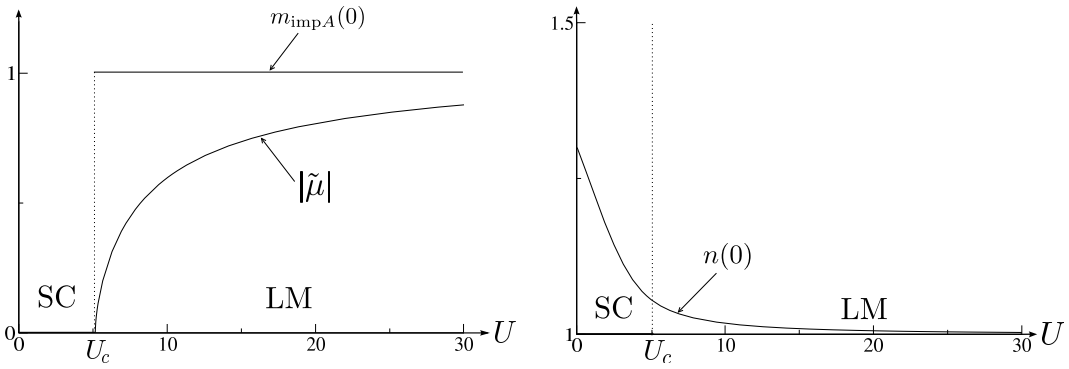


Figure 4.3: Left: FDM-NRG calculation for the evolution of the zero-field, permanent local moment, $|\tilde{\mu}|$ ($= m_A(0) = m(0^+)$), and the *excess* magnetization $m_{\mathrm{imp},A}(0) = (m_{\mathrm{imp}}(0^+))$, on crossing the transition at $U = U_c$ to the LM phase (shown here for $x = -0.4$, $r = 0.4$). The local moment, $|\tilde{\mu}|$ vanishes continuously as $U \to U_c^+(r)$, whilst $m_{\mathrm{imp},A}(0)$ changes discontinuously to full saturation on crossing the transition. Right: NRG calculation for the local charge, $n(0) = n_\uparrow(0) + n_\downarrow(0)$ as a function of U for the same parameters. In contrast, to $|\tilde{\mu}|$, $n(0)$ is continuous across $U = U_c$. Once again, the unit of energy is set to $[\Gamma_0^{1/(1-r)}] \equiv 1$.

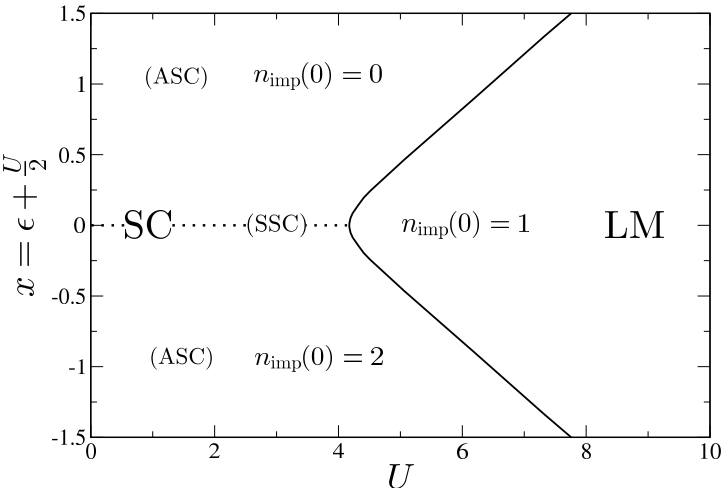


Figure 4.4: NRG phase diagram for the PAIM for $r = 0.4$. $x = \varepsilon + \frac{U}{2}$ is plotted versus U . The solid line shows the transition, where $U = U_c(r)$ (the unit of energy is set to $[\Gamma_0^{1/(1-r)}] \equiv 1$), obtained from where the local moment $m_A(0) = |\tilde{\mu}|$ vanishes. The dotted line shows the SSC phase where $x = \varepsilon + \frac{U}{2} = 0$, and $n_{\mathrm{imp}}(0) = 1$.

4.4 The Luttinger integral, I_L

We now address the issue of the Luttinger integral, I_L, eq. (3.75) in a LM phase in a single-self-energy description. From the general analysis of Section 3.5, we may now relate the phase shift, δ, in a SSE description to the Luttinger integral, I_L, in the specific case of the pseudogap AIM.

4.4.1 General ph asymmetry

Recall that in a LM phase at zero-field, the SSE, $\Sigma(\omega,0) \equiv \Sigma_\sigma(\omega,0) = \Sigma^R_\sigma(\omega,0) - i\Sigma^I_\sigma(\omega,0)$, may be related to the TSEs, $\Sigma_{A\sigma}(\omega,0)$, via eq. (3.30). From considering diagrammatic arguments in the spirit of Luttinger [60] for the low-ω dependence of the two self-energies, (which we specifically undertake in Section 4.6) it may be shown that $\Sigma^I_{A\sigma}(0,0) = 0$ for all U in a LM phase and hence the TSEs are purely real at the Fermi level. Thus, by inserting $\Sigma_{A\sigma}(0) \equiv \Sigma^R_{A\sigma}(0)$ into eq. (3.30) it directly follows that $\Sigma^I_\sigma(0,0)$ also vanishes at the Fermi level. The zero-field (spin independent) renormalized level, $\varepsilon^*(0) = \varepsilon + \Sigma^R(0,0)$, may be related to the renormalized levels $\varepsilon^*_{A\sigma}(0) = \varepsilon + \Sigma^R_{A\sigma}(0,0)$ via eq. (3.30) (noting that $\Gamma_\sigma(0,0) = 0$):

$$\varepsilon^*(0) = \varepsilon + \Sigma^R(0,0) = \tfrac{1}{2}[\varepsilon^*_{A\uparrow}(0) + \varepsilon^*_{A\downarrow}(0)] + \frac{(\frac{1}{2}[[\varepsilon^*_{A\uparrow}(0) - \varepsilon^*_{A\downarrow}(0)])^2}{\frac{1}{2}[\varepsilon^*_{A\uparrow}(0) + \varepsilon^*_{A\downarrow}(0)]}, \tag{4.12}$$

or alternatively

$$\varepsilon^* = \frac{2\varepsilon^*_{A\uparrow}\varepsilon^*_{A\downarrow}}{\varepsilon^*_{A\uparrow} + \varepsilon^*_{A\downarrow}}, \qquad \frac{1}{\varepsilon^*} = \frac{1}{2}\left[\frac{1}{\varepsilon^*_{A\uparrow}} + \frac{1}{\varepsilon^*_{A\downarrow}}\right] \tag{4.13}$$

where we suppress the explicit field-dependence in the following, i.e. $\varepsilon^* \equiv \varepsilon^*(0)$, $\varepsilon^*_{A\sigma} \equiv \varepsilon^*_{A\sigma}(0)$. From eq. (4.9) we know that the LM phase renormalized levels are sign definite. Hence we may replace $\varepsilon^*_{A\uparrow} = -|\varepsilon_{A\uparrow}|$ and $\varepsilon^*_{A\downarrow} = -|\varepsilon_{A\downarrow}|$ in eq. (4.13) to obtain

$$\varepsilon^* = \frac{2|\varepsilon^*_{A\uparrow}||\varepsilon^*_{A\downarrow}|}{|\varepsilon^*_{A\uparrow}| - |\varepsilon^*_{A\downarrow}|} \tag{4.14}$$

The results above now put us in a position to be able to determine the Luttinger integral, I_L - given by eq. (3.75) - specifically for the PAIM. Using the Friedel sum rule, eq. (4.8), we showed above that in a LM phase the excess charge of the system is always $n_{\rm imp}(0) = 1$. Taking this result together with eq. (3.74) implies that the phase shift is given by

$$\delta = \frac{\pi}{2} n_{\rm imp}(0) + I_L \tag{4.15a}$$

$$= \frac{\pi}{2} + I_L \tag{4.15b}$$

The phase shift δ is also related to the renormalized level via eq. (3.76) as

$$\delta = \frac{\pi}{2} - \tan^{-1}\left[\frac{\varepsilon^*}{\eta}\right] \tag{4.16}$$

where we have used $\Sigma^I(0,0) = 0$ as stated above. Moreover, eq. (4.14) may be used

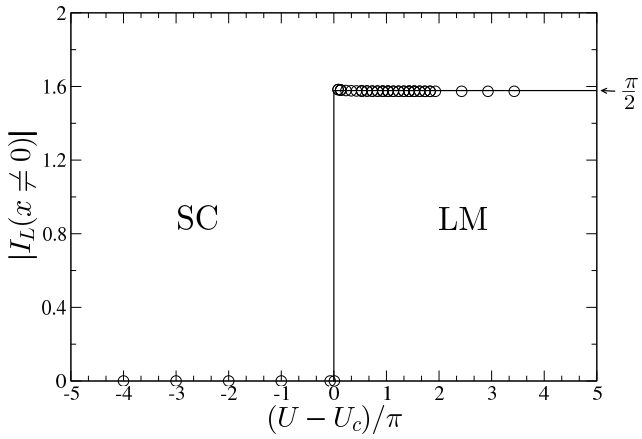


Figure 4.5: Particle-hole asymmetric NRG results for $r = 0.4$, $\varepsilon = -5\pi$, and therefore $x < 0$ ($U_c/\pi \approx 6.1$). $|I_L(x \neq 0)|$ is plotted versus $(U - U_c)/\pi$. In the SC (ASC) phase, we find $I_L(x) = 0$. For the LM phase we find $I_L(x < 0) = -\frac{\pi}{2}$, $I_L(x > 0) = \frac{\pi}{2}$.

to determine the sign of ε^*. If $|\varepsilon^*_{A\uparrow}| > |\varepsilon^*_{A\downarrow}|$, then $\varepsilon^* > 0$, and hence eq. (4.16) gives $\delta = 0$. In contrast, if $|\varepsilon^*_{A\uparrow}| < |\varepsilon^*_{A\downarrow}|$, then $\varepsilon^* < 0$ and $\delta = \pi$. Direct comparison of eq. (4.15b), with eq. (4.16) then gives

$$I_L = \mathrm{Im}\int_{-\infty}^{0} \mathrm{d}\omega \frac{\partial\Sigma(\omega)}{\partial\omega} G_\sigma(\omega, 0) = -\frac{\pi}{2} \quad \text{if} \quad |\varepsilon^*_{A\uparrow}| > |\varepsilon^*_{A\downarrow}| \tag{4.17a}$$

$$= +\frac{\pi}{2} \quad \text{if} \quad |\varepsilon^*_{A\uparrow}| < |\varepsilon^*_{A\downarrow}| \tag{4.17b}$$

The sign change here is completely natural as a consequence of a ph transformation. As detailed in Section 4.1.2, it is readily shown that $\varepsilon^*_{A\uparrow}(x, |h|) = -\varepsilon^*_{A\downarrow}(-x, |h|)$ - and therefore $I_L \equiv I_L(x)$ satisfies

$$I_L(x) = -I_L(-x), \tag{4.18}$$

i.e. it is an odd function of x. We may numerically confirm the result, eq. (4.17) via NRG. Fig. 4.5 shows the Luttinger integral, I_L, versus $(U - U_c)$, calculated from FDM-NRG for the PAIM $r = 0.4$ at a generic ph asymmetry, $x \neq 0$. For $U < U_c$ in the ASC phase, we find $I_L = 0$ as expected. In contrast, for $U > U_c$, in the LM phase, we find $I_L(x < 0) = -\frac{\pi}{2}$, and $I_L(x > 0) = +\frac{\pi}{2}$, in accordance with eq. (4.17).

So far we have only discussed the general asymmetric model. At the unique ph symmetric point, where $x = \varepsilon + \frac{U}{2} = 0$, eq. (4.18) implies that $I_L(x = 0) = 0$, as may be obtained via direct analysis.

4.4.2 Particle-hole symmetry

From a particle hole transformation (where $x \to -x$), the renormalized levels are related by eq. (4.3d), such that identically at $x = 0$, the levels are equal and opposite of each other, i.e. $\varepsilon^*_{A\uparrow}(0, |h|) = -\varepsilon^*_{A\downarrow}(0, |h|)$, and as such $|\varepsilon^*_{A\uparrow}(0, |h|)| = |\varepsilon^*_{A\downarrow}(0, |h|)|$. Thus, the denominator of eq. (4.14) vanishes and in consequence the renormalized level, ε^* diverges at $x = 0$. This singular behaviour of ε^* demonstrates that the SSE, $\Sigma^R(\omega)$, diverges as $\omega \to 0^{\pm}$ as we explicitly consider below in Section 4.5. Making use of the arguments in Appendix A, Section A.3, it may be shown that the phase shift, $\tilde{\delta}(\omega)$ (where $\tilde{\delta}(\omega = 0) = \delta$ is discontinuous across the Fermi level).[6] Specifically, from eq. (A.19), we obtain

$$\tilde{\delta}^{\pm} = \lim_{\omega \to 0^{\pm}} \tilde{\delta}(\omega) = \tfrac{\pi}{2} \mp \tfrac{\pi}{2} r, \tag{4.19}$$

Thus, the phase shift is discontinuous across the Fermi level with $\tilde{\delta}^{\pm} = \delta \mp \frac{\pi}{2} r$. However, from eq. (3.74) I_L is related specifically to δ and not $\tilde{\delta}^{\pm}$, such that $\delta = \frac{\pi}{2} = \frac{\pi}{2} + I_L$ (with $n_{\rm imp}(0) = 1$), indicating that $I_L \equiv I_L(x = 0) = 0$.

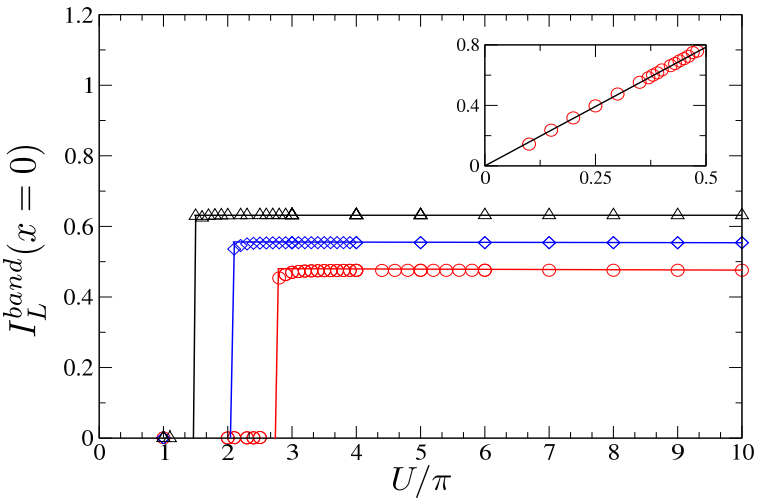


Figure 4.6: Particle-hole symmetry NRG results for $r = 0.3$ (red-circles), $r = 0.35$ (blue-diamonds), $r = 0.4$ (black-triangles). $I_L^{band} \equiv I_L^{band}(x = 0)$ is plotted versus U/π in both phases. In the SSC phase, the numerics show that $I_L(x = 0) = 0$ for all r. By contrast, in the LM phase, I_L^{band} reaches an r dependent plateau value. The inset shows the LM plateau value as a function of r. It found to go as $I_L^{band} = \frac{\pi}{2} r$.

From the NRG we explicitly calculate $I_L(x = 0)$ numerically from eq. (3.75).

[6] As considered in Appendix A, the phase shift $\tilde{\delta}(\omega) = \delta(\omega) + \pi$ (with $\delta(\omega)$ defined by eq. (A.4a)), such that $\tilde{\delta}(\omega) = 0$.

Fig. 4.6 shows results for $r = 0.3, 0.35, 0.4$, where it appears that $I_L = \frac{\pi}{2}r$. However, we show in Appendix A, Section A.4, that the integrand of I_L has an explicit zero-ω pole contribution of $I_L^P = -\frac{\pi}{2}r$ that is crucially not picked up in the numerical calculations of Fig. 4.6, and hence $I_L(x = 0) = I_L^{band} + I_L^P$ does indeed vanish at $x = 0$, as expected from the general argument above.

Before we proceed we make some important comments about the results obtained above for the Luttinger integral, $I_L(x)$. First, we emphasize that the I_L considered here is the analog of the Luttinger integral relevant in the SC phase, both quantities being written in terms of the conventional single-self-energy, $\Sigma(\omega) \equiv \Sigma_\sigma(\omega, 0)$. In a SC phase where the system is a Fermi liquid, I_L, is argued to vanish by the general diagrammatic arguments of Section 3.4, and as such is completely independent of any bare model parameters. Moreover, the above argument shows that the result, $|I_L| = \frac{\pi}{2}$ (for any $x \neq 0$), is an intrinsic property of the LM phase.

Second, the result of eq. (4.17) is precisely the same as what we found for the singly-occupied regime in the atomic limit, as shown in Section 3.6.1, eq. (3.90). Furthermore, we underline that the result $|I_L| = \frac{\pi}{2}$ is not specific to the PAIM explicity considered here, but may also be shown for the the LM phase arising in the gapped AIM (where $\Gamma(\omega = 0) = 0$), as well as other multi-impurity/multi-band models with LM phases [103].

Finally, we emphasize that the conclusions of this section are strictly applicable to $h = 0$, where the QCP is pristine. For any non-zero h, the QCP is destroyed and thus everywhere in the (U, h) plane (apart from $U > U_c$, $h = 0$), the system is a Fermi liquid perturbatively connected to the NIL. In other words, for any finite field, all Luttinger integrals in all cases vanish.

4.5 Low-ω behaviour: LM phase

In this section we consider and discuss the low-ω asymptotic forms of both the propagators and self-energies, paying particular attention to the underlying behaviour in the zero-field LM phase of the PAIM.

In a LM phase it is useful to define a low-energy scale, ω_* [34], that vanishes continously as the quantum phase transition is approached from above ($U \to U_c^+$)

$$\Gamma_0 \omega_*^r = \tfrac{1}{2}|\varepsilon_{A\uparrow}^* - \varepsilon_{A\downarrow}^*|, \tag{4.20}$$

where the $\frac{1}{2}$ prefactor is chosen for convenience. The only assumption that we make here is that each of the renormalized levels, $\varepsilon_{A\sigma}^*$, are continuous as the transition is approached as a function of U.[7] By virtue of the fact that in a SC phase at zero-field, the renormalized level, $\varepsilon^*(0)$, is independent of spin-σ, the energy difference

[7] However, as shown by FDM-NRG in Fig. 4.2, this is indeed the case.

$[\varepsilon^*_{A\uparrow} - \varepsilon^*_{A\downarrow}]$, must vanish as the transition is approached for $U \to U_c^+(r)$.

As discussed previously in Chapter 1, close to a quantum phase transition (as $U \to U_c^{\pm}$) there is only one characteristic scale, ω_*, which vanishes at the critical point coming from each phase. On considering the limit $\omega_* \to 0$, physical quantities of the system, such as the single-particle spectrum and the self-energies, exhibit *universal* scaling in terms of the ratio (ω/ω_*). In other words by recasting these quantities in terms of (ω/ω_*) close to the QCP (also known as the scaling regime), all curves scale onto a single *universal* curve independent of the initial 'bare' parameters of the model. Later on in this chapter we calculate full scaling curves (from NRG) for the dynamics of the system as the QCP is approached from each of the distinct phases.

Returning to the argument above, from eq. (4.9), both renormalized levels in a LM phase are sign definite and therefore the difference between them may be written as the sum of their magnitudes

$$|\varepsilon^*_{A\uparrow} - \varepsilon^*_{A\downarrow}| = |\varepsilon^*_{A\downarrow}| + |\varepsilon^*_{A\uparrow}|. \tag{4.21}$$

This in turn has the implication that not only must their difference vanish, but *both levels must separately vanish as* $U \to U_c^+$ (as the numerical calculations of Fig. 4.2 indeed show). In order to discuss the LM phase, both at $x = 0$ and in general, it is necessary to define a ratio, γ, as

$$\gamma = \frac{\varepsilon^*_{A\uparrow} + \varepsilon^*_{A\downarrow}}{|\varepsilon^*_{A\uparrow} - \varepsilon^*_{A\downarrow}|} = \frac{\frac{1}{2}(\varepsilon^*_{A\uparrow} + \varepsilon^*_{A\downarrow})}{\Gamma_0 \omega^r_*} = \frac{|\varepsilon^*_{A\downarrow}| - |\varepsilon^*_{A\uparrow}|}{|\varepsilon^*_{A\uparrow}| + |\varepsilon^*_{A\downarrow}|}, \tag{4.22}$$

where *both* the sum and difference of the renormalized levels vanish as $U \to U_c^+(r)$. From eq. (4.3d), at $x = 0$ the sum of the levels vanish by symmetry and therefore γ is identically zero everywhere in the LM phase. In contrast, away from the ph symmetric point ($x \neq 0$), γ is in general non-zero, with $\gamma(x) = -\gamma(-x)$, odd in x. In addition, γ is strictly bounded between ± 1 and importantly *does not vanish as* $U \to U_c^+$ where both the sum and differences *separately* vanish, but tends to a finite value.

4.5.1 Particle-hole asymmetry

We initially consider the general asymmetric model, where $x \neq 0$ and hence γ does not vanish by eq. (4.22). By expressing the renormalized level, ε^* via eq. (4.14) and the low-energy scale via eq. (4.20), their ratio is readily shown to be given by

$$\frac{\varepsilon^*}{\Gamma_0 \omega^r_*} = \gamma - \frac{1}{\gamma}, \tag{4.23}$$

in terms of the dimensionless ratio, γ. As explained above, since γ is finite as $U \to U_c^+$, eq. (4.23) also shows that the renormalized level $\varepsilon^* \propto \omega_*^r$ as the QCP is approached.

In the next section we consider a diagrammatic self-consistency argument to obtain the *exact* leading low-ω behaviour of the TSEs, $\Sigma_{A\sigma}(\omega, 0)$ to all-orders of perturbation theory in a LM phase. However, provided the leading low-ω dependence is given by

$$\Sigma^I_{A\sigma}(\omega, 0) \overset{\omega \to 0}{\sim} |\omega|^m \qquad : \; m \geq r, \tag{4.24}$$

such that the TSEs vanish at least as rapidly as the hybridization function, $\Gamma(\omega)$, direct analysis of eq. (3.30) yields

$$\frac{1}{\Gamma_0 \omega_*^r} \Sigma^I(\omega, 0) \overset{\tilde{\omega} \to 0}{\sim} a_a |\tilde{\omega}|^r, \tag{4.25}$$

with $a_a \propto \frac{1}{\gamma^2}$ and $\tilde{\omega} = (\omega/\omega_*)$. As we shall see subsequently, this result is *exact*, holding to all-orders in perturbation theory (in U) and self-consistent in the sense of ref [60]. From eq. (4.25) the SSE, $\Sigma^I(\omega, 0)$, therefore vanishes with the same power as the hybridization function, $\Gamma(\omega)$. This behaviour, i.e. when the conventional single-self-energy vanishes no faster than the hybridization function, is symptomatic of a non-Fermi liquid. For the (metallic) $r = 0$ case, this would simply correspond to a constant $\Sigma^I(\omega = 0, 0)$.

The reader should also notice that the (dimensionless)[8] quantity, $\Sigma^I(\omega, 0)/\Gamma_0 \omega_*^r$ exhibits scaling in terms of (ω/ω_*) as the QCP is approached. In other words, the self-energy function, $\Sigma^I(\omega, 0)/\Gamma_0 \omega_*^r$, becomes independent of the specific 'bare' choices of U, ε in the initial Hamiltonian. This scaling behaviour legitimizes the choice of ω_* via eq. (4.20), as the appropriate low-energy scale in the LM phase.

The low-ω dependence of the real part of the SSE, $\Sigma^R(\omega, 0)$ can be obtained via similar direct analysis of eq. (3.30). Alternatively, the leading low-ω behaviour of $\Sigma^R(\omega)$ can be obtained by considering a Hilbert transform [104] similar to eq. (2.14), but for a general retarded function of the form $F(\omega) = F^R(\omega) - iF^I(\omega)$ (where $F(\omega)$ is analytic in the upper half plane)

$$F^R(\omega) = \frac{1}{\pi} \int_{-\infty}^{\infty} \mathrm{d}\omega' \; F^I(\omega') \mathrm{P}\left(\frac{1}{\omega - \omega'}\right), \tag{4.26}$$

where once again P denotes the Cauchy principal value. Furthermore, if the low-ω form of $F^I(\omega) \overset{\omega \to 0^\pm}{\sim} A_a^\pm |\omega|^\lambda$ with $-1 < \lambda < +1$ (and $A_a^\pm$ are real coefficients, where in general $A_a^+ \neq A_a^-$), the $\omega \to 0$ behaviour of the leading low-ω correction to the

[8] Γ_0 has units E^{1-r}, such that $\Gamma_0 \omega_*^r$ has units of E (E =energy).

real part, $[F^R(\omega) - F^R(0)]$, is readily shown to be

$$F^R(\omega) - F^R(0) \overset{\omega\to 0}{\sim} -\mathrm{sgn}(\omega)|\omega|^\lambda \left(\frac{\beta(r)}{2}[A_a^+ + A_a^-] - \mathrm{sgn}(\omega)\frac{1}{2\beta(r)}[A_a^+ - A_a^-] \right). \tag{4.27}$$

If $F^I(\omega)$ vanishes with the same coefficient on both sides of the Fermi level, i.e. $A_a^+ = A_a^- = A_a$, then eq. (4.27) simply reduces to

$$F^R(\omega) - F^R(0) \overset{\omega\to 0}{\sim} -\mathrm{sgn}(\omega)\beta(r)F^I(\omega), \tag{4.28}$$

with $\beta(r) = \tan(\frac{\pi}{2}r)$.[9] For the PAIM, we consider r in the range $0 < r < 1$, and assume that the coefficient of the leading low-ω behaviour of $\Sigma^I(\omega)$ is independent of $\mathrm{sgn}(\omega)$. Hence $\Sigma^R(\omega)$ is given from eq. (4.28) by

$$\Sigma^R(\omega) - \Sigma^R(0) \overset{\omega\to 0}{\sim} -\mathrm{sgn}(\omega)\beta(r)\Sigma^I(\omega). \tag{4.29}$$

Now writing eq. (4.25) as $\Sigma^I(\omega)/\Gamma_0\omega_*^r \overset{\omega\to 0}{\sim} a_a|\tilde{\omega}|^r$, with coefficient of proportionality $a_a = O(1)$, and $\tilde{\omega} = (\omega/\omega_*)$, the low-$\omega$ form of the local propagator, given via the Dyson equation, $G_\sigma(\omega, 0) \equiv G(\omega) = [\omega^+ - \varepsilon - \Gamma(\omega, 0) - \Sigma(\omega)]^{-1}$ may be obtained. By inserting eqs. (4.23, 4.25, 4.29), together with eq. (4.1b) for $\Gamma(\omega)$, into the Dyson equation we find

$$\Gamma_0\omega_*^r G(\omega) \overset{|\tilde{\omega}|\ll 1}{\sim} \left[\frac{\omega^+}{\Gamma_0\omega_*^r} - \frac{\varepsilon^*}{\Gamma_0\omega_*^r} + (\mathrm{sgn}(\tilde{\omega})\beta(r) + i)(1 + a_a)|\tilde{\omega}|^r \right]^{-1}, \tag{4.30a}$$

$$\overset{|\tilde{\omega}|\ll 1}{\sim} \left[\frac{\omega_*^{1-r}}{\Gamma_0}\tilde{\omega}^+ - \left(\gamma - \frac{1}{\gamma}\right) + (\mathrm{sgn}(\tilde{\omega})\beta(r) + i)(1 + a_a)|\tilde{\omega}|^r \right]^{-1}. \tag{4.30b}$$

This is the 'quasiparticle scaling form' of the Green function in the zero-field LM phase. In the scaling regime where $U \to U_c^+(r)$, such that $\tilde{\omega}$ is finite in the limit that $\omega_* \to 0$, the first term in eq. (4.30) simply vanishes. Thus, the corresponding scaling-form of the local spectrum, $\pi D(\omega) = -\mathrm{Im}G(\omega)$, may be expressed as

$$\pi\Gamma_0\omega_*^r D(\omega) \overset{|\tilde{\omega}|\ll 1}{\sim} \frac{(1 + a_a)|\tilde{\omega}|^r}{[\gamma - \frac{1}{\gamma} - \mathrm{sgn}(\tilde{\omega})\beta(r)(1 + a_a)|\tilde{\omega}|^r]^2 + [(1 + a_a)|\tilde{\omega}|^r]^2} \tag{4.31a}$$

$$\overset{\tilde{\omega}\to 0}{\sim} \frac{(1 + a_a)}{(\gamma - \frac{1}{\gamma})^2}|\tilde{\omega}|^r. \tag{4.31b}$$

This low-$\tilde{\omega}$ form is known from previous NRG calculations [35], but here we have obtained it as a simple consequence of the underlying structure of the TSEs. In Section 4.8 we also confirm this result through our own NRG calculations.

[9] For a λ in the interval $-1 < \lambda < 0$, $F^R(0)$ is the leading $O(1)$ correction to the leading low-ω divergence and not $F^R(\omega)$ at $\omega = 0$ itself.

4.5.2 Particle-hole symmetry

We now consider the unique ph symmetric case where $x = \varepsilon + \frac{U}{2} = 0$. As stated above at ph symmetry the renormalized levels, $\varepsilon^*_{A\uparrow}$, $\varepsilon^*_{A\downarrow}$ are equal and opposite and therefore their sum vanishes. The low-ω LM scale, eq. (4.20), then simply reduces to

$$\Gamma_0 \omega_*^r = |\varepsilon^*_{A\sigma}|, \tag{4.32}$$

and from eq. (4.22), the ratio $\gamma(x = 0)$ also vanishes. Thus, from eq. (4.23), the spin-independent renormalized level ε^* is divergent for the entire phase.

In order to proceed, once again we assume that the TSEs, $\Sigma^I_{A\sigma}(\omega, 0)$ vanish as $\omega \to 0$ at least as fast as the hybridization function, $\Gamma(\omega)$. From direct analysis of eq. (3.30), it is once again a matter of algebra to show that the leading low-ω behaviour of the SSE is given in scaling form by

$$\frac{1}{\Gamma_0 \omega_*^r} \Sigma^I(\omega) \overset{\omega \to 0}{\sim} a_s |\tilde{\omega}|^{-r}. \tag{4.33}$$

where a_s is a coefficient of $O(1)$ and specifically at $x = 0$, $\Sigma^I(\omega) = \Sigma^I(-\omega)$ is an even function of ω. The SSE thus diverges in the LM phase - this behaviour is again indicative of the underlying non-Fermi liquid nature of the phase. The real part, $\Sigma^R(\omega)$ follows from eq. (4.28)

$$\Sigma^R(\omega) - \Sigma^R(0) \overset{\omega \to 0}{\sim} -\operatorname{sgn}(\omega)\beta(-r)\Sigma^I(\omega) = \operatorname{sgn}(\omega)\beta(r)\Sigma^I(\omega), \tag{4.34}$$

and therefore the low-ω form of the SSE is given by

$$\Sigma(\omega) \overset{\omega \to 0}{\sim} \Sigma^R(0) - [-\operatorname{sgn}(\omega)\beta(r) + i]\Sigma^I(\omega). \tag{4.35}$$

Furthermore, it may be shown simply that $\varepsilon + \Sigma^R(0)$[10] vanishes by symmetry. Hence, by inserting eq. (4.35) into the Dyson equation for the propagator, $G(\omega)$, eq. (2.50), the leading low-ω scaling 'quasiparticle' behaviour is given by

$$\Gamma_0 \omega_*^r G(\omega) \overset{|\tilde{\omega}| \ll 1}{\sim} [(\operatorname{sgn}(\tilde{\omega})\beta(r)|\tilde{\omega}|^r + (-\operatorname{sgn}(\tilde{\omega})\beta(r) + i)a_s|\tilde{\omega}|^{-r}]^{-1} \tag{4.36}$$

where we neglect both the ω and ε contributions in the denominator of eq. (2.50). The scaling spectrum in the limit $|\tilde{\omega}| \to 0$ then becomes

$$\pi \Gamma_0 \omega_*^r D(\omega) \overset{\tilde{\omega} \to 0}{\sim} \frac{1}{a_s} \frac{1}{1 + \beta^2(r)} |\tilde{\omega}|^r, \tag{4.37}$$

where in analogy with the asymmetric case, eq. (4.31b), the spectrum vanishes at

[10] $\Sigma^R(0)$ is the $O(1)$ correction to the divergence of eq. (4.33) and not $\Sigma^R(\omega)$ at $\omega = 0$ itself.

the Fermi level with the same power as the hybridization function. This power dependence was first found from the NRG calculations of ref [39], but has also been found from the LMA [64] and within a perturbative RG framework [46]. Moreover, on multiplying eq. (4.33) and eq. (4.37) together we obtain the generalized pinning condition in the LM phase at ph symmetry

$$\lim_{\omega\to 0^{\pm}}[\pi(1+\beta^2(r))\Sigma^I(\omega)D(\omega)] = 1. \tag{4.38}$$

Fig. 4.7 confirms the low-ω spectral pinning of eq. (4.38) for $r = 0.4$ from direct NRG calculations. We find that in a LM phase for all $U > U_c$, eq. (4.38) is satified - the bottom panel clearly shows that all curves are pinned to unity for small-ω. The inset shows the *universal* scaling curve for all $\tilde{\omega}$, demonstrating clearly the asymptotic behaviour for both $|\tilde{\omega}| \ll 1$ and $|\tilde{\omega}| \gg 1$. We do not refer further to the large-$|\tilde{\omega}|$ behaviour here, but a full discussion is given in Section 4.8. The LM

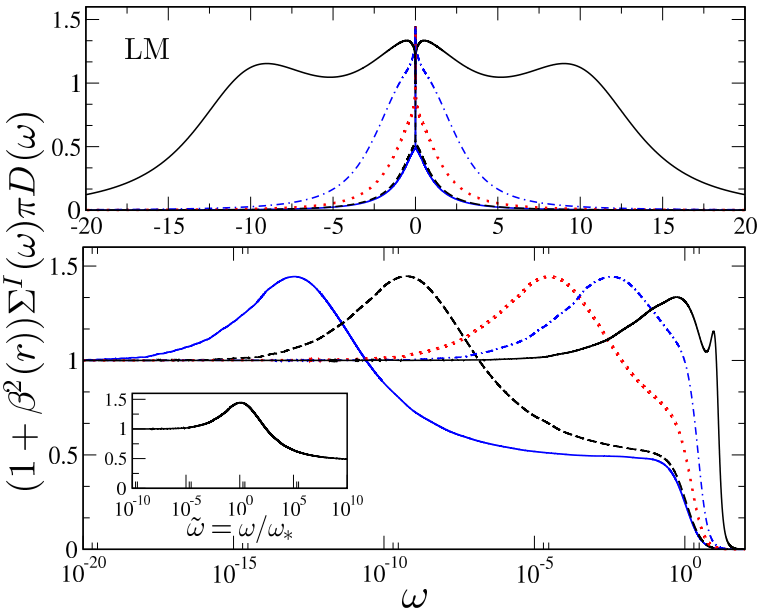


Figure 4.7: Top panel: $\pi(1+\beta^2(r))\Sigma^I(\omega)D(\omega)$ is plotted versus ω for $r = 0.4$, $x = 0$, for different U as U_c is approached. The solid black line shows $U/\pi = 10$, dot-dashed blue shows $U/\pi = 3$, dotted red shows $U/\pi = 2$, dashed black shows $U/\pi = 1.5$, solid blue shows $U/\pi = 1.44$, with $U_c(r)/\pi \simeq 1.438$. The bottom panel shows the same data with ω on a log-scale. The inset shows the full-scaling function for all $\tilde{\omega}$, ω_* has been (freely) chosen such that the peak position occurs at $|\tilde{\omega}|$=1. (The unit of energy is set to $[\Gamma_0^{1/(1-r)}] \equiv 1$.)

pinning condition of eq. (4.38) is the analog of the well known [34, 44] SSC phase pinning condition given for $U < U_c$ by

$$\lim_{\omega\to 0^{\pm}}[\pi(1+\beta^2(r))\Gamma^I(\omega)D(\omega)] = 1. \tag{4.39}$$

This condition is also satisfied in the non-interacting limit, given by eq. (4.5b). Thus, on the lowest-ω scales the spectrum is unrenormalized from its non-interacting value, which is the hallmark of a Fermi liquid.

Both conditions, eqs. (4.38-4.39), are a reflection of the fact that the phase shift, $\tilde{\delta}(\omega)$ discussed in Appendix A (given by eq. (A.14)), is discontinuous across the Fermi level in both phases at ph symmetry. The pinning conditions relations are derived explicitly in Section A.3 from direct analysis of the phase shift.

4.6 Luttinger self-consistency

In the previous section we considered the low-ω asymptotics of both the conventional SSE, $\Sigma(\omega)$, and the propagator, $G(\omega)$, in the LM phase by simply stating that the TSEs, $\Sigma^I_{A\sigma}(\omega, 0)$ vanish with a power $m \geq r$. In this present section, by adapting the original analysis of Luttinger [60] we use a diagrammatic argument to obtain the leading low-ω behaviour of the self-energies, $\Sigma_{A\sigma}(\omega, 0)$ (for $U > U_c(r)$), $\Sigma_\sigma(\omega, 0)$ (for $U < U_c(r)$) in the unique phases of the PAIM.

As discussed previously in Section 2.2.1, in a Fermi liquid phase the interacting ground state is *adiabatically* connected to the non-interacting ground state. As a consequence, the propagator, and hence the self-energy may be written as a perturbation series order by order in the interaction, U, in terms of the non-interacting propagator, $g_\sigma(\omega)$. The (time-ordered) self-energy may then be written in terms of the *skeleton expansion* as a *functional* of the interacting propagator, i.e. $\Sigma_\sigma(\omega) = \Sigma[G_\uparrow, G_\downarrow]$. Moreover, the interacting propagator, G_σ may be expressed by the Dyson equation, eq. (2.50), back in terms of the self-energy. Together the skeleton expansion and the Dyson equation then provide a self-consistency procedure for the determination of both the propagator and self-energy. In principle, if all possible Feynman diagrams are included in the skeleton expansion for Σ_σ, then the *exact* propagator may be obtained. Obviously there are an infinite number of such diagrams and including them all in the skeleton expansion would prove impossible for any practical purpose. However, it is possible, following the original analysis of Luttinger [60] to obtain exact results for the low-ω dependence of the self-energy, by considering the structure of a generic *nth*-order contribution.

The proceeding analysis can be done even in the non-Fermi liquid LM phase of the PAIM. As discussed in Section 3.5, in a LM phase ($U > U_c$, at zero-field) the TSEs, $\Sigma_{A\uparrow}(\omega, 0)$, $\Sigma_{A\downarrow}(\omega, 0)$ can be expressed in skeleton form in terms of the broken symmetry propagators, $G_{A\sigma}(\omega, 0)$. In what is to follow we explicitly consider the TSEs; however, results for the SC phase (and finite-field) follow by simply dropping the A labels as usual.

As considered in Section 2.3.4, a contribution to the self-energy involves any diagram which may be sandwiched between an ingoing and outgoing line. Recall

that a skeleton diagram contribution to the self-energy has no *self-energy insertions* on any of the propagator lines, and as shown in Fig. 2.4 involves replacing (single) non-interacting propagator lines with full propagator (double) lines. For a more in depth analysis of how to construct the diagrams, we refer the reader to ref [63] page 165 or ref [62] Chapter 3.

4.6.1 First-order contribution

Using the standard diagrammatic rules, it is readily shown that the first-order 'bubble' contribution to the self-energy (as shown in Fig. 3.4) is purely static (ω-independent) given by[11]:

$$\Sigma^{(1)}_{A\sigma}(\omega, |h|) = U \int_{-\infty}^{\infty} \frac{\mathrm{d}\omega'}{2\pi i} G_{A-\sigma}(\omega', 0) \mathrm{e}^{i\omega' 0^+} = U\langle \hat{n}_{A-\sigma} \rangle = U n_{A-\sigma}(|h|). \tag{4.40a}$$

Eq. (2.12) may then be used to express the local charge, $n_{A-\sigma}(|h|) \equiv n_{-\sigma}(h)$, as an integral up to the Fermi level of the local spectrum, $D_{A-\sigma}(\omega, |h|)$. By taking a linear combination of the spectral functions, the first-order contribution to the self-energy can then be rewritten as

$$\Sigma^{(1)}_{A\sigma}(\omega) = \frac{U}{2} \int_{-\infty}^{0} \mathrm{d}\omega [(D_{A\uparrow}(\omega) + D_{A\downarrow}(\omega)) - \sigma(D_{A\uparrow}(\omega) - D_{A\downarrow}(\omega))], \tag{4.40b}$$

$$= \tfrac{U}{2}[n(h) - \sigma m_A(|h|)], \tag{4.40c}$$

where we have dropped the explicit field dependence in the propagators and self-energies in the interest of brevity. The integrals in eq. (4.40b) are simply expressed in terms of the local charge, $n(h)$, (given by eq. (3.16)) and the local magnetization, $m_A(|h|)$ (given by eq. (3.17)). If the skeleton expansion were truncated at first-order level, then the self-energy takes on this purely static form, in which all dynamic (ω-dependent) correlations are neglected and the effect of interactions is solely embodied in the renormalized levels, $\varepsilon^*_{A\sigma}(|h|) = \varepsilon + \frac{U}{2}[n(h) - \sigma m_A(h)]$. This is the so-called 'mean-field' unrestricted Hartree-Fock (UHF) approximation, in which a σ spin electron 'experiences' a $-\sigma$ spin average environment coming from all of the other particles in the system [62].

[11] We have used the Fourier transform- $G_{A\sigma}(t, |h|) = \int_{-\infty}^{\infty} \frac{\mathrm{d}\omega}{2\pi} G_{A\sigma}(\omega, |h|) \mathrm{e}^{-i\omega t}$ together with the definition of the propagator, eq. (2.1): $iG_\sigma(t = 0^-, h) = -\langle \hat{c}^\dagger_\sigma \hat{c}_\sigma \rangle = -\langle \hat{n}_{-\sigma} \rangle$, in order to express the self-energy in terms of the local charge, $n_{-\sigma}(h)$.

4.6.2 Second-order diagram

Also following the standard diagrammatic rules, the second-order skeleton diagram may also be written in terms of the propagators via

$$\Sigma^{(2)}_{A\sigma}(\omega) = U^2 \int_{-\infty}^{\infty} \prod_{i=1}^{3} \frac{\mathrm{d}\omega_i}{2\pi} G_{A\sigma}(\omega_1) G_{A-\sigma}(\omega_2) G_{A-\sigma}(\omega_3) \times 2\pi\delta(\omega_1 + \omega_2 - \omega_3 - \omega), \tag{4.41}$$

where the delta function reflects frequency conservation at the vertices of the diagram.

Inserting the integral representation of the delta function, $2\pi\delta(\omega_1+\omega_2-\omega_3-\omega) = \int_{-\infty}^{\infty} \mathrm{d}t\ \mathrm{e}^{-i(\omega_1+\omega_2-\omega_3-\omega)t}$ into eq. (4.41), $\Sigma^{(2)}_{A\sigma}(\omega)$ becomes

$$\Sigma^{(2)}_{A\sigma}(\omega) = \int_{-\infty}^{\infty} \mathrm{d}t \mathrm{e}^{i\omega t} \Bigg\{ U^2 \int_{-\infty}^{\infty} \prod_{i=1}^{3} \frac{\mathrm{d}\omega_i}{2\pi} G_{A\sigma}(\omega_1) \mathrm{e}^{-i\omega_1 t} \tag{4.42a}$$
$$\times G_{A-\sigma}(\omega_2) \mathrm{e}^{-i\omega_2 t} G_{A-\sigma}(\omega_3) \mathrm{e}^{i\omega_3 t} \Bigg\}.$$

On recognising that $G_{A\sigma}(t) = \int_{-\infty}^{\infty} \frac{\mathrm{d}\omega}{2\pi} G_{A\sigma}(\omega) \mathrm{e}^{-i\omega t}$, eq. (4.42a) may be written as

$$\Sigma^{(2)}_{A\sigma}(\omega) = \int_{-\infty}^{\infty} \mathrm{d}t \mathrm{e}^{i\omega t} \Big\{ U^2 G_{A\sigma}(t) G_{A-\sigma}(t) G_{A-\sigma}(-t) \Big\} \equiv \int_{-\infty}^{\infty} \mathrm{d}t \mathrm{e}^{i\omega t} \Sigma^{(2)}_{A\sigma}(t), \tag{4.42b}$$

which is just the Fourier transform of the self-energy in the time domain. By considering a one-sided Hilbert transform, eq. (2.8), it is readily shown that the (time-dependent) Green function is given in terms of the spectral functions, $\pi D_{A\sigma}(\omega_i) = -\operatorname{sgn}(\omega_i) \mathrm{Im} G_\sigma(\omega_i)$, via

$$G_{A\sigma}(t) = -i \int_{-\infty}^{\infty} \mathrm{d}\omega_1 \mathrm{e}^{-i\omega_1 t} D_{A\sigma}(\omega_1) \Big[\theta(\omega_1)\theta(t) - \theta(-\omega_1)\theta(-t) \Big]. \tag{4.43}$$

This equation is very useful and shows that the signs of the frequencies and the signs of the times are 'slaved' to each other by virtue of the step functions. Inserting eq. (4.43) into eq. (4.42b) (for $\Sigma^{(2)}_{A\sigma}(t)$) we obtain

$$\Sigma^{(2)}_{A\sigma}(t) = -iU^2 \int_{-\infty}^{\infty} \prod_{i=1}^{3} \mathrm{d}\omega_i \mathrm{e}^{-i\omega_1 t} D_{A\sigma}(\omega_1) \mathrm{e}^{-i\omega_2 t} D_{A-\sigma}(\omega_2) \mathrm{e}^{i\omega_3 t} D_{A-\sigma}(\omega_3) \tag{4.44}$$
$$\times [\theta(t)\theta(\omega_1)\theta(\omega_2)\theta(-\omega_3) - \theta(-t)\theta(-\omega_1)\theta(-\omega_2)\theta(\omega_3)].$$

We see that the self-energy is written as the sum of two step function terms, one for $t > 0$, the other for $t < 0$. Each term corresponds to a different 'Goldstone' time-

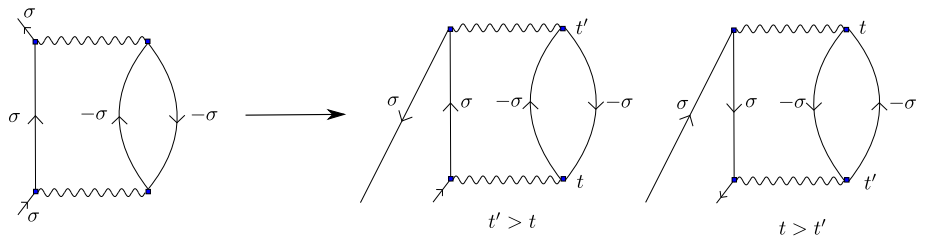


Figure 4.8: The second-order (skeleton) contribution to $\Sigma_{A\sigma}(t)$ (left) can be expressed into two time-ordered Goldstone diagrams (right). The diagrams are shown with single lines for simplicity.

ordering [62] of the diagram. The LHS of Fig. 4.8 shows the second-order skeleton diagram, given in mathematical form by eq. (4.44). The RHS shows the two time-orderings of the diagram, one for $t > t' = 0$ (left) and the other for $t < t' = 0$ (right). In general for any *nth*-order Feynman diagram, there are $n!$ time-orderings, corresponding to the ordering of the interaction vertices. On Fourier transformation of eq. (4.44) it is readily shown that

$$\Sigma^{(2)}_{A\sigma}(\omega) = U^2 \int_{-\infty}^{\infty} \prod_{i=1}^{3} \mathrm{d}\omega_i D_{A\sigma}(\omega_1) D_{A-\sigma}(\omega_2) D_{A-\sigma}(\omega_3) \tag{4.45}$$
$$\times [\theta(\omega_1)\theta(\omega_2)\theta(-\omega_3) + \theta(-\omega_1)\theta(-\omega_2)\theta(\omega_3)][z - \omega_1 - \omega_2 + \omega_3]^{-1},$$

expressed solely in terms of the spectral functions, where $z = \omega + i\eta\,\mathrm{sgn}(\omega)$. As we shall see, this is the form that we require in order to fully elucidate the low-ω behaviour of the self-energy.

4.6.3 Low-ω behaviour of the second-order diagram

We now proceed to use the form of eq. (4.45) in order to analyse the low-ω behaviour of $\Sigma^{(2)}_{A\sigma}(\omega)$. Using the standard relation $[z - \varepsilon]^{-1} = \mathrm{P}[\omega - \varepsilon]^{-1} - i\pi\,\mathrm{sgn}(\omega)\delta(\omega - \varepsilon)$, $\Sigma^{I(2)}_{A\sigma}(\omega) = -i\,\mathrm{sgn}(\omega)\mathrm{Im}\Sigma^{(2)}_{A\sigma}(\omega)$ may be expressed as:

$$\Sigma^{I(2)}_{A\sigma}(\omega) = U^2 \int_{-\infty}^{\infty} \prod_{i=1}^{3} \mathrm{d}\omega_i D_{A\sigma}(\omega_1) D_{A-\sigma}(\omega_2) D_{A-\sigma}(\omega_3) \tag{4.46}$$
$$\times [\theta(\omega_1)\theta(\omega_2)\theta(-\omega_3) + \theta(-\omega_1)\theta(-\omega_2)\theta(\omega_3)]\delta(\omega - [\omega_1 + \omega_2 - \omega_3])$$

Taking the $t > 0$ time-ordering (the first product of step functions in eq. (4.46)) of this diagram and making the substitution $v_i = \omega_i$ for $i = 1, 2$ (for particles) and $-v_i = \omega_i$ for $i = 3$ (for holes) we find:

$$\Sigma^{I(2)}_{A\sigma}(\omega) \propto U^2 \int_0^{\infty} \ldots \int_0^{\infty} \prod_{i=1}^{3} \mathrm{d}v_i D_{A\sigma}(v_1) D_{A-\sigma}(v_2) D_{A-\sigma}(-v_3)\delta(\omega - [v_1 + v_2 + v_3]).$$

Since $v_1, v_2, v_3 > 0$, the delta function contraint means that this diagram only gives a contribution for $\omega > 0$. Furthermore, if we take the limit $\omega \to 0$, then each of v_1, v_2, v_3 *do not exceed* ω. This puts a constraint on the integration limits

$$\Sigma^{I(2)}_{A\sigma}(\omega) \propto U^2 \int_0^{|\omega|} \dots \int_0^{|\omega|} \prod_{i=1}^{3} \mathrm{d}v_i D_{A\sigma}(v_1) D_{A-\sigma}(v_2) D_{A-\sigma}(-v_3) \delta(\omega - [v_1 + v_2 + v_3]).$$

Rescaling the integrals by $v_i = |\omega|\nu_i$ and assuming the low-ω form of the spectral functions $D_{A\sigma}(\omega) \propto |\omega|^{\lambda_\sigma}$ (with $\lambda_\sigma > -1$ and $\lambda_\uparrow$ and $\lambda_\downarrow$ in general distinct) we find[12]

$$\Sigma^{I(2)}_{A\sigma}(\omega) \propto U^2 |\omega|^{2+\lambda_\sigma+2\lambda_{-\sigma}} \left[\int_0^1 \dots \int_0^1 \prod_{i=1}^{3} \mathrm{d}\nu_i |\nu_1|^{\lambda_\sigma} |\nu_2\nu_3|^{\lambda_{-\sigma}} \delta(1 - [\nu_1 + \nu_2 + \nu_3]) \right],$$

where the term is brackets is a purely real, ω-independent, multiplicative constant. Similar analysis for the other time-ordering $t < 0$ (coming from the other theta-contribution in eq. (4.46)), gives the same low-ω power dependence, but for $\omega < 0$. The low-ω behaviour of the second-order self energy, given the spectral functions $D_{A\sigma}(\omega) \propto |\omega|^{\lambda_\sigma}$ is therefore

$$\Sigma^{I(2)}_{A\sigma}(\omega) \overset{\omega \to 0^{\pm}}{\sim} B^{(2)} |\omega|^{2+\lambda_\sigma+2\lambda_{-\sigma}} \tag{4.47}$$

where $B^{(2)}$ is a coefficient independent of $\mathrm{sgn}(\omega)$.

4.6.4 Infinite-order perturbation theory

Now that we have explicitly considered both the first and and second-order contributions, we proceed to discuss the higher-order terms in the skeleton expansion. As considered in the context of the second-order diagram above, each *nth*-order skeleton diagram has $n!$ Goldstone time-orderings. In Fig. 4.9 a third-order skeleton diagram is expressed in terms of its $(6 = 3!)$ time ordered Goldstone contributions. Following Luttinger's analysis [60], the prescription for constructing any *nth* order Goldstone diagram is as follows (we neglect real multiplicative factors that have no bearing on the analysis that is to follow):[13]

1. For a given *nth*-order Feynman (skeleton) diagram, constructed by the standard rules [62,63], label each internal propagator line with an energy label, ω_i for particle (ascending) line, and $\bar{\omega}_i$ for each (descending) hole line. Draw the external lines coming from below in all cases.

[12] We assume a power $\lambda_\sigma > -1$ such that the spectra are integrable.

[13] This prescription allows us to bypass the laborious analysis that we undertook above to write the second-order Feynman diagram in terms of its corresponding Goldstone parts.

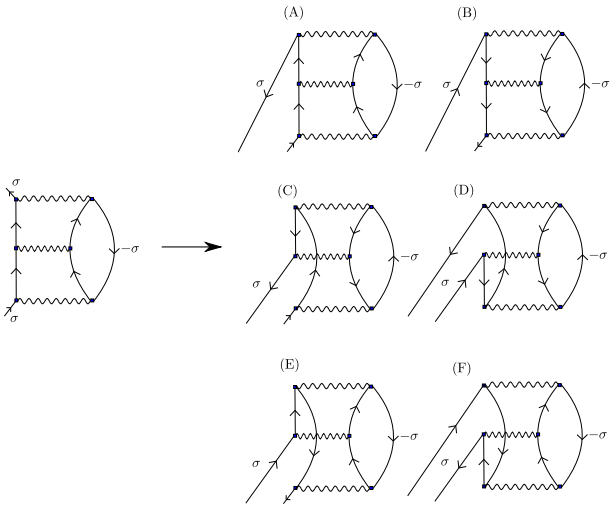


Figure 4.9: Third-order skeleton diagram expressed in terms of its 6 time-ordered Goldstone contributions, labelled (A)-(F).

2. Label each propagator line with an associated spin label such that spin-σ is conserved at each vertex.

3. Define a purely real multiplicative factor S that is proportional to each diagram.

4. For every particle line, multiply S by $\theta(\omega_i)D_{A\sigma'}(\omega_i)$, and for every hole line, by $\theta(-\bar{\omega}_i)D_{A\sigma'}(\bar{\omega}_i)$. The step function ensure that particles/holes have energy greater/less than the Fermi energy.

5. Draw a horizontal line across a diagram between each pair of interactions. With each horizontal line, associate a factor W. Divide S by each W; W is calculated via step (6).

6. For a given horizontal cut across the diagram, W is calculated by adding up all of the particle energies, ω_i, and subtracting the hole energies, $\bar{\omega}_i$. If an external line is crossed by the horizontal line, then associate a factor $z = \omega + i\eta\,\mathrm{sgn}(\omega)$ (it could be a particle or hole line). The contributions of each W make up the so-called 'energy denominator' of the diagram. For an nth-order diagram there are $(n-1)$ W contributions to each energy denominator.

7. Finally, each internal energy, ω_i or $\bar{\omega}_i$, is integrated over from $-\infty$ to ∞.

For example, the 3rd-order Goldstone diagram (F), is shown in Fig. 4.10, with energy/spin labels on each of the lines. Using the rules stated above, the contribution

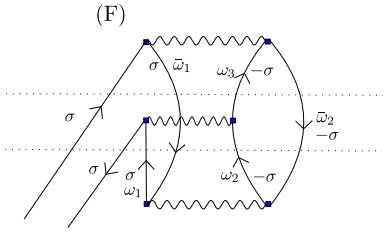


Figure 4.10: Goldstone 3rd-order skeleton diagram contribution. The horizontal lines correspond to the energy denominators discussed explicitly in the text.

of this diagram is given by

$$(F) \propto \int \ldots \int_{-\infty}^{\infty} \mathrm{d}\omega_1 \, \mathrm{d}\omega_2 \, \mathrm{d}\omega_3 \, \mathrm{d}\bar{\omega}_1 \, \mathrm{d}\bar{\omega}_2 D_{A\sigma}(\omega_1) D_{A-\sigma}(\omega_2) \tag{4.48}$$
$$\times D_{A-\sigma}(\omega_3) D_{A\sigma}(\bar{\omega}_1) D_{A-\sigma}(\bar{\omega}_2) \frac{\theta(\omega_1)\theta(\omega_2)\theta(\omega_3)\theta(-\bar{\omega}_1)\theta(-\bar{\omega}_2)}{(\omega_1+\omega_2-\bar{\omega}_1-\bar{\omega}_2)(z+\omega_3-\bar{\omega}_1-\bar{\omega}_2)}$$

The top horizontal (dotted) line in Fig. 4.10 gives rise to the $[z+\omega_3-\bar{\omega}_1-\bar{\omega}_2]$ factor in the energy denominator, the z coming from the external particle line. In contrast, since both incoming and outgoing external lines are crossed, the lower horizontal line in the figure generates a purely real contribution to the energy denominator $[\omega_1+\omega_2-\bar{\omega}_1-\bar{\omega}_2]$. We do not consider this 3rd-order diagram further, but move to the general *nth* order case.

nth-order generalisation

We now use the rules stated above to evaluate a completely general arbitrary *nth*-order Goldstone contribution to the skeleton expansion. The general form of a typical contribution is given by

$$\Sigma^{(n)}_{A\sigma} \propto \int \ldots \int_{-\infty}^{\infty} [\, \mathrm{d}\omega_1 \ldots \, \mathrm{d}\omega_m \, \mathrm{d}\bar{\omega}_1 \ldots \, \mathrm{d}\bar{\omega}_{m'}][D_{A\sigma'}(\omega_1) \ldots D_{A\sigma'}(\omega_m)$$
$$\times D_{A\sigma'}(\bar{\omega}_1) \ldots D_{A\sigma'}(\bar{\omega}_{m'})] \times \prod_i \frac{\Theta_i}{z-\varepsilon_i}, \tag{4.49}$$

where ε_i is the difference in the energies of a *collection* of internal ascending (particle-m) and descending (hole-m') lines, given by

$$\varepsilon_i = [(\omega_1+\omega_2+\ldots+\omega_m)-(\bar{\omega}_1+\bar{\omega}_2+\ldots+\bar{\omega}_{m'})], \tag{4.50a}$$

and Θ_i is a factor involving the associated step functions

$$\Theta_i = \theta(\omega_1)\ldots\theta(\omega_m)\theta(-\bar{\omega}_1)\ldots\theta(-\bar{\omega}_{m'}). \tag{4.50b}$$

In any arbitrary nth-order skeleton diagram, from conservation of particle number, the number of ascending (particle) and descending (hole) lines (including external lines) are equal at any point. In order to obtain the ω-dependence of a general nth-order diagram, we focus on the denominators involving $z = \omega + i\,\mathrm{sgn}(\omega)\eta$ ($[z - \varepsilon_i]$ or $[\varepsilon - z]$). These denominators come from taking horizontal cuts that cross precisely one (ingoing or outgoing) external line. The external line can be either a particle or a hole. If the external line is a particle, then there must be m internal particle lines and $m+1$ internal hole lines. Whereas, if the external line is a hole, then there are m internal particle lines and $m-1$ internal hole lines. In other words, the difference in the number of internal particle and hole lines is ± 1, i.e. the number of particle lines is given by: $m = m' \pm 1$.

Explicitly considering the case where $m = m' - 1$ (i.e. there is one more internal hole line than particle line), then it follows that a contribution to $\Sigma^{I(n)}_{A\sigma}(\omega) = -\,\mathrm{sgn}(\omega)\mathrm{Im}\Sigma^{I(n)}_{A\sigma}(\omega)$ is given by

$$\Sigma^{I(n)}_{A\sigma} \propto \int \ldots \int_{-\infty}^{\infty} [\,\mathrm{d}\omega_1 \ldots\, \mathrm{d}\omega_m\, \mathrm{d}\bar{\omega}_1 \ldots\, \mathrm{d}\bar{\omega}_{m+1}]\Theta_i[D_{A\sigma'}(\omega_1)\ldots D_{A\sigma'}(\omega_m) \times D_{A\sigma'}(\bar{\omega}_1)\ldots D_{A\sigma'}(\bar{\omega}_{m+1})] \times \delta(\omega - [(\bar{\omega}_1 + \ldots + \bar{\omega}_{m+1}) - (\omega_1 + \ldots + \omega_m)]). \tag{4.51}$$

where for the moment we ignore the spin-dependence of the spectral functions (σ' could be either $\uparrow$ or $\downarrow$). In relation to this equation we emphasize that a contribution to $\Sigma^{I(n)}_{A\sigma}$ will always involve *at least one* delta function constraint. Thus, on making the substitutions $\omega_i = v_i$ (for particles), $\bar{\omega}_i = -\bar{v}_i$ (for holes), eq. (4.51) becomes

$$\Sigma^{I(n)}_{A\sigma} \propto \int \ldots \int_{0}^{|\omega|} [\,\mathrm{d}v_1 \ldots\, \mathrm{d}v_m\, \mathrm{d}\bar{v}_1 \ldots\, \mathrm{d}\bar{v}_{m+1}][D_{A\sigma'}(v_1)\ldots D_{A\sigma'}(v_m) \times D_{A\sigma'}(-\bar{v}_1)\ldots D_{A\sigma'}(-\bar{v}_{m+1})] \times \delta(\omega - [\bar{v}_1 + \ldots + \bar{v}_{m+1} + v_1 + \ldots + v_m]), \tag{4.52}$$

where once again, the delta function constrains the integration limits: Since all v_i and $\bar{v}_i$ are positive, for low-ω the delta function constraint means that $v_1 \ldots v_m$, $\bar{v}_1 \ldots \bar{v}_{m+1}$ do not exceed $|\omega|$.

Spin-dependence

We now consider the aspect of spin dependence in the propagators. Once again, we assume that the low-ω form of the spectral functions is $D_{A\sigma}(\omega) \propto |\omega|^{\lambda_\sigma}$ (where $\lambda_\uparrow \neq \lambda_\downarrow$ in general, and $\lambda_\sigma > -1$). By virtue of spin conservation, for any horizontal cut between 2 interaction vertices there will be an odd number of *internal* σ lines and an even number of internal $-\sigma$ lines, for any contribution to the σ-spin self-energy, $\Sigma_{A\sigma}(\omega)$. We denote the number of $-\sigma$ lines by $2p$, with $p = 1, 2, 3, \ldots$.

Moreover, since we are considering a general cut across a diagram of m particle

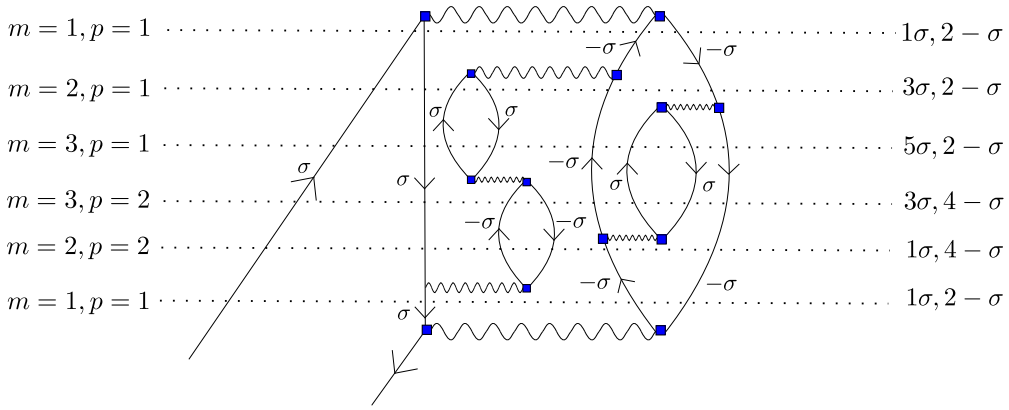


Figure 4.11: 7th-order skeleton diagram Goldstone contribution for $m + 1 = m'$. The horizontal dotted lines correspond to specific values of m and p. There are $[2p]$ $-\sigma$-lines and $[2m + 1 - 2p]$ σ-lines in each horizontal cut. In addition, there are m particle ($m + 1$ hole) lines in each horizontal cut.

lines and $m' = m + 1$ hole lines, there are a collection of $2m + 1$ lines in total. Therefore, generally there are $2m + 1 - 2p$ σ-lines in a horizontal cut of a diagram (with $p \leq m$, such that there is always at least one σ-line). A 7th-order skeleton diagram contribution is shown in Fig. 4.11. For each horizontal cut of the diagram between 2 interaction vertices (shown via the dotted lines) there is an associated energy denominator of the form $[z - \varepsilon_i]$. The values of the integers p and m are shown on the LHS, together with the corresponding number of σ and $-\sigma$ lines that are crossed in each cut on the RHS. Once again, making the substitutions $v_i = |\omega|\nu_i, \bar{v}_i = |\omega|\nu_i$ in eq. (4.52), the general form of an *nth* order contribution to the self-energy is

$$\Sigma^{I(n)}_{A\sigma} \propto |\omega|^{2m+(2m+1-2p)\lambda_\sigma+2p\lambda_{-\sigma}} \text{ for } m = 1, 2, 3, \ldots, \quad p = 1, 2, 3 \ldots m. \tag{4.53}$$

Explicitly considering the $(m = 1, p = 1)$ case yields the same power dependence as the second-order diagram, eq. (4.47), i.e. $\Sigma^{(n)I}_{A\sigma}(\omega) \propto |\omega|^{2+\lambda_\sigma+2\lambda_\sigma}$. For this form to be the leading order contribution for *any nth*-order skeleton diagram then the following inequality must be satisfied:

$$2 + \lambda_\sigma + 2\lambda_{-\sigma} \leq 2m + (2m + 1 - 2p)\lambda_\sigma + 2p\lambda_{-\sigma} \text{ for } m = 2, 3, \ldots, \quad p = 2, 3 \ldots m,$$

which can alternatively be written as

$$0 \leq (m - p)(\lambda_\sigma + 1) + (p - 1)(\lambda_{-\sigma} + 1). \tag{4.54}$$

Both $(m - p) \geq 0$, and $(p - 1) \geq 1$, and therefore provided that $\lambda_\sigma, \lambda_{-\sigma} \geq -1$, which they are for the spectra to be integrable, this inequality holds for all m, p.

The leading power dependence for any *nth*-order skeleton diagram is therefore the $m = 1$, $p = 1$ case - the same as for the second-order diagram. This analysis also may be shown to hold explicitly for the $m = m' + 1$ case, where there is one more particle line than hole lines in each horizontal cut across the diagram. Hence, we have shown to all orders in perturbation theory that the low-ω dependence of the self-energies, given spectra that have the form, $D_{A\sigma}(\omega) \overset{\omega\to 0}{\sim} |\omega|^{\lambda_\sigma}$, are

$$\boxed{\Sigma^I_{A\sigma}(\omega) \overset{\omega\to 0}{\sim} B|\omega|^{2+\lambda_\sigma+2\lambda_{-\sigma}}} \tag{4.55}$$

where B is a real coefficient, which in general has contributions from all orders in perturbation theory. If both λ_σ and $\lambda_{-\sigma} = 0$, such that the spectral functions reach a constant at the Fermi level (as they do for the metallic AIM [2]), then eq. (4.55) reduces to the familiar Fermi liquid result $\Sigma^I_\sigma(\omega) \propto \omega^2$, eq. (2.52b), originally derived by Luttinger [60]. However, we emphasize that the result in its present context is not just applicable to the SC Fermi liquid phase where $\Sigma_{A\sigma}(\omega)$ and $\Sigma_\sigma(\omega)$ coincide, but also to the LM phase where the TSE, $\Sigma_{A\sigma}(\omega) = \Sigma[G_{A\uparrow}, G_{A\downarrow}]$ is a functional of the broken symmetry propagators.

The corresponding low-ω form of the real part, $\Sigma^R_{A\sigma}(\omega)$ is readily determined from Hilbert transform, eq. (4.26). In summary if $[2 + \lambda_\sigma + 2\lambda_{-\sigma}] > 1$, then the real part is simply expressed as a Taylor series

$$[\Sigma^R_{A\sigma}(\omega) - \Sigma^R_{A\sigma}(0)] \overset{\omega\to 0}{\sim} \omega\left(\frac{\partial\Sigma^R_{A\sigma}(\omega)}{\partial\omega}\right)_{\omega=0} + \ldots. \tag{4.56a}$$

By contrast, if $-1 < [2 + \lambda_\sigma + 2\lambda_{-\sigma}] < 1$ (c.f. eq. (4.27)), then

$$[\Sigma^R_{A\sigma}(\omega) - \Sigma^R_{A\sigma}(0)] \overset{\omega\to 0}{\propto} |\omega|^{2+\lambda_\sigma+2\lambda_{-\sigma}}, \tag{4.56b}$$

i.e. the low-ω correction goes with the same power as the imaginary part.

4.6.5 Self-consistency for the PAIM

In the previous section we derived the low-ω dependence of the self-energy, $\Sigma_{A\sigma}(\omega)$, order-by-order in perturbation theory. For the pseudogap AIM we now show what solutions are internally *self-consistent*. By inserting the low-ω forms of the self-energy, eqs. (4.55-4.56) into the spectral function, and then comparing the result with the assumed low-ω form, $\pi D_{A\sigma}(\omega) \overset{\omega\to 0}{\sim} |\omega|^{\lambda_\sigma}$, we may determine what conditions are imposed on the exponents, $\lambda_\uparrow$, $\lambda_\downarrow$. As we examine below, for the solution to be *self-consistent*, the input and output values of the exponents must be equivalent.

By inserting the hybridization function (eq. (4.1b)) into the Dyson equation

(eq. (3.23)), and using $D_{A\sigma}(\omega) = -\frac{1}{\pi}\,\mathrm{sgn}(\omega) G^{t}_{A\sigma}(\omega)$, the broken-symmetry spectral functions for the pseudogap AIM may be written as

$$\pi D_{A\sigma}(\omega) = \frac{|\omega|^{r} + \Sigma^{I}_{A\sigma}(\omega)}{[\omega - \varepsilon^{*}_{A\sigma} + \mathrm{sgn}(\omega)\beta(r)|\omega|^{r} - [\Sigma^{R}_{A\sigma}(\omega) - \Sigma^{R}_{A\sigma}(0)]]^{2} + [|\omega|^{r} + \Sigma^{I}_{A\sigma}(\omega)]^{2}} \tag{4.57}$$

where we have set the unit of energy, $\Gamma_{0}^{\frac{1}{1-r}} \equiv 1$ (for reasons of brevity). By inserting the low-ω form of the self-energy $\Sigma_{A\sigma}(\omega)$ from eq. (4.55) into eq. (4.57), we may obtain the low-ω dependence of $\pi D_{A\sigma}(\omega)$. Then on comparison of this form to the low-ω dependence we initially assumed, i.e. $D_{A\sigma}(\omega) \propto |\omega|^{\lambda_{\sigma}}$, we may obtain specific self-consistent values of the exponents, λ_{σ}.

The distinct solutions that we may obtain are explicitly dependent on whether the renormalized levels, $\varepsilon^{*}_{A\sigma}$ are finite or vanishing and also on whether $r \lessgtr 2 + \lambda_{\sigma} + 2\lambda_{-\sigma}$. In all cases we consider r in the range $0 < r < 1$.

Finite renormalized levels

We first consider the generic case where both renormalized levels, $\varepsilon^{*}_{A\uparrow}$, $\varepsilon^{*}_{A\downarrow} \neq 0$. On insertion of eq. (4.55) into eq. (4.57) we obtain

$$\pi D_{A\sigma}(\omega) \overset{\omega\to 0}{\sim} \frac{|\omega|^{r} + B|\omega|^{2+\lambda_{\sigma}+2\lambda_{-\sigma}}}{[\varepsilon^{*}_{A\sigma}]^{2}}. \tag{4.58}$$

There are two distinct cases we must now consider:

1. If $r < 2 + \lambda_{\sigma} + 2\lambda_{-\sigma}$, the low-$\omega$ form of eq. (4.58) simply becomes

$$\pi D_{A\sigma}(\omega) \overset{\omega\to 0}{\sim} \frac{|\omega|^{r}}{[\varepsilon^{*}_{A\sigma}]^{2}}, \tag{4.59a}$$

which (on comparison with $D_{A\sigma}(\omega) \propto |\omega|^{\lambda_{\sigma}}$) indicates that $r = \lambda_{\uparrow} = \lambda_{\downarrow}$, and from eqs. (4.55-4.56) the TSEs become

$$\Sigma^{I}_{A\sigma}(\omega) \propto |\omega|^{2+3r}, \qquad [\Sigma^{R}_{A\sigma}(\omega) - \Sigma^{R}_{A\sigma}(0)] \propto \omega. \tag{4.59b}$$

This result is self-consistent for the entire r range that we consider.

2. If $r \geq 2 + \lambda_{\sigma} + 2\lambda_{-\sigma}$, then eq. (4.58) becomes

$$\pi D_{A\sigma}(\omega) \overset{\omega\to 0}{\sim} \frac{B|\omega|^{2+\lambda_{\sigma}+2\lambda_{-\sigma}}}{[\varepsilon^{*}_{A\sigma}]^{2}} \tag{4.60}$$

and therefore $\lambda_{\sigma} = 2 + \lambda_{\sigma} + 2\lambda_{-\sigma}$, such that $\lambda_{-\sigma} = -1$. However, we initially assumed that both $\lambda_{\uparrow}, \lambda_{\downarrow} > -1$, so this solution is not self-consistent.

Vanishing renormalized levels

Alternatively, both renormalized levels may vanish, i.e. $\varepsilon^*_{A\uparrow}$, $\varepsilon^*_{A\downarrow} = 0$. In this case:

1. If $r < 2 + \lambda_\sigma + 2\lambda_{-\sigma}$, the the low-$\omega$ form of the spectrum, eq. (4.57), reduces to

$$\pi D_{A\sigma}(\omega) \overset{\omega\to 0}{\sim} \frac{|\omega|^{-r}}{[1+\beta^2(r)]}, \tag{4.61}$$

   and therefore $-r = \lambda_\uparrow = \lambda_\downarrow$, provided $r < \frac{1}{2}$. The self-energy is then given from eqs. (4.55-4.56) by

$$\Sigma^I_{A\sigma}(\omega) \propto |\omega|^{2-3r}, \qquad [\Sigma^R_{A\sigma}(\omega) - \Sigma^R_{A\sigma}(0)] \propto \omega \qquad : 0 < r < \tfrac{1}{3}, \tag{4.62a}$$

$$\propto |\omega|^{2-3r} \quad : \tfrac{1}{3} < r < \tfrac{1}{2}, \tag{4.62b}$$

   (for $r = \frac{1}{3}$, $\Sigma^R_{A\sigma}(\omega) - \Sigma^R_{A\sigma}(0) \propto \omega \ln|\omega|$).

2. If $r \geq 2 + \lambda_\sigma + 2\lambda_{-\sigma}$, then eq. (4.57) becomes

$$\pi D_{A\sigma}(\omega) \propto |\omega|^{-2-\lambda_\sigma - 2\lambda_{-\sigma}} \tag{4.63}$$

   and therefore $\lambda_\sigma = -2 - \lambda_\sigma - 2\lambda_{-\sigma}$. $\lambda_\sigma + \lambda_{-\sigma} = -1$ is also a self-consistent solution.

One vanishing renormalized level

The third and final case that we consider is if one renormalized level vanishes, for example $\varepsilon^*_{A\uparrow} = 0$, but $\varepsilon^*_{A\downarrow} \neq 0$. In this case there are 4 distinct scenarios:

1. If $r < 2 + \lambda_\uparrow + 2\lambda_\downarrow$, $r < 2 + \lambda_\downarrow + 2\lambda_\uparrow$, then eq. (4.57) becomes

$$\pi D_{A\uparrow}(\omega) \propto |\omega|^{-r}, \qquad \pi D_{A\downarrow}(\omega) \propto |\omega|^{r}, \tag{4.64a}$$

   therefore $\lambda_\uparrow = -r$ and $\lambda_\downarrow = r$. The corresponding self-energies are

$$\Sigma^I_{A\uparrow}(\omega) \propto |\omega|^{2+r}, \quad \Sigma^I_{A\downarrow}(\omega) \propto |\omega|^{2-r}, \qquad [\Sigma^R_{A\sigma}(\omega) - \Sigma^R_{A\sigma}(0)] \propto \omega. \tag{4.64b}$$

2. If $r \geq 2 + \lambda_\uparrow + 2\lambda_\downarrow$, $r \geq 2 + \lambda_\downarrow + 2\lambda_\uparrow$, then

$$\pi D_{A\uparrow}(\omega) \propto |\omega|^{-2-\lambda_\uparrow - 2\lambda_\downarrow} \qquad \pi D_{A\downarrow}(\omega) \propto |\omega|^{2+\lambda_\downarrow + 2\lambda_\uparrow} \tag{4.65}$$

   and therefore $\lambda_\uparrow = -2 - \lambda_\uparrow - 2\lambda_\downarrow$, $\lambda_\uparrow + \lambda_\downarrow = -1$. Also, $\lambda_\downarrow = 2 + \lambda_\downarrow + 2\lambda_\uparrow$, $\lambda_\uparrow = -1$. Both $D_{A\uparrow}(\omega)$ and $D_{A\downarrow}(\omega)$ are not integrable and therefore this

solution is not self-consistent.

3. If $r < 2 + \lambda_\uparrow + 2\lambda_\downarrow$, but $r \geq 2 + \lambda_\downarrow + 2\lambda_\uparrow$ then

$$\pi D_{A\uparrow}(\omega) \propto |\omega|^{-r}, \qquad \pi D_{A\downarrow}(\omega) \propto |\omega|^{2+\lambda_\downarrow+2\lambda_\uparrow}, \tag{4.66}$$

and therefore $\lambda_\uparrow = -r$. Also, $\lambda_\downarrow = 2 + \lambda_\downarrow + 2\lambda_\uparrow$, $\lambda_\uparrow = r = -1$, so once again this solution is not self-consistent.

4. If $r \geq 2 + \lambda_\uparrow + 2\lambda_\downarrow$, but $r < 2 + \lambda_\downarrow + 2\lambda_\uparrow$ then

$$\pi D_{A\uparrow}(\omega) \propto |\omega|^{-2-\lambda_\uparrow-2\lambda_\downarrow}, \qquad \pi D_{A\downarrow}(\omega) \propto |\omega|^{r}, \tag{4.67}$$

and therefore $\lambda_\uparrow + \lambda_\downarrow = -1$. Also, $\lambda_\downarrow = r$, $\lambda_\uparrow = -1 - r$. We are considering the case of $r > 0$, so once again this solution is not self-consistent, as $\pi D_{A\uparrow}(\omega)$ is not integrable.

Therefore the only case that is self-consistent is the first scenario given by eq. (4.64).

4.6.6 Phases of the PAIM

	Self-energies	Spectra	Renormalized levels	r range	Applicable to
(A)	$\Sigma^I_{A\sigma}(\omega) \propto \lvert\omega\rvert^{2+3r}$	$D_{A\sigma}(\omega) \propto \lvert\omega\rvert^{r}$	$\epsilon^*_{A\sigma} \neq 0$	$0 < r < 1$	ASC - $\lvert h\rvert \geq 0$ LM - $h = 0$
(B)	$\Sigma^I_{A\sigma}(\omega) \propto \lvert\omega\rvert^{2-3r}$	$D_{A\sigma}(\omega) \propto \lvert\omega\rvert^{-r}$	$\epsilon^*_{A\sigma} = 0$	$-1 < r < \frac{1}{2}$	SSC - $h = 0$
(C)	$\Sigma^I_{A\sigma}(\omega) \propto \lvert\omega\rvert^{2+r}$ $\Sigma^I_{A-\sigma}(\omega) \propto \lvert\omega\rvert^{2-r}$	$D_{A\sigma}(\omega) \propto \lvert\omega\rvert^{-r}$ $D_{A-\sigma}(\omega) \propto \lvert\omega\rvert^{r}$	$\epsilon^*_{A\sigma} = 0$ $\epsilon^*_{A-\sigma} \neq 0$	$0 < r < 1$	finite-field- $h = h'$
(D)	$\Sigma^I_{A\sigma}(\omega) \propto \lvert\omega\rvert^{2+\lambda_\sigma+2\lambda_{-\sigma}}$	$D_{A\sigma}(\omega) \propto \lvert\omega\rvert^{-2-\lambda_\sigma-2\lambda_{-\sigma}}$	$\epsilon^*_{A\sigma} = 0$	$-1 = \lambda_\sigma + \lambda_{-\sigma}$ $r \geq 1 + \lambda_{-\sigma}$	NA

Figure 4.12: Summary of the self-consistent solutions found from the order by order analysis above.

Fig. 4.12 shows a summary of the self-consistent solutions found above. Case (A), corresponding to eq. (4.59), applies to the general LM phase where both renormalized levels are non-zero and distinct, $\varepsilon^*_{A\uparrow}(0) \neq \varepsilon^*_{A\downarrow}(0)$ (as shown from the Friedel sum rule in Section 4.3.2). The TSEs therefore vanish with a power *greater* than the hybridization function and the analysis of Section 4.5 for the low-ω behaviour of the SSEs holds, i.e. $\Sigma^I(\omega) \propto |\omega|^r$ $(x \neq 0)$, $\Sigma^I(\omega) \propto |\omega|^{-r}$ $(x = 0)$.

Case (A) also applies to the zero-field ASC phase where the renormalized levels $\varepsilon^*_{A\uparrow}(0) = \varepsilon^*_{A\downarrow}(0) = \varepsilon^*(0)$ are independent of spin. In any SC phase the TSES and SSEs coincide, the self-energy, $\Sigma^I(\omega) \equiv \Sigma^I_{A\sigma}(\omega) \propto |\omega|^{2+3r}$, vanishes faster than the hybridization function. The low-ω behaviour of the propagator is thus determined

solely by the vanishing of the hybridization, and therefore $D(\omega) = D_{A\sigma}(\omega)$ has the same asymptotic behaviour as the non-interacting limit - eq. (4.6), but with ε replaced by $\varepsilon^*(0)$.

As we shall see in Section 4.10, the third scenario that case (A) applies to is the case of a finite (local) field, h, when both renormalized levels are non-zero, $\varepsilon^*_{A\uparrow}(|h|), \varepsilon^*_{A\downarrow}(|h|) \neq 0$. The spin-dependent self-energies $\Sigma_\sigma(\omega, h) \equiv \Sigma_{A\sigma}(\omega, |h|) \propto |\omega|^{2+3r}$, once again vanish faster than the hybridization. The spectra, $D_\sigma(\omega, h) \equiv D_{A\sigma}(\omega, |h|) \propto |\omega|^r$, with the same low-$\omega$ dependence as the non-interacting limit with $[\varepsilon - \sigma h]$ replaced by $\varepsilon^*_\sigma(h)$.

Case (B) where both renormalized levels vanish, $\varepsilon^*_{A\uparrow} = \varepsilon^*_{A\downarrow} = \varepsilon^* = 0$, applies to the ph symmetric ($x = 0$) SC (SSC) phase at zero-field. The self-energy, $\Sigma^I(\omega) \propto |\omega|^{2-3r}$ vanishes faster than the hybridization provided that $r < \frac{1}{2}$. The spectral function thus diverges $D(\omega) \equiv D_\sigma(\omega) \propto |\omega|^{-r}$ as $\omega \to 0$ with the same form as the non-interacting limit, eq. (4.5a). The fact that the low-ω form of the self-energy only vanishes with an exponent greater than the hybridization if $r < \frac{1}{2}$ means that the symmetric SC (Fermi liquid) phase can only exist in this range. It is known from direct NRG results (and an analysis of the relevant operators around the NRG fixed point) [43] that this is indeed the case; the ground state of the interacting model for any $r > \frac{1}{2}$ is a non-Fermi liquid LM moment phase for any infinitesimal interaction, $U = 0^+$. The low-ω behaviour derived here from general diagrammatic arguments [60] therefore predict that the SSC phase cannot exist for $r > \frac{1}{2}$.

As we shall see in Section 4.10, Case (C) applies to a specific line of points in the (U, h) plane for a fixed $x \neq 0$ where one of the renormalized levels, $\varepsilon^*_{A\sigma}(|h|)$ crosses the Fermi level at finite-field, whilst the other level, $\varepsilon^*_{A-\sigma}(|h|)$ remains finite. At this fixed h for a given U and x, one of the spectral functions effectively becomes ph symmetric on the lowest ω-scales, and diverges, $D_{A\sigma}(\omega, |h|) \propto |\omega|^{-r}$, while the other spectral function vanishes, $D_{A-\sigma}(\omega, |h|) \propto |\omega|^r$.

Finally we note that the final self-consistent solution, Case (D), does not apply to any specific phase of the PAIM.

4.6.7 Self-consistency in the atomic limit

Before proceeding further we comment on Luttinger self-consistency for the simple atomic limit. In Section 3.6 we simply asserted that first-order self-consistent perturbation theory (within a SSE description for the empty/doubly-occupied regimes, and within a TSE description for the singly-occupied regime) was exact. In this present section we show that this assertion is indeed correct by a simple diagrammatic argument.

For the empty regime where $\varepsilon > 0$, the spectral function is given simply from eq. (3.80) by the delta function $\pi D_{A\sigma}(\omega) = \pi D_{A-\sigma}(\omega) = \pi D(\omega) = \delta(\omega - \varepsilon)$. Thus,

the spectral function clearly only has poles at positive-ω; however as we have seen above, every nth-order skeleton diagram (above 1st-order) contains m particle lines and $m \pm 1$ hole lines (with $m \geq 1$). Each dynamical skeleton diagram contains at least one hole line and consequently an associated step function that is only non-zero for negative-ω. Therefore any diagram above 1st-order level involves factors-$\delta(\omega - \varepsilon)\theta(-\omega)$ which vanish for $\varepsilon > 0$.

In the case where the impurity is doubly occupied and $\varepsilon + U < 0$, the spectrum is $\pi D(\omega) = \delta(\omega - \varepsilon - U)$, and so clearly only has poles at negative-ω. By the same argument as above, any dynamical skeleton diagram must contain at least one particle line and therefore factors of the form $\delta(\omega - \varepsilon - U)\theta(+\omega) = 0$ arise. Thus, once again all $n > 1$ diagrams vanish in the contribution to $\Sigma(\omega)$.

The final case is where the system is in the singly-occupied LM regime. In this scenario the level energy lies in the range $\varepsilon + U > 0$, $\varepsilon < 0$. From eq. (3.82) the spectral functions are spin-dependent given by $\pi D_{A\sigma}(\omega) = \delta(\omega - \varepsilon - (1 - \sigma)\frac{1}{2}U)$ (with $\sigma = \pm 1$). Thus all $D_{A\uparrow}(\omega)$ have poles for $\omega < 0$ and all $D_{A\downarrow}(\omega)$ have poles for $\omega > 0$. For any dynamical contribution to the skeleton expansion to be non-zero, all $\uparrow$-propagators would have to be particle lines and all $\downarrow$-propagators hole lines. However, this scenario would violate spin conservation at the vertices: As discussed above, for any nth-order ($n > 1$) contribution to $\Sigma_{A\uparrow}(\omega)$, there are an even number of $\downarrow$-lines at any point in the diagram. Therefore for any dynamical contribution to $\Sigma_{A\uparrow}(\omega)$ there is at least one $\downarrow$-particle line with an associated factor of $\theta(+\omega)D_{A\downarrow}(\omega) = \theta(+\omega)\delta(\omega - \varepsilon)$ which vanishes for $\varepsilon < 0$.

These results in each regime are clearly self-consistent as all dynamical contributions (diagrams above 1st-order) to the skeleton expansion vanish. As a consequence, the first-order bubble diagram (shown in Fig. 3.4) is the only diagram which makes a finite contribution to $\Sigma_{A\sigma}(\omega)$ in the singly-occupied regime and to $\Sigma_{\sigma}(\omega)$ in the empty/doubly-occupied regimes.

4.7 Low-ω behaviour: SC phase

Using the self-consistent results above for the low-ω form of the SSE, $\Sigma(\omega)$, we now move to consider the low-ω behaviour of the propagator, $G(\omega)$, in each of the zero-field SC phases (ASC and SSC).

4.7.1 ASC phase: $x \neq 0$

At zero-field in any SC phase, all propagators are spin-independent and the SSE and TSE descriptions coincide. We therefore may drop all $A\sigma$ labels from the relevant quantities in the discussion that follows.

Away from ph symmetry the renormalized level, $\varepsilon^*(0) \equiv \varepsilon^* = \varepsilon + \Sigma^R(0)$, is

non-vanishing for all $U < U_c$. From the self-consistent deductions of the last section we found when $\varepsilon^* \neq 0$ that the unique self-consistent solution is given by (case (A) above):

$$\Sigma^I(\omega) \overset{\omega\to 0}{\sim} a_{ASC}|\omega|^{2+3r}. \tag{4.68a}$$

where a_{ASC} is a real coefficient. From Hilbert transform, eq. (4.26), the real part as $\omega \to 0$ can be obtained, its behaviour is readily shown to be linear in ω and given by

$$\Sigma^R(\omega) - \Sigma^R(0) \overset{\omega\to 0}{\sim} -(\tfrac{1}{Z} - 1)\omega, \tag{4.68b}$$

with Z the usual 'quasiparticle-weight' given by eq. (2.55), considering a Taylor expansion for $\Sigma^R(\omega)$ about $\omega = 0$, eq. (2.53). The low-ω form of the propagator can then be obtained via the Dyson equation, eq. (2.50), as

$$G(\omega) \overset{\omega\to 0}{\sim} [\omega^+ - \varepsilon^* - (\mathrm{sgn}(\omega)\beta(r) + i)|\omega|^r + (\tfrac{1}{Z} - 1)\omega - ia_{ASC}|\omega|^{2+3r}]^{-1}. \tag{4.69}$$

Furthermore, we may define a low energy (Kondo) scale in the SC phase in terms of Z that vanishes at the QCP as $U \to U_c^-(r)$ via

$$\omega_* \equiv \omega_K = [\Gamma_0 Z]^{\frac{1}{1-r}} \tag{4.70}$$

where for the metallic $r = 0$ case, the scale simply reduces to $\omega_K = \Gamma_0 Z$ [2]. With this choice of the low-energy scale, the low-$\tilde{\omega} = (\omega/\omega_*)$ *scaling form* of eq. (4.69) can be written as

$$\Gamma_0\omega_*^r G(\omega) \overset{\tilde{\omega}\to 0}{\sim} \left[\tilde{\omega}^+ - \frac{\varepsilon^*}{\Gamma_0\omega_*^r} - (\mathrm{sgn}(\tilde{\omega})\beta(r) + i)|\tilde{\omega}|^r\right]^{-1}. \tag{4.71}$$

The contribution from $\Sigma^I(\omega)$ has been neglected in this 'quasiparticle form' as it vanishes more rapidly than both the hybridization function and $\tilde{\omega}$. This equation is the ASC phase analog of the LM phase scaling form of eq. (4.30). The local single particle spectrum is then given in (non-scaling) and scaling form by

$$\pi D(\omega) \overset{\omega\to 0}{\sim} \frac{\Gamma_0|\omega|^r}{[\varepsilon^*]^2}, \qquad \pi\Gamma_0\omega_*^r D(\omega) \overset{\tilde{\omega}\to 0}{\sim} \frac{|\tilde{\omega}|^r}{(\varepsilon^*/\Gamma_0\omega_*^r)^2}, \tag{4.72}$$

where we implicitly assume that the ratio $\varepsilon^*/[\Gamma_0\omega_*^r]$ is finite as $U \to U_c^-$. In other words, $\varepsilon^* \propto \omega_*^r \to 0$ as the transition is approached (this is indeed the case as shown by the numerical calculations of Fig. 4.2). As is true for any Fermi liquid, the low-ω behaviour of eq. (4.72) has precisely the same structure as that of the non-interacting limit, such that as interactions are slowly switched off, the form of

eq. (4.6) is recovered. This low-ω form for $D(\omega)$ was first found from the NRG calculations of ref [35], and also within the LMA [34]. However, here we emphasize that we have deduced its form *exactly* within the Luttinger self-consistency [60] framework of the last section.

4.7.2 SSC phase: $x = 0$

In the zero-field ph symmetric strong-coupling phase, the spin-independent renormalized level $\varepsilon^*(x = 0)$ vanishes by symmetry (obtained from eq. (4.3d) with both $h = 0, x = 0$). It is then case (B) of the above analysis that applies to the phase, with the low-ω form of the SSE given by

$$\Sigma^I(\omega) \overset{\omega\to 0}{\sim} a_{SSC}|\omega|^{2-3r} \qquad : r < \frac{1}{2}. \tag{4.73}$$

In order for the SSE to be subsidiary to the hybridization function at low-ω, i.e. $2 - 3r > r$, the solutions are only self-consistently possible for $r < \frac{1}{2}$, confirming the known fact [39, 43, 46] that as $r \to \frac{1}{2}^-$, $U_c(r) \to 0$. In contrast for $r > \frac{1}{2}$ for any finite U only LM phase solutions exist. Fig. 4.13 shows a schematic representation of the phase diagram for $x = 0$ in the (U, r) plane. (For $r \to 0$ it is known [39, 43] that $U_c(r)$ diverges as $1/r$ and hence for the metallic $r = 0$ model there is no phase transition, with only SSC Fermi liquid solutions possible.)

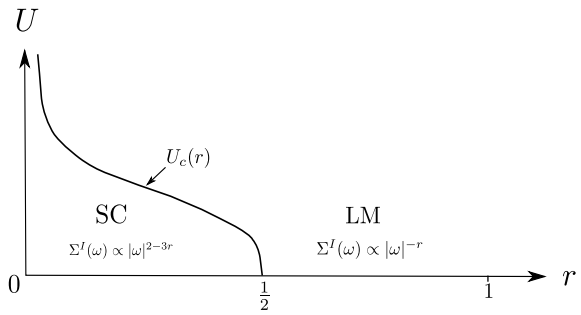


Figure 4.13: Schematic phase diagram in the (r, U) plane for $x = 0$, reproduced from ref [100].

The corresponding low-ω form of $\Sigma^R(\omega)$ follows from the Hilbert transform, eq. (4.26). In accordance with eq. (4.62), for $r < \frac{1}{3}$, such that $2 - 3r > 1$, $[\Sigma^R(\omega) - \Sigma^R(0)] \overset{\omega\to 0}{\sim} -(\frac{1}{Z} - 1)\omega$, i.e. the same form as eq. (4.68b). The resultant quasiparticle form of $G(\omega)$ is then given by eq. (4.71) with $\varepsilon^* = 0$. By contrast for $r > \frac{1}{3}$, such that $2 - 3r < 1$, $[\Sigma^R(\omega) - \Sigma^R(0)] \overset{\omega\to 0}{\sim} -\mathrm{sgn}(\omega)\beta(2 - 3r)a_{SSC}|\omega|^{2-3r}$ in accordance with eq. (4.28). The quasiparticle form of $G(\omega)$ then becomes

$$\Gamma_0\omega_*^r G(\omega) \overset{\tilde{\omega}\to 0}{\sim} \left[\frac{\omega_*^{1-r}}{\Gamma_0}\tilde{\omega}^+ - (\mathrm{sgn}(\tilde{\omega})\beta(r) + i)|\tilde{\omega}|^r\right]^{-1}, \tag{4.74}$$

with $\omega_* \equiv \omega_K$ from eq. (4.70). The low-ω form of the spectral function, $D(\omega) = -\frac{1}{\pi}\mathrm{Im}G(\omega)$, for $0 < r < \frac{1}{2}$ then reduces to

$$\pi D(\omega) \overset{\omega\to 0}{\sim} \frac{|\omega|^{-r}}{\Gamma_0[1+\beta^2(r)]}, \qquad \pi\Gamma_0\omega_*^r D(\omega) \overset{\tilde{\omega}\to 0}{\sim} \frac{|\tilde{\omega}|^{-r}}{1+\beta^2(r)}, \tag{4.75}$$

such that the behaviour is the same as the non-interacting limit, eq. (4.5a), once again reflecting adiabatic continuity and the inherent Fermi liquid nature of the SSC phase. Furthermore, the well known [100] spectral pinning condition eq. (4.39) is satisfied.

4.8 Scaling arguments as the QCP is approached

We now consider the quantum critical point (QCP), and more specifically the behaviour of the single particle propagator, $G(\omega) = G_\sigma(\omega, h = 0)$ as the QCP is approached from either phase. As discussed above, at zero-field there is a low-energy scale, ω_*, defined in each phase via eqs. (4.20, 4.70), that vanishes at the QCP as $U \to U_c^{\pm}(r)$. We define a (dimensionless) function of U/U_c that vanishes at the QCP from either phase

$$u = |1 - \tfrac{U}{U_c}| \to 0 \qquad : U \to U_c^{\pm}, \tag{4.76}$$

such that the low-energy scale, $\omega_*/\Gamma_0^{1/(1-r)} = u^a$, with a power a. We set the unit of energy $[\Gamma_0^{1/(1-r)}] = 1$ in the proceeding discussion for simplicity.[14] In the scaling regime (near the QCP in either phase, where u vanishes), the propagator, $G(\omega)$ can then be written in the general scaling form [34]

$$G(\omega) \sim u^{-ab}\Psi_\alpha\left(\frac{\omega}{u^a}\right) = \omega_*^{-b}\Psi_\alpha\left(\frac{\omega}{\omega_*}\right), \tag{4.77}$$

where a, b are exponents and $\Psi_\alpha(y)$ is a function of y with $\alpha =$ LM or SC. The quantity $\omega_*^b G(\omega)$ is therefore a *universal* function of $\tilde{\omega} = \omega/\omega_*$ as the transition is approached, independent of the intitial 'bare' parameters in the Hamiltonian. The scaling equation, eq. (4.77), strictly holds for *any*-$\tilde{\omega}$ in the scaling regime (where the limit $\omega_* \to 0$ is taken).

In eq. (4.77) we have eliminated the exponent a from consideration by writing the scale, $\omega_* = u^a$. The exponent b can be determined by direct consideration of the low-$\tilde{\omega}$ 'quasiparticle' forms in each phase, eqs. (4.30, 4.36) for the LM phase, and eqs. (4.71, 4.74) for the SC phase. We find that in all cases, regardless of phase or particle-hole asymmetry, that the exponent $b = r$. The general scaling form of the

[14] If $\Gamma_0^{1/(1-r)}$ is explicitly kept in the equations we find: $\Gamma_0^{1/(1-r)}G(\omega) \sim u^{-ab}\Psi_\alpha\big(\omega/[\Gamma_0^{1/(1-r)}]u^a\big) = \omega_*^{-b}[\Gamma_0^{1/(1-r)}]^b\Psi_\alpha(\frac{\omega}{\omega_*})$, such that $\Gamma_0^{\frac{1-b}{1-r}}\omega_*^b G(\omega) \sim \Psi_\alpha(\frac{\omega}{\omega_*})$

propagator (for *any*-$\tilde{\omega}$) is then given by

$$\Gamma_0 \omega_*^r G(\omega) = \Psi_\alpha(\tilde{\omega}), \tag{4.78a}$$

and therefore the corresponding scaling form of the spectrum, $D(\omega) = -\frac{1}{\pi}\mathrm{Im}G^r(\omega)$ is

$$\pi\Gamma_0 \omega_*^r D(\omega) = \Psi_\alpha^I(\tilde{\omega}), \tag{4.78b}$$

with $\Psi_\alpha(\tilde{\omega}) = \Psi_\alpha^R(\tilde{\omega}) - i\Psi_\alpha^I(\tilde{\omega})$ (for the retarded functions). As we have seen, the low-$\tilde{\omega}$ behaviour of this scaling function characterizes the behaviour in each distinct phase. In Section 4.5 we showed via eq. (4.31b) that for $|\tilde{\omega}| \ll 1$, $\Psi_{LM}^I(\tilde{\omega}) \propto |\tilde{\omega}|^r$ (for any x). Similarly, in the ASC phase for $|\tilde{\omega}| \ll 1$, $\Psi_{SC}^I(\tilde{\omega}) \propto |\tilde{\omega}|^r$ via eq. (4.72). By contrast, for the SSC phase the renormalized level $\varepsilon^*(0)$ vanishes by symmetry, and in consequence, the scaling function has the divergent behaviour, $\Psi_{SC}^I(\tilde{\omega}) \propto |\tilde{\omega}|^{-r}$ via eq. (4.75).

Furthermore, the low-$\tilde{\omega}$ behaviour of $\Psi_\alpha^I(\tilde{\omega})$ described above has been shown via numerically exact NRG calculations for the ph symmetric [39, 41], and also for the ph asymmetric models [35], as well as arising from the local moment approach (LMA) [34,44,45]. We also confirm these numerical results explicitly here. Fig. 4.14 shows the $x = -10$ low-$\tilde{\omega}$ of $|\omega|^r \Psi_\alpha^I(\tilde{\omega}) = \pi\Gamma_0|\omega|^r D(\omega)$ in the ASC phase ($U < U_c$), and LM phase ($U > U_c$) for $r = 0.45$, calculated via NRG. Interestingly, Fig. 4.14

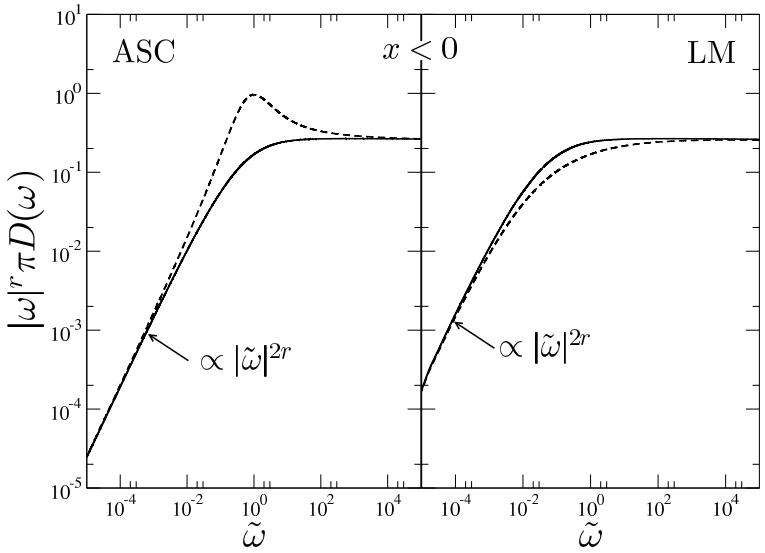


Figure 4.14: NRG scaling spectra $|\tilde{\omega}|^r \Psi_\alpha^I(\tilde{\omega}) = \pi\Gamma_0|\omega|^r D(\omega)$, in both phases plotted versus $\tilde{\omega} = \omega/\omega_*$ on a log-scale for $x = -10$, $r = 0.45$ (where $U_c/\pi \sim 9.5$). The LHS shows the ASC phase, the RHS shows the LM phase. Dotted lines show spectra for $\tilde{\omega} < 0$, and solid lines show $\tilde{\omega} > 0$. For the ASC phase, the peak is for $\omega < 0$, for the LM phase, the peak is for $\omega > 0$. Once again, we have set the energy scale $\Gamma_0^{1/(1-r)} = 1$.

demonstrates, as has been shown previously [35], that the coefficients of the leading low-$\tilde{\omega}$ dependence of $\Psi^I_{SC}(\tilde{\omega})$, $\Psi^I_{LM}(\tilde{\omega})$ are equal for both positive and negative frequencies, regardless of whether the model is ph symmetric/asymmetric. In other words, on the very lowest-energy scales any spectral asymmetry goes away, and the spectra, regardless of the initial x, become ph symmetric. In the ASC phase this is entirely natural, coming from the form of eq. (4.72). Since the self-energy vanishes with an exponent greater than r, the $|\tilde{\omega}| \ll 1$ behaviour of $\Psi^I_{SC}(\tilde{\omega})$ is controlled solely by the hybridization function, $\Gamma^I(\omega)$, which is an even function of ω. In the LM phase, renormalization group arguments show that the same fixed point arises for any x [35, 40, 43]. Furthermore, this LM fixed point is ph symmetric in nature (with an effective $x = 0$), such that any ph asymmetry in the spectral function flows to zero on the lowest frequency scales.[15]

The x-dependence of the scaling spectra may be explicitly labeled, i.e. $\Psi_\alpha(\tilde{\omega}) \equiv \Psi_\alpha(\tilde{\omega}, x)$. From a ph transformation $[x \to -x]$ at zero-field, the spectral function is related by, $D(\omega, x) = D(-\omega, -x)$ (eq. (4.3b)). In consequence from eq. (4.78b) the scaling spectra have the symmetry

$$\Psi^I_\alpha(\tilde{\omega}, x) = \Psi^I_\alpha(-\tilde{\omega}, -x), \tag{4.79}$$

and therefore only $x \leq 0$ or $x > 0$ need be explicitly considered. In fact, as we shall see below from direct NRG calculations, the full scaling spectra in each phase, $\Psi^I_\alpha(\tilde{\omega}, x)$, for a given $\mathrm{sgn}(x)$ are entirely independent of $|x|$.

4.9 Quantum critical point

The QCP occurs at the point $U = U_c(r)$ where the low-energy scale, ω_*, vanishes coming from either phase. As a consequence, it follows immediately that precisely at the QCP, the system is scale-free. In addition, the QCP may also be accessed by considering a fixed $\tilde{\omega}$ in the limit that $\omega_* \to 0$. It is then the large $|\tilde{\omega}| = |\omega|/\omega_*$ behaviour of the scaling functions that give the QCP behaviour. In order for the QCP to be scale free and the scaling spectrum, $\Psi^I_\alpha(\tilde{\omega}, x)$, to be a universal function of $\tilde{\omega}$ in the large-$|\tilde{\omega}|$ limit, eq. (4.78b) must take the form

$$\Psi^I_\alpha(\tilde{\omega}, x) = \pi\Gamma_0\omega_*^r D(\omega) \propto \left(\frac{|\omega|}{\omega_*}\right)^{-r} \qquad : |\tilde{\omega}| \gg 1, \tag{4.80a}$$

such that the ω_* dependence cancels on both sides of the equation and the low-ω dependence *identically at the QCP* is given by

$$\pi\Gamma_0 D(\omega) \propto |\omega|^{-r} \qquad : \omega_* = 0. \tag{4.80b}$$

[15] We refer the reader to the NRG flow diagrams of Fig. C.3 in Appendix C for further clarification.

As a consequence of the form of eq. (4.80a), the QCP behaviour may be obtained by considering a U close to $U_c(r)$ (such that ω_* is small). On plotting the scaling spectrum, $\Psi^I_\alpha(\tilde{\omega}, x)$, it is then the large-$\tilde{\omega}$ 'tails' that give the behaviour of the QCP. It is only precisely at the QCP itself, where $U = U_c(r)$ (and $\omega_* = 0$), that the large-$|\tilde{\omega}|$ tails persist all the way down to $\omega = 0$.

The above scaling analysis holds regardless of the value of x, and hence applies to both the model at and away from particle-hole symmetry. This behaviour has been found from direct NRG calculations [35, 41]. For further details on the scaling analysis described here, we refer the reader to refs [34, 45, 65, 103].

4.9.1 Scaling behaviour as the QCP is approached

In this section we examine the large-$\tilde{\omega}$ ($|\tilde{\omega}| \gg 1$) scaling behaviour of the spectral functions and self-energies as the QCP is approached from both phases. Firstly, we focus on what forms the self-energies must take in order for $\pi\omega_*\Gamma_0 D(\omega)$ to have the scaling form of eq. (4.80a). Secondly, we examine the specific coefficients of the leading large-$|\tilde{\omega}|$ behaviour of eq. (4.80a).

Approach from the strong coupling phase

We now consider the QCP as approached from below within a conventional single self-energy description. In the SC phase (SSC or ASC) for $U < U_c(r)$, the Dyson equation, eq. (2.50), for the zero-field (retarded) propagator gives $G^r(\omega) \equiv G(\omega) = [\omega^+ - \varepsilon - \Gamma(\omega) - \Sigma(\omega)]^{-1}$ (with $\omega^+ = \omega + i\eta$). Rescaling this equation in terms of the SC low-energy 'Kondo' scale, $\omega_* = \omega_K$ (given by eq. (4.70)) we obtain the scaling form of the propagator

$$\Psi_{SC}(\tilde{\omega}) \equiv \Gamma_0\omega_*^r G(\omega) = \left[\frac{\tilde{\omega}^+}{\Gamma_0}\omega_*^{1-r} - \frac{\varepsilon^*(0)}{\Gamma_0\omega_*^r} - \frac{1}{\Gamma_0\omega_*^r}\Gamma(\omega) - \frac{1}{\Gamma_0\omega_*^r}\delta\Sigma(\omega)\right]^{-1} \tag{4.81a}$$

where as usual the renormalized level is given by $\varepsilon^*(0) = \varepsilon + \Sigma^R(0)$ and $\delta\Sigma(\omega) = [\Sigma(\omega) - \Sigma^R(0)]$, with $\tilde{\omega} = \omega/\omega_*$. In the limit that the QCP is approached, such that $\omega_* \ll |\omega|$ (or equivalently $|\tilde{\omega}| \gg 1$), the scaling spectrum has the form

$$\Psi^I_{SC}(\tilde{\omega}) \equiv \pi\Gamma_0\omega_*^r D(\omega) \overset{|\tilde{\omega}|\gg 1}{\sim} -\mathrm{Im}[-\tilde{\varepsilon}^*(0) + \mathrm{sgn}(\tilde{\omega})|\tilde{\omega}|^r[\beta(r) + i] - \delta\tilde{\Sigma}(\tilde{\omega})]^{-1} \tag{4.81b}$$

where the quantities have been rescaled via $\tilde{\varepsilon}^*(0) = \varepsilon^*/(\Gamma_0\omega_*^r)$, $\delta\tilde{\Sigma}(\tilde{\omega}) = \delta\Sigma(\omega)/(\Gamma_0\omega_*^r)$, and the rescaled hybridization function is given from eq. (4.1b) by $\Gamma(\omega)/(\Gamma_0\omega_*^r) = -|\tilde{\omega}|^r[\mathrm{sgn}(\tilde{\omega})\beta(r) + i]$. As mentioned previously in Section 4.7.2, we assume that the scaled renormalized level, $\tilde{\varepsilon}^*(0)$, is strictly bounded and approaches a finite-value as the transition is approached, i.e. in other words, $\varepsilon^*(0) \propto \omega_*^r$. In consequence, for

$|\tilde{\omega}| \gg 1$, the scaling spectrum, eq. (4.81b), then reduces simply to

$$\pi\Gamma_0\omega_*^r D(\omega) \overset{|\tilde{\omega}|\gg 1}{\sim} \frac{(|\tilde{\omega}|^r + \tilde{\Sigma}^I(\tilde{\omega}))}{[\mathrm{sgn}(\tilde{\omega})\beta(r)|\tilde{\omega}|^r - \delta\tilde{\Sigma}^R(\tilde{\omega})]^2 + [|\tilde{\omega}|^r + \tilde{\Sigma}^I(\tilde{\omega})]^2}. \tag{4.82}$$

In the previous section we showed by general scaling arguments that eq. (4.80a) gives $\Psi^I_{SC}(\tilde{\omega}) = \pi\Gamma_0\omega_*^r D(\omega) \propto |\tilde{\omega}|^{-r}$ for $|\tilde{\omega}| \gg 1$. In order for eq. (4.82) to have this large-$|\tilde{\omega}|$ dependence, the SSE must vanish *at least as rapidly* as the hybridization, i.e. $\tilde{\Sigma}^I(\tilde{\omega}) \propto |\tilde{\omega}|^\phi$, with $\phi \geq r$. The cases $\phi > r$ and $\phi = r$ are distinct. In the case that $\phi > r$, such that for $|\tilde{\omega}| \gg 1$ the self-energies vanish faster than the hybridization, then the QCP would be a non-interacting critical point. In other words, the large-$|\tilde{\omega}|$ behaviour of eq. (4.82) would be controlled exclusively by the hybridization function. However, it is known [37, 43, 46–48], and as we confirm explicitly from NRG, that the QCP is *interacting* in nature. The exponent $\phi = r$ is thus required such that the self-energy vanishes with precisely the same power as the hybridization function. In consequence, the $|\tilde{\omega}| \gg 1$ behaviour of the self-energy is given by

$$\tilde{\Sigma}^I(\tilde{\omega}) \overset{|\tilde{\omega}|\gg 1}{\sim} |\tilde{\omega}|^r[\alpha^+_{sc}\theta(\tilde{\omega}) + \alpha^-_{sc}\theta(-\tilde{\omega})], \tag{4.83a}$$

or equivalently, using $\tilde{\Sigma}^I(\tilde{\omega}) = \Sigma^I(\omega)/\Gamma_0\omega_*^r$ on the LHS, in scale-free form

$$\Sigma^I(\omega) \overset{\omega\to 0}{\sim} \Gamma_0|\omega|^r[\alpha^+_{sc}\theta(\omega) + \alpha^-_{sc}\theta(-\omega)], \qquad : U = U_c(r) \tag{4.83b}$$

where $\alpha^\pm_{sc}$ are coefficients of $O(1)$. Eq. (4.83a) gives the large-$|\tilde{\omega}|$ 'tails' of the scaling self-energy. In contrast, eq. (4.83b) gives the low-ω behaviour identically at $U = U_c(r)$ where the low-energy scale, ω_* has vanished, and the large-$\tilde{\omega}$ tails of eq. (4.83a) persist all the way down to $\omega = 0$.

The corresponding real part of the self-energy may be obtained by inserting the low-ω form of eq. (4.83b) into eq. (4.27), we obtain

$$\delta\Sigma^R(\omega) \overset{\omega\to 0}{\sim} -\Gamma_0|\omega|^r\big(\mathrm{sgn}(\omega)\beta(r)\tfrac{1}{2}[\alpha^+_{sc} + \alpha^-_{sc}] - \beta^{-1}(r)\tfrac{1}{2}[\alpha^+_{sc} - \alpha^-_{sc}]\big), \tag{4.84a}$$

also vanishing with the same power as the hybridization function. If $\alpha^+_{sc} = \alpha^-_{sc} = \alpha_{sc}$, eq. (4.84a) (c.f. eq. (4.28)) simply reduces to

$$\delta\Sigma^R(\omega) \overset{\omega\to 0}{\sim} -\mathrm{sgn}(\omega)\beta(r)\Sigma^I(\omega). \tag{4.84b}$$

The general form of the low-ω QCP spectral function, eq. (4.80b), then follows as

$$\pi\Gamma_0 D(\omega) \overset{\omega\to 0}{\sim} |\omega|^{-r}[C_+\theta(\omega) + C_-\theta(\omega)] \tag{4.85}$$

with dimensionless coefficients, $C_\pm$. The coefficients, $C_\pm$ may also be obtained in

terms of $\alpha_{sc}^{\pm}$, by inserting eqs. (4.83b-4.84a) into eq. (4.82):

$$C_{\pm} = \frac{1+\alpha_{sc}^{\pm}}{\left(\beta(r)[1+\frac{1}{2}(\alpha_{sc}^{+}+\alpha_{sc}^{-})] \mp \frac{1}{\beta(r)}\frac{1}{2}(\alpha_{sc}^{+}-\alpha_{sc}^{-})\right)^2 + (1+\alpha_{sc}^{\pm})^2}. \tag{4.86}$$

At ph symmetry, from eq. (4.3b), the spin-independent spectral function is an even function of ω, and therefore $C = C_{-} = C_{+}$ is guaranteed by symmetry. Furthermore, $\Sigma^{I}(\omega, x=0)$ is also an even function at $x=0$, such that $\alpha_{sc}^{+} = \alpha_{sc}^{-}$.

From direct NRG calculations we find that $\alpha_{sc}^{+} = \alpha_{sc}^{-} = \alpha_{sc}(r)$ arises *independently of the asymmetry* x. Therefore for both $x=0$, as is guaranteed by symmetry, but also for the generic asymmetric case, the coefficients $\alpha_{sc}^{\pm}$ are equal. There is therefore an *emergent* ph symmetry at the QCP. Eq. 4.86, then reduces to

$$C(r) = C_{\pm}(r) = \cos^2(\tfrac{\pi}{2}r)\frac{1}{[1+\alpha_{sc}(r)]^2}, \tag{4.87}$$

where $[1+\beta^2(r)]^{-1} = \cos(\frac{\pi}{2}r)$. The low-$\omega$ form of the spectral function is thus

$$\pi\Gamma_0 D(\omega) \overset{\omega\to 0}{\sim} C(r)|\omega|^{-r} \qquad : \omega_* = 0, \tag{4.88}$$

or equivalently the 'tails' of the scaling spectrum for large-$|\tilde{\omega}|$

$$\pi\Gamma_0\omega_*^{r} D(\omega) = \Psi_{SC}^{I}(\tilde{\omega}) \overset{|\tilde{\omega}|\gg 1}{\sim} C|\tilde{\omega}|^{-r}. \tag{4.89}$$

As has been noted from previous NRG studies [35], and also shown in Fig. 4.14, the ASC scaling spectrum, $\Psi_{SC}^{I}(\tilde{\omega})$ is asymptotically ph symmetric for both $|\tilde{\omega}| \ll 1$, and $|\tilde{\omega}| \gg 1$ for *any* x.

Recall that from extensive NRG studies, notably refs [37,43], it is well known that two distinct quantum critical points exist. The first QCP is entirely ph symmetric in nature, which we denote as the SQCP. It occurs in the $x=0$ case in the range $0 < r < \frac{1}{2}$. It also arises in the asymmetric ($x \neq 0$) case in the range $0 < r < r_*$, where $r_* \simeq \frac{3}{8}$ as is determined numerically [43]. In direct contrast, for $r_* < r < 1$, the transition is captured by an asymmetric QCP, we denote as AQCP [43]. In the range $r_* < r < \frac{1}{2}$, both critical points coexist, such that the SQCP governs the transition for the symmetric model, whereas the AQCP persists in the asymmetric model.

In the r range where the two distinct critical points exist ($r_* < r < \frac{1}{2}$), we find from the NRG numerics that the difference between the SQCP and AQCPs reside in the coefficients, $C \equiv C(r)$. The coefficients are different for the SQCP and the AQCP, but in both cases are independent of x. For the SQCP we denote the coefficient $C \equiv C_s(r)$, whereas for the AQCP, we denote the coefficient $C \equiv C_a(r)$. In consequence, the AQCP is the same regardless of the initial 'bare' $x = \varepsilon + \frac{U}{2}$

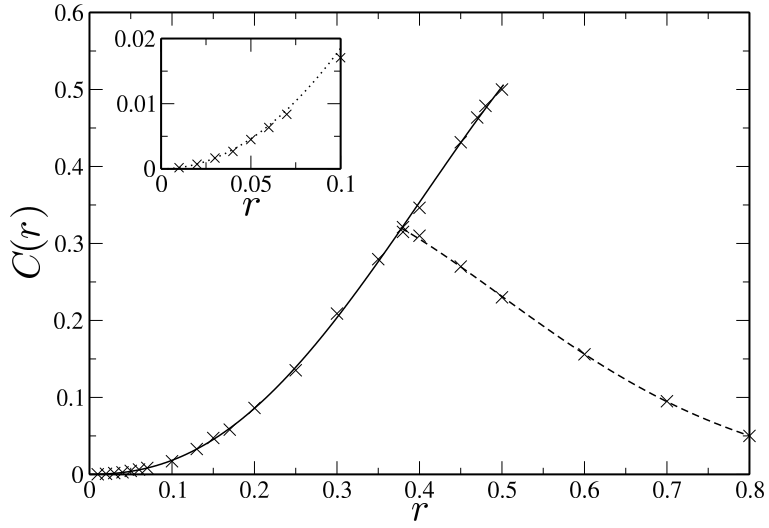


Figure 4.15: The critical point spectral coefficients $C(r)$ (from the low-ω dependence, $\pi\Gamma_0 D(\omega) \overset{\omega\to 0}{\sim} C(r)|\omega|^r$), for both the SQCP, $C(r) = C_s(r)$ (solid line), and the AQCP, $C(r) = C_a(r)$ (dashed line), plotted versus r. The inset shows the behaviour of $C_s(r)$ on a magnified scale for small r.

that is inserted into the Hamiltonian. In other words there is a single AQCP for any $x \neq 0$ and not a line of critical points parameterized by x.[16] This property is also deduced from a perturbative renormalization group treatment of the maximally asymmetric model ($U = \infty, \varepsilon =$ finite), for values of r close to $\frac{1}{2}$ and 1 [46]. Fig. 4.15 shows NRG results for the coefficients, $C(r)$, as a function of r for both the SQCP and AQCP critical points. As the figure shows, precisely at $r = r_*$, the critical coefficients coincide, whereas for $r > r_*$, they are in general distinct.

Approach from the LM phase

We have considered the approach to the critical point coming from the SC phase for $U \to U_c^-(r)$. In this present section we explicitly consider the approach from the LM phase, where $U \to U_c^+(r)$.

In a LM phase at zero-field, since the spin independent propagator can be written from eq. (3.11) as $G(\omega) = \frac{1}{2}[G_{A\sigma}(\omega) + G_{A-\sigma}(\omega)]$, the spectral function, $\pi D(\omega) = -\mathrm{Im}G(\omega)$ may be expressed as

$$\pi D(\omega) = \frac{1}{2}\sum_\sigma \frac{\big(\Gamma_I(\omega) + \Sigma^I_{A\sigma}(\omega)\big)}{\big(\omega - \varepsilon^*_{A\sigma} + \mathrm{sgn}(\omega)\beta(r)\Gamma_I(\omega) - \delta\Sigma^R_{A\sigma}(\omega)\big)^2 + \big(\Gamma^I(\omega) + \Sigma^I_{A\sigma}(\omega)\big)^2}, \tag{4.90a}$$

[16] There are actually a pair of AQCPs, one for $x > 0$ and one for $x < 0$, related by a ph transformation.

where $\delta\Sigma^R_{A\sigma}(\omega) = \Sigma^R_{A\sigma}(\omega) - \Sigma^R_{A\sigma}(0)$. Using eq. (4.1b) for $\Gamma(\omega)$ and rescaling eq. (4.90a) by the LM low-energy scale, ω_* (given by eq. (4.20)), the spectral scaling function, $\Psi^I_{LM}(\tilde{\omega}) \equiv \pi\Gamma_0\omega_*^r D(\omega)$ follows as

$$\Psi^I_{LM}(\tilde{\omega}) = \frac{1}{2}\sum_\sigma \frac{\big(|\tilde{\omega}|^r + \tilde{\Sigma}^I_{A\sigma}(\tilde{\omega})\big)}{\big(\tilde{\omega}\omega_*^{1-r} - \tilde{\varepsilon}^*_{A\sigma} + \mathrm{sgn}(\tilde{\omega})\beta(r)|\tilde{\omega}|^r - \delta\tilde{\Sigma}^R_{A\sigma}(\tilde{\omega})\big)^2 + \big(|\tilde{\omega}|^r + \tilde{\Sigma}^I_{A\sigma}(\tilde{\omega})\big)^2},$$

where $\tilde{\varepsilon}^*_{A\sigma} = \varepsilon^*_{A\sigma}/\Gamma_0\omega_*^r$, and $\tilde{\Sigma}_{A\sigma}(\tilde{\omega}) = \Sigma_{A\sigma}(\omega)/\Gamma_0\omega_*^r$. It is readily shown, using eq. (4.22) that the ratio $\tilde{\varepsilon}^*_{A\sigma} = \varepsilon^*_{A\sigma}/\Gamma_0\omega_*^r = [\gamma - \sigma]$, and therefore reaches a finite value as $\omega_* \to 0$ (for any x). Thus, taking the limit that the QCP is approached such that $|\tilde{\omega}| \gg 1$, the $\tilde{\omega}\omega_*^{1-r}$ and $\tilde{\varepsilon}^*_{A\sigma}$ terms in the denominator may be neglected and we obtain

$$\Psi^I_{LM}(\tilde{\omega}) \overset{|\tilde{\omega}|\gg 1}{\sim} \frac{1}{2}\sum_\sigma \frac{\big(|\tilde{\omega}|^r + \tilde{\Sigma}^I_{A\sigma}(\tilde{\omega})\big)}{\big(\mathrm{sgn}(\tilde{\omega})\beta(r)|\tilde{\omega}|^r - \delta\tilde{\Sigma}^R_{A\sigma}(\tilde{\omega})\big)^2 + \big(|\tilde{\omega}|^r + \tilde{\Sigma}^I_{A\sigma}(\tilde{\omega})\big)^2}. \quad (4.90b)$$

For the same reasoning as above, the QCP is *interacting* and hence the large-$|\tilde{\omega}|$ scaling behaviour of the two-self-energies must be of the form

$$\tilde{\Sigma}^I_{A\sigma}(\tilde{\omega}) \overset{|\tilde{\omega}|\gg 1}{\sim} \Gamma_0|\tilde{\omega}|^r[\alpha^+_\sigma\theta(\tilde{\omega}) + \alpha^-_\sigma\theta(-\tilde{\omega})], \quad (4.91a)$$

or equivalently identically at the QCP where the large-$|\tilde{\omega}|$ behaviour holds all the way down to $\omega = 0$ and hence the self-energy is scale-free:

$$\Sigma^I_{A\sigma}(\omega) \overset{\omega\to 0}{\sim} \Gamma_0|\omega|^r[\alpha^+_\sigma\theta(\omega) + \alpha^-_\sigma\theta(-\omega)] \qquad : \omega_* = 0. \quad (4.91b)$$

Inserting eq. (4.91a), together with its real part, $\tilde{\Sigma}^R_{A\sigma}(\tilde{\omega})$, given by Hilbert transform (c.f. eq. (4.84a)), the spectral function coefficient, $C_\pm$ follows as

$$C_\pm = \frac{1}{2}\sum_\sigma \frac{1 + \alpha^\pm_\sigma}{\big(\beta(r)[1 + \frac{1}{2}(\alpha^+_\sigma + \alpha^-_\sigma)] \mp \frac{1}{\beta(r)}\frac{1}{2}(\alpha^+_\sigma - \alpha^-_\sigma)\big)^2 + \big(1 + \alpha^\pm_\sigma\big)^2}. \quad (4.92)$$

If the spectral function coefficient is to be independent of the sign of ω, i.e. $C = C_+ = C_-$, then either of two conditions on the self-energy coefficients must be separately satisfied: $\alpha^+_\sigma = \alpha^-_{-\sigma}$ or $\alpha^+_\sigma = \alpha^-_\sigma$. At ph symmetry the latter condition is guaranteed where $\Sigma^I_{A\sigma}(\omega) = \Sigma^I_{A-\sigma}(-\omega)$. From direct NRG calculations[17] we find that both these conditions are satisfied, such that $\alpha^\pm_\sigma \equiv \alpha_{sc}(r)$, i.e. all 4 coefficients are the same. As a consequence, the precise QCP behaviour is the same coming from both phases with the self-energy given by $\Sigma^I_{A\sigma}(\omega) = \Sigma^I(\omega) \overset{\omega\to 0}{\sim} \alpha_{sc}(r)|\omega|^r$, and the spectral function by $\pi\Gamma_0 D(\omega) \overset{\omega\to 0}{\sim} C(r)|\omega|^{-r}$ (with $C(r) = \cos^2(\frac{\pi}{2}r)/[1 + \alpha_{sc}(r)]$).

[17] We explicitly calculate the propagators and self-energies at $T = 0$ with an infinitesimal local field, $h = 0^+$, such that A state functions are 'picked out' of the degenerate LM ground state.

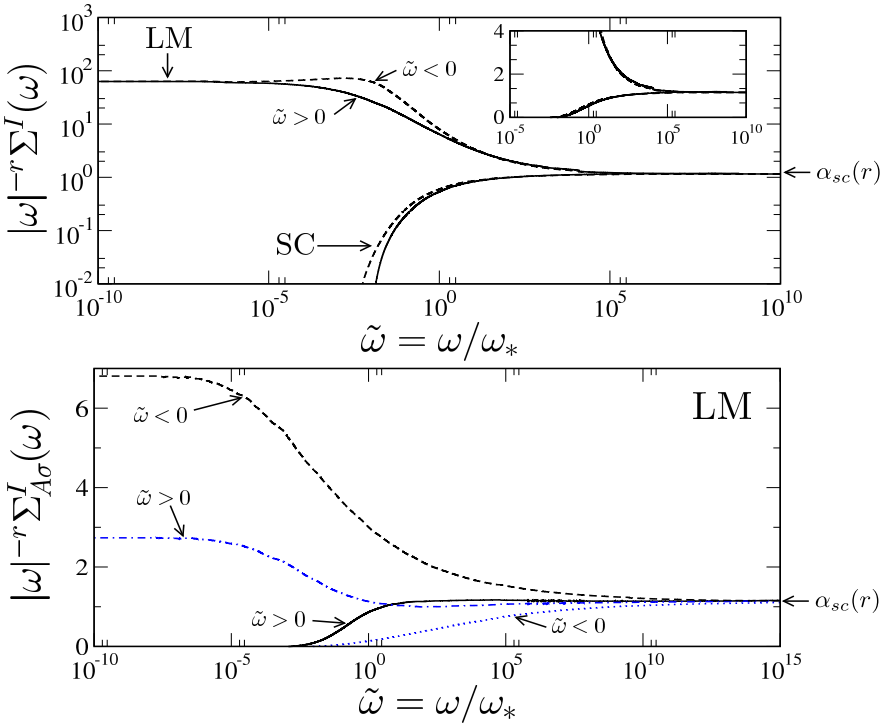


Figure 4.16: NRG results for $r_* < r = 0.45 < \frac{1}{2}$, and asymmetry: $\eta = 2x/U = -0.4$, $U_c/\pi \simeq 2.6$. The upper panel shows the (spin-independent) SSE scaling functions, $|\omega|^{-r}\Sigma^I(\omega)$, versus $\tilde{\omega}$ on a log-log plot, in LM and SC (ASC) phases. The curves for $\tilde{\omega} < 0$ are shown with a dashed line, whereas for $\tilde{\omega} > 0$, a solid line, as indicated. For $|\tilde{\omega}| \gg 1$, all curves tend to the same value, $\alpha_{sc}(r)$, indicative of the QCP. The inset shows the large-$|\tilde{\omega}|$ scaling behaviour with a linear vertical axis. The bottom panel shows the scaling behaviour of the TSEs in the LM phase. $|\omega|^{-r}\Sigma^I_{A\uparrow}(\omega)$ is shown with a solid line for $\tilde{\omega} > 0$ and a dashed line for $\tilde{\omega} < 0$. $|\omega|^{-r}\Sigma^I_{A\downarrow}(\omega)$ is shown with a dot-dashed line for $\tilde{\omega} > 0$ and a dotted line for $\tilde{\omega} < 0$. (We have set the unit of energy $\Gamma_0^{1/(1-r)} \equiv 1$.)

4.9.2 Numerical results for the SC and LM scaling functions

Before proceeding to discuss the physics of the PAIM at a finite field, in this section we show results using FDM-NRG[18] for the scaling spectra in the three distinct regimes of critical behaviour detailed above. The first regime we consider is the range ($r_* < r < \frac{1}{2}$) where both critical points (the SQCP and the AQCP) coexist.

$r_* < r < \frac{1}{2}$

Fig. 4.16 shows the full-$\tilde{\omega}$ dependence of the self-energy scaling functions for $r > r_* = 0.45$, and $x < 0$. The upper panel shows the (spin-independent) SSE scaling

[18]NRG technical details: To obtain the scaling functions exhibited in this section we keep 2500 states at each iteration, for 181 iterations, with a discretization parameter $\lambda = 2$, and broadening parameter, $b = 0.6$. (See Appendix C for further details of the NRG procedure.) For all numerical NRG results in this chapter for convenience we set the unit of energy $\Gamma_0^{1/(1-r)} \equiv 1$.

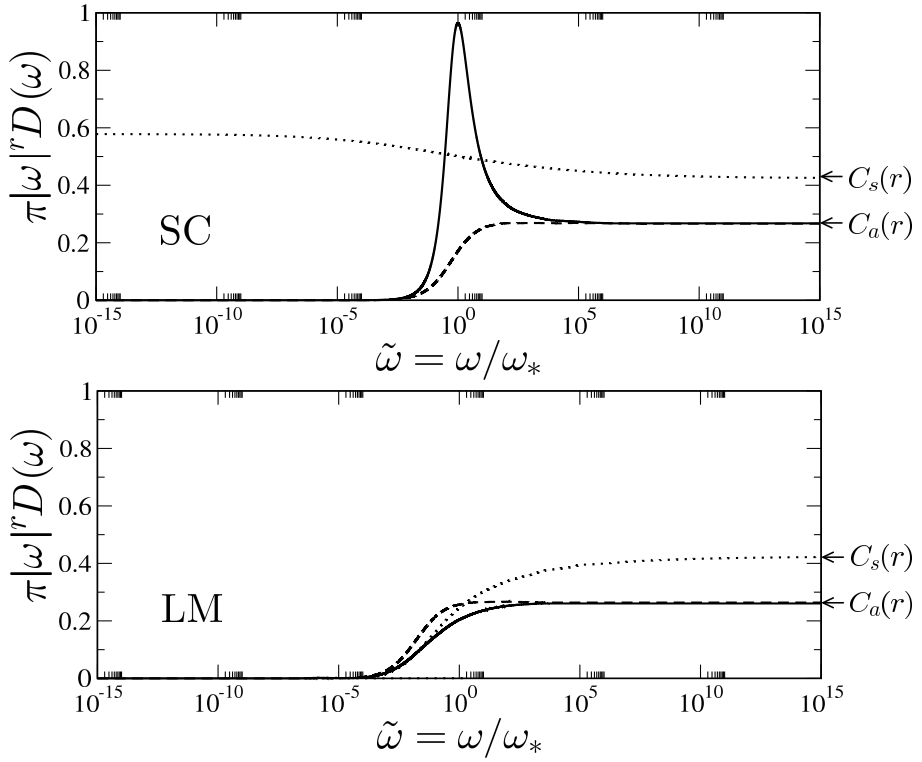


Figure 4.17: NRG results for the same parameters as Fig. 4.16. Scaling spectra, $\pi\Gamma_0|\omega|^r D(\omega) \equiv |\tilde{\omega}|^r \Psi^I_\alpha(\tilde{\omega})$ are plotted versus, $\tilde{\omega} = \omega/\omega_*$ on a log-scale. The upper panel shows the ASC phase spectra for $x = \varepsilon + \frac{U}{2} < 0$ for both $|\tilde{\omega}| < 0$ (solid line), and $|\tilde{\omega}| > 0$ (dashed line). The $x = 0$ scaling spectra is also shown with a dotted line. The lower panel shows the corresponding LM phase spectra for both the symmetric and asymmetric cases. For the asymmetric model, the scaling spectra, $\Psi^I_\alpha(\omega, x)$, are independent of $|x|$. The large-$|\tilde{\omega}|$ critical plateau coefficients, $C(r) = C_a(r)$ or $C_s(r)$, are marked on by arrows. The low-energy scale, ω_* has been freely chosen such that the peak maxima are centred at $|\tilde{\omega}| = 1$.

functions, $\Gamma_0^{-1}|\omega|^{-r}\Sigma^I(\omega)$, versus $\tilde{\omega}$ on a log-log plot in *both* phases.[19] The large-$|\tilde{\omega}|$ tails show that as the QCP is approached, the same plateau value, $\alpha_{sc}(r)$, is reached coming from both phases as expected. The lower panel shows the LM phase two self-energy scaling functions, $\Gamma_0^{-1}|\omega|^{-r}\Sigma_{A\uparrow}(\omega)$, $\Gamma_0^{-1}|\omega|^{-r}\Sigma_{A\downarrow}(\omega)$, versus $\tilde{\omega}$ (on a log-scale). Once again, clearly for $|\tilde{\omega}| \gg 1$, the functions for both $\tilde{\omega} > 0$ and $\tilde{\omega} < 0$ reach the same value, $\alpha_{sc}(r)$. The upper and lower panels of Fig. 4.16 together, show that as the QCP is approached from either phase, all self-energies, $\Sigma(\omega)$, $\Sigma_{A\uparrow}(\omega)$, $\Sigma_{A\downarrow}(\omega)$ are asymptotically coincident, such that the large-$|\tilde{\omega}|$ tails of the scaling functions have the same form coming from either phase, i.e.

$$\frac{1}{\Gamma_0\omega_*^r}\Sigma^I(\omega) = \frac{1}{\Gamma_0\omega_*^r}\Sigma^I_{A\sigma}(\omega) \overset{|\tilde{\omega}|\gg 1}{\sim} \alpha_{sc}(r)|\tilde{\omega}|^r. \tag{4.93a}$$

[19] The LM phase SSE, $\Sigma^I(\omega)$, has been obtained from the TSE functions via eq. (3.30).

Once again, we emphasize that precisely at the QCP, where $\omega_* = 0$ and the system is scale free, the large-$|\tilde{\omega}|$ behaviour holds all the way down to $\omega = 0$:

$$\Gamma_0^{-1}|\omega|^{-r}\Sigma^I(\omega) = \Gamma_0^{-1}|\omega|^{-r}\Sigma^I_{A\sigma}(\omega) \overset{\omega\to 0}{\sim} \alpha_{sc}(r). \tag{4.93b}$$

Fig. 4.16 also shows the asymptotic low-$\tilde{\omega}$ forms in each of the phases. The top panel confirms the result of eq. (4.68a), i.e. that in the ASC phase the SSE $\Sigma^I(\omega) \propto |\omega|^{2+3r}$ (or equivalently $|\omega|^{-r}\Sigma^I(\omega) \propto |\tilde{\omega}|^{2+2r}$). In addition, the top panel shows that the SSE in a LM phase has the form of eq. (4.25), $\Sigma^I(\omega) \overset{\tilde{\omega}\to 0}{\sim} a_a|\tilde{\omega}|^r$ (or equivalently $|\omega|^{-r}\Sigma^I(\omega) \overset{\tilde{\omega}\to 0}{\sim} a_a$), where $a_a = a_a^+ = a_a^-$.

The bottom panel of Fig. 4.16 shows the small-$|\tilde{\omega}|$ behaviour of the TSEs in the LM phase, where we find that $|\omega|^{-r}\Sigma^I_{A\sigma}(\omega) \overset{\tilde{\omega}\to 0}{\sim} \theta(-\sigma\tilde{\omega})b_\sigma^\pm$. This low-$\tilde{\omega}$ behaviour is clearly at odds with the dependence, $\Sigma_{A\sigma}(\omega) \overset{\tilde{\omega}\to 0}{\sim} |\tilde{\omega}|^{2+3r}$ - case (A) in Fig. 4.12, derived from the order by order Luttinger self-consistency analysis of Section 4.6.5. We do not comment further on this issue here, but return to it in Section 4.11.

Fig. 4.17 shows the scaling spectra $|\tilde{\omega}|^r\Psi^I_\alpha(\tilde{\omega}) = \pi\Gamma_0|\omega|^r D(\omega)$, versus $\tilde{\omega}$ (on a log-scale) in both phases, once again for $r = 0.45$ and a typical $x < 0$. In this range $r_* < r < \frac{1}{2}$, the AQCP and SQCP critical points are distinct and therefore have different critical plateau values, $C(r)$ for large-$|\tilde{\omega}|$. For $x < 0$ in the ASC phase, the scaling spectra, $|\tilde{\omega}|^r\Psi_{SC}(\tilde{\omega})$, has a peak for $\tilde{\omega} < 0$, whereas in the LM phase the peak is for $|\tilde{\omega}| > 0$, as has previously been reported [35]. For large-$|\tilde{\omega}|$, the spectra in both phases for both $\tilde{\omega} > 0$ and $\tilde{\omega} < 0$ reach the same plateau value, $C_a(r)$. The scaling spectra for the ph symmetric point ($x = 0$) are also shown (dotted lines), reaching a distinct plateau value of $C_s(r) \neq C_a(r)$ coming from each side of the transition. The low-$|\tilde{\omega}|$ behaviour indicative of the distinct phases are given via the quasiparticle-forms eqs. (4.30, 4.36) for the LM phase and eqs. (4.71, 4.74) for the SC phases (ASC and SSC).

$r > \frac{1}{2}$: Asymmetric critical point

We now consider numerical NRG results for the scaling spectra, $\Psi^I_\alpha(\tilde{\omega}, x)$ in the range $r > \frac{1}{2}$. The relevant quantum critical point for the range $r > \frac{1}{2}$, when $x \neq 0$, is the AQCP. (As mentioned above, in the ph symmetric case for $r > \frac{1}{2}$ there is no critical behaviour — the model has a LM ground-state for all $U > 0$.)

Fig. 4.18 shows the scaling spectra, $|\tilde{\omega}|^r\Psi^I_\alpha(\tilde{\omega}, x)$ in both phases for $r = 0.6$. The top left panel shows the ASC spectrum, $\pi\Gamma_0|\omega|^r D(\omega)$, versus ω (on a log-scale) for a fixed $x = -1$ as $U_c(r)$ is progressively approached from below. Curves for both $\omega > 0$ and $\omega < 0$ are shown, where it can be seen that there is clearly a pronounced maximum for $\omega < 0$. In contrast, the top right panel shows the equivalent LM spectra as $U_c(r)$ is approached from above. The peak maximum in the LM phase occurs for $\omega > 0$, but with the peak less pronounced than for the ASC phase.

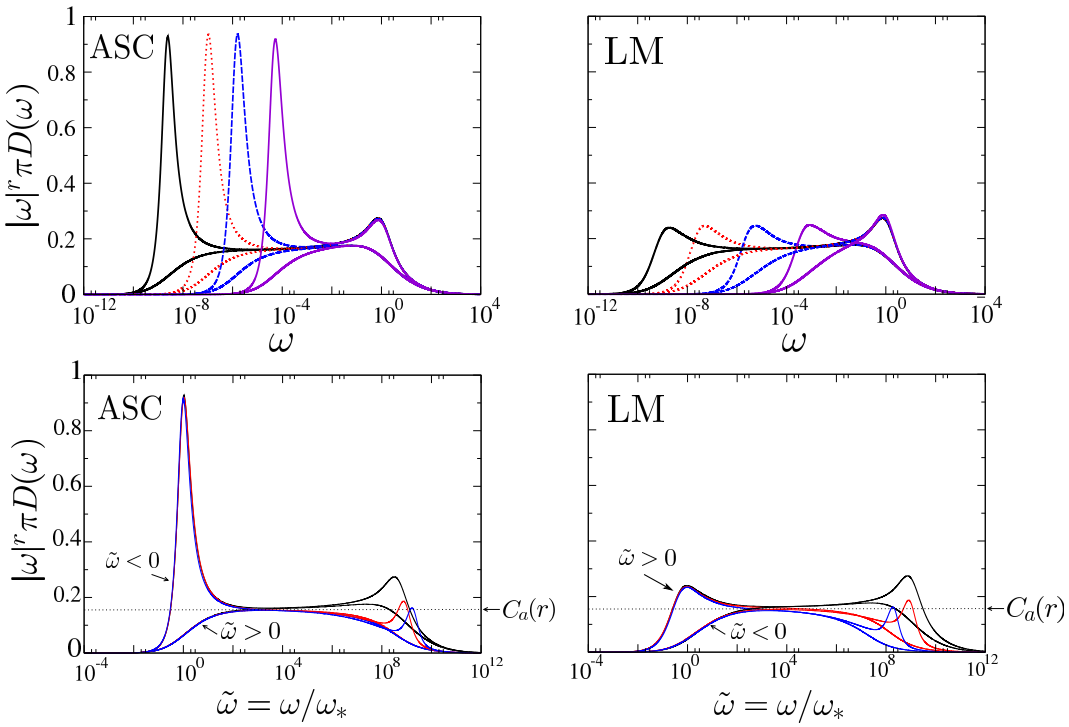


Figure 4.18: Top (left and right): NRG results for a fixed asymmetry, $x = -1$, and band exponent $r = 0.6$. $\pi\Gamma_0|\omega|^r D(\omega)$ is plotted versus ω (on a log-scale) in both phases getting progressively closer to the AQCP, where the critical $U = U_c/\pi \approx 2.0676$. The left panel shows results for the ASC phase with curves plotted for $U/\pi = 2.05$, 2.065, 2.067 and 2.0675. The right panel shows results for the LM phase with curves plotted for $U/\pi = 2.0677$, 2.068, 2.07 and 2.08. For the ASC phase, a peak occurs for $\omega < 0$; whereas for the LM phase, a peak occurs for $\omega > 0$. Bottom (left and right): Scaling spectra ($r = 0.6$), $|\tilde{\omega}|^r \Psi^I_\alpha(\tilde{\omega}) = \Gamma_0|\omega|^r \pi D(\omega)$, are plotted in both phases versus $\tilde{\omega}$ on a log-scale for $x = -1$, $U_c/\pi \approx 2.0676$ in black, $x = -10$, $U_c/\pi \sim 11.0883$ in red, $x = -20$, $U_c/\pi \approx 19.63558$ in blue. Left shows the ASC phase, right the LM phase. The scale, ω_*, has been freely chosen such that the peak maximum in each scaling spectrum occurs at $|\tilde{\omega}| = |\omega/\omega_*| = 1$.

The behaviour occurring at $\omega \simeq O(U)$ on the RHS of both plots are non-universal Hubbard satellite peaks.[20]

The bottom (left and right) panels of Fig. 4.18 show the scaling spectra, $|\tilde{\omega}|^r \Psi^I_\alpha(\tilde{\omega})$ versus $\tilde{\omega}$ for three distinct values of x ($x = -1, -10, -20$). The spectra collapse onto the same universal curve in all cases for $\tilde{\omega} \lesssim 10^4$. (Once again, on the RHS of the figure, non-universal Hubbard satellite peaks are shown which differ for different x.) Thus, we find that for a fixed r and for any $x < 0$, the scaling spectra are independent of x in both phases, i.e. in other words $\Psi^I_\alpha(\tilde{\omega}, x)$ is independent of $|x|$. The corresponding scaling spectra for $x > 0$ can then be determined via eq. (4.79).

[20]The non-universal Hubbard satellite peaks arise at $\omega \simeq \varepsilon$ and $\omega \simeq \varepsilon + U$, corresponding to the atomic limit single-particle processes involving adding and removing an electron from the impurity level. The delta functions of eqs. (2.47-2.48) are broadened by coupling to the conduction band, and a consequence the width of the peaks is of $O(\Gamma_0)$.

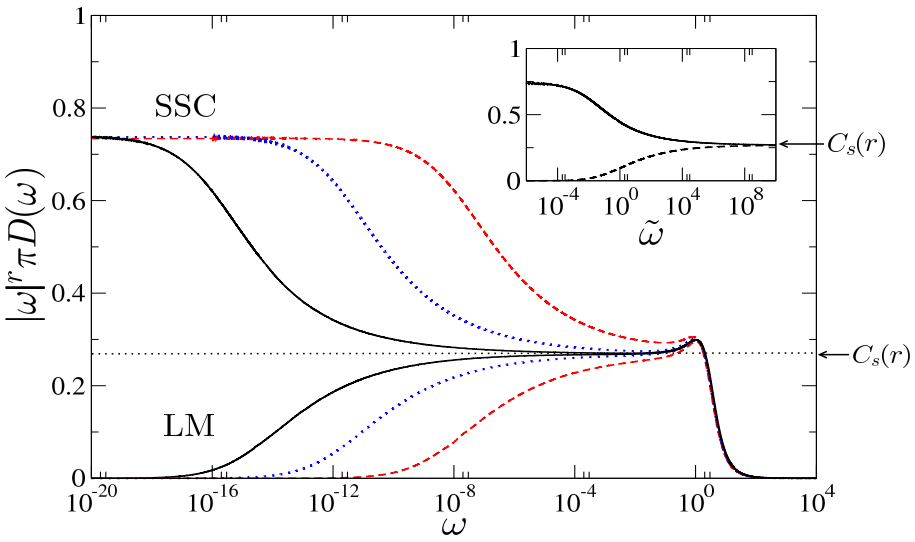


Figure 4.19: NRG results for $r = 0.35 < r_*$, $x = 0$. Spectra, $\Gamma_0|\omega|^r \pi D(\omega)$, are plotted in both phases versus ω on a log-scale for $x = 0$, where $U_c/\pi \approx 2.127$. Specifically, SSC spectra are plotted for $U/\pi = 2.0$, 2.1 and 2.12, whereas for the LM phase spectra are plotted for $U/\pi = 2.128$, 2.14 and 2.2. At ph symmetry the spectra, $D(\omega)$, are even functions of ω, so only $\omega > 0$ need be considered explicitly. We freely choose the low-energy scale, ω_*, as the ω at which $\Gamma_0|\omega|^r \pi D(\omega)$ reaches 0.5 for the SSC phase and 0.1 for the LM phase. For $\omega \ll \omega_*$, the SSC phase plateau value is $\cos^2(\frac{\pi}{2}r)$ in accordance with eq. (4.75). The LM spectra vanish ($\propto |\omega|^{2r}$) for $\omega \ll \omega_*$. By contrast for $\omega_* \ll \omega \ll$ non-universal scales of $O(U)$, all spectra fall onto the critical plateau value, $C_s(r)$. For $\omega \gg O(U)$ all spectra vanish. The inset shows $\Gamma_0|\omega|^r \pi D(\omega)$ plotted versus $\tilde{\omega}$ (on a log-scale), showing just the universal scaling behaviour.

$r < r_*$: Symmetric critical point

As stated above, for $r < r_*$ the critical behaviour of the model is determined solely by the SQCP. In this section we consider NRG results for the scaling spectra for both $x = 0$ and $x < 0$.

Precisely at the ph symmetric point ($x = 0$) the SQCP separates the SSC phase, with low-$\tilde{\omega}$ behaviour $\pi\Gamma_0|\omega|^r D(\omega) \overset{\tilde{\omega}\to 0}{\sim} \cos^2(\frac{\pi}{2}r)$ given via eq. (4.75), from the LM phase with $\pi\Gamma_0|\omega|^r D(\omega) \propto |\tilde{\omega}|^{2r}$, given by eq. (4.37). Fig. 4.19 shows the spectra, $\pi\Gamma_0|\omega|^r D(\omega)$ versus ω (on a log-scale) for $x = 0$, $r = 0.35$, on both sides of $U_c(r)$. All spectra are even functions of ω at $x = 0$ so only $\omega > 0$ or $\omega < 0$ need be considered explicitly. Each curve is plotted for a specific U close to $U_c(r)$. The SQCP plateau value, $C_s(r)$ is indicated by a dotted line. (Once again, the non-universal behaviour sets in on an energy scale of $\omega \simeq O(U)$. Specifically, since $\varepsilon = -\frac{U}{2}$ at ph symmetry, the Hubbard satellite peaks occur at $\omega \simeq \varepsilon = -\frac{U}{2}$ and $\omega \simeq \varepsilon + U = +\frac{U}{2}$, such that they are symmetrically disposed about the Fermi level.)

Fig. 4.20 shows $\pi\Gamma_0|\omega|^r D(\omega) = |\tilde{\omega}|^r \Psi_\alpha^I(\tilde{\omega})$ in both phases versus $\tilde{\omega}$ (on a log-scale) away from ph symmetry (for $x < 0$). From the numerical calculations we

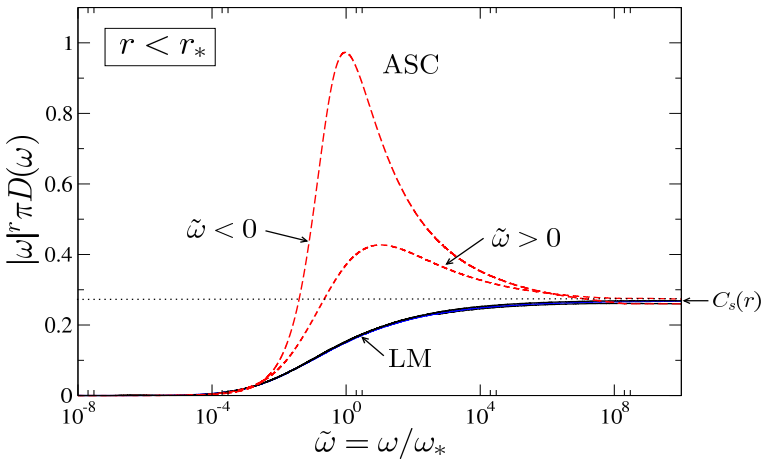


Figure 4.20: NRG calculations for $r = 0.35$. $\pi\Gamma_0|\omega|^r D(\omega)$, is plotted in both phases versus $\tilde{\omega}$ on a log-scale for $x \neq 0$. Results are shown for $x = -1$, where $U_c/\pi \approx 2.5$, and $x = -20$, where $U_c/\pi \approx 19.6$. Scaling spectra for different $|x|$ fall on top of each other. For $\omega/\omega_* \gg 1$, all spectra fall onto the symmetric critical plateau value, $C_s(r)$.

find that the LM scaling spectrum becomes completely independent of x, such that $\Psi^I_{LM}(\tilde{\omega}, x) = \Psi^I_{LM}(-\tilde{\omega}, -x) = \Psi^I_{LM}(\tilde{\omega}, x = 0)$ is an even function of $\tilde{\omega}$. The solid (blue) line shows the LM spectra. The dashed (red) lines show the ASC scaling spectra; we find that there is a larger peak for $\tilde{\omega} < 0$ than $\tilde{\omega} > 0$ for $x < 0$. For any $x < 0$, the scaling spectra are independent of x. In the figure, spectra for two distinct x's ($x = -1, = -20$) are plotted on top of each other and found to be identical for both the ASC and LM phases.

One final comment should be made before we proceed. As noted above, we find that for $r < r_*$, $\Psi^I_{LM}(\tilde{\omega}, x)$ is completely independent of x and hence is an even function of $\tilde{\omega}$ with no asymmetric peak structure - just a smooth crossover from the $|\tilde{\omega}| \ll 1$ behaviour to the $|\tilde{\omega}| \gg 1$ form. By contrast for $r > r_*$ and $x < 0$, the LM scaling spectrum acquires a peak for $\tilde{\omega} < 0$. As r increases in the range $r_* < r < 1$, we notice that the peak height increases. (The peak height of LM scaling spectra in Fig. 4.18 for $r = 0.6$ is greater than in Fig. 4.17 for $r = 0.45$.)

Symmetric critical coefficient

Before moving on, we comment briefly on the r-dependence of the SQCP coefficient $C_s(r)$ in the limit that $r \to 0$. From NRG the value of $C_s(r)$ has been calculated and is shown in Fig. 4.15. We find from NRG that as $r \to 0$, $C_s(r) \propto r^2$ and hence from eq. (4.92), the self-energy coefficient $\alpha_{sc}(r) = (\alpha^{\pm}_{\sigma}) \propto \frac{1}{r^2}$, diverges at low-$r$. Specifically the numerics, as shown in the inset of Fig. 4.15, give the coefficient vanishing as

$$C_s(r) \overset{r\to 0}{\sim} \frac{3\pi^2 r^2}{16} \tag{4.94}$$

which is what is found from a local moment approach (LMA) description [45] of the QCP at ph symmetry. At ph symmetry within the LMA it is found that $\alpha_\sigma^+ = \alpha_{-\sigma}^-$ and hence $C_+ = C_-$ arises; but that $\alpha_\sigma^+ \neq \alpha_\sigma^-$, with $\alpha_\uparrow^- = 4$ and $\alpha_\uparrow^+ = 0$ as $r \to 0$. From eq. (4.92) the value of C_s then follows as

$$C_s(r) \overset{r\to 0}{\sim} \frac{1}{2}\pi^2 r^2 \sum_\sigma \frac{(1+\alpha_\sigma^\pm)}{(\alpha_\sigma^+ - \alpha_\sigma^-)^2} = \frac{3\pi^2 r^2}{16}, \tag{4.95}$$

which captures the correct *exact* behaviour from NRG - eq. (4.94). The LMA however does not predict the correct critical behaviour away from ph symmetry [34]. Within the LMA, the relation $[\alpha_\sigma^+ = \alpha_{-\sigma}^-]$ does not hold generally away from ph symmetry, and therefore $C^+(r,x) \neq C^-(r,x)$. In other words, in contrast to the exact results from NRG which show that there is one distinct critical point (for $r < r_*$), the LMA predicts that there is a line of quantum critical points in the (r,x) plane.

We make one final remark about the r-dependence of $C_s(r)$. As may be seen from Fig. 4.15, we find from the numerics that $C_s(r) \to \frac{1}{2}$ as $r \to \frac{1}{2}^-$. The reason for this is as follows: For the model at ph symmetry, as discussed in Section 4.7.2, the critical $U = U_c \to 0$ as $r \to \frac{1}{2}$. The SQCP thus becomes non-interacting at $r = \frac{1}{2}$, and hence $\alpha_{sc}(r) = \alpha_\sigma^\pm$ vanishes. The spectral coefficient then is given from eq. (4.92) by $C_s(r) = \cos^2(\frac{\pi}{4}) = \frac{1}{2}$, which is the same as eq. (4.75) above.

4.10 Finite field

So far we have explicitly considered the zero field case where the quantum critical point between the two distinct phases is pristine. In this section we discuss the case where there is a finite-field, h, applied either globally (to both the impurity level and the conduction band states), or purely locally (where a field is applied solely to the impurity level). Specifically we consider what can be said about the system at finite field from the Luttinger self-consistency arguments of Section 4.6.5. Once again, we supplement the analytical arguments with exact numerical results from NRG.

4.10.1 Global field

If a field is applied globally to both the conduction band and the impurity level, the hybridization function, $\Gamma_\sigma(\omega, h)$ does not vanish at the Fermi level. Generally at finite-field, the hybridization function $\Gamma_\sigma(\omega, h)$ is given by eq. (4.1). Thus, at the Fermi level where $\omega = 0$, $\Gamma_\sigma(\omega, h)$ tends to a constant, given by

$$\Gamma_\sigma(0,h) = -\Gamma_0(\mathrm{sgn}(\sigma h)\beta(r) + i)|h|^r. \tag{4.96}$$

Provided $\Sigma^I_\sigma(0,h)=0$, the spectral function, $\pi D_\sigma(\omega=0,h)$, then follows as

$$\pi D_\sigma(0,h)=\frac{\Gamma_0|h|^r}{[-\varepsilon^*_\sigma(|h|)+\mathrm{sgn}(\sigma h)\beta(r)|h|^r]^2+[\Gamma_0|h|^r]^2}. \tag{4.97}$$

where $\varepsilon^*_\sigma(h)=\varepsilon-\sigma h+\Sigma^R_\sigma(0,h)\neq 0$ and $\delta\Sigma^R_\sigma(\omega,h)=\Sigma^R_\sigma(\omega,h)-\Sigma^R_\sigma(0,h)$. The spectral function thus reaches a constant at the Fermi level.

From the order by order perturbative arguments of Section 4.6, taking $\pi D_{A\sigma}(\omega)\overset{\omega\to 0}{\sim}|\omega|^{\lambda_\sigma}$ with $\lambda_\sigma=0$, eq. (4.55) simply reduces to

$$\Sigma^I_\sigma(\omega,h)\propto|\omega|^2, \tag{4.98}$$

(thus validating the initial assumption that $\Sigma^I_\sigma(0,h)=0$). Inserting this low-ω behaviour back into $D_\sigma(\omega,h)$, we once again obtain eq. (4.97) for $D_\sigma(0,h)$, and therefore eq. (4.98) is fully self-consistent. This low-ω form of the self-energy is the standard Fermi liquid result originally obtained by Luttinger [60], which also arises for the zero-field $r=0$ metallic AIM, where the hybridization function reaches a constant at the Fermi level - $\Gamma^I_\sigma(\omega,0)=\Gamma_0$. In consequence, in direct analogy with the zero-field metallic case, the PAIM for any finite global field is a Fermi liquid phase for all U and h.

4.10.2 Local field

Self-consistency considerations

The self-consistent results of Section 4.6.5 apply equally well to the case of a finite local-field, h, where the hybridization function, $\Gamma_\sigma(\omega,h)\equiv\Gamma(\omega)=-\Gamma_0(\mathrm{sgn}(\omega)\beta(r)+i)|\omega|^r$, is independent of field. As discussed previously in Chapter 3, recall that for any finite h, e.g. for $h>0$, the propagator, $G_\sigma(\omega,h)\equiv G_{A\sigma}(\omega,|h|)$, and the self-energy, $\Sigma_\sigma(\omega,h)\equiv\Sigma_{A\sigma}(\omega,|h|)$, such that *only* a SSE description arises for both $U>U_c$ and $U<U_c$, reflecting the fact that the phase transition is strictly destroyed. From Fig. 4.12 it is case (A), where the renormalized levels, $\varepsilon^*_{A\sigma}(|h|)\equiv\varepsilon^*_\sigma(h)$, are finite that specifically applies in general to finite-field. The self-consistent self-energy is then given by

$$\Sigma^I_\sigma(\omega,h\neq 0)\propto|\omega|^{2+3r}, \tag{4.99a}$$

with a real part, $\delta\Sigma^R(\omega,h)\overset{\omega\to 0}{\sim}-(\frac{1}{Z}-1)\omega$ (obtained in direct analogy with eq. (4.68b)). The low-ω form of the spectral function is then simply given by

$$\pi D_\sigma(\omega,h)\overset{\omega\to 0}{\sim}\frac{\Gamma_0|\omega|^r}{[\varepsilon^*_\sigma(h)]^2}, \tag{4.99b}$$

which is exactly the same form as the zero-field ASC phase spectral function, eq. (4.72), with $\varepsilon^*(0)$ replaced by $\varepsilon^*_\sigma(h) = \varepsilon - \sigma h + \Sigma^R_\sigma(0,h)$. Thus, this solution describes a ASC Fermi liquid phase perturbatively connected to the non-interacting limit for all finite h.

Case (A) (and hence eq. (4.99a)) is not the only self-consistent possibility that arises at finite-field. For general h, the spin-dependent renormalized levels, $\varepsilon^*_\sigma(h)$ ($\equiv \varepsilon^*_{A\sigma}(|h|)$ for $h > 0$, $\sigma = \uparrow, \downarrow$) are both non-zero. As described above, Luttinger-Ward self-consistency then yields the solution eq. (4.99a). However, it is possible to tune the value of the field, h, to a particular value, we denote h', at which one of the renormalized levels, $\varepsilon^*_\sigma(h)$, vanishes, whilst the other, $\varepsilon^*_{-\sigma}(h)$, stays finite. At this unique point, it is case (C) in Fig. 4.12 that specifically arises. Furthermore, this situation only ensues for the ph asymmetric model where $x \neq 0$. The $x = 0$ case is precluded since the renormalized levels for opposite spins are equal and opposite for all h. For $x \neq 0$, and $h = h'$, the self-consistent self-energies are given from eq. (4.64) by

$$\Sigma^I_\sigma(\omega, h') \propto |\omega|^{2+r}, \qquad : \varepsilon^*_\sigma(h') = 0 \tag{4.100a}$$

$$\Sigma^I_{-\sigma}(\omega, h') \propto |\omega|^{2-r}, \qquad : \varepsilon^*_{-\sigma}(h') \neq 0 \tag{4.100b}$$

with $\delta\Sigma^I_\sigma(\omega, h') \overset{\omega\to 0}{\sim} -(\frac{1}{Z} - 1)\omega$ given once again from eq. (4.68b) for both $\sigma = \uparrow, \downarrow$. By inserting these forms of the self-energies into eq. (4.57), the low-ω forms of the spectral functions, $D_\sigma(\omega, h')$ are specifically given by

$$\pi\Gamma_0 D_\sigma(\omega, h') \overset{\omega\to 0}{\sim} \cos^2(\tfrac{\pi}{2}r)|\omega|^{-r} \qquad : \varepsilon^*_\sigma(h') = 0 \tag{4.101a}$$

$$\pi D_{-\sigma}(\omega, h') \overset{\omega\to 0}{\sim} \frac{\Gamma_0|\omega|^r}{(\varepsilon^*_{-\sigma}(h'))^2} \qquad : \varepsilon^*_{-\sigma}(h') \neq 0. \tag{4.101b}$$

In each case in eq. (4.100), the self-energies vanish with a power greater than the hybridization function, and thus are irrelevant on the very lowest energy scales. In consequence, the low-ω behaviour of the spectral functions, eq. (4.101) are precisely the same form as the non-interacting limit. The σ-spin spectrum effectively becomes ph symmetric at low-energies - eq. (4.101a) having exactly the same form as for the zero-field SSC phase, eq. (4.75), and satisfying the generalized pinning condition, eq. (4.39). By contrast, the $-\sigma$-spin spectrum has the same form as eq. (4.99b), and hence the zero-field ASC phase behaviour of eq. (4.72). Furthermore, we emphasize that for all finite h, for both $h = h'$ and $h \neq h'$, the system behaves as Fermi liquid, perturbatively connected to the NIL.

Fig. 4.21 shows NRG calculations for $\Gamma_0|\omega|^r \pi D_\downarrow(\omega, h')$, where for $h = h'$, $\varepsilon^*_\downarrow(h) = 0$. We have tuned U for $h = 0$, $h = 10^{-7}$ and $h = 10^{-4}$, such that in each case $h = h'$. For $h = h' = 0$, the case corresponds to the zero-field *interacting* QCP,

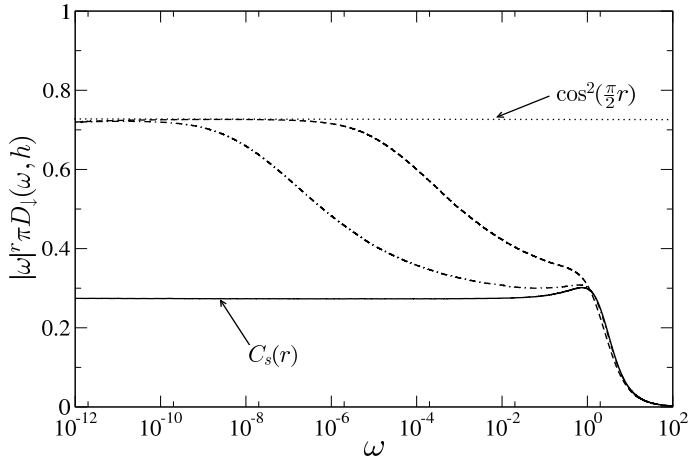


Figure 4.21: NRG results for $r = 0.35$ (such that $r < r_*$) and $\eta = 2x/U = -0.1$. The spectral function, $|\omega|^r \pi D_\downarrow(\omega, h = h')$ is plotted versus ω for $h = h'$ such that $\varepsilon_\downarrow(h)^* = 0$, whilst $\varepsilon_\uparrow(h)^* \neq 0$. $h = 0$ is the solid line, $h = 10^{-7}$, $U/\pi \simeq 2.035$, is the dot-dashed line, $h = 10^{-4}$, $U/\pi \simeq 1.614$ is the dashed line. At $h = 0$, for $U = U_c(r) \simeq 2.107\pi$, the spectra goes to the SQCP plateau value, $C_s(r)$ for $\omega \to 0$. By contrast for $h > 0$, for $h = h'$, $|\omega|^r \pi D_\downarrow(\omega, h = h') \overset{\omega \to 0}{\sim} \cos^2(\frac{\pi}{2}r)$, the ph symmetric NIL.

where both zero-field renormalized levels, $\varepsilon^*_{A\uparrow}(0), \varepsilon^*_{A\downarrow}(0)$, vanish. The spectra thus reaches a renormalized plateau-value, $C_s(r)$, as discussed in Section 4.9 and shown as a function of r in Fig. 4.15. By contrast for $h = h' > 0$, only one renormalized level vanishes (here $\varepsilon^*_\downarrow(h') = 0$, whilst $\varepsilon^*_\uparrow(h')$ remains finite) and consequently $\pi\Gamma_0 |\omega|^r D_\downarrow(\omega, h) \overset{\omega \to 0}{\sim} \cos^2(\frac{\pi}{2}r)$ by eq. (4.101a).

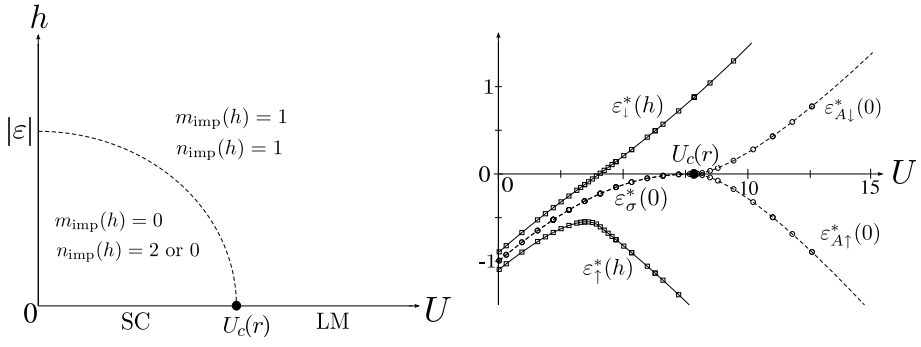


Figure 4.22: The LHS shows a schematic in the (U, h) plane for the asymmetric PAIM ($x = \varepsilon + \frac{U}{2} \neq 0$), and a typical r in the range $0 < r < 1$. The dashed line shows points for which $\varepsilon^*_\sigma(h) = 0$ with $\varepsilon^*_{-\sigma}(h) \neq 0$ terminating at $h = |\varepsilon|$ for $U = 0$. The zero field interacting *local* QCP is indicated. The RHS shows the renormalized levels, $\varepsilon^*_\sigma(h)$ versus U for $h = 10^{-1}$, squares (with a solid line as a guide to the eye) and $h = 0$ (circles and dashed line); shown for $r = 0.35$ and fixed $x = -1$, and calculated from NRG. For $h = 10^{-1}$, $\varepsilon^*_\downarrow(h)$ changes sign at $U \simeq 4.1$ ($< U_c(r) \simeq 7.8$), whilst $\varepsilon^*_\uparrow(h) < 0$ remains.

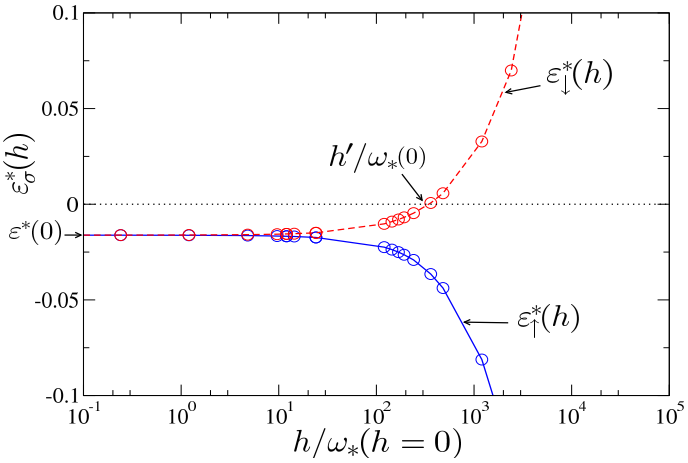


Figure 4.23: NRG results for a fixed $U/\pi = 1.2 < U_c(r)$, $r = 0.35$, $\eta = 2x/U = -0.1$. The renormalized levels, $\varepsilon^*_\uparrow(h)$, $\varepsilon^*_\downarrow(h)$ are plotted versus $h/\omega_*(0)$, where $\omega_*(h=0) \simeq 5 \times 10^{-6}$.

Renormalized levels

For a typical r in the range $0 < r < 1$, the left panel of Fig. 4.22 illustrates the behaviour schematically in the (U, h) plane (for a fixed $x \neq 0$). The dashed line shows the points for which $\varepsilon^*_\sigma(h') = 0$ (whilst $\varepsilon^*_{-\sigma}(h')$ remains finite), terminating at $h' = |\varepsilon|$ for $U = 0$. The figure emphasizes the point that $\varepsilon^*_\sigma(h) = 0$ only occurs for a single field $h = h'$ for $U < U_c$ (i.e. for the ASC phase only). For $h = h' \to 0$, $U \to U_c^-(r)$, the zero-field QCP indicated with a black circle. This is the only *local* interacting QCP in the (U, h)-plane, reflecting the fact that for any non-zero field the local phase transition is destroyed. As discussed above, the dashed line where $\varepsilon^*_\sigma(h') = 0$ then simply corresponds to a phase 'transition' between two equivalent Fermi liquid SC phases.

The right panel of Fig. 4.22 shows numerical NRG results for both the zero-field renormalized levels, $\varepsilon^*_\sigma(0) \equiv \varepsilon^*(0)$ - ASC phase, $\varepsilon^*_{A\uparrow}(0), \varepsilon^*_{A\downarrow}(0)$ - LM phase, and the finite-field levels, $\varepsilon^*_\uparrow(h), \varepsilon^*_\downarrow(h)$, as a function of U for a typical r and $x \neq 0$. The zero-field QCP, where $U = U_c(r)$, is once again indicated by the black circle. The figure illustrates that in contrast to the situation of zero-field, where all levels vanish at the local QCP, at finite-field the transition is destroyed. While $\varepsilon^*_\uparrow(h) < 0$ for all U, $\varepsilon^*_\downarrow(h)$ crosses the Fermi level at a particular $U < U_c(r)$ and $h = h'$.

To elucidate the finite-field behaviour further, Fig. 4.23 shows NRG results for the renormalized levels, $\varepsilon^*_\sigma(h)$, as a function of the rescaled local field (h/ω_*) and for fixed $U < U_c(r)$ (with $x < 0$) ($\omega_* \equiv \omega_*(h = 0)$ is the zero-field low-energy Kondo scale defined by eq. (4.70)). For $h/\omega_*(0) \ll 1$, the levels approach their zero-field (spin-independent) ASC value ($\varepsilon^*(0) < 0$). In contrast, for $h/\omega_*(0) \gg 1$, the levels become distinct, and at $h = h'$ (as indicated), $\varepsilon^*_\downarrow(h)$ crosses the Fermi level, such that for $h > h'$ the renormalized levels are sign-definite.

Excess quantities

In order to fully illustrate the finite-field PAIM physics, recall that the Friedel sum rule given by eq. (3.73b) in Section 3.4.2, relating the renormalized levels to the excess charges, holds equally well for any finite-field. From this equation (together with $\Gamma^I_\sigma(0,h) \equiv \Gamma^I(0) = 0$ for a purely local field), it follows that if $\varepsilon^*_\sigma(h) > 0$ then $n_{\mathrm{imp};\sigma}(h) = 0$, and if $\varepsilon^*_\sigma(h) < 0$ then $n_{\mathrm{imp};\sigma}(h) = 1$. If $\varepsilon^*_\sigma(h) = 0$ then $n_{\mathrm{imp};\sigma}(h) = \frac{1}{2}$. Now with reference to the LHS of Fig. 4.22, consider fixing a $U < U_c(r)$ and steadily increasing h (for $x < 0$). Initially (as for the zero-field ASC phase) both levels, $\varepsilon^*_\uparrow(h), \varepsilon^*_\downarrow(h) < 0$, so that from eq. (3.73b) both excess charges $n_{\mathrm{imp};\uparrow}(h), n_{\mathrm{imp};\downarrow}(h) = 1$. The total charge is then given by: $n_{\mathrm{imp}}(h) = n_{\mathrm{imp};\uparrow}(h) + n_{\mathrm{imp};\downarrow}(h) = 2$. The corresponding excess magnetization also follows as $m_{\mathrm{imp}}(h) = n_{\mathrm{imp};\uparrow}(h) - n_{\mathrm{imp};\downarrow}(h) = 0$. On increasing h through h', $\varepsilon^*_\downarrow(h)$ crosses the Fermi level and from eq. (3.73b), $n_{\mathrm{imp};\downarrow}(h)$ drops discontinuously from 1 to 0. Thus, as the point $h = h'$ is traversed, both the total charge and the magnetization change abruptly, such that for $h > h'$, both $n_{\mathrm{imp}}(h), m_{\mathrm{imp}}(h) = 1$.

Local quantities

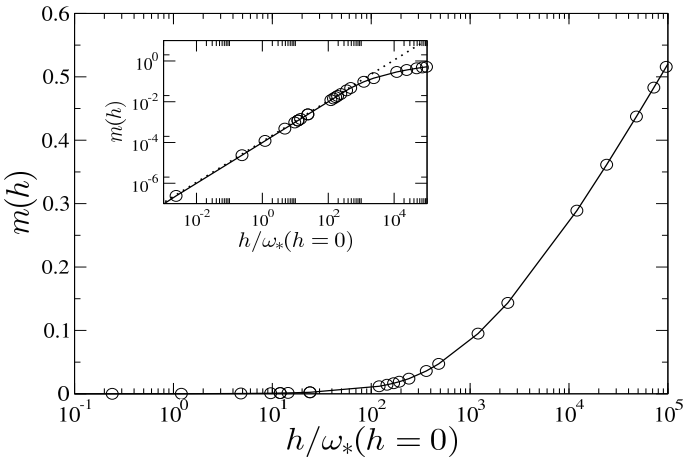


Figure 4.24: NRG results for the same parameters as Fig. 4.23 and with $U < U_c(r) \simeq 2.1\pi$. The local magnetization, $m(h)$, is plotted versus $h/\omega_*(h=0)$ (on a log-scale). $m(h)$ remains finite for all h; the inset shows the same data on a log:log plot. For $h/\omega_*(h=0) \ll 1$, $m(h)$ vanishes linearly in h.

In contrast to the excess magnetization, $m_{\mathrm{imp}}(h)$, the local impurity magnetization, $m(h)$, defined by eq. (3.1a), behaves very differently as a function of field. For any non-zero field (and $U < U_c(r)$, such that the system is in the ASC phase at zero-field) $m(h)$ is non-zero evolving continuously as a function of h. Fig. 4.24 shows $m(h)$ plotted as a function of $h/\omega_*(0)$ (with $\omega_*(0)$ once again the zero-field Kondo scale). The inset shows that for $h/\omega_*(0) \ll 1$, $m(h)$ vanishes linearly in h.

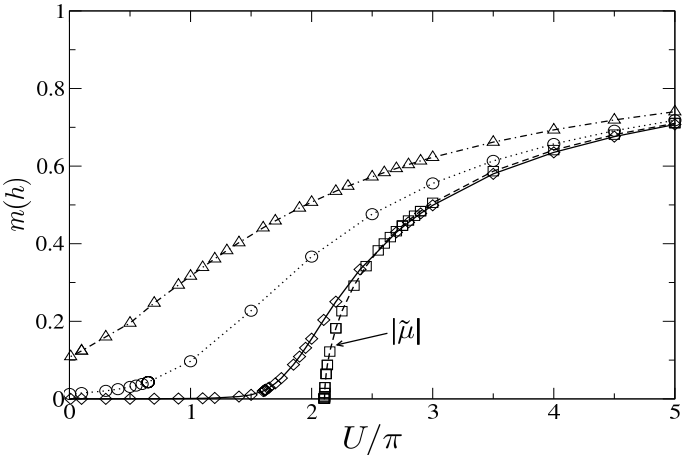


Figure 4.25: NRG results for $r = 0.35$, $\eta = 2x/U = -0.1$. The local magnetization, $m(h)$, is plotted versus U for a range of local fields, h. For $h = 0$ (dashed line-squares), the QCP is pristine and the local magnetization, $m_A(0) \equiv |\tilde{\mu}|$ is shown, vanishing as $U \to U_c^+(r)$, here $U_c/\pi \simeq 2.1$. $m(h)$ is then shown for $h = 10^{-4}$ (diamonds), $h = 10^{-2}$ (circles), $h = 10^{-1}$ (triangles). For any finite-h, the local QCP is destroyed and $m(h)$ is finite for any U.

Further numerical results are shown in Fig. 4.25, where the local magnetization, $m(h)$, is plotted versus U for a range of local fields. As previously discussed in Section 4.3.2 and shown in Fig. 4.3, the zero-field local moment $|\tilde{\mu}| \equiv m_A(0) \equiv m(0^+)$ is the order-parameter for the zero-field phase transition. In Fig. 4.25, $|\tilde{\mu}|$ is shown to vanish as expected for $U \to U_c^+(r)$, such that in the zero-field ASC phase for $U < U_c$, $|\tilde{\mu}| = 0$. By contrast, three further curves are shown in the figure, each for a finite-h, where we find that $m(h)$ is non-vanishing for *any* U.

Relating the excess and local quantities

Recall that the 'excess' magnetization, $m_{\rm imp}(h)$, is defined as the magnetization of the entire system with the impurity present, minus that with the impurity absent. Since the applied field is purely local, the magnetization of the system in the absence of the impurity vanishes, and therefore $m_{\rm imp}(h)$ is the magnetization for the entire system, $M(h)$. As a consequence, $m_{\rm imp}(h)$ may be separated into a local contribution, $m(h)$, together with the magnetization of the conduction band, $M_{CB}(h)$, i.e.

$$m_{\rm imp}(h) = m(h) + M_{CB}(h). \tag{4.102}$$

As discussed above and shown schematically on the LHS of Fig. 4.22, for $U < U_c(r)$ and $h < h'$, $m_{\rm imp}(h) = 0$. By contrast $m(h)$ is finite and continuously increases for any finite h. Therefore, eq. (4.102) implies that $M_{CB}(h) = -m(h)$, the conduction band magnetization taking an equal and opposite value to the magnetization localized on the impurity. By contrast for $h > h'$, $m_{\rm imp}(h) = 1$ and therefore

from eq. (4.102), $M_{CB}(h) = -m(h) + 1$. Thus, the physical picture is that when $h = h'$ is traversed, the conduction band magnetization changes discontinuously, i.e. $\delta M_{CB}(h') = M_{CB}(h = h'^{+}) - M_{CB}(h = h'^{-}) = +1$, whereas $m(h)$ evolves smoothly for all h. In other words, the abrupt discontinuous change in $m_{\rm imp}(h)$ on crossing $h = h'$, is localized solely on the conduction band and has no weight on the impurity itself.

A similar argument allows us to write the excess charge, $n_{\rm imp}(h)$, in terms of the local charge, $n(h)$ and the conduction band charge $N_{CB}(h)$

$$n_{\rm imp}(h) = n(h) + N_{CB}(h) - N^0_{CB}, \tag{4.103}$$

where N^0_{CB} is the charge of the system in the absence of the impurity, independent of the local-field, h. Once again, $n(h)$ is continuous across $h = h'$, whereas by contrast the excess quantity $\delta n_{\rm imp}(h') = n_{\rm imp}(h'^{+}) - n_{\rm imp}(h'^{-}) = -1$ changes abruptly. Hence, from eq. (4.103)

$$n_{\rm imp}(h'^{+}) - n_{\rm imp}(h'^{-}) = N_{CB}(h'^{+}) - N_{CB}(h'^{-}) = -1, \tag{4.104}$$

and therefore an entire electron is lost from the conduction band as $h = h'$ is traversed.

In conclusion, the physical picture when $h = h'$ is crossed is that an electron of definite spin is lost by the entire system, but has no weight on the impurity itself. The resulting discontinuous change of both $m_{\rm imp}(h)$ and $n_{\rm imp}(h)$ when $h = h'$ is crossed correspond to a simple bulk level-crossing transition where the ground-state charge of the system changes by unity. This 'transition' is analogous to the behaviour at zero-field for a fixed U on varying x (denoted by the dotted line in Fig. 4.4), where on crossing $x = 0$, the ASC phase for $x < 0$ and $n_{\rm imp}(0) = 2$ goes to the ASC phase for $x > 0$ and $n_{\rm imp}(0) = 0$. This bulk transition is distinct from the zero-field *local* quantum phase transition between the SC and LM phases, where $m(0^{+}) = |\tilde{\mu}|$ is the order parameter, vanishing continuously as $U \to U_c^{+}(r)$. A previous NRG study [36] suggested that the phase transition at finite-field is a "field-induced Kondo transition". However, as we have shown here this is simply not the case - $m(h)$ is non-vanishing as $h = h'$ is traversed.

4.11 Infinite-order Luttinger self-consistency

To conclude this chapter we make some general comments about the Luttinger self-consistency analysis of Section 4.6.

From direct NRG calculations, we find that everywhere in the (U, h) plane the self-consistent results of Fig. 4.12 hold, showing the exactness of the Luttinger con-

sistency arguments of Section 4.6. However, there is one exception where these order by order arguments do not predict the low-ω form of the self-energy. In the LM phase, identically at zero-field (for any x), we find that the two self-energies have the low-ω behaviour

$$\Sigma^I_{A\sigma}(\omega,0) \propto \theta(-\sigma\omega)|\omega|^r + \theta(\sigma\omega)|\omega|^{3r}, \tag{4.105}$$

with $\sigma = \pm 1$ as usual. This one-sided behaviour is shown in Fig. 4.26, where $\Sigma^I_{A\uparrow}(\omega,0)$ is plotted versus ω on a log:log plot for a typical r and $x < 0$ and both $\omega < 0$ and $\omega > 0$.

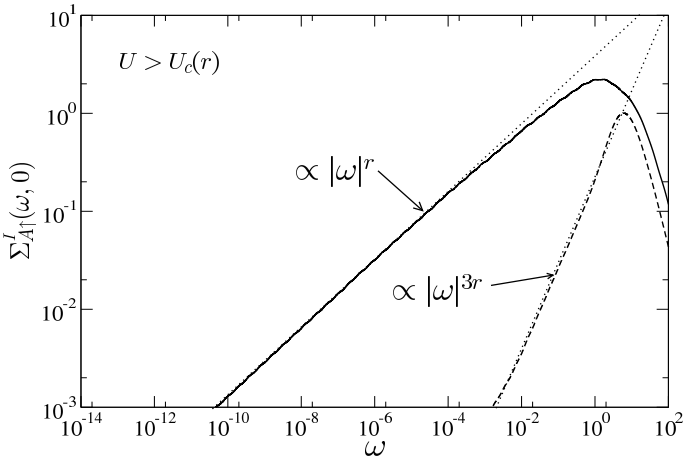


Figure 4.26: The self-energy for $r = 0.35$, $\eta = 1 + \frac{2\varepsilon}{U} = \frac{2x}{U} = -0.1$, $U/\pi = 5$, such that $x \simeq -0.785$. $\Sigma^I_{A\uparrow}(\omega,0)$ is plotted versus ω with both axes on a log-scale, shown for $\omega < 0$ (solid line) and $\omega > 0$ (dashed line). For $h = 0$, the low-ω form of the TSE for $\omega < 0$ in a LM phase, $\Sigma^I_{A\uparrow}(\omega,0) \propto |\omega|^r$, whereas for $\omega > 0$, $\Sigma^I_{A\uparrow}(\omega,0) \propto |\omega|^{3r}$. The dotted lines indicate the power dependences.

The self-consistent low-ω results exhibited in Fig. 4.12 are obtained from an order by order analysis of the self-energies (SSE in the SC phase, TSEs in the LM phase) expressed in terms of the skeleton expansion. (Even though from the underlying self-consistency, each skeleton diagram corresponds to an infinite-order summation in U, the self-energies are still in essence perturbative.) However, it is possible that Luttinger self-consistency can arise in a different sense. Imagine that a particular class of diagrams are summed to infinite-order yielding an integrable singularity in an internal (integrated-over) frequency index. Then by virtue of the fact that this type of contribution is not present in the order by order expansion, the resultant self-consistent low-ω form of the self-energy would be distinct.

We have identified an infinite-order subset of diagrams that can self-consistently generate the low-ω self-energy dependence of eq. (4.105). In Chapter 6 we explicitly consider a self-consistency scheme, similar to that of Section 4.6, but involving the

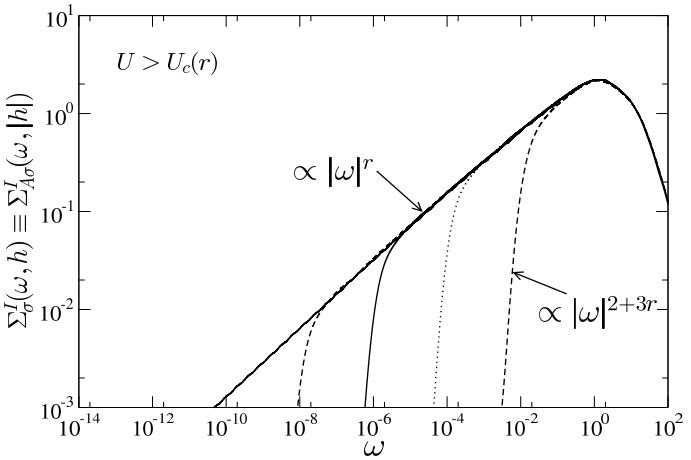


Figure 4.27: NRG results for the same parameters as Fig. 4.26. $\Sigma^I_\uparrow(\omega,h)$ is plotted versus ω with both axes on a log-scale, shown for $\omega < 0$ for different local fields, $h = 0$, 10^{-8}, 10^{-6}, 10^{-4}, 10^{-2}. For $h = 0$, the low-ω form of the TSE for $\omega < 0$ in a LM phase, $\Sigma^I_{A\uparrow}(\omega,0) \propto |\omega|^r$. By contrast, for any finite-field, $h > 0$, for $|\omega| < h$, the low-ω form becomes $\Sigma^I_{A\uparrow}(\omega,|h|) \propto |\omega|^{2+3r}$.

relevant class of diagrams. However, we emphasize that since $\Sigma_{A\sigma}(\omega,0)$ vanishes *at least as rapidly* as the hybridization function, $\Gamma(\omega)$, the exact low-ω deductions of Section 4.5 for the zero-field SSE, $\Sigma(\omega)$, still hold.

We explicitly confirm the preceding results for the self-energy in Fig. 4.27. The finite-field self-energy, $\Sigma^I_\sigma(\omega,h) \equiv \Sigma^I_{A\sigma}(\omega,|h|)$ is plotted versus ω for $U > U_c(r)$ on a log:log plot for $\omega < 0$. As discussed above, at zero-field from eq. (4.105), $\Sigma^I_{A\sigma}(\omega,0) \propto |\omega|^r$. However, for *any* finite-field, for $|\omega|/h \ll 1$, $\Sigma_\sigma(\omega,h) \propto |\omega|^{2+3r}$ as expected from eq. (4.99a). As $h \to 0$, the finite-field curves fall onto the zero-field curve, such that for $|\omega|/h \gg 1$, $\Sigma_\sigma(\omega,h) \equiv \Sigma_{A\sigma}(\omega,0) \propto |\omega|^r$.

4.12 Concluding remarks

In this chapter we have fully described both the static and dynamic behaviour of the PAIM, focusing on what can be said exactly about both phases, with particular emphasis on the non-Fermi liquid LM phase. Using the TSE formalism of Chapter 3 has allowed us to obtain a number of entirely new results in the LM phase.

In the next chapter we move to discuss application of an approximate technique to the PAIM, where the skeleton expansion is truncated at second-order level.

CHAPTER 5

Self-consistent second-order perturbation theory

In this chapter we consider the application of self-consistent second-order perturbation theory (in U) to the zero-field pseudogap AIM studied in the previous chapter. The essential idea is that the skeleton expansion for the self-energy, as shown in Fig. 2.4, is truncated at second-order level such that only the first-order Hartree-Fock 'bubble' diagram (as shown in Fig. 3.4 and discussed in section 4.6.1) and the second-order diagram (as discussed in Section 4.6.2) are explicitly included in the approximation.

Formally, recall that in a Fermi liquid SC phase, the single-self-energy, $\Sigma_\sigma(\omega, 0)$, is expressed in terms of the functional derivative of the Luttinger-Ward functional, i.e. $\Sigma_\sigma(\omega, 0) \equiv \delta\Phi_{LW}/\delta G_\sigma(\omega, 0)$ and in consequence is a functional of the propagators determined via the skeleton expansion, $\Sigma_\sigma(\omega, 0) \equiv \Sigma[\{G_{\sigma'}\}]$. By contrast, in a doubly degenerate LM phase, it is the TSEs, $\Sigma_{A\sigma}(\omega, 0)$ that are obtained via $\Sigma_{A\sigma}(\omega, 0) \equiv \delta\Phi_{LW}/\delta G_{A\sigma}(\omega, 0)$, where Φ_{LW} is precisely the same functional of the broken-symmetry propagators in the LM phase, as it is of the usual propagators in the SC phase, i.e. $\Phi[\{G_{\sigma'}\}] \equiv \Phi[\{G_{A\sigma'}\}]$. The SSE in the LM phase can then be calculated as a derivative quantity from eq. (3.30) in terms of the distinct TSEs.

As discussed previously in Chapter 3, because the self-energies are functionals of the propagators, and in turn, the propagators are obtained in terms of their corresponding self-energies, the Dyson equation, eq. (3.23), and the skeleton expansion provide a self-consistency condition for the determination of the propagators as *entire* functions of ω. In this chapter we seek to numerically obtain self-consistent solutions to the model in each of the unique phases by truncating the skeleton expansion at second-order level. In order to correctly capture the underlying physics of both phases, we generally allow the possibility that broken-symmetry solutions, $G_{A\sigma}(\omega)$ (with a non-zero-local moment $|\tilde{\mu}|$) can exist. As we explicitly discuss below,

the numerical procedure may then converge to a solution with a non-zero value of $|\tilde{\mu}|$ - with $G_{A\uparrow}(\omega,0) \neq G_{A\downarrow}(\omega,0)$ (we denote a LM solution), or by contrast $|\tilde{\mu}|$ may converge to zero, with an associated single propagator, $G_\sigma(\omega,0) \equiv G_{A\sigma}(\omega)$ (which we denote as a SC solution).

Even though second-order perturbation theory is a naive approach, and may only be able to capture the underlying physics for small U, the reasons we consider it here are threefold. Firstly, as explained in Section 4.6.2, second-order is the first level of approximation to the skeleton expansion that generates a non-trivial *dynamic* (ω-dependent) contribution to $\Sigma_{A\sigma}(\omega)$. Secondly, we want to find out whether it is possible to obtain fully converged numerical self-consistent solutions in the *broken-symmetry* LM phase. Finally, we want to answer the question of whether the unique interacting nature of the QCP, as discussed in Section 4.9, is captured coming from both phases.

Before proceeding, we make another important point. For the approximation considered here, as a consequence of the fact that the self-energy is obtained from a generating functional, Φ_{LW}, macroscopic conservation laws for quantities such as energy, spin and particle number are respected [66, 67]. For techniques of this type, known as 'conserving approximations', the general arguments of Section 3.4 hold, i.e. in *any* contribution to Φ_{LW} a finite frequency shift, $\delta\omega$, in the σ-spin propagators leaves Φ_{LW} unchanged (i.e. $\delta\Phi_{LW} = 0$). As a direct consequence, the Luttinger integrals, $I_{L_\sigma}(h)$ and $I_{L_{A\sigma}}(|h|)$ (for $U < U_c$ and $U > U_c$ respectively) are both argued to vanish, eq. (3.72). Exact relations such as the Friedel sum rules, eqs. (3.73a-3.73b), relating the excess charge to the renormalized levels in each phase are then satisfied, even at the approximate second-order level discussed here.

An outline of the chapter is as follows. We first consider the underlying equations relevant to implement this simple level of approximation. Subsequently, we discuss the low-ω asymptotic functional forms of both the relevant propagators and self-energies, in each of the unique phases. In each case a comparison is made to the *exact* results of the previous chapter. We then move to discuss the relevant algorithm used in order to obtain numerical results. Finally we present results for both static and dynamical quantities at both ph symmetry and the more general model.

5.1 Diagrams

The self-energy truncated at second-order level is given simply (and shown diagrammatically in Fig.5.1) by

$$\Sigma_{A\sigma}(\omega) = \Sigma^{(1)}_{A\sigma} + \Sigma^{(2)}_{A\sigma}(\omega), \tag{5.1}$$

where $\Sigma^{(1)}_{A\sigma}$ denotes the first-order unrestricted Hartree-Fock *static* (ω-independent) contribution. $\Sigma^{(1)}_{A\sigma}$ is given via eq. (4.40) in terms of the local charge, $\bar{n} \equiv n(h=0)$

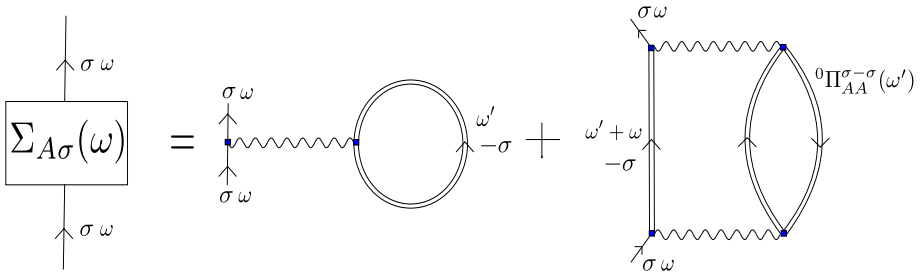


Figure 5.1: $\Sigma_{A\sigma}(\omega)$, first and second order contributions to the skeleton expansion. All double lines denote full self-consistent propagators, $G^{(2)}_{A\sigma}(\omega)$, wiggly lines denote the on-site interaction energy, "U". All frequencies and spins are conserved at each vertex.

and magnetization, $|\tilde{\mu}|$, by

$$\Sigma^{(1)}_{A\sigma} = U\langle\hat{n}_{-\sigma}\rangle = \tfrac{U}{2}[\bar{n} - \sigma|\tilde{\mu}|]. \tag{5.2}$$

The local charge, $\bar{n}$ and local magnetization, $|\tilde{\mu}| \equiv m_A(0) = m(h \to 0^+)$ are given at zero-field via eqs. (3.16, 3.20b) as

$$\bar{n} = \int_{-\infty}^{0} \mathrm{d}\omega[D_{A\uparrow}(\omega) + D_{A\downarrow}(\omega)], \tag{5.3a}$$

$$|\tilde{\mu}| = \int_{-\infty}^{0} \mathrm{d}\omega[D_{A\uparrow}(\omega) - D_{A\downarrow}(\omega)]. \tag{5.3b}$$

The second-order *dynamical* contribution in terms of broken-symmetry propagators is given via eq. (4.41), as

$$\Sigma^{(2)}_{A\sigma}(\omega) = U^2 \iiint_{-\infty}^{\infty} \prod_{i=1}^{3} \frac{\mathrm{d}\omega_i}{2\pi} G_{A\sigma}(\omega_1) G_{A-\sigma}(\omega_2) G_{A-\sigma}(\omega_3) \times 2\pi\delta(\omega_1 + \omega_2 - \omega_3 - \omega).$$

Using the delta function to eliminate one of the internal frequency integrals, we may rewrite this equation in the form

$$\Sigma^{(2)}_{A\sigma}(\omega) = U^2 \int_{-\infty}^{\infty} \frac{\mathrm{d}\omega''}{2\pi i} G_{A-\sigma}(\omega + \omega'') \left[i \int_{-\infty}^{\infty} \frac{\mathrm{d}\omega''}{2\pi} G_{A\sigma}(\omega' - \omega'') G_{A-\sigma}(\omega') \right], \tag{5.4}$$

where we define the term in square brackets as a so-called 'polarization propagator' (also known as a polarization bubble, or polarization part) [62, 63] as

$${}^0\Pi^{\sigma-\sigma}_{AA}(\omega) = i \int_{-\infty}^{\infty} \frac{\mathrm{d}\omega'}{2\pi} G_{A\sigma}(\omega' - \omega) G_{A-\sigma}(\omega'). \tag{5.5}$$

A polarization propagator is any part of a diagram that can be fitted between two interaction lines. Specifically, ${}^0\Pi^{\sigma-\sigma}_{AA}(\omega)$ is known as the transverse spin polarization propagator [62], and is shown in Fig. 5.1. The dynamical contribution to the self-

energy, eq. (5.4), then follows as

$$\Sigma^{(2)}_{A\sigma}(\omega) = U^2 \int_{-\infty}^{\infty} \frac{\mathrm{d}\omega'}{2\pi i} G_{A-\sigma}(\omega+\omega')\,{}^0\Pi^{\sigma-\sigma}_{AA}(\omega'). \tag{5.6}$$

A simple calculation, analogous to the considerations of eq. (4.6.2) then allows us to write this polarization propagator, ${}^0\Pi^{\sigma-\sigma}_{AA}(\omega)$, in terms of its real and imaginary parts. The imaginary part, which is important in what is to follow, is given by

$$\begin{aligned}\frac{1}{\pi}\mathrm{Im}\,{}^0\Pi^{\sigma-\sigma}_{AA}(\omega) = \theta(\omega)\int_0^{|\omega|} \mathrm{d}\omega' D_{A\sigma}(\omega'-\omega)D_{A-\sigma}(\omega') \\ + \theta(-\omega)\int_{-|\omega|}^{0} \mathrm{d}\omega' D_{A\sigma}(\omega'-\omega)D_{A-\sigma}(\omega')\end{aligned} \tag{5.7}$$

By virtue of the fact that the spectral functions, $D_{A\sigma}(\omega) = -\frac{1}{\pi}\,\mathrm{sgn}(\omega)\mathrm{Im}G^t_{A\sigma}(\omega)$, have positive weight for all ω, the polarization propagator also has this property, i.e. $\frac{1}{\pi}\mathrm{Im}\,{}^0\Pi^{\sigma-\sigma}_{AA}(\omega) \geq 0$. It is then straightforward to show by inserting eq. (5.7) into eq. (4.45), that the second-order contribution, $\Sigma^{I(2)}_{A\sigma}(\omega) = -\,\mathrm{sgn}(\omega)\mathrm{Im}\Sigma^{I(2)}_{A\sigma}(\omega)$ may then be written in terms of $D_{A\sigma}(\omega)$ and $\mathrm{Im}\,{}^0\Pi^{\sigma-\sigma}_{AA}(\omega)$ via

$$\begin{aligned}\Sigma^{I(2)}_{A\sigma}(\omega) = U^2\theta(\omega)\int_{-|\omega|}^{0} \mathrm{d}\omega' \mathrm{Im}\,{}^0\Pi^{\sigma-\sigma}_{AA}(\omega')D_{A-\sigma}(\omega'+\omega) \\ + U^2\theta(-\omega)\int_0^{|\omega|} \mathrm{d}\omega' \mathrm{Im}\,{}^0\Pi^{\sigma-\sigma}_{AA}(\omega')D_{A-\sigma}(\omega'+\omega)\end{aligned} \tag{5.8}$$

where $\Sigma^{I(2)}_{A\sigma}(\omega) \geq 0$ for all ω. The second-order broken-symmetry propagator itself, $G^{(2)}_{A\sigma}(\omega)$, may be written from the Dyson equation, eq. (3.23), as

$$G^{(2)}_{A\sigma}(\omega) = [\omega^+ - \varepsilon^*_{A\sigma} - \Gamma(\omega) - [\Sigma^{(2)}_{A\sigma}(\omega) - \Sigma^{(2)}_{A\sigma}(0)]]^{-1}, \tag{5.9}$$

with renormalized level energy given by

$$\varepsilon^*_{A\sigma} = \varepsilon + \tfrac{U}{2}(\bar{n} - \sigma|\tilde{\mu}|) + \Sigma^{(2)}_{A\sigma}(\omega=0). \tag{5.10}$$

The spectral function, $D^{(2)}_{A\sigma}(\omega) = -\frac{1}{\pi}\,\mathrm{sgn}(\omega)\mathrm{Im}G_{A\sigma}(\omega)$ is then given by

$$D^{(2)}_{A\sigma}(\omega) = \frac{\Gamma^I(\omega) + \Sigma^I_{A\sigma}(\omega)}{[\omega - \varepsilon^*_{A\sigma} - \Gamma^R(\omega) - [\Sigma^{R(2)}_{A\sigma}(\omega) - \Sigma^{R(2)}_{A\sigma}(0)]]^2 + [\Gamma_I(\omega) + \Sigma^I_{A\sigma}(\omega)]^2}, \tag{5.11}$$

with $\omega^+ = \omega + i\,\mathrm{sgn}(\omega)\eta$.

In the special case of ph symmetry where $x = \varepsilon + \frac{U}{2} = 0$, we may utilize the symmetries of Section 4.1.2. By inserting eq. (4.3b) into eq. (5.3a), it is readily

shown as a consequence of the spectral function $D_{A\sigma}(\omega)$ being normalized, that the local charge $\bar{n} = 1$. Thus, at $x = 0$, the renormalized levels, $\varepsilon^*_{A\sigma}$, given by eq. (5.10), reduce to

$$\varepsilon^*_{A\sigma} = -\sigma\tfrac{U}{2}|\tilde{\mu}| + \Sigma^{(2)}_{A\sigma}(\omega = 0). \tag{5.12}$$

Now inserting the symmetry, eq. (4.3c), into eq. (5.12), the levels are sign definite at $x = 0$, given by

$$\varepsilon^*_{A\uparrow} < 0, \qquad \varepsilon^*_{A\downarrow} = -\varepsilon^*_{A\uparrow} > 0. \tag{5.13}$$

In a LM phase *away from ph symmetry* (where $x \neq 0$), the renormalized levels, $\varepsilon^*_{A\uparrow}, \varepsilon^*_{A\downarrow}$, are not necessarily sign definite.[1]

We now have all of the relevant equations in order to be able to implement a numerical procedure to determine the self-consistent propagator, $G_{A\sigma}(\omega)$. However, before proceeding, we examine the low-ω behaviour in each of the distinct phases.

5.2 Low-ω asymptotics

In section 4.6 we used Luttinger self-consistency arguments [60] to obtain the *exact* low-ω forms of the self-energies in each of the distinct phases to all orders (in U). In this section, we determine the precise coefficients of the leading low-ω behaviour at the (self-consistent) second-order level of approximation. (Here we note that for reasons of brevity we set the unit of energy, $\Gamma_0^{1/(1-r)} \equiv 1$ in the rest of this chapter.)[2]

5.2.1 SSC phase

We first consider the unique case of ph symmetry where $x = \varepsilon + \frac{U}{2} = 0$, and start with the strong coupling (SC) phase. As discussed in Section 3.1, the local moment, $|\tilde{\mu}|$, is necessarily zero in a SC phase at zero-field, and consequently the propagators are independent of spin (and we may drop both the A and σ labels from the propagators). The symmetries, eqs. (4.3a-4.3d) then give

$$\begin{aligned} G(\omega) &= -G(-\omega), \qquad D(\omega) = D(-\omega), \\ \Sigma(\omega) &= -\Sigma(-\omega), \qquad \Sigma^I(\omega) = \Sigma^I(-\omega), \qquad \varepsilon^* = 0. \end{aligned} \tag{5.14}$$

[1] In Section 4.3.2 we argued that if the local and excess magnetizations lie in the same direction, then for *any* x $(= \varepsilon + \frac{U}{2})$ the renormalized levels *are* sign definite. (This result is also satisfied from the numerically exact NRG calculations of Fig. 4.2.) However, here at the (crude) second-order level of approximation the levels may be of either sign.

[2] The hybridization function then becomes: $\Gamma^I(\omega) = \Gamma_0|\omega|^r = \Gamma_0^{1/(1-r)}|\omega/\Gamma_0^{1/(1-r)}|^r \equiv |\omega|^r$. When plotting numerical results all quantities are rescaled in terms of $\Gamma_0^{1/(1-r)}$, e.g. $\omega = \omega/\Gamma_0^{1/(1-r)}$, $U = U/\Gamma_0^{1/(1-r)}$, $\varepsilon = \varepsilon/\Gamma_0^{1/(1-r)}$ are dimensionless.

From the (order by order) Luttinger self-consistency arguments [60] of Section 4.6, in the SSC phase the *self-consistent* low-ω behaviour of the single self-energy is given by $\Sigma^I(\omega) \overset{\omega\to 0}{\sim} \propto |\omega|^{2-3r}$ (eq. (4.73)). At the second-order level considered here the self-energy also has the same form:

$$\Sigma^{I(2)}(\omega) \overset{\omega\to 0}{\sim} \alpha_{2s}(r)|\omega|^{2-3r}. \tag{5.15}$$

The coefficient, $\alpha_{2s}(r)$, may be obtained at the specific second-order level described here.

Since the self-energy (eq. (5.15)) vanishes with an exponent greater than the hybridization function ($\Gamma^I(\omega) \propto |\omega|^r$) for $r < \frac{1}{2}$, on the very lowest frequency scales the spectral function, $D(\omega)$, must have the same form as the non-interacting function, $D^0(\omega)$ (c.f. eq. (4.75)):[3]

$$\pi\Gamma_0 D^{(2)}(\omega) \overset{\omega\to 0}{\sim} \cos^2(\tfrac{\pi}{2})|\omega|^{-r} = \lim_{\omega\to 0}[\pi\Gamma_0 D^0(\omega)]. \tag{5.16}$$

Inserting eq. (5.16) into eq. (5.7) for $\mathrm{Im}^0\Pi(\omega) \equiv \mathrm{Im}^0\Pi^{\sigma-\sigma}_{AA}(\omega)$, it is readily shown that its low-ω behaviour is of the form

$$\mathrm{Im}^0\Pi(\omega) \overset{\omega\to 0}{\sim} \frac{1}{\pi}\cos^4(\tfrac{\pi}{2}r)\int_0^{|\omega|} \mathrm{d}\omega' |\omega' - |\omega||^{-r}|\omega'|^{-r}. \tag{5.17a}$$

Making the substitution, $\omega' = y|\omega|$, this equation reduces to

$$\mathrm{Im}^0\Pi(\omega) \overset{\omega\to 0}{\sim} \frac{1}{\pi}\cos^4(\tfrac{\pi}{2}r)\left[\int_0^1 \mathrm{d}y (1-y)^{-r}y^{-r}\right]|\omega|^{1-2r} \tag{5.17b}$$

$$\overset{\omega\to 0}{\sim} \mathcal{A}_{2s}(r)|\omega|^{1-2r}, \text{ with coefficient:} \tag{5.17c}$$

$$\mathcal{A}_{2s}(r) = \frac{1}{\pi}\cos^4(\tfrac{\pi}{2}r)\left[\frac{\Gamma(1-r)^2}{\Gamma(2-2r)}\right], \tag{5.17d}$$

where the integral in square brackets may be given in terms of the gamma function, $\Gamma(y)$. Thus, by inserting eq. (5.17c) and eq. (4.75) into eq. (5.8), it is readily shown by an analogous argument to that leading to eq. (5.17d) above, that the leading low-ω behaviour of $\Sigma^{I(2)}(\omega)$ is given by

$$\Sigma^{I(2)}(\omega) \overset{\omega\to 0}{\sim} \alpha_{2s}(r)|\omega|^{2-3r}, \text{ with coefficient:} \tag{5.18a}$$

$$\alpha_{2s}(r) = U^2\mathcal{A}_{2s}(r)\frac{1}{\pi}\cos^2(\tfrac{\pi}{2}r)\left[\frac{\Gamma(1-r)\Gamma(2-2r)}{\Gamma(3-3r)}\right], \tag{5.18b}$$

which as expected from the underlying self-consistency is the ω-dependence that

[3] The low-ω forms of both $D(\omega)$ and $\Sigma(\omega)$ in a SSC phase at second-order level are essentially the same as those discussed in Section 4.7.2. It is the precise second-order coefficients that we determine in this section.

we started with for $\Sigma^{I(2)}(\omega)$ in eq. (5.15). The fact that the second-order coefficient $a_{2s}(r) \propto U^2$ naturally reflects the second-order level of the calculation. As a consequence of the fact that $\Sigma^{I(2)}(\omega)$ vanishes more rapidly than the hybridization function, the low-ω *self-consistent* results described here are identical to those obtained for a one-loop (i.e. not self-consistent) second-order perturbative calculation as described in ref [100].

5.2.2 LM phase: General PH symmetry/asymmetry

As discussed in Section 3.1, in a LM phase there is a non-zero local moment, $|\tilde{\mu}|$ in the system. Both the spectra, $D_{A\sigma}(\omega)$, and self-energies, $\Sigma_{A\sigma}(\omega)$ are thus dependent on spin σ. As a consequence of the non-vanishing local moment, the renormalized levels, $\varepsilon^*_{A\sigma}$, given via eq. (5.10), are necessarily non-zero in a LM phase. Once again, from the order by order Luttinger self-consistency arguments of Section 4.6, in a LM phase, $\Sigma^{I(2)}_{A\sigma}(\omega)$ has the following dependence (and holds *self-consistently* in the range $0 < r < 1$)

$$\Sigma^{I(2)}_{A\sigma}(\omega) \overset{\omega\to 0}{\sim} \alpha_{A\sigma}(r)|\omega|^{2+3r} \tag{5.19a}$$

$$[\Sigma^{R(2)}_{A\sigma}(\omega) - \Sigma^{R(2)}_{A\sigma}(0)] \overset{\omega\to 0}{\sim} -\gamma_{A\sigma}\omega \tag{5.19b}$$

where $\alpha_{A\sigma}(r)$ is a specific second-order coefficient with $\gamma_{A\sigma} = \frac{1}{\pi}\int_{-\infty}^{\infty} \mathrm{d}\omega P(\Sigma^{I(2)}_{A\sigma}(\omega)/\omega^2)$, obtained from eq. (4.26). Thus by inserting eq. (5.19), together with eq. (4.1b) into eq. (5.11), the low-ω form of the broken-symmetry spectral function follows as

$$\pi D^{(2)}_{A\sigma}(\omega) \overset{\omega\to 0}{\sim} \frac{|\omega|^r}{[\varepsilon^*_{A\sigma}]^2}, \tag{5.20}$$

vanishing as $\omega \to 0$. By using eq. (5.20) in eq. (5.7), it is readily shown that the low-ω behaviour of the polarization bubble, $\mathrm{Im}^0\Pi^{\sigma-\sigma}_{AA}(\omega)$ is

$$\mathrm{Im}^0\Pi^{\sigma-\sigma}_{AA}(\omega) \overset{\omega\to 0}{\sim} \mathcal{A}_{AA}(r)|\omega|^{1+2r}, \text{ with coefficient:} \tag{5.21a}$$

$$\mathcal{A}_{AA}(r) = \frac{1}{\pi}\frac{1}{[\varepsilon^*_{A\sigma}\varepsilon^*_{A-\sigma}]^2}\left[\frac{\Gamma(1+r)^2}{\Gamma(2+2r)}\right], \tag{5.21b}$$

where $\mathcal{A}_{AA}(r)$ is independent of spin-σ and the coefficient is the same for both $\omega > 0$ and $\omega < 0$, i.e. $\mathcal{A}^+_{AA}(r) = \mathcal{A}^-_{AA}(r)$. Now inserting eq. (5.21a), together with eq. (5.20) into eq. (5.8), we find that the low-ω form of the two-self energy function is

$$\Sigma^{I(2)}_{A\sigma}(\omega) \overset{\omega\to 0}{\sim} \alpha_{A\sigma}(r)|\omega|^{2+3r}, \text{ with coefficient:} \tag{5.22a}$$

$$\alpha_{A\sigma}(r) = U^2\mathcal{A}_{AA}(r)\frac{1}{\pi}\frac{1}{[\varepsilon^*_{A-\sigma}]^2}\left[\frac{\Gamma(1+r)\Gamma(2+2r)}{\Gamma(3+3r)}\right], \tag{5.22b}$$

once again $\propto U^2$. If the system is at ph symmetry, then the renormalized levels are equal and opposite via eq. (5.13), and therefore the leading dependence of the two-self-energies are spin-independent, i.e. $\alpha_{A\sigma}(r) = \alpha_{A-\sigma}(r) = \alpha_A(r)$, but this is not generally true for $x \neq 0$.

5.2.3 ASC phase

For general $x \neq 0$, away from ph symmetry, the (spin-independent) renormalized level, $\varepsilon^* \equiv \varepsilon^*_{A\sigma}$, is generally non-zero in a ASC phase (as shown from NRG in Fig. 4.2). In fact, the low-ω behaviour of the propagators and self-energies are exactly the same as for the general LM phase if the A and σ subscripts on all quantities are dropped. Once again, the order by order self-consistency analysis of Section 4.6 gives the low-ω form of the SSE as $\Sigma^I(\omega) \propto |\omega|^{2+3r}$, eq. (4.68a), holding in the range $0 < r < 1$. Specifically at second-order level this may be written as

$$\Sigma^{I(2)}(\omega) \overset{\omega\to 0}{\sim} \alpha_{2a}(r)|\omega|^{2+3r}, \tag{5.23}$$

with $\alpha_{2a}(r)$ a second-order coefficient. By analogy with the last section, the single-particle spectrum is then given by

$$\pi D^{(2)}(\omega) \overset{\omega\to 0}{\sim} \frac{|\omega|^r}{[\varepsilon^*]^2}, \tag{5.24}$$

where the coefficient $\alpha_{2a}(r)$ is given via eq. (5.22b) on dropping the A and σ subscripts.

5.2.4 Single self-energy in the LM phase

Given the low-ω dependence of the TSEs in the LM phase, eq. (5.22a), we can now obtain the corresponding low-ω form of the single self-energy, $\Sigma^I(\omega)$, from eq. (3.30). It is readily shown that

$$\Sigma^{I(2)}(\omega) \overset{\omega\to 0}{\sim} \frac{1}{\gamma^2}|\omega|^r \qquad : x \neq 0 \tag{5.25a}$$

$$\Sigma^{I(2)}(\omega) \overset{\omega\to 0}{\sim} [\varepsilon^*_{A\sigma}\cos(\tfrac{\pi}{2}r)]^2|\omega|^{-r} \qquad : x = 0 \tag{5.25b}$$

where as defined by eq. (4.22), $\gamma = [(\varepsilon^*_{A\sigma} + \varepsilon^*_{A-\sigma})/(\varepsilon^*_{A\sigma} - \varepsilon^*_{A-\sigma})]$, is the ratio of the sum and differences of the renormalized levels.[4] The self-energies may then be rescaled by the natural LM phase low-energy scale, ω_*, given in terms of the

[4]Note that at $x = 0$, $\gamma = 0$ as a consequence of eq. (5.13).

difference of the renormalized levels by eq. (4.20):

$$\frac{1}{\omega_*^r}\Sigma^{I(2)}(\omega) \overset{\tilde{\omega}\to 0}{\sim} \frac{1}{\gamma^2}|\tilde{\omega}|^r \qquad : x \neq 0, \tag{5.26a}$$

$$\frac{1}{\omega_*^r}\Sigma^{I(2)}(\omega) \overset{\tilde{\omega}\to 0}{\sim} \cos^2(\tfrac{\pi}{2}r)|\tilde{\omega}|^{-r} \qquad : x = 0, \tag{5.26b}$$

where, as a consequence of eq. (5.13), we have used $\omega_*^r = \frac{1}{2}|\varepsilon^*_{A\sigma} - \varepsilon^*_{A-\sigma}| = |\varepsilon^*_{A\sigma}|$ for $x = 0$. The eqs. (5.26a-5.26b) are the specific second-order analogs of the general forms given by eqs. (4.25, 4.33). Thus, the second-order values of the coefficients a_a, a_s are given simply by $a_a = 1/\gamma^2$, and $a_s = \cos^2(\frac{\pi}{2}r)$. The absence of any specific U dependence in these coefficients arises as a consequence that the TSEs, $\Sigma_{A\sigma}(\omega)$, vanish with a power greater than the hybridization function as $\omega \to 0$. We emphasize that the low-ω forms of $\Sigma^I(\omega)$, eq. (5.25), obtained even at this simple second-order level of approximation reflect that the LM phase is a non-Fermi liquid. The self-energies vanish at least as slowly as the hybridization function, i.e. $\Sigma^I(\omega) \overset{\omega\to 0}{\sim} |\omega|^\lambda$, $\lambda \leq r$ such that the spectral function, $D(\omega)$ is wholly influenced by the form of $\Sigma^I(\omega)$ on the lowest frequency scales.

By inserting eqs. (5.25a-5.25b) into eq. (5.11) for $D(\omega)$, the low-ω form of the total (σ-independent) spectrum in a LM phase, $D(\omega) = \frac{1}{2}[D_{A\sigma}(\omega)+D_{A-\sigma}(\omega)]$, given via eq. (3.13) becomes

$$\pi D^{(2)}(\omega) \overset{\omega\to 0}{\sim} \frac{|\omega|^r[1+\frac{1}{\gamma^2}]}{[\frac{1}{2}|\varepsilon^*_{A\sigma} - \varepsilon^*_{A-\sigma}|]^2[\gamma - \frac{1}{\gamma}]^2}, \tag{5.27a}$$

for *any* x. Once again, using eq. (4.20) for ω_*, the low-$\tilde{\omega}$ scaling behaviour of the spectrum is written as

$$\pi\omega_*^r D^{(2)}(\omega) \overset{\tilde{\omega}\to 0}{\sim} \frac{[1+\frac{1}{\gamma^2}]|\tilde{\omega}|^r}{[\gamma - \frac{1}{\gamma}]^2}, \tag{5.27b}$$

such that precisely at $x = 0$, where $\gamma = 0$, the scaling spectrum simply has the form

$$\pi\omega_*^r D^{(2)}(\omega) \overset{\tilde{\omega}\to 0}{\sim} |\tilde{\omega}|^r \qquad : x = 0. \tag{5.27c}$$

For general $x \neq 0$, eq. (5.27b) has exactly the same form as the exact case given by eq. (4.31b), but with a specific second-order coefficient $a_a = \gamma^{-2}$. By contrast, at $x = 0$, eq. (5.27c) is consistent with eq. (4.37), with $a_s = \cos^2(\frac{\pi}{2}r) = [1+\beta^2(r)]^{-1}$.

Combining eqs. (5.26b) and (5.27c), we recover the generalized pinning condition in a LM phase, given *exactly* by eq. (4.38), but here satisfied at the level of self-

consistent second-order perturbation theory:

$$\pi[1+\beta^2(r)]\Sigma^{I(2)}(\omega)D^{(2)}(\omega) \overset{\tilde{\omega}\to 0}{\sim} 1. \tag{5.28}$$

5.3 Second-order numerical procedure

Having considered the low-ω asymptotics in both phases, we now look to implement a numerical algorithm which is capable of obtaining self-consistent solutions for the propagators, $G^{(2)}_{A\sigma}(\omega)$, converged for all ω.

5.3.1 Algorithm

We have performed the calculations on a logarithmic grid (that samples the states around the Fermi level most extensively) using approx 10,000 grid points spanning $\omega_{min} = 10^{-30}$ to $\omega_{max} = 10^{8}$. We make ω_{max} so large such that we consider the infinite band limit ($D = \omega_{max} \to \infty$) of the model. The steps in the numerical algorithm are as follows:

1. For a fixed band exponent, r, and a given U and x, calculate the first-order unrestricted Hartree-Fock (UHF) propagators, here we denote them as: $G^{(1)}_{A\sigma}(\omega) = [\omega^+ - \varepsilon^*_{A\sigma} - \Gamma(\omega)]^{-1}$, with $\varepsilon^*_{A\sigma} = x + \frac{U}{2}[(\bar{n}-1) - \sigma|\tilde{\mu}|]$. Convergence can be achieved very easily as the first-order approximation to the self-energy is purely static.

2. Calculate the transverse polarization bubble, $\mathrm{Im}^0\Pi^{\sigma-\sigma}_{AA}(\omega)$ from eq. (5.7) with the $\pi D^{(1)}_{A\sigma}(\omega) = -\,\mathrm{sgn}(\omega)\mathrm{Im}G^{(1)}_{A\sigma}(\omega)$ from step 1.

3. Determine the second-order contribution to the TSEs, $\Sigma^{I(2)}_{A\sigma}(\omega)$, from eq. (5.8) using the polarization bubble, $\mathrm{Im}^0\Pi^{\sigma-\sigma}_{AA}(\omega)$, and the UHF spectral functions, $D^{(1)}_{A\sigma}(\omega) = \frac{1}{\pi}\,\mathrm{sgn}(\omega)\mathrm{Im}G^{(1)}(\omega)$. $\Sigma^{R(2)}_{A\sigma}(\omega)$ is then calculated numerically from $\Sigma^{I(2)}_{A\sigma}(\omega)$ via Hilbert transformation, eq. (4.26).

4. Find the local moment, $|\tilde{\mu}|$, from eq. (5.3b), and the local charge, $\bar{n}$, from eq. (5.3a), then input these, plus the second-order approximation for $\Sigma^{(2)}_{A\sigma}(\omega)$ into eq. (5.11) for a new spectrum, $D^{(2)}_{A\sigma}(\omega)$.

5. Iterate steps (2)-(4), putting the new second-order approximation for the spectral functions, $D^{(2)}_{A\sigma}(\omega)$ back into calculate $\Sigma^{(2)}_{A\sigma}(\omega)$ each time. Do this until full self-consistency is reached, i.e. when the full ω dependence of the propagators has converged.

From the spectra, $D^{(2)}_{A\sigma}(\omega)$, the real part of the propagator, $G^{R(2)}_{A\sigma}(\omega)$, may be calculated via eq. (2.14). However, $G^{R(2)}_{A\sigma}(\omega)$ is not needed at any point of the self-consistent process. The spectra, $D^{(2)}(\omega)$, together with the SSEs, $\Sigma^{(2)}(\omega)$ may be

calculated from eqs. (3.13, 3.30) respectively from the fully converged $D^{(2)}_{A\sigma}(\omega)$ and $\Sigma^{(2)}_{A\sigma}(\omega)$ at the end of the procedure.

5.3.2 Technical details

In order to control the iteration procedure, at each iteration a linear combination of the spectral functions from the current and previous iteration is taken

$$D_{A\sigma}(\omega) = \lambda D^{current}_{A\sigma}(\omega) + (1-\lambda) D^{prev}_{A\sigma}(\omega) \tag{5.29}$$

The parameter λ can be varied throughout the iterative procedure in order to achieve convergence in a stable manner. The larger λ is, the faster convergence is achieved, such that if $\lambda = 1$, the spectral function is just the spectral function for the current iteration. Decreasing λ allows a more stable, if slower path to convergence.

5.4 Numerical results

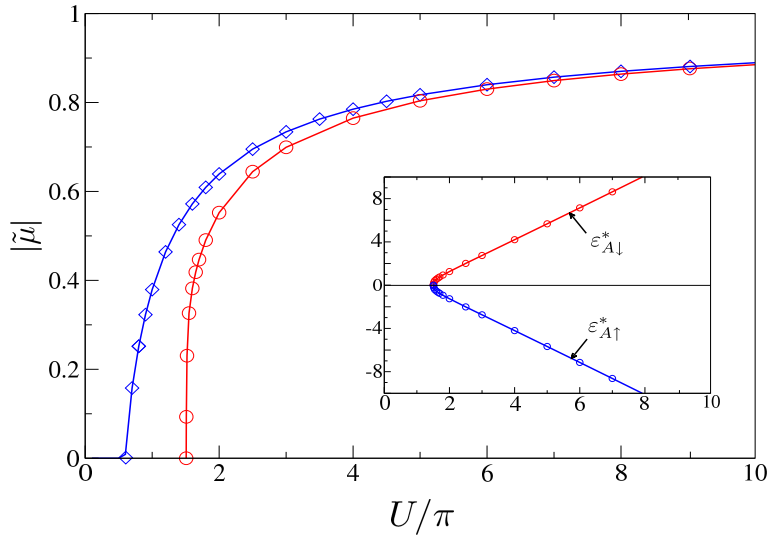


Figure 5.2: The local moment, $|\tilde{\mu}|$, versus U/π, for $r = 0.3$ and $x = 0$. Self-consistent second-order perturbation theory is shown in red (circles), first-order UHF is shown in blue (diamonds). $U_c/\pi \simeq 1.5$ (2nd-order); $U_c/\pi \simeq 0.8$ (UHF). The inset shows the 2nd-order renormalized levels, $\varepsilon^*_{A\sigma}$, versus U/π for the same parameters.

5.4.1 Particle-hole symmetry

Here we present the numerical results from the algorithm stated above, firstly for the case of ph symmetry where $x = \varepsilon + \frac{U}{2} = 0$, and the local charge, $\bar{n} = 1$. The idea is to start with a broken-symmetry (mean-field UHF) starting 'seed' solution, $D^{(1)}_{A\sigma}(\omega)$,

and iterate using the steps above to full self-consistency. Ultimately, the algorithm will either flow towards a solution with a converged *finite* local moment, $|\tilde{\mu}|$ (we denote a local moment phase solution), or alternatively to a solution with $|\tilde{\mu}| = 0$, (a SC (Fermi liquid) phase solution). The U at which converged LM solutions are no longer possible (and $|\tilde{\mu}|$ vanishes) we define as our critical, $U = U_c$, such that for $U < U_c$ *only* SC solutions exist.

Numerically we find that the converged self-consistent local moment, $|\tilde{\mu}|$, vanishes continuously to the critical $U = U_c(r)$ for all r in the range $0 < r < 1$. Fig. 5.2 shows the moment, $|\tilde{\mu}|$, for both first and second-order perturbation theory at $x = 0$ and a typical r in the range. The inset of Fig. 5.2 shows the second-order renormalized levels, $\varepsilon^*_{A\sigma}$, (equal and opposite for $x = 0$) for the same parameters, vanishing continuously at the same $U = U_c$ as $|\tilde{\mu}|$. As expected via the general arguments of Section 4.5, the local moment low-energy scale, $\omega_* = |\varepsilon^*_{A\sigma}|^{1/r}$, given via eq. (4.20), thus vanishes at $U = U_c(r)$. By contrast, for $U < U_c$, the local moment converges to $|\tilde{\mu}| = 0$, and thus only SC solutions exist, where specifically for $x = 0$ the spin independent level vanishes, $\varepsilon^*_{A\sigma} = \varepsilon^* = 0$.

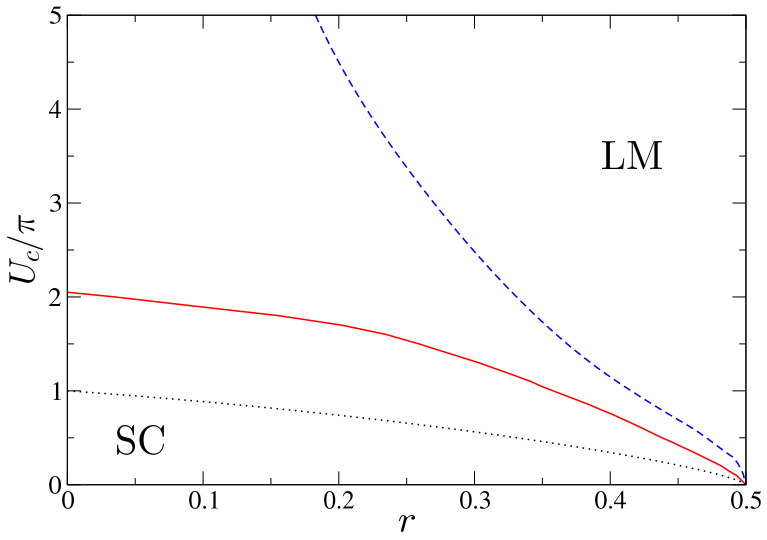


Figure 5.3: Phase diagram for $x = 0$. r is plotted versus U. First-order UHF is plotted in black. second-order self-consistent perturbation theory in red. Exact NRG data is plotted in blue.

Fig. 5.3 shows the phase boundary (where $U = U_c$) in the (r, U) plane. Second-order self-consistent perturbation theory is shown with a solid (red) line. First-order UHF is also shown with a dotted (black) line together with numerically exact NRG results (dashed blue line). In the limit that $r \to 0$, such that the model reduces to the standard AIM coupled to a metallic band, the NRG phase boundary diverges, $U_c(r) \propto \frac{1}{r}$ as is well known from previous studies [39,41,43] (this result is also found within the local moment approach [44]). Hence from exact calculations for $r = 0$

only the SC (non-magnetic) Fermi liquid phase persists, with Kondo quenching of the local moment for all U. By contrast, both first and second-order self-consistent theories predict a spurious phase transition at $r = 0$. UHF is well known [2, 7] to predict a phase transition at $U_c/\pi = 1$ for the metallic model. Second-order thus exhibits the same failing as UHF, albeit at a larger $U_c(r = 0)$. In contrast however, in the limit that $r \to \frac{1}{2}$, both first and second-order correctly predict that $U_c \to 0$, such that the symmetric SC phase cannot exist for $r > \frac{1}{2}$. Furthermore, as one might expect, for small U, the second-order boundary is closer to the exact phase boundary as $r \to \frac{1}{2}$ than mean-field level.

In the discussion thus far we have considered how the transition is reached coming from the $|\tilde{\mu}| \to 0^+$, $U \to U_c^+(r)$, LM side of the transition, where the scale ω_*, vanishes. By contrast, for SC solutions the renormalized level vanishes for the whole phase, and the propagators are independent of spin-σ. In order to capture the low-energy behaviour in the SSC phase, we define a low-energy (Kondo) scale, ω_K, by the width of the central resonance[5] in the modified spectral function, given by

$$F(\omega) = \pi|\omega|^r(1 + \beta^2(r))D(\omega), \tag{5.30}$$

which just as for the non-interacting limit is pinned to unity at the Fermi level in a SSC phase via eq. (4.5b).

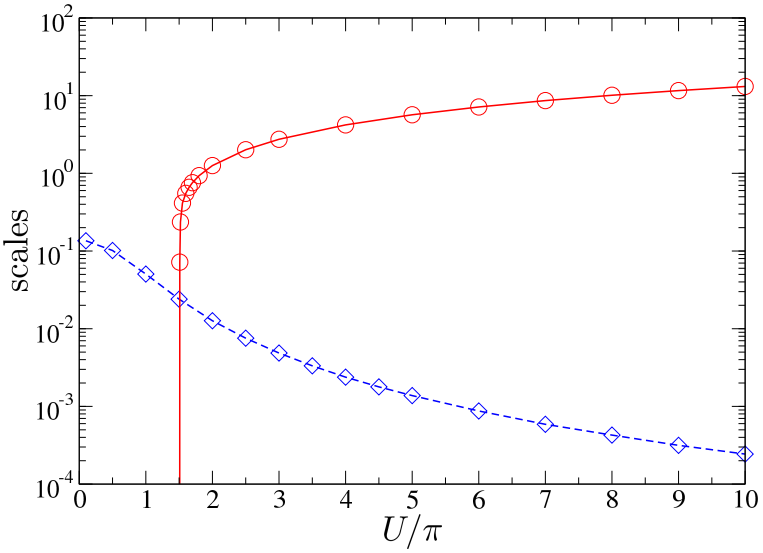


Figure 5.4: Second-order results for $x = 0$, $r = 0.3$. The LM phase scale, $\omega_*^r = |\varepsilon_{A\sigma}^*|$, shown in red, vanishes at U_c. LM states arise for $U > U_c$. The SC scale, defined as the width of the central resonance at 0.8 of its maximum, is shown in blue. At second order level, for $U > U_c$ it is possible to get SC solutions, when $|\tilde{\mu}| = 0$.

[5]Specifically we define the scale, ω_K as the width of the central resonance in $F(\omega)$ at 0.8 of its maximum.

If the quantum phase transition is to be coherently described coming from both phases at this level of approximation, the scale, ω_K, must vanish at the same $U = U_c$ as the LM scale, ω_*. We find from the numerical procedure that ω_K *does not vanish* as $U \to U_c^-(r)$. In fact it is possible to get SC solutions for $U > U_c$ if $|\tilde{\mu}|$ is set to zero in the calculation from the outset. Fig. 5.4 shows the low-energy scales versus U, coming from either phase for a fixed $r = 0.3$. The LM scale, $\omega_*^r = |\varepsilon_{A\sigma}^*|$ (in red-circles) vanishes as $U \to U_c^+(r)$. In contrast, the SC scale, ω_K, vanishes algebraically - $\omega_K \propto U^{-|s(r)|}$, where $s(r)$ is a number of $O(1)$ (for $r = 0.3$ $|s(r)| \simeq 2.5$) as $U/\pi \gg 1$, and therefore never vanishes for any finite U. This is the second-order analogue of a first-order restricted Hartree-Fock calculation [62], such that SC solutions persist for all U and the system effectively "has no knowledge" of the LM phase as $U_c(r)$ is crossed.

Before proceeding to discuss the second-order results for the spectral functions, we make a brief comment about the numerical procedure. With some particular parameters, convergence of the algorithm detailed above is achieved in as few as 5-10 iterations and with a $\lambda = 1$ in eq. (5.29). This facile convergence is generally achieved in either phase far from the 'transition' such that $|1 - U/U_c| \gg 1$. However, for some other combinations of parameters, particularly for small values of the LM scale, ω_*, as $U \to U_c^+(r)$, the procedure is numerically more delicate. In order to achieve convergence as $U_c(r)$ is approached from above, it is necessary to obtain convergence for a particular fixed U, and then use that solution as the 'seed' for the next calculation (for a slightly smaller U). In this way, together with lowering λ in eq. (5.29), it is feasible to progressively decrease U towards $U_c(r)$ maintaining stable convergence in as few iterations as possible.

Spectral functions

The LM phase modified spectrum, $F(\omega)$, given via eq. (5.30), is shown versus ω in Fig. 5.5, once again for $r = 0.3$. As U is progressively increased, the high energy (non-universal) Hubbard satellite peaks, roughly positioned at $\omega \approx \pm\frac{U}{2}$, split from a central resonance. As previously discussed, these high-energy spectral features occur at energies $\omega \approx \varepsilon$ and $\omega \approx \varepsilon + U$,[6] corresponding to the atomic limit single-particle processes (as detailed in Section 2.3), between the empty, singly and doubly occupied states of the impurity level. The atomic limit poles, given by eq. (2.45), are broadened by coupling to the conduction band and thus have width $O(\Gamma_0)$. The inset shows the LM spectra as $U \to U_c^+(r)$, with ω plotted on a log-scale. As discussed previously, and shown in Fig. 5.2, the LM phase renormalized levels $\varepsilon_{A\sigma}^*$, are always finite, and so the spectra always vanish via eq. (5.20). The LM phase modified spectra thus vanish via eq. (5.30) as $F(\omega) \propto |\omega|^{2r}$.

[6] For $x = \varepsilon + \frac{U}{2} = 0$, such that $\varepsilon = -\frac{U}{2}$, the Hubbard satellite peaks occur at $\omega \approx \pm\frac{U}{2}$ for $x = 0$.

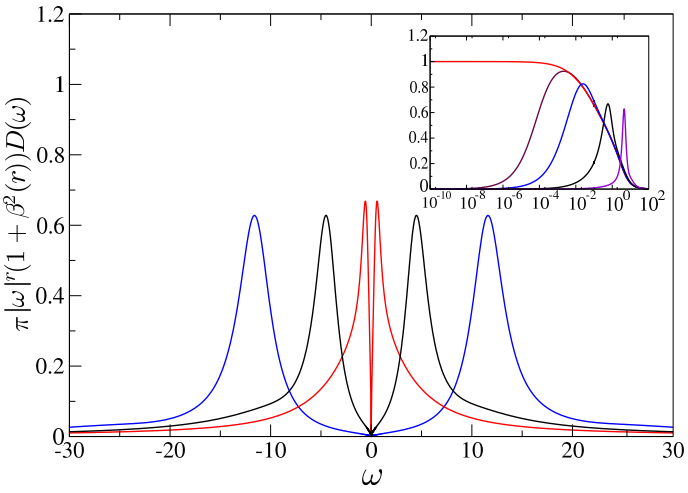


Figure 5.5: Second-order, $F(\omega)$ is plotted versus ω for U progressively getting closer to the transition for $r = 0.3$, $x = 0$. $U/\pi = 2$ red, =5 black, =10 blue. The inset shows $F(\omega)$ versus ω on a logarithmic scale for U progressively getting closer to U_c. $U/\pi = 1.5$ red, =1.51 violet, =1.52 blue, =2 black and =10 purple.

As can be seen from the inset of Fig. 5.5, as $U \to U_c^+(r)$, the LM spectra fold onto the equivalent SC spectra (where $\varepsilon^* = 0$), with $F(\omega = 0) = 1$. In consequence, the low-ω behaviour of $D^{(2)}(\omega)$ at $U = U_c(r)$ is given by eq. (4.5a), i.e. $D^{(2)}(\omega) \overset{\omega\to 0}{\sim} \cos^2(\frac{\pi}{2}r)|\omega|^{-r}$, and is thus the same as that of the non-interacting limit. By contrast in Section 4.9 we found that precisely at $U = U_c(r)$, the *exact* spectral function has the low-ω form, $D(\omega) \overset{\omega\to 0}{\sim} C(r)|\omega|^{-r}$, with $C(r) \neq \cos(\frac{\pi}{2}r)$ in general, taking a value which is renormalized by interactions (given by eq. (4.87)). Second-order self-consistent perturbation theory thus fails to capture the known interacting nature (as found from previous studies [34, 37, 46, 47]) of the QCP.

Fig. 5.6 shows the SSC phase modified spectra, $F(\omega)$, versus ω as U is steadily increased. On increasing U, the central resonance narrows in width, and hence the strong-coupling scale, ω_K, vanishes. On high-energy scales of $O(U)$, in contrast to the LM phase spectra, instead of having pronounced Hubbard satellites at $\omega \simeq \pm U/2$, shoulders of the central resonance emerge. This smearing out of the high-energy features in a SC phase is clearly an artifact of the self-consistent procedure. This effect has been observed before for other self-consistent calculations using non-broken-symmetry propagators [72, 105, 106]. The inset of Fig. 5.6, shows the SC phase modified spectra, $F(\omega)$, as a function of ω on a log-scale, where the Hubbard band shoulders are clearly pronounced for large U.

We conclude the discussion of second-order self-consistent perturbation theory at particle-hole symmetry with numerical confirmation of the low-ω forms of both the TSEs and SSEs (as discussed in Section 5.2). The self-energies are shown in Fig.5.7 on a log:log scale as a function of ω for $U/\pi = 5$, where $U > U_c(r)$ such

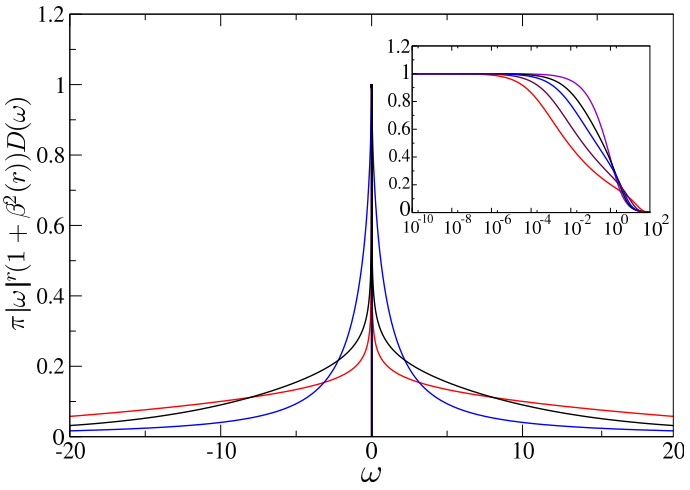


Figure 5.6: Second-order, $F(\omega)$ is plotted versus ω in the SC phase for $r = 0.3$, $x = 0$. $U/\pi = 0.5$ blue, =5 black and =10 red. The inset shows $F(\omega)$ versus ω (on a logscale). $U/\pi = 0.5$ violet, =1.5 black, =2.5 blue, =5 purple and =10 red.

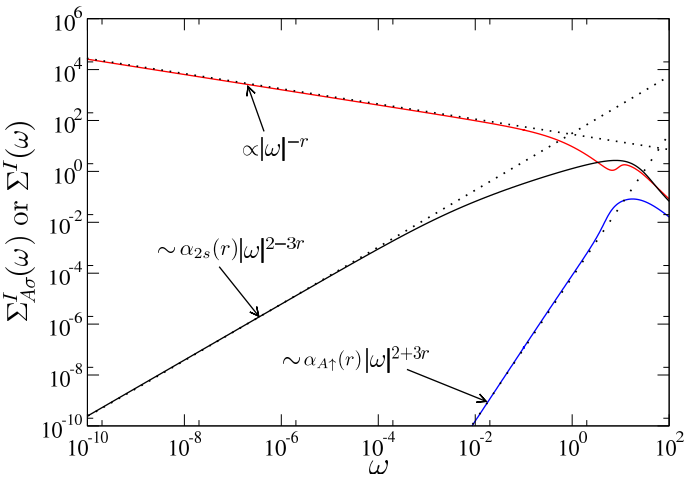


Figure 5.7: Self-energies, $\Sigma^{I(2)}_{A\sigma}(\omega)$ plotted versus ω on a log:log plot for $U/\pi = 5$, $r = 0.3$, $x = 0$. Black is the SSE, $\Sigma^{I(2)}(\omega)$ for a SC solution. Blue is the TSE, $\Sigma^{I(2)}_{A\uparrow}(\omega)$ for a LM solution. Red is the corresponding SSE, $\Sigma^{I(2)}(\omega)$, for the LM solution. The asymptotic forms of each function are shown with dotted lines.

that both SC and LM phase solutions coexist. In black the SC phase SSE is shown, $\Sigma^{I(2)}(\omega) \overset{\omega\to 0}{\sim} \alpha_{2s}(r)|\omega|^{2-3r}$ (given via eq. (5.18b)). The LM phase TSE, $\Sigma^{I(2)}_{A\uparrow}(\omega) \overset{\omega\to 0}{\sim} \alpha_{A\uparrow}(r)|\omega|^{2+3r}$ (given via eq. (5.19)) is shown in blue. The corresponding SSE in the LM phase, is shown diverging in r as $\omega \to 0$: $\Sigma^{I(2)}(\omega) \propto |\omega|^{-r}$, is shown in red, given via eq. (5.25b).

5.4.2 General particle-hole asymmetry: $x \neq 0$

We now discuss the second-order numerical results for the model away from ph symmetry ($x \neq 0$). We concentrate on the case for $x < 0$, however the propagators (and corresponding self-energies) for $x > 0$ can easily be obtained via a ph transformation ($x \to -x$) as detailed in Section 4.1.2 and Appendix B.

Static quantities

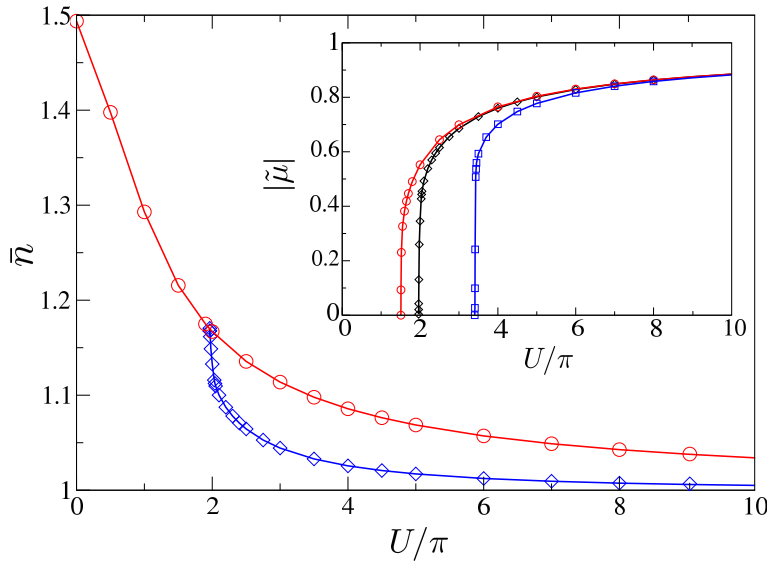


Figure 5.8: Second-order self-consistent perturbation theory for $r = 0.3$. Local charge, $\bar{n}$, shown versus U/π for $x = -1$. Red is the ASC phase, blue is the LM phase. Inset shows second-order SC perturbation theory for $r = 0.3$. The inset shows $|\tilde{\mu}|$ versus U/π for different x. Red is $x = 0$, black is $x = -1$, blue is $x = -3$.

As discussed in Section 3.1, generally in a LM phase regardless of asymmetry (embodied by x), the local moment, $|\tilde{\mu}|$ is finite and vanishes at the critical $U \to U_c^+(r, x)$. The inset of Fig. 5.8 shows the self-consistent values of $|\tilde{\mu}|$, determined here at second-order level, versus U for three different values of x. The figure shows that as $|x|$ increases, the value of $U_c(r, x)$, increases in magnitude. By contrast, for $U < U_c(r, x)$, in the asymmetric SC (ASC) phase, we find that the self-consistently determined value of $|\tilde{\mu}|$ vanishes. Fig. 5.9 shows the phase diagram in the (U, x) plane for $r = 0.2$, with $U_c(r, x)$ defined by where $|\tilde{\mu}|$ vanishes for each x. The figure shows that second-order perturbation theory is closer to the exact NRG phase boundary, than first-order UHF. The dotted line denotes the ph symmetric point where $x = 0$.

Once again, in analogy to the ph symmetric case discussed above, we find from numerical calculations that ASC solutions may be obtained for all U by requiring that $|\tilde{\mu}| = 0$ from the outset. In consequence for $U > U_c(r, x)$ within the numerical

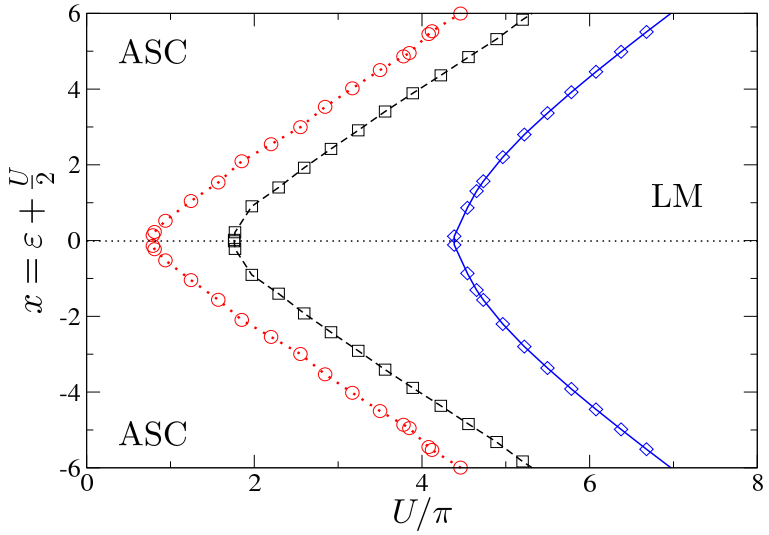


Figure 5.9: Phase diagram in the (U, x) plane for $r = 0.2$. The red-circles show first-order UHF, the black-squares show second-order, exact NRG data is shown with blue-diamonds.

algorithm it is possible to obtain both LM, where $|\tilde{\mu}|$ is allowed to be non-zero, and ASC type solutions, where $|\tilde{\mu}| = 0$ is required. Away from $x = 0$, the local charge, $\bar{n}$, given via eq. (5.3a), deviates away from unity (for $x < 0$, it lies in the range $1 \leq \bar{n} < 2$). The main panel of Fig. 5.8 shows $\bar{n}$, for $x = -1$ and $r = 0.3$. For the ASC phase, we find that $\bar{n}$ decreases smoothly towards unity as U increases. In contrast, $\bar{n}$ for the LM phase descends much more rapidly towards 1.

Scales and renormalized levels

In the ASC phase, we find from the numerics that the renormalized level, $\varepsilon^* = [x + \frac{U}{2}(\bar{n} - 1) + \Sigma^{(2)}(0)]$, does not vanish, for any finite U. At ph symmetry we defined a low-energy scale, ω_K, by the width of the central spectral maximum in $F(\omega)$, given by eq. (5.30). However, in the ASC phase, the spectrum vanishes for low-ω via eq. (5.24), and hence $F(\omega)$ also vanishes - $F(\omega) \propto |\omega|^{2r}$. In order to define a low-energy scale in the ASC phase, we write the spectrum via eq. (5.11), and neglect both the ω term and the low-ω form of the SSE to give

$$\pi D(\omega) \overset{\omega\to 0}{\sim} \frac{|\omega|^r}{[-\varepsilon^* + \mathrm{sgn}(\omega)\beta(r)|\omega|^r]^2 + [|\omega|^r]^2} \tag{5.31a}$$

$$\overset{\omega\to 0}{\sim} \frac{|\omega|^r}{[\varepsilon^*]^2 - 2\varepsilon^* \,\mathrm{sgn}(\omega)\beta(r)|\omega|^r + (1 + \beta^2(r))|\omega|^{2r}} \tag{5.31b}$$

$$\overset{\omega\to 0}{\sim} \frac{\cos^2(\frac{\pi}{2}r)|\omega|^r}{[\varepsilon^* \cos(\frac{\pi}{2}r)]^2 - 2\varepsilon^* \,\mathrm{sgn}(\omega)\cos(\frac{\pi}{2}r)\sin(\frac{\pi}{2}r)|\omega|^r + |\omega|^{2r}} \tag{5.31c}$$

$$\overset{\tilde{\omega}\to 0}{\sim} \frac{\cos(\frac{\pi}{2}r)}{\omega_*^r}\left[\frac{|\tilde{\omega}|^r}{1 - 2\,\mathrm{sgn}(\tilde{\omega})\sin(\frac{\pi}{2}r)|\tilde{\omega}|^r + |\tilde{\omega}|^{2r}}\right] \tag{5.31d}$$

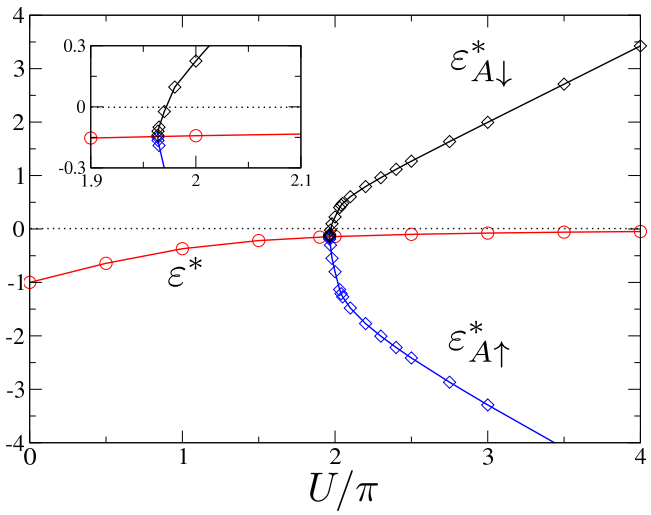


Figure 5.10: Renormalized levels, shown versus U/π for $x = -1$, $r = 0.3$. Red is ε^*(ASC), blue is $\varepsilon^*_{A\uparrow}$, black is $\varepsilon^*_{A\downarrow}$. Inset shows the levels vanishing on a magnified scale near the QCP. $U = U'$ is the point where $\varepsilon^*_{A\downarrow}$ crosses the Fermi level. Here, the specific values of $U_c/\pi \simeq 1.96$ and $U'/\pi \simeq 1.975$.

where the last equation has been rescaled in terms of a low-energy scale, $\omega_* \equiv \omega_K(x \neq 0)$ (with $\tilde{\omega} = \omega/\omega_*$ as usual) chosen to be

$$\omega_* = \omega_K(x \neq 0) = |\varepsilon^* \cos(\tfrac{\pi}{2} r)|^{\frac{1}{r}}, \tag{5.32}$$

such that the term in square brackets in eq. (5.31d) has a maximum at $\tilde{\omega} = \pm 1$. Hence, $\omega_*^r(1+\beta^2(r))\pi D(\omega)$ is a universal function of $\tilde{\omega}$ with a spectral maximum at $|\tilde{\omega}| = 1$. The corresponding modified spectral function, eq. (5.30), is then also given solely as a function of $\tilde{\omega}$. For $\tilde{\omega} \ll 1$ from eq. (5.31d) $F(\omega)$ becomes:

$$F(\omega) = [1+\beta^2(r)]|\omega|^r \pi D(\omega) \overset{\omega \to 0}{\sim} \frac{|\omega|^{2r}}{[\varepsilon^* \cos(\frac{\pi}{2} r)]^2} \overset{\tilde{\omega} \to 0}{\sim} |\tilde{\omega}|^{2r} \tag{5.33}$$

vanishing for the whole phase $\propto |\omega|^{2r}$ as stated above.

We find from the numerics that the scale, ω_K, decays algebraically in U for $U \gg 1$: $\omega_K(x) \sim U^{-|d(r)|}$, with $d(r)$ an exponent of $O(1)$. In Fig. 5.10, the ASC phase renormalized level, $\varepsilon^* = -|\omega_K^r / \cos(\frac{\pi}{2} r)|$, is shown in red versus U/π for $x = -1$ and $r = 0.3$. The scale never vanishes, such that the ASC phase persists for all U. In other words, just as for the $x = 0$ case examined above, the ASC phase is effectively 'blind' to local moment formation as $U \to U_c^-(r)$ leading to an unsatisfactory description of the phase transition.

In the LM phase, we find once again that the scale, $\omega_*^r = \frac{1}{2}|\varepsilon^*_{A\uparrow} - \varepsilon^*_{A\downarrow}|$, vanishes as $U \to U_c^+(r, x)$. However, the symmetry of eq. (5.13) does not generally hold for $x \neq 0$, i.e. the renormalized levels, $\varepsilon^*_{A\uparrow}$, $\varepsilon^*_{A\downarrow}$, are not sign definite, and therefore do

not independently vanish at $U_c(r,x)$. Instead, the levels lose their spin dependence at the transition, approaching the renormalized level of the ASC phase, i.e. $\varepsilon^*_{A\uparrow}$, $\varepsilon^*_{A\downarrow} \to \varepsilon^*$, as $U \to U_c^+(r,x)$. Fig. 5.10 shows the behaviour of all three distinct renormalized levels as a function of U - where the inset shows the dependence on a magnified scale in the vicinity of $U_c(r,x)$.

As a consequence of the fact that the levels are not sign-definite away from ph symmetry, one of the two LM phase levels, $\varepsilon^*_{A\uparrow}$ or $\varepsilon^*_{A\downarrow}$, must cross the Fermi level at a specific $U > U_c(r,x)$. We denote this value by U'. This behaviour is shown by the inset of Fig. 5.10, where specifically, it is $\varepsilon^*_{A\downarrow}$ that crosses the Fermi level. Moreover, at this unique point (where $\varepsilon^*_{A\downarrow}(U=U')=0$), the other level, $\varepsilon^*_{A\uparrow}(U=U')<0$ for all $x<0$. Thus, from the order by order Luttinger self-consistency arguments of Section 4.6, the low-ω form of the TSEs, are given by case (C) in Fig. 4.12, i.e.

$$\Sigma^{I(2)}_{A\uparrow}(\omega, U=U') \overset{\omega\to 0}{\sim} |\omega|^{2-r} \qquad : \varepsilon^*_{A\uparrow}(U=U')<0, \tag{5.34a}$$

$$\Sigma^{I(2)}_{A\downarrow}(\omega, U=U') \overset{\omega\to 0}{\sim} |\omega|^{2+r} \qquad : \varepsilon^*_{A\downarrow}(U=U')=0. \tag{5.34b}$$

This self-energy behaviour is analogous to what happens from exact calculations for a specific finite local field, $h = h'$ (see Section 4.10), where one of the field-dependent renormalized levels, $\varepsilon^*_\sigma(h=h')$, crosses the Fermi level, whilst the other remains finite. On inserting the forms of eqs. (5.34a-5.34b) into eq. (5.11), the low-ω form the spectral functions, $D_{A\sigma}(\omega)$, follow as

$$\pi D^{(2)}_{A\uparrow}(\omega, U=U') \overset{\omega\to 0}{\sim} \frac{|\omega|^r}{[\varepsilon^*_{A\uparrow}]^2}, \tag{5.35a}$$

$$\pi D^{(2)}_{A\downarrow}(\omega, U=U') \overset{\omega\to 0}{\sim} \cos^2(\tfrac{\pi}{2}r)|\omega|^{-r}, \tag{5.35b}$$

such that $D_{A\uparrow}(\omega, U=U')$ is simply given via eq. (5.20), whereas, $D_{A\downarrow}(\omega, U=U')$ effectively becomes ph symmetric on the lowest frequency scales, with the same form as eq. (4.75).

Friedel-sum rule

In Section 4.3.2, we argued that at zero-field, the renormalized levels $\varepsilon^*_{A\uparrow}$, $\varepsilon^*_{A\downarrow}$, should be sign definite and of opposite sign everywhere in the LM phase (and not just at $x=0$, where this condition is guaranteed by symmetry). This is a result of the form of the Friedel sum rule, eq. (4.8), provided the *local* magnetization, $m(h = 0^+) = m_A(0) = +|\tilde{\mu}|$ has the same sign as the *excess* magnetization, $m_{\rm imp}(h=0^+)$ (which we conjecture to hold for all x). This conjecture is backed up by the NRG calculations of Fig. 4.2, which shows that the LM phase ($U > U_c(r,x)$) renormalized levels are indeed sign definite for any x at zero-field.

Here, at the second-order level of approximation, as can be seen from Fig. 5.10,

for $U > U'$ the renormalized levels are of opposite sign and hence from eq. (4.8), the excess magnetization is given by $m_{\rm imp}(0^+) = n_{{\rm imp},A\uparrow}(0) - n_{{\rm imp},A\downarrow}(0) = 1$. For any $U > U_c(r,x)$, the converged local moment, $|\tilde{\mu}| > 0$, and thus the signs of $|\tilde{\mu}|$ and $m_{\rm imp}(0^+)$ are indeed the same. By contrast, in the regime $U_c < U < U'$, both levels lie below the Fermi level, and therefore from eq. (4.8), $n_{{\rm imp},A\uparrow}(0), n_{{\rm imp},A\downarrow}(0) = 1$. The excess magnetization then follows as $m_{\rm imp}(0^+) = n_{{\rm imp},A\uparrow}(0) - n_{{\rm imp},A\downarrow}(0) = 0$. In this range, the local moment, $|\tilde{\mu}|$, is still positive (as it is for any $U > U_c(r,x)$) and therefore ${\rm sgn}(m_{\rm imp}(0^+)) \neq {\rm sgn}(|\tilde{\mu}|)$. The regime, $U_c < U < U'$, is thus unphysical, spuriously arising as a consequence of the crude level of approximation employed here.

For all values of $U \lesseqgtr U'$ in the LM phase, both levels, $\varepsilon^*_{A\sigma} \neq 0$, and we find that the TSEs $\Sigma^{I(2)}_{A\sigma}(\omega) \propto |\omega|^{2+3r}$ in accordance with eq. (5.19). The corresponding LM phase SSE, is then given via eq. (5.25a), i.e. $\Sigma^{I(2)}(\omega) \propto |\omega|^r$. The low-$\omega$ dependencies of the LM self-energies are shown in Fig. 5.11 together with the ASC phase SSE, eq. (5.23), for $U/\pi = 5$ (for $U > U_c$ both ASC and LM solutions coexist).

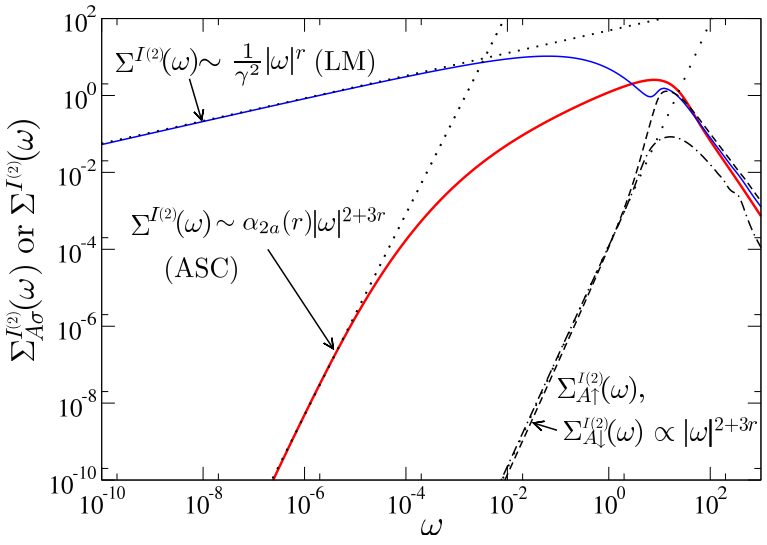


Figure 5.11: The self-energies, $\Sigma^{I(2)}_{A\sigma}(\omega)$ or $\Sigma^{I(2)}(\omega)$ plotted versus ω on a log-scale for $\omega > 0$, $U/\pi = 5$, $r = 0.3$. The solid red line shows the SSEs in the ASC phase, the solid blue line shows the SSE in the LM phase, the dot-dashed black line shows $\Sigma^{I(2)}_{A\uparrow}(\omega)$, and the dashed black line shows $\Sigma^{I(2)}_{A\downarrow}(\omega)$. The dotted lines show the low-ω asymptotic forms.

Spectral functions

As explained above, for $U = U_c(r,x)$, where $|\tilde{\mu}|$ vanishes (by definition), the converged solution has a renormalized level, $\varepsilon^* \equiv \varepsilon^*_{A\sigma}$, such that it is equivalent to a Fermi liquid ASC solution. In consequence, the low-ω behaviour of $D(\omega)$ precisely

at $U = U_c(r,x)$ is the same as eq. (5.24), i.e. $D(\omega) \propto |\omega|^r$. By contrast, from the general arguments of Section 4.8, we showed that for any-x, the QCP low-ω behaviour is given by eq. (4.87), i.e. $D(\omega) \overset{\omega\to 0}{\sim} C(r)|\omega|^{-r}$. Thus, this non-trivial QCP behaviour is simply not captured by second-order level of approximation considered here.

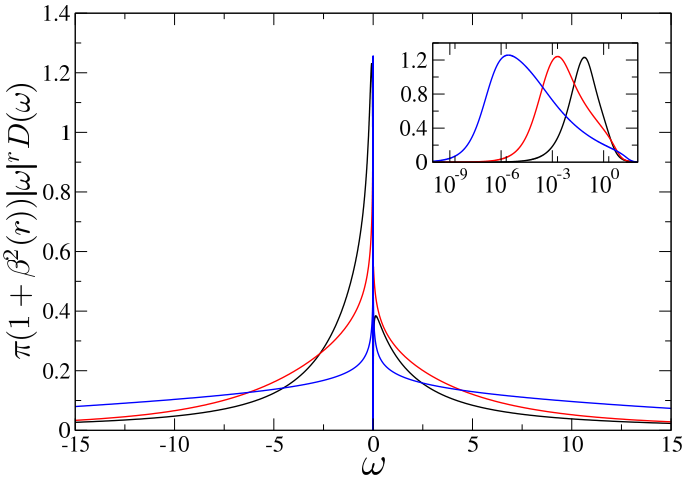


Figure 5.12: The modified spectral function, $F(\omega)$, in the ASC phase plotted versus ω for $r = 0.3$, $x = -1$. Blue shows $U/\pi = 6$, red is $U/\pi = 2.5$, black is $U/\pi = 1$. The inset shows the same data with ω on a log-scale for $\omega < 0$.

We can confirm numerically that the spectra in both phases for $x \neq 0$ obey the low-ω eqs. (5.20, 5.24). Fig. 5.12 shows ASC phase modified spectra, $F(\omega)$, for increasing U. Once again, in analogy with the ph symmetric case, the high-energy Hubbard satellite peaks, occuring at $\omega \simeq \varepsilon$, and $\omega \simeq \varepsilon + U$, are smeared out into shoulders by the self-consistency process[7]. The inset shows the modified spectra, $F(\omega)$ ultimately vanishing for low-ω - $F(\omega) \propto |\omega|^{2r}$, via eq. (5.30). The inset also shows the low-energy peak, occurring at $\omega \simeq \omega_K$, the maxima position never vanishes for any finite U.

By contrast Fig. 5.13 shows $F(\omega)$ versus ω in the LM phase. At high energies the Hubbard satellites are shown as distinct peaks, occuring at $\omega \simeq \varepsilon$, and $\omega \simeq \varepsilon + U$. As discussed above, as $U \to U_c^+(r,x)$, shown in black, $U_c \simeq 1.96$, the spectra become the same as the equivalent ASC spectra.

5.4.3 Excess charges and Luttinger integrals

Before proceeding, we make one final comment about the nature of the converged solutions obtained here. As a consequence of the fact that the approximation employed here is conserving - i.e. derived from a generating functional, Φ_{LW}, in both

[7] As is also obtained via a self-consistent study of the asymmetric metallic AIM within a parquet approach [107]

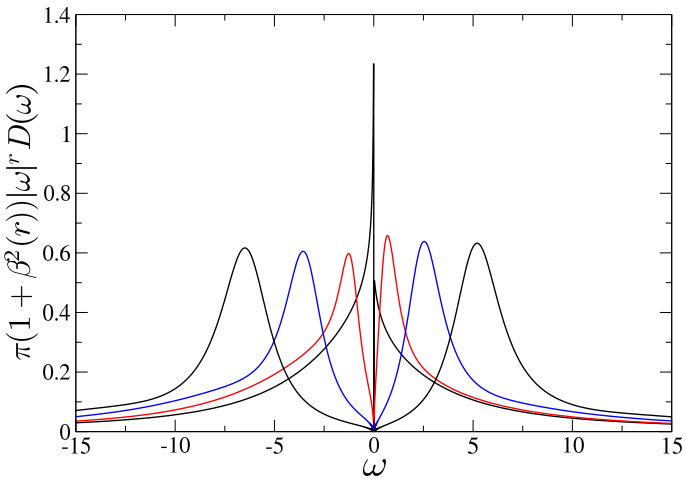


Figure 5.13: The modified spectral function, $F(\omega)$, in the LM phase plotted versus ω for $r = 0.3$, $x = -1$. Progressively from outside to in: Black shows $U/\pi = 6$, blue shows $U/\pi = 3$, red is $U/\pi = 2$, black is $U/\pi \simeq U_c/\pi = 1.96$

phases, the general arguments of Section 3.4 for the vanishing of the Luttinger integrals, I_{L_σ} for $U < U_c$ given by eq. (3.50), and $I_{L_{A\sigma}}$ for $U > U_c(r, x)$ given by eq. (3.55), holds. We have explicitly calculated both eq. (3.50) and eq. (3.55) in each phase[8] from the converged second-order propagators and self-energies. We find in both cases that the integrals vanish, consistent with the general arguments leading to eq. (3.72). Furthermore, we may also calculate the Luttinger integral of eq. (3.75) from both the (converged) SSE, $\Sigma(\omega)$, and the spin-independent full propagator, $G(\omega)$, for $U > U_c(r, x)$ in the LM phase. From the explicit numerical integration we find $I_L(x) = \mathrm{sgn}(x)\frac{\pi}{2}$, which is indeed consistent with the exact proof leading to eq. (4.17).

A further result of the approximation being conserving, is that the Friedel sum rules, eqs. (4.7-4.8) also hold, relating the excess charges $n_{\mathrm{imp};\sigma}(0)$ and $n_{\mathrm{imp};\mathrm{A}\sigma}(0)$ to the renormalized levels ε^* and $\varepsilon^*_{A\sigma}$ respectively. We have explicitly calculated each of the excess charges by integrating over the relevant excess density of states, $\Delta\rho_{\mathrm{imp};\sigma}(\omega)$, or $\Delta\rho_{\mathrm{imp};\sigma}(\omega)$, from eq. (3.38). We explicitly find that all results are entirely consistent with the Friedel sum rules of Section 4.3.

5.5 Concluding remarks

In this chapter we have presented the results of second-order *self-consistent* perturbation theory applied to the PAIM at zero-field. Although a naive approximation, an advantage of truncating the skeleton expansion at this simple level is that it

[8] We have actually only calculated $I_{L_{A\sigma}}$ in the LM phase for $U > U'$, and not in the unphysical regime $U_c < U < U'$ detailed above.

is the first order that builds in a non-trivial ω-dependent self-energy. The low-ω asymptotics of Section 5.2 backed up by the numerics of Section 5.4, show that at second-order level, the exponent of the self-energy in all of the phases discussed here are consistent with the order-by-order self-consistent Luttinger arguments of Section 4.6.5. By undertaking this perturbative procedure using broken-symmetry propagators, $G_{A\sigma}(\omega)$, we see that it is possible to obtain fully converged self-consistent local moment solutions above the trivial static first-order mean-field level.

We emphasize that self-consistent second-order perturbation theory does remarkably well for small values of the interaction strength U. For example, Fig. 5.3 shows the phase boundary for $x = 0$; as $r \to \frac{1}{2}$, the second-order phase boundary actually is not far off the numerically-exact NRG result. However, in the SC phases (SSC or ASC) of the model, second-order level suffers from the same deficiencies as a first-order treatment. The system in a SC phase is effectively 'blind' to local moment formation as U_c is approached, and SC solutions may be obtained for all U. In analogy with the *exact* deductions of Section 4.5, the method described here predicts a low-energy scale, ω_*, vanishing from the LM phase at a finite $U \to U_c^+(r, x)$ for all x. However, second-order level does not capture an equivalent (Kondo) scale, ω_K, vanishing at the same $U = U_c$ coming from the SC (ASC or SSC) phase. Moreover, since the two low-energy scales do not vanish at the same finite U, the method is incapable of capturing the *interacting* nature of the QCP, with a diverging low-ω spectral function for low-ω, $D(\omega) \propto C(r)|\omega|^{-r}$ (given by eq. (4.87)).

As explained in Section 4.11, another important point to make is that *any* order by order perturbative treatment, such as the method studied here, is incapable of capturing the underlying behaviour in the zero-field LM phase. As we have seen from direct NRG results (Fig. 4.26), the TSEs in a LM phase vanish with the same power as the hybridization function for low-ω, eq. (4.105) - $\Sigma_{A\sigma}(\omega) \propto |\omega|^r$. Thus, an inherently non-perturbative method is clearly needed in order to capture this non-trivial behaviour.

In conclusion, an approximation to the skeleton expansion for the self-energy is needed which is capable of capturing the underlying physics of both LM and SC phases and the non-trivial *interacting* nature of the QCP. Thus, in the next chapter we consider an approximation to the skeleton expansion that contains a resummation of Feynman diagrams to infinite-order in the interaction strength U.

CHAPTER 6

Fluctuation exchange approximation

6.1 Preliminaries

In this chapter we apply a more sophisticated 'conserving' approximation [66,67] to examine the PAIM at zero-field. The fluctuation exchange approximation (FLEX) [69–72], once again a Φ_{LW} derivable technique, involves the resummation of particular classes of Feynman diagrams (as discussed below) in the approximation to the self-energy. As for the second-order self-consistent approximation considered in the previous chapter, the self-energies in each phase — the SSE in the SC phase and the TSEs in the LM phase — are given by the functional derivatives of the Luttinger-Ward functional, i.e. $\Sigma_\sigma(\omega,0) = \delta\Phi_{LW}/\delta G_\sigma(\omega,0)$ for $U < U_c(r)$ and $\Sigma_{A\sigma}(\omega,0) = \delta\Phi_{LW}/\delta G_{A\sigma}(\omega,0)$ for $U > U_c(r)$. As a consequence, the general arguments of Section 3.4 leading to the vanishing of the relevant Luttinger integrals, $I_{L_\sigma}(0)$ for $U < U_c(r)$, eq. (3.50), and $I_{L_{A\sigma}}(0)$ for $U > U_c(r)$, eq. (3.55), once again hold in each distinct phase. Furthermore, the Friedel sum rules, given by eqs. (4.7-4.8), are also satisfied at the level of approximation as a consequence of the Luttinger integrals vanishing.

The motivation for considering FLEX for the pseudogap AIM is that since it is an infinite-order approximation, it may be capable of capturing the large U behaviour associated with both the *interacting* QCP, as well as the underlying behaviour in each of the SC and LM phases. In fact (as we explain below) we find that FLEX does indeed predict an SC $\leftrightarrow$ LM phase transition at a finite $U = U_c(r)$ with a scale, ω_*, that vanishes coming from *both phases* [108]. (This behaviour is unlike the second-order self-consistent perturbative treatment of the last chapter that only predicted a vanishing low-energy scale coming from the LM phase.)

Summary

We first lay out the key equations needed to implement the FLEX approximation for the PAIM, before proceeding to discuss a numerical algorithm capable of self-consistently capturing the behaviour in each phase. Focusing initially on the specific ph symmetric ($x = 0$) model, we examine the low-ω asymptotics coming from the SC (SSC) phase, and more specifically on the scaling of the propagators and self-energies as the QCP approached for $U \to U_c^-(r)$. This analysis allows us to gain an insight into the behaviour of the self-energy precisely at the QCP where $U = U_c(r)$ and the system is scale free. Moreover, as a consequence of the underlying self-consistency, we may determine the condition for which an analytic self-energy at the QCP is possible. Before proceeding to discuss the doubly degenerate LM phase, we examine the numerical results in the SSC phase and obtain scaling spectra as entire functions of $\tilde{\omega} = \omega/\omega_*$ (with $\omega_* = \omega_K$ the low-energy Kondo scale).

In the next part of the chapter, we analyse both the low-ω behaviour in the LM phase and consider a general Luttinger self-consistency [60] scheme, distinct from the order by order considerations of Section 4.6, in an attempt to explain the underlying behaviour of eq. (4.105) - found from the NRG calculations of Fig. 4.26. Subsequently, we move to consider how the numerical algorithm should be implemented specifically in the LM phase. We obtain converged self-consistent numerical results for the LM phase as $U \to U_c^+(r)$.

In the final part of the chapter we consider briefly the implementation of the FLEX algorithm for the general asymmetric model for $x = \varepsilon + \frac{U}{2} \neq 0$. Before concluding, we then analyse the behaviour of the symmetric model ($x = 0$) within FLEX at a finite a local-field, h.

6.2 Diagrams

6.2.1 Self-energies

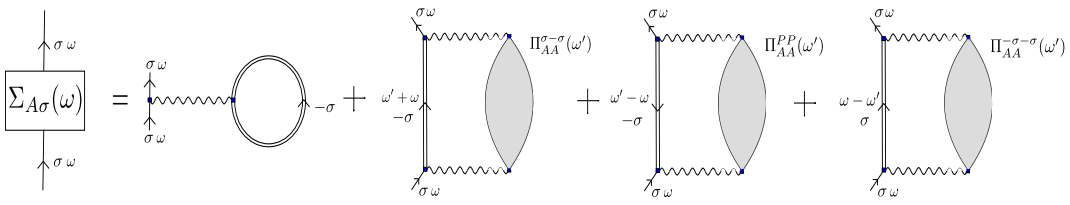


Figure 6.1: FLEX approximation to the skeleton expansion for the two-self-energy. The self-energy is made up of the static first-order Hartree-Fock contribution (the bubble diagram), plus 3 infinite sums in the transverse spin channel, the particle-particle channel and the longitudinal spin channel.

The full dynamical self-energy within the FLEX approximation [69–72] is shown

diagrammatically in Fig. 6.1. $\Sigma_{A\sigma}(\omega)$ is given by the first-order UHF static piece, $\Sigma^{(1)}_{A\sigma} = \frac{U}{2}[\bar{n} - \sigma|\tilde{\mu}|])$, with the local charge, $\bar{n}$, and local moment, $|\tilde{\mu}|$, given respectively by eq. (5.3a) and eq. (5.3b), plus the dynamical contributions from three infinite sums of polarization propagators. The two-self-energies are therefore written as

$$\Sigma_{A\sigma}(\omega) = \tfrac{U}{2}[\bar{n} - \sigma|\tilde{\mu}|] + \tilde{\Sigma}_{A\sigma}(\omega), \tag{6.1a}$$

$$\tilde{\Sigma}_{A\sigma}(\omega) = \Sigma^{PH}_{A\sigma}(\omega) + \Sigma^{PP}_{A\sigma}(\omega) + \Sigma^{bub}_{A\sigma}(\omega). \tag{6.1b}$$

$\tilde{\Sigma}_{A\sigma}(\omega)$ is a purely *dynamical* contribution to the self-energy given by the final three diagrams shown in Fig. 6.1. Each contribution may be expressed in terms of an integral over a propagator and a polarization part, given by

$$\Sigma^{PH}_{A\sigma}(\omega) = U^2 \int_{-\infty}^{\infty} \frac{\mathrm{d}\omega'}{2\pi i}\, \Pi^{\sigma-\sigma}_{AA}(\omega') G_{A-\sigma}(\omega+\omega'), \tag{6.2a}$$

$$\Sigma^{PP}_{A\sigma}(\omega) = -U^2 \int_{-\infty}^{\infty} \frac{\mathrm{d}\omega'}{2\pi i}\, \Pi^{PP}_{AA}(\omega') G_{A-\sigma}(\omega'-\omega), \tag{6.2b}$$

$$\Sigma^{bub}_{A\sigma}(\omega) = U^2 \int_{-\infty}^{\infty} \frac{\mathrm{d}\omega'}{2\pi i}\, \Pi^{-\sigma-\sigma}_{AA}(\omega') G_{A\sigma}(\omega-\omega'). \tag{6.2c}$$

$\Pi^{\sigma-\sigma}_{AA}(\omega)$ is the so-called transverse-spin (particle-hole) polarization propagator, which as shown in Fig. 6.2, involves skeleton diagrams exhibiting repeated interactions between a σ-spin electron and a $-\sigma$ hole in a ladder summation[1]. The second polarization part, $\Pi^{PP}_{AA}(\omega)$, the so-called particle-particle propagator also shown in Fig. 6.2, includes skeleton diagrams with repeated interactions between two electrons (particles) of opposite spin. The third contribution to the self-energy in eq. (6.2) involves the longitudinal-spin (bubble) polarization propagator, $\Pi^{\sigma\sigma}_{AA}(\omega)$, as shown at the bottom of Fig. 6.3. This polarization part includes the repeated interactions between 'bubbles' of opposite spin.

There is one main reason that we include the diagrams shown in Fig. 6.1 in the approximation for the self-energy. As shown in Fig. 6.3, the diagrams in each polarization propagator can be written as an infinite geometric series involving 'bare' polarization bubbles given by

[1]The diagrams that make up the transverse-spin polarization propagator are the principal set of diagrams included in the random phase approximation (RPA) [63] and also the local moment approach (LMA) [28]. However, we emphasize that in contrast to the RPA and the LMA, their use in this current context involves full-interacting propagators on all of the individual lines (as denoted with double lines).

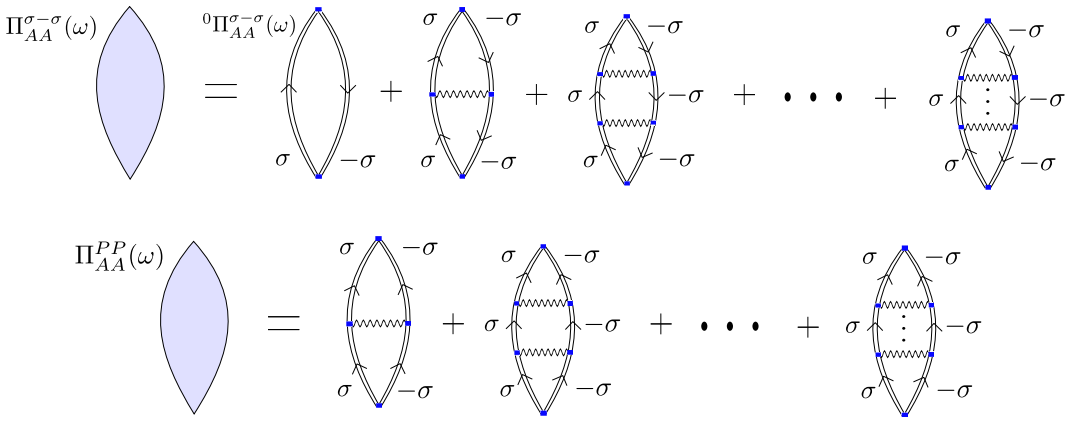


Figure 6.2: Ladder summations for repeated interactions in the transverse-spin channel to give $\Pi_{AA}^{\sigma-\sigma}(\omega)$ (top), and in the particle-particle (PP) channel to give $\Pi_{AA}^{PP}(\omega)$ (bottom).

$$\Pi_{AA}^{\sigma-\sigma}(\omega) = \frac{{}^0\Pi_{AA}^{\sigma-\sigma}(\omega)}{1 - U\,{}^0\Pi_{AA}^{\sigma-\sigma}(\omega)}, \tag{6.3a}$$

$$\Pi_{AA}^{PP}(\omega) = \frac{{}^0\Pi_{AA}^{PP}(\omega)}{1 + U\,{}^0\Pi_{AA}^{PP}(\omega)} - {}^0\Pi_{AA}^{PP}(\omega), \tag{6.3b}$$

$$\Pi_{AA}^{\sigma\sigma}(\omega) = \frac{{}^0\Pi_{AA}^{\sigma\sigma}(\omega)}{1 - U^2[{}^0\Pi_{AA}^{\sigma\sigma}(\omega)\,{}^0\Pi_{AA}^{-\sigma-\sigma}(\omega)]} - {}^0\Pi_{AA}^{\sigma\sigma}(\omega). \tag{6.3c}$$

We note that the ladder summations for $\Pi_{AA}^{\sigma-\sigma}(\omega)$ and $\Pi_{AA}^{PP}(\omega)$ shown in Fig. 6.2 can be simply reformulated as the diagrams shown in Fig. 6.3. The explicit minus signs that occur in the series for both $\Pi_{AA}^{\sigma-\sigma}(\omega)$ and $\Pi_{AA}^{\sigma\sigma}(\omega)$ are as a consequence of the presence of 'Fermi loops' in the diagrams [62, 63]. In the last chapter we defined the 'bare' transverse-spin polarization bubble via eq. (5.5), given by the convolution of two propagators as

$${}^0\Pi_{AA}^{\sigma-\sigma}(\omega) = i\int_{-\infty}^{\infty}\frac{\mathrm{d}\omega'}{2\pi}G_{A\sigma}(\omega'-\omega)G_{A-\sigma}(\omega'). \tag{6.4a}$$

Similarly, the 'bare' particle-particle polarization bubble and the 'bare' longitudinal-spin polarization bubble are given by

$${}^0\Pi_{AA}^{PP}(\omega) = -i\int_{-\infty}^{\infty}\frac{\mathrm{d}\omega'}{2\pi}G_{A\sigma}(\omega-\omega')G_{A-\sigma}(\omega'), \tag{6.4b}$$

$${}^0\Pi_{AA}^{\sigma\sigma}(\omega) = i\int_{-\infty}^{\infty}\frac{\mathrm{d}\omega'}{2\pi}G_{A\sigma}(\omega'+\omega)G_{A\sigma}(\omega'). \tag{6.4c}$$

From the general structure of the polarization diagrams the symmetries,

$${}^0\Pi_{AA}^{\sigma\sigma'}(\omega) = {}^0\Pi_{AA}^{\sigma'\sigma}(-\omega), \qquad \Pi_{AA}^{\sigma\sigma'}(\omega) = \Pi_{AA}^{\sigma'\sigma}(-\omega), \tag{6.5}$$

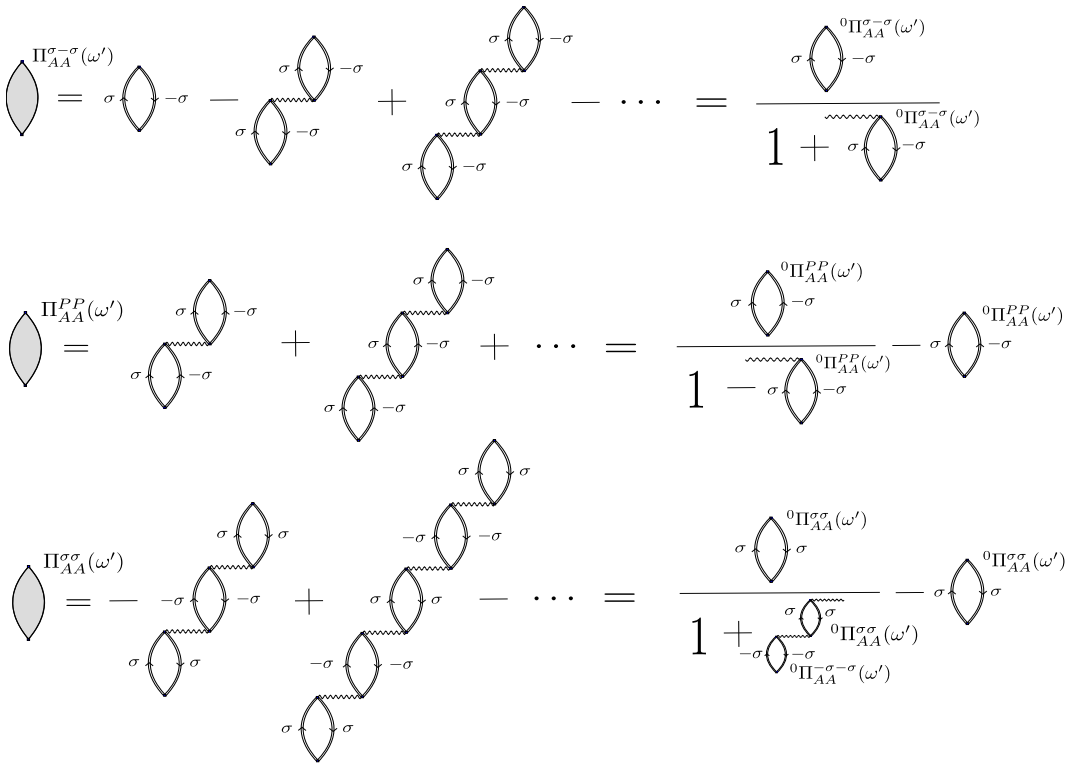


Figure 6.3: Infinite resummation of diagrams to form the three polarization propagators in the FLEX approximation to the self-energy. Top is an infinite sum in the transverse spin channel, middle is an infinite sum in the PP channel. Bottom is an infinite sum in the longitudinal spin (bubble) channel. Second-order contributions are subtracted in two of the three channels to avoid overcounting of diagrams.

hold regardless of phase or ph asymmetry, such that ${}^0\Pi^{\sigma\sigma}_{AA}(\omega)$ and $\Pi^{\sigma\sigma}_{AA}(\omega)$ are even functions of ω.

By summing up the repeated interactions as geometric series in each of the three channels, the self-energy can now be calculated to infinite-order, essential to any theory capable of capturing the large U strong-coupling limit. A second motivation for specifically including the transverse-spin diagrams of $\Pi^{\sigma-\sigma}_{AA}(\omega)$ in the approximation for the self-energy, is that they encompass the most important physical processes occurring on the impurity site. It is well known [2, 18] that the Kondo effect occurs as a consequence of 'spin-flip' processes occurring on the impurity level. It is these processes which are captured by the diagrams included in $\Pi^{\sigma-\sigma}_{AA}(\omega)$ as we now discuss.

The LHS of Fig. 6.4 shows a particular time-ordered contribution to $\Sigma^{PH}_{A\downarrow}(t)$ (just the Fourier transform of $\Sigma^{PH}_{A\downarrow}(\omega)$). Now, we explicitly consider the doubly degenerate LM phase. As discussed in Section 4.3.2, in an 'A' type state the overall excess magnetic moment in the system is $m_{\mathrm{imp}A}(0) = +1$, eq. (4.11), with the local moment $m_A(0) = |\tilde{\mu}|$. Now imagine we are deep in a LM phase such that

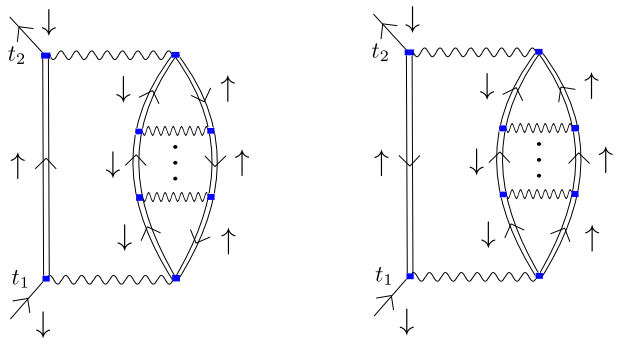


Figure 6.4: Time-ordered (Goldstone) contributions to $\Sigma^{PH}_{A\downarrow}(t)$ (left) and $\Sigma^{PP}_{A\downarrow}(t)$ (right). See text for discussion.

$U/U_c \gg 1$, and $|\tilde{\mu}| \to 1$ (in this limit the impurity level is essentially occupied with an $\uparrow$ electron). For a contribution to $\Sigma^{PH}_{A\downarrow}(\omega)$, as shown in Fig. 6.4,[2] envisage that at time t_1 a $\downarrow$ electron is added to the impurity level, such that at the same time an $\uparrow$ electron 'hops off' leaving a $\downarrow$-particle/$\uparrow$-hole left on the impurity level. The polarization propagator, $\Pi^{-+}_{AA}(\omega)$, then essentially describes the repeated interactions between the particle-hole pair as time progresses. At a later time, t_2, another spin-flip process occurs restoring the 'A'-type state of the system. The diagrams involved in $\Sigma^{PH}_{A\sigma}(\omega)$ thus describe the underlying processes that convert the A and B states, essential to the underlying physics of the model.

Whilst the processes contributing to $\Sigma^{PH}_{A\sigma}(\omega)$ involve spin-fluctuations on the impurity, the other diagrams, those in the pp and bubble channels contributing to $\Sigma^{PP}_{A\sigma}(\omega)$ and $\Sigma^{bub}_{A\sigma}(\omega)$ respectively, may be broadly thought of as involving charge fluctuations [71, 72]. The RHS of Fig. 6.4 shows a particular time-ordered contribution to $\Sigma^{PP}_{A\downarrow}(t)$ (once again, the Fourier transform of $\Sigma^{PP}_{A\downarrow}(\omega)$). This diagram involves repeated interactions between electrons where the impurity must be doubly occupied. Thus, these diagrams may be more important to the overall self-energy *away from ph symmetry* where the local charge, $\bar{n} \neq 1$.[3]

6.2.2 Propagators

The eqs. (6.1-6.4) completely define the FLEX approximation for the self-energy, $\Sigma_{A\sigma}(\omega)$, in terms of the full self-consistent propagators, $G_{A\sigma}(\omega)$, (shown by double lines in figures (6.1-6.3). The FLEX broken-symmetry propagators, $G_{A\sigma}(\omega)$, are given as usual via the Dyson equation, eq. (3.23), in terms of the self-energy, $\tilde{\Sigma}_{A\sigma}(\omega)$,

[2] The diagram can be thought of in the time-ordered Goldstone sense, which as discussed in Section 4.6.2, involves an explicit vertical time-axis.

[3] As stated in the previous chapter, the local charge $\bar{n}$ given by eq. (5.3a) is unity in both the SSC and LM phases at $x = 0$.

by

$$G_{A\sigma}(\omega) = [\omega^+ - \varepsilon^*_{A\sigma} - \Gamma(\omega) - [\tilde{\Sigma}_{A\sigma}(\omega) - \tilde{\Sigma}_{A\sigma}(0)]]^{-1}, \tag{6.6a}$$

$$\text{with} \quad D_{A\sigma}(\omega) = -\tfrac{1}{\pi}\,\mathrm{sgn}(\omega)\mathrm{Im}G_{A\sigma}(\omega) = \frac{\pi^{-1}[\Gamma^I(\omega) + \tilde{\Sigma}^I_{A\sigma}(\omega)]}{[\omega - \varepsilon^*_{A\sigma} - \Gamma^R(\omega) - [\tilde{\Sigma}^R_{A\sigma}(\omega) - \tilde{\Sigma}^R_{A\sigma}(0)]]^2 + [\Gamma^I(\omega) + \tilde{\Sigma}^I_{A\sigma}(\omega)]^2} \tag{6.6b}$$

with $\omega^+ = \omega + i\,\mathrm{sgn}(\omega)\eta$ such that we refer to the time-ordered propagator. The renormalized level is given by $\varepsilon^*_{A\sigma} = x + \frac{U}{2}[(\bar{n}-1) - \sigma|\tilde{\mu}|] + \tilde{\Sigma}^R_{A\sigma}(\omega = 0)$, encapsulating the entire static part of $\Sigma_{A\sigma}(\omega)$. By contrast, $[\tilde{\Sigma}_{A\sigma}(\omega) - \tilde{\Sigma}_{A\sigma}(0)] = \delta\Sigma_{A\sigma}(\omega)$ is purely a dynamical (ω-dependent) contribution to $\Sigma_{A\sigma}(\omega)$. The eqs. (6.1, 6.6) thus provide a self-consistency condition for the determination of the propagator and self-energy within the FLEX approximation.

6.3 Implementing the approximation

6.3.1 Polarization propagators

In this section we present the important equations for implementing the FLEX approximation numerically. In order to calculate the relevant self-energies and polarization propagators, which are all complex functions of ω, it is convenient to first calculate their imaginary parts. We may then make use of analyticity to obtain the corresponding real parts by Hilbert transform, eq. (4.26). In order to achieve this, the spectral representation of the broken symmetry propagator as eq. (2.8) is given by

$$G^{\pm}_{A\sigma}(\omega) = \int_{-\infty}^{\infty} \mathrm{d}\omega' \frac{D_{A\sigma}(\omega')\theta(\pm\omega')}{\omega - \omega' \pm i\eta} \tag{6.7}$$

where $G_{A\sigma}(\omega) = G^+_{A\sigma}(\omega) + G^-_{A\sigma}(\omega)$. By inserting this equation into eqs. (6.4a-6.4c), it is readily shown that the imaginary parts of the bare polarization propagators are given by

$$\frac{1}{\pi}\mathrm{Im}^0\Pi^{\sigma\sigma'}_{AA}(\omega) = \theta(\omega)\int_0^{|\omega|} \mathrm{d}\omega' D_{A\sigma}(\omega' - \omega)D_{A\sigma'}(\omega') + \theta(-\omega)\int_{-|\omega|}^{0} \mathrm{d}\omega' D_{A\sigma}(\omega' - \omega)D_{A\sigma'}(\omega'), \tag{6.8a}$$

$$\frac{1}{\pi}\mathrm{Im}^0\Pi^{PP}_{AA}(\omega) = \theta(\omega)\int_0^{|\omega|} \mathrm{d}\omega' D_{A\sigma}(\omega - \omega')D_{A-\sigma}(\omega') + \theta(-\omega)\int_{-|\omega|}^{0} \mathrm{d}\omega' D_{A\sigma}(\omega - \omega')D_{A-\sigma}(\omega'), \tag{6.8b}$$

with $\sigma' = \sigma$ for the longitudinal spin (bubble) channel and $\sigma' = -\sigma$ for the transverse spin (ph) channel. Since $D_{A\sigma}(\omega) \geq 0$, it is clear from eq. (6.8) that the imaginary parts of all bare polarization propagators also exhibit this property, i.e. $\mathrm{Im}^0\Pi^{\sigma\sigma'}_{AA}(\omega)$, $\mathrm{Im}^0\Pi^{PP}_{AA}(\omega) \geq 0$ for all ω. By analogy with eq. (2.13), the spectral representation of ${}^0\Pi^{\sigma\sigma'}_{AA}(\omega)$, may also be written as

$$ {}^0\Pi^{\sigma\sigma'}_{AA}(\omega) = \frac{1}{\pi}\int_{-\infty}^{\infty} \mathrm{d}\omega' \frac{\mathrm{Im}^0\Pi^{\sigma\sigma'}_{AA}(\omega')\,\mathrm{sgn}(\omega')}{\omega' - \omega - \mathrm{sgn}(\omega')i\eta}, \tag{6.9} $$

which allows the real part to be obtained via

$$ \mathrm{Re}^0\Pi^{\sigma\sigma'}_{AA}(\omega) = \frac{1}{\pi}\int_{-\infty}^{\infty} \mathrm{d}\omega' P\left(\frac{\mathrm{Im}^0\Pi^{\sigma\sigma'}_{AA}(\omega')\,\mathrm{sgn}(\omega')}{\omega' - \omega}\right), \tag{6.10} $$

where P denotes the principal value integral as usual. A similar relation also holds for the particle-particle polarization bubble, ${}^0\Pi^{PP}_{AA}(\omega)$, although we do not write it explicitly for reasons of space.

The real and imaginary parts of the 'full' polarization propagators, given by eqs. (6.3a-6.3c) may be calculated in term of the real and imaginary parts of the corresponding bare polarization propagators. From eq. (6.3a), the imaginary part of the transverse-spin polarization propagator is readily shown to be

$$ \mathrm{Im}\Pi^{\sigma-\sigma}_{AA}(\omega) = \frac{\mathrm{Im}^0\Pi^{\sigma-\sigma}_{AA}(\omega)}{[1 - U\mathrm{Re}^0\Pi^{\sigma-\sigma}_{AA}(\omega)]^2 + [U\mathrm{Im}^0\Pi^{\sigma-\sigma}_{AA}(\omega)]^2}, \tag{6.11} $$

where the imaginary parts of the other propagators, $\Pi^{\sigma\sigma}_{AA}(\omega)$ and $\Pi^{PP}_{AA}(\omega)$, may also be obtained in a similar way. The corresponding real part of $\Pi^{\sigma-\sigma}_{AA}(\omega)$ is calculated via a similar Hilbert transform relation to eq. (6.10), such that by inserting $\mathrm{Im}^0\Pi^{\sigma-\sigma}_{AA}(\omega) \geq 0$, eq. (6.11) shows that $\mathrm{Im}\Pi^{\sigma-\sigma}_{AA}(\omega) \geq 0$ for all ω.

By inserting eq. (6.9) for ${}^0\Pi^{\sigma-\sigma}_{AA}(\omega)$ into eq. (6.2a), and by writing $G_{A\sigma}(\omega) = G^+_{A\sigma}(\omega) + G^-_{A\sigma}(\omega)$, it may be shown by a simple contour integration that the self-energy in the transverse spin channel is expressed as

$$ \Sigma^{PH}_{A\sigma}(\omega) = \frac{U^2}{\pi}\int_{-\infty}^{\infty} \mathrm{d}\omega' \mathrm{Im}\Pi^{\sigma-\sigma}_{AA}(\omega')[\theta(\omega')G^-_{A-\sigma}(\omega'+\omega) + \theta(-\omega')G^+_{A-\sigma}(\omega'+\omega)]. $$

Hence, using the fact that $D_{A\sigma}(\omega) = \mp\frac{1}{\pi}\theta(\pm\omega)\mathrm{Im}G^{\pm}_{A\sigma}(\omega)$, which follows from eq. (6.7), it may be shown that

$$ \begin{aligned} \Sigma^{(PH)I}_{A\sigma}(\omega) = U^2\theta(-\omega)\int_0^{|\omega|} \mathrm{d}\omega' D_{A-\sigma}(\omega+\omega')\mathrm{Im}\Pi^{\sigma-\sigma}_{AA}(\omega') \\ + U^2\theta(\omega)\int_{-|\omega|}^{0} \mathrm{d}\omega' D_{A-\sigma}(\omega+\omega')\mathrm{Im}\Pi^{\sigma-\sigma}_{AA}(\omega'), \end{aligned} \tag{6.12a} $$

with $\Sigma^{PH}_{A\sigma}(\omega) = \Sigma^{PH(R)}_{A\sigma}(\omega) - i\,\mathrm{sgn}(\omega)\Sigma^{PH(I)}_{A\sigma}(\omega)$. Thus, with both $\mathrm{Im}\Pi^{\sigma-\sigma}_{AA}(\omega)$, $D_{A\sigma}(\omega) \geq 0$, it follows from eq. (6.12a) that $\Sigma^{I(PH)}_{A\sigma}(\omega) \geq 0$. From similar arguments it is readily shown that the self-energies in the other two channels are also expressed in terms of the spectral functions and the imaginary parts of the relevant polarization propagators, given by

$$\Sigma^{I(PP)}_{A\sigma}(\omega) = U^2\theta(-\omega)\int_{-|\omega|}^{0} \mathrm{d}\omega' D_{A-\sigma}(\omega'-\omega)\mathrm{Im}\Pi^{PP}_{AA}(\omega') + U^2\theta(\omega)\int_{0}^{|\omega|} \mathrm{d}\omega' D_{A-\sigma}(\omega'-\omega)\mathrm{Im}\Pi^{PP}_{AA}(\omega'), \tag{6.12b}$$

in the particle-particle channel, and

$$\Sigma^{I(bub)}_{A\sigma}(\omega) = U^2\theta(-\omega)\int_{-|\omega|}^{0} \mathrm{d}\omega' D_{A\sigma}(\omega-\omega')\mathrm{Im}\Pi^{-\sigma-\sigma}_{AA}(\omega') + U^2\theta(\omega)\int_{0}^{|\omega|} \mathrm{d}\omega' D_{A\sigma}(\omega-\omega')\mathrm{Im}\Pi^{-\sigma-\sigma}_{AA}(\omega'), \tag{6.12c}$$

in the bubble channel. The real part of any of the (time-ordered) self-energy functions may be obtained via the Hilbert transform relation (c.f. eq. (4.26))

$$F^R(\omega) = \frac{1}{\pi}\mathrm{P}\int_{-\infty}^{\infty} \mathrm{d}\omega'\, F^I(\omega')\left(\frac{1}{\omega-\omega'}\right) \tag{6.13}$$

with $F(\omega) = F^R(\omega) - i\,\mathrm{sgn}(\omega)F^I(\omega)$.

6.3.2 Stability criteria

We now have all of the relevant equations needed to implement the FLEX approximation within a numerical algorithm. However, before we proceed, we analyse the stability of the relevant polarization propagators in the complex plane, initially focusing on the transverse-spin propagator, $\Pi^{\sigma-\sigma}_{AA}(\omega)$.

In order for the approximation to be valid, all propagators and self-energies must remain analytic.[4] For the AIM coupled to a metallic conduction band, it is well known, [2, 109] that if (zero-field) non-interacting propagators are used as the basis Green functions, that the RPA $\Pi(\omega) \equiv \Pi^{\sigma-\sigma}_{AA}(\omega)$ is non-analytic in ω for $U/\pi > 1$. This 'breaking down' of perturbation-theory reflects the fact that the system is unstable to local moment formation.[5]

[4] As considered in Section 2.1, the time-ordered propagators must remain analytic in the UHP for $\omega > 0$ and the LHP for $\omega < 0$.

[5] The local moment approach (LMA) [28, 34, 51, 64, 65] gets around this issue by allowing the existence of broken symmetry, using unrestricted Hartree Fock mean-field propagators as the basis

The stability of $\Pi_{AA}^{\sigma-\sigma}(\omega)$ can in fact be deduced simply from its zero-frequency value. If $\Pi_{AA}^{\sigma-\sigma}(\omega)$ is analytic in ω, then its real part must be obtainable via Hilbert transform from its imaginary part. On replacing ${}^0\Pi_{AA}^{\sigma-\sigma}(\omega)$ with $\Pi_{AA}^{\sigma-\sigma}(\omega)$ in eq. (6.10), the zero-frequency value of the real part is given by

$$\mathrm{Re}\Pi_{AA}^{\sigma-\sigma}(\omega=0)=\frac{1}{\pi}\int_{-\infty}^{\infty}\mathrm{d}\omega'\mathrm{P}\left(\frac{\mathrm{Im}\Pi_{AA}^{\sigma-\sigma}(\omega')}{|\omega'|}\right)\geq 0. \tag{6.14}$$

Thus, by virtue of the fact that $\mathrm{Im}\Pi_{AA}^{\sigma-\sigma}(\omega)\geq 0$ for all ω, the real part must also exhibit the property $\mathrm{Re}\Pi_{AA}^{\sigma-\sigma}(\omega=0)\geq 0$. $\mathrm{Re}\Pi_{AA}^{\sigma-\sigma}(\omega=0)$ may also be given via eq. (6.3a) in terms of the real and imaginary parts of ${}^0\Pi_{AA}^{\sigma-\sigma}(\omega=0)$

$$\mathrm{Re}\Pi_{AA}^{\sigma-\sigma}(\omega=0)=\frac{\mathrm{Re}{}^0\Pi_{AA}^{\sigma-\sigma}(\omega=0)}{1-U\mathrm{Re}{}^0\Pi_{AA}^{\sigma-\sigma}(\omega=0)}. \tag{6.15}$$

From eq. (6.10), it may also be shown that $\mathrm{Re}{}^0\Pi_{AA}^{\sigma-\sigma}(\omega=0)\geq 0$. By comparing eqs. (6.14-6.15), the fact that the denominator of eq. (6.15) must be positive means that we obtain the stability condition

$$0<U\mathrm{Re}{}^0\Pi_{AA}^{\sigma-\sigma}(\omega=0)\leq 1. \tag{6.16a}$$

In the other two polarization channels, similar analysis leads to

$$0\leq U\mathrm{Re}{}^0\Pi_{AA}^{PP}(\omega=0), \tag{6.16b}$$

$$0<U\mathrm{Re}{}^0\Pi_{AA}^{\sigma\sigma}(\omega=0)\leq 1. \tag{6.16c}$$

These stability conditions must be satisfied within the FLEX algorithm; special care must be taken to make sure that the analyticity of the propagators is not violated at any point of the self-consistency process.

6.3.3 General algorithm

Here we outline the general FLEX algorithm within a TSE description for general $x=\varepsilon+\frac{U}{2}$ at zero-field. Once again, as for self-consistent second-order treatment of the previous chapter, we define all functions of ω on a logarithmic grid, such that frequencies around the Fermi level are well sampled. We implement the numerical procedure as follows

1. For a fixed $x=\varepsilon+\frac{U}{2}$, an initial U, and a fixed band exponent, r, calculate an initial UHF propagator, $G_{A\sigma}^{(1)}(\omega)=[\omega^+-\varepsilon_{A\sigma}^*-\Gamma(\omega)]^{-1}$ with $\varepsilon_{A\sigma}^*=x+\frac{U}{2}[(\bar{n}-1)-\sigma|\tilde{\mu}|]$. Use eqs. (5.3a-5.3b) to calculate $\bar{n}$ and $|\tilde{\mu}|$ respectively at this

functions.

simple static level of approximation to $\Sigma_{A\sigma}(\omega)$. Calculate the corresponding UHF spectral function, $D^{(1)}_{A\sigma}(\omega) = -\frac{1}{\pi}\,\mathrm{sgn}(\omega)\mathrm{Im}G^{(1)}_{A\sigma}(\omega)$.

2. Using eqs. (6.8a-6.8b), calculate the imaginary parts of the 'bare' polarization propagators, $\mathrm{Im}^0\Pi^{+-}_{AA}(\omega)$, $\mathrm{Im}^0\Pi^{PP}_{AA}(\omega)$, $\mathrm{Im}^0\Pi^{--}_{AA}(\omega)$, $\mathrm{Im}^0\Pi^{++}_{AA}(\omega)$ using the UHF spectral functions from step (1).

3. Calculate the corresponding real parts, $\mathrm{Re}^0\Pi^{+-}_{AA}(\omega)$, $\mathrm{Re}^0\Pi^{PP}_{AA}(\omega)$, $\mathrm{Re}^0\Pi^{++}_{AA}(\omega)$, $\mathrm{Re}^0\Pi^{--}_{AA}(\omega)$ via Hilbert transform, eq. (6.10).

4. Using eqs. (6.3a-6.3c), calculate the imaginary parts of the full polarization propagators, $\mathrm{Im}\Pi^{+-}_{AA}(\omega)$, $\mathrm{Im}\Pi^{PP}_{AA}(\omega)$, $\mathrm{Im}\Pi^{--}_{AA}(\omega)$, $\mathrm{Im}\Pi^{++}_{AA}(\omega)$.

5. Calculate the dynamical contribution to the TSEs, $\tilde{\Sigma}^{I}_{A\sigma}(\omega)$, via eqs. (6.12a-6.12c), from the $D_{A\sigma}(\omega)$ in step (1) and the full polarization propagators from step (4).

6. Use eq. (6.13) to calculate the static contribution, $\tilde{\Sigma}^{R}_{A\sigma}(\omega)$.

7. Determine new spectral functions, $D_{A\sigma}(\omega)$, via eq. (6.6b), using the real and imaginary parts of the TSEs from steps (5-6), and renormalized levels $\varepsilon^{*}_{A\sigma} = x + \frac{U}{2}[(\bar{n}-1) - \sigma|\tilde{\mu}|] + \tilde{\Sigma}^{R}_{A\sigma}(0)$.

8. Using eqs. (5.3a, 5.3b), calculate new $\bar{n}$ and $|\tilde{\mu}|$ from the $D_{A\sigma}(\omega)$ in step (7).

9. Repeat steps (2)-(8), using the $D_{A\sigma}(\omega)$ calculated in step (6) as the new input in step (2), until all functions of ω converge. Output the converged $D_{A\sigma}(\omega)$ and $\Sigma_{A\sigma}(\omega)$.

10. For a converged $|\tilde{\mu}| > 0$, the SSE, $\Sigma(\omega)$, in the LM phase, can be calculated via eq. (3.30). The spin independent spectral function is calculated via $D(\omega) = \frac{1}{2}[D_{A\uparrow}(\omega) + D_{A\downarrow}(\omega)]$.

Once again, as for the second-order approximation of the last chapter, at no point in this algorithm is it necessary to calculate, $G^{R}_{A\sigma}(\omega)$; only the $D_{A\sigma}(\omega)$ are needed to calculate the polarization propagators and the TSEs at each of the steps. This makes the process numerically easier to implement as the spectral functions all have positive definite weight, $D_{A\sigma}(\omega) \geq 0$ for all ω. However, the converged $G^{R}_{A\sigma}(\omega)$ can easily be obtained via eq. (2.14) at the end of the calculation. Moreover, since $\tilde{\Sigma}^{I}_{A\sigma}(\omega)$ can be calculated solely via the imaginary parts of the polarization propagators and the spectral functions, it is not necessary to calculate $\mathrm{Re}\Pi^{\sigma-\sigma}_{AA}(\omega)$, $\mathrm{Re}\Pi^{PP}_{AA}(\omega)$, $\mathrm{Re}\Pi^{\sigma-\sigma}_{AA}(\omega)$ at any point of the numerical process.

6.4 Phase diagram at ph symmetry

We first use the numerical algorithm discussed above to find the $U_c(r)$ as a function of r at ph symmetry (where $x = \varepsilon + \frac{U}{2} = 0$). As we detail below, for a fixed r it is possible to find the U at which it is no longer possible to obtain SC solutions (and the low-energy (Kondo) scale, ω_*, vanishes).[6] From the LM phase it is also possible to deduce the same phase boundary, but with a small modification to the algorithm above, which we detail in Section 6.8.4. (We also note here that for reasons of brevity we set the unit of energy, $\Gamma_0^{1/(1-r)} \equiv 1$ in the rest of this chapter.)[7]

From the numerics we find that for r below a certain value, we denote $r_c(\approx 0.271)$, the algorithm always converges to a SC phase solution for any U. By contrast for $r \geq r_c$, we find that SC solutions only exist below a certain $U = U_c(r)$. Whereas, for $U > U_c(r)$, only LM phase solutions exist. The essential behaviour is shown in Fig. 6.5, which exhibits the phase diagram in the (r, U) plane. Phase boundary curves are shown for FLEX, together with NRG, first and second-order self-consistent perturbation theories.

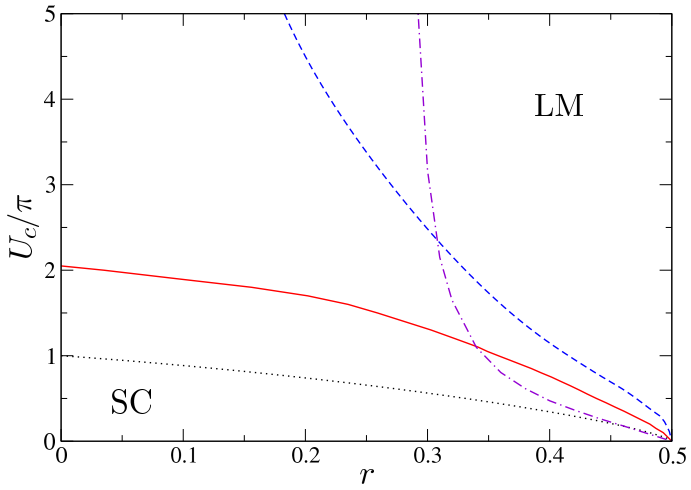


Figure 6.5: Phase diagram for $x = 0$, $U_c(r)/\pi$ plotted versus r. FLEX (violet-dot-dash), NRG (blue-dashed), self-consistent second-order (red-solid), UHF (black-dotted).

From the FLEX algorithm, we find that as $r \to r_c^+$, the critical U diverges via

$$U_c(r) \overset{r \to r_c^+}{\sim} \frac{\mathcal{B}}{r - r_c}, \tag{6.17}$$

[6] The important point to note here is that by using the general numerical algorithm detailed in Section 6.3.3, we may determine the FLEX phase boundary. The precise definition of the SC (Kondo) scale, ω_*, is unimportant at this point.

[7] The hybridization function then becomes: $\Gamma^I(\omega) = \Gamma_0|\omega|^r = \Gamma_0^{1/(1-r)}|\omega/\Gamma_0^{1/(1-r)}|^r \equiv |\omega|^r$. When plotting numerical results all quantities are rescaled in terms of $\Gamma_0^{1/(1-r)}$, e.g. $\omega = \omega/\Gamma_0^{1/(1-r)}$, $U = U/\Gamma_0^{1/(1-r)}$, $\varepsilon = \varepsilon/\Gamma_0^{1/(1-r)}$ are dimensionless.

where $\mathcal{B}$ is a coefficient of $O(1)$ (we find numerically that $\mathcal{B} \approx \frac{1}{4}$). For all four techniques, $U_c(r) \to 0$ as $r \to \frac{1}{2}$, indicating that the symmetric SC phase cannot exist for $r > \frac{1}{2}$. By contrast, in the limit $r \to 0$, whereas first and second-order theories predict a spurious unphysical phase transition, both FLEX and NRG predict that the SSC phase persists for all U. Furthermore, whilst the numerically exact NRG curve diverges as $1/r$, the FLEX curve diverges via eq. (6.17) as $r \to r_c^+$. In other words, FLEX gets this diverging behaviour correct, but just for the wrong value of r, i.e. as $r \to r_c$, rather than $r \to 0$.

6.5 Analytic results in the symmetric strong coupling phase

In the previous section we applied the general FLEX numerical algorithm to obtain the phase diagram depicted in Fig. 6.5. However, before we consider the implementation of the algorithm described above in more detail, in this section we specifically examine the forms of the propagators (and self-energies) in the ph symmetric SC (SSC) phase from an analytic viewpoint.

6.5.1 Symmetries of the propagators

As explained in Section 3.1, in any SC phase at zero-field, all propagators are naturally independent of spin-σ, and the SSE and TSE descriptions coincide. As a consequence we may drop both the A and σ subscripts from the propagators, i.e. $G_{A\sigma}(\omega) = G_{A-\sigma}(\omega) = G(\omega)$. Furthermore, in the SSC phase from eq. (5.14), both the propagator, $G(\omega)$, and the self-energy, $\Sigma(\omega)$, are odd functions of ω and the renormalized level, ε^* vanishes.

Since the propagators exhibit the symmetries of eq. (5.14), the 'bare' polarization propagators, given by eqs. (6.4a-6.4c) can all be shown to be equivalent, i.e

$$ {}^0\Pi^{+-}(\omega) = {}^0\Pi^{-+}(\omega) = {}^0\Pi^{++}(\omega) = {}^0\Pi^{--}(\omega) = {}^0\Pi^{PP}(\omega) \equiv {}^0\Pi(\omega). \tag{6.18} $$

In addition, from eq. (6.5), ${}^0\Pi(\omega)$ is an even function of ω. Using these symmetries, the full polarization propagators, given by eqs. (6.3a-6.3c) simply reduce to

$$ \Pi^{\sigma-\sigma}_{AA}(\omega) = \Pi^{PH}(\omega) = \frac{{}^0\Pi(\omega)}{1 - U\,{}^0\Pi(\omega)}, \tag{6.19a} $$

$$ \Pi^{PP}_{AA}(\omega) = \Pi^{PP}(\omega) = \frac{{}^0\Pi(\omega)}{1 + U\,{}^0\Pi(\omega)} - {}^0\Pi(\omega), \tag{6.19b} $$

$$ \Pi^{\sigma\sigma}_{AA}(\omega) = \Pi^{bub}(\omega) = \tfrac{1}{2}[\Pi^{PH}(\omega) + \Pi^{PP}(\omega)] - \tfrac{1}{2}{}^0\Pi(\omega), \tag{6.19c} $$

with $\Pi^{PH}(\omega)$, $\Pi^{PP}(\omega)$, $\Pi^{bub}(\omega)$ also even functions of ω. As a consequence, the polarization propagator in the bubble (longitudinal-spin) channel can be written

solely in terms of the propagators in the other two channels. Thus, by inserting the forms of eq. (6.19) into eq. (6.2), the contributions to the dynamical self-energy in each channel may be written as

$$\Sigma^{PH}(\omega) = U^2 \int_{-\infty}^{\infty} \frac{\mathrm{d}\omega'}{2\pi i}\, \Pi^{PH}(\omega') G(\omega+\omega'), \tag{6.20a}$$

$$\Sigma^{PP}(\omega) = U^2 \int_{-\infty}^{\infty} \frac{\mathrm{d}\omega'}{2\pi i}\, \Pi^{PP}(\omega') G(\omega+\omega'), \tag{6.20b}$$

$$\Sigma^{bub}(\omega) = U^2 \int_{-\infty}^{\infty} \frac{\mathrm{d}\omega'}{2\pi i}\, \Pi^{bub}(\omega') G(\omega+\omega'). \tag{6.20c}$$

where to obtain these forms we have used the fact that *all* polarization propagators are even functions of ω, and $G(\omega) = -G(-\omega)$. The total dynamic self-energy, given by the sum of the self-energies from the three channels, eq. (6.1b), can then be written as

$$\tilde{\Sigma}(\omega) = U^2 \int_{-\infty}^{\infty} \frac{\mathrm{d}\omega'}{2\pi i}\, [\Pi^{PH}(\omega') + \Pi^{PP}(\omega') + \Pi^{bub}(\omega')] G(\omega+\omega'), \tag{6.21a}$$

$$= U^2 \int_{-\infty}^{\infty} \frac{\mathrm{d}\omega'}{2\pi i}\, [\Pi'(\omega') + \Pi''(\omega')] G(\omega+\omega'), \tag{6.21b}$$

where it is convenient to define two new effective polarization channels using eq. (6.19c), with polarization propagators given by

$$\Pi'(\omega) = \tfrac{3}{2}\Pi^{PH}(\omega), \tag{6.22a}$$

$$\Pi''(\omega) = \tfrac{3}{2}\Pi^{PP}(\omega) - \tfrac{1}{2}{}^{0}\Pi(\omega). \tag{6.22b}$$

The corresponding self-energies are given by

$$\Sigma'(\omega) = U^2 \int_{-\infty}^{\infty} \frac{\mathrm{d}\omega'}{2\pi i}\, \Pi'(\omega') G(\omega+\omega'), \tag{6.23a}$$

$$\Sigma''(\omega) = U^2 \int_{-\infty}^{\infty} \frac{\mathrm{d}\omega'}{2\pi i}\, \Pi''(\omega') G(\omega+\omega'). \tag{6.23b}$$

The full dynamical self-energy, $\tilde{\Sigma}(\omega)$, then follows as

$$\tilde{\Sigma}(\omega) = \Sigma'(\omega) + \Sigma''(\omega), \tag{6.23c}$$

$$\text{with} \quad \Sigma'(\omega) = \tfrac{3}{2}\Sigma^{PH}(\omega), \qquad \Sigma''(\omega) = \Sigma^{PP}(\omega) + \tfrac{1}{2}\Sigma^{bub}(\omega) - \tfrac{1}{2}\Sigma^{PH}(\omega). \tag{6.23d}$$

As we shall see, the reason that we define the self-energies in this way is that $\Sigma'(\omega)$ becomes important to the underlying physics of the model as $U_c(r)$ is approached from below. By contrast, $\Sigma''(\omega)$ proves to be inconsequential to the critical behaviour. $\Sigma'^{I}(\omega)$ and $\Sigma''^{I}(\omega)$ can be obtained via eq. (6.12a), with $\mathrm{Im}\Pi_{AA}^{\sigma-\sigma}(\omega)$

replaced with $\mathrm{Im}\Pi'(\omega)$ and $\mathrm{Im}\Pi''(\omega)$ respectively

$$\Sigma'^{I}(\omega) = U^2 \int_0^{|\omega|} \mathrm{d}\omega' D(\omega' - |\omega|)\mathrm{Im}\Pi'(\omega'), \tag{6.24a}$$

$$\Sigma''^{I}(\omega) = U^2 \int_0^{|\omega|} \mathrm{d}\omega' D(\omega' - |\omega|)\mathrm{Im}\Pi''(\omega'), \tag{6.24b}$$

where we have also made use of the fact that both $D(\omega) = -\frac{1}{\pi}\,\mathrm{sgn}(\omega)G(\omega)$ and the polarization propagators are even functions of ω to simplify the integrals.

6.5.2 Low-ω behaviour of the self-energy, $\Sigma'(\omega)$

We now have all of the underlying equations in place to be able to implement the FLEX algorithm numerically, and also consider what happens to the low-energy physics in the symmetric SC phase.

Recall that in any SC phase, the model possesses a *global* singlet ground-state where the Kondo effect persists. The system is characterized by a low-energy Kondo scale, $\omega_K \equiv \omega_*$, that for the metallic AIM vanishes exponentially in the interaction strength and thus never vanishes for any finite U. The spin degree of freedom located on the impurity is completely screened by the itinerant electrons of the conduction band. In consequence, ω_*, can be broadly thought of as the energy cost at which a spin is flipped on the impurity level. As stated in Chapter 1, for the PAIM, it is known [33, 43] that $U_c(r)$, the point at which ω_* vanishes, moves to a finite U (as shown by the NRG phase boundary in Fig. 5.3). The QCP, where ω_* vanishes as $U \to U_c^-(r)$ can be thought of as the point at which the energy cost to flip a spin on the impurity vanishes.

In Section 4.7.2, we defined a Kondo scale vanishing at the QCP in terms of the quasiparticle weight Z, given by eq. (2.55). However, as we shall see, within the FLEX approximation considered here, it is more convenient (and essential to the numerical algorithm) to define a scale in terms of the position of a low-ω resonance in the polarization propagator, $\mathrm{Im}\Pi'(\omega)$. The QCP is then the point where the position of this resonance vanishes. This is the approach originally taken by White [72], when analysing the strong-coupling behaviour of the metallic ($r = 0$) AIM. In this section we generalize White's analysis to encompass the case of finite r.

With this in mind, we now examine the low-ω behaviour of the self-energy. In Section 4.6 we showed by general Luttinger self-consistency arguments, order by order in U, that the SSE, $\Sigma(\omega)$, in a Fermi liquid phase vanishes with a power greater than the hybridization function, $\Gamma(\omega)$ as $\omega \to 0$. As a consequence, at $x = 0$, where the renormalized level, ε^*, vanishes by symmetry, the low-ω behaviour of the spectrum is simply given by eq. (4.75). The modified spectral function $F(\omega)$, eq. (5.30), is then pinned to unity. Thus, by inserting the low-ω form of $D(\omega)$,

eq. (4.75), into eq. (6.8a), the low-ω behaviour of the 'bare' polarization bubble is given by (c.f. eq. (5.17c))

$$\mathrm{Im}^0\Pi(\omega) \overset{\omega\to 0}{\sim} \mathcal{A}_{2s}(r)|\omega|^{1-2r} \tag{6.25}$$

with coefficient given via eq. (5.17d). For $r \leq \frac{1}{2}$, it is readily shown by considering the Hilbert transform, eq. (6.10), that $\mathrm{Re}^0\Pi(\omega)$ has the following low-ω behaviour

$$\mathrm{Re}^0\Pi(\omega) \overset{\omega\to 0}{\sim} \mathrm{Re}^0\Pi(\omega=0) - \tan(\pi r)\mathcal{A}_{2s}(r)|\omega|^{1-2r} + \ldots, \tag{6.26}$$

vanishing with the same exponent as $\mathrm{Im}^0\Pi(\omega)$. The imaginary part of the full polarization propagator, $\Pi'(\omega)$, obtained from eqs. (6.19a, 6.22a), can then be written as

$$\mathrm{Im}\Pi'(\omega) = \frac{\frac{3}{2}(\mathrm{Im}^0\Pi(\omega)+\eta)}{[1-U\mathrm{Re}^0\Pi(\omega)]^2 + [U(\mathrm{Im}^0\Pi(\omega)+\eta)]^2}. \tag{6.27}$$

where $\eta = 0^+$ is put in to deal correctly with the unique case if the denominator of this equation vanishes. Inserting the low-ω forms of eqs. (6.25-6.26) into this equation we obtain

$$\mathrm{Im}\Pi'(\omega) \overset{\omega\to 0}{\sim} \frac{\frac{3}{2}\mathcal{A}_{2s}(r)|\omega|^{1-2r}}{[1-U\mathrm{Re}^0\Pi(0)+\tan(\pi r)\mathcal{A}_{2s}(r)|\omega|^{1-2r}]^2 + [U\mathcal{A}_{2s}(r)|\omega|^{1-2r}]^2}.$$

Furthermore, from expanding the denominator of this equation it may be shown that the low-ω form of $\mathrm{Im}\Pi'(\omega)$ is given by

$$\mathrm{Im}\Pi'(\omega) \overset{\omega\to 0}{\sim} \frac{3}{2}\frac{\cos^2(\pi r)}{U^2\mathcal{A}_{2s}(r)}\omega_*^{2r-1}H(\tilde{\omega}), \tag{6.28a}$$

where we define a low-energy (Kondo) scale $\omega_m(=\omega_*)$ as

$$\omega_m = \left[\frac{[1-U\mathrm{Re}^0\Pi(\omega=0)]}{\mathcal{A}_{2s}(r)U\sqrt{1+\tan^2(\pi r)}}\right]^{\frac{1}{1-2r}}. \tag{6.28b}$$

such that the (universal) function

$$H(\tilde{\omega}) = \frac{|\tilde{\omega}|^{1-2r}}{1+\sin(\pi r)|\tilde{\omega}|^{1-2r}+|\tilde{\omega}|^{2-4r}} \tag{6.28c}$$

has a peak maximum at $\tilde{\omega} = \omega/\omega_* = \pm 1$. From eq. (6.28a), $\mathrm{Im}\Pi'(\omega)$ therefore has a peak maximum positioned at $\omega = \omega_*$ (as argued at the beginning of this section). For small-$\tilde{\omega}$, such that $|\omega| \gg \omega_*$, $H(\tilde{\omega}) \overset{\tilde{\omega}\to 0}{\sim} |\tilde{\omega}|^{1-2r}$, and hence from eq. (6.28a), the

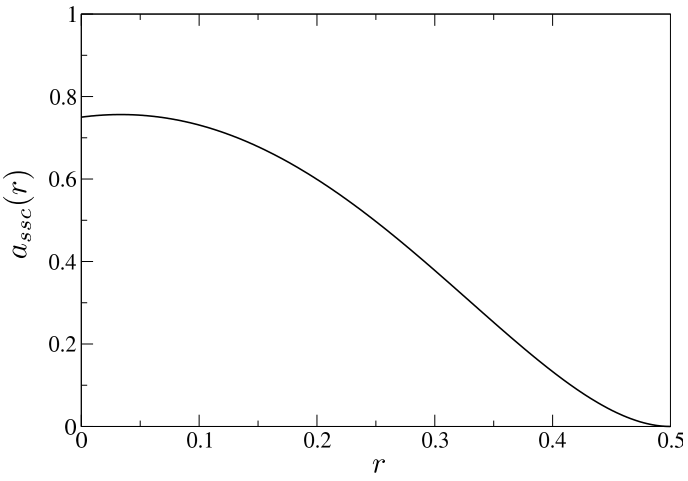


Figure 6.6: The self-energy coefficient, $a_{ssc}(r)$, given by eq. (6.31), plotted versus r.

scaling function simply becomes

$$\omega_*^{1-2r}\,\mathrm{Im}\Pi'(\omega) \overset{\omega\to 0}{\sim} \frac{3}{2}\frac{\cos^2(\pi r)}{U^2\mathcal{A}_{2s}(r)}|\tilde{\omega}|^{1-2r}, \tag{6.29}$$

such that $\omega_*^{1-2r}\mathrm{Im}\Pi'(\omega)$ is a *universal* scaling function of $\tilde{\omega}$. We may rescale eqs. (4.75, 6.25) via the low-energy scale ω_* to give the low-$|\tilde{\omega}|$ scaling functions

$$\Psi^I_{SC}(\tilde{\omega}) = \pi\omega_*^r D(\omega) \overset{\tilde{\omega}\to 0}{\sim} \cos^2(\tfrac{\pi}{2}r)|\tilde{\omega}|^{-r}, \tag{6.30a}$$

$$F(\omega) = (1+\beta^2(r))|\tilde{\omega}|^r\Psi^I_{SC}(\tilde{\omega}) = \pi(1+\beta^2(r))|\omega|^r D(\omega) \overset{\tilde{\omega}\to 0}{\sim} 1, \tag{6.30b}$$

$$\omega_*^{2r-1}\,\mathrm{Im}^0\Pi(\omega) \overset{\tilde{\omega}\to 0}{\sim} \mathcal{A}_{2s}(r)|\tilde{\omega}|^{1-2r}, \tag{6.30c}$$

respectively. Thus, by inserting eqs. (6.29, 6.30a) into eq. (6.24a), the low-$\tilde{\omega}$ scaling form of $\Sigma'^I(\omega)$ is readily shown to be

$$\frac{1}{\omega_*^r}\Sigma'^I(\omega) \overset{\tilde{\omega}\to 0}{\sim} \frac{3}{2}\left[\frac{\cos^2(\pi r)}{\cos^2(\frac{\pi r}{2})}\right]\left[\int_0^1 \mathrm{d}y(1-y)^{-r}y^{1-2r}\right]|\tilde{\omega}|^{2-3r} \tag{6.31a}$$

$$\overset{\tilde{\omega}\to 0}{\sim} a_{ssc}(r)|\tilde{\omega}|^{2-3r} \tag{6.31b}$$

with precise coefficient (obtained at the FLEX level of approximation) given by

$$a_{ssc}(r) = \frac{3}{2}\left[\frac{\cos^2(\pi r)}{\cos^2(\frac{\pi r}{2})}\right]\left[\frac{\Gamma(2-2r)^2}{\Gamma(1-r)\Gamma(3-3r)}\right], \tag{6.31c}$$

where $\Gamma(x)$ once again denotes the gamma function. Furthermore, the real part is given from eq. (6.13). However, since $\Sigma'^I(\omega)$ is even in ω, its real part at $\omega = 0$

vanishes.[8] Thus, the low-$\tilde{\omega}$ behaviour is [100]

$$\frac{1}{\omega_*^r}\Sigma'^R(\omega) \overset{\tilde{\omega}\to 0}{\sim} -\gamma'(r)\tilde{\omega} \qquad : \quad 0 < r < \tfrac{1}{3} \tag{6.32a}$$

$$\overset{\tilde{\omega}\to 0}{\sim} -\beta(2-3r)a_{ssc}(r)|\tilde{\omega}|^{2-3r} \qquad : \quad \tfrac{1}{3} < r < \tfrac{1}{2} \tag{6.32b}$$

where $\gamma'(r)$ is a dimensionless quantity given by $\gamma'(r) = \int_{-\infty}^{\infty} \mathrm{d}\tilde{\omega}\ \mathrm{P}[L(\tilde{\omega})/\tilde{\omega}^2]$, and $L(\tilde{\omega}) = \omega_*^{-r}\Sigma^I(\omega)$. For the limiting case $r = \frac{1}{3}$, the real part has logarithmic corrections - $\Sigma^R(\omega) \overset{\omega\to 0}{\propto} \omega \ln|\omega|$, but does not scale in terms of $\tilde{\omega}$. The low-$\tilde{\omega}$ form of the FLEX self-energy given by eqs. (6.31-6.32), *self-consistent* for $r < \frac{1}{2}$, takes precisely the same form as eq. (4.73) obtained from the order by order analysis of Section 4.6. As shown in Fig. 6.6, in the limit that $r \to 0$, such that the impurity is coupled to a metallic conduction band, the coefficient $a_{ssc}(r) \to \frac{3}{4}$, and the self-energy is given by the familiar quadratic Fermi liquid behaviour

$$\Sigma'^I(\omega) \overset{\tilde{\omega}\to 0}{\sim} \tfrac{3}{4}\,\tilde{\omega}^2 + \ldots. \tag{6.33}$$

In contrast, in the limit that $r \to \frac{1}{2}$, the coefficient $a_{ssc}(r) \to 0$, such that identically at $r = \frac{1}{2}$ the SSC phase can no longer exist for any finite U.

The low-energy scale

Before we proceed, two comments should be made about the low-energy scale, $\omega_m \equiv \omega_*$, defined by eq. (6.28b).

Firstly, as stated above, since $H(\tilde{\omega})$, eq. (6.28c), has a maximum at $\tilde{\omega} = \pm 1$, the scale gives the position of a low-ω resonance in $\mathrm{Im}\Pi'(\omega)$. As the QCP is approached, the scale naturally vanishes and the position of the peak moves towards the Fermi level. As a consequence, identically at the QCP itself, the resonance has reached $\omega = 0$ and there is now a pole located precisely at the Fermi level. We will discuss this important feature in the next section where we consider the precise details of the QCP.

Secondly, as $\omega_m \to 0$, since the terms in the denominator of eq. (6.28b) remain finite as $U \to U_c^-(r)$, implies that the numerator must vanish, or equivalently $U\mathrm{Re}^0\Pi(\omega = 0) \to 1$ at the transition. Thus, identically at the QCP, the critical U within FLEX is given by the relation

$$U_c(r) = [\mathrm{Re}^0\Pi(\omega = 0)]^{-1}. \tag{6.34}$$

(Note that this condition gives the upper bound of the stability condition of eq. (6.16a) above.)

[8] The integrand of eq. (6.13) for $F^R(\omega = 0)$ is odd in ω' when $F^I(\omega')$ is even.

6.5.3 Low-ω behaviour of the self-energy, $\Sigma''(\omega)$

We now briefly describe the low-energy behaviour of the other effective polarization channel defined by eq. (6.22b). On insertion of eqs. (6.25-6.26) into eqs. (6.19, 6.22b), by analogy with eq. (6.28a) the low-ω form of the imaginary part of $\Pi''(\omega)$ is readily shown to be given by

$$\mathrm{Im}\Pi''(\omega) \overset{\omega\to 0}{\sim} \frac{\frac{3}{2}\mathcal{A}_{2s}(r)|\omega|^{1-2r}}{[1+U\mathrm{Re}^0\Pi(\omega=0)]^2} - 2\mathcal{A}_{2s}(r)|\omega|^{1-2r}. \tag{6.35}$$

Furthermore, as the low-energy scale vanishes, and hence from eq. (6.34), $U\mathrm{Re}^0\Pi(\omega = 0) \to 1$, the denominator of this expression does not vanish (instead it tends to 2). We may recast the equation by rescaling in terms of ω_*, eq. (6.28b):

$$\omega_*^{1-2r}\mathrm{Im}\Pi''(\omega) \propto \omega_*^{2(1-2r)}|\tilde{\omega}|^{1-2r} \tag{6.36}$$

and therefore, unlike $\omega_*^{1-2r}\mathrm{Im}\Pi'(\omega)$ given by eq. (6.29), $\omega_*^{1-2r}\mathrm{Im}\Pi''(\omega)$ is *not* a universal function of $\tilde{\omega}$ for small-$\tilde{\omega}$. By inserting eq. (6.36) together with the low-$\tilde{\omega}$ form of $D(\omega)$, eq. (4.75), into eq. (6.24b), the (dimensionless) low-$\tilde{\omega}$ scaling form of $\Sigma''^I(\omega)$ is then given by

$$\frac{1}{\Gamma_0\omega_*^r}\Sigma''^I(\omega) \equiv \frac{1}{\omega_*^r}\Sigma''^I(\omega) \propto |\tilde{\omega}|^{2-3r}\omega_*^{2(1-2r)}. \tag{6.37}$$

Hence, on taking the limit $\omega_* \to 0$, such that the system is in the scaling regime (i.e. close to the QCP), this contribution to $\Sigma^I(\omega)$ can be neglected compared to the other scaling contribution coming from eq. (6.31).

6.6 Analytic results for the QCP at ph symmetry

Before moving to a discussion of the numerics in the SC phase, in this section we examine the low-ω behaviour precisely at the QCP within FLEX.

As considered in Section 4.8, the QCP is the point at which the low-energy scales vanish coming from either phase. Recall that from general scaling arguments, the low-ω form of the spectral function identically at the QCP is given from eq. (4.88) by $\pi D(\omega) \overset{\omega\to 0}{\sim} C_s(r)|\omega|^{-r}$ (with $C_s(r)$ a coefficient that depends on the leading coefficient of the self-energy via eq. (4.87)). (Recall that this behaviour is also seen *away* from the QCP (in either phase), in the high frequency ($|\tilde{\omega}| \gg 1$) forms (tails) of the scaling functions, e.g. the spectral scaling function is given from eq. (4.89) as $\Psi_\alpha^I(\tilde{\omega}) \equiv \pi\omega_*^r D(\omega) \overset{|\tilde{\omega}|\gg 1}{\sim} C_s(r)|\tilde{\omega}|^{-r}$.)

In order for the QCP spectral function to have this *interacting* behaviour, the single-self-energy must vanish as $\Sigma^I(\omega) \overset{\omega\to 0}{\sim} \alpha_{sc}|\omega|^r$, eq. (4.83b). In the last chapter

we found that the simple level of second-order perturbation theory, although performed self-consistently, failed to capture this non-trivial phenomenon, predicting a vanishing scale coming exclusively from the LM phase. In this section we analyse whether the more sophisticated conserving approximation of FLEX can correctly predict the interacting QCP behaviour.

6.6.1 Low-ω behaviour

To proceed, we initially assume that identically at the QCP the low-ω behaviour of the spectrum has the form of eq. (4.88) (obtained from exact arguments)

$$\pi D(\omega) \overset{\omega\to 0}{\sim} C_s(r)|\omega|^{-r} \qquad : \omega_* = 0, \quad U = U_c(r). \tag{6.38}$$

Inserting this form into eq. (6.11), the low-ω behaviour of $\mathrm{Im}^0\Pi(\omega)$ is

$$\mathrm{Im}^0\Pi(\omega) \overset{\omega\to 0}{\sim} \mathcal{A}(r)|\omega|^{1-2r}, \qquad : U = U_c(r), \tag{6.39}$$

where $\mathcal{A}(r)$ is a coefficient to be determined. At the QCP we know from eq. (6.34) that the critical U is given by $[U_c]^{-1} = \mathrm{Re}^0\Pi(0)$. Inserting this condition into eq. (6.26) (and replacing $\mathcal{A}_{2s}(r)$ with $\mathcal{A}(r)$) we obtain

$$\mathrm{Re}^0\Pi(\omega) \overset{\omega\to 0}{\sim} \frac{1}{U_c} - \tan(\pi r)\mathcal{A}(r)|\omega|^{1-2r} + \ldots, \tag{6.40}$$

once again, precisely at $U = U_c(r)$. The low-ω behaviour of $\mathrm{Im}\Pi'(\omega)$ is then obtained by inserting eqs. (6.39-6.40) into eq. (6.27). We obtain

$$\mathrm{Im}\Pi'(\omega) \overset{\omega\to 0}{\sim} \frac{\frac{3}{2}\mathcal{A}(r)|\omega|^{1-2r} + \eta}{[-U_c\tan(\pi r)\mathcal{A}(r)|\omega|^{1-2r}]^2 + [U_c(\mathcal{A}(r)|\omega|^{1-2r} + \eta)]^2} \tag{6.41a}$$

$$\overset{\omega\to 0}{\sim} \frac{3}{2}\frac{\cos^2(\frac{\pi}{2}r)}{U_c^2\mathcal{A}(r)}|\omega|^{2r-1} + \mathrm{Im}\Pi'^{pole}(\omega). \tag{6.41b}$$

The first term gives the 'band' contribution to $\mathrm{Im}\Pi'(\omega)$, which diverges for $r < \frac{1}{2}$. The second term gives a zero-frequency pole contribution to $\mathrm{Im}\Pi'(\omega)$ of the form [100]

$$\mathrm{Im}\Pi'^{pole}(\omega) \equiv L(\mathrm{Im}^0\Pi(\omega); r), \tag{6.42a}$$

with

$$L(y;r) = \frac{1}{U_c^2}\frac{\eta}{[\tan(\pi r)y]^2 + [y+\eta]^2} \quad : \eta \to 0^+, \tag{6.42b}$$

$$= \frac{2r}{U_c^2\tan(\pi r)}\pi\delta(y). \tag{6.42c}$$

where it is simply a matter of algebra to show the last line. The pole contribution to $\mathrm{Im}\Pi'(\omega)$ given by eq. (6.42a), reduces to

$$\mathrm{Im}\Pi'^{pole}(\omega) = \frac{2\pi r|\omega|^{2r}}{U_c^2(1-2r)\mathcal{A}(r)\tan(\pi r)}\delta(\omega) = 0, \tag{6.43}$$

Thus, the explicit pole part of $\mathrm{Im}\Pi'(\omega)$ is 'dead' and makes no contribution - as a consequence we neglect it from further consideration in what is to follow. Furthermore, by inserting eq. (6.41), together with the assumed behaviour of eq. (6.38), into eq. (6.24a), it follows that the self-energy has the low-ω form

$$\Sigma'^I(\omega) \overset{\omega\to 0}{\sim} \frac{3}{2}\frac{\cos^2(\pi r)C_s(r)}{\mathcal{A}(r)\pi}\left[\int_0^{|\omega|} \mathrm{d}\omega' |\omega' - |\omega||^{-r}|\omega'|^{2r-1}\right] \tag{6.44a}$$

$$\overset{\omega\to 0}{\sim} \frac{3}{2}\frac{\cos^2(\pi r)C_s(r)}{\mathcal{A}(r)\pi}\left[\int_0^1 \mathrm{d}y (1-y)^{-r}y^{2r-1}\right]|\omega|^r \tag{6.44b}$$

$$\overset{\omega\to 0}{\sim} \alpha_{sc}(r)|\omega|^r, \qquad \text{with real part given by} \tag{6.44c}$$

$$\Sigma'^R(\omega) \overset{\omega\to 0}{\sim} -\mathrm{sgn}(\omega)\beta(r)\alpha_{sc}(r)|\omega|^r, \tag{6.44d}$$

where the behaviour of $\Sigma'^R(\omega)$ has been obtained from eq. (6.13), taking the form of eq. (6.44d) by analogy with eq. (4.28) (and once again, $\Sigma'^R(0)$ vanishes by symmetry). The coefficient, $\alpha_{sc} \equiv \alpha_{sc}(r)$, is independent of $\mathrm{sgn}(\omega)$ as a consequence of the fact that $\Sigma'^I(\omega)$ is an even function at $x = 0$. Furthermore, by inserting eq. (6.44), together with the (time-ordered) hybridization function, $\Gamma(\omega) = -\mathrm{sgn}(\omega)(\beta(r)+i)|\omega|^r$, into eq. (6.6b) for the spectral function, we obtain

$$\begin{aligned}\pi D(\omega) &\overset{\omega\to 0}{\sim} \frac{(1+\alpha_{sc})|\omega|^r}{[\omega + \mathrm{sgn}(\omega)\beta(r)(1+\alpha_{sc})|\omega|^r]^2 + [(1+\alpha_{sc})|\omega|^r]^2} \\ &\overset{\omega\to 0}{\sim} \frac{\cos^2(\frac{\pi}{2}r)}{1+\alpha_{sc}}|\omega|^{-r}\end{aligned} \tag{6.45}$$

where the ω term is neglected in the limit that $\omega \to 0$. On comparison of this equation with eq. (6.38), we see that this form of the spectral function is self-consistent with precise coefficient given by $C_s(r) = \cos^2(\frac{\pi}{2}r)/(1+\alpha_{sc})$.

Alternatively, the QCP behaviour of eq. (6.45) may be accessed by examining the high-frequency tails ($|\tilde{\omega}| \gg 1$) of the scaling spectrum *away from the QCP* in either phase (where we consider a finite $\tilde{\omega}$ in the limit that $\omega_* \to 0$). The scaling

spectrum is written as[9]

$$\Psi^I_\alpha(\tilde{\omega}) \equiv \pi\omega_*^r D(\omega) \overset{|\tilde{\omega}|\gg 1}{\sim} \frac{\cos^2(\frac{\pi}{2}r)}{1+\alpha_{sc}}|\tilde{\omega}|^{-r} \tag{6.46}$$

with $\alpha =$ SC or LM. Furthermore, the scaling behaviour of eq. (6.46) has exactly the same form as eq. (4.89) obtained via general scaling arguments in Section 4.9. The only difference between the exact case of eq. (4.89) and the case considered here is that the precise value of the coefficient, α_{sc}, may be determined here at the FLEX level of approximation.[10] We now explain how this calculation unfolds.

6.6.2 Determining the coefficient, $\alpha_{sc}(r)$

The self-consistent value of $\alpha_{sc}(r)$, is determined by inserting $C_s(r) = \cos^2(\frac{\pi}{2}r)/(1+\alpha_{sc})$ and $\mathcal{A}(r) = \mathcal{A}_{2s}(r)[1+\alpha_{sc}(r)]^{-2}$ into eq. (6.44b) (and then comparing with eq. (6.44c)). We obtain the simple form

$$\alpha_{sc}(r) = [1+\alpha_{sc}(r)]K(r), \tag{6.47a}$$

where

$$K(r) = \frac{3}{2}\frac{\cos^2(\pi r)}{\cos^2(\frac{\pi}{2}r)}\left[\frac{\Gamma(2-2r)\Gamma(2r)}{\Gamma(1+r)\Gamma(1-r)}\right] \geq 0, \tag{6.47b}$$

which is always positive in the range $0 < r < 1$, and we have used the fact that the integral in eq. (6.44b) may be represented in terms of gamma functions. On rearranging eq. (6.47a) into closed form we obtain

$$\alpha_{sc}(r) = \frac{K(r)}{1-K(r)}. \tag{6.47c}$$

Thus, it is possible to determine $\alpha_{sc}(r)$ over the full range of r from this simple "RPA"-like form. By inserting eq. (6.47c) into eq. (6.46), we may write the modified spectral function given by eq. (6.30b) in terms of $K(r)$

$$F(\omega) = [1+\beta^2(r)]|\tilde{\omega}|^r \Psi^I_\alpha(\tilde{\omega}) \overset{|\tilde{\omega}|\gg 1}{\sim} \frac{1}{1+\alpha_{sc}(r)} = 1-K(r). \tag{6.48}$$

As a consequence, the function, $K(r)$, effectively renormalizes the spectral pinning condition, eq. (6.30b), found in the SSC phase, away from unity. Thus, as the QCP

[9] In the scaling regime, where $\omega_* \to 0$, the contribution, $\Sigma''(\omega)$, coming from the other effective polarization channel, does not show any singular behaviour as $U \to U_c(r)$ (see eq. (6.37)). As a consequence, $\Sigma''(\omega)$, may be neglected from consideration in the large-$|\tilde{\omega}|$ form of the spectral function.

[10] By inserting eq. (6.45) into eq. (6.11), it is readily shown that the 'bare' polarization propagator has the scaling form of eq. (6.39) with coefficient $\mathcal{A}(r) = \mathcal{A}_{2s}(r)[1+\alpha_{sc}(r)]^{-2}$.

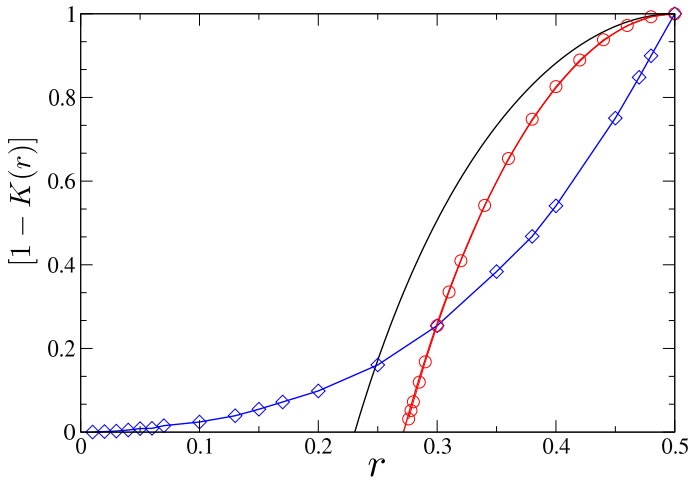


Figure 6.7: Spectrum plateau values, $[1-K(r)]$, versus r at the QCP from full FLEX (red)(analytic line with numerical results to confirm), just PH diagrams (black), NRG (blue).

is approached, the large-$|\tilde{\omega}|$ tails of the scaling function in eq. (6.48) reach an r-dependent plateau value $= [1-K(r)]$. This behaviour is analogous to the results of Section 4.9 - the exact NRG calculations of Fig. 4.19 shows the high-$\tilde{\omega}$ r-dependent plateau in $\Psi^I_\alpha(\tilde{\omega})$.

6.6.3 QCP plateau value

We now ask the question of what values the coefficient, $\alpha_{sc}(r)$, can take as a function of r by explicitly considering the form of eq. (6.47c). In order for the self-energy to remain analytic and the Hilbert transform relation of eq. (6.13) to hold, $\Sigma'^I(\omega)$ must be positive for all ω. Thus, the condition for the QCP solution to have an analytic self energy is clearly, $K(r) \leq 1$, such that the coefficient $\alpha_{sc}(r)$ is always positive and the denominator of eq. (6.47c) does not become negative. Fig.6.7 shows the spectral plateau value, $[1-K(r)]$ (given by eq. (6.48)), as a function of r (FLEX in red-circles). The first thing to notice is that as $r \to \frac{1}{2}$, the value of $K(r)$ vanishes, and hence the coefficient $\alpha_{sc}(r)$ also vanishes via eq. (6.47c). The plateau value, $[1-K(r)]$, then simply moves to unity such that eq. (6.48) has the same form as the SSC phase.

The second important feature of the curve in Fig. 6.7 is that at some non-zero $r \approx 0.271$ $(= r_c)$, $[1-K(r)] \to 0$. (The value $r = r_c$ is the same r that we find the FLEX phase boundary diverges at from the numerics shown in Fig. 6.5.) For $r \geq r_c$, $[1-K(r)] \geq 0$, there is a QCP solution with an analytic self-energy of the form discussed above, i.e. $\Sigma^I(\omega) \overset{\omega\to 0}{\sim} \alpha_{sc}|\omega|^r$. In this scenario, the scale, ω_m, vanishes at a critical $U = U_c(r)$ self-consistently determined by eq. (6.34). By contrast, for $r < r_c$, the plateau value $[1-K(r)]$, becomes negative, which leads to a negative

value of $\alpha_{sc}(r)$. However, as we have already shown via the phase diagram in Fig. 6.5, what actually happens within the numerics is that for $r < r_c$, only SSC solutions exist, with ω_* (given by eq. (6.28b)), non-vanishing for all U.[11]

The blue curve (with diamonds) in Fig. 6.7 shows data for the plateau value of the ph symmetric QCP (SQCP) from NRG (the same data as Fig. 4.15 - with plateau value $= [1+\beta^2(r)]C_s(r)$). As discussed in Section 4.9, we remind the reader that when the model is solved exactly there is a finite $U_c(r)$ for all $r > 0$, with $U_c(r) \overset{r\to 0}{\propto} \frac{1}{r}$. The NRG plateau value shown in the figure is $\propto r^2$ as $r \to 0$, given via eq. (4.95), such that the self-energy coefficient $\alpha_{sc}(r) \propto \frac{1}{r^2}$.

To conclude this section we remark that whilst FLEX does not predict the correct quantitative behaviour of the phase boundary at $x = 0$ for all r, it does give a qualitative insight into the *exact* underlying physics of the problem. Within FLEX, the value of the QCP plateau in the modified spectrum, $F(\omega)$, is wholly influenced by the low-ω self-energy asymptotics. For instance, if the PP/bubble channel diagrams are taken out of the approximation for the skeleton expansion completely such that only the transverse-spin (particle-hole) diagrams remain (eqs. (6.22a-6.23a) give $\Sigma'(\omega) = \Sigma^{PH}(\omega)$ and $\Sigma''(\omega) = 0$), the critical plateau value changes ($K(r) \to \frac{2}{3}K(r)$). The black line in Fig. 6.7 shows the spectrum plateau value with only the ph diagrams included in the self-energy, $[1 - \frac{2}{3}K(r)]$.

6.7 Numerics in the SSC phase

Using the basic FLEX algorithm stated above in Section 6.3.3, we now discuss the specific process for implementing FLEX in the SSC phase, moving towards the QCP as $U \to U_c^-(r)$.

6.7.1 Flow equation

In parallel with White's original analysis for the metallic AIM [72], eq. (6.28b) for the SSC phase low-energy scale, $\omega_m \equiv \omega_*$, may be rearranged to make U the subject:

$$U = \left[\omega_m^{1-2r}\sec(\pi r)\mathcal{A}_{2s}(r) + \mathrm{Re}^0\Pi(\omega = 0)\right]^{-1}. \tag{6.49}$$

This equation may be used within the numerical procedure to *target* a particular scale, ω_m, from the outset, such that we find a stable numerical path to convergence. The idea is that an initial ω_m is chosen and kept fixed for all iterations, such that the peak position in $\mathrm{Im}\Pi'(\omega)$ remains fixed throughout the numerical process. There are two reasons for doing this; firstly and most importantly, it is so that for all iterations

[11] In this case, $U_c(r) \to \infty$, but $\mathrm{Re}^0\Pi(\omega = 0) \to 0$ faster still, such that $U\mathrm{Re}^0\Pi(\omega = 0)$ never reaches unity, and as a result the condition eq. (6.34) is never satisfied.

the stability condition of eq. (6.16a), i.e. $0 < U\mathrm{Re}^0\Pi(\omega = 0) \leq 1$, is guaranteed and propagators do not violate analyticity at any point of the procedure. Secondly, we find that if the resonance position is pinned to ω_m, the algorithm is most stable and leads to fast convergence in as few iterations as is possible, therefore minimizing errors.

In order to implement the algorithm with a fixed low-energy scale, an initial ω_m is chosen and then at each iteration a new U is determined from eq. (6.49). The U then 'flows' throughout the procedure until it converges on a particular *self-consistent* value. For the metallic $r = 0$ case, eq. (6.49) reduces to White's [72] original flow equation, given by

$$U = \left[\omega_m/\pi + \mathrm{Re}^0\Pi(\omega = 0)\right]^{-1} = \left[\omega_m D(\omega = 0) + \mathrm{Re}^0\Pi(\omega = 0)\right]^{-1}, \tag{6.50}$$

where $\pi D(\omega)$ is pinned to unity at the Fermi level for $r = 0$ given via eq. (6.30b).

6.7.2 Algorithm specifics

For a fixed $x = 0$, and a chosen U and r, we initially start with the non-interacting spectral function $D^{(0)}(\omega)$, obtained by setting $\varepsilon^*_{A\sigma} = 0$ in $D^{(1)}_{A\sigma}(\omega)$, step (1) of the general algorithm stated in Section 6.3.3. We next calculate the real and imaginary parts of the bare polarization propagators, ${}^0\Pi(\omega)$ via steps (2) and (3). Subsequently as discussed above, we fix a scale, ω_m, such that a new U is chosen via eq. (6.49). The polarization propagators, $\Pi'(\omega)$, $\Pi''(\omega)$ via eqs. (6.22a-6.22b), and dynamical self-energy, $\tilde{\Sigma}^I(\omega)$ via eqs. (6.23c-6.24b), are calculated via steps (4-6). The real part, $\tilde{\Sigma}^R(\omega)$ is then obtained from eq. (6.13). The spectral function, $D(\omega)$, is obtained via eq. (6.6b), with the new self-energy, $\Sigma(\omega)$ ($= \tilde{\Sigma}(\omega)$).[12] This process is then repeated until U, and all entire functions of ω converge. The converged $D(\omega)$ and $\Sigma^I(\omega)$ are then outputted.

The disadvantage of this specific SSC phase algorithm is that the U cannot be chosen explicitly - the output U is determined by the input scale, ω_m via eq. (6.49). However as above, we emphasize that it is important to implement the calculation in this way such that $U\mathrm{Re}^0\Pi(\omega = 0)$ never exceeds unity and the stability condition of eq. (6.16a) holds for all iterations. By contrast, one advantage of this algorithm is that by setting $\omega_m = 0$ from the outset, we may easily find $U_c(r)$, i.e. eq. (6.49) simply reduces to $U = U_c(r) = [\mathrm{Re}^0\Pi(\omega = 0)]^{-1}$, which is the same condition as eq. (6.34).

Once again, as detailed in Section 5.3.2, we make use of the parameter, λ, to take

[12] The self-energy is purely dynamic as a consequence of the fact that the renormalized level vanishes at $x = 0$ in the SC phase. Furthermore, the local charge, $\bar{n} = 1$ for all U and in any SC phase the local moment $|\tilde{\mu}| = 0$, and so neither need to be explicitly calculated. The numerical process in the SSC phase is somewhat simplified as a consequence of these symmetry properties.

linear combinations of the spectral functions from current and previous iterations, in order to obtain stable convergence towards the required SSC solution.

6.7.3 Numerical results for the low-energy scale

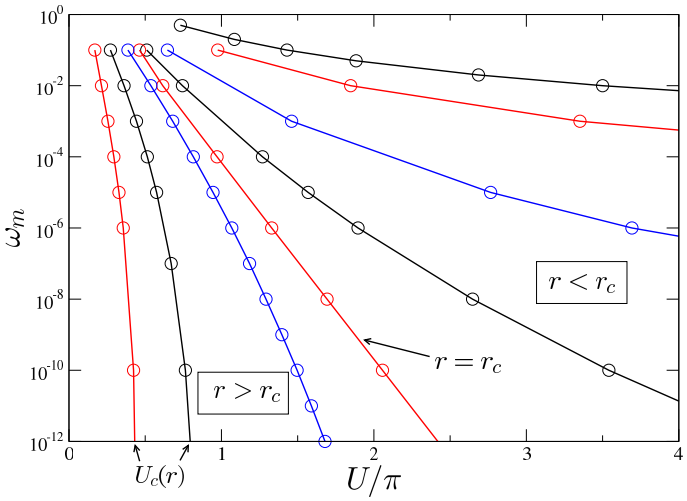


Figure 6.8: The scale, ω_m, is plotted (on a log-scale) versus U/π for progressive r. From right to left, $r = 0$, 0.1. 0.2, 0.25, 0.271, 0.3, 0.35, 0.4. See text for discussion.

We now proceed to discuss the behaviour of the low-energy scale, $\omega_m \equiv \omega_*$, as a function of r in the range $0 < r < \frac{1}{2}$. Data is obtained by fixing an ω_m in the algorithm above and converging for U via eq. (6.49). (If we set $\omega_m = 0$ in eq. (6.49) from the outset we seek the critical value of $U = U_c(r)$ - this is how we determined the phase boundary in Fig. 6.5.)

Fig. 6.8 shows ω_m plotted on a log-scale versus U for different value of r. By fitting a curve to the results for each fixed r, we find that for $r > r_c$, the scale has the r dependence

$$\omega_m \propto \left(1 - \tfrac{U}{U_c}\right)^{\frac{1}{r-r_c}}, \tag{6.51}$$

vanishing for a finite $U = U_c(r)$. On the LHS of Fig. 6.8 (as indicated), ω_m is shown to vanish for $r = 0.4$ and $r = 0.35$ at $U_c/\pi \simeq 0.45$ and $U_c/\pi \simeq 0.9$ respectively.

As $r \to r_c^+$, the denominator of the exponent in eq. (6.51) vanishes, but also $U_c(r)$ diverges via eq. (6.17). Thus, by inserting eq. (6.17) into eq. (6.51), ω_m may be expressed as

$$\omega_m \overset{r \to r_c^+}{\propto} [1 - \mathcal{B}^{-1} U (r - r_c)]^{\frac{1}{r-r_c}}. \tag{6.52}$$

On using the definition of the exponential function $\exp(-x) = \lim_{n\to\infty}(1 - \frac{x}{n})^n$, it

follows that in the limit $r \to r_c^+$, eq. (6.52) may be simply written as

$$\omega_m \overset{r\to r_c^+}{\propto} \exp[-U/\mathcal{B}]. \tag{6.53}$$

Thus, the system behaves like an impurity coupled to a metal[13] for $r = r_c$, with a low-energy Kondo scale that becomes exponentially small in the interaction strength, U. By contrast, for $r < r_c$, we find that the scale

$$\omega_m \propto U^{-\frac{1}{|r-r_c|}}, \tag{6.54}$$

decays algebraically and never vanishes for any finite U. In consequence the SSC phase persists for all U. This behaviour, shown on the RHS of Fig. 6.8, is analogous what happens in the SSC phase at the second-order level detailed in the last chapter. As a result, for the $r = 0$, metallic case (as originally studied by White [72]) we find from eq. (6.54), FLEX predicts an algebraic Kondo scale, i.e. $\omega_m(r = 0) \propto U^{-\frac{1}{r_c}}$ (with $\frac{1}{r_c} \approx 3.7$).

To conclude this section we briefly summarize the key results. For $r \geq r_c$, FLEX gives a sensible, if not quantitatively correct, description of the QCP coming from the SSC phase. However, for $r < r_c$, FLEX predicts that the SSC phase persists for all U with a low-energy scale algebraic in U. At $r = r_c$ the scale becomes exponential in U, analogous to the exact well known behaviour of the metallic ($r = 0$) single impurity Anderson model.

6.7.4 Results for the dynamics

We now discuss the numerical results for the dynamics in the symmetric SC phase in the two distinct regimes, $r < r_c$ and $r \geq r_c$. In Fig. 6.9, the modified spectral function, $F(\omega)$, is plotted versus ω for $r = 0.2 < r_c$. All spectra are pinned to unity, as expected from eq. (6.30b). As U is progressively increased, the central resonance narrows and the shoulders move apart. On high-energy scales the Hubbard satellites, occurring $\omega \simeq \pm\frac{U}{2}$, are completely smeared out. This is because, as consequence of the self-consistency procedure, universal scaling behaviour sets in at a high energy scale, $O(U)$, as is known from previous studies of the Hubbard and metallic Anderson models [105, 106]. The inset of Fig. 6.9 shows $F(\omega)$ as a function of $\tilde{\omega} = \omega/\omega_*$ on a log-scale, explicitly showing the spectral pinning at the Fermi level. The scale, $\omega_m \equiv \omega_*$ vanishes algebraically via eq. (6.54), and as a consequence we get no high-$|\tilde{\omega}|$ QCP plateau arising in the spectra. Instead, $F(\omega)$ simply vanishes in the limit $|\tilde{\omega}| \to \infty$.

For $r = 0.35 > r_c$, Fig. 6.10 shows the behaviour of the polarization propagator,

[13] When the $r = 0$ (metallic) model is solved exactly it is well known [2] that the Kondo scale is exponentially small in the interaction U.

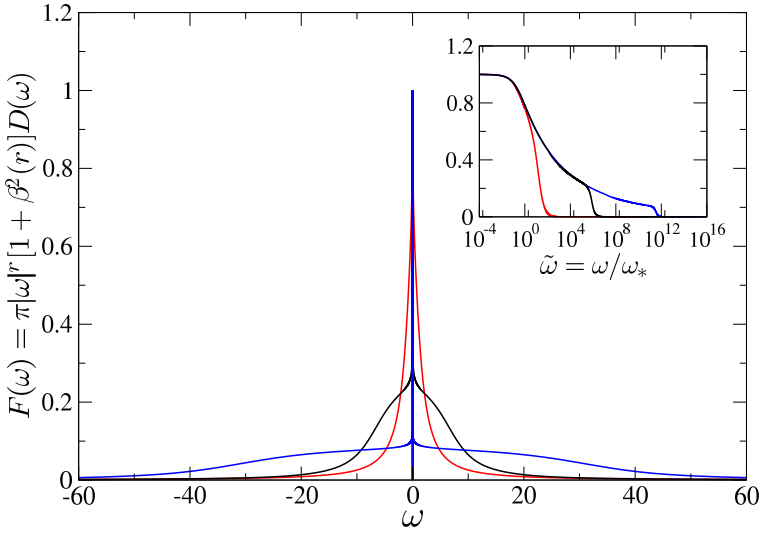


Figure 6.9: The modified spectral function, $F(\omega)$, plotted versus ω for $r = 0.2$. Red is for $\omega_m = 0.1$, $U/\pi \simeq 0.65$, Black is for $\omega_m = 10^{-5}$, $U/\pi \simeq 2.8$, Blue is for $\omega_m = 10^{-10}$, $U/\pi \simeq 10.6$. Inset shows the same data, but plotted versus ω/ω_* on a log-scale.

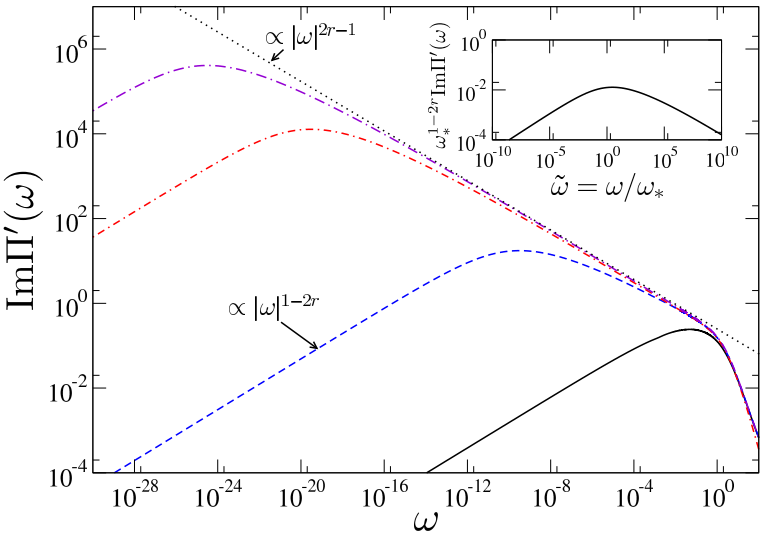


Figure 6.10: The imaginary part of the polarization propagator, $\mathrm{Im}\Pi(\omega)$, plotted versus ω as ω_m is gradually decreased towards $U_c(r)$, for $r = 0.35$, $x = 0$ on a log:log plot ($U_c(r)/\pi \simeq 0.9$). From left to right, $\omega_m = 10^{-25}$, $= 10^{-20}$, $= 10^{-10}$, $= 10^{-1}$ are shown. The inset shows the universal scaling function, $\omega_*^{1-2r}\mathrm{Im}(\omega)$, versus $\tilde{\omega}$, also on a log:log plot.

$\mathrm{Im}\Pi'(\omega)$, as a function of ω as ω_m is progressively lowered, such that the critical U is approached. For each curve the resonance maximum occurs at $\omega = \omega_m$ - as guaranteed by eq. (6.49). The inset shows the full-scaling behaviour of $\omega_*^{1-2r}\mathrm{Im}\Pi'(\omega)$ plotted as a function of $\tilde{\omega}$. For $|\tilde{\omega}| \ll 1$, $\omega_*^{1-2r}\mathrm{Im}\Pi'(\omega) \propto |\tilde{\omega}|^{1-2r}$, vanishing as expected from eq. (6.29). By contrast, for $|\tilde{\omega}| \ll 1$, $\omega_*^{1-2r}\mathrm{Im}\Pi'(\omega) \propto |\tilde{\omega}|^{2r-1}$, diverging with the form of eq. (6.41).

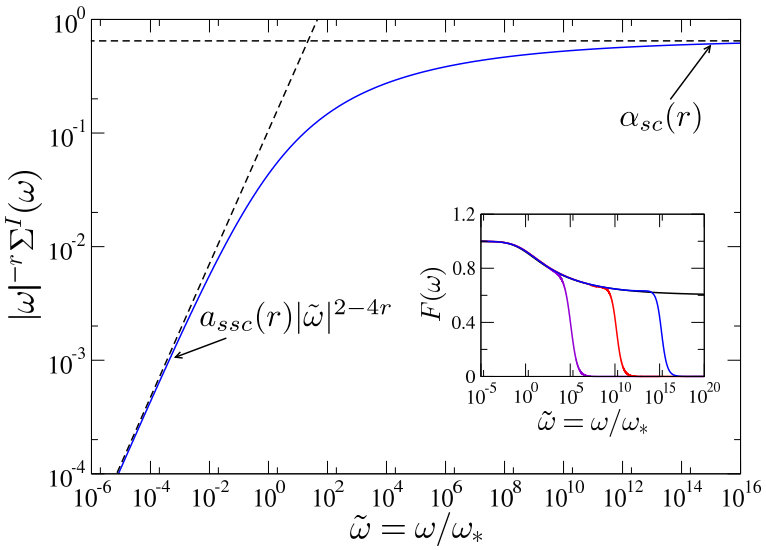


Figure 6.11: The self-energy scaling function, $|\omega|^{-r}\Sigma^I(\omega)$ plotted versus $\tilde{\omega}$ on a log:log plot, for $r = 0.35$, $x = 0$. The dotted lines show the asymptotic behaviour given by the scaling equations for both critical behaviour, $\tilde{\omega} \gg 1$ and Fermi liquid behaviour, $\tilde{\omega} \ll 1$. The inset shows the full modified scaling spectrum, $F(\omega)$ versus $\tilde{\omega}$ on a logscale for $r = 0.35$. The critical plateau value, $[1 - K(r)] \approx 0.6$, for $r = 0.35$ (and $U_c(r)/\pi \simeq 0.9$).

Fig. 6.11 shows the full $\tilde{\omega}$-dependence of the SSE scaling function, $|\omega|^{-r}\Sigma^I(\omega)$, once again for $r = 0.35 > r_c$ where $U_c(r)$ is finite. For $\tilde{\omega} \ll 1$, the Fermi liquid behaviour of eq. (6.31) is shown. By contrast, for $|\tilde{\omega}| \gg 1$, $|\omega|^{-r}\Sigma^I(\omega) \to \alpha_{sc}(r)$, as expected from eq. (6.44). The inset shows the modified spectral function, $F(\omega)$ as a complete universal function of $\tilde{\omega}$ on a log-scale. For $\tilde{\omega} \ll 1$, the spectra are pinned to unity with low-$|\tilde{\omega}|$ behaviour given by eq. (6.30b). In contrast, for $\tilde{\omega} \gg 1$, the spectra approach the renormalized plateau value, $[1 - K(r)]$, given by eq. (6.48).

To conclude this section, in Fig. 6.12 we show results for $F(\omega)$ versus ω from both FLEX and NRG. In this small U regime, where both $U < U_c(r)$ and $U/\pi < 1$, the FLEX and NRG results are virtually identical (with the curves lying precisely on top of each other).

6.8 Local moment phase at ph symmetry

In this chapter up until this point, we have focused solely on the SSC Fermi liquid phase, where both the TSEs and SSEs coincide, and approaching the QCP with $U \to U_c^-(r)$. We now move to describe the zero-field LM phase within TSE description for $U > U_c(r)$.

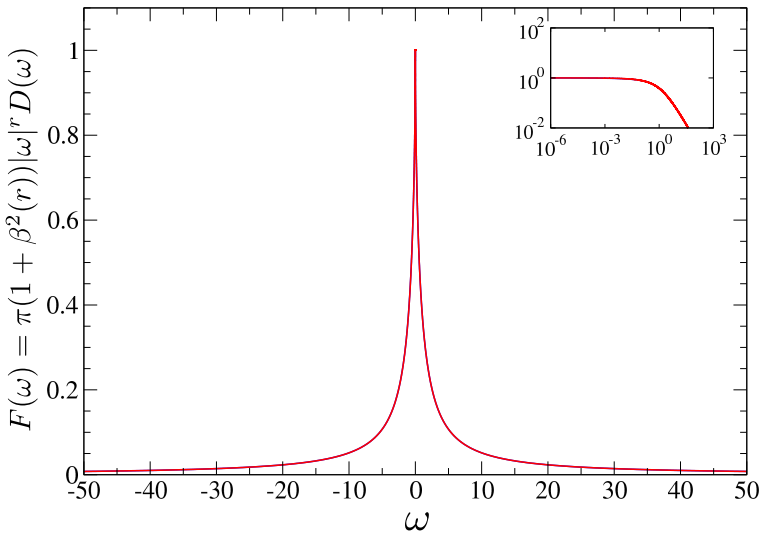


Figure 6.12: The modified spectral function, $F(\omega)$, plotted versus ω for $U/\pi = 0.8$, $r = 0.35$, $x = 0$ from both FLEX and NRG. The inset shows the same data on a log:log plot.

Physical motivation

As discussed in relation to the SSC phase, the Kondo scale, ω_m, can be thought of as the energy cost for flipping a spin on the impurity level. As the QCP is approached from below, the scale vanishes and in consequence the position of the resonance in $\mathrm{Im}\Pi'(\omega)$ also vanishes. Furthermore, precisely at $U = U_c$, the system is left with a 'dead' pole at the Fermi level in $\mathrm{Im}\Pi'(\omega)$, reflecting the zero-energy cost of flipping a spin on the impurity.

As explained in Chapter 3, the local moment phase comprises of two broken-symmetry many-body states, 'A' and 'B'. Since the two states are degenerate, we argue on physical grounds that there should be no energy cost for flipping a spin on the impurity for the *entire* LM phase (and not just at $U = U_c(r)$). Thus, before moving to a description of the model within the FLEX approximation in the LM phase, we first consider a general Luttinger self-consistency argument [60] in the spirit of the order by order analysis of Section 4.6, but with an explicit pole located at the Fermi level in the transverse-spin polarization propagator, $\mathrm{Im}\Pi^{\sigma-\sigma}_{AA}(\omega)$. Primarily the aim is to see if the self-consistent low-ω behaviour of the self-energy that arises in this case is distinct from the results of Section 4.6.

6.8.1 Luttinger self-consistency

The arguments here are for the leading low-ω behaviour of the spectrum and self-energies, holding for *any* x (not just $x = 0$). We neglect the contributions coming from the other polarization channels in the following, i.e. eq. (6.1b) simply reduces

to $\tilde{\Sigma}_{A\sigma}(\omega) = \Sigma^{PH}_{A\sigma}(\omega)$.[14] Furthermore, we initially assume that the broken-symmetry spectral functions have the leading low-ω dependence

$$\pi D_{A\sigma}(\omega) \overset{\omega\to 0}{\sim} [\theta(\omega)a^{+}_{\sigma} + \theta(\omega)a^{-}_{\sigma}]|\omega|^{\lambda_\sigma}. \tag{6.55}$$

Thus, we consider the case where there are two spin-dependent exponents, $\lambda_\uparrow$, $\lambda_\downarrow > -1$, with four distinct coefficients, $a^{\pm}_{\uparrow}$, and $a^{\pm}_{\downarrow}$. In a LM phase as shown by the general arguments of Section 4.3, the renormalized levels, $\varepsilon^{*}_{A\sigma}$, are always finite and never vanish for any $U > U_c(r)$. We initially assume this to be the case and as a consequence that the spectra vanish, i.e. $\lambda_\sigma > 0$. We return to this argument in due course to show that this indeed must be the case.

By inserting the low-ω form of eq. (6.55) into eq. (6.8a) (with $\sigma' = -\sigma$) it is straightforward to show that

$$\mathrm{Im}^0\Pi^{\sigma-\sigma}_{AA}(\omega) \overset{\omega\to 0}{\sim} A^{\pm}_{\sigma-\sigma}|\omega|^{1+\lambda_\sigma+\lambda_{-\sigma}}, \tag{6.56a}$$

with leading coefficient given by

$$A^{\pm}_{\sigma-\sigma} = \frac{1}{\pi}\left[\int_0^1 \mathrm{d}y(1-y)^{\lambda_\sigma}y^{\lambda_{-\sigma}}\right]\left[\theta(\omega)a^{-}_{\sigma}a^{+}_{-\sigma} + \theta(-\omega)a^{+}_{\sigma}a^{-}_{-\sigma}\right]. \tag{6.56b}$$

The real part, $\mathrm{Re}^0\Pi^{\sigma-\sigma}_{AA}(\omega)$, may subsequently be calculated from $\mathrm{Im}^0\Pi^{\sigma-\sigma}_{AA}(\omega)$ via eq. (6.10). In fact it is given simply by the Taylor series

$$\mathrm{Re}^0\Pi^{\sigma-\sigma}_{AA}(\omega) \overset{\omega\to 0}{\sim} \mathrm{Re}^0\Pi^{\sigma-\sigma}_{AA}(\omega=0) + \alpha_{\sigma-\sigma}\omega + \ldots, \tag{6.57}$$

provided that $[\lambda_\sigma + \lambda_{-\sigma}] > 0$ (which we assumed from the outset). The linear coefficient, $\alpha_{\sigma-\sigma}$, equivalent to the first derivative, is given by the integral

$$\alpha_{\sigma-\sigma} = \left(\frac{\partial \mathrm{Re}^0\Pi^{\sigma-\sigma}_{AA}(\omega)}{\partial\omega}\right)_{\omega=0} = \int_0^\infty \frac{\mathrm{d}\omega'}{\pi}\mathrm{P}\frac{[\mathrm{Im}^0\Pi^{\sigma-\sigma}_{AA}(\omega') - \mathrm{Im}^0\Pi^{\sigma-\sigma}_{AA}(-\omega')]}{(\omega')^2}, \tag{6.58}$$

which is obtained on differentiation of eq. (6.10). We also note that from eq. (6.5), $\alpha_{\sigma-\sigma} = -\alpha_{-\sigma\sigma}$ (with $|\alpha_{\sigma-\sigma}| = \alpha_{+-} > 0$).

In fact, $|\alpha_{\sigma-\sigma}|$ is a measure of whether the system is in the local moment phase or not, and therefore a suitable candidate (together with the local moment, $|\tilde{\mu}|$) for an *order-parameter* for the transition. In a SC phase (and also at the QCP), the polarization propagators lose any spin dependence and become even functions of ω

[14] We will consider the case where there is an $\omega = 0$ 'spin-flip' pole in the transverse spin polarization propagator. The self-energy contributions coming from the other polarization channels, $\Sigma^{PP}_{A\sigma}(\omega)$ and $\Sigma^{bub}_{A\sigma}(\omega)$ may then be shown to be insignificant at low-ω in comparison to the contribution from $\Sigma^{PH}_{A\sigma}(\omega)$.

via eq. (6.5), such that the numerator in eq. (6.58) vanishes. By contrast in a LM phase, since the propagators are spin-dependent, the numerator in eq. (6.58) must be non-zero. Moreover, as the QCP is approached from the LM phase, such that $U \to U_c^+(r)$, the spin dependence in the propagators vanishes and therefore $|\alpha_{\sigma-\sigma}|$ must *continuously* vanish at the transition.

The ph channel polarization propagator, $\mathrm{Im}\Pi_{AA}^{\sigma-\sigma}(\omega)$, is given by eq. (6.11). If there is to be a pole in this object located at the Fermi level, then it is required that $[1 - U\mathrm{Re}^0\Pi_{AA}^{+-}(\omega = 0)] \to 0^+$ as $\omega \to 0$. In order to examine this case we Taylor expand $[1 - U\mathrm{Re}\Pi^{+-}(\omega)]$ around the point $\omega = \delta$ (where δ is a small positive constant) to obtain

$$[1 - U\mathrm{Re}^0\Pi^{+-}(\omega)] \overset{\omega\to\delta}{\sim} [1 - U\mathrm{Re}^0\Pi^{+-}(\delta)] - U\alpha_{+-}^{\delta}(\omega - \delta) + \ldots \tag{6.59}$$

where $\alpha_{+-}^{\delta} = (\partial\mathrm{Re}^0\Pi^{+-}(\omega)/\partial\omega)_{\omega=\delta} > 0$ (such that as $\delta \to 0^+$, $\alpha_{+-}^{\delta} \to \alpha_{+-}$). Moreover, we take the frequency $\omega = \delta$ to be the point at which $[1 - U\mathrm{Re}\Pi^{+-}(\omega = \delta)]$ vanishes (such that the first term on the RHS of eq. (6.59) is zero). By virtue of the fact that $\alpha_{+-}^{\delta} > 0$, it follows that δ *must be positive* for the stability condition of eq. (6.16a), $[0 < \mathrm{Re}^0\Pi^{+-}(\omega) < \frac{1}{U}]$, to hold. Thus, we insert eq. (6.59) together with the low-ω behaviour of the imaginary part (eq. (6.56a)) into eq. (6.3a) to obtain

$$\Pi_{AA}^{+-}(\omega) \overset{\omega\to 0}{\sim} \frac{[\frac{1}{U} - \alpha_{+-}^{\delta}(\omega - \delta) + \ldots] + i[A_{\uparrow\downarrow}^{\pm}|\omega|^{1+\lambda_\uparrow+\lambda_\downarrow}]}{[-U\alpha_{+-}^{\delta}(\omega - \delta) + \ldots] - i[UA_{\uparrow\downarrow}^{\pm}|\omega|^{1+\lambda_\uparrow+\lambda_\downarrow}]} \tag{6.60a}$$

$$\overset{\omega\to 0}{\sim} -\left(\frac{\frac{1}{U} + i\eta}{U\alpha_{+-}^{\delta}(\omega - \delta) + i\eta}\right), \tag{6.60b}$$

with $\eta = A_{\uparrow\downarrow}^{\pm}|\delta|^{1+\lambda_\uparrow+\lambda_\downarrow}$. Taking the limit that $\delta \to 0^+$ (such that $\eta \to 0^+$),[15] eq. (6.60b) becomes

$$\Pi_{AA}^{+-}(\omega) \overset{\omega\to 0^+}{\sim} -Q\left[P\left(\frac{1}{\omega - 0^+}\right) - i\pi\delta(\omega - 0^+)\right] \tag{6.61}$$

with $Q = [\alpha_{+-}U^2]^{-1} \geq 0$. (From the symmetry $\Pi_{AA}^{+-}(\omega) = \Pi_{AA}^{-+}(-\omega)$, $\mathrm{Im}\Pi_{AA}^{-+}(\omega)$ has a pole at $\omega = 0^-$.)

By inserting eqs. (6.56a, 6.57) into eq. (6.11) we obtain the low-ω form of the band contribution to $\mathrm{Im}\Pi_{AA}^{\sigma-\sigma}(\omega)$. This, together with the pole piece is given by

$$\mathrm{Im}\Pi_{AA}^{\sigma-\sigma}(\omega) \overset{\omega\to 0}{\sim} \pi Q\delta(\omega) + \frac{A_{\sigma-\sigma}^{\pm}}{(U\alpha)^2}|\omega|^{\lambda_{-\sigma}+\lambda_\sigma-1}, \tag{6.62}$$

where for convenience we denote $\alpha \equiv \alpha_{+-}$, and the delta function piece strictly denotes a pole at $\omega = 0^+$ for the $\mathrm{Im}\Pi_{AA}^{+-}(\omega)$ function, and a pole at $\omega = 0^-$ for

[15] Since $[\lambda_\uparrow + \lambda_\downarrow] > 0$, $\eta = A_{\uparrow\downarrow}^{\pm}|\delta|^{1+\lambda_\uparrow+\lambda_\downarrow}$ vanishes faster than δ.

$\mathrm{Im}\Pi^{-+}_{AA}(\omega)$. Now, inserting this equation, together with the low-ω form of the spectral function, eq. (6.55), into eq. (6.12a), it is readily shown that

$$\Sigma^{I(PH)}_{A\sigma}(\omega) = \Sigma^{I(PH)pb}_{A\sigma}(\omega) + \Sigma^{I(PH)bb}_{A\sigma}(\omega), \tag{6.63a}$$

$$\Sigma^{I(PH)pb}_{A\sigma}(\omega) = \theta(-\sigma\omega)\pi Q D_{A-\sigma}(\omega) \overset{\omega\to 0}{\sim} b^{\pm}_{\sigma}|\omega|^{\lambda_{-\sigma}} \tag{6.63b}$$

$$\Sigma^{I(PH)bb}_{A\sigma}(\omega) = \overset{\omega\to 0}{\sim} g^{\pm}_{\sigma}|\omega|^{2\lambda_{-\sigma}+\lambda_{\sigma}}, \tag{6.63c}$$

where $\Sigma^{I(PH)bb}_{A\sigma}(\omega)$ is purely a band-band (bb) contribution to $\Sigma^{I(PH)}_{A\sigma}(\omega)$, obtained by inserting just the band contribution to $\mathrm{Im}\Pi^{\sigma-\sigma}_{AA}(\omega)$, together with $D_{A-\sigma}(\omega)$, into eq. (6.12a). By contrast, the pole-band (pb) contribution, $\Sigma^{I(PH)bb}_{A\sigma}(\omega)$, comes from the pole contribution in eq. (6.62). The specific coefficients are then given by

$$b^{\pm}_{\sigma} = \theta(-\sigma\omega)\frac{a^{-\sigma}_{-\sigma}}{\alpha}, \tag{6.64a}$$

$$l^{\pm}_{\sigma} = \left[\int_0^1 \mathrm{d}y(1-y)^{\lambda_{-\sigma}} y^{\lambda_{-\sigma}+\lambda_{\sigma}-1}\right]\left[\theta(\omega)\frac{a^{+}_{-\sigma}A^{-}_{\sigma-\sigma}}{\alpha^2} + \theta(-\omega)\frac{a^{-}_{-\sigma}A^{+}_{\sigma-\sigma}}{\alpha^2}\right]. \tag{6.64b}$$

Since we are considering the case where $\lambda_{\uparrow}, \lambda_{\downarrow} > 0$, the exponent $[2\lambda_{-\sigma} + \lambda_{\sigma}]$ is greater than $\lambda_{-\sigma}$, and consequently the first term in eq. (6.63a) vanishes less rapidly than the second term. Under these conditions it may be shown from the Hilbert transform, eq. (6.13) that the low-ω behaviour of the real part is

$$\Sigma^{R(PH)}_{A\sigma}(\omega) \overset{\omega\to 0}{\sim} \Sigma^{R(PH)}_{A\sigma}(\omega=0) + k^{\pm}_{\sigma}|\omega|^{\lambda_{-\sigma}}, \text{ with coefficient:} \tag{6.65a}$$

$$k^{\pm}_{\sigma} = -\tfrac{1}{2}[\beta(\lambda_{-\sigma})\,\mathrm{sgn}(\omega)(b^{+}_{\sigma} + b^{-}_{\sigma}) - \beta^{-1}(\lambda_{-\sigma})(b^{+}_{\sigma} - b^{-}_{\sigma})], \tag{6.65b}$$

such that if $b^{+}_{\sigma} = b^{-}_{\sigma} = b_{\sigma}$, it simply reduces to $k^{\pm}_{\sigma} = k_{\sigma} = -\,\mathrm{sgn}(\omega)\beta(\lambda_{-\sigma})b_{\sigma}$. This Hilbert transform relationship is the same as that used in Section 4.5.1, eq. (4.27), and holds for $[-1 < \lambda_{-\sigma} < 1]$. In consequence, the leading low-ω behaviour of the real part of the self-energy has the same power as the imaginary part, but for $\omega > 0$ *and* $\omega < 0$ (as opposed to $\Sigma^{I(PH)}_{A\sigma}(\omega)$ which is governed by the spin dependent step function in the first term of eq. (6.63c)). Using the low-ω equations, (6.63c) and (6.65a), together with the hybridization function, $\Gamma(\omega) = -\,\mathrm{sgn}(\omega)[\beta(r) + i]|\omega|^{r}$ in eq. (6.6b) we obtain

$$\pi D_{A\sigma}(\omega) \overset{\omega\to 0}{\sim} \frac{|\omega|^{r} + b^{\pm}_{\sigma}|\omega|^{\lambda_{-\sigma}}}{[\omega - \varepsilon^{*}_{A\sigma} + \mathrm{sgn}(\omega)\beta(r)|\omega|^{r} - k^{\pm}_{\sigma}|\omega|^{\lambda_{-\sigma}}]^2 + [|\omega|^{r} + b^{\pm}_{\sigma}|\omega|^{\lambda_{-\sigma}}]^2}.$$

With the condition that the renormalized levels are finite,[16] the vanishing terms in

[16] From the general arguments of Section 4.3, the renormalized levels are always finite in a LM phase, only vanishing at the transition. Therefore this is the case we consider here.

the denominator may be neglected to obtain

$$\pi D_{A\sigma}(\omega) \overset{\omega\to 0}{\sim} \frac{|\omega|^r + b_\sigma^\pm |\omega|^{\lambda_{-\sigma}}}{[\varepsilon^*_{A\sigma}]^2}. \tag{6.66}$$

Self-consistency requirements

On comparison of eq. (6.66) with what we started with, eq. (6.55), there are 2 distinct scenarios we must consider:

1. If $r \leq \lambda_{-\sigma}$, then self-consistently it is required that $\lambda_\uparrow = \lambda_\downarrow = r$. The low-$\omega$ form of the two-self-energies then become

$$\Sigma^I_{A\sigma}(\omega) \overset{\omega\to 0}{\sim} b_\sigma^\pm(r)|\omega|^r + l_\sigma^\pm(r)|\omega|^{3r} \tag{6.67a}$$

$$\Sigma^R_{A\sigma}(\omega) \overset{\omega\to 0}{\sim} k_\sigma^\pm(r)|\omega|^r. \tag{6.67b}$$

   Inserting these self-energies into eq. (6.66) we obtain

$$\pi D_{A\sigma}(\omega) \overset{\omega\to 0}{\sim} \frac{[1 + b_\sigma^\pm(r)]|\omega|^r}{[\varepsilon^*_{A\sigma}]^2}, \tag{6.68}$$

   which is a fully self-consistent solution to the problem.

2. If $r > \lambda_{-\sigma}$ then it is required that $\lambda_\uparrow = \lambda_\downarrow$ and $\lambda_\sigma = 2\lambda_{-\sigma} + \lambda_\sigma$, and therefore $\lambda_\downarrow = \lambda_\uparrow = 0$. However, we assumed from the start that $\lambda_\uparrow, \lambda_\downarrow > 0$, and therefore this solution is crucially *not* self-consistent.

Argument for $\lambda_\sigma > 0$

From the outset in eq. (6.55), we assumed that the exponents $\lambda_\uparrow, \lambda_\downarrow > 0$ (i.e. that both spectra vanish as $\omega \to 0$). Here we argue that provided the renormalized levels, $\varepsilon^*_{A\sigma}$, are non-zero (which they always are in an LM phase), this always has to be the case.

In the above analysis we found that if $\lambda_\sigma > 0$, then the self-energy, $\Sigma^I_{A\sigma}(\omega)$ must vanish with a power $m \geq r$ (i.e. no less slowly than the hybridization function, $\Gamma^I(\omega)$). We now consider the alternative case where $\Sigma^I_{A\sigma}(\omega) \overset{\omega\to 0}{\sim} j_\sigma^\pm |\omega|^m$ (with $j_\sigma^\pm$ an arbitrary coefficient) goes with a power less than the hybridization (i.e $m < r$). In this scenario, then either

1. The self-energy is divergent (i.e. $m < 0$). For $(-1 < m < 0)$ from eq. (4.27), the real part would have the same leading-order dependence, i.e. $[\Sigma^R_{A\sigma}(\omega) - \Sigma^R_{A\sigma}(0)] \overset{\omega\to 0}{\sim} q_\sigma^\pm |\omega|^m$ (where $q_\sigma^\pm$ is another coefficient). The low-ω form of eq. (6.6b) then becomes (we may neglect the renormalized levels, $\varepsilon^*_{A\sigma}$, com-

pared to the diverging self-energy on the lowest frequency scales)

$$\pi D_{A\sigma}(\omega) \overset{\omega\to 0}{\sim} \frac{j_\sigma^{\pm}|\omega|^{-m}}{[j_\sigma^{\pm 2} + q_\sigma^{\pm 2}]}. \tag{6.69}$$

As a consequence, the spectra vanish ($\lambda_\sigma = -m > 0$), even if the self-energies diverge.

2. The second case to consider is if the self-energy vanishes with a power less than r, i.e. $0 < m < r$. If this occurs, then the $\varepsilon^*_{A\sigma}$ 'wins' in the denominator of the spectral function, eq. (6.66), and therefore the spectra must also vanish.

3. The third marginal case is when $\Sigma^I_{A\sigma}(\omega) \overset{\omega\to 0}{\sim} j_\sigma^{\pm}$, i.e. the self-energy goes to a constant value as $\omega \to 0$ ($m = 0$). This solution however, may also be shown to be not self-consistent. On examination of the specific case it may be shown that the leading low-ω behaviour of the real part of the bare polarization propagator is given by $[\mathrm{Re}^0\Pi^{\sigma-\sigma}_{AA}(\omega) - \mathrm{Re}^0\Pi^{\sigma-\sigma}_{AA}(0)] \overset{\omega\to 0}{\propto} \omega \ln|\omega| + \ldots$, i.e. there are logarithmic corrections to the linear term. As a consequence, the first derivative of $\mathrm{Re}^0\Pi^{\sigma-\sigma}_{AA}(\omega)$ as $\omega \to 0$ is divergent. It then follows that the pole contribution to $\mathrm{Im}\Pi^{\sigma-\sigma}_{AA}(\omega)$ has a vanishing weight, $Q = 0$.

Concluding remarks

We conclude that eqs. (6.67-6.68) give the *only self-consistent solution* when there is a pole located precisely at $\omega = 0^+$ in $\mathrm{Im}\Pi^{+-}_{AA}(\omega)$ (or at $\omega = 0^-$ in $\mathrm{Im}\Pi^{-+}_{AA}(\omega)$) with finite weight, Q (and holding generally for any x).

We now refer back to the NRG calculations of Section 4.11. The numerical results of Fig. 4.26 show the low-ω behaviour of the zero-field TSE, $\Sigma^I_{A\uparrow}(\omega)$, plotted versus ω on a log-log scale for an arbitrary (r, x). The NRG data indeed shows that the low-ω behaviour of $\Sigma^I_{A\sigma}(\omega)$ (given by eq. (4.105)) is in agreement with form deduced here from eq. (6.67). Thus, the exact numerical NRG results are telling us that the self-consistent solution of eq. (6.67) captures the *correct* low-ω dependence of the self-energy in the LM phase. As a consequence, in the FLEX numerical algorithm that follows, we specifically look for LM solutions that have a pole in $\mathrm{Im}\Pi^{+-}(\omega)$ at $\omega = 0^+$.

We make one final important point before proceeding. In this section we have shown that the order by order analysis of Section 4.6 is not the only case where Luttinger self-consistency [60] can arise.[17] By explicitly considering the pole-contribution (integrable singularity) to $\mathrm{Im}\Pi^{+-}_{AA}(\omega)$, we have self-consistently determined the *correct* low-ω dependence of $\Sigma^I_{A\sigma}(\omega)$ in the doubly degenerate LM phase at zero-field.

[17] For non-zero renormalized levels, $\varepsilon^*_{A\uparrow}$, $\varepsilon^*_{A\downarrow}$, the order by order results of Section 4.6 give the self-energy vanishing as $\Sigma^I_{A\sigma}(\omega) \propto |\omega|^{2+3r}$ (case A of Fig. 4.12). By contrast, the self-consistency argument above gives $\Sigma^I_{A\sigma}(\omega) \propto |\omega|^r$.

6.8.2 Low-$\tilde{\omega}$ scaling behaviour

In the light of the low-ω self-consistency analysis of the previous section, in this section we consider the low-$\tilde{\omega}$ scaling functions in the LM phase within FLEX.

In a LM phase, we may write the renormalized levels in terms of the UHF static self-energy $\Sigma^{(1)}_{A\sigma} = x + \frac{U}{2}([\bar{n}-1]-\sigma|\tilde{\mu}|)$, plus the zero-frequency part of the dynamical self-energy, $\tilde{\Sigma}^R_{A\sigma}(0)$, as

$$\varepsilon^*_{A\sigma} = x + \tfrac{U}{2}([\bar{n}-1] - \sigma|\tilde{\mu}|) + \tilde{\Sigma}^R_{A\sigma}(0). \tag{6.70}$$

At ph symmetry (where $x = 0$), the local charge, $\bar{n} = 1$, and also it follows from eq. (4.3c) that $\tilde{\Sigma}^R_{A\sigma}(0) = -\tilde{\Sigma}^R_{A\sigma}(0)$. The eq. (6.70) then reduces to

$$\varepsilon^*_{A\sigma} = -\sigma[\tfrac{U}{2}|\tilde{\mu}| - |\tilde{\Sigma}^R_{A\sigma}(0)|] = -\varepsilon^*_{A-\sigma},. \tag{6.71}$$

such that the renormalized levels are sign definite with ($\varepsilon^*_{A\uparrow} < 0$ and $\varepsilon^*_{A\downarrow} > 0$).[18]

In order to capture the unique behaviour of the QCP coming from the LM phase, each of the renormalized levels, $\varepsilon^*_{A\sigma}$, must vanish as $U \to U^+_c(r)$, such that we get the low-ω form of eq. (6.44) for $\Sigma^I(\omega)$. Once again, we define the LM low-energy scale here in exactly the same way we did in Chapter 4-5, i.e. via eq. (4.20) in terms of the difference in the renormalized levels, $\omega_* = \frac{1}{2}|\varepsilon^*_{A\sigma} - \varepsilon^*_{A-\sigma}|^{\frac{1}{r}}$. (In the proceeding discussion we also refer to the ratio, γ defined by eq. (4.22).)

Given that the TSEs have the *self-consistent* form of eq. (6.67), and inserting these, together with $\Gamma(\omega) = -\operatorname{sgn}(\omega)[\beta(r) + i]|\omega|^r$ into eq. (6.6b) for $D_{A\sigma}(\omega)$, along with the low-energy scale, ω_*, it is readily shown that the low-$\tilde{\omega}$ scaling form of the broken-symmetry spectra are given by

$$\omega^r_* \pi D_{A\sigma}(\omega) \overset{\tilde{\omega}\to 0}{\sim} \frac{[1 + b^{\pm}_{\sigma}]}{[1 - \sigma\gamma]^2}|\tilde{\omega}|^r, \tag{6.72}$$

for *any* asymmetry, x. On comparison of this form with eq. (6.55) (with $\lambda_\sigma = r$), we see that the coefficient, $a^{\pm}_{\sigma}$, is expressed as

$$a^{\pm}_{\sigma} = \frac{1}{\omega^{2r}_*}\frac{[1 + b^{\pm}_{\sigma}]}{[1 - \sigma\gamma]^2}. \tag{6.73}$$

The bare polarization propagator given by eq. (6.56a) may be rescaled in terms of the low-energy scale (with $\lambda_\sigma = r$) to give

$$\omega^{2r-1}_* \operatorname{Im}^0\Pi^{\sigma-\sigma}_{AA}(\omega) \overset{\tilde{\omega}\to 0}{\sim} \mathcal{A}^{\pm}_{\sigma-\sigma}|\tilde{\omega}|^{1+2r} \tag{6.74}$$

[18] We obtain the specific form of eq. (6.71) from the observation that within the numerics: $\tilde{\Sigma}^R_{A\uparrow}(0) > 0$, whilst $\tilde{\Sigma}^R_{A\downarrow}(0) < 0$.

with the scale-free coefficient, $\mathcal{A}^{\pm}_{\sigma-\sigma} = \omega_*^{-4r} A^{\pm}_{\sigma-\sigma}$, given by

$$\mathcal{A}^{\pm}_{\sigma-\sigma} = \frac{1}{\pi}\left[\frac{\Gamma(1+r)^2}{\Gamma(2+2r)}\right]\frac{1}{[1-\gamma^2]^2}[[1+b^{\mp}_{\sigma}][1+b^{\pm}_{-\sigma}]. \tag{6.75}$$

where we have expressed the integral in eq. (6.56b) in terms of gamma functions, and used eq. (6.73) for the form of $a^{\pm}_{\sigma}$. From eq. (6.62), the scaling form of the full polarization propagator is given by

$$\omega_*^{1-2r}\ \mathrm{Im}\Pi^{\sigma-\sigma}_{AA}(\omega) \overset{\tilde{\omega}\to 0}{\sim} \pi Q'\delta(\tilde{\omega}) + \frac{\mathcal{A}^{\pm}_{\sigma-\sigma}|\tilde{\omega}|^{2r-1}}{U^2[\alpha'(r)]^2}, \tag{6.76}$$

with the (scale-free) poleweight given by $Q' = [\alpha'(r)U^2]^{-1}$. The quantity, $\alpha'(r) = \omega_*^{2r}\alpha$, with $\alpha \equiv \alpha_{+-}$ given by the integral in eq. (6.58). Thus, the low-$\tilde{\omega}$ scaling form of $\Sigma^I_{A\sigma}(\omega)$ is given from eq. (6.67)

$$\frac{1}{\omega_*^r}\ \Sigma^I_{A\sigma}(\omega) \overset{\tilde{\omega}\to 0}{\sim} b^{\pm}_{\sigma}(r)|\tilde{\omega}|^r + \mathcal{L}^{\pm}_{\sigma}(r)|\tilde{\omega}|^{3r} \tag{6.77a}$$

with (scale-free) coefficients given from eq. (6.64) (with $\lambda_\sigma = r$ and using eqs. (6.73, 6.75))

$$b^{\pm}_{\sigma}(r) = \theta(-\sigma\tilde{\omega})\frac{[1+b^{-\sigma}_{-\sigma}]}{|\alpha'(r)|[1+\sigma\gamma]^2}, \tag{6.77b}$$

$$\mathcal{L}^{\pm}_{\sigma}(r) = \frac{1}{\pi}\left[\frac{\Gamma(2r)\Gamma(1+r)}{\Gamma(1+3r)}\right]\left[\frac{[1+b^{\pm}_{-\sigma}]}{[1\pm\sigma\gamma]^2}\left[\frac{\mathcal{A}^{\mp}_{\sigma-\sigma}}{[\alpha'(r)]^2}\right]\right]. \tag{6.77c}$$

where $\mathcal{L}^{\pm}_{\sigma}(r) = \omega_*^{2r} l^{\pm}_{\sigma}(r)$, and we express the integral in eq. (6.64) in terms of gamma functions.

Writing the self-energy coefficient, $b^{\pm}_{\sigma}(r)$, in the form of eq. (6.77b), allows us to specify the precise values it may take. We obtain

$$b^{+}_{\uparrow} = b^{-}_{\downarrow} = 0, \quad b^{-}_{\uparrow} = \frac{b}{[1+\gamma]^2}, \quad b^{+}_{\downarrow} = \frac{b}{[1-\gamma]^2}, \tag{6.78}$$

where $b = [\alpha'(r)]^{-1}$. For the specific case of ph symmetry, the quantity $\gamma = 0$ and therefore from eq. (6.78), $b^{-}_{\uparrow} = b^{+}_{\downarrow} = b$. The spectral scaling function, eq. (6.72), then simply reduces to

$$\omega_*^r \pi D_{A\sigma}(\omega) \overset{\tilde{\omega}\to 0}{\sim} [1+\theta(-\sigma\tilde{\omega})b]|\tilde{\omega}|^r. \tag{6.79}$$

The full spin-independent spectral function can be determined via the average of the TSE spectral functions from eq. (3.13), i.e. $D(\omega) = \frac{1}{2}[D_{A\uparrow}(\omega) + D_{A\downarrow}(\omega)]$. In consequence, the asymptotic low-$\tilde{\omega}$ form of the LM phase scaling spectrum,

$\Psi^I_{LM}(\tilde{\omega}) \equiv \omega_*^r \pi D(\omega)$ is given by

$$\begin{aligned}\omega_*^r \pi \tfrac{1}{2}[D_{A\uparrow}(\omega) + D_{A\downarrow}(\omega)] &\overset{\tilde{\omega}\to 0}{\sim} \tfrac{1}{2}([1+\theta(-\tilde{\omega})b]|\tilde{\omega}|^r + [1+\theta(\tilde{\omega})b]|\tilde{\omega}|^r) \\ \Psi^I_{LM}(\tilde{\omega}) = \omega_*^r \pi D(\omega) &\overset{\tilde{\omega}\to 0}{\sim} [1+\tfrac{1}{2}b]|\tilde{\omega}|^r, \end{aligned} \tag{6.80}$$

which is independent of $\mathrm{sgn}(\tilde{\omega})$, as expected for $x = 0$ since $D(\omega)$ is an even function of ω (from eq. (4.3b)). Finally, by inserting the low-$\tilde{\omega}$ forms of the TSES, eq. (6.77a), into eq. (3.30) for the single-self-energy, a simple, if lengthy calculation shows that the low-$\tilde{\omega}$ scaling function has the form

$$\frac{1}{\omega_*^r}\,\Sigma^I(\omega) \overset{\tilde{\omega}\to 0}{\sim} a_s(r)|\tilde{\omega}|^{-r} = \frac{\cos^2(\frac{\pi}{2}r)}{[1+\frac{1}{2}b]}|\tilde{\omega}|^{-r}, \tag{6.81}$$

capturing the *exact* divergent low-$\tilde{\omega}$ form of eq. (4.33). Whilst both FLEX and the second-order self-consistent perturbation theory of the last chapter capture the diverging behaviour of $\frac{1}{\omega_*^r}\,\Sigma^I(\omega)$, since the FLEX TSEs vanish with the same power as the hybridization function, the coefficient is renormalized from its value at second-order level, given by eq. (5.26b). Furthermore, on multiplying eqs. (6.80-6.81) together we find that the spectral pinning condition for the LM phase, given exactly by eq. (4.38), and shown via NRG results in Fig. 4.7 holds at the FLEX level of approximation

$$\pi[1+\beta^2(r)]\Sigma^I(\omega)D(\omega) \overset{\tilde{\omega}\to 0}{\sim} 1 \qquad : x = 0, \tag{6.82}$$

where $\beta(r) = \tan(\frac{\pi}{2}r)$ as usual.

6.8.3 LM phase numerical procedure

We now proceed to a discussion of how the FLEX algorithm may be implemented in the LM phase, before proceeding to numerical results.

Symmetries

At ph symmetry, where $x = 0$, the symmetries of eqs. (4.3a-4.3c) give

$$\begin{aligned} G_{A\sigma}(\omega) &= -G_{A-\sigma}(-\omega), \qquad D_{A\sigma}(\omega) = D_{A-\sigma}(-\omega), \\ \Sigma_{A\sigma}(\omega) &= U - \Sigma_{A-\sigma}(-\omega), \qquad \Sigma^I_{A\sigma}(\omega) = \Sigma^I_{A-\sigma}(-\omega). \end{aligned} \tag{6.83}$$

By inserting the symmetry of the propagator into eq. (6.4) we obtain the symmetry relations for the bare polarization propagators

$${}^0\Pi^{++}_{AA}(\omega) = {}^0\Pi^{--}_{\bar{A}\bar{A}}(\omega) = {}^0\Pi^{PP}_{A\bar{A}}(\omega) = {}^0\Pi^{PP}_{\bar{A}A}(-\omega), \tag{6.84}$$

such that only ${}^0\Pi^{PP}_{AA}(\omega)$ and ${}^0\Pi^{+-}_{AA}(\omega)$ (${}^0\Pi^{-+}_{AA}(\omega) = {}^0\Pi^{+-}_{AA}(-\omega)$ from eq. (6.5)) need be calculated explicictly at a specific iteration.

Algorithm

Now that we have discussed the low-$\tilde{\omega}$ asymptotics in the LM phase, we proceed to consider how the general FLEX algorithm stated above in Section 6.3.3 may be implemented in practice. Our main target is to show that numerical self-consistent solutions are possible within FLEX for a finite local moment, $|\tilde{\mu}|$. Specifically we want to iterate within a TSE framework such that there is an $\omega = 0^+$ pole in $\mathrm{Im}\Pi^{+-}_{AA}(\omega)$, and thus the correct low-ω form of the TSEs (shown in Fig. 4.26 obtained from direct NRG calculations), are realized within the FLEX numerics.

The specific process is as follows: As in step (1) of the general algorithm, we initially fix U, r, $x = 0$, and 'seed' the process with a UHF spectral function, $D^{(1)}_{A\sigma}(\omega)$. The bare polarization propagators, ${}^0\Pi^{+-}_{AA}(\omega)$, ${}^0\Pi^{PP}_{AA}(\omega)$, are then calculated via steps (2) and (3) above. To guarantee a pole at the Fermi level in $\mathrm{Im}\Pi^{+-}_{AA}(\omega)$, at each iteration we set $U = [\mathrm{Re}{}^0\Pi^{+-}_{AA}(\omega = 0)]^{-1}$, such that U is not fixed to a specific value and 'flows' throughout the process. The TSEs, $\Sigma^I_{A\sigma}(\omega)$, are then calculated via step (5) above, specifically including the pole-band contribution to $\Sigma^{(PH)I}_{A\sigma}(\omega)$ (given by eq. (6.63b)). New spectral functions, $D_{A\sigma}(\omega)$, are then calculated, with the real part of the self-energy, $[\tilde{\Sigma}^R_{A\sigma}(\omega) - \tilde{\Sigma}^R_{A\sigma}(0)]$ determined from step (6). The renormalized levels, $\varepsilon^*_{A\sigma}$, given via eq. (6.71), are equal and opposite of each other at ph symmetry and thus only one needs to be explicitly calculated. This process, must then be repeated until U, and all functions of ω converge. The converged $D_{A\sigma}(\omega)$ and $\Sigma^I_{A\sigma}(\omega)$ are then outputted, and the SSE, $\Sigma(\omega)$, can then be calculated from the two self energies via eq. (3.30).

6.8.4 Methodology

Unfortunately, if the numerical algorithm is implemented in the way detailed above, we find that self-consistent solutions are not possible for any finite $|\tilde{\mu}|$. Fig. 6.13 shows how the numerical solution flows in the $(U, |\tilde{\mu}|)$ plane as the algorithm is implemented, with each point corresponding to a specific iteration number, n. The algorithm is started with a mean-field UHF solution that has a large $|\tilde{\mu}|$ (here $|\tilde{\mu}| \simeq 0.8$), and a $U/\pi = 10$. However, as the figure shows, we find that as the iteration number, n, increases, the local moment $|\tilde{\mu}| \to 0$ and $U \to U^+_c(r)$, such that the system converges to the QCP solution. We find that the poleweight, Q, also vanishes, as well as both the renormalized levels, $\varepsilon^*_{A\uparrow} = -\varepsilon^*_{A\downarrow}$. In other words, all of the spin-dependence in the propagators vanish as the algorithm is implemented and

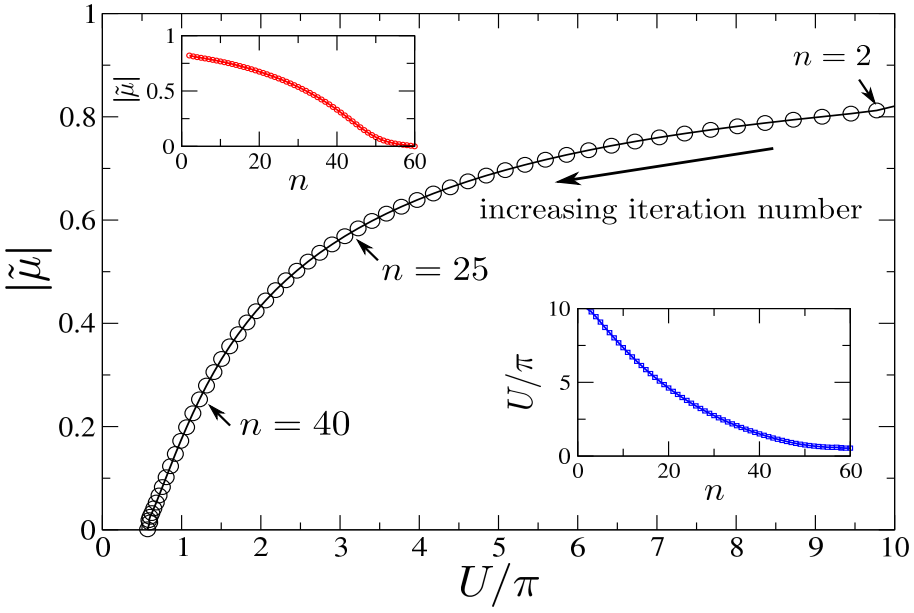


Figure 6.13: The main panel shows $|\tilde{\mu}|$ plotted versus U/π for $r = 0.4$, $x = 0$ as the algorithm is iterated. Each point corresponds to an iteration number. The top left inset shows $|\tilde{\mu}|$ plotted versus iteration number, n, converging to 0. The bottom right inset shows U/π plotted versus n, converging to $U_c(r)/\pi \simeq 0.5$.

$U \to U_c^+(r)$.[19]

From extensive calculations using the algorithm detailed above for the whole range of r, we conclude that a fully self-consistent numerical solution using broken-symmetry propagators is unfortunately not possible for any finite $|\tilde{\mu}|$ (such that $G_{A\sigma}(\omega) \neq G_{A-\sigma}(\omega)$). However, we may proceed by making a small modification to the purely *static* part of the self-energies, embodied by the renormalized levels, $\varepsilon^*_{A\sigma}$, as we now explain. Instead of working with the self-consistently determined value of the local moment, $|\tilde{\mu}|$, given by eq. (5.3b), we choose to replace it in the renormalized levels by another quantity, we denote $|\mu_0|$. The renormalized levels then become

$$\varepsilon^*_{A\sigma} = -\tfrac{U}{2}\sigma|\mu_0| + \tilde{\Sigma}_{A\sigma}(\omega = 0). \tag{6.85}$$

with $|\mu_0| \neq |\tilde{\mu}|$. In order that we continue to iterate such that there is a pole at located at $\omega = 0^+$ in $\mathrm{Im}\Pi^{+-}_{AA}(\omega)$, we vary $|\mu_0|$ at each iteration such that the condition $U\mathrm{Re}^0\Pi^{+-}_{AA}(\omega = 0) = 1$ is satisfied. The specific process is as follows: The spectral functions are determined via eq. (6.6b) with the renormalized levels given

[19] We may equally well choose to implement the FLEX algorithm in the same way as we did in the SSC phase, targeting a specific finite ω_*, and allowing the U to flow, such that the position of a low-ω resonance in $\mathrm{Im}\Pi^{+-}_{AA}(\omega)$ is fixed. However, by iterating in this way, the local moment, $|\tilde{\mu}|$, once again flows to zero, and the algorithm simply converges to a SSC solution, with $U < U_c(r)$.

by eq. (6.85) at each iteration. From these spectra the value of $U\mathrm{Re}^0\Pi^{+-}_{AA}(\omega = 0)$ is calculated. The quantity $|\mu_0|$ is then varied in $\varepsilon^*_{A\sigma}$, and inserted in the spectral functions, such that the condition $[U\mathrm{Re}^0\Pi^{+-}_{AA}(\omega = 0) = 1]$ is satisfied to high numerical accuracy at a given iteration. The TSE functions, $\Sigma_{A\sigma}(\omega)$, may then be calculated in the usual way as stated above.

Numerically we find that the modification of replacing $|\tilde{\mu}|$, by $|\mu_0|$ in the renormalized levels, means that $|\mu_0|$ vanishes at precisely the same $U = U^+_c(r)$, as $|\tilde{\mu}| \to 0$. Furthermore, we find that both $|\tilde{\mu}|$ and $|\mu_0|$ vanish at the same U coming from above as the SC low-energy scale, ω_m, vanishes from below. Thus, the quantum phase transition is described *coherently* coming from either phase. (This behaviour is in direct contrast to that of the second-order perturbative solutions of Chapter 5, where the low-energy scale only vanished coming from the LM side.)

Physically, the quantity, $|\mu_0|$, may be thought of as the local moment that is needed to negate the fact that we are not including all possible diagrams in our approximation for the skeleton expansion. It is our belief that if were possible to include all Feynman diagrams in the approximation to $\Sigma_{A\sigma}(\omega)$, then the *exact* result would have $|\mu_0| \equiv |\tilde{\mu}|$, and the whole numerical process would be *entirely* self-consistent.

6.8.5 Numerical results for the static quantities

We now move to discuss the numerical results from the LM algorithm stated above.

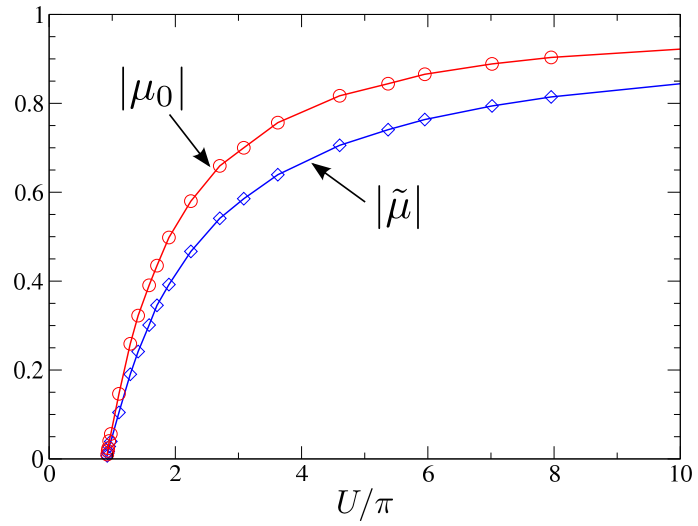


Figure 6.14: Converged self-consistently determined $|\tilde{\mu}|$ (blue-circles), and $|\mu_0|$ (red-diamonds) versus U/π for $x = \varepsilon + \frac{U}{2} = 0$ and $r = 0.35$, with $U_c(r)/\pi \simeq 0.9$.

Fig. 6.14 shows the local moment, $|\tilde{\mu}|$, calculated in the usual way from eq. (5.3b),

and $|\mu_0|$ for the converged FLEX LM solutions for a typical r $(= 0.35)$. As stated above, one can see that both quantities vanish at the same critical $U = U_c^+(r)$, which is also equal to the $U_c(r)$ at which the scale $\omega_m \equiv \omega_*$ vanishes in the SSC phase (as shown by the $r = 0.35$ curve in Fig. 6.8). Moreover, in the limit that $U/U_c \gg 1$, the local moment, $|\tilde{\mu}|$, approaches unity. By contrast, we find that it is possible for $|\mu_0|$ to take a value greater than 1, but this simply reflects the crude nature of the approximation of replacing $|\tilde{\mu}|$ by $|\mu_0|$ in eq. (6.85). We also note that in all cases, for $U > U_c(r)$, we find that $|\mu_0| > |\tilde{\mu}|$ (as shown in Fig. 6.14).

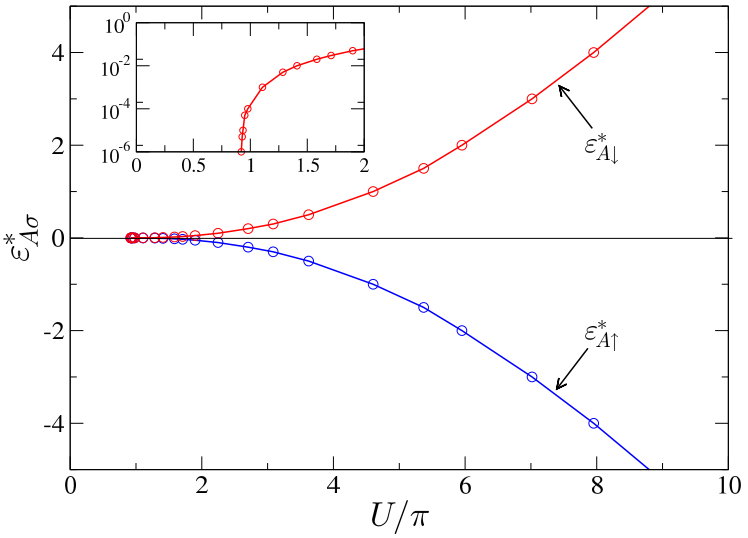


Figure 6.15: The renormalized levels, $\varepsilon^*_{A\uparrow}(< 0)$ (in blue), and $\varepsilon^*_{A\uparrow}(> 0)$ (in red) plotted versus U/π for $x = 0$ and $r = 0.35$. The inset shows the LM scale $\omega^r_* = \frac{1}{2}|\varepsilon^*_{A\uparrow} - \varepsilon^*_{A\downarrow}| = |\varepsilon^*_{A\sigma}(x = 0)|$ on a log-scale versus U/π. $(U_c/\pi \simeq 0.9)$.

The (sign-definite) renormalized levels, $\varepsilon^*_{A\uparrow}$, $\varepsilon^*_{A\downarrow}$, given via eq. (6.85), are shown in Fig. 6.15. The figure shows that the levels vanish very slowly as the QCP is approached. As a consequence, the low-energy scale $\omega^r_* = |\varepsilon^*_{A\downarrow}|$ is also found to vanish - $\omega^r_* \propto |1 - \frac{U}{U_c}|^{y(r)}$, with exponent, $y(r) > 1$. This behaviour is also consistent with what we find from NRG calculations, (as shown in Fig. 4.2 for a typical (r, x)). The inset of Fig. 6.15 shows $|\varepsilon^*_{A\uparrow}|$ on a log-scale confirming that it vanishes at the same $U_c(r)$ as $|\tilde{\mu}|$.

Furthermore, the local moments, $|\tilde{\mu}|$, obtained via eq. (5.3b), are shown in Fig. 6.16, calculated at the approximate levels of UHF and FLEX, together with numerically exact NRG. For small $(1 - U/U_c(r))$, such that the system is near the QCP, FLEX does not capture the correct $U_c(r)$ from NRG, or the correct power dependence $|\tilde{\mu}| \overset{U \to U_c^+}{\sim} |1 - U/U_c|^{z(r)}$ $(z(r) < 1)$. However, the FLEX data does fall onto the NRG curve remarkably well for $|\tilde{\mu}| \gtrsim 0.6$, and appears to become exact in the limit $U/U_c \gg 1$.

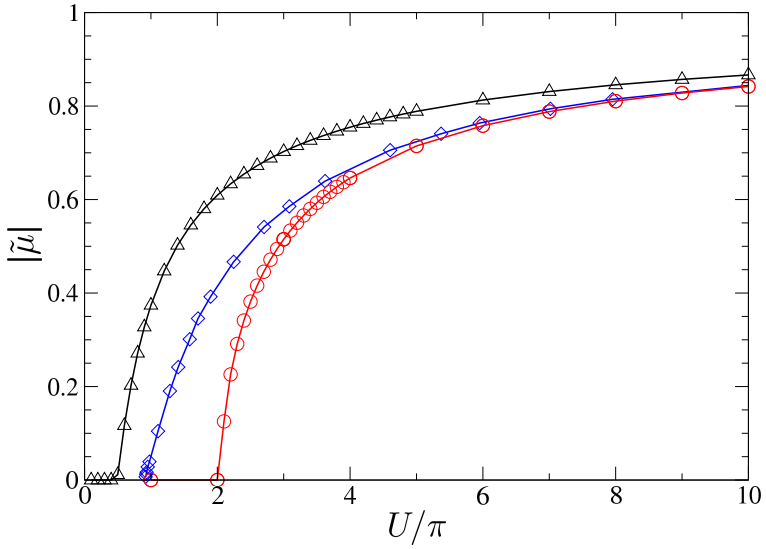


Figure 6.16: The local moment, $|\tilde{\mu}|$, plotted as a function of U/π for $r = 0.35$ and $x = 0$. Red-circles shows NRG calculations, blue-diamonds show FLEX calculations, and black-triangles show first-order UHF results.

6.8.6 Numerical results for the dynamics

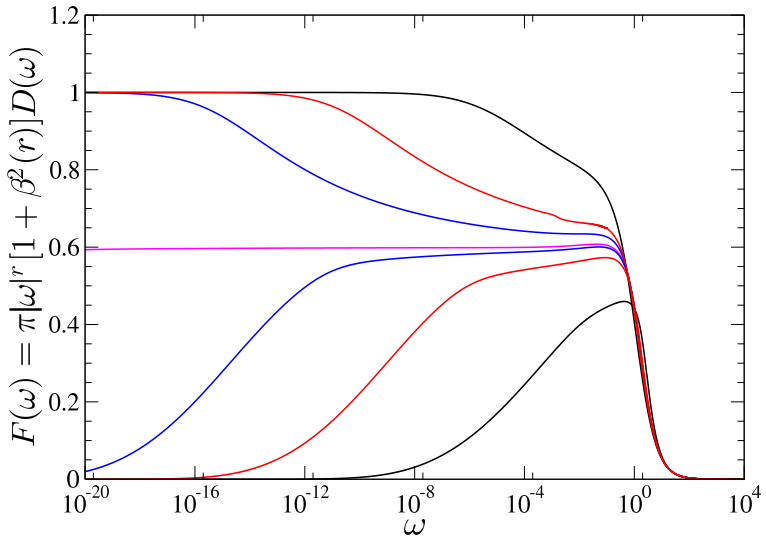


Figure 6.17: The modified spectra, $F(\omega)$, close to the QCP, where $U_c(r) \simeq 0.9$, coming from both phases versus ω on a log-scale for $r = 0.35$, $x = 0$. SC phase: black: $\omega_m = 10^{-4}$, red: $\omega_m = 10^{-6}$, blue: $\omega_m = 10^{-10}$. Magenta, is QCP spectra where the system is scale free. LM phase: blue: $\varepsilon^*_{A\sigma} = 10^{-8}$, red: $\varepsilon^*_{A\sigma} = 10^{-5}$, black: $\varepsilon^*_{A\sigma} = 10^{-2}$. At ph symmetry the LM low-energy scale is given by $\omega_* = |\varepsilon^*_{A\sigma}|^{\frac{1}{r}}$.

The modified spectral function, $F(\omega)$, is shown plotted versus ω in Fig. 6.17, coming from both sides of the transition for $r = 0.35$. As discussed in Section 6.6,

in the limit that $U \to U_c^{\pm}(r)$, the spectra collapse onto a single universal plateau value, $[1 - K(r)]$, given via eq. (6.48) (for $r = 0.35$, $[1 - K(r)] \simeq 0.6$). Away from criticality in the SSC phase, the spectra are pinned to unity, as is consistent with eq. (6.30b). In the LM phase by contrast, on multiplying both sides of eq. (6.80) by $[1 + \beta^2(r)]|\tilde{\omega}|^r$, the modified spectra vanish via

$$F(\omega) = \pi|\omega|^r(1 + \beta^2(r))D(\omega) \overset{\tilde{\omega}\to 0}{\sim} [1 + \tfrac{1}{2}b][1 + \beta^2(r)]|\tilde{\omega}|^{2r}. \tag{6.86}$$

This figure should be compared with the exact NRG calculations of Fig. 4.19, which shows $|\omega|^r \pi D(\omega)$ plotted versus ω either side of the transition at ph symmetry. The FLEX results of Fig. 6.17 essentially capture all of the main features of the exact case, predicting an r dependent plateau value for $\omega \gg \omega_*$ (that is the same coming from both unique phases). Furthermore, as stated above, FLEX correctly predicts the form of the $\omega \ll \omega_*$ behaviour in both SSC and LM phases.

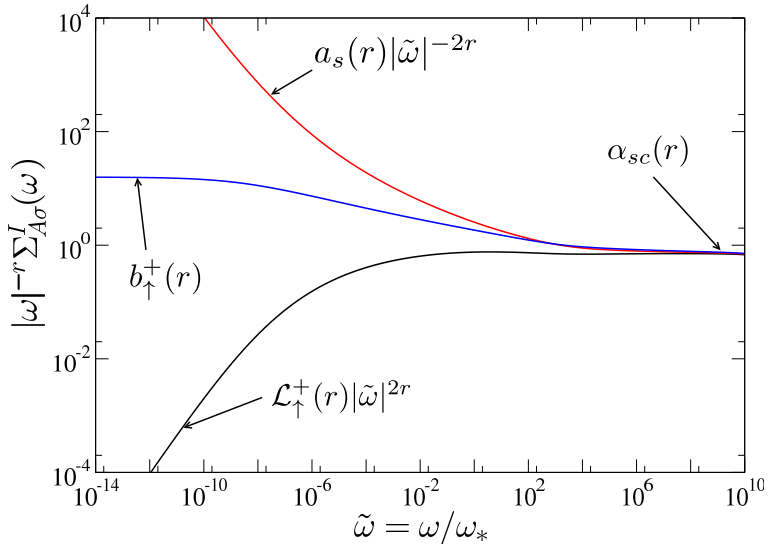


Figure 6.18: The LM phase self-energy scaling functions, $|\omega|^{-r}\Sigma^I_{A\sigma}(\omega)$ versus $\tilde{\omega}$ on a log:log plot for $r = 0.35$, $x = 0$. The TSE function, $|\tilde{\omega}|^{-r}\Sigma^I_{A\uparrow}(\omega)$ is shown in blue for $\tilde{\omega} < 0$ and black for $\tilde{\omega} > 0$. The SSE is shown in red (which is an even function of $\tilde{\omega}$). Both the large-$\tilde{\omega}$ spectral tails giving the QCP behaviour, and also the small-$\tilde{\omega}$ LM phase behaviour are shown.

The self-energy scaling functions for both the SSE and the TSEs (for $\omega \to 0^{\pm}$) are shown in Fig. 6.18. The high-$|\tilde{\omega}|$ tails of all three scaling functions reach the same plateau value as expected $|\omega|^{-r}\Sigma^I(\omega) \overset{|\tilde{\omega}|\gg 1}{\sim} \alpha_{sc}(r) = K(r)/[1 - K(r)]$, given by eq. (6.47c). In contrast for $|\tilde{\omega}| \ll 1$, the scaling functions give the characteristic behaviour of the LM phase. The SSE has the dependence, $|\omega|^{-r}\Sigma^I(\omega) \propto |\tilde{\omega}|^{-2r}$, as expected from eq. (6.81) (on multiplying both sides of the equation by $|\tilde{\omega}|^{-r}$). The low-$\tilde{\omega}$ form of the TSE scaling functions, $|\omega|^{-r}\Sigma^I_{A\uparrow}(\omega)$, which at ph symmetry

$= |\omega|^{-r}\Sigma^I_{A\downarrow}(-\omega)$ given via eq. (6.77a), are distinct depending on $\mathrm{sgn}(\tilde{\omega})$. In the limit that $\tilde{\omega} \to 0^+$, the self-energy scaling function has the dependence $|\omega|^{-r}\Sigma^I_{A\uparrow}(\omega) \propto |\tilde{\omega}|^{2r}$, whilst in contrast for $\tilde{\omega} \to 0^-$, $|\omega|^{-r}\Sigma^I_{A\uparrow}(\omega) \propto b(r)$. This low-$\tilde{\omega}$ single-sided behaviour has essentially the same form as found from the NRG calculations of Fig. 4.26.

To conclude this section, Fig. 6.19 shows $F(\omega)$, plotted versus ω on a linear scale for $U/\pi = 10$ and $r = 0.35$, calculated at second-order self-consistent level, FLEX and NRG. All three techniques exhibit high-energy Hubbard satellite peaks located approximately at $\omega \simeq \pm\frac{U}{2}$. The FLEX peaks are renormalized to approximately double the width of the second-order peaks, and show reasonably good agreement with the NRG peaks.[20] The inset shows the low-ω behaviour on a log:log plot; where all three spectra, $F(\omega) \propto |\omega|^{2r}$. The FLEX curve is much closer to the NRG curve than UHF as a consequence of the low-ω form of eq. (6.80).

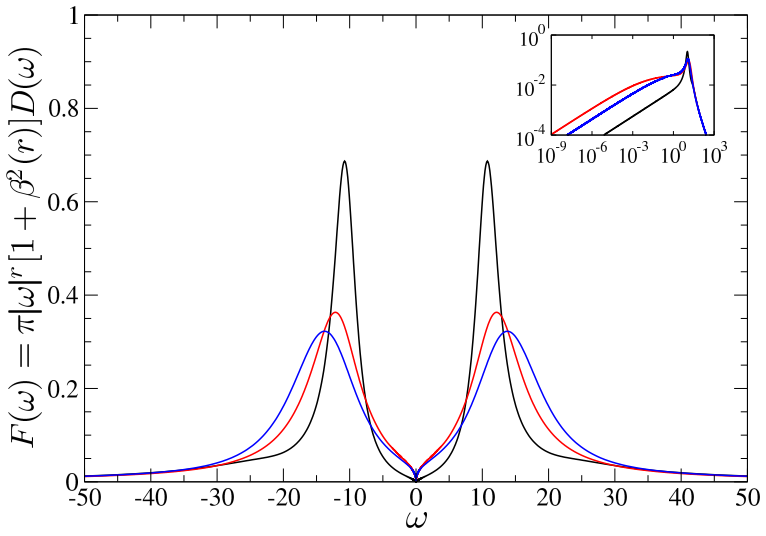


Figure 6.19: The modified spectral function, $F(\omega)$ is plotted versus ω deep in the LM phase for $U/U_c \gg 1$, $r = 0.35$, $x = 0$, $U/\pi = 10$. The red curve shows NRG data, blue is FLEX, and black is data from 2nd-order self-consistent perturbation theory. The inset shows the same data on a log:log plot.

6.9 Asymmetric strong coupling phase

Up until this point we have focused on the ph symmetric ($x = 0$) model. We now move to implement the FLEX approximation to the more general case of ph asymmetry, where $x = \varepsilon + \frac{U}{2} \neq 0$. We choose to fix $x < 0$, but propagators/self-energies for $x > 0$ can easily by obtained easily via the symmetries of eqs. (4.3a-4.3c).

[20] The reason for this broadening is discussed extensively in ref. [28].

For the ASC phase at zero-field, the propagators (and self-energies) are naturally spin-independent, i.e. $G_{A\sigma}(\omega) = G_{A-\sigma}(\omega) = G(\omega)$. However, they are not odd functions of ω as they were at ph symmetry. Furthermore, in contrast to the ph symmetric case, the local charge, $\bar{n}$, takes a non-integer value between 0 and 2 (for $x < 0$, $\bar{n}$ lies in the range $[1, 2]$, whereas for $x > 0$, $\bar{n}$ lies in the range $[0, 1]$). As a consequence, at each iteration of the numerical algorithm, $\bar{n}$ must be explicitly calculated (via eq. (5.3a)).[21] Moreover, the spin-independent renormalized level, ε^*, is always finite, given by

$$\varepsilon^* = \varepsilon + \Sigma^R(0) = x + \tfrac{U}{2}[\bar{n} - 1] + \tilde{\Sigma}^R(0). \tag{6.87}$$

where we have used $x = \varepsilon + \frac{U}{2}$ and expressed $\Sigma^R(0)$ via eq. (6.1).

Away from ph symmetry, the bare polarization propagators have the symmetries

$${}^0\Pi^{\sigma-\sigma}(\omega) = {}^0\Pi^{\sigma\sigma}(\omega) = {}^0\Pi(\omega) = {}^0\Pi(-\omega), \quad \text{but} \quad {}^0\Pi^{PP}(\omega) \neq {}^0\Pi(\omega) \tag{6.88}$$

The full polarization propagators, eqs. (6.3a-6.3c), then simply reduce to

$$\Pi^{PH}(\omega) = \frac{{}^0\Pi(\omega)}{1 - U\,{}^0\Pi(\omega)} \tag{6.89a}$$

$$\Pi^{PP}(\omega) = \frac{{}^0\Pi^{PP}(\omega)}{1 + U\,{}^0\Pi^{PP}(\omega)} - {}^0\Pi^{PP}(\omega) \tag{6.89b}$$

$$\Pi^{bub}(\omega) = \frac{1}{2}\left[\frac{{}^0\Pi(\omega)}{1 - U\,{}^0\Pi(\omega)} + \frac{{}^0\Pi(\omega)}{1 + U\,{}^0\Pi(\omega)}\right] - {}^0\Pi(\omega) \tag{6.89c}$$

Once again, as for the SSC phase, we define two new effective self-energies. Both $\Sigma'(\omega)$ and $\Sigma''(\omega)$ are defined in exactly the same way as eq. (6.23d) (with each self-energy defined by eq. (6.2)). $\Sigma'(\omega)$ is given by eq. (6.23a) involving an integral over $\Pi'(\omega) = \frac{3}{2}\Pi^{PH}(\omega)$, which has the 'RPA' form of eq. (6.89a). Within FLEX it is these diagrams which become critical as $U \to U_c(r)$. By contrast $\Sigma''(\omega)$ essentially includes all of the other non-critical contributions to $\tilde{\Sigma}(\omega)$.

6.9.1 Low-$\tilde{\omega}$ scaling behaviour

In this section we examine the low-$\tilde{\omega}$ scaling functions in the ASC phase, determining the precise coefficients of the leading behaviour at the FLEX level of approximation.

In order for the ASC phase to be described as a Fermi liquid within FLEX, the single self-energy must vanish with a power greater than the hybridization function. Hence, $\Sigma^I(\omega)$ must have the general Luttinger self-consistent form of eq. (4.68a), i.e. $\Sigma^I(\omega) \propto |\omega|^{2+3r}$ (which is the only self-consistent form where the power is greater

[21] The added complexity of calculating $\bar{n}$ at each iteration makes the numerical procedure for the ASC phase more unstable than for the SSC phase.

than r when $\varepsilon^* \neq 0$). As a consequence, the low-ω behaviour of the spectral function must be the same as eq. (4.72), i.e.

$$\pi D(\omega) \overset{\omega\to 0}{\sim} \frac{|\omega|^r}{[\varepsilon^*]^2}, \qquad \pi\omega_*^r D(\omega) \overset{\tilde{\omega}\to 0}{\sim} \frac{|\tilde{\omega}|^r}{(\varepsilon^*/\omega_*^r)^2} \tag{6.90}$$

where in the second expression, we have rescaled in terms of a low-energy Kondo scale, ω_* (which vanishes at the QCP as $U \to U_c^-(r)$). For FLEX to exhibit scaling in terms of $|\tilde{\omega}|$, the ratio $(\varepsilon^*/\omega_*^r)$ must remain finite, or in other words $\varepsilon^* \propto \omega_*^r$. As a consequence, the renormalized level must also vanish as the QCP is approached from below (from the NRG results of Fig. 4.2 we know this to be the case when the model is solved exactly).

On inserting the low-ω form of eq. (6.90) into eq. (6.8a), it is readily shown that $\mathrm{Im}^0\Pi(\omega)$ has the low-ω form

$$\mathrm{Im}^0\Pi(\omega) \overset{\omega\to 0}{\sim} \mathcal{A}_{ASC}(r)|\omega|^{1+2r}, \text{ with coefficient given by :} \tag{6.91a}$$

$$\mathcal{A}_{ASC}(r) = \frac{1}{\pi}\frac{1}{[\varepsilon^*]^4}\left[\frac{\Gamma(1+r)^2}{\Gamma(2+2r)}\right] = \frac{(\omega_*^r/\varepsilon^*)^4}{\pi\omega_*^{4r}}\left[\frac{\Gamma(1+r)^2}{\Gamma(2+2r)}\right] = \frac{1}{\omega_*^{4r}}\mathcal{A}'_{ASC}(r), \tag{6.91b}$$

such that we obtain the scaling form

$$\omega_*^{2r-1}\mathrm{Im}^0\Pi(\omega) \overset{\tilde{\omega}\to 0}{\sim} \mathcal{A}'_{ASC}(r)|\tilde{\omega}|^{1+2r}, \tag{6.91c}$$

where $\mathcal{A}'_{ASC}(r)$ is a scale-free coefficient. The low-ω form of the real part may then be determined via the Hilbert transform relation, eq. (6.10). It is readily shown to have the behaviour[22]

$$\omega_*^{2r-1}[\mathrm{Re}^0\Pi(\omega) - \mathrm{Re}^0\Pi(0)] \overset{\tilde{\omega}\to 0}{\sim} \tan(\pi r)\mathcal{A}'_{ASC}(r)|\tilde{\omega}|^{1+2r} \qquad : r < \tfrac{1}{2}, \tag{6.92}$$

vanishing with the same power as the imaginary part. In the following we focus on the $0 < r < \frac{1}{2}$ case, although it is equally possible to obtain relations for the range $\frac{1}{2} < r < 1$ (we do not consider this case explicitly for reasons of space).[23] Inserting this equation (for $\mathrm{Re}^0\Pi(\omega)$) together with eq. (6.91a) into eq. (6.89a), it follows that the low-ω behaviour of $\mathrm{Im}\Pi'(\omega)$ is given by

$$\mathrm{Im}\Pi'(\omega) \overset{\omega\to 0}{\sim} \frac{\frac{3}{2}\mathcal{A}_{ASC}(r)|\omega|^{1+2r}}{[1 - U\mathrm{Re}^0\Pi(0) - U\tan(\pi r)\mathcal{A}_{ASC}(r)|\omega|^{1+2r}]^2 + [U\mathcal{A}_{ASC}|\omega|^{1+2r}]^2}.$$

[22] The ω term in the Taylor expansion for $\mathrm{Re}^0\Pi(\omega)$ vanishes because in a SC phase ${}^0\Pi(\omega)$ is an even function (from eq. (6.88)). The leading low-ω behaviour of $\mathrm{Re}^0\Pi(\omega)$ may then be shown to vanish with the same exponent as the imaginary part, c.f. eq. (6.26).

[23] For $\frac{1}{2} \leq r < 1$ it is readily shown that $[\mathrm{Re}^0\Pi(\omega) - \mathrm{Re}^0\Pi(0)] \overset{\omega\to 0}{\sim} \mathcal{B}_{ASC}(r)\omega^2$, with $\mathcal{B}_{ASC}(r) = (\partial^2\mathrm{Im}^0\Pi(\omega)/\partial\omega^2)_{\omega=0}$.

This equation may be recast as

$$\mathrm{Im}\Pi'(\omega) \overset{\omega\to 0}{\sim} \frac{3\cos^2(\frac{\pi}{2}r)\omega_*^{2r-1}}{2U^2\mathcal{A}_{ASC}(r)}\left[\frac{|\tilde{\omega}|^{1+2r}}{1-2\sin(\pi r)|\tilde{\omega}|^{1+2r}+|\tilde{\omega}|^{2+4r}}\right], \tag{6.93}$$

where as usual $\tilde{\omega}=\omega/\omega_*$, with

$$\omega_m \equiv \omega_* = \left[\frac{[1-U\mathrm{Re}^0\Pi(0)]}{U\mathcal{A}_{ASC}(r)\sqrt{1+\tan^2(\pi r)}}\right]^{\frac{1}{1+2r}}, \tag{6.94}$$

such that the function in square brackets in eq. (6.93) has a peak maximum at $\tilde{\omega}=\pm 1$. Thus, in analogy with eq. (6.28b) (the low-energy scale for the SSC phase), we define the Kondo scale, ω_m, by the position of a low-ω resonance in $\mathrm{Im}\Pi'(\omega)$.

We now show explicitly that the scale, ω_* (defined as the peak maximum in $\mathrm{Im}\Pi'(\omega)$), is proportional to the renormalized level, $|\varepsilon^*|^{\frac{1}{r}}$. Fig. 6.20 shows a plot (obtained from the numerical algorithm) of $|\varepsilon^*|$ versus $\omega_m \equiv \omega_*$ for a particular r and x. The figure shows that for small values of the scale, the coefficient of proportionality is approximately 1 and thus we take $\omega_* = |\varepsilon_*|^{\frac{1}{r}}$ hereafter. As a consequence, by inserting this form into eq. (6.91b), eq. (6.94) becomes

$$\omega_m \equiv \omega_* = |\varepsilon^*|^{\frac{1}{r}} = \left[\frac{[1-U\mathrm{Re}^0\Pi(0)]}{U\mathcal{A}'_{ASC}(r)\sqrt{1+\tan^2(\pi r)}}\right]^{\frac{1}{1-2r}}. \tag{6.95}$$

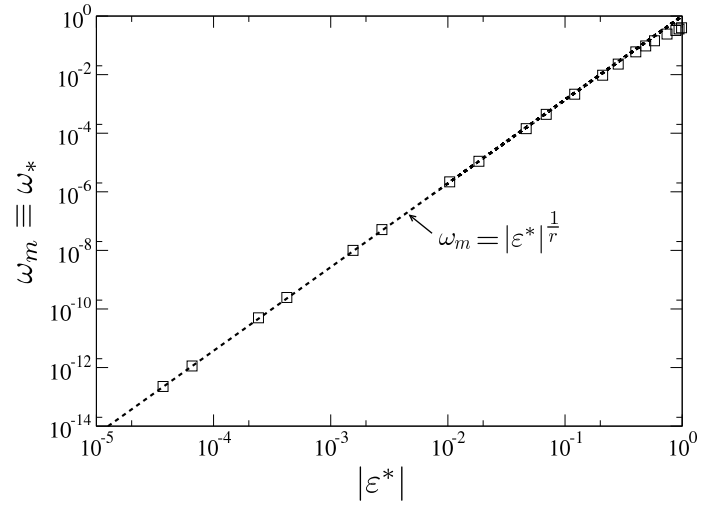


Figure 6.20: The scales: ω_m, defined by the position of the peak maximum in $\mathrm{Im}\Pi'(\omega)$ are plotted versus the renormalized level, $|\varepsilon^*|$ (shown with squares) on a log:log plot for $r=0.35$, $x=-1$. The dashed line shows $\omega_m = |\varepsilon^*|^{1/r}$.

Once again, as for the ph symmetric case of Section 6.5, as the QCP is approached and the low-energy scale vanishes, $\omega_* \to 0$, (and also the renormalized level) from

the numerator of the condition for the transition is that $U\mathrm{Re}^0\Pi(0) \to 1$. By rescaling eq. (6.93) (and taking the small-$|\tilde{\omega}|$ limit of the term in brackets), the low-$|\tilde{\omega}|$ scaling form of $\mathrm{Im}\Pi'(\omega)$ is given by

$$\omega_*^{1-2r}\mathrm{Im}\Pi'(\omega) \overset{\tilde{\omega}\to 0}{\sim} \frac{3}{2}\frac{\cos^2(\frac{\pi}{2}r)}{U^2\mathcal{A}'_{ASC}(r)}|\tilde{\omega}|^{1+2r}, \tag{6.96}$$

Finally, by inserting the low-$\tilde{\omega}$ functional form of eq. (6.96) together with eq. (6.90) into eq. (6.24a), the universal self-energy scaling function in the ASC phase is given by

$$\frac{1}{\omega_*^r}\,\Sigma'^I(\omega) \overset{\tilde{\omega}\to 0}{\sim} b_{ASC}(r)|\tilde{\omega}|^{2+3r}, \text{ with coefficient:} \tag{6.97a}$$

$$b_{ASC}(r) = \frac{3}{2}\cos^2(\tfrac{\pi}{2}r)\left[\frac{\Gamma(2+2r)^2}{\Gamma(1+r)\Gamma(3+3r)}\right]. \tag{6.97b}$$

In the scaling regime (where the limit that $\omega_* \to 0$ is considered), it is readily shown that the other self-energy contribution to $\tilde{\Sigma}(\omega)$, $\Sigma''(\omega)$ - defined by eq. (6.37), does not show universal scaling in the same way as $\Sigma'(\omega)$, and therefore for reasons of space we do not consider any further here. In other words, it is $\Sigma'(\omega)$ that shows critical behaviour as $U \to U_c^-(r)$, whereas $\Sigma''(\omega)$ does not.

6.9.2 Approaching the QCP

We now proceed to discuss the low-ω (high-$|\tilde{\omega}|$) behaviour as the QCP is approached from the ASC phase. Recall that from the arguments of Section 4.8 we find that precisely at the QCP the (spin-independent) spectral function has the form, $D(\omega) \overset{\omega\to 0}{\sim} C^{\pm}(r)|\omega|^{-r}$, with $C^{\pm}(r)$ a coefficient of $O(1)$, dependent on the low-ω form of the self-energy via eq. (4.86). At ph symmetry the spectrum, $D(\omega)$, is simply an even function of ω, and thus $C^+(r) = C^-(r) \equiv C(r)$ is guaranteed. However, we find from the detailed NRG calculations of Section 4.9 that regardless of the degree of ph symmetry, the leading coefficient is in fact the same coming from both sides of the Fermi level in all cases. Furthermore, both the symmetric QCP (SQCP) (approached for $x = 0$ in the range $0 < r < \frac{1}{2}$, and for $r < r_*$ for $x \neq 0$) and the asymmetric QCP (AQCP) (approached in the range $r_* < r < 1$ for $x \neq 0$) have a coefficient $C^{\pm}(r) \equiv C(r)$. The difference between the QCPs (in the range $r_* < r < \frac{1}{2}$ - where they coexist) lies in the precise values that the coefficients $C_s(r)$ and $C_a(r)$ take (as shown in Fig. 4.15). In other words, at both QCPs there is an emergent ph symmetry. We now examine whether this symmetry arises within the FLEX approximation by considering the high-$\tilde{\omega}$ scaling functions.

Once again, as for the ph symmetric case that we analysed in Section 6.6, within FLEX the QCP is captured by a 'dead' $\omega = 0$ pole in $\mathrm{Im}\Pi'(\omega)$. We initially assume

that the high-$|\tilde{\omega}|$ scaling forms of the self-energies in the SC phase have the same forms as eqs. (4.83a, 4.84a), given by

$$\frac{1}{\omega_*^r}\Sigma^I(\omega) \overset{|\tilde{\omega}|\gg 1}{\sim} [\theta(\tilde{\omega})\alpha_{sc}^+ + \theta(-\tilde{\omega})\alpha_{sc}^-]|\tilde{\omega}|^r, \tag{6.98}$$
$$\frac{1}{\omega_*^r}[\Sigma^R(\omega) - \Sigma^R(0)] \overset{|\tilde{\omega}|\gg 1}{\sim} -\tfrac{1}{2}|\tilde{\omega}|^r[\mathrm{sgn}(\omega)\beta(r)(\alpha_{sc}^+ + \alpha_{sc}^-) - \beta^{-1}(r)(\alpha_{sc}^+ - \alpha_{sc}^-)] + \ldots,$$

such that if $\alpha_{sc}^+ = \alpha_{sc}^-$, the $x = 0$ limit of eq. (6.44) is recovered. Thus, by inserting these forms, together with $\omega_*^{-r}\Gamma(\omega) = -\,\mathrm{sgn}(\tilde{\omega})[\beta(r) + i]|\tilde{\omega}|^r$, into eq. (6.6b), it is readily shown that we obtain the large-$|\tilde{\omega}|$ form

$$\Psi_{SC}^I(\tilde{\omega}) \equiv \omega_*^r \pi D(\omega) \overset{|\tilde{\omega}|\gg 1}{\sim} \frac{|\tilde{\omega}|^{-r}}{(1+\alpha_{sc}^{\pm})[1+[B^{\pm}(r)]^2]}, \tag{6.99}$$

where

$$B^{\pm}(r) = \pm\beta(r)\left[\frac{1+\frac{1}{2}(\alpha_{sc}^+ + \alpha_{sc}^-)}{(1+\alpha_{sc}^{\pm})}\right] - \frac{1}{\beta(r)}\left[\frac{\frac{1}{2}(\alpha_{sc}^+ - \alpha_{sc}^-)}{(1+\alpha_{sc}^{\pm})}\right], \tag{6.100}$$

such that the coefficient reduces to $B^{\pm}(r) = \pm\beta(r)$, if $\alpha_{sc}^+ = \alpha_{sc}^-$, and eq. (6.99) reduces to eq. (6.45). Thus, by inserting the scaling form of eq. (6.99) into eq. (6.8a), it follows that the polarization bubble has the dependence

$$\omega_*^{2r-1}\mathrm{Im}^0\Pi(\omega) \overset{|\tilde{\omega}|\gg 1}{\sim} [\theta(\tilde{\omega})\mathcal{A}_a^+(r) + \theta(-\tilde{\omega})\mathcal{A}_a^-(r)]|\tilde{\omega}|^{1-2r}, \tag{6.101a}$$

where

$$\mathcal{A}_a^{\pm}(r) = \left[\frac{\pi^{-1}}{(1+[B^+(r)]^2)(1+[B^-(r)]^2)(1+\alpha_{sc}^+)(1+\alpha_{sc}^-)}\right]\left[\frac{\Gamma(1-r)^2}{\Gamma(2-2r)}\right] \tag{6.101b}$$

such that $\mathcal{A}_a^{\pm}(r) = \mathcal{A}_a(r)$, is independent of $\mathrm{sgn}(\tilde{\omega})$.[24] The real part, $\mathrm{Re}^0\Pi(\omega)$, then has the form as eq. (6.40) (with $\mathcal{A}(r)$ replaced by $\mathcal{A}_a(r)$). Now, inserting these forms into eq. (6.11), together with recognising that as $U \to U_c(r)$, $U\mathrm{Re}^0\Pi(\omega) \to 1$, we obtain

$$\omega_*^{1-2r}\mathrm{Im}\Pi'(\omega) \overset{|\tilde{\omega}|\gg 1}{\sim} \frac{\cos^2(\pi r)}{U_c^2\mathcal{A}_a(r)}|\tilde{\omega}|^{2r-1}, \tag{6.102}$$

which has precisely the same form as the ph symmetric case, eq. (6.41), but with $\mathcal{A}(r)$ replaced by $\mathcal{A}_a(r)$. We note that the explicit pole contribution to $\mathrm{Im}\Pi'(\omega)$ is once again 'dead' as explained above in Section 6.6. Thus, by inserting eq. (6.102)

[24] In fact this symmetry is guaranteed by virtue of the fact that $\mathrm{Im}^0\Pi(\omega)$ is an even function from eq. (6.88), regardless of x.

and eq. (6.99) into eq. (6.24a) for the form of $\Sigma'^I(\omega)$, it is readily shown that

$$\tfrac{1}{\omega_*^r}\Sigma'^I(\omega) \overset{|\tilde{\omega}|\gg 1}{\sim} [\theta(\tilde{\omega})\alpha_{sc}^+ + \theta(-\tilde{\omega})\alpha_{sc}^-]|\tilde{\omega}|^r, \quad \text{or alternatively at the QCP:} \tag{6.103a}$$

$$\Sigma'^I(\omega) \overset{\omega\to 0}{\sim} [\theta(\omega)\alpha_{sc}^+ + \theta(-\omega)\alpha_{sc}^-]|\omega|^r \qquad : \omega_* = 0. \tag{6.103b}$$

(At the QCP (where $U = U_c(r)$) the high-$|\tilde{\omega}|$ behaviour persists all the way down to $\omega = 0$, such that the system is scale-free.) The coefficient values are given by

$$\alpha_{sc}^{\pm} = (1 + \alpha_{sc}^{\mp})\left[K(r)\frac{1 + [B^{\mp}(r)]^2}{1 + \beta^2(r)}\right]. \tag{6.104}$$

The function, $K(r)$, is given via eq. (6.47b), and as a consequence, the function in square brackets is positive for all r. This equation reduces to the ph symmetric case of eq. (6.47c), (where it can be written in closed form) if the coefficients for both $\omega < 0$ and $\omega > 0$ are equal ($\alpha_{sc}^+ = \alpha_{sc}^-$). However, in general from eq. (6.104), we must assume (as we indeed find numerically in the next section) that the coefficients α_{sc}^+, α_{sc}^- are distinct for arbitrary x.

To conclude this section we make some important comments. We have shown that FLEX predicts the correct non-trivial power dependence of the self-energy *self-consistently* at the QCP for *any* x, i.e. $\Sigma(\omega) \overset{\omega\to 0}{\propto} |\omega|^r$. However, for any non-zero x, as is also found from the local moment approach [34], we find that the coefficients of the self-energy given by eq. (6.104) are distinct, i.e. $\alpha_{sc}^+ \neq \alpha_{sc}^-$. As a consequence, FLEX effectively predicts a line of QCPs, each for a distinct x, with different values of $\alpha_{sc}^{\pm}$. The only case where the coefficients are equal is at ph symmetry where it is guaranteed by the symmetry of eq. (4.3b). Hence, the approximation used here fails to capture the emergent ph symmetry found from the exact results of Section 4.9.

6.9.3 Algorithm specifics

We now proceed to describing the specifics for implementing the FLEX algorithm described in Section 6.3.3, in the ASC phase approaching the QCP for $U \to U_c^-(r, x)$.

As our starting 'seed' solution we input a first-order Hartree spectral function, $\pi D^{(1)}(\omega) = [\omega^+ - \varepsilon^* - \Gamma(\omega)]^{-1}$, with $\varepsilon^* = \varepsilon + \Sigma^R(0) = x + \frac{U}{2}[\bar{n} - 1]$, for a fixed $x = \varepsilon + \frac{U}{2}$, an initial U, and a fixed r. The polarization propagators are then determined in exactly the same way as for the SSC phase as described in Section 6.7. By analogy with the $x = 0$ case, we choose to fix a low-energy scale, ω_m, and by rearranging eq. (6.95) we obtain

$$U = [\mathrm{Re}^0\Pi(0) + \omega_m^{1-2r}\mathcal{A}'_{ASC}(r)\sec(\pi r)]^{-1}, \tag{6.105}$$

such that we choose a new U at each iteration. Once again, we emphasize that this

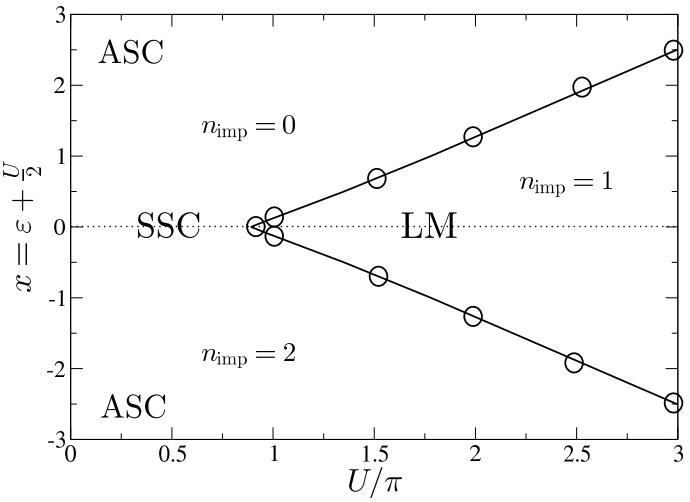


Figure 6.21: FLEX phase diagram: U_c/π versus x for $r = 0.35$. The phase boundary line is obtained coming from the asymmetric strong coupling side of the transition at the point at which ω_m vanishes.

particular process ensures that $U\mathrm{Re}^0\Pi(\omega) \leq 1$, and the analyticity of the polarization propagators are never violated. The SSE, $\tilde{\Sigma}^I(\omega)$, is then calculated numerically via eq. (6.1b) and $\tilde{\Sigma}^R(\omega)$ via eq. (6.13). A spectral function $D(\omega)$ is then determined via eq. (6.6b) from the new $\Sigma(\omega) = \varepsilon^* + [\tilde{\Sigma}(\omega) - \tilde{\Sigma}^R(0)]$. An added complexity is that the local charge, $\bar{n}$, must be calculated at each iteration via eq. (5.3a), to determine the corresponding $\varepsilon^* = x + \frac{U}{2}[\bar{n} - 1] + \tilde{\Sigma}^R(0)$. These steps are then repeated until U, and all functions of ω converge.

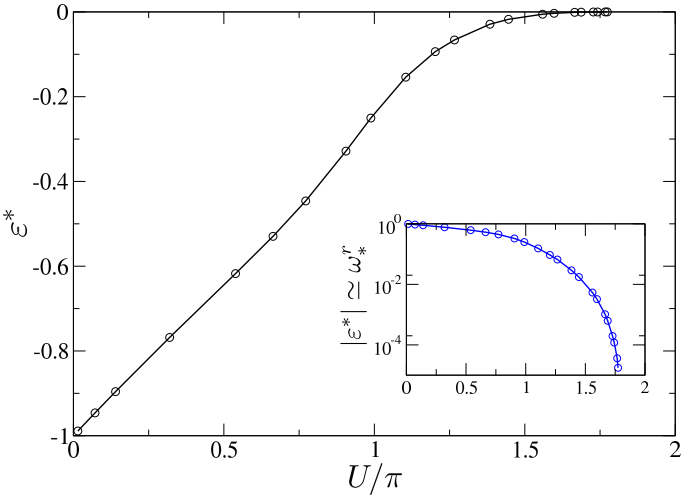


Figure 6.22: ε^* is plotted versus U/π in the ASC phase for $x = -1$ and $r = 0.35$. The inset shows $|\varepsilon^*|$ on a log-scale, again versus U/π.

6.9.4 Numerical results in the ASC phase

The phase diagram for general ph asymmetry is shown in Fig. 6.21, where $U_c(r, x)$ is plotted in the (U, x) plane for a fixed r. This figure was obtained by applying the algorithm explained above for different fixed ph asymmetries (parameterized by x).

In order to achieve stable convergence in as few iterations as possible, instead of using the Hartree spectral function, $D^{(1)}(\omega)$ as the input function, we choose to start with a previously converged FLEX solution as the input 'seed' for a slightly different U. In other words, by fixing the input scale, ω_m, and converging for an output U, and then using that solution as the input for a slightly smaller ω_m, we may progressively get closer to the QCP (where $U = U_c(r, x)$) in a stable manner (in as few iterations as possible). By proceeding in this way, we are able to achieve results down to a scale of $\omega_*^r \simeq |\varepsilon| \approx 10^{-5}$.

By contrast, if we simply input $\omega_m = 0$, such that from eq. (6.105), $U = [\mathrm{Re}^0\Pi(\omega = 0)]^{-1}$, and the renormalized level, ε^*, vanishes (via eq. (6.95)), the self-consistent procedure causes the solution to converge to the ph symmetric $U_c(r)$. This occurs because all of the ph asymmetry that enters the algorithm is embodied by the x that appears specifically in ε^*. In other words, if the renormalized level, ε^*, is set to zero, all spectral asymmetry in the functions is lost.

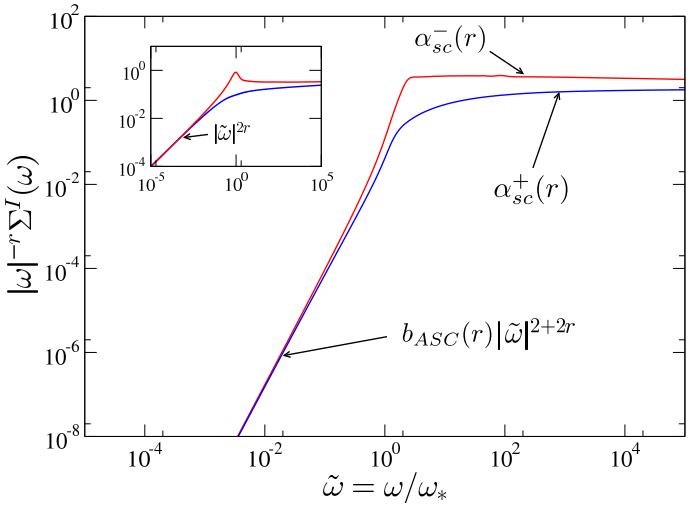


Figure 6.23: The self-energy scaling function, $|\omega|^{-r}\Sigma^I(\omega)$, versus $\tilde{\omega}$ on a log:log plot in the ASC phase for $r = 0.35$, $x = -1$. The inset shows the scaling spectrum, $|\tilde{\omega}|^r\Psi^I_{SC}(\tilde{\omega}) = |\omega|^r\pi D(\omega)$ versus $\tilde{\omega}$ on a log:log plot for the same parameters. Once again, the red curve shows data for $\tilde{\omega} < 0$, whereas blue shows $\tilde{\omega} > 0$.

Fig. 6.22 shows the renormalized level, ε^*, as a function of U for $x = -1$ and a typical r $(= 0.35)$. As one would expect, in the non-interacting limit the renormalized level goes to its 'bare' level value, i.e $\varepsilon^* = \varepsilon (= x = -1$ in this case). As U is increased, the magnitude of ε^*, $|\varepsilon^*| \simeq \omega_*^r$ vanishes at a particular $U = U_c$. By

contrast above this value of U, ASC solutions can no longer be found. The inset of Fig. 6.22 shows $|\varepsilon^*|$ vanishing on a log-scale as $U \to U_c(r,x)$, (in this particular case $U_c(r,x)/\pi \simeq 1.8$).

In Fig. 6.23 the self-energy scaling function $|\omega|^{-r}\Sigma^I(\omega)$ is shown plotted as an entire function of $\tilde{\omega}$ for the same r and x as considered above. The figure confirms the low-$\tilde{\omega}$ scaling behaviour of eq. (6.97a), i.e. $|\omega|^{-r}\Sigma^I(\omega) \propto |\tilde{\omega}|^{2+2r}$ (or equivalently $\omega_*^{-r}\Sigma^I(\omega) \propto |\tilde{\omega}|^{2+3r}$). The large-$|\tilde{\omega}|$ (QCP) behaviour is also shown. As mentioned above, the curves reach different plateau values, $\alpha_{sc}^{\pm}$, on each side of the Fermi level. The inset shows the spectral scaling function, $|\tilde{\omega}|\Psi_{SC}(\tilde{\omega}) = \pi|\omega|^r D(\omega)$, plotted as a function of $\tilde{\omega}$ over the whole range. For low-$\tilde{\omega}$ the function vanishes as $\pi|\omega|^r D(\omega) \propto |\tilde{\omega}|^{2r}$, with the behaviour of eq. (6.90). For large-$|\tilde{\omega}|$, the function reaches a plateau value with the form of eq. (6.99). The inset of the figure is the FLEX analogue of the exact NRG calculations for $|\tilde{\omega}|\Psi_{SC}(\tilde{\omega})$ shown on the LHS of Fig. 4.14. On comparison of the two, it may be seen that FLEX gets both the low-$\tilde{\omega}$ and high-$\tilde{\omega}$ behaviour qualitatively correct.

6.10 Local moment phase for general particle-hole asymmetry

6.10.1 Low-$\tilde{\omega}$ scaling behaviour

The low-$\tilde{\omega}$ results for the LM TSE scaling functions of Section 6.8.2 (eqs. (6.72-6.77)) hold generally in a LM phase away from ph symmetry. For $x \neq 0$, the renormalized level ratio, γ, given by eq. (4.22), is generically non-zero. Hence, by using $D(\omega) = \frac{1}{2}[D_{A\uparrow}(\omega) + D_{A\downarrow}(\omega)]$ and combining the broken-symmetry spectral functions of eq. (6.72), it is readily shown that the LM spectral scaling function has the low-$\tilde{\omega}$ form

$$\Psi^I_{LM}(\tilde{\omega}) \equiv \omega_*^r \pi D(\omega) \overset{\tilde{\omega}\to 0}{\sim} \frac{[1+a_a^{\pm}]}{[\gamma - \frac{1}{\gamma}]^2}|\tilde{\omega}|^r. \tag{6.106}$$

The low-$\tilde{\omega}$ SSE scaling function is then obtained by inserting eq. (6.77a) into eq. (3.30). Some straightforward, if lengthy algebra shows that the SSE has the general scaling form

$$\frac{1}{\omega_*^r}\,\Sigma^I(\omega) \overset{\tilde{\omega}\to 0}{\sim} a_a^{\pm}|\tilde{\omega}|^r, \tag{6.107a}$$

with leading coefficient given by

$$a_a^{\pm} = \tfrac{1}{\gamma^2}[1 + \tfrac{1}{2}(b_\uparrow^{\pm} + b_\downarrow^{\pm})] + \tfrac{1}{\gamma}[b_\uparrow^{\pm} - b_\downarrow^{\pm}] + \tfrac{1}{2}(b_\uparrow^{\pm} + b_\downarrow^{\pm}). \tag{6.107b}$$

Furthermore, away from ph symmetry the FLEX coefficients $b_\uparrow^-$ and $b_\downarrow^+$ are distinct given via eq. (6.78) (whilst $b_\uparrow^+, b_\downarrow^- = 0$). On insertion of these forms into eq. (6.107b)

it follows that

$$\begin{aligned} a_a^{\pm} &= \frac{b}{2}\left[\frac{1}{[1\mp\gamma]^2}\right]\left[\frac{1}{\gamma^2}\mp\frac{2}{\gamma}+1\right]+\frac{1}{\gamma^2} \\ &= \frac{1}{\gamma^2}\left[1+\frac{b}{2}\right], \end{aligned} \tag{6.108}$$

and therefore $a_a^+ = a_a^- = a_a$. The coefficient is independent of $\mathrm{sgn}(\tilde{\omega})$, indicating an *emergent* ph symmetry in the LM phase within FLEX. As a consequence, the precise form of eq. (6.106) is the same as the *exact* behaviour of eq. (4.31b), showing that the correct low-$\tilde{\omega}$ asymptotics in a LM phase are captured within the FLEX approximation.[25]

6.10.2 Numerical implementation and algorithm

In the LM phase for $x \neq 0$, implementation of the FLEX algorithm becomes much more challenging by virtue of the fact that there are no explicit symmetries of the propagators that allow the algorithm explained in Section 6.3.3 to be simplified.

Once again, as for the ph symmetric case of Section 6.8, we iterate such that there is a $\omega = 0^+$ pole in $\mathrm{Im}\Pi_{AA}^{+-}(\omega)$, with weight, Q. We use the same technique to 'pin' the pole to the Fermi level, varying $|\mu_0| \neq |\tilde{\mu}|$ at each iteration, such that $U\mathrm{Re}^0\Pi_{AA}^{+-}(0) = 1$ is satisfied to high numerical accuracy. The TSEs, $\Sigma_{A\sigma}(\omega)$, are then calculated in the same way as before, explicitly including the contribution from the pole in $\mathrm{Im}\Pi_{AA}^{+-}(\omega)$ (eq. (6.63b)). Generally, the LM phase renormalized levels, $\varepsilon_{A\uparrow}^*$, $\varepsilon_{A\downarrow}^*$, are given by

$$\varepsilon_{A\sigma}^*(x) = x + \tfrac{U}{2}[\bar{n}-1] - \sigma\tfrac{U}{2}|\mu_0| + \tilde{\Sigma}_{A\sigma}^R(\omega=0). \tag{6.109}$$

Since each level is distinct, we must calculate both explicitly at each iteration (with the local charge, $\bar{n}$ given by eq. (5.3a)).

6.10.3 Numerical results

Using the FLEX algorithm as detailed above, it is possible to obtain converged LM solutions for $G_{A\sigma}(\omega)$, with a pair of (sign-definite) renormalized levels ($\varepsilon_{A\uparrow}^* < 0$, $\varepsilon_{A\downarrow}^* > 0$). However, as we explain below, in contrast to the results at ph symmetry, we find that the local moment $|\mu_0|$ (and $|\tilde{\mu}|$) *does not* vanish at the $U_c(r,x)$, where the scale, $\omega_m \equiv \omega_*$, vanishes coming from the ASC phase.

Specifically, it is possible to obtain converged LM solutions far from the transition where the scale ω_* is large (such that $|1 - U/U_c| \gg 1$), and the local charge $\bar{n}$ is close to unity. We then use a converged FLEX propagator, $G_{A\sigma}(\omega)$, as the 'seed'

[25] The precise values that γ and b take are determined self-consistently at the FLEX level of approximation.

solution for a slightly smaller value of the scale, ω_*. In this way it is possible to obtain convergence as the scale is progressively lowered as $U_c(r,x)$ is approached.[26]

Fig. 6.24 shows the scale, ω_*, coming from both phases for $x=0$ and $x=-1$.[27] In the ph symmetric case, numerically we achieve values of the scale down to $\omega_* \simeq 10^{-18}$ (where $|\varepsilon^*_\sigma| \simeq 10^{-7}$). The figure shows that the scales vanish at precisely the same $U = U_c(r, x=0)$ coming from both sides. By contrast, in the asymmetric case we achieve convergence for scales down to $\omega_* \approx 10^{-10}$. The figure shows that it is possible to obtain LM solutions for $U < U_c(r,x)$ (where $U_c(r,x)$ is defined as the point at which the ASC phase scale vanishes). Furthermore, the inset of Fig. 6.24 shows the converged local moments, $|\tilde{\mu}|$ and $|\mu_0|$ as a function of U/π. Whilst at ph symmetry, both $|\tilde{\mu}|$ and $|\mu_0|$ vanish as $U \to U_c^+(r)$, for $x=-1$ we find that the moments are still large and finite, *even* when the scale is tiny - $\omega_* \approx 10^{-10}$.

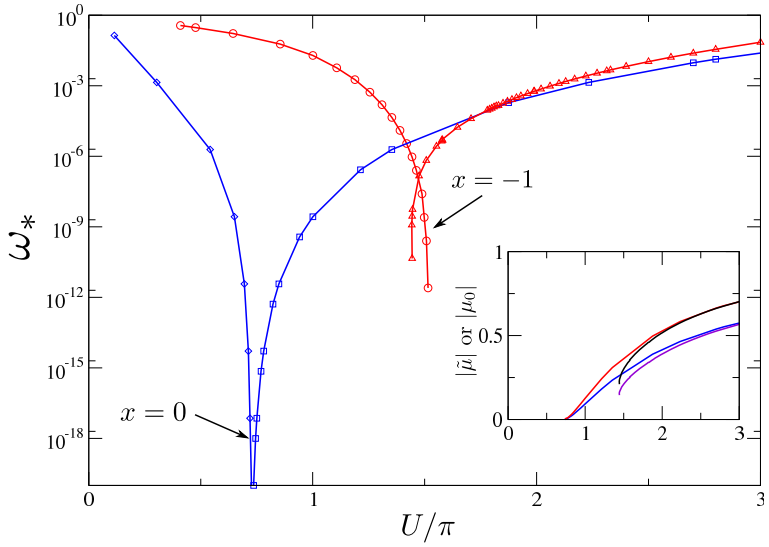


Figure 6.24: The low-energy scale, ω_*, is plotted versus U/π coming from both phases for $x=0$ and $x=-1$, each for $r=0.35$. In the LM phase the scale is given by $\omega_* = \frac{1}{2}|\varepsilon_{A\uparrow} - \varepsilon_{A\downarrow}|^{1/r}$, whereas in the SC (both SSC and ASC) phase $\omega_* = \omega_m$. The inset shows the local moments, $|\tilde{\mu}|$ and $|\mu_0|$ plotted versus U/π for the same parameters. The local moment, $|\tilde{\mu}|$, is plotted with a blue line for $x=0$ and a violet line for $x=-1$. The moment, $|\mu_0|$ is plotted with a red line for $x=0$ and a black line for $x=-1$.

The added complexity comes from having to explicitly calculate the local charge, $\bar{n}$, via eq. (5.3a) at every iteration. This, together with the already crude approximation of replacing $|\tilde{\mu}|$ by $|\mu_0|$ in $\varepsilon^*_\sigma(h)$, makes describing the QCP unfeasible within the self-consistent algorithm. It may be possible to introduce another parameter, $\bar{n}_0$, replacing $\bar{n}$ in eq. (6.109). Both $|\mu_0|$ and $\bar{n}_0$ could then be varied in such a way

[26] Care must be taken to ensure that the signs of the renormalized levels do not change at any point of the numerical process, if they do then the algorithm quickly becomes unstable.

[27] In this figure for simplicity we choose to only include the transverse spin channel diagrams in the approximation to the dynamical self-energy, such that $\tilde{\Sigma}_{A\sigma}(\omega) = \Sigma^{PH}_{A\sigma}(\omega)$.

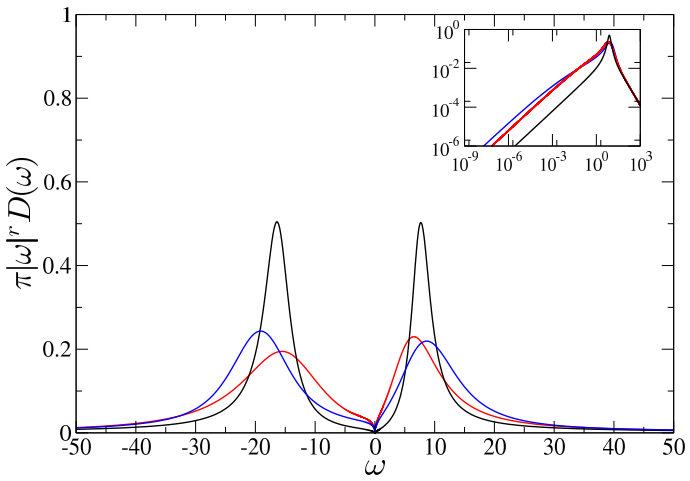


Figure 6.25: Asymmetric LM phase: $|\omega|^r \pi D(\omega)$ versus ω for $r = 0.35$, $x = -5$, $U/\pi = 10$. NRG is shown in red, FLEX is shown in blue, UHF is shown in black. Deep in the LM phase (FLEX $|\tilde{\mu}| \sim 0.84$). The inset shows same data on a log:log plot (for $\omega > 0$) to show the low-ω behaviour.

so that the condition $U\mathrm{Re}\Pi^{+-}_{AA}(0) = 1$ is met. However, we do not consider this approximation any further here.

As alluded to above, away from ph symmetry it is known that charge fluctuations become more important to the underlying physics of the Anderson model [2]. Since FLEX breaks down in describing the transition coherently from both phases, we argue that more diagrams are needed in the approximation to the skeleton expansion to capture the correct underlying behaviour.

In contrast to the limiting behaviour as the QCP is approached, deep in the LM phase, where $|1 - U/U_c| \gg 1$, the local charge $\bar{n}$ approaches unity, and stable LM solutions may be obtained with $|\mu_0| \neq |\tilde{\mu}|$. Fig. 6.25 shows, $\pi|\omega|^r D(\omega)$ versus ω for a typical r and $x < 0$. First-order mean-field theory is shown, together with results from FLEX and NRG. The figure shows that FLEX does remarkably well in this large U limit - the spectra on large energy scales look very similar to the corresponding NRG data. FLEX does much better at capturing the broadening of the Hubbard satellite peaks (occurring at $\omega \simeq \varepsilon$ and $\omega \simeq \varepsilon + U$) than the first-order approximation. The inset shows the low-ω behaviour of the same data on a log:log plot, showing that the FLEX-$|\omega|^r$ dependence (given via eq. (6.106)), and the NRG curve are very similar.

6.11 Finite field effects

We now discuss briefly the case where there is a local field, h, on the impurity level within FLEX. We refer back to the exact finite-field results of Section 4.10 at various

points in the discussion.

At finite-field the renormalized level becomes[28]

$$\varepsilon^*_\sigma(h) = \varepsilon - \sigma h + \tfrac{U}{2}[n(h) - \sigma m_0(h)] + \Sigma^R_\sigma(\omega = 0; h), \tag{6.110}$$

where $m_0(h) = m(h) + [|\mu_0| - |\tilde{\mu}|]$, and we also add an explicit Zeeman term, $-\sigma h$. The local magnetization, $m(h)$, and charge, $n(h)$, are defined via eqs. (3.3a-3.3b) respectively. The quantity $m_0(h)$ is chosen in this way such that the zero-field limit in the LM phase is captured correctly within the approximation as $h \to 0^+$, and $\lim_{h\to 0^+}[m_0(h)] = |\mu_0|$. For $U > U_c(r)$, as $h \to 0^+$, the renormalized levels vanish to give, $\varepsilon^*_\sigma(h) \to \varepsilon^*_{A\sigma}(0)$, and $U\mathrm{Re}\Pi^{+-}(0, h \to 0^+) \to 1$. By contrast, for $U < U_c(r)$, as $h \to 0^+$, $\varepsilon^*_\sigma(h) \to \varepsilon^*(0)$, i.e. the level is spin independent with $m_0(h = 0) = |\mu_0| = 0$.

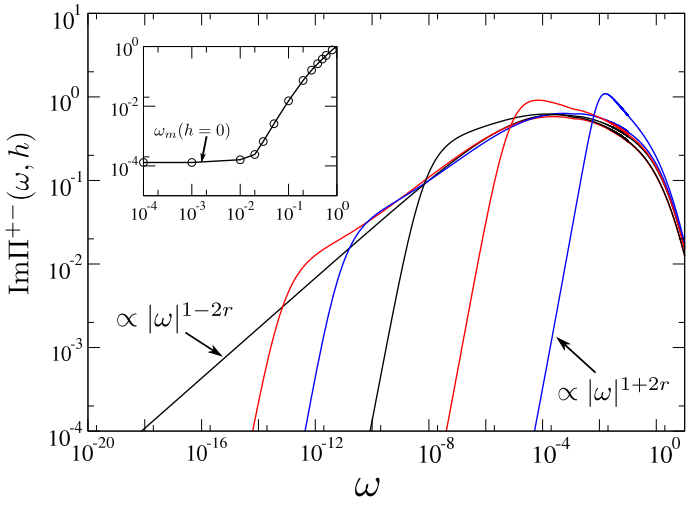


Figure 6.26: The transverse spin polarization propagator, $\mathrm{Im}\Pi^{+-}(\omega, h)$, plotted versus ω (with both on log-scales) for different local fields with $r = 0.35$, $U/\pi = 0.5$ and $x = 0$. Results are plotted from left to right for $h = 0$, 10^{-6}, 10^{-4}, 10^{-3}, 10^{-2}, 10^{-1}. The inset shows the Kondo scale, $\omega_m \equiv \omega_*$ (here $\omega_m \simeq 10^{-4}$), defined as the position of the peak maximum in $\mathrm{Im}\Pi^{+-}(\omega, h)$, versus h.

In agreement with the exact results of Section 4.10, within FLEX we find that for any finite h, the local magnetization, $m(h)$ (and also, $m_0(h)$), is non-zero for any U. In a zero-field SC (either SSC or ASC) phase, where $|\mu_0| = |\tilde{\mu}| = 0$, the effect of a finite local field, h, is to break the spin symmetry of the propagators. The finite-ω resonance located at $\omega = \omega_m$ in $\mathrm{Im}\Pi^{+-}(\omega, h = 0)$ moves from $\omega_m(h = 0) \to \omega_m(h = 0) + \beta h$, where β is a coefficient of $O(1)$. This behaviour is shown Fig. 6.26, where $\mathrm{Im}\Pi^{+-}(\omega, h)$ is plotted versus ω for a range of fields. At zero-field $\mathrm{Im}\Pi^{+-}(\omega, h = 0) \equiv \mathrm{Im}\Pi^{PH}(\omega) = \frac{2}{3}\mathrm{Im}\Pi'(\omega)$ has the low-ω behaviour of eq. (6.28a) as indicated. By contrast for $h \gg \omega_*(h = 0)$, $\mathrm{Im}\Pi^{+-}(\omega, h) \propto |\omega|^{1+2r}$ has the low-ω

[28] Any explicit A labeling may be dropped at finite field. For $h > 0$ and $U > U_c(r)$, $\varepsilon^*_\sigma(h) \equiv \varepsilon^*_{A\sigma}(|h|)$.

behaviour of eq. (6.93) (with ε^* replaced by $\varepsilon^*_\sigma(h)$ in $\mathcal{A}_{ASC}(r)$). The inset shows the scale, $\omega_m(h)$ versus h, displaying the behaviour stated above.

Recall that in a LM phase, the effect of any finite infinitesimal field, $h = 0^\pm$, is to break the spin degeneracy of the A and B states. If $h > 0$, then the A state is favoured, whereas if $h < 0$ then the B state is picked out. Within FLEX, the effect of this is embodied in the fact that the 'spin-flip' pole located in $\mathrm{Im}\Pi^{\sigma-\sigma}_{AA}(\omega)$ at the Fermi level, moves to finite-ω for any finite h. The scale at which this occurs is linear in the field, $\omega_*(h) \propto \beta h$.

As a consequence of the fact that the degeneracy of the LM phase is lifted, the QCP is strictly destroyed for any finite h. The QCP is characterized within FLEX by a 'dead' $\omega = 0$ pole in $\mathrm{Im}\Pi^{+-}_{AA}(\omega)$, with vanishing renormalized levels, $\varepsilon^*(0) = \varepsilon^*_{A\sigma}(0) = 0$. Once again (as for the LM phase), on application of a field we find that the pole moves to become a resonance at finite-ω and the renormalized levels, given via eq. (6.110) become finite and distinct. Thus, the physical picture is that for any finite h, the system for all U is perturbatively connected to the non-interacting limit. The propagators and self-energies have the self-consistent low-ω forms as described in Section 4.10, i.e. $D_\sigma(\omega, h) \propto |\omega|^r$, via eq. (4.99b), and $\Sigma_\sigma(\omega, h) \propto |\omega|^{2+3r}$, via eq. (4.99a).

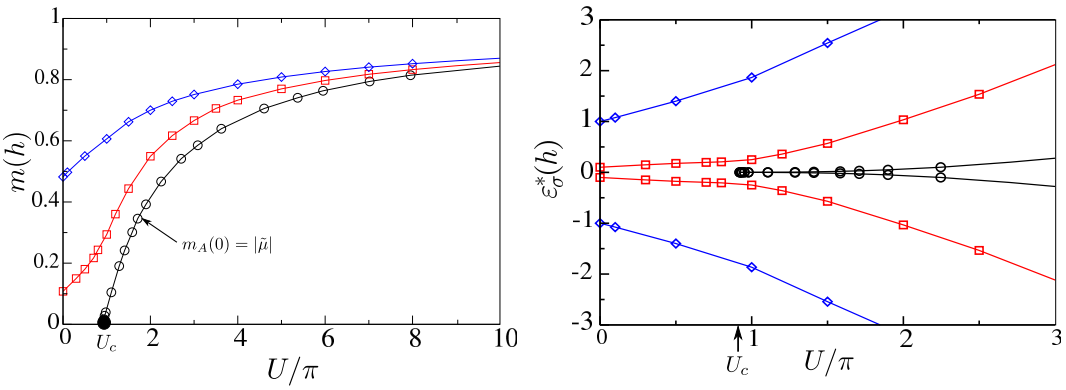


Figure 6.27: LHS: The local magnetization, $m(h)$, plotted versus U/π for different h, with $r = 0.35$, $x = 0$. The black curve shows $h = 0$, the red curve shows $h = 0.1$, and the blue curve shows $h = 1$. RHS: The renormalized levels, $\varepsilon_\sigma(h)$, are plotted versus U/π for the same parameters (with $\varepsilon^*_\uparrow(h) < 0$ and $\varepsilon^*_\downarrow(h) = -\varepsilon^*_\uparrow(h) > 0$).

The finite-h physics is embodied by the LHS of Fig. 6.27, which shows the local magnetization, $m(h)$, as a function of U for different local fields at ph symmetry. For $h = 0$, the local order parameter, $m_A(0) \equiv |\tilde{\mu}|$, vanishes as $U \to U_c^+(r)$. By contrast, for $h > 0$, $m(h)$ does not vanish for any U. The picture here is essentially the same as that found from the exact numerical calculations of Fig. 4.25. Moreover, the RHS of Fig. 6.27 shows the renormalized levels, $\varepsilon^*_\sigma(h)$ as a function of U. At $h = 0$, both levels $\varepsilon^*_\sigma(h = 0^+) \equiv \varepsilon^*_{A\sigma}(0)$ vanish as $U \to U_c^+(r)$. By contrast, for any

finite-field, the levels are finite (and of opposite sign for $x = 0$) for all finite h.

Away from ph symmetry, as explained in Section 4.10, the renormalized levels, $\varepsilon^*_\sigma(h)$, are not in general sign-definite. In consequence, one of them may cross the Fermi level at a finite (h, U). This leads to a simple level crossing transition as discussed extensively in text leading to eq. (4.100). However, for reasons of space we do not focus on this point any further here.

6.12 Excess quantities

As stated above, FLEX is a conserving approximation [66, 67], with the self-energy in each phase being obtained as a functional derivative of the Luttinger-Ward functional, Φ_{LW} with respect to the appropriate propagator in each phase. Since the self-energies are obtained in this way, the general arguments for the vanishing of the Luttinger integrals, I_{L_σ} for $U < U_c(r)$ given by eq. (3.50), and $I_{L_{A\sigma}}$ for $U > U_c(r)$, given by eq. (3.55), hold at the FLEX level of approximation.

We have explicitly calculated each of the Luttinger integrals from the FLEX converged propagators and self-energies. We can confirm that in both (zero-field) cases the Luttinger integrals, $I_{L_\sigma}(0)$, $I_{L_{A\sigma}}(0)$, vanish as expected.[29] By contrast, in the LM phase at zero-field where $\Sigma_\sigma(\omega)$ and $\Sigma_{A\sigma}(\omega)$ are in general distinct, we have also explicitly calculated the Luttinger integral (in terms of the SSE), eq. (3.75), finding

$$I_L(h = 0) = \tfrac{\pi}{2}\,\mathrm{sgn}(x), \tag{6.111}$$

which has the same form as found from the exact phase-shift arguments of Section 4.4 via eq. (4.17).

The excess charges, $n_{\mathrm{imp};\sigma}(h)$ and $n_{\mathrm{imp};A\sigma}(|h|)$, may also be determined in each phase from an integral over the appropriate excess density of states via eq. (3.38). On numerical calculation of these quantities we find that all results are consistent with the exact relations of the Friedel sum rules for both $U > U_c(r)$ and $U < U_c(r)$ given by eqs. (4.7-4.8). The zero-field phase diagram, Fig. 6.21, shows the calculated values of $n_{\mathrm{imp}}(0)$ for the different phases as a function of x. The picture here is essentially the same as that obtained from NRG in Fig. 4.4.

6.13 Concluding remarks

In this chapter we have used local broken-symmetry propagators, $G_{A\sigma}(\omega)$, within the FLEX [69–72] (conserving) approximation to investigate the distinct phases of the PAIM, and the QCP between them.

[29] The finite-field Luttinger integral, $I_{L_\sigma}(h)$, is also found to vanish in all cases.

The two different phases of the model and scaling behaviour near the QCP were examined both at particle-hole symmetry and more general $x \neq 0$ case. Analytical results were obtained for the scaling behaviour of the propagators and self-energies in each phase. We find that the non-trivial *interacting* nature of the QCP is captured within FLEX by an $\omega = 0$ 'dead' pole in the polarization propagator, $\mathrm{Im}\Pi^{+-}_{AA}(\omega)$. Moreover, infinite-order Luttinger self-consistency arguments also suggest that the same propagator has a pole at $\omega = 0^+$ in the doubly degenerate LM phase, but with a finite weight, Q. This form of Luttinger self-consistency, distinct from the order by order analysis of Section 4.6, predicts the low-ω behaviour of the zero-field TSEs, known from the NRG results of Fig. 4.26 ($\Sigma^I(\omega) \propto |\omega|^r$).

Numerically, we were able to model the QCP with self-consistent solutions coming from both phases at ph symmetry (with a small modification to the static part of the self-energy in the LM phase). In contrast, away from ph symmetry for the more general $x \neq 0$ model, the FLEX algorithm is more challenging to implement. We were successful in describing the ASC phase as the QCP is approached from below. However, whilst it was possible to obtain LM solutions away from ph symmetry, describing the QCP coming from this phase was found to be beyond the scope of the approximation.

Finally, we note that in consequence of the conserving nature of the approximation, the Friedel sum rules of eqs. (4.7-4.8), together with the general results of Section 3.4 for the vanishing of the Luttinger integrals, holds in both phases.

CHAPTER 7

Spin susceptibilities

In this chapter we study the exact low-temperature behaviour of a range of different static spin susceptibilities. As discussed previously in Chapter 3, in a LM phase the $T \to 0$ and $h \to 0^{\pm}$ limits do not commute. As a consequence, we consider the distinct susceptibilities that arise in each unique case.

The chapter begins with a discussion of the local static susceptibility, χ_s, precisely at $T = 0$, as the local field $h \to 0^{\pm}$. By writing the local magnetization, $m(h)$, in terms of the impurity Green function and expressing the local self-energy in terms of a functional of the propagators (via the skeleton expansion), we derive an *exact* result for the form of χ_s as the QCP is approached from both the LM and SC phases. In consequence, we then determine the condition for the quantum phase transition, once again using the fact that the self-energy is a functional of the propagators, to show that χ_s diverges as the QCP is approached as $U \to U^{\pm}$. Subsequently, we use the NRG to numerically confirm the exact analytic results derived for the form of χ_s, and find that both are in remarkable agreement. Before proceeding, in analogy with the exact results determined for χ_s, we consider the zero temperature local *charge* susceptibility, χ_c, deriving a similar exact form to χ_s. Moreover, we find that our analytic results for both χ_s and χ_c, agree perfectly with the numerical calculations of ref [42] for the pseudogap Anderson model away from particle-hole symmetry.

In the second half of this chapter we consider taking the (non-commuting) limits $h \to 0^{\pm}$, $T \to 0$ the opposite way around, such that we allow the field to vanish at finite temperature before letting $T \to 0$. This is the more conventional limiting process that has been more extensively examined in the literature for the pseudogap Anderson model [37, 43, 46, 49] and other impurity models with quantum phase transitions between LM and SC [54, 55, 57]. Firstly, we consider the susceptibilities in response to a global field applied to both the impurity level and conduction band states, before proceeding to the more subtle case where a field is applied locally solely to the impurity level. We use physical arguments based on the nature of the doubly

degenerate local moment ground-state to determine the low-T forms of both the global susceptibility in response to a global field, $\chi_{u,u}(T)$, and also the local susceptibility in response to a global field, $\chi_{u,loc}(T)$. In addition, from a detailed analysis of the Lehmann (spectral) representation of the general dynamic local susceptibility, $\chi_{loc,loc}(i\omega)$, we develop a microscopic argument to determine the known [37, 47, 48] form of the local static susceptibility, $\chi_{loc,loc}(T)$. We then explain how each of the susceptibilities may be calculated from NRG [110].

We conclude the chapter by considering the excess susceptibility, $\chi_{\rm imp}(T)$, defined as the spin susceptibility of the whole system (with the impurity present) minus the contribution of the free conduction band (when the impurity is absent). From analytic arguments, we derive the LM phase result, $\lim_{T\to 0}\chi_{\rm imp}(T) \to \frac{1}{2}$, i.e. that the susceptibility has the full free-spin Curie law behaviour, previously known from NRG calculations [43] for the PAIM.

Before we proceed to the analysis detailed above, we briefly consider the nature of the two distinct non-commuting limiting processes that arise when the ground-state of a system is a doubly degenerate LM phase. Fig. 7.1 shows the two scenarios: The left panel shows the behaviour of the local magnetization, $m(h)$, identically at zero temperature, as $h \to 0^{\pm}$. In this thesis so far, this is the case that has been largely considered, with the limiting value of the local magnetization, $m(h = 0^{\pm}) = \pm|\tilde{\mu}|$. By contrast, the right panel shows the case where the limits are taken in the opposite order. The local magnetization, $m(h)$, is continuous across $h = 0$ in this instance, vanishing as $h \to 0^{\pm}$. In both limiting processes, the magnetization precisely at zero field is zero, $m(h = 0) = 0$. In the former case, this distinct point is accessed discontinuously as a function of field; and as discussed in Chapter 3, a TSE description is necessary to determine the underlying behaviour. In the latter case by contrast, for any finite temperature the degeneracy of the LM ground-state is destroyed, and $m(h = 0) = 0$ is continuously accessed as $T \to 0$.

7.1 Local moment phase: susceptibilities at zero temperature

7.1.1 Spin susceptibility and local moment formation

As in the rest of this thesis, we consider a general impurity model with a phase transition between a SC and a LM phase. Although, we naturally have in mind the pseudogap AIM, essentially there is nothing specific to that particular case in the proceeding analysis.

In this section, we consider the impurity *static* spin susceptibility, in response to a magnetic field, $h = \frac{1}{2}g\mu_B B$ applied locally to the impurity level (and not to the conduction band). In recognition that the results of this chapter are for general finite field, we drop any explicit 'A' (or 'B') labeling in the propagators, i.e. for

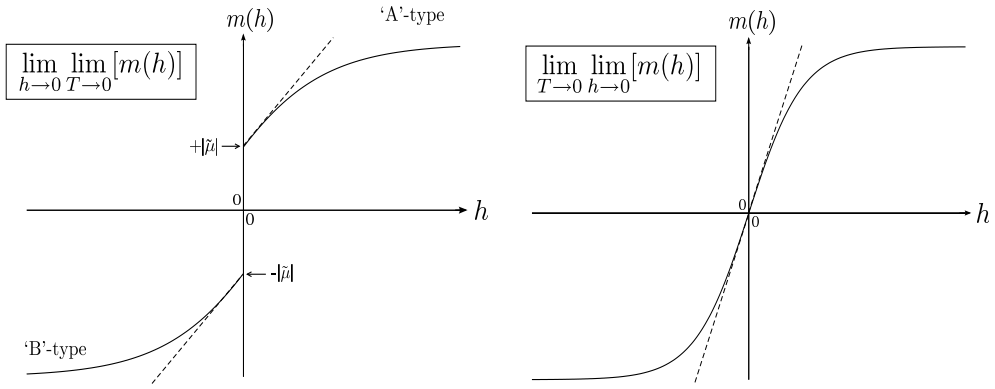


Figure 7.1: Schematic showing the difference in taking the two non-commuting limits in a degenerate local moment phase. The local magnetization, $m(h) = -m(-h) = 2\langle \hat{s}_z \rangle$, is shown versus a local field, h. The left panel shows the $\lim_{h\to 0}\lim_{T\to 0}[m(h)]$, whereas the right panel shows $\lim_{h\to 0}\lim_{T\to 0}[m(h)]$. The associated susceptibilities are given by the gradients of the dashed lines.

$U > U_c$ ($G_\sigma(\omega, h) \equiv G_{A\sigma}(\omega, |h|)$ for $h > 0$ and $G_\sigma(\omega, h) \equiv G_{B\sigma}(\omega, -|h|)$ for $h < 0$. The local magnetization, $m(h)$, is given at zero-temperature by (c.f. eq. (3.1a))

$$m(h) = \int_{-\infty}^{\mu} \mathrm{d}\omega [D_\uparrow(\omega, h) - D_\downarrow(\omega, h)] \tag{7.1a}$$

$$= -\frac{1}{\pi}\mathrm{Im}\int_{-\infty}^{\mu} \mathrm{d}\omega \sum_\sigma \sigma G^r_\sigma(\omega) \tag{7.1b}$$

$$= \frac{1}{2\pi}\int_{-\infty}^{\infty} \mathrm{d}\omega \mathrm{e}^{(i\omega+\mu)0^+} \sum_\sigma \sigma G_\sigma(i\omega). \tag{7.1c}$$

Here $G^r_\sigma(\omega)$ is the retarded propagator; whilst $G_\sigma(i\omega)$ is the Matsubara imaginary-time (zero-temperature) Green function obtained via the analytic continuation, $\omega + i\eta \to i\omega + \mu$ [62].[1] There is no restriction to either zero-field phase; the system could be in either the SC or LM phases in the following analysis. For $h \neq 0$ the pristine QCP is destroyed and the system is strictly a Fermi liquid for all finite-h (see Fig. 1.4).

The local Matsubara Green function for the single-impurity Anderson model is given by

$$G_\sigma(i\omega) = [i\omega + \mu + \sigma h - \varepsilon - \Gamma(i\omega) - \Sigma_\sigma(i\omega)]^{-1}, \tag{7.2}$$

where since we consider a magnetic field applied purely locally, the hybridization function, $\Gamma(i\omega)$ is independent of h. With this in mind, together with $\mathrm{sgn}(h) =$

[1] It is convenient to use the Matsubara propagator, $G_\sigma(i\omega)$, in the following argument. We also explicitly include the chemical potential, μ, in the propagator so that we may consider the local charge susceptibility, $\chi_c = \frac{1}{2}\partial n/\partial\mu$ in Section 7.1.3.

$\mathrm{sgn}(m(h))$ (eq. (3.5)), we define the local static spin susceptibility specifically as

$$\chi_s = \left(\frac{\partial\langle\hat{s}_z\rangle}{\partial h}\right)_{h=0} = \frac{1}{2}\left(\frac{\partial m(h)}{\partial h}\right)_{h=0}, \tag{7.3}$$

where the $\frac{1}{2}$ accounts for the fact that, as defined above, the high field limit of $|m(h)|$ is 1 rather than a $\frac{1}{2}$ (and we set $g\mu_B \equiv 1$).

Before we proceed we make some comments about the precise nature of χ_s, particularly in the LM phase (where $U > U_c$). As stated in Section 3.1, the magnetization in either phase is odd in the field, i.e. $m(h) = -m(-h)$. In the SC phase the zero-field magnetization simply vanishes, $m(h \to 0^{\pm}) = 0$. By contrast, in the LM phase, $m(h)$ is discontinuous across $h = 0$, as illustrated on the LHS of Fig. 7.1.

We remind the reader that as $h \to 0^+$, $m(0^+) = +|\tilde{\mu}|$ (what we call an 'A type' state), while as $h \to 0^-$, $m(0^-) = -|\tilde{\mu}|$ (a 'B type' state). The magnetization as a function of field is then given by

$$m(h) = |\tilde{\mu}|[\theta(h) - \theta(-h)] + \delta m(h), \tag{7.4}$$

where $\delta m(h)$ is given for $h > 0$ by

$$\delta m(h) = m(h) - m(0^+) = m(h) - |\tilde{\mu}| \quad : \quad h > 0 \tag{7.5}$$

and $\delta m(h)$ for $h < 0$ follows from $\delta m(h) = -\delta m(-h)$. The overall $\delta m(h)$ thus corresponds to simply removing the full discontinuously from $m(h)$, and as such is continuous across $h = 0$.

The h-dependent spin susceptibility is given by inserting eq. (7.4) into eq. (7.3), $\chi_s(h) = |\tilde{\mu}|\delta(h) + \frac{1}{2}\frac{\partial}{\partial h}\delta m(h)$. The delta-function pole piece does not of course contribute to $\chi_s(h)$ as $h \to 0^{\pm}$; and therefore $\chi_s(h = 0^{\pm}) = \frac{1}{2}(\frac{\partial}{\partial h}\delta m(h))_{h=0^{\pm}}$. Hence, the overall susceptibility for $h \to 0$ can be written as

$$\chi_s(h \to 0) = |\tilde{\mu}|\delta(h) + \chi_s(h = 0^{\pm}) \tag{7.6}$$

and is separable into two distinct contributions[2]. The first contribution is the δ-singularity (which is mirrored in the $h = 0$ $(= T)$ dynamical spin susceptibility containing an $\omega = 0$ pole in the LM phase as found by ref [37]), which is known explicitly given the zero-field moment, $|\tilde{\mu}|$. The *non-trivial* part of the full susceptibility is thus $\chi_s(h = 0^{\pm})$. It is this quantity that we calculate explicitly in the LM

[2]This form is analogous to case of a free spin where $|\tilde{\mu}| = 1$ and $\chi_s(h = 0^{\pm}) = 0$. We refer the reader to Appendix E for further details.

phase; for brevity we denote it simply by χ_s, so that in the following we denote

$$\chi_s \equiv \frac{1}{2}\left(\frac{\partial m(h)}{\partial h}\right)_{h=0^{\pm}}. \tag{7.7}$$

From a physical point of view, and in keeping with the arguments of Chapter 3, what we are calculating is clear. Applying a small field in an arbitrary direction, 'picks out' one component of the $h = 0$ LM ground-state. The 'A state' is picked out if we choose $h > 0$, or the equivalently the 'B state' if $h < 0$ is chosen. We may then calculate the $h \to 0^+$ local spin susceptibility of the system with $G_\sigma(\omega, h) \equiv G_{A\sigma}(\omega, |h|)$ 'A' propagators in eq. (7.1) for $m(h)$ (or equivalently $G_\sigma(\omega, h) \equiv G_{B\sigma}(\omega, -|h|)$ for $h < 0$).

Before proceeding, we make an important comment about the SC phase. In a SC phase, since there is no permanent local moment at zero-field, the issues considered above (surrounding the order of limits) simply do not arise, and $\chi_s(h = 0) \equiv \chi_s(h = 0^{\pm})$. As we shall see, it is χ_s — as we have defined it, $\chi_s(h = 0^{\pm})$, in the LM phase or $\chi_s(h = 0)$ in the SC phase, which diverges as the QCP is approached from either side of the transition, $U \to U_c^{\pm}$.

Our natural focus is on the magnetization, $m(h)$, as given by eq. (7.1). However, in order to obtain it, we also consider the local impurity charge, $n(h)$, given by eq. (3.1b), shown to be even in the field via eq. (3.7b) and *continuous* across $h = 0$.[3] More precisely, we need to consider the zero-field value of the susceptibility $\chi_c'(h) = \frac{1}{2}(\frac{\partial n(h)}{\partial h})$ (which should not be confused with the charge susceptibility - given by $\chi_c \propto \partial n/\partial \mu$, which we also discuss below). In the following we explicitly consider the case where

$$\chi_c' \equiv \chi_c'(h = 0) = \frac{1}{2}\left(\frac{\partial n(h)}{\partial h}\right)_{h=0} = 0. \tag{7.8}$$

This condition holds at ph symmetry in both phases where the local charge, $n(h) = 1$, for all h. Furthermore, it may be shown by the symmetries of the propagators that it also holds away from ph symmetry in the SC (ASC) phase. For general $x = \varepsilon + \frac{U}{2}$ in the LM phase, a lengthy calculation shows that whilst eq. (7.8) does not hold, the essential result of this section, eq. (7.23), has precisely the same form.

To proceed, we may write the local σ-spin charge in the following form, $n_\sigma(h) \equiv \langle \hat{n}_\sigma \rangle = \frac{1}{2}\langle \hat{n}_\uparrow + \hat{n}_\downarrow + \sigma(\hat{n}_\uparrow - \hat{n}_\downarrow)\rangle = \frac{1}{2}[n(h) + \sigma m(h)]$. From this it follows simply from eqs. (7.7-7.8) that the spin-suceptibility may be recast as

$$\chi_s = \sigma\left(\frac{\partial n_\sigma(h)}{\partial h}\right)_{h=0^{\pm}}, \tag{7.9}$$

[3]For the PAIM, the local charge, $n(0)$ is shown on the RHS of Fig. 4.3 as a function of U as the QCP is traversed.

where we have used $\sigma^2 = 1$. Furthermore, the local σ-spin charge, $n_\sigma(h)$, may be written as an integral over the Matsubara propagator (obtained from the analytic continuation, $\omega + i\eta \to i\omega + \mu$ from eq. (3.2)), given by

$$n_\sigma(h) = \int_{-\infty}^{\infty} \frac{\mathrm{d}\omega}{2\pi} \mathrm{e}^{(i\omega+\mu)0^+} G_\sigma(i\omega). \tag{7.10}$$

Thus, the spin-susceptibility, χ_s, can either be obtained directly from eqs. (7.1, 7.7), or alternatively via eqs. (7.9-7.10). For convenience we choose the latter in the following analysis. From now on, $\partial/\partial h$ implicitly means evaluated at $h = 0^{\pm}$, we just will not write it explicitly for reasons of brevity. On differentiation of eq. (7.2) with respect to the field we simply obtain

$$\frac{\partial G_\sigma(i\omega)}{\partial h} = -\sigma G_\sigma^2(i\omega)\left[1 - \sigma \frac{\partial \Sigma_\sigma(i\omega)}{\partial h}\right]. \tag{7.11}$$

Therefore, by differentiating eq. (7.10) and inserting the form of eq. (7.11), χ_s follows as

$$\chi_s = -\int_{-\infty}^{\infty} \frac{\mathrm{d}\omega}{2\pi} \mathrm{e}^{(i\omega+\mu)0^+} G_\sigma^2(i\omega)\left[1 - \sigma \frac{\partial \Sigma_\sigma(i\omega)}{\partial h}\right] \tag{7.12}$$

where we may simply drop the convergence factor, $\mathrm{e}^{(i\omega+\mu)0^+}$ in the following. We now decompose the skeleton expansion for the self-energy as

$$\Sigma_\sigma(i\omega) = \Sigma_\sigma^{(1)} + \Sigma'_\sigma(i\omega), \tag{7.13}$$

where $\Sigma_\sigma^{(1)}$ denotes the purely static first-order UHF contribution (given by the first-order bubble diagram shown in Fig. 3.4), and $\Sigma'_\sigma(i\omega)$ refers to *all dynamical contributions* as shown in Fig. 7.2. The first-order contribution is simply given from eq. (4.40) by

$$\Sigma_\sigma^{(1)} = U\langle \hat{n}_{-\sigma} \rangle = \tfrac{U}{2}[n(h) - \sigma m(h)]. \tag{7.14}$$

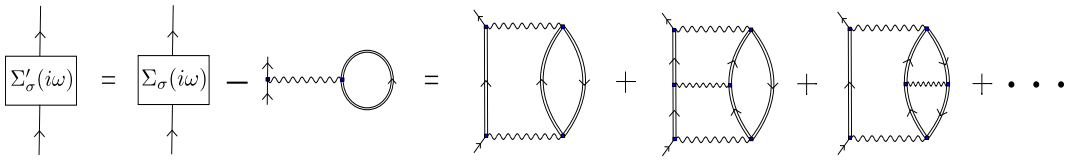


Figure 7.2: $\Sigma'_\sigma(i\omega)$ expressed as a functional of the propagators, via the skeleton expansion. The first-order bubble diagram is subtracted in the contribution to $\Sigma'_\sigma(i\omega)$. All double lines denote full interacting propagators as usual.

Thus, differentiating the self-energy, eq. (7.13), then gives

$$\sigma\frac{\partial\Sigma(i\omega)}{\partial h} = \sigma\frac{\partial}{\partial h}(\tfrac{U}{2}[n(h)-\sigma m(h)]) + \sigma\frac{\partial\Sigma'_\sigma(i\omega)}{\partial h}, \tag{7.15a}$$

$$= -U\chi_s + \sigma\frac{\partial\Sigma'_\sigma(i\omega)}{\partial h}, \tag{7.15b}$$

where we have used eq. (7.8) in the second line. As a consequence, eq. (7.12) then becomes

$$\chi_s = -\int_{-\infty}^{\infty}\frac{\mathrm{d}\omega}{2\pi}G_\sigma^2(i\omega)\left[(1+U\chi_s) - \sigma\frac{\partial\Sigma'_\sigma(i\omega)}{\partial h}\right]$$

$$\text{i.e. } \frac{\chi_s}{1+U\chi_s} = -\int_{-\infty}^{\infty}\frac{\mathrm{d}\omega}{2\pi}G_\sigma^2(i\omega)\left[1 - \frac{1}{(1+U\chi_s)}\sigma\frac{\partial\Sigma'_\sigma(i\omega)}{\partial h}\right] \tag{7.16}$$

Dynamical self-energy

We now choose to focus explicitly on $\partial\Sigma'_\sigma(i\omega)/\partial h$. As a consequence of the fact that $\Sigma'_\sigma(i\omega)$ is made up of all dynamical contributions to the skeleton expansion and hence is a functional of the propagators, its derivative can be written via a chain rule in terms of the functional derivative [111]

$$\frac{\partial\Sigma'_\sigma(i\omega)}{\partial h} = \sum_{\sigma'}\int\frac{\mathrm{d}\omega'}{2\pi}\frac{\delta\Sigma'_\sigma(i\omega)}{\delta G_{\sigma'}(i\omega')}\frac{\partial G_{\sigma'}(i\omega')}{\partial h}. \tag{7.17}$$

We define the irreducible two-particle, four-point vertex function $I'_{\sigma\sigma'}(i\omega, i\omega')$ by

$$I'_{\sigma\sigma'}(i\omega, i\omega') = \frac{\delta\Sigma'_\sigma(i\omega)}{\delta G_{\sigma'}(i\omega')} = \frac{\delta^2\Phi'_{LW}}{\delta G_\sigma(i\omega)\delta G_{\sigma'}(i\omega')}. \tag{7.18}$$

As discussed in Section 2.4.1, functional differentiation is equivalent to cutting a single propagator line. The self-energy is given by the functional derivative of the Luttinger-Ward functional, $\Sigma'_\sigma(i\omega) = \delta\Phi'_{LW}/\delta G_{\sigma'}(i\omega)$, where Φ'_{LW} is made up of all closed linked skeleton diagrams with the first-order term removed. $I'_{\sigma\sigma'}(i\omega, i\omega')$ is thus constructed diagrammatically by cutting a further propagator line in all skeleton diagrams for $\Sigma'_\sigma(i\omega)$, or alternatively as the second-functional-derivative of Φ'_{LW} (as indicated). We emphasize that $I'_{\sigma\sigma'}(i\omega, i\omega')$ is not the same as the usual 'full' four-point vertex function, $I_{\sigma\sigma'}(i\omega, i\omega') = \delta\Sigma_\sigma(i\omega)/\delta G_{\sigma'}(i\omega')$ - defined in terms of all diagrammatic contributions to the skeleton expansion, because the first-order contribution to the self-energy is excluded in $\Sigma'_\sigma(i\omega)$. We also note, that the function satisfies the symmetry relation - $I'_{\sigma\sigma'}(i\omega, i\omega') = I'_{\sigma'\sigma}(i\omega', i\omega)$.

Hence, by inserting eq. (7.11) into eq. (7.17), and using eq. (7.15b), we obtain

$$-\sigma\frac{\partial\Sigma'_\sigma(i\omega)}{\partial h} = \sum_{\sigma'}\int\frac{\mathrm{d}\omega'}{2\pi}I'_{\sigma\sigma'}(i\omega,i\omega')\sigma\sigma'G^2_{\sigma'}(i\omega')\left[(1+U\chi_s)-\sigma'\frac{\partial\Sigma'_{\sigma'}(i\omega')}{\partial h}\right],$$

and therefore

$$\frac{-1}{(1+U\chi_s)}\sigma\frac{\partial\Sigma'_\sigma(i\omega)}{\partial h} = \sum_{\sigma'}\int\frac{\mathrm{d}\omega'}{2\pi}I'_{\sigma\sigma'}(i\omega,i\omega')\sigma\sigma'G^2_{\sigma'}(i\omega')\left[1-\frac{1}{1+U\chi_s}\sigma'\frac{\partial\Sigma'_{\sigma'}(i\omega')}{\partial h}\right]. \tag{7.19}$$

On iteration of this equation we obtain

$$\frac{-1}{(1+U\chi_s)}\sigma\frac{\partial\Sigma'_\sigma(i\omega)}{\partial h} = \sum_{\sigma'}\sigma\sigma'\int\frac{\mathrm{d}\omega'}{2\pi}\Gamma'_{\sigma\sigma'}(i\omega,i\omega')G^2_{\sigma'}(i\omega'), \tag{7.20}$$

where the *reducible* vertex function $\Gamma'_{\sigma\sigma'}(i\omega,i\omega')$ is obtained in terms of $I'_{\sigma\sigma'}(i\omega,i\omega')$ via a Bethe-Salpeter equation [62, 111]

$$\Gamma'_{\sigma\sigma'}(i\omega,i\omega') = I'_{\sigma\sigma'}(i\omega,i\omega') + \sum_{\sigma''}\int\frac{\mathrm{d}\omega''}{2\pi}I'_{\sigma\sigma''}(i\omega,i\omega'')G^2_{\sigma''}(i\omega'')\Gamma'_{\sigma''\sigma'}(i\omega'',i\omega'). \tag{7.21}$$

This equation is shown diagrammatically in Fig. 7.3. The vertex function, $\Gamma'_{\sigma\sigma'}(i\omega,i\omega')$, is reducible in the sense that it contains diagrams with two propagator lines, which may be cut to yield contributions to $I'_{\sigma\sigma'}(i\omega,i\omega')$.

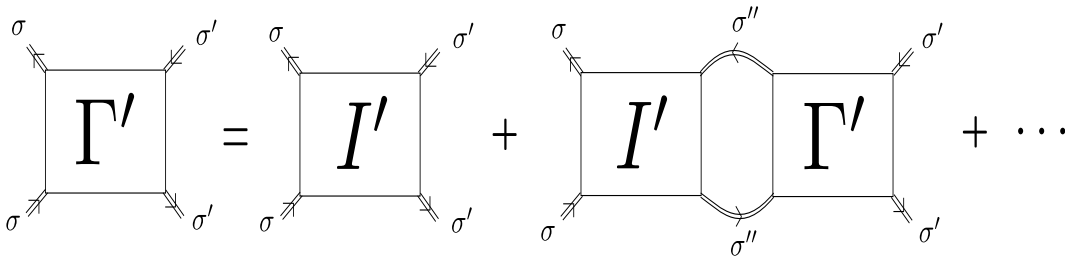


Figure 7.3: Diagrammatic form of the Bethe-Salpeter equation, eq. (7.21), for the reducible vertex function, $\Gamma_{\sigma\sigma'}(i\omega,i\omega')$, in terms of the irreducible vertex function, $I_{\sigma\sigma'}(i\omega,i\omega')$.

Hence, by inserting eq. (7.20) into eq. (7.16) we obtain

$$\frac{\chi_s}{1+U\chi_s} = -\int_{-\infty}^{\infty}\frac{\mathrm{d}\omega}{2\pi}G^2_\sigma(i\omega)\left[1+\sum_{\sigma'}\sigma\sigma'\int\frac{\mathrm{d}\omega'}{2\pi}\Gamma'_{\sigma\sigma'}(i\omega,i\omega')G^2_{\sigma'}(i\omega')\right] \tag{7.22a}$$

$$\equiv {}^0\tilde{\Pi}^{\sigma\sigma}, \tag{7.22b}$$

with ${}^0\tilde{\Pi}^{\sigma\sigma}$, a *static* polarization bubble. By rearranging this equation, the static

spin susceptibility can then be written in closed form via

$$\chi_s = \frac{{}^0\tilde{\Pi}^{\sigma\sigma}}{1 - U\,{}^0\tilde{\Pi}^{\sigma\sigma}}. \tag{7.23}$$

This result is entirely non-trivial, as it shows that the *exact* spin susceptibility, χ_s, has a simple 'RPA'-like form [62], and not just at the simple level of 'mean-field plus fluctuations' (FLEX) that we studied in the previous chapter. We also note here that if $\Gamma'_{\sigma\sigma'}(i\omega, i\omega') = 0$, eq. (7.22) reduces to

$${}^0\Pi^{\sigma\sigma} = -\int_{-\infty}^{\infty} \frac{\mathrm{d}\omega}{2\pi} G_\sigma^2(i\omega), \tag{7.24}$$

which is the usual 'bare' polarization bubble encountered at the FLEX level of approximation, where *vertex* correction terms are neglected in the approximation to the self-energy.[4] It is also readily shown by analytic continuation ($i\omega + \mu \to \omega + i\,\mathrm{sgn}(\omega)\eta$) of the Matsubara Green functions to time-ordered functions that

$${}^0\Pi^{\sigma\sigma} \equiv \mathrm{Re}\,{}^0\Pi^{\sigma\sigma}(\omega = 0) = i\int_{-\infty}^{\infty} \frac{\mathrm{d}\omega}{2\pi} [G_\sigma^t(\omega)]^2 \tag{7.25}$$

i.e. ${}^0\Pi^{\sigma\sigma}$ is equivalent to the static polarization part used in FLEX, where $G_\sigma^t(\omega)$ denotes the time-ordered Green function.

In deriving the key result, eq. (7.23), the central element has been the decomposition of the self-energy into static plus dynamic contributions as in eq. (7.13), and recognition that the exact static contribution $\Sigma_\sigma^{(1)}$ contains the magnetization, $m \equiv m(h)$, again. It is also physically rather natural, since the symmetry that is broken in the LM phase ($m(h = 0^\pm) \neq 0$) is explicitly contained in the static contribution to the self-energy; and indeed is effectively accessible also in the SC phase by applying the appropriate field (h in this case).

We make one final important point before proceeding. If we had not decomposed the self-energy into static plus dynamic contributions (in eq. (7.13)), and then proceeded in direct parallel from eq. (7.12), we would simply yield the result

$$\chi_s = -\int_{-\infty}^{\infty} \frac{\mathrm{d}\omega}{2\pi} G_\sigma^2(i\omega)\left[1 + \sum_{\sigma'} \sigma\sigma' \int \frac{\mathrm{d}\omega'}{2\pi} \Gamma_{\sigma\sigma'}(i\omega, i\omega') G_{\sigma'}^2(i\omega')\right], \tag{7.26}$$

which is the analog of eq. (7.22). $\Gamma_{\sigma\sigma'}(i\omega, i\omega')$ is a reducible vertex function given by the (usual) Bethe-Salpeter equation

$$\Gamma_{\sigma\sigma'}(i\omega, i\omega') = I_{\sigma\sigma'}(i\omega, i\omega') + \sum_{\sigma''} \int \frac{\mathrm{d}\omega''}{2\pi} I_{\sigma\sigma''}(i\omega, i\omega'') G_{\sigma''}^2(i\omega'') \Gamma'_{\sigma''\sigma'}(i\omega'', i\omega').$$

[4] We emphasize that the propagators, $G_\sigma(i\omega)$, are *self-consistent* at whatever level of approximation they are calculated.

where $I_{\sigma\sigma'}(i\omega, i\omega')$ is an irreducible vertex function obtained via the functional derivative

$$I_{\sigma\sigma'}(i\omega, i\omega') = \frac{\delta\Sigma_\sigma(i\omega)}{\delta G_{\sigma'}(i\omega')} = \frac{\delta^2\Phi_{LW}}{\delta G_\sigma(i\omega)\delta G_{\sigma'}(i\omega')}. \tag{7.27}$$

In this equation both Φ_{LW} and $\Sigma_\sigma(i\omega)$ contain all skeleton diagrams including the static first-order bubble diagram.

In comparison to eq. (7.22), the result, eq. (7.26), is not terribly illuminating, further accentuating the advantage of rewriting the self-energy in terms of its static and dynamic parts.

7.1.2 Condition for the QCP

In this section we obtain a condition for the quantum phase transition coming from the LM side of the transition where the order parameter, $m(h = 0^+) \equiv m_A(0) = |\tilde{\mu}|$, (as shown via NRG calculations for the PAIM in Fig. 4.3) continuously vanishes as $U \to U_c^+$.

In the following it is convenient to define the quantity

$$y = \tfrac{1}{2}U|\tilde{\mu}|, \tag{7.28}$$

which must vanish at $U = U_c$ (where $|\tilde{\mu}| \to 0$). Once again, by separating the self-energy, $\Sigma_\sigma(i\omega)$, into its static and dynamical components via eq. (7.13) and using eq. (7.28), the static part is written in terms of y as

$$\Sigma_\sigma^0 = \tfrac{U}{2}n - \sigma y. \tag{7.29}$$

Inserting this form into eq. (7.2) for the propagator, we obtain

$$G_\sigma(i\omega) = [i\omega + \mu - \varepsilon - (\tfrac{U}{2}n - \sigma y) - \Gamma(i\omega) - \Sigma'_\sigma(i\omega)]^{-1}, \tag{7.30}$$

where from now on we set the chemical potential, $\mu = 0$ for convenience. Eq. (7.1) for $m(h = 0^+) \equiv |\tilde{\mu}| = 2y/U$ then gives

$$\frac{2}{U}y = \sum_\sigma \sigma \int_{-\infty}^{\infty} \frac{\mathrm{d}\omega}{2\pi} \mathrm{e}^{i\omega 0^+} G_\sigma(i\omega) \equiv f(y; U). \tag{7.31}$$

The function $f(y; U)$ is odd in y, because from eq. (7.30) it may be easily shown that $G_\sigma(i\omega) \equiv G_\sigma(i\omega, y) = G_{-\sigma}(i\omega, -y)$. Thus, on the natural assumption that as $U \to U_c^+$, $f(y; U)$ vanishes linearly in y, the condition for the transition is

$$\frac{2}{U_c} = \left(\frac{\partial f(y; U)}{\partial y}\right)_{y=0}, \tag{7.32}$$

and hence $1 = \frac{1}{2}U_c(\partial f(y;U)/\partial y)_{y=0}$. The symmetry $G_\sigma(i\omega, y) = G_{-\sigma}(i\omega, -y)$ can be used to show that the local charge is even in y, i,e $n(y) = n(-y)$. Here we explicitly consider the case where $(\partial n/\partial y)_{y=0} = 0$. On differentiating eqs. (7.30-7.31) with respect to y we obtain

$$\left(\frac{\partial f(y;U_c)}{\partial y}\right) = -\sum_\sigma \sigma \int_{-\infty}^{\infty} \frac{\mathrm{d}\omega}{2\pi} G_\sigma^2(i\omega)\left[1 - \sigma\frac{\partial \Sigma'_\sigma(i\omega)}{\partial y}\right] \tag{7.33}$$

where $\partial/\partial y$ means implicitly evaluated at $y = 0$ (and hence $U = U_c$) from now on. Once again, in analogy with eq. (7.17), as a consequence of the fact that $\Sigma'_\sigma(i\omega)$ is a functional of the propagators via the skeleton expansion, we may write the chain rule

$$\frac{\partial \Sigma'_\sigma(i\omega)}{\partial y} = \sum_{\sigma'} \int \frac{\mathrm{d}\omega'}{2\pi} \frac{\delta \Sigma'_\sigma(i\omega)}{\delta G_{\sigma'}(i\omega')} \frac{\partial G_{\sigma'}(i\omega')}{\partial y}. \tag{7.34}$$

Thus, proceeding in direct parallel with eqs. (7.17-7.20), we obtain

$$-\sigma\frac{\partial \Sigma'_\sigma(i\omega)}{\partial y} = \sum_{\sigma'} \sigma\sigma' \int \frac{\mathrm{d}\omega'}{2\pi} \Gamma'_{\sigma\sigma'}(i\omega, i\omega') G^2_{\sigma'}(i\omega'), \tag{7.35}$$

where the reducible vertex function, $\Gamma'_{\sigma\sigma'}(i\omega, i\omega')$ is defined as before, via the Bethe-Salpeter equation, eq. (7.21). Inserting eq. (7.35) into eq. (7.33) we obtain

$$\begin{aligned}\left(\frac{\partial f(y;U_c)}{\partial y}\right) &= -\sum_\sigma \sigma \int_{-\infty}^{\infty} \frac{\mathrm{d}\omega}{2\pi} G_\sigma^2(i\omega)\left[1 + \sum_{\sigma'} \sigma\sigma' \int \frac{\mathrm{d}\omega'}{2\pi} \Gamma'_{\sigma\sigma'}(i\omega, i\omega') G^2_{\sigma'}(i\omega')\right] \\ &= 2^0 \tilde{\Pi}^{\sigma\sigma}(U_c)\end{aligned} \tag{7.36}$$

where we have used the definition eq. (7.22) in the second line. Thus, on comparison of this equation with eq. (7.32), we obtain the condition for the quantum phase transition coming from the doubly degenerate LM phase:

$$1 = {U_c}^0 \tilde{\Pi}^{\sigma\sigma}(U_c). \tag{7.37}$$

As a consequence, the denominator of eq. (7.23) vanishes at the transition as $U \to U_c^{\pm}$, and the spin susceptibility, χ_s diverges at the same point as the local moment, $|\tilde{\mu}|$, vanishes. From eq. (7.7), χ_s is positive for all U, hence we obtain the condition

$$0 \leq {U_c}^0 \tilde{\Pi}^{\sigma\sigma}(U) \leq 1, \tag{7.38}$$

where the upper limit corresponds to the QCP where $U = U_c$, and with χ_s finite throughout the LM and SC phases. This is precisely the same (stability) condition,

eq. (6.16c), found within the FLEX approximation in Chapter 6 for the PAIM, but with ${}^0\tilde{\Pi}^{\sigma\sigma}(U)$ replaced by ${}^0\Pi^{\sigma\sigma}(U)$.

NRG calculations for the PAIM

In order to confirm the analytic results above for the *non-trivial* local spin susceptibility, $\chi_s \equiv \chi_s(h \to 0^{\pm})$, we calculate it from NRG for the pseudogap AIM. We now describe how we may calculate χ_s from NRG and provide numerical results for both ph symmetry and for general x.

For a given calculation, we fix r, U and $T = 10^{-20}$ (such that we effectively take the zero-temperature limit), and vary h, such that the ratio $h/T \gg 1$ (and thus we consider the physical picture shown on the LHS of Fig. 7.1). For each value of h we calculate the magnetization via eq. (7.1), i.e.

$$m(h) = 2\langle \hat{s}_z \rangle = \int_{-\infty}^{0} \mathrm{d}\omega [D_{\uparrow}(\omega, h) - D_{\downarrow}(\omega, h)], \tag{7.39}$$

with the operator, $\hat{s}_z = \frac{1}{2}[\hat{n}_{\uparrow} - \hat{n}_{\downarrow}]$ as usual. Once we have enough points, we may then plot $m(h)$ versus h for a fixed U, which allows us to fit a straight line to the data in the limit that $h \to 0$. The spin susceptibility can then be calculated via (analogous to the method of ref [43])

$$\chi_s(T = 0, h \to 0^{\pm}) = \frac{1}{2}\left[\frac{\partial m(h)}{\partial h}\right]_{h=0^{\pm}} \simeq \lim_{h \to 0^{\pm}} \frac{1}{2}\left[\frac{m(h)}{h}\right]. \tag{7.40}$$

The whole process can be repeated for a fixed r, x and different U, such that we may plot $\chi_s(T = 0, h \to 0^{\pm})$ versus U as the transition is crossed. We have calculated $\chi_s(T = 0, h \to 0^{\pm})$ for $r = 0.4$ (such that $r_* < r < \frac{1}{2}$ and both distinct critical points exist) for both ph symmetry, where the transition is governed by the SQCP, and also for $r = 0.4$ for $x = -5$, where the transition is captured by the AQCP. We find that in both cases $\chi_s(h \to 0^{\pm})$ diverges at the transition as $U \to U_c^{\pm}$ from both sides of the transition, confirming the results of the previous section.

Fig. 7.4 shows $\chi_s(h \to 0^{\pm})$ for $x = 0$, while Fig. 7.5 shows $\chi_s(h \to 0^{\pm})$ for $x = -5$. These results are consistent with the NRG calculations of ref [42], who find a divergent spin susceptibility as U_c is approached from the SC phase, but also a divergent χ_s throughout the entire LM phase. The latter reflects the $|\tilde{\mu}|\delta(h)$ contribution to $\chi_s(T = 0, h)$ (the first term in eq. (7.6)), whilst $\chi_s(h \to 0^{\pm})$, eq. (7.7), is finite throughout the LM phase, diverging only as $U \to U_c^{+}$ (as shown in Figs. (7.4-7.5)).

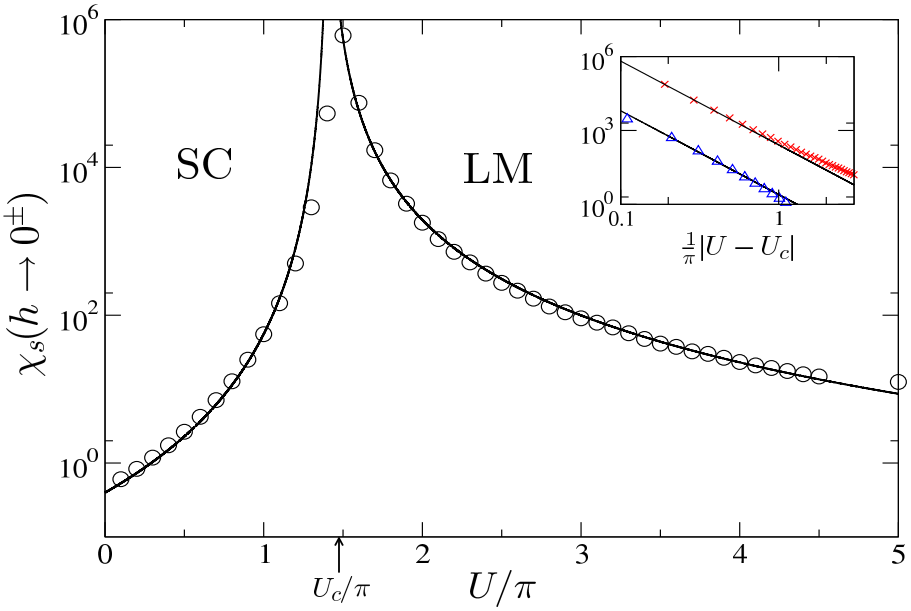


Figure 7.4: NRG results for the PAIM: $\chi_s(h \to 0^{\pm})$ is plotted versus U/π as the transition (characterized by the SQCP) is crossed for $r = 0.4$, $x = 0$. The susceptibility is finite in both phases, but diverges at $U = U_c(r)$. In this case $U_c/\pi \simeq 1.41$. Data points are shown, the lines are shown as a guide to the eye. The inset shows $\chi_s(h \to 0^{\pm})$ plotted versus $\frac{1}{\pi}|U - U_c|$ on a log:log plot for both phases (SC phase - with triangles, LM phase - with crosses). The numerics suggest that $\chi_s(h \to 0^{\pm}) \sim C_\alpha(r)|U - U_c|^{-|y(r)|}$ arises in both phases with the same exponent, $y(r)$, but with different coefficients, $C_\alpha(r)$, α = SC or LM. In this case $y(r) \simeq 3.4$, $C_{LM}(r) = 260$, $C_{SC}(r) = 2.5$. The unit of energy is set to $[\Gamma_0^{1/(1-r)}] \equiv 1$.

7.1.3 Local charge susceptibility

From direct NRG calculations for the PAIM explicitly away from ph symmetry, it is found by Pixley *et al.* [42], that in addition to the local spin susceptibility, the local charge susceptibility also diverges as the transition is approached from either phase. We have also explicitly reproduced their calculations as shown in Fig. 7.6. In this section we use similar arguments to those in Section 7.1.1 to derive an exact form for the local charge susceptibility, χ_c.

By analogy with eq. (7.6), we define the zero-temperature charge susceptibility by

$$\chi_c = \frac{1}{2}\left(\frac{\partial n}{\partial \mu}\right)_{\mu=0}, \tag{7.41}$$

where μ is the chemical potential. Physically the system may be in either the SC or LM phase at zero temperature and zero field[5]. The system may then be described within a conventional SSE description and the local magnetization $m \equiv m(h = 0) =$

[5]Here we take the limits $h \to 0^{\pm}$ followed by $T \to 0$, such that the physical picture for $m(h)$ is that of the RHS of Fig. 7.1

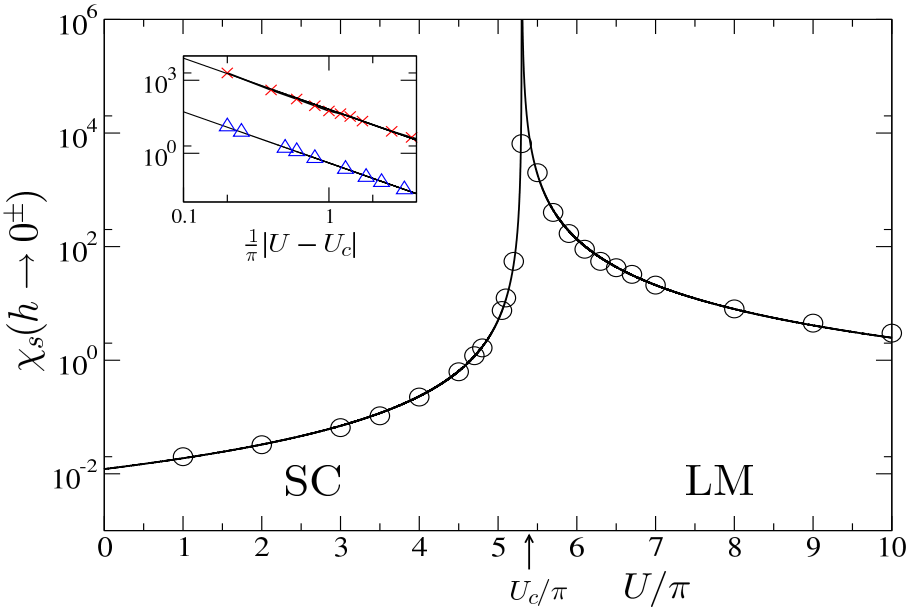


Figure 7.5: NRG results for the pseudogap model: $\chi_s(h \to 0^{\pm})$ is plotted versus U/π as the transition (characterized by the AQCP) is crossed for $r = 0.4$, $x = -5$. The susceptibility is finite in both phases, but diverges at $U = U_c(r)$. In this case $U_c/\pi \simeq 5.3$. Data points are shown, the lines are shown as a guide to the eye. The inset shows $\chi_s(h \to 0^{\pm})$ plotted versus $\frac{1}{\pi}|U - U_c|$ on a log:log plot for both phases (SC phase - with triangles, LM phase - with crosses).The numerics suggest that $\chi_s(h \to 0^{\pm}) \sim C_\alpha(r)|U - U_c|^{-|y(r)|}$ arises in both phases with the same exponent, $y(r)$, but with different coefficients, $C_\alpha(r)$, $\alpha =$ SC or LM. In this case $y(r) \simeq 2.1$, $C_{LM}(r) = 130$, $C_{SC}(r) = 0.8$. The unit of energy is set to $[\Gamma_0^{1/(1-r)}] \equiv 1$.

0 in all cases. Once again, by writing $n_\sigma = \frac{1}{2}[n + \sigma m]$ (with $m = 0$) the charge susceptibility is simply

$$\chi_c = \left(\frac{\partial n_\sigma}{\partial \mu}\right), \tag{7.42}$$

where all derivatives are evaluated at $\mu = 0$ (but we remove the explicit dependence for reasons of brevity). We also make the point that results of this section hold exclusively away from ph symmetry (where $x \neq 0$). At the ph symmetric point, the local charge, $n = 1$, for all U, and hence from eq. (7.41), χ_c vanishes in this case. Thus, proceeding in direct parallel with eqs. (7.11-7.15b), recognizing that

$$\frac{\partial \Sigma_\sigma(i\omega)}{\partial \mu} = U\chi_c + \frac{\partial \Sigma'_\sigma(i\omega)}{\partial \mu}, \tag{7.43}$$

where $\Sigma_\sigma(i\omega) = \frac{U}{2}n + \Sigma'_\sigma(i\omega)$, we obtain

$$\frac{\chi_c}{1 + U\chi_c} = -\int_{-\infty}^{\infty} \frac{\mathrm{d}\omega}{2\pi} G_\sigma^2(i\omega)\left[1 - \frac{1}{(1 + U\chi_c)}\frac{\partial \Sigma'_\sigma(i\omega)}{\partial \mu}\right] \tag{7.44}$$

Once again, in analogy with eq. (7.17), since $\Sigma'_\sigma(i\omega)$ is a functional of the propagators via the skeleton expansion, we may write the chain rule

$$\frac{\partial \Sigma'_\sigma(i\omega)}{\partial \mu} = \sum_{\sigma'} \int \frac{\mathrm{d}\omega'}{2\pi} \frac{\delta \Sigma'_\sigma(i\omega)}{\delta G_{\sigma'}(i\omega')} \frac{\partial G_{\sigma'}(i\omega')}{\partial \mu}. \tag{7.45}$$

From this equation we may proceed in direct parallel with eqs. (7.17-7.21) to obtain the relation

$$\frac{\chi_c}{1 - U\chi_c} = -\int_{-\infty}^{\infty} \frac{\mathrm{d}\omega}{2\pi} G_\sigma^2(i\omega) \left[1 + \sum_{\sigma'} \int \frac{\mathrm{d}\omega'}{2\pi} \Gamma'_{\sigma\sigma'}(i\omega, i\omega') G_{\sigma'}^2(i\omega') \right] \tag{7.46a}$$

$$\equiv {}^0\tilde{\Pi}_c^{\sigma\sigma}(U), \tag{7.46b}$$

the charge susceptibility analog of eq. (7.22), and hence

$$\chi_c = \frac{{}^0\tilde{\Pi}_c^{\sigma\sigma}(U)}{1 + U {}^0\tilde{\Pi}_c^{\sigma\sigma}(U)}. \tag{7.47}$$

We obtain the *exact* form for the charge susceptibility, χ_c. In order for the charge susceptibility to diverge at the transition (as found by ref [42] and shown in Fig. 7.6), the denominator of this expression must vanish at $U = U_c$, and hence

$$U_c {}^0\tilde{\Pi}_c^{\sigma\sigma}(U_c) = -1, \tag{7.48}$$

which along with eq. (7.37), provides another condition for the quantum phase transition. On comparison of eq. (7.22) with eq. (7.46), we may write $U^0\tilde{\Pi}_c^{\sigma\sigma}$ in terms of $U^0\tilde{\Pi}^{\sigma\sigma}$. We obtain

$$\begin{aligned} U^0\tilde{\Pi}_c^{\sigma\sigma} &= U^0\tilde{\Pi}^{\sigma\sigma} - U \int_{-\infty}^{\infty} \frac{\mathrm{d}\omega}{2\pi} G_\sigma^2(i\omega) \left[\sum_{\sigma'} (1 - \sigma\sigma') \int \frac{\mathrm{d}\omega'}{2\pi} \Gamma'_{\sigma\sigma'}(i\omega, i\omega') G_{\sigma'}^2(i\omega') \right] \\ &= U^0\tilde{\Pi}^{\sigma\sigma} - 2U \left(\int_{-\infty}^{\infty} \frac{\mathrm{d}\omega}{2\pi} G_\sigma^2(i\omega) \left[\int \frac{\mathrm{d}\omega'}{2\pi} \Gamma'_{\sigma-\sigma}(i\omega, i\omega') G_{-\sigma}^2(i\omega') \right] \right). \end{aligned} \tag{7.49}$$

At the transition in order for both eq. (7.37) and eq. (7.48) to be satisfied such that both spin and charge susceptibilities diverge, the term in curved brackets in eq. (7.49) must go to 1. As a consequence, in order for χ_c to diverge at U_c (and for the correct underlying physics to be captured), vertex function terms *must* be included in any approximation. If vertex terms are neglected, i.e. if $\Gamma'_{\sigma\sigma'}(i\omega, i\omega') = 0$, then ${}^0\tilde{\Pi}_c^\sigma$ simply reduces to

$${}^0\Pi_c^{\sigma\sigma} = -\int_{-\infty}^{\infty} \frac{\mathrm{d}\omega}{2\pi} G_\sigma^2(i\omega) = {}^0\Pi^{\sigma\sigma} = \mathrm{Re}\, {}^0\Pi^{\sigma\sigma}(\omega = 0) \tag{7.50}$$

which is the object considered at the simple level of FLEX in Chapter 6. Hence,

we conclude that at the FLEX level of approximation it is impossible for both $U_c^0\Pi^{\sigma\sigma} = 1$ and $U_c^0\Pi_c^{\sigma\sigma} = -1$ simultaneously. As discussed in the previous chapter, FLEX does predict the former condition, arising from the singular behaviour in the ph/bubble channels as $U \to U_c(r)$. However, FLEX fails to capture any singular behaviour arising as a consequence of charge fluctuations. This may be a reason that the numerical calculations of section 6.10 for ph asymmetry in the LM phase fail to capture the QCP.

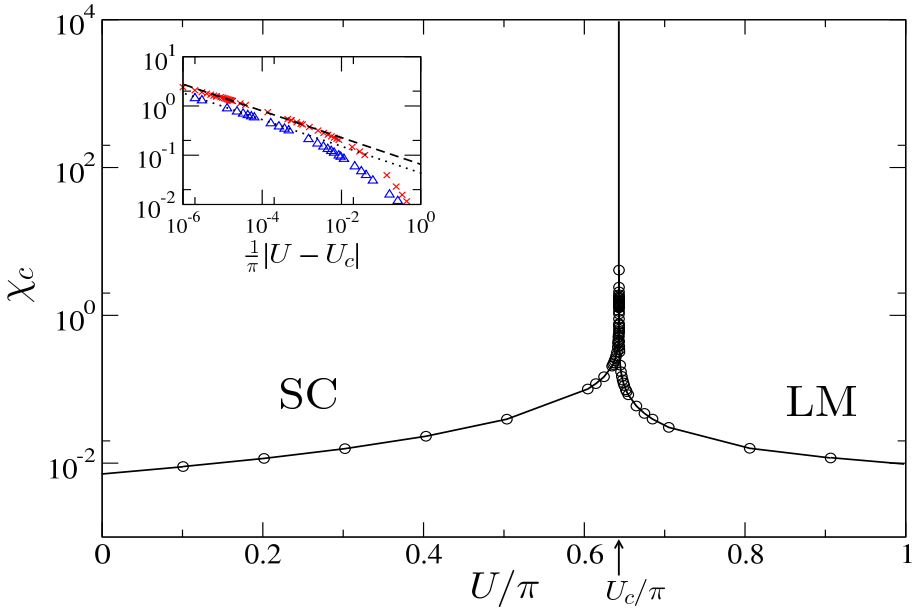


Figure 7.6: NRG results for the pseudogap model. The local charge susceptibility, χ_c, is plotted versus U/π as the transition (characterized by the AQCP) is crossed for $r = 0.6$, $\varepsilon/D = -0.05$ (reproduced for the same parameters as ref [42]). The susceptibility is finite in both phases, but diverges at $U = U_c(r)$. In this case $U_c/\pi \simeq 0.643$. Data points are shown, the lines are shown as a guide to the eye. The inset shows χ_c plotted versus $\frac{1}{\pi}|U - U_c|$ on a log-log plot (SC phase - with triangles, LM phase - with crosses). The numerics suggest that $\chi_c \sim C_\alpha(r)/\pi|U - U_c|^{-|y(r)|}$ arises in both phases with the same exponent, $y(r)$, but with different coefficients, $C_\alpha(r)$, $\alpha =$ SC or LM. In this case $y(r) \simeq 0.25$, $C_{LM}(r) = 0.052$, $C_{SC}(r) = 0.079$. The unit of energy is set to $[\Gamma_0^{1/(1-r)}] \equiv 1$.

7.2 Local moment phase susceptibilities: $h = 0$, $T \to 0$

In this section we pursue the $T \to 0$, $h = 0$ limit as shown on the right panel of Fig. 7.1. To proceed, we write the model Hamiltonian in the form

$$\hat{H} = \hat{H}_0 + \hat{H}_{\text{field}}, \tag{7.51}$$

where $\hat{H}_0$ is the zero-field single-impurity Anderson model Hamiltonian given by eq. (1.1). The field part of the Hamiltonian, with a magnetic field $h = \frac{1}{2}g\mu_B B$ acts

globally (both on the impurity level and conduction band states), is given by

$$\hat{H}_{\text{field}} = -2h\hat{S}_{\text{z}} = -2h\left(\hat{s}_{\text{z}} + \sum_{\mathbf{k}} \hat{s}_{\mathbf{k}\text{z}}\right) \qquad : h = h_u, \tag{7.52}$$

such that $\hat{S}_{\text{z}}$ ($\hat{S}_{\text{z}}$ is the overall spin z-component in the system) is given by $\hat{S}_{\text{z}} = (\hat{s}_{\text{z}} + \sum_{\mathbf{k}} \hat{s}_{\mathbf{k}\text{z}})$. The local and conduction band operators are given by $s_{\text{z}} = \frac{1}{2}\sum_{\sigma} \sigma \hat{n}_{\sigma}$, and $s_{\mathbf{k}} = \frac{1}{2}\sum_{\sigma} \sigma \hat{n}_{\mathbf{k}\sigma}$ respectively. We denote $\hat{s}_{\text{z}}^{bath} = \sum_{\mathbf{k}} \hat{s}_{\mathbf{k}\text{z}}$. Alternatively, a field may be applied locally solely to the impurity level. In this case $\hat{H}_{\text{field}}$ becomes

$$\hat{H}_{\text{field}} = -2h\hat{s}_{\text{z}} \qquad : h = h_{loc}. \tag{7.53}$$

With the forms of eqs. (7.52-7.53) we can separately treat the two distinct cases.

The expectation value of any arbitrary operator, $\hat{X}$, at finite temperature is given simply by the thermal average

$$\langle \hat{X} \rangle = \frac{1}{Z}\text{Tr}[\hat{X}\text{e}^{(-\beta\hat{H})}] = \frac{1}{Z}\text{Tr}[\hat{X}\text{e}^{(-\beta[\hat{H}_0 + \hat{H}_{\text{field}}])}] \tag{7.54}$$

where $Z = \text{Tre}^{(-\beta\hat{H})}$ is the partition function and $\text{Tr} = \sum_n \langle n| \dots |n\rangle$, with $|n\rangle = |\Psi_n\rangle$, the nth excited state of the many-body system, and $\beta = 1/T$ (such that $k_B = 1$).

7.2.1 Global uniform field

Firstly, we consider a global field, $h \equiv h_u$, that acts on both the impurity level and also the conduction band states. As a consequence of the fact that the overall z-component of spin, $\hat{S}_z$, commutes with the overall Hamiltonian, on differentiating eq. (7.54), with respect to a global field, $h = h_u$, it is trivially shown that

$$\frac{\partial \langle \hat{X} \rangle}{\partial h} = 2\beta[\langle \hat{X}\hat{S}_{\text{z}} \rangle - \langle \hat{S}_{\text{z}} \rangle \langle \hat{X} \rangle]. \tag{7.55}$$

where the derivative is evaluated at $h = 0$ (as are all derivatives in the following discussion, but we drop the explicit labelling). Thus, we may define three distinct spin-susceptibilities in response to a global field, given by

$$\chi_{u,u}(T) = \frac{\partial \langle \hat{S}_{\text{z}} \rangle}{\partial h} = 2\beta[\langle \hat{S}_{\text{z}}^2 \rangle - \langle \hat{S}_{\text{z}} \rangle^2] \tag{7.56a}$$

$$\chi_{u,loc}(T) = \frac{\partial \langle \hat{s}_{\text{z}} \rangle}{\partial h} = 2\beta[\langle \hat{s}_{\text{z}}\hat{S}_{\text{z}} \rangle - \langle \hat{s}_{\text{z}} \rangle \langle \hat{S}_{\text{z}} \rangle], \tag{7.56b}$$

$$\chi_{u,bath}(T) = \frac{\partial \langle \hat{s}_{\text{z}}^{bath} \rangle}{\partial h} = 2\beta[\langle \hat{s}_{\text{z}}^{bath}\hat{S}_{\text{z}} \rangle - \langle \hat{s}_{\text{z}}^{bath} \rangle \langle \hat{S}_{\text{z}} \rangle]. \tag{7.56c}$$

The first equation gives a global response, the second gives a local (impurity) response, and the third is a conduction band response, all to a global magnetic field, $h \equiv h_u$

In any phase of the model, identically at zero-field, and at zero-temperature there is no overall magnetic moment in the system. In other words, the expectation value of the z-component of the total spin is zero, i.e. $\langle \hat{S}_{\rm z} \rangle = 0$. As a consequence, the second terms in eqs. (7.56a-7.56c) vanish. Furthermore, by inserting eq. (7.52) in eq. (7.56a), we may express the 'global-global' susceptibility, $\chi_{u,u}(T)$, in terms of the other two, i.e.

$$\chi_{u,u}(T) = \chi_{u,loc}(T) + \chi_{u,bath}(T) = 2\beta\langle \hat{S}_{\rm z}^2 \rangle = 2\beta[\langle \hat{s}_{\rm z}\hat{S}_{\rm z}\rangle + \langle \hat{s}_{\rm z}^{bath}\hat{S}_{\rm z}\rangle]. \tag{7.57}$$

We will explicitly make use of this expression in due course, although for now we focus specifically on $\chi_{u,u}(T)$.

In *any* SC phase, the spin degree of freedom on the impurity is screened by the delocalized electrons of the conduction band. As a consequence, the many-body ground-state is a non-magnetic *global* singlet state, with no excess spin in the system. Thus, at $T = 0$, when the operator $\hat{S}_{\rm z}$ acts on the ground-state we simply obtain

$$\hat{S}_{\rm z}|0\rangle = 0, \tag{7.58}$$

where $|0\rangle$ denotes $|\Psi_0\rangle$, the zero-temperature ground-state of the entire system. From eq. (7.57) as $T \to 0$, we obtain $T\chi_{u,u}(T) = 2\langle \hat{S}_{\rm z}^2 \rangle = 0$.

By contrast, in a LM phase the ground-state precisely at zero-temperature is doubly degenerate. The system has equal probability of being in either one of two states:

$$|0\rangle = |A\rangle \quad \text{or} \quad = |B\rangle \quad \text{with } E_A = E_B = E_0, \tag{7.59}$$

where E_A and E_B are the energies of the 'A' and 'B' states respectively. As previously discussed, applying an infinitesimal field, $h = 0^{\pm}$, 'picks out' either the A or B components of the zero-field ground-state. However, in this present argument we consider the case where the field is identically zero, such that the A and B states are strictly degenerate in energy. From eq. (7.56a), in the $T \to 0$ limit, we may write

$$T\chi_{u,u}(T) = \frac{2}{Z}{\rm Tr}\langle n|{\rm e}^{-\beta\hat{H}}\hat{S}_{\rm z}^2|n\rangle = \frac{2\sum_n {\rm e}^{-\beta[E_n - E_0]}\langle n|\hat{S}_{\rm z}^2|n\rangle}{\sum_n {\rm e}^{-\beta[E_n-E_0]}} \overset{T\to 0}{\sim} \frac{2}{g_0}\sum_{\alpha}\langle \alpha|\hat{S}_{\rm z}^2|\alpha\rangle \tag{7.60}$$

where g_0 is the $T = 0$ ground-state degeneracy, and α runs over the degenerate states of the ground-state. In a doubly-degenerate LM phase, $g_0 = 2$, and $\alpha \in \{A, B\}$. Eq.

(7.60) then reduces to

$$T\chi_{u,u}(T) \overset{T\to 0}{\sim} \langle A|\hat{S}_{\rm z}^2|A\rangle + \langle B|\hat{S}_{\rm z}^2|B\rangle. \tag{7.61}$$

As discussed in Chapter 3, in a LM phase there is an unquenched SU(2) spin degree of freedom in the entire system at zero-temperature. As a consequence, each of the degenerate A or B states, are eigenstates of the overall $\hat{S}_{\rm z}$ operator (with eigenvalues $\pm\frac{1}{2}$), i.e.

$$\hat{S}_{\rm z}|A\rangle = \tfrac{1}{2}|A\rangle, \tag{7.62a}$$
$$\hat{S}_{\rm z}|B\rangle = -\tfrac{1}{2}|B\rangle. \tag{7.62b}$$

Therefore, by inserting eqs. (7.62a-7.62b) into eq. (7.60) we simply obtain

$$\lim_{T\to 0} T\chi_{u,u}(T) = 2\langle \hat{S}_{\rm z}^2\rangle = \tfrac{1}{2}, \tag{7.63}$$

which exhibits the 'full' free spin-$\frac{1}{2}$ Curie law behaviour.[6]

Equivalently, by a similar argument we may write, the 'mixed' susceptibility, $\chi_{u,loc}(T)$, given by eq. (7.56b), at zero-temperature as

$$T\chi_{u,loc}(T) = {\rm Tr}\tfrac{1}{Z}\langle n|{\rm e}^{-\beta\hat{H}}\hat{s}_{\rm z}\hat{S}_{\rm z}|n\rangle \overset{T\to 0}{\sim} \frac{2}{g_0}\Big[\langle A|\hat{s}_{\rm z}\hat{S}_{\rm z}|A\rangle + \langle B|\hat{s}_{\rm z}\hat{S}_{\rm z}|B\rangle\Big]. \tag{7.64a}$$

Allowing $\hat{S}_{\rm z}$ to act on the ground-states, we are then left with

$$T\chi_{u,loc}(T) \overset{T\to 0}{\sim} \Big[\frac{1}{2}\langle A|\hat{s}_{\rm z}|A\rangle - \frac{1}{2}\langle B|\hat{s}_{\rm z}|B\rangle\Big]. \tag{7.64b}$$

The purely local magnetization, $m(h)$, is defined by $m(h) = 2\langle\hat{s}_{\rm z}\rangle$. For the A and B states, as discussed in Section 3.1, $m_A(0) = m(h\to 0^+) = +|\tilde{\mu}|$, whereas $m_B(0) = m(h\to 0^-) = -|\tilde{\mu}|$. Thus, the matrix elements of the local-spin operator, $\hat{s}_{\rm z}$, are given by[7]

$$\langle A|\hat{s}_{\rm z}|A\rangle = +\tfrac{1}{2}|\tilde{\mu}|, \tag{7.65a}$$
$$\langle B|\hat{s}_{\rm z}|B\rangle = -\tfrac{1}{2}|\tilde{\mu}|, \tag{7.65b}$$

In light of this, inserting eqs. (7.65a-7.65b) into eq. (7.64b), we may write $T\chi_{u,loc}(T)$ as

$$T\chi_{u,loc}(T) \overset{T\to 0}{\sim} \big[+\tfrac{1}{4}|\tilde{\mu}| - (-)\tfrac{1}{4}|\tilde{\mu}|\big] = \tfrac{1}{2}|\tilde{\mu}|. \tag{7.66}$$

[6] The very simple case of a free-spin is analysed in Appendix E.

[7] Since the local operator, $\hat{s}_{\rm z}$, does not commute with $\hat{H}$, the A and B states are not eigenstates, as they are of $\hat{S}_{\rm z}$.

In consequence, the 'mixed' susceptibility, $T\chi_{u,loc}(T)$, at zero-temperature is proportional to the local *order parameter*, $|\tilde{\mu}|$. Moreover, whilst $T\chi_{u,loc}(T=0)$ vanishes in a SC phase, on crossing the transition into the LM phase, it evolves continuously as U increases above U_c. Hence, in the limit that $U/U_c \to \infty$, $T\chi_{u,loc}(T=0)$ saturates to the free-spin value of a $\frac{1}{2}$.

7.2.2 Conduction band susceptibility

We now consider the conduction band susceptibility, $T\chi_{u,bath}(T)$, given by eq. (7.56c). By inserting eqs. (7.63, 7.66) into eq. (7.57) we obtain

$$T\chi_{u,bath}(T) = T\chi_{u,u}(T) - \chi_{u,loc}(T) \overset{T\to 0}{\sim} \tfrac{1}{2}[1-|\tilde{\mu}|] = \tfrac{1}{2}[M_{CB}], \tag{7.67}$$

where $M_{CB} = [1-|\tilde{\mu}|]$ is a moment that is delocalised across all of the conduction band states. The physical picture is clear: On crossing $U = U_c$, moving into the local moment phase, a whole excess spin condenses in the system and the conduction band acquires a fully saturated moment, i.e. M_{CB} changes discontinuously from 0 to 1. By contrast, the local moment, $|\tilde{\mu}|$ evolves continuously as U_c is traversed. As the system moves deeper into the LM phase, $M_{CB} \to 0$, as the excess spin becomes localized on the impurity level (the limit of a free-spin, completely decoupled from the band).

7.3 Local field: Susceptibilities from correlation functions

So far we have considered a global field, $h \equiv h_u$, applied to the entire system. Alternatively, we may like to consider the local susceptibility in response to a local field, $h \equiv h_{loc}$, applied solely on the impurity level. The situation here is not as simple, as the local-operator $\hat{s}_z$ *does not* commute with the overall Hamiltonian, $\hat{H}$. We cannot simply differentiate with respect to h as we did in going from eq. (7.54) to eq. (7.55). However, it may be shown [110, 112] that the general *exact* dynamic Matsubara local spin susceptibility when applying an infinitesimal perturbation, $\hat{H}^I = -2h\hat{s}_z$, is given by[8]

$$\chi_{loc,loc}(T, i\omega_q) = 2\int_0^\beta \mathrm{d}\tau \mathrm{e}^{i\omega_q\tau}\langle \hat{T}_\tau[\hat{s}_z(\tau)\hat{s}_z]\rangle \tag{7.68a}$$

where $\hat{T}_\tau[\ldots]$ is the time-ordered product of the operators (with $\tau = it$), $\omega_q = 2q\pi/\beta$ is a *bosonic* Matsubara frequency with q an integer, and expectation values are evaluated at $h = 0$. Using the definition of the thermal average (eq. (7.54)),

[8] We set the chemical potential, $\mu = 0$ for convenience.

eq. (7.68a), becomes

$$\chi_{loc,loc}(T,i\omega_q) = 2\int_0^\beta \mathrm{d}\tau \mathrm{e}^{i\omega_q\tau} \sum_n \tfrac{1}{Z}\langle n|\mathrm{e}^{-\beta\hat{H}}[\mathrm{e}^{\tau\hat{H}}\hat{s}_\mathrm{z}\mathrm{e}^{-\tau\hat{H}}]\hat{s}_\mathrm{z}|n\rangle \tag{7.68b}$$

$$= 2\int_0^\beta \mathrm{d}\tau \mathrm{e}^{i\omega_q\tau} \sum_{n,m} \tfrac{1}{Z}\mathrm{e}^{-\beta E_n}|\langle n|\hat{s}_\mathrm{z}|m\rangle|^2 \mathrm{e}^{\tau[E_n-E_m]} \tag{7.68c}$$

where we have used the fact that a general operator in the Heisenberg picture is given by $\hat{X}(\tau) = \mathrm{e}^{\tau\hat{H}}\hat{X}\mathrm{e}^{-\tau\hat{H}}$, inserted a complete set of states $\hat{1} = \sum_m |m\rangle\langle m|$, and used $\hat{H}|n\rangle = E_n|n\rangle$. Thus, on performing the integration we obtain the spectral (Lehmann) representation of the quantity

$$\chi_{loc,loc}(T,i\omega_q) = \frac{2}{Z}\sum_{n,m} \mathrm{e}^{-\beta E_n}|\langle n|\hat{s}_\mathrm{z}|m\rangle|^2 \left[\frac{\mathrm{e}^{\beta(i\omega_q-[E_m-E_n])}-1}{i\omega_q-[E_m-E_n]}\right] \tag{7.68d}$$

Now, we make the analytic continuation, $i\omega_q \to \omega + i\eta$, from the imaginary axis to the real axis, such that we consider the retarded function, given by

$$\chi^r_{loc,loc}(T,\omega) = \frac{2}{Z}\sum_{n,m} \mathrm{e}^{-\beta E_n}|\langle n|\hat{s}_\mathrm{z}|m\rangle|^2 \left[\frac{\mathrm{e}^{\beta((\omega+i\eta)-[E_m-E_n])}-1}{\omega+i\eta-[E_m-E_n]}\right]. \tag{7.69}$$

Taking the $\omega = 0$ limit of this equation, as is appropriate to find the (purely thermodynamic) static susceptibility $\chi^r_{loc,loc}(T,\omega=0) \equiv \chi_{loc,loc}(T)$, we obtain

$$\chi_{loc,loc}(T) = \frac{2}{Z}\sum_{n,m} |\langle n|\hat{s}_\mathrm{z}|m\rangle|^2 \left[\frac{\mathrm{e}^{\beta[i\eta-E_m]}-\mathrm{e}^{-\beta E_n}}{i\eta-[E_m-E_n]}\right] \tag{7.70a}$$

By swapping n and m in the first term, the equation reduces to

$$\chi_{loc,loc}(T) = -\frac{2}{Z}\sum_{n,m} \mathrm{e}^{-\beta E_n}|\langle n|\hat{s}_\mathrm{z}|m\rangle|^2 \left[\frac{\mathrm{e}^{i\beta\eta}}{[E_n-E_m]-i\eta} + \frac{1}{[E_n-E_m]+i\eta}\right]. \tag{7.71}$$

We have kept in the explicit $\eta = 0^+$ dependence in order to deal correctly with the limit that $E_n \to E_m$. By contrast, if $E_m \neq E_n$, then we may take safely take the limit $\eta \to 0^+$, to yield

$$\chi^{(1)}_{loc,loc}(T) = -\frac{4}{Z}\sum_{\substack{n,m \\ (E_n\neq E_m)}} \mathrm{e}^{-\beta E_n}|\langle n|\hat{s}_\mathrm{z}|m\rangle|^2 \left[\frac{1}{E_n-E_m}\right] \tag{7.72}$$

However, if $[E_n = E_m]$, then we may expand the exponential function as a Taylor series for small $\beta\eta$, i.e.

$$\chi^{(2)}_{loc,loc}(T) = \lim_{\substack{\eta\to 0^+ \\ \eta\beta\to 0^+}} \left[-\frac{2}{Z} \sum_{\substack{n,m \\ (E_n=E_m)}} \mathrm{e}^{-\beta E_n} |\langle n|\hat{s}_\mathrm{z}|m\rangle|^2 \left[\frac{1}{i\eta}\left(1-\mathrm{e}^{i\beta\eta}\right)\right]\right] \tag{7.73a}$$

$$= \lim_{\eta\to 0^+} \left[\frac{2}{Z} \sum_{\substack{n,m \\ (E_n=E_m)}} \mathrm{e}^{-\beta E_n} |\langle n|\hat{s}_\mathrm{z}|m\rangle|^2 \left[\frac{i\eta\beta}{i\eta}\right]\right] \tag{7.73b}$$

$$= \frac{2\beta}{Z} \sum_{\substack{n,m \\ (E_n=E_m)}} \mathrm{e}^{-\beta E_n} |\langle n|\hat{s}_\mathrm{z}|m\rangle|^2. \tag{7.73c}$$

The full expression for the susceptibility is then given by the sum of the non-degenerate, eq. (7.72), and degenerate, eq. (7.73c), terms. We obtain

$$\begin{aligned} &\chi_{loc,loc}(T) = \chi^{(1)}_{loc,loc}(T) + \chi^{(2)}_{loc,loc}(T) \\ =&\frac{4}{Z} \sum_{\substack{n,m \\ (E_n\neq E_m)}} \mathrm{e}^{-\beta E_n} |\langle n|\hat{s}_\mathrm{z}|m\rangle|^2 \left[\frac{1}{E_m - E_n}\right] + \frac{2\beta}{Z} \sum_{\substack{n,m \\ (E_n=E_m)}} \mathrm{e}^{-\beta E_n} |\langle n|\hat{s}_\mathrm{z}|m\rangle|^2 \end{aligned} \tag{7.74}$$

We now take the limit of zero-temperature ($\beta \to \infty$). For a general degenerate $T = 0$ ground-state, $\chi^{(2)}_{loc,loc}(T)$ becomes[9]

$$\chi^{(2)}_{loc,loc}(T) = \sum_{n,m} \frac{2\beta}{Z} \mathrm{e}^{-\beta E_n} |\langle n|\hat{s}_\mathrm{z}|m\rangle|^2 = 2\beta \frac{\sum_{n,m} \mathrm{e}^{-\beta[E_n - E_0]} |\langle n|\hat{s}_\mathrm{z}|m\rangle|^2}{\sum_n \mathrm{e}^{-\beta[E_n-E_0]}}$$

$$\overset{T\to 0}{\sim} \frac{2\beta}{g_0} \sum_{\alpha,\alpha'} |\langle \alpha|\hat{s}_\mathrm{z}|\alpha'\rangle|^2, \tag{7.75}$$

where g_0 is, once again, the ground-state degeneracy, and α, α' run over the degenerate states with energy E_0. For the LM phase, where the system is doubly-degenerate, it follows that

$$\begin{aligned} T\chi^{(2)}_{loc,loc}(T) &\overset{T\to 0}{\sim} \left[|\langle A|\hat{s}_\mathrm{z}|A\rangle|^2 + |\langle B|\hat{s}_\mathrm{z}|B\rangle|^2 + 2|\langle A|\hat{s}_\mathrm{z}|B\rangle|^2 \right] \\ &= \left[\frac{1}{4}|\tilde{\mu}|^2 + \frac{1}{4}|\tilde{\mu}|^2 + \frac{1}{2}|\tilde{\gamma}|^2 \right] = \frac{1}{2}[|\tilde{\mu}|^2 + |\tilde{\gamma}|^2]. \end{aligned} \tag{7.76}$$

where $|\tilde{\gamma}| = \frac{1}{2}\langle A|\hat{s}_\mathrm{z}|B\rangle$, and the diagonal matrix elements are given from eqs. (7.65a-7.65b). This term thus represents excitations between the degenerate LM ground-state A and B states. By virtue of the fact that the operators $\hat{S}_\mathrm{z}$ and $\hat{s}_\mathrm{z}$ commute

[9] On taking the $T \to 0$ limit we implicitly assume that there is an energy gap between the ground-state energy, E_0 and all excited state energies.

with each other, we may simply write

$$\langle A|\hat{s}_{\rm z}\hat{S}_z|B\rangle = \langle A|\hat{S}_z\hat{s}_{\rm z}|B\rangle. \tag{7.77}$$

Therefore, allowing $\hat{S}_{\rm z}$ to act on the states, via eqs. (7.62a-7.62b), we obtain

$$-\tfrac{1}{2}\langle A|\hat{s}_{\rm z}|B\rangle = \tfrac{1}{2}\langle A|\hat{s}_{\rm z}|B\rangle = 0, \tag{7.78}$$

such that the off-diagonal matrix element, $|\tilde{\gamma}|$, vanishes.

In contrast, on taking the $T \to 0$ limit, the first non-degenerate term in eq. (7.74) becomes

$$\chi^{(1)}_{loc,loc}(T) \overset{T\to 0}{\sim} \frac{4}{g_0} \sum_{\substack{m\notin\{A,B\} \\ \alpha\in\{A,B\}}} |\langle\alpha|\hat{s}_{\rm z}|m\rangle|^2 \left[\frac{1}{E_m - E_0}\right]. \tag{7.79}$$

Hence, this term reaches a finite value in the zero temperature limit. Overall, by putting together eqs. (7.76, 7.79), we find that the static local-local susceptibility in the limit that $T \to 0$ is given by

$$\chi_{loc,loc}(T) \overset{T\to 0}{\sim} \frac{1}{2T}|\tilde{\mu}|^2 + 2 \sum_{\substack{m\notin\{A,B\} \\ \alpha\in\{A,B\}}} |\langle\alpha|\hat{s}_{\rm z}|m\rangle|^2 \left[\frac{1}{E_m - E_0}\right]. \tag{7.80}$$

Therefore, the first term dominates in the zero-temperature limit, diverging with a simple Curie Law form. By contrast, the second term goes to a constant finite value and may be neglected in comparison to the first term in a LM phase.

Before proceeding, we make an important point. The fact that $T\chi_{loc,loc}(T=0)$ vanishes with an exponent twice that of the local moment, $|\tilde{\mu}|$, has previously been deduced by a hyperscaling analysis [37].[10] By considering a scaling ansatz for the singular part of the free energy as the critical point is approached (as a function of $h = h_{loc}$, T and $|U - U_c|$), Ingersent *et al.* [37] were able to deduce a number of relations between the exponents of the local magnetization and susceptibility. In Appendix D, Section D.3, we consider a scaling analysis of the free-energy in detail. However, in this present section, we emphasize that the result of eq. (7.80), obtained via a direct (microscopic) analysis of the Lehmann representation, allows us to determine both the *exponent* and the exact *coefficient* of the vanishing of $T\chi_{loc,loc}(T \to 0)$ in the LM phase.

[10] Later, in similar vein to ref [37], others have considered similar scaling relations for the local-susceptibility [46, 48, 79].

High temperature

In contrast to the low-temperature results detailed above, at large temperature (such that $T \to \infty$, or equivalently $\beta \to 0$), $T\chi_{loc,loc}(T)$ is given via eq. (7.70a) as

$$\chi_{loc,loc}(T) = \frac{2}{Z}\sum_{n,m} \mathrm{e}^{-\beta E_n} |\langle n|\hat{s}_\mathrm{z}|m\rangle|^2 \left[\frac{\mathrm{e}^{\beta(i\eta+[E_n-E_m])}-1}{i\eta+[E_n-E_m]}\right] \tag{7.81a}$$

$$= \frac{2\beta}{Z}\sum_{n,m} \mathrm{e}^{-\beta E_n} |\langle n|\hat{s}_\mathrm{z}|m\rangle|^2 = \frac{2\beta}{Z}\sum_{n} \mathrm{e}^{-\beta E_n}\langle n|\hat{s}_\mathrm{z}^2|n\rangle = \frac{2}{T}\langle \hat{s}_\mathrm{z}^2\rangle, \tag{7.81b}$$

where we have expanded the exponential function in the numerator of eq. (7.81a) for small β. This result, once again having a simple Curie-Law form, is the same as we would obtain if we simply differentiated eq. (7.54) w.r.t. h (with $\hat{X} = \hat{s}_\mathrm{z}$) if the local operator $\hat{s}_\mathrm{z}$ actually commuted with the overall Hamiltonian.

7.4 Verification from NRG

From the NRG we may calculate *dynamic* correlation functions of the form[11]

$$A(T,\omega) = i\int_0^\infty \mathrm{e}^{-i(\omega+i\eta)t}\langle \hat{X}(t)\hat{Y}(0)\rangle \,\mathrm{d}t \tag{7.82}$$

where the operators $\hat{X}(t) = \mathrm{e}^{-i\hat{H}t}\hat{X}\mathrm{e}^{i\hat{H}t}$ and $\hat{Y}$ need not be specified at this point. It may be shown by an analogous argument to that leading to eq. (7.68d), that the Lehmann representation of this quantity is given by

$$A(T,\omega) = \frac{1}{Z}\sum_{n,m} \mathrm{e}^{-\beta E_n}\frac{\langle n|\hat{X}|m\rangle\langle m|\hat{Y}|n\rangle}{\omega+i\eta-[E_m-E_n]} \tag{7.83}$$

such that the function has poles just off the real axis and is analytic in the upper half of the complex plane. Thus, on using the relation $[(\omega-\varepsilon)+i\eta]^{-1} = \mathrm{P}[\omega-\varepsilon]^{-1} - i\pi\delta(\omega-\varepsilon)$, we may write

$$A^I(T,\omega) = \frac{1}{Z}\sum_{n,m} \mathrm{e}^{-\beta E_n}\langle n|\hat{X}|m\rangle\langle m|\hat{Y}|n\rangle\delta(\omega-[E_m-E_n]), \tag{7.84}$$

where $A^I(T,\omega) = -\frac{1}{\pi}\mathrm{Im}A(T,\omega)$. This quantity has poles at the excitation energies of the many-body system weighted by the matrix elements $\langle n|\hat{X}|m\rangle\langle m|\hat{Y}|n\rangle$. On

[11] In Appendix C, we briefly describe how correlators of this form may be calculated from NRG. For a comprehensive explanation we refer the reader to refs: [102, 113].

integration of this function over all ω we obtain the sum rule

$$\int_{-\infty}^{\infty} \mathrm{d}\omega\ A^I(T,\omega) = \frac{1}{Z}\sum_{n,m} \mathrm{e}^{-\beta E_n}\langle n|\hat{X}|m\rangle\langle m|\hat{Y}|n\rangle\left[\int_{-\infty}^{\infty} \mathrm{d}\omega\ \delta(\omega - [E_m - E_n])\right]$$
$$= \frac{1}{Z}\sum_{n} \mathrm{e}^{-\beta E_n}\langle n|\hat{X}\hat{Y}|n\rangle = \langle \hat{X}\hat{Y}\rangle, \tag{7.85}$$

where we have used the fact that the delta function is normalized to unity. We make use of this result below. Furthermore, as above, we may split up eq. (7.84) into two distinct contributions, one representing the non-degenerate excitations of the system and a degenerate zero-energy term containing an $\omega = 0$ pole, i.e.

$$A^I(T,\omega) = \frac{1}{Z}\sum_{\substack{n,m \\ (E_n \neq E_m)}} \mathrm{e}^{-\beta E_n}\langle n|\hat{X}|m\rangle\langle m|\hat{Y}|n\rangle\delta(\omega - [E_m - E_n])$$
$$+\frac{1}{Z}\sum_{\substack{n,m \\ (E_n = E_m)}} \mathrm{e}^{-\beta E_n}\langle n|\hat{X}|m\rangle\langle m|\hat{Y}|n\rangle\delta(\omega). \tag{7.86a}$$

Taking the zero-temperature limit of this equation, it is readily shown that

$$A^I(T,\omega) \overset{T\to 0}{\sim} \frac{1}{g_0}\sum_{\alpha,m\neq\alpha} \langle\alpha|\hat{X}|m\rangle\langle m|\hat{Y}|\alpha\rangle\delta(\omega - [E_m - E_0]) + Q\delta(\omega) \tag{7.86b}$$

where once again, $\{\alpha\}$, denotes the degenerate states of the ground-state and g_0 is the degeneracy. At zero-temperature, the poleweight of the zero-ω pole, Q, is given by

$$Q = \frac{1}{g_0}\sum_{\alpha,\beta}\langle\alpha|\hat{X}|\beta\rangle\langle\beta|\hat{Y}|\alpha\rangle = \lim_{\delta\to 0}\left[\int_{-\infty}^{\infty} - \int_{\delta}^{\infty} - \int_{-\infty}^{-\delta}\right][A^I(\omega, T=0)]\ \mathrm{d}\omega, \tag{7.87}$$

where the matrix elements are between the degenerate states of the ground-state manifold. As specified, integrating over the function over all frequency and then subtracting off the finite-frequency parts allows us to calculate the poleweight, Q.

The two cases we now consider are, firstly, when $\hat{X} = \hat{s}_\mathrm{z}$, and $\hat{Y} = \hat{S}_\mathrm{z}$, appropriate to the 'mixed' susceptibility, $\chi_{u,loc}(T)$, of Section 7.2, and secondly when both $\hat{X}$, $\hat{Y} = \hat{s}_\mathrm{z}$, appropriate to the local-local susceptibility, $\chi_{loc,loc}(T)$, of Section 7.3.

Mixed susceptibility

In a LM phase where $g_0 = 2$ and $\alpha \in \{A, B\}$, on setting $\hat{X} = \hat{s}_\mathrm{z}$, and $\hat{Y} = \hat{S}_\mathrm{z}$, eq. (7.86b) becomes

$$A^I_{u,l}(T,\omega) \overset{T\to 0}{\sim} \frac{1}{2} \sum_{\substack{\alpha\in\{A,B\} \\ m\notin\{A,B\}}} \langle\alpha|\hat{s}_\mathrm{z}|m\rangle\langle m|\hat{S}_\mathrm{z}|\alpha\rangle\delta(\omega - [E_m - E_0]) + Q_{u,l}\delta(\omega), \tag{7.88}$$

where the subscript u, l simply denotes that we are considering a correlation function between the global (uniform) operator, $\hat{S}_\mathrm{z}$, and the local operator, $\hat{s}_\mathrm{z}$. Moreover, $\hat{S}_\mathrm{z}$ is a purely diagonal operator (the states $|\alpha\rangle$ are eigenstates of $\hat{S}_\mathrm{z}$). As a consequence, the first term in eq. (7.88) vanishes and $A^I(T,\omega)$ is a purely static quantity containing a single pole at the Fermi level, i.e. $A^I_{u,l}(T,\omega) = A^I_{u,l}(T,\omega=0) = Q_{u,l}\delta(\omega)$. Thus, in order to obtain $Q_{u,l} \equiv \langle\hat{s}_\mathrm{z}\hat{S}_\mathrm{z}\rangle$, we simply integrate over all ω. With α (and β) $\in \{A, B\}$, eq. (7.87) becomes

$$Q_{u,l} = \int_{-\infty}^{\infty} \mathrm{d}\omega\ A^I_{u,l}(T=0,\omega) = \frac{1}{2}\Big[\langle A|\hat{s}_\mathrm{z}|A\rangle\langle A|\hat{S}_\mathrm{z}|A\rangle + \langle B|\hat{s}_\mathrm{z}|B\rangle\langle B|\hat{S}_\mathrm{z}|B\rangle\Big] \tag{7.89a}$$

$$= \frac{1}{2}\left[\frac{1}{4}|\tilde{\mu}| - (-)\frac{1}{4}|\tilde{\mu}|\right] = \frac{1}{4}|\tilde{\mu}|, \tag{7.89b}$$

and therefore by comparison with eqs. (7.64a, 7.66), we find $Q_{u,l} = \frac{1}{2}T\chi_{u,loc}(T=0)$.

Local susceptibility

Alternatively, we may set both $\hat{X}$, $\hat{Y} = \hat{s}_\mathrm{z}$ in eq. (7.86b) to obtain

$$A^I_{l,l}(T,\omega) \overset{T\to 0}{\sim} \frac{1}{2} \sum_{\substack{\alpha\in\{A,B\} \\ m\notin\{A,B\}}} \langle\alpha|\hat{s}_\mathrm{z}|m\rangle\langle m|\hat{s}_\mathrm{z}|\alpha\rangle\delta(\omega - [E_m - E_0]) + Q_{l,l}\delta(\omega), \tag{7.90}$$

where the l, l simply denote that we consider the local-local correlator. By virtue of the fact that the operator $\hat{s}_\mathrm{z}$ is not diagonal, the first term in eq. (7.90) does not vanish. As a consequence, the correlation function, $A^I_{l,l}(T=0,\omega)$, unlike $A^I_{u,l}(T=0,\omega)$, is a *dynamic* quantity with positive weight for all ω. If we integrate the function over all ω, from the sum-rule, eq. (7.85), we simply obtain

$$\int_{-\infty}^{\infty} \mathrm{d}\omega\ A^I_{l,l}(T=0,\omega) = \langle\hat{s}^2_\mathrm{z}\rangle. \tag{7.91}$$

By contrast, in order to obtain the poleweight, $Q_{l,l}$, we make use of eq. (7.87), i.e.

$$Q_{l,l} = \lim_{\delta\to 0}\left[\int_{-\infty}^{\infty} - \int_{\delta}^{\infty} - \int_{-\infty}^{-\delta}\right][A^I_{l,l}(\omega, T=0)]\,\mathrm{d}\omega = \frac{1}{2}\left[|\langle A|\hat{s}_z|A\rangle|^2 + |\langle B|\hat{s}_z|B\rangle|^2\right] \tag{7.92a}$$

$$= \frac{1}{2}\left[\frac{1}{4}|\tilde{\mu}|^2 + \frac{1}{4}|\tilde{\mu}|^2\right] = \frac{1}{4}|\tilde{\mu}|^2, \tag{7.92b}$$

where we have used $\langle A|\hat{s}_z|B\rangle = 0$, eq. (7.78). On comparison of this equation with eq. (7.76), we see that $Q_{l,l} = \frac{1}{2}T\chi_{loc,loc}(T=0)$.

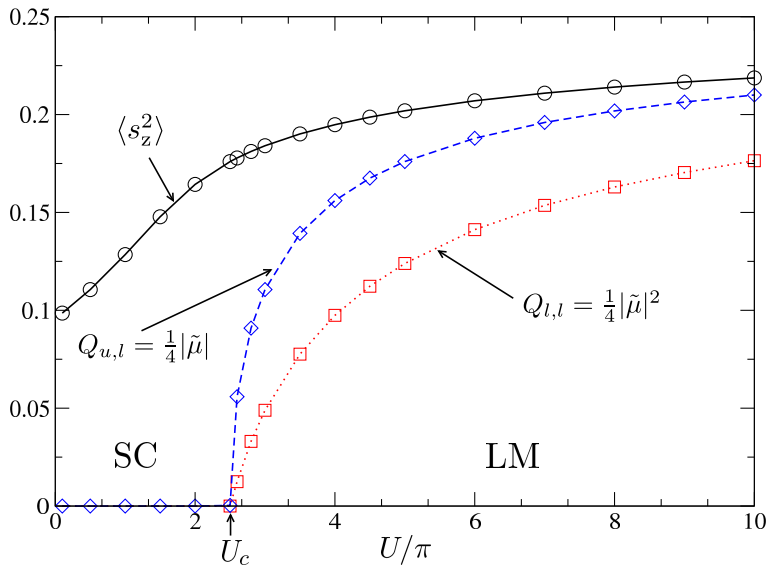


Figure 7.7: NRG results for the PAIM: $r = 0.35$, $x = -1$, $h \equiv h_u, h_{loc} = 0$, $T \to 0$ ($T/D = 10^{-20}$ where D is the bandwidth). Correlation functions are plotted versus U/π. $\langle \hat{s}_z^2\rangle$ is shown with a solid black line (circles). $Q_{u,l} \equiv \langle \hat{s}_z \hat{S}_z\rangle$ is shown with a dashed blue line (diamonds). The poleweight $Q_{l,l}$ from $A^I_{l,l}(\omega)$ is shown with dotted red (squares).

Using FDM-NRG [101, 102] we have calculated both $A^I_{u,l}(T=0,\omega)$, eq. (7.88) and $A^I_{u,l}(T=0,\omega)$, eq. (7.90) for the pseudogap AIM for a typical $r \in [0,1]$. From these dynamic functions we have determined $Q_{u,l} \equiv \langle \hat{s}_z \hat{S}_z\rangle$ from eq. (7.89a), $\langle \hat{s}_z^2\rangle$ from eq. (7.91), and $Q_{l,l}$ from eq. (7.92a). Fig. 7.7 shows NRG calculations for $r = 0.35$ and $x = \varepsilon + \frac{U}{2} = -1$. As shown, the results confirm the deductions above; both $Q_{u,l} = \frac{1}{4}|\tilde{\mu}| = \frac{1}{2}T\chi_{u,loc}(T=0)$ and $Q_{l,l} = \frac{1}{4}|\tilde{\mu}|^2 = \frac{1}{2}T\chi_{loc,loc}(T=0)$ vanishing as $U \to U_c^+(r)$. By contrast for $U < U_c$, both $Q_{u,l}$ and $Q_{l,l}$ vanish by virtue of the fact that the $T=0$ ground-state is non-degenerate. We also find that $\langle \hat{s}_z^2\rangle$ is finite for all U and is continuous across $U = U_c$. Furthermore, all three curves naturally approach $\frac{1}{4}$ as U/U_c becomes large and the local moment, $|\tilde{\mu}|$ saturates to unity, as the system moves deep into the LM phase.

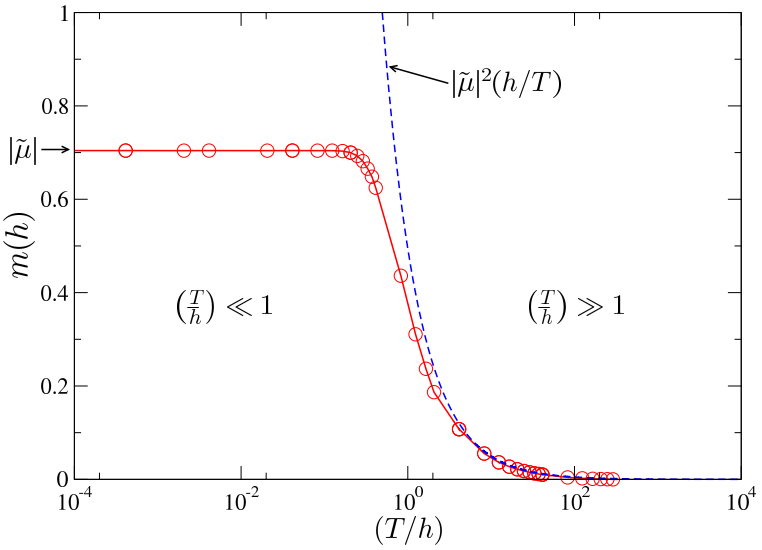


Figure 7.8: NRG results for the PAIM: $r = 0.35$, $x = -1$, $U/\pi = 5$, $h \equiv h_{loc} = 10^{-8}$ for a range of temperatures. The local magnetization, $m(h) = 2\langle s_z \rangle$ is plotted versus T/h (calculated from the NRG spectral functions, eq. (5.3b)), shown in red. The dashed line in blue shows the $T/h \ll 1$ asymptote discussed in the text.

7.4.1 Alternative calculation from NRG

Alternatively, we may wish to calculate $T\chi_{loc,loc}(T)$ from NRG in the same way as Section 7.1.2, once again using the method of Ingersent et al [37, 43]. In direct analogy to eq. (7.40), the local susceptibility may be calculated from

$$\chi_{loc,loc}(T \to 0, h = 0) = \frac{1}{2}\left[\frac{\partial m(h)}{\partial h}\right]_{h=0^{\pm}} \simeq \lim_{h\to 0} \frac{1}{2}\left[\frac{m(h)}{h}\right], \tag{7.93}$$

but here we determine it in the case where $h/T \ll 1$. For a given calculation, we fix U and $h \equiv h_{loc} = 10^{-8}$, then vary T in the range $10^{-10} < T < 10^{-5}$.[12] Each time we calculate $m(h) = 2\langle \hat{s}_z \rangle$ from the spectral functions via

$$m(h) = \int_{-\infty}^{\infty} f(\omega, T)[D_{\uparrow}(\omega; h) - D_{\downarrow}(\omega; h)]\, \mathrm{d}\omega \tag{7.94}$$

which is the finite temperature generalization of eq. (3.3a), with $f(\omega, T) = [1 + \mathrm{e}^{\omega/T}]^{-1}$ the Fermi function, such that $f(\omega, T = 0) = \theta(-\omega)$. Fig. 7.8, shows $m(h)$ plotted versus T/h for a fixed $U/\pi = 5$. As expected, for $T/h \ll 1$ (equivalent to taking the limits $\lim_{h\to 0^+} \lim_{T\to 0}[m(h)]$, see the left panel of Fig. 7.1), the local magnetization saturates to the *permanent* local moment $|\tilde{\mu}|$. By contrast for $T/h \gg 1$, we find that the $m(h)/h$ diverges $\propto a/T$, with a a coefficient of $O(1)$. Using eq. (7.93), it is possible to fit a curve to the $2\chi_{loc,loc}(T) \simeq [m(h)/h] \sim a/T$

[12] All quantities are in units of the energy scale $[\Gamma_0^{1/(1-r)}]$, which we set to 1 for simplicity.

dependence in order to determine a. We find

$$T\chi_{loc,loc}(T/h \gg 1) = \frac{a}{2} = \frac{1}{2}|\tilde{\mu}|^2 \tag{7.95}$$

such that $a = |\tilde{\mu}|^2$, which confirms once again the analytic result of eq. (7.80), and the NRG results of Section 7.4.

7.4.2 Excess spin susceptibility

To conclude this chapter we consider the *excess* susceptibility, $\chi_{imp}(T)$. As discussed in Section 3.2, for quantum impurity problems 'excess' quantities are usually defined via [2]

$$\chi_{\rm imp}(T) = [\chi_{u,u}(T) - \chi^{(0)}_{u,bath}(T)], \tag{7.96}$$

i.e. the global susceptibility for the entire system (in the presence of the impurity), minus the global susceptibility for a free conduction band in the absence of the impurity. We recognise that the free conduction band susceptibility, $\chi^{(0)}_{u,bath}(T \to 0)$, is given via a simple Pauli susceptibility [112], and thus reaches a constant at zero temperature. Therefore by inserting eq. (7.63) into eq. (7.96) we find that

$$\lim_{T\to 0} T\chi_{imp}(T) = \lim_{T\to 0} T\chi_{u,u}(T) = \frac{1}{2}, \tag{7.97}$$

i.e. the zero temperature excess quantity $T\chi_{imp}(T)$ has exactly the same form as $T\chi_{u,u}(T)$ in the LM phase. By contrast, in the SC phase, $\chi_{u,u}(T = 0)$ is finite, and therefore on crossing the transition $U = U_c$, $T\chi_{\rm imp}(T = 0)$ changes discontinuously from 0 to a $\frac{1}{2}$. The form of eq. (7.97) is known from extensive NRG studies for the PAIM [43] and also other impurity models such as the gapped model [50] and the Bose-Fermi Anderson model [55,65]. However, we emphasize that its deduction here is from exact analytical arguments.

7.5 Concluding remarks

In this chapter we have considered a number of spin susceptibilities applicable to impurity models with a zero-temperature phase transition between a non-degenerate SC phase and a doubly-degenerate LM phase. The essential point is that in a LM phase, the limits $T \to 0$ and $h \to 0^{\pm}$ do not commute, such that both must be examined explicitly (the distinct underlying behaviour of the local magnetization, $m(h)$, in each case is shown in Fig. 7.1).

In Section 7.1, by considering the self-energy as a functional derivative of the Luttinger-Ward functional, we were able to deduce previously unknown *exact* forms

for both the local static spin and charge susceptibilities, χ_s, and χ_c at zero-temperature (with $h \to 0^{\pm}$). Furthermore, we were able to determine the exact condition for the phase transition coming from the LM phase as $U \to U_c^+$, finding that in consequence, χ_s, is finite in both phases, but divergent precisely at the critical point (where $U = U_c$). Finally, we used NRG to calculate χ_s (and χ_c) for the pseudogap model (both at $x = 0$ and $x \neq 0$) to verify the exact deductions made.

In the second part of the chapter we consider taking the opposite order of limits, i.e. $h \to 0^{\pm}$ and then $T \to 0$. We have analysed both the response of the system in a LM phase to a global magnetic field, $h = h_u$ and also a local magnetic field, $h = h_{loc}$. We have determined the forms of $\chi_{u,u}(T = 0)$, the global susceptibility in response to a global field, $\chi_{u,loc}(T = 0)$, the local response to a global field, and finally, $\chi_{loc,loc}(T = 0)$, the local susceptibility in response to a local field. In all cases we find that the susceptibilities have simple Curie Law forms, with the Curie coefficient proportional to differing powers of the order parameter, the local moment, $|\tilde{\mu}|$. Finally we calculate the excess spin susceptibility, $T\chi_{imp}(T)$, finding that it takes the Curie law form of a decoupled free-spin in the LM phase.

CHAPTER 8

Summary

In this thesis we have developed a many-body theory for the low-temperature behaviour of doubly-degenerate local moment phases arising in quantum impurity problems. By considering general impurity models possessing a quantum phase transition, we made a number of exact analytic arguments about the underlying non-Fermi liquid nature of local moment phases. Focusing on the pseudogap Anderson model as one such paradigmatic example, we have fully elucidated the exact behaviour in each of its distinct phases. In addition, we have developed the fluctuation exchange approximation to describe the underlying physics of the PAIM.

In Chapter 3 we developed the analytic framework to describe LM phases. We focused initially on the *local* impurity charge, $n(h)$ and magnetization, $m(h)$ as a function of magnetic field, h. Whilst the local charge, $n(h)$, is shown to be continuous across $h = 0$ in both phases, we asserted that in a LM phase (where $U > U_c$) the local magnetization, $m(h)$, is discontinuous across $h = 0$, leading to the existence of a permanent local moment as $h \to 0^{\pm}$, i.e. $m(h \to 0^{\pm}) = \pm|\tilde{\mu}|$. By contrast, in a SC phase (where $U < U_c$), $m(h)$ is continuous across $h = 0$, vanishing as $h \to 0^{\pm}$. This behaviour of $m(h)$ means that it is an appropriate order parameter for the zero-field quantum phase transition, vanishing continuously coming from the LM phase as $U \to U_c^{+}$.

The underlying form of the propagators in each phase was discussed in the light of the behaviour of $m(h)$ as $h \to 0^{\pm}$. Defining $G_{A/B\sigma}(\omega, \pm|h|) \equiv G_{\sigma}(\omega, h)$ for $h \gtrless 0$ in a LM phase, and considering the $h \to 0^{\pm}$ limit, we found that the full (rotationally invariant) propagator could be expressed as a simple average over the broken symmetry functions, i.e. $G(\omega, h = 0) = \frac{1}{2}[G_{A\sigma}(\omega, 0) + G_{B\sigma}(\omega, 0)]$ (where $G_{A\sigma}(\omega, 0) \equiv G_{\sigma}(\omega, 0^{+})$ and $G_{B\sigma}(\omega, 0) \equiv G_{\sigma}(\omega, 0^{-})$). Furthermore, by expressing each of the propagators in terms of an appropriate Dyson equation, we defined two self-energy functions, $\Sigma_{A\sigma}(\omega, 0)$ and $\Sigma_{B\sigma}(\omega, 0)$, distinct from the conventional zero-field (single) self-energy $\Sigma_{\sigma}(\omega, 0)$. By comparing the relevant Dyson equations,

the (zero-field) propagator $G_\sigma(\omega,0)$ (and self-energy $\Sigma_\sigma(\omega,0)$) may be expressed in terms of the two self-energies $\Sigma_{A\sigma}(\omega,0)$ and $\Sigma_{B\sigma}(\omega,0)$.[1] The same approach in a SC phase yielded equivalence of the SSE and TSEs, such that all propagators $G_\sigma(\omega,0)$, $G_{A\sigma}(\omega,0)$, $G_{B\sigma}(\omega,0)$ are identical; the TSE description therefore provides a framework for describing both phases on an equal footing.

Proceeding further in Chapter 3, we noted that in a LM phase the TSEs, $\Sigma_{A/B\sigma}(\omega,0)$, may be obtained via functional differentiation of the LW functional (Φ_{LW}) w.r.t. $G_{A/B\sigma}(\omega,0)$, by analogy to the SSE, $\Sigma_\sigma(\omega,0)$ ($=\delta\Phi_{LW}/\delta G_\sigma(\omega,0)$) in a SC phase. In other words for $U<U_c$, $\Sigma_\sigma(\omega,0)\equiv\Sigma[\{G_{\sigma'}\}]$, whereas for $U>U_c$, $\Sigma_{A\sigma}(\omega,0)\equiv\Sigma[\{G_{A\sigma'}\}]$, where $[\ldots]$ denotes the same functional in each case. The LM phase SSE, $\Sigma_\sigma(\omega,0)$, is then a derivative quantity, obtained as a direct consequence of the underlying behaviour of the TSEs.

We then discussed the excess charge, $n_{\rm imp}(h)$, and magnetization, $m_{\rm imp}(h)$, in both phases. By considering a Friedel-Luttinger sum rule [96] in both phases, the scattering phase shifts, $\delta_\sigma(h)$ for $U<U_c$, and $\delta_{A\sigma}(|h|)$ for $U>U_c$, may be related to the relevant excess charges and Luttinger integrals. In Section 3.4, we generalized Luttinger and Ward's diagrammatic analysis [59] for the vanishing of the Luttinger integral, $I_{L_\sigma}(h)$, (in a Fermi liquid phase), to the case of a LM phase for a Luttinger integral, $I_{L_{A\sigma}}(|h|)$, defined in terms of the broken-symmetry propagators and TSEs. This general (diagrammatic) argument allowed us to relate the excess charges, $n_{{\rm imp};\sigma}(h)$, $n_{{\rm imp};{\rm A}\sigma}(h)$, for $U\lessgtr U_c$, to the impurity renormalized levels, $\varepsilon^*_\sigma(h)$, $\varepsilon^*_{A\sigma}(|h|)$, via two *distinct* Friedel sum rules. A further Luttinger integral, I_L, was then defined in terms of the SSE, $\Sigma_\sigma(\omega,0)$, in a LM phase. However, since the SSE is not directly expressible via a functional derivative of Φ_{LW}, this Luttinger integral cannot be argued to vanish. We concluded the chapter with an analysis of the exactly soluble atomic limit, finding that in the singly-occupied regime the system may be examined using a TSE description. In this regime we determined $I_L(h=0)$ (the Luttinger integral in terms of the SSE), finding that it takes on the value, $|I_L|=\frac{\pi}{2}$.

In Chapter 4 we considered the pseudogap AIM in both phases, but with particular emphasis on what could be said *exactly* about the doubly-degenerate LM phase (using the TSE formalism developed previously). We made use of the Friedel sum rules derived in the previous chapter to determine the excess charges (and magnetizations) in both phases. The physical picture of the transition is that the local moment, $|\tilde{\mu}|$, evolves continuously on entering the LM phase, whereas $m_{{\rm imp};A}(0)$ changes discontinuously from 0 to 1. Precisely at the QCP (where $U=U_c$), an excess moment condenses in the entire system, but has no weight on the impurity itself. In the next part of the chapter we showed that the Luttinger integral, I_L,

[1] The TSE formalism also underlies the local moment approach (LMA) [28, 29, 34, 45, 64], but in an approximate sense.

(defined in terms of the SSE in the LM phase) takes the universal value, $|I_L| = \frac{\pi}{2}$ (the same value as the singly occupied regime of the atomic limit) for general $x \neq 0$.

In Section 4.6 we generalized Luttinger's order by order diagrammatic analysis [60] for the low-ω dependence of the self-energy to the case where the spectral functions have the form, $D_{A\sigma}(\omega, |h|) \overset{\omega \to 0}{\propto} |\omega|^{\lambda_\sigma}$ (with λ_σ a spin-dependent exponent). Since the TSEs, $\Sigma_{A\sigma}(\omega, 0)$, may be expressed in skeleton form as a functional derivative of Φ_{LW}, the analysis holds for both $U \lessgtr U_c$ (where the A labels may simply be dropped for $U < U_c$). As a consequence, the *exact* low-ω behaviour of the self-energies was determined *self-consistently* in each phase to all orders. Proceeding to a discussion of the QPT, we deduced the scaling behaviour of the propagators and self-energies coming from each phase. From the NRG technique we then performed detailed numerical calculations to obtain full scaling functions for the single-particle dynamics for $U \gtrless U_c$, finding that the deduced analytic forms are indeed correct.

In Section 4.10 we analysed the PAIM for the cases of finite global and local magnetic fields applied to the system. Once again, focusing on what could be said about the low-ω forms of the self-energies from Luttinger self-consistency considerations, the essential conclusion is that for any finite h, the local magnetization, $m(h)$, is finite and the QCP is destroyed. The analytic arguments were supplemented by exact numerical data from NRG.

The chapter concluded with a comment about the LM phase precisely at zero-field. On performing direct NRG calculations, we found that the TSE vanishes as $\Sigma^I_{A\sigma}(\omega, 0) \propto |\omega|^r$, a form at odds with the order by order deductions of Section 4.6. We concluded that Luttinger self-consistency can arise in a different sense, where a certain class of Feynman diagrams may be summed to infinite order: an important point returned to in Chapter 6.

In Chapter 5 we analysed the specific case where the skeleton expansion for the self-energy, $\Sigma_\sigma(\omega, 0)$ in the SC phase, and $\Sigma_{A\sigma}(\omega, 0)$ in the LM phase, is truncated at second-order level. We deduced the precise low-ω forms of the propagators and self-energies, and developed a numerical algorithm capable of obtaining self-consistent converged solutions in each phase at the second-order level of approximation. The essential result is that whilst it is possible to find solutions in both phases, the QCP is not adequately described coming from either phase. In fact, it is always possible to obtain SC solutions. In addition, we found that LM solutions (with $|\tilde{\mu}| \neq 0$) are only possible above a finite $U = U_c(r)$, such that for $U > U_c(r)$, both SC and LM solutions coexist. Hence, the second-order treatment fails to capture the underlying interacting nature of the QCP, simply predicting a SC solution at the point $U = U_c$ where $|\tilde{\mu}|$ vanishes.

In Chapter 6 we applied the fluctuation exchange approximation (FLEX) to the PAIM, developing a numerical algorithm capable of self-consistently capturing the correct low-ω behaviour of the propagators in each phase. In a particular range of r

we also found that it is possible to capture the precise low-ω *interacting* behaviour of the QCP previously found in Chapter 4 (from scaling arguments). For the LM phase, a Luttinger self-consistency argument in the vein of the order by order analysis of Chapter 4 is considered, but with a pole contribution located precisely at the Fermi level in the transverse spin polarization propagator, $\Pi^{+-}_{AA}(\omega)$. This argument allowed us to deduce that the low-ω form of the TSE is $\Sigma_{A\sigma}(\omega) \propto |\omega|^r$, distinct from the order by order forms of Section 4.6, and as found from exact numerical NRG calculations of Section 4.11. On implementing the algorithm numerically in the LM phase (specifically at ph symmetry), we found it necessary to make a small modification of replacing $|\tilde{\mu}|$ with $|\mu_0|$ in the static part of the self-energy, in order to describe the QCP coming from both phases.

In the second part of Chapter 6, we applied the FLEX approximation to the pseudogap model away from ph symmetry. Whilst it is possible to obtain fully-self-consistent solutions in the ASC phase, capturing the essential physics of the QCP coming from the LM phase was found to be beyond the scope of the approximation. Moving on, we examined the (local) finite field behaviour of the model within FLEX. The essential result is that the field has the effect of moving the $\omega = 0$ pole in $\mathrm{Im}\Pi^{+-}_{AA}(\omega)$ to finite ω, and as a consequence destroying the QCP.

In Chapter 7 we focused on the *exact* behaviour of an array of spin susceptibilities in coupling to both a local and global magnetic field applied to a general quantum impurity system (with a QPT between LM and SC phases). One of the essential results is that the limits $T \to 0$ and $h \to 0^{\pm}$ do not commute in a LM phase. Firstly, we concentrated on the local spin susceptibility, $\chi_s \equiv \chi_s(h \to 0^+)$, in response to a local magnetic field (applied just to the impurity level) precisely at $T = 0$. We showed that χ_s has an 'RPA' form, remaining finite in each zero-field phase and diverging at the QCP. Considering a similar argument for the local charge susceptibility, χ_c, we found that it too diverges precisely at the QCP in the general asymmetric model. The forms of both χ_s and χ_c were confirmed with exact numerical calculations from NRG.

In the second half of the chapter, the opposite order of limits (i.e. the $h = 0$, and $T \to 0$ case) was considered. Focusing initially on the response of the system to a global magnetic field it was deduced that in a LM phase, the global spin susceptibility takes the simple Curie Law form of a free-spin, i.e. $T\chi_{u,u}(T) \overset{T\to 0}{\sim} \frac{1}{2}$. By investigating the local susceptibility in response to a global field, $\chi_{u,loc}(T)$, and the local susceptibility in response to a local field, $\chi_{loc,loc}(T)$, it was also readily shown that in the LM phase, each were dependent on the local moment, $|\tilde{\mu}|$, taking the forms $T\chi_{u,loc}(T) \overset{T\to 0}{\sim} \frac{1}{2}|\tilde{\mu}|$, $T\chi_{loc,loc}(T) \overset{T\to 0}{\sim} \frac{1}{2}|\tilde{\mu}|^2$. By contrast, in a SC phase, we found that $T\chi_{u,u}(T), T\chi_{u,loc}(T), T\chi_{loc,loc}(T)$ all vanish in the limit $T \to 0$. To conclude the chapter, we considered the excess static spin susceptibility, $T\chi_{\mathrm{imp}}(T = 0)$, finding that it takes the same form as $T\chi_{u,u}(T)$, and hence is discontinuous across

$U = U_c$ vanishing in the SC phase, but equal to a half in the LM phase.

In conclusion, we have undertaken a detailed theoretical study of the underlying behaviour of quantum impurity models that exhibit a quantum phase transition between a (Fermi liquid) SC phase and a (non-Fermi liquid) LM phase. The essential result is that by using the TSE formulation, it is possible to describe the exact behaviour of doubly degenerate phases within a diagrammatic framework. There are a number of possible extensions to the work described here. The TSE description may be explicitly applied to other quantum impurity problems that exhibit a LM phase, such as the gapped Anderson model [50–53, 82], as well as other multi-impurity/multi-channel models [91–94, 96, 97, 114]. Furthermore, we believe that the TSE formalism may be applied to lattice models that have doubly degenerate ground-states, such as the Mott insulating phase in the Hubbard model.

APPENDIX A

Phase shifts and Luttinger integrals

In the first part of this appendix, we (i) relate the phase shift to the renormalized level, eq. (A.8), and (ii) show that the local single-particle spectrum at the Fermi level is determined by the phase shift, eq. (A.13). In the second part of this appendix we consider the ph symmetric PAIM, where the phase shift is discontinuous across the Fermi level in both phases. Furthermore, in Section A.4, we show that by direct consideration of the low-ω forms of both the SSE, $\Sigma(\omega)$, and the propagator, $G(\omega)$, the Luttinger integral, I_L, at ph symmetry in the LM phase has a finite $\omega = 0$ pole contribution.

A.1 Relating the phase shift to the renormalized level

The results derived here are entirely general, independent of whether the zero-field phase is LM or SC, and also applicable to finite field, h (whether it be applied globally or locally). For notational convenience we work explicitly below with propagators, $G_{A\sigma}(\omega, |h|)$ appropriate to the LM phase; but the corresponding results for the SC phase (or more generally in terms of $G_\sigma(\omega, h)$ and the single self-energy, $\Sigma_\sigma(\omega, h)$ follow directly from those given below by simply dropping the A labels).

The retarded broken symmetry Green function, $G_{A\sigma}(\omega, |h|) \equiv G^r_{A\sigma}(\omega, |h|)$, is given by the Dyson equation, eq. (3.23):

$$\begin{aligned} G_{A\sigma}(\omega, |h|) =& [\omega + i\eta - \varepsilon_\sigma - \Gamma_\sigma(\omega, h) - \Sigma_{A\sigma}(\omega, |h|)]^{-1} \\ =& [(\omega - \varepsilon_\sigma - \Gamma^R_\sigma(\omega, h) - \Sigma^R_{A\sigma}(\omega, |h|)) + i(\eta + \Gamma^I_\sigma(\omega, h) + \Sigma^I_{A\sigma}(\omega, |h|))]^{-1} \end{aligned} \tag{A.1}$$

where $\eta = 0^+$ and $\varepsilon_\sigma = \varepsilon - \sigma h$, and the (retarded) hybridization and self-energies are given by $\Gamma_\sigma(\omega, h) = \Gamma^R_\sigma(\omega, h) - i\Gamma^I_\sigma(\omega, h)$ and $\Sigma_{A\sigma}(\omega, |h|) = \Sigma^R_{A\sigma}(\omega, |h|) - i\Sigma^I_{A\sigma}(\omega, |h|)$ respectively. In the following derivation in the interest of conciseness, we suppress the explicit h-dependences of the propagators. The scattering phase shift [2] (for an

'A' state) is then defined by

$$\delta_{A\sigma} = \int_{-\infty}^{0} \mathrm{d}\omega \frac{\partial \delta_{A\sigma}(\omega)}{\partial \omega} = \mathrm{Im} \int_{-\infty}^{0} \mathrm{d}\omega \frac{\partial}{\partial \omega} \ln G_{A\sigma}(\omega). \tag{A.2}$$

In order to relate this quantity to impurity renormalized level, $\varepsilon^*_{A\sigma}$, eq. (A.2) may be rewritten as

$$\delta_{A\sigma} = [\arg(G_{A\sigma}(\omega))]^{\omega=0}_{\omega=-\infty} = [\mathrm{Im} \ln G_{A\sigma}(\omega)]^{\omega=0}_{\omega=-\infty} = [\delta_{A\sigma}(\omega)]^{\omega=0}_{\omega=-\infty}. \tag{A.3}$$

Now writing $\ln z = \ln|z| + i \tan^{-1}(\frac{y}{x})$, with $z = x + iy$, and expressing $G_{A\sigma}(\omega) = [a + ib]^{-1} = (a - ib)/(a^2 + b^2)$, such that $\mathrm{Im} \ln G_{A\sigma}(\omega) = \tan^{-1}(-b/a)$. eq. (A.1) gives

$$\delta_{A\sigma}(\omega) = \mathrm{Im} \ln G_{A\sigma}(\omega) = \tan^{-1}\left[\frac{-(\eta + \Gamma^I_\sigma(\omega) + \Sigma^I_{A\sigma}(\omega))}{(\omega - \varepsilon_\sigma - \Gamma^R_\sigma(\omega) - \Sigma^R_{A\sigma}(\omega))}\right] \tag{A.4a}$$

$$\overset{\omega \to -\infty}{\sim} -\pi \tag{A.4b}$$

where the last result is obtained as a consequence of the $\tan^{-1}(\alpha)$ function being defined in the interval $[-\pi, 0]$ (with both $\Gamma^I_\sigma(\omega)$ and $\Sigma^I_{A\sigma}(\omega)$ positive for all ω). For convenience we define $\tilde{\delta}_{A\sigma}(\omega) = \delta_{A\sigma}(\omega) - \delta_{A\sigma}(-\infty) = \delta_{A\sigma}(\omega) + \pi$ such that from eq. (A.2) the static phase shift is given simply by $\delta_{A\sigma} \equiv \tilde{\delta}_{A\sigma}(\omega = 0)$. With this transformation eq. (A.4a) becomes

$$\tilde{\delta}_{A\sigma}(\omega) = \pi + \tan^{-1}\left[\frac{-(\eta + \Gamma^I_\sigma(\omega) + \Sigma^I_{A\sigma}(\omega))}{(\omega - \varepsilon_\sigma - \Gamma^R_\sigma(\omega) - \Sigma^R_{A\sigma}(\omega))}\right] \tag{A.5}$$

We may now invert the argument of the $\tan^{-1}(\alpha)$ function. If we take $\tan^{-1}(\frac{1}{\alpha})$ to lie in the range $[-\frac{\pi}{2}, +\frac{\pi}{2}]$ then since $\tan^{-1}(\alpha)$ lies in the range $[-\pi, 0]$, we have the identity $\tan^{-1}(\alpha) + \tan^{-1}(\frac{1}{\alpha}) = -\frac{\pi}{2}$. Hence

$$\tan^{-1}\left[\frac{-(\eta + \Gamma^I_\sigma(\omega) + \Sigma^I_{A\sigma}(\omega))}{(\omega - \varepsilon_\sigma - \Gamma^R_\sigma(\omega) - \Sigma^R_{A\sigma}(\omega))}\right] = -\frac{\pi}{2} - \tan^{-1}\left[\frac{\varepsilon_\sigma - \omega + \Gamma^R_\sigma(\omega) + \Sigma^R_{A\sigma}(\omega)}{\eta + \Gamma^I_\sigma(\omega) + \Sigma^I_{A\sigma}(\omega)}\right]. \tag{A.6}$$

Inserting this form into eq. (A.5), we obtain

$$\tilde{\delta}_{A\sigma}(\omega) = \frac{\pi}{2} - \tan^{-1}\left[\frac{\varepsilon_\sigma - \omega + \Gamma^R_\sigma(\omega) + \Sigma^R_{A\sigma}(\omega)}{\eta + \Gamma^I_\sigma(\omega) + \Sigma^I_{A\sigma}(\omega)}\right]. \tag{A.7}$$

Thus setting $\omega = 0$, the static phase shift $\delta_{A\sigma} = \tilde{\delta}_{A\sigma}(0)$ is given by

$$\delta_{A\sigma} = \frac{\pi}{2} - \tan^{-1}\left[\frac{\varepsilon^*_{A\sigma}}{\eta + \Gamma^I_\sigma(0) + \Sigma^I_{A\sigma}(0)}\right] \tag{A.8}$$

where now the $\tan^{-1}(\alpha)$ factor lies in the range $[-\frac{\pi}{2}, +\frac{\pi}{2}]$, and the renormalized level, $\varepsilon^*_{A\sigma} \equiv \varepsilon^*_{A\sigma}(|h|)$ is given by

$$\varepsilon^*_{A\sigma} = \varepsilon - \sigma h + \Gamma^R_\sigma(0) + \Sigma^R_{A\sigma}(0). \tag{A.9}$$

For most problems that we consider in this thesis (as we shall see the only exception is the particle-hole symmetric case of the pseudogap AIM) $\Sigma^I_{A\sigma}(\omega)$ vanishes (continuously) at the Fermi level, and hence may be neglected in the denominator of eq. (A.8). We consequently obtain

$$\boxed{\delta_{A\sigma}(|h|) = \pi n_{\mathrm{imp};A\sigma}(|h|) + I_{L_{A\sigma}}(|h|) = \frac{\pi}{2} - \tan^{-1}\left[\frac{\varepsilon^*_{A\sigma}(|h|)}{\eta + \Gamma^I_\sigma(0,h)}\right],} \tag{A.10}$$

where we have used eq. (3.49) to relate $\delta_{A\sigma}(|h|)$ to the excess charge $n_{\mathrm{imp};A\sigma}(|h|)$ and Luttinger integral, $I_{L_{A\sigma}}(|h|)$ (defined by eq. (3.50)). This equation is the desired result, the so-called Friedel-Luttinger sum rule [96] that we use in Section 3.3 (eqs. 3.52, 3.56).

A.2 Relating the phase shift to the spectral function

The single-particle impurity spectrum $\pi D_{A\sigma}(\omega) = -\mathrm{Im}G_{A\sigma}(\omega)$, simply obtained from eq. (A.1), may be written as

$$\pi D_{A\sigma}(\omega) = \frac{[\eta + \Gamma^I_\sigma(\omega) + \Sigma^I_{A\sigma}(\omega)]}{[\omega - \varepsilon_\sigma - \Gamma^R_\sigma(\omega) - \Sigma^R_{A\sigma}(\omega)]^2 + [\eta + \Gamma^I_\sigma(\omega) + \Sigma^I_{A\sigma}(\omega)]^2} \tag{A.11}$$

If $D_{A\sigma}(\omega)$ is non-divergent (which is the generic case) as $\omega \to 0$ and Fermi level is approached, then eq. (A.11) may be rewritten as

$$\begin{aligned}\pi[\Gamma^I_\sigma(0) + \Sigma^I_\sigma(0)]D_{A\sigma}(0) &= \frac{1}{1 + \left[\frac{\varepsilon_\sigma + \Gamma^R_\sigma(0) + \Sigma^R_{A\sigma}(0)}{\eta + \Gamma^I_\sigma(0) + \Sigma^I_{A\sigma}(0)}\right]^2} \\ &= \frac{1}{1 + \tan^2(\frac{\pi}{2} - \delta_{A\sigma})} = \cos^2(\tfrac{\pi}{2} - \delta_{A\sigma}) = \sin^2(\delta_{A\sigma}),\end{aligned} \tag{A.12}$$

where we have used eq. (A.7) to express the square bracket in terms of $\delta_{A\sigma}$. Using eq. (A.8) and $\Sigma^I_{A\sigma}(0) = 0$, we obtain

$$\pi[\Gamma^I_\sigma(0)]D_{A\sigma}(0) = \sin^2(\delta_{A\sigma}) = \sin^2(\pi n_{\mathrm{imp},A\sigma} + I_{L_{A\sigma}}) \tag{A.13}$$

where if $\Gamma^I_\sigma(0) = \Gamma_0$, this equation reduces to the well known case [2] for the Anderson model coupled to a metallic conduction band.

A.3 Discontinuous phase shift: PAIM ph symmetry

We add a supplement to the arguments that lead to eqs. (A.12-A.13) above (which in practice is relevant only to the ph symmetric PAIM at $h = 0$). The issue centres on the possibility that the phase shift, $\tilde{\delta}_{A\sigma}(\omega)$, may be discontinuous across the Fermi level ($\omega = 0$). From eq. (A.7), $\tilde{\delta}_{A\sigma}(\omega)$ is expressed as

$$\tilde{\delta}_{A\sigma}(\omega) = \frac{\pi}{2} - \tan^{-1}\left[\frac{\varepsilon_\sigma - \omega + \Gamma^R_\sigma(\omega) + \Sigma^R_{A\sigma}(\omega)}{\eta + \Gamma^I_\sigma(\omega) + \Sigma^I_{A\sigma}(\omega)}\right] \tag{A.14}$$

Now consider the case where the numerator of the $\tan^{-1}$ function vanishes continuously at $\omega = 0$, then

$$\delta_{A\sigma} = \tilde{\delta}_{A\sigma}(\omega = 0) = \frac{\pi}{2} \tag{A.15}$$

as ensured by the $\eta = 0^+$ in the denominator.

A.3.1 SC phase

However, suppose that in addition to the numerator vanishing, the denominator $[\Gamma^I_\sigma(\omega) + \Sigma^I_{A\sigma}(\omega)]$ also vanishes continuously (where $\Gamma^I_\sigma(\omega)$ and $\Sigma^I_{A\sigma}(\omega)$ each vanish) as $\omega \to 0$. In this case, notice from eq. (A.11) that the spectral function, $D_{A\sigma}(\omega)$ continuously diverges as $\omega \to 0$, and therefore we cannot simply set $\omega = 0$ as we did in eq. (A.12). Crucially if the ratio

$$\lim_{\omega\to 0^\pm}\left[\frac{\varepsilon_\sigma - \omega + \Gamma^R_\sigma(\omega) + \Sigma^R_{A\sigma}(\omega)}{\Gamma^I_\sigma(0) + \Sigma^I_{A\sigma}(\omega)}\right] \tag{A.16}$$

is finite as $\omega \to 0^\pm$ and different as $\omega \to 0^+$ or $\omega \to 0^-$, then $\tilde{\delta}_{A\sigma}(\omega)$ will be discontinuous across $\omega = 0$. This behaviour is applicable to the $h = 0$ ph symmetric SC phase of the PAIM, where the renormalized level, $\varepsilon^*_{A\sigma} \equiv \varepsilon^*$, vanishes by symmetry.[1] From eq. (4.73) we know that the self-energy, $\Sigma^I(\omega)$, vanishes as $\propto |\omega|^{2-3r}$, with an exponent larger than r for $r < \frac{1}{2}$.[2] Thus, the low-ω dependence of $\Sigma(\omega)$ may be neglected as $\omega \to 0$, compared to the hybridization. On inserting the hybridization function given by eq. (4.1b), into eq. (A.14) we obtain

$$\tilde{\delta}^\pm = \tilde{\delta}(\omega \to 0^\pm) = \frac{\pi}{2} - \tan^{-1}\left(\frac{\mp\tan(\frac{\pi}{2}r)\Gamma_0|\omega|^r}{\Gamma_0|\omega|^r}\right) \tag{A.17a}$$

$$= \frac{\pi}{2} \pm \frac{\pi}{2}r, \tag{A.17b}$$

[1] All A and σ subscripts may be dropped in the SC phase at zero field.

[2] From the arguments of Section 4.7.2, the real part, $\Sigma^R(\omega)$, also vanishes with a power greater than $\Gamma(\omega)$.

such that $\tilde{\delta}^{\pm} = \delta \pm \frac{\pi}{2}$. By analogy with eq. (A.12) we may then write the low-ω behaviour of the spectral function as

$$\lim_{\omega \to 0^{\pm}} \pi \Gamma^I(\omega) D(\omega) = \sin^2(\tfrac{\pi}{2} \pm \tfrac{\pi}{2} r) = [1 + \tan^2(\tfrac{\pi}{2} r)]^{-1}, \tag{A.18}$$

where we have used the fact that $\Sigma^I(\omega)$ vanishes more rapidly tham $\Gamma^I(\omega)$ as $\omega \to 0$. This result simply recovers the well known [64, 100] Fermi liquid spectral pinning condition of eq. (4.39), i.e. $\lim_{\omega \to 0^{\pm}} [[1 + \tan^2(\frac{\pi}{2} r)] \Gamma_0 |\omega|^r D(\omega)] \to 1$.

A.3.2 LM phase

We now turn to the ph symmetric LM phase. From eqs. (4.33-4.34), the low-ω dependence of the SSE at $h = 0$ is given by $\Sigma(\omega) \overset{\omega \to 0}{\sim} a_s[\mathrm{sgn}(\omega)\beta(r) - i]|\omega|^{-r}$. Inserting this form into eq. (A.14) for $\tilde{\delta}_{A\sigma}(\omega)$ (where we may drop A and σ subscripts at zero-field within a SSE description) we simply obtain[3]

$$\tilde{\delta}^{\pm} = \tilde{\delta}(\omega \to 0^{\pm}) = \frac{\pi}{2} - \tan^{-1}\left(\frac{\pm \tan(\frac{\pi}{2} r) a_s |\omega|^{-r}}{a_s |\omega|^{-r}} \right) \tag{A.19a}$$

$$= \frac{\pi}{2} \mp \frac{\pi}{2} r, \tag{A.19b}$$

Thus, once again relating the spectral function, eq. (A.11), to this quantity we obtain

$$\lim_{\omega \to 0^{\pm}} \pi \Sigma^I(\omega) D(\omega) = \sin^2(\tfrac{\pi}{2} \mp \tfrac{\pi}{2} r) = [1 + \tan^2(\tfrac{\pi}{2} r)]^{-1}, \tag{A.20}$$

where we have used the fact that $\Gamma^I(\omega)$ vanishes as $\omega \to 0^{\pm}$, whilst $\Sigma^I(\omega)$ is divergent. Thus, we have obtained the LM phase spectral pinning condition of eq. (4.38), i.e. $\lim_{\omega \to 0^{\pm}} [[1 + \tan^2(\frac{\pi}{2} r)] \Sigma^I(\omega) D(\omega)] \to 1$.

A.4 LM phase: Luttinger integral pole contribution

In this section we show that at ph symmetry in the LM phase there is a finite pole contribution to the Luttinger integral, I_L (given by eq. (3.75)), not picked up by the numerics of Fig. 4.6.

With the low-ω form of the SSE, given by eqs. (4.33-4.34), the low-ω dependence of the spin-independent propagator, $G(\omega) = G^R(\omega) - i\pi D(\omega)$, eq. (A.1) (with A and

[3] All other terms in eq. (A.14) are irrelevant compared to the divergent form of $\Sigma(\omega)$ on the lowest frequency scales.

σ subscripts dropped), is simply given by

$$G(\omega) = [\omega - \varepsilon - \Gamma(\omega) - \Sigma(\omega)]^{-1}, \tag{A.21a}$$

$$\overset{\omega\to 0}{\sim} [a_s[\mathrm{sgn}(\omega)\beta(r) - i]|\omega|^{-r}]^{-1}. \tag{A.21b}$$

(All the other terms in eq. (A.21a) are insignificant compared to the divergent self-energy behaviour in the limit that $\omega \to 0$.) The low-ω forms of the real part and spectral function follow as

$$G^R(\omega) \overset{\omega\to 0}{\sim} -\frac{\mathrm{sgn}(\omega)\beta(r)|\omega|^r}{a_s[1+\beta^2(r)]}, \quad \pi D(\omega) \overset{\omega\to 0}{\sim} \frac{|\omega|^r}{a_s[1+\beta^2(r)]}. \tag{A.21c}$$

In Section 4.5, in order to obtain the low-ω form of the SSE, eq. (4.33), we assumed that the TSEs, $\Sigma_{A\sigma}(\omega) \equiv \Sigma_{A\sigma}(\omega, 0)$, vanish with a power $\lambda \geq r$ (as we later show explicitly by self-consistency considerations in Section 4.6). Now assuming that $\Sigma_{A\sigma}(\omega) \overset{\omega\to 0}{\sim} b^{\pm}_{A\sigma}|\omega|^r[\mathrm{sgn}(\omega)\beta(r) - i]$ (with $b^{\pm}_{A\sigma} = b^{\mp}_{A-\sigma}$ at $x = 0$ from the symmetry relation of eq. (4.3c)), such that $\lambda(= r)$ takes its smallest permitted value. Inserting this low-ω form into eq. (3.30), it is possible to show that in addition to the low-ω dependences of eq. (A.21c), there is a zero-ω pole contribution to $\Sigma^I(\omega)$. It is simply a matter of algebra to show that

$$\Sigma^I_P(\omega) = \frac{\pi a_s[1+\beta^2(r)]}{\beta(r)}|\omega|^{1-r}\delta(\omega), \tag{A.22}$$

where the P subscript denotes 'pole', and the coefficient is given by $a_s = [\varepsilon^*_{A\sigma}]^2/(1 + \frac{1}{2}[b^{\pm}_{A\uparrow} + b^{\mp}_{A\downarrow}])[1+\beta^2(r)]$. Hence, this pole contribution is 'dead', vanishing at $\omega = 0$ (and therefore does not feature explicitly in $\Sigma^I(\omega)$). However, before discounting this contribution, let us first consider the explicit pole contribution to the Luttinger integral, I_L, eq. (3.75),

$$I^P_L = -\int_{-\infty}^{0} \mathrm{d}\omega \frac{\partial \Sigma^I_P(\omega)}{\partial \omega} G^R(\omega) = -[G^R(\omega)\Sigma^I_P(\omega)]^0_{-\infty} + \int_{-\infty}^{0} \mathrm{d}\omega \frac{\partial G^R(\omega)}{\partial \omega}\Sigma^I_P(\omega). \tag{A.23}$$

where we have used integration by parts to re-express the integral (in order to avoid differentiating the delta function). On differentiation of $G^R(\omega)$, eq. (A.21c), we obtain $\partial G^R(\omega)/\partial\omega = -r\beta(r)|\omega|^{r-1}/(a_s[1+\beta^2(r)])$. Thus, inserting this form, together with eq. (A.22) into eq. (A.23), and recognising that the first term on the RHS vanishes, we obtain

$$I^P_L = -\pi r \int_{-\infty}^{0} \mathrm{d}\omega\ |\omega|^{r-1} \times |\omega|^{1-r}\delta(\omega) = -\frac{\pi}{2} r \left[\int_{-\infty}^{\infty} \mathrm{d}\omega\ \delta(\omega)\right] = -\frac{\pi}{2} r, \tag{A.24}$$

where we have used that $\delta(\omega)$ is both an even function and normalized to unity. Hence, eq. (A.24) shows that the ω-dependence in front of the delta function exactly cancels, and thus there is a finite contribution to I_L coming from the 'dead' pole contribution in $\Sigma^I(\omega)$, eq. (A.22). From the numerical NRG results (shown in Fig. 4.6), this $\omega = 0$ pole contribution is not picked up, and we find $I_L^{band} = +\frac{\pi}{2}r$. However, putting this contribution together with I_L^P gives the required result (as expected from the phase shift arguments of Section 4.4) that (the total) $I_L = I_L^P + I_L^{band}$ vanishes in the LM phase at ph symmetry (where $x = 0$).

APPENDIX B

Symmetries of the Hamiltonian

B.1 Particle-hole transforms

In this appendix we establish what symmetry relations there are between the propagators (and self-energies) as a consequence of the Hamiltonian being invariant under certain canonical transformations of operators.

The single impurity Anderson model Hamiltonian may be written in the form

$$\hat{H} = \sum_{\sigma}(\varepsilon - \sigma h)\hat{n}_{\sigma} + U\hat{n}_{\uparrow}\hat{n}_{\downarrow} + \sum_{\mathbf{k},\sigma}(\varepsilon_{\mathbf{k}} - \sigma h)\hat{n}_{\mathbf{k}\sigma} + \sum_{\mathbf{k},\sigma}\left(V_{\mathbf{k}}\hat{c}^{\dagger}_{\sigma}\hat{c}_{\mathbf{k}\sigma} + \text{h.c.}\right) \tag{B.1a}$$

$$= \varepsilon\hat{n} - 2h\hat{s}_{\text{z}} + U\hat{n}_{\uparrow}\hat{n}_{\downarrow} + \sum_{\mathbf{k}}\varepsilon_{\mathbf{k}}\hat{n}_{\mathbf{k}} - 2h\sum_{\mathbf{k}}\hat{s}_{\mathbf{k}\text{z}} + \left(V_{\mathbf{k}}\hat{c}^{\dagger}_{\sigma}\hat{c}_{\mathbf{k}\sigma} + \text{h.c.}\right) \tag{B.1b}$$

where $\hat{n}_{\sigma} = \hat{c}^{\dagger}_{\sigma}\hat{c}_{\sigma}$, is the impurity occupancy operator, and $\hat{s}_z = \frac{1}{2}\sum_{\sigma}\sigma\hat{n}_{\sigma}$. The total $\hat{S}_{\text{z}}$ operator is given via $\hat{S}_{\text{z}} = \hat{s}_{\text{z}} + \sum_{\mathbf{k}}\hat{s}_{\mathbf{k}\text{z}}$, with the field h acting globally (both on the conduction band states and the impurity level). The case of a purely local field is recovered by simply neglecting the $-2h\sum_{\mathbf{k}}\hat{s}_{\mathbf{k}\text{z}}$ term in the Hamiltonian. The conduction band is assumed to be symmetric, such that $\varepsilon_{\mathbf{k}} = -\varepsilon_{-\mathbf{k}}$, so that $\sum_{\mathbf{k}}\varepsilon_{\mathbf{k}} = \int_{-\infty}^{\infty}\mathrm{d}\varepsilon\;\varepsilon\;\rho_b(\varepsilon) = 0$; with $V_{\mathbf{k}} = V_{-\mathbf{k}}$ for the hybridization matrix elements. The impurity energy level may be expressed as

$$\varepsilon = x - \tfrac{U}{2}, \tag{B.2}$$

which defines the asymmetry parameter, x ($x = 0$ corresponds to the unique particle-hole symmetric point where $\varepsilon = -\frac{U}{2}$). The Hamiltonian, $\hat{H} \equiv \hat{H}(x,h)$, may then be written as

$$\hat{H}(x,h) = (x - \tfrac{U}{2})\hat{n} - 2h\hat{s}_{\text{z}} + U\hat{n}_{\uparrow}\hat{n}_{\downarrow} - 2h\sum_{\mathbf{k}}\hat{s}_{\mathbf{k}\text{z}} + \hat{H}_{CB} + \hat{H}_{hyb}, \tag{B.3}$$

where $\hat{H}_{CB}$ and $\hat{H}_{hyb}$ denote the conduction band and hybridization terms in eq. (B.1a) respectively. Now consider the following particle-hole transform ('pht'):

$$\hat{c}_\sigma \leftrightarrow \hat{c}^\dagger_{-\sigma} \qquad \hat{c}_{\mathbf{k}\sigma} \leftrightarrow -\hat{c}^\dagger_{-\mathbf{k}-\sigma}. \tag{B.4}$$

This transform exchanges both particles/holes and also spins. Both the $\hat{H}_{CB}$ and $\hat{H}_{hyb}$ remain completely unchanged by the pht as is readily checked. Now we consider the remaining terms in the Hamiltonian. Under the pht the operators become

$$\hat{n}_\sigma = \hat{c}^\dagger_\sigma \hat{c}_\sigma \leftrightarrow 1 - \hat{n}_{-\sigma}, \qquad \hat{n}_{\mathbf{k}\sigma} = \hat{c}^\dagger_{\mathbf{k}\sigma}\hat{c}_{\mathbf{k}\sigma} \leftrightarrow 1 - \hat{n}_{-\mathbf{k}-\sigma}, \tag{B.5}$$

and hence

$$\hat{n} = \sum_\sigma \hat{n}_\sigma \leftrightarrow 2 - \hat{n} \qquad \hat{s}_z = \frac{1}{2}\sum_\sigma \sigma \hat{n}_\sigma \leftrightarrow \hat{s}_z, \tag{B.6a}$$

$$\hat{n}_{\mathbf{k}} = \sum_\sigma \hat{n}_{\mathbf{k}\sigma} \leftrightarrow 2 - \hat{n}_{-\mathbf{k}} \qquad \hat{s}_{\mathbf{k}z} = \frac{1}{2}\sum_\sigma \sigma \hat{n}_{\mathbf{k}\sigma} \leftrightarrow \hat{s}_{-\mathbf{k}z}. \tag{B.6b}$$

Inserting these transforms into the Hamiltonian, eq. (B.3), under the pht it is changed to

$$\hat{H}(x,h) \to 2x + \big(-\tfrac{U}{2} - x\big)\hat{n} - 2h\hat{s}_z + U\hat{n}_\uparrow\hat{n}_\downarrow - 2h\sum_{\mathbf{k}} \hat{s}_{\mathbf{k}z} + H_{CB} + \hat{H}_{hyb} \tag{B.7a}$$

$$= \hat{H}(-x,h) + 2x. \tag{B.7b}$$

Therefore $\hat{H}$ is invariant under the pht at the ph symmetric point, $x = 0$ (where $\varepsilon = -\frac{U}{2}$). More generally, the transformation relates the Hamiltonian for a given x, to the Hamiltonian for $-x$, at precisely the same value of the field h. (The $2x$ in eq. (B.7b) is an irrelevant constant term.)

We may also consider a ph transformation in which particles/holes are exchanged, but spins remain unchanged, such that

$$\hat{c}_\sigma \leftrightarrow \hat{c}^\dagger_\sigma \qquad \hat{c}_{\mathbf{k}\sigma} \leftrightarrow -\hat{c}^\dagger_{-\mathbf{k}\sigma}. \tag{B.8}$$

In this case the spin operators transform as

$$\hat{s}_z \leftrightarrow -\hat{s}_z \qquad \hat{s}_{\mathbf{k}z} \leftrightarrow -\hat{s}_{-\mathbf{k}z}, \tag{B.9}$$

such that the Hamiltonian becomes

$$\hat{H}(x,h) = \hat{H}(-x,-h) + 2x. \tag{B.10}$$

B.2 Physical properties

A pht is a canonical transform, and just amounts to a different way of representing the fermions in the system. Moreover, this means that the expectation value of any operator must remain unchanged under a pht, i.e.

$$\langle \hat{A}(x,h)\rangle \equiv A(x,h) = \frac{\mathrm{Tr}\hat{A}\mathrm{e}^{-\beta\hat{H}(x,h)}}{\mathrm{Tr}\mathrm{e}^{-\beta\hat{H}(x,h)}} = \left[\frac{\mathrm{Tr}\hat{A}\mathrm{e}^{-\beta\hat{H}(x,h)}}{\mathrm{Tr}\mathrm{e}^{-\beta\hat{H}(x,h)}}\right]_{pht}. \tag{B.11}$$

From eq. (B.7b), $\hat{H}(x,h) = \hat{H}(-x,h) + 2x$, the constant $2x$ term clearly cancels in eq. (B.11):

$$A(x,h) = \frac{\mathrm{Tr}\hat{A}\mathrm{e}^{-\beta\hat{H}(-x,h)}}{\mathrm{Tr}\mathrm{e}^{-\beta\hat{H}(-x,h)}} = A_p(-x,h), \tag{B.12}$$

where $\hat{A}_p = [\hat{A}]_{pht}$. If $\hat{A} = \hat{n}$, then from eq. (B.6a), eq. (B.12) relates the local (impurity) charge at x to that at $-x$, $n(x,h) = 2 - n(-x,h)$.

The same reasoning applies to any physical property. We now consider the time-ordered local propagator

$$G_\sigma(t) = -i\langle\hat{T}(\hat{c}_\sigma(t)\hat{c}^\dagger_\sigma)\rangle = -i\langle\hat{T}(\hat{c}_\sigma\hat{c}^\dagger_\sigma(-t))\rangle = +i\langle\hat{T}(\hat{c}^\dagger_\sigma(-t)\hat{c}_\sigma)\rangle, \tag{B.13}$$

with $\hat{T}$ the Wick time-ordering operator. Explicitly labeling the x and h dependence of the propagator, we have

$$\begin{aligned} G_\sigma(t;x,h) &= -i\langle\hat{T}(\hat{c}_\sigma(t)\hat{c}^\dagger_\sigma)\rangle_x && \text{(B.14a)}\\ &= -i\left[\langle\hat{T}(\hat{c}_\sigma(t)\hat{c}^\dagger_\sigma)\rangle\right]_{pht} = -i\langle\hat{T}(\hat{c}^\dagger_{-\sigma}(t)\hat{c}_{-\sigma})\rangle_{-x} && \text{(B.14b)}\\ &= -G_{-\sigma}(-t;-x,h). && \text{(B.14c)} \end{aligned}$$

Where we have used

$$\begin{aligned} [\hat{c}_\sigma(t)]_{pht} &= [\mathrm{e}^{-i\hat{H}(x,h)t}\hat{c}_\sigma\mathrm{e}^{i\hat{H}(x,h)t}]_{pht} && \text{(B.15a)}\\ &= \mathrm{e}^{-i[\hat{H}(-x,h)+2x]t}\hat{c}^\dagger_{-\sigma}\mathrm{e}^{i[\hat{H}(-x,h)+2x]t} && \text{(B.15b)}\\ &= \mathrm{e}^{-i\hat{H}(-x,h)t}\hat{c}^\dagger_{-\sigma}\mathrm{e}^{i\hat{H}(-x,h)t}. && \text{(B.15c)} \end{aligned}$$

Expressing eq. (B.14c) in the frequency domain gives the key result

$$G_\sigma(\omega;x,h) = -G_{-\sigma}(-\omega;-x,h), \tag{B.16}$$

which relates the σ spin propagator at a frequency ω and a given value $x = \varepsilon + \frac{U}{2}$ to the $-\sigma$ spin propagator at frequency $-\omega$ and $-x$ for the same value of the field h.

In order to establish the corresponding pht relation between the self-energies we write the time-ordered propagator in terms of a Dyson equation (eq. (2.50)):

$$G_\sigma(\omega; x, h) = [\omega + i\eta\,\mathrm{sgn}(\omega) - \varepsilon + \sigma h - \Gamma_\sigma(\omega, h) - \Sigma_\sigma(\omega; x, h)]^{-1}. \tag{B.17}$$

In this thesis we consider a (time-ordered) hybridization function $\Gamma_\sigma(\omega, h) = \Gamma^R_\sigma(\omega, h) - i\,\mathrm{sgn}(\omega)\Gamma_\sigma(\omega, h)$, which for the pseudogap Anderson model satisfies (c.f. eq. (4.1))

$$\Gamma^I_\sigma(\omega, h) = \Gamma_0|\omega + \sigma h|^r, \qquad \Gamma^R_\sigma(\omega, h) = -\,\mathrm{sgn}(\omega)\beta(r)\Gamma_0|\omega + \sigma h|^r. \tag{B.18}$$

For a fixed h, the following relation then holds

$$\Gamma_\sigma(\omega, h) = -\Gamma_{-\sigma}(-\omega, h). \tag{B.19}$$

Inserting this relation into eq. (B.17), along with $\varepsilon = x - \frac{U}{2}$ we find

$$\begin{aligned} G_\sigma(\omega; x, h) &= -[-\omega - i\eta\,\mathrm{sgn}(\omega) + x - \tfrac{U}{2} - \sigma h - \Gamma_{-\sigma}(-\omega, h) + \Sigma_\sigma(\omega; x, h)]^{-1}, \\ &= -[-\omega + i\eta\,\mathrm{sgn}(-\omega) + x + \tfrac{U}{2} - \sigma h - \Gamma_{-\sigma}(-\omega, h) - (U - \Sigma_\sigma(\omega; x, h))]^{-1}. \end{aligned} \tag{B.20}$$

Expressing $-G_{-\sigma}(-\omega; -x, h)$ in terms of an equivalent Dyson equation yields

$$\begin{aligned} &-G_{-\sigma}(-\omega; -x, h) = \\ &\quad - [-\omega + i\eta\,\mathrm{sgn}(-\omega) + x + \tfrac{U}{2} - \sigma h - \Gamma_{-\sigma}(-\omega, h) - \Sigma_{-\sigma}(-\omega; -x, h)]^{-1}. \end{aligned} \tag{B.21}$$

On comparing eqs. (B.20-B.21) and using the relation eq. (B.16), we find

$$\Sigma_{-\sigma}(-\omega; -x, h) = U - \Sigma_\sigma(\omega; x, h)), \tag{B.22}$$

which relates the (time-ordered) self-energies, $\Sigma_\sigma(\omega; x, h) = \Sigma^R_\sigma(\omega; x, h) - i\,\mathrm{sgn}(\omega)\,\Sigma^I_\sigma(\omega; x, h)$, at the same value of the field, h.

A similar relation can be obtained for the renormalized levels. The field dependent renormalized level may be expressed as

$$\varepsilon^*_\sigma(x, h) = \varepsilon - \sigma h + \Gamma_\sigma(0, h) + \Sigma^R_\sigma(0, h) = x - \tfrac{U}{2} - \sigma h + \Gamma_\sigma(0, h) + \Sigma^R_\sigma(0, h). \tag{B.23}$$

From this

$$\varepsilon^*_\sigma(x,h) = -[-x + \tfrac{U}{2} + \sigma h - \Gamma_\sigma(0,h) - \Sigma^R_\sigma(0,h)] \tag{B.24a}$$
$$= -[-x + \tfrac{U}{2} + \sigma h + \Gamma_{-\sigma}(0,h) - (U - \Sigma^R_{-\sigma}(0,h)] \tag{B.24b}$$
$$= -[-x - \tfrac{U}{2} + \sigma h - \Gamma_{-\sigma}(0,h) - \Sigma^R_{-\sigma}(0,h)]. \tag{B.24c}$$

Thus, we obtain the relation

$$\varepsilon^*_\sigma(x,h) = -\varepsilon^*_{-\sigma}(-x,h). \tag{B.25}$$

B.3 A and B propagators

In this appendix so far we have not labeled the explicit A or B dependence of the propagators because we have been analysing a ph transform (eq. (B.4)) at the precisely the same field, h. However, for $U > U_c$ for $h = |h| > 0$ we may simply add A labels, and for $h = -|h| < 0$ we may add B labels. The pht equations relating the propagators, self-energies and renormalized levels, eqs. (B.16, B.22, B.25), may be written with explicit A (or B) labels

$$G_{A\sigma}(\omega; x, |h|) = -G_{A-\sigma}(-\omega; -x, |h|), \tag{B.26a}$$
$$\Sigma_{A-\sigma}(-\omega; -x, |h|) = U - \Sigma_{A\sigma}(\omega; x, |h|), \tag{B.26b}$$
$$\varepsilon^*_{A\sigma}(x, |h|) = -\varepsilon^*_{A-\sigma}(-x, |h|). \tag{B.26c}$$

At the specific ph symmetric point (where $x = 0$), eq. (B.26c) shows that the renormalized levels are sign definite for any field $|h|$, i.e. $\varepsilon^*_{A\sigma}(x = 0, |h|) = -\varepsilon^*_{A-\sigma}(x = 0, |h|)$. By contrast for $U < U_c$ in a SC phase, these relations hold if the explicit A labels are dropped. At ph symmetry in the zero field SC phase the self-energy is spin independent; eq. (B.25) then implies that the renormalized level must vanish, $\varepsilon^*(0,0) = 0$ for $x = 0$, $U < U_c$.

B.4 Reversing the field

There is another symmetry of the Hamiltonian that we may exploit. The Hamiltonian is invariant if for a given fixed x, we reverse the polarity of the field, $h \leftrightarrow -h$ and swap σ for $-\sigma$. This implies that the propagators exhibit the symmetry

$$G_{\alpha\sigma}(\omega; x, h) = G_{\bar{\alpha}-\sigma}(\omega; x, -h) \tag{B.27}$$

where $\alpha = A, B$, $\bar{\alpha} = B, A$, with $h = |h| > 0$ for A and $h = -|h| < 0$ for B. The $\alpha, \bar{\alpha}$ labels can of course be dropped once again for $U < U_c$ in the SC phase. Applying

this symmetry to the self-energies and the renormalized levels yields

$$\Sigma_{\alpha\sigma}(\omega; x, h) = \Sigma_{\bar{\alpha}-\sigma}(\omega; x, -h), \tag{B.28}$$

$$\varepsilon^*_{\alpha\sigma}(x, h) = \varepsilon^*_{\bar{\alpha}-\sigma}(x, -h). \tag{B.29}$$

Combining eqs. (B.27-B.29), with the pht relations eqs. (B.26a-B.26c) gives

$$G_{A\sigma}(\omega; x, |h|) = -G_{B\sigma}(-\omega; -x, -|h|), \tag{B.30a}$$

$$\Sigma_{A\sigma}(\omega; x, |h|) = U - \Sigma_{B-\sigma}(-\omega; -x, -|h|), \tag{B.30b}$$

$$\varepsilon^*_{A\sigma}(x, |h|) = -\varepsilon^*_{B\sigma}(-x, -|h|), \tag{B.30c}$$

which relate the A and B quantities, for $\sigma \to -\sigma$, $h \to -h$.

The pht considered (eq. (B.4)), in which particles and holes are exchanged as well as $\sigma \to -\sigma$, relates the physical properties of the system for $x \to -x$ for the same value of the magnetic field h. As mentioned above, we could have also considered the physical properties of the system under a ph transformation, eq. (B.8) where spins were not exchanged, yielding eq. (B.10), $\hat{H}(x, h) = \hat{H}(-x, -h)+2x$. Using this relation one could have proceeded to determine the resultant symmetries satisfied by $G_\sigma(\omega, x, h)$ and $\varepsilon^*_\sigma(x, h)$. However, if this analysis is undertaken, we yield the same results as eqs. (B.30a-B.30c). This is telling us that consideration of the pht eq. (B.4), and of $\uparrow$, $\downarrow$ spin symmetry (embodied by eqs. (B.27-B.29)) together encompass the results obtained from a straight ph transform.

APPENDIX C

Numerical renormalization group

In this appendix we discuss briefly the ideas and concepts behind the numerical renormalization group (NRG), originally developed by Wilson for the Kondo model [10]. The NRG was subsequently applied to the metallic Anderson model by Krishnamurthy *et al.* [11, 12], and to the pseudogap Anderson model by refs [35–39, 41, 43]. NRG has also been used to solve a range of other impurity models including the multi-impurity and multi-channel Kondo/Anderson models - for a comprehensive review, see ref: [113]. The NRG provides an extremely powerful *non-perturbative* tool, able to provide numerically exact results for both thermodynamic quantities and also dynamic functions such as the impurity propagator. The technique also provides a non-perturbative way of thinking about quantum impurity problems, based on the renormalization group concept and building on Anderson's ideas of scaling [18].

In this thesis we use the full density matrix (FDM) formulation of NRG to obtain exact numerical results for the dynamics of the pseudogap Anderson impurity model in order to: provide evidence for the exact analytic results of Chapters 4, 7; and also to give exact comparisons to the approximate results of Chapters 5-6. In this appendix we briefly review the NRG approach and its implementation. Naturally, the discussion follows closely the more detailed explanation found in, e.g. ref [113]; although our focus here is on the differences encountered on application to the pseudogap Anderson impurity model.

The first step of the NRG is to discretize logarithmically the states of the conduction band, such that all energy scales of the problem are equally well-sampled. The band is divided into logarithmic intervals and only the symmetric combination of states in each interval is retained. The Anderson model is then cast in the form of a linear chain, with couplings that exponentially decrease in magnitude along the chain. The Hamiltonian can then be solved numerically by a process of iterative diagonalization and truncation. At each step, the lowest N_k states are kept, avoid-

ing the exponential scaling of the calculation with chain length, and allowing the physics to be investigated on progressively lower energy/temperature scales.

C.1 Linear-chain Hamiltonian

Here we briefly outline the NRG procedure. We start with the (zero-field) single impurity Anderson model Hamiltonian (c.f. eq. (1.1)):

$$\hat{H} = \sum_{\sigma} \varepsilon d_{\sigma}^{\dagger} d_{\sigma} + U \hat{n}_{\uparrow} \hat{n}_{\downarrow} + \sum_{\mathbf{k}\,\sigma} \varepsilon_{\mathbf{k}} c_{\mathbf{k}\sigma}^{\dagger} c_{\mathbf{k}\sigma} + \sum_{\mathbf{k}\,\sigma} (V_{i\mathbf{k}} d_{\sigma}^{\dagger} c_{\mathbf{k}\sigma} + \text{h.c.}). \tag{C.1}$$

We take the conduction band to be isotropic such that $\varepsilon_{\mathbf{k}} = \varepsilon_{|\mathbf{k}|}$, and of finite width (with halfwidth D). In addition, the conduction band is assumed to be symmetric, and also we take $V_{\mathbf{k}i} = V_{i\mathbf{k}} = V$. The conduction band states are expanded in terms of spherical harmonics centred on the impurity site [11]. Since the conduction band is isotropic, the impurity only couples to the s-wave spherical harmonics. In a dimensionless integral energy representation,

$$\frac{\hat{H}}{D} = \sum_{\sigma} \left[\frac{\varepsilon}{D} d_{\sigma}^{\dagger} d_{\sigma} + \frac{U}{2D} \hat{n}_{\sigma} \hat{n}_{\sigma'} + \int_{-1}^{1} \mathrm{d}k g(k) a_{k\sigma}^{\dagger} a_{k\sigma} + \int_{-1}^{1} \mathrm{d}k h(k) \big(d_{\sigma}^{\dagger} a_{k\sigma} + a_{k\sigma}^{\dagger} d_{\sigma} \big) \right] \tag{C.2}$$

where $\hat{a}_{k\sigma}^{\dagger}, \hat{a}_{k\sigma}$ are fermionic conduction band operators satisfying the usual anti-commutation relation, $\{\hat{a}_{k\sigma}^{\dagger}, \hat{a}_{k'\sigma'}\} = \delta_{\sigma\sigma'}\delta(k-k')$. Here the conduction band states span the energy range, $-1 < k < +1$. The effect of the conduction electron bath on the impurity is captured in a single hybridization function [113],

$$\Gamma(\omega) = \pi \frac{\mathrm{d}\varepsilon(\omega)}{\mathrm{d}\omega} h[\varepsilon(\omega)]^2, \tag{C.3}$$

where $g[\varepsilon(\omega)] = \omega$. The imaginary part is thus,

$$\Gamma^I(\omega) = \pi V^2 \sum_{\mathbf{k}} \delta(\omega - \varepsilon_{\mathbf{k}}), \tag{C.4}$$

in terms of $\varepsilon_{\mathbf{k}}$ and $V = V_{i\mathbf{k}}$ appearing in eq. (C.1). In the pseudogap context, we take $\Gamma^I(\omega) = \Gamma|\omega/D|^r \equiv \Gamma_0|\omega|^r$ ($\Gamma(\omega)$ is ph symmetric), where $\Gamma_0 = \Gamma/D^r = \pi\rho_0 V^2$.[1]

[1] The quantity Γ has units of energy, E. By contrast, the quantity Γ_0 has units of E^{1-r}, such that $\Gamma_0^{1/(1-r)}$ has units of energy. Γ is the usual NRG unit of energy, whereas $\Gamma_0^{1/(1-r)}$ is the energy unit that we use in this thesis.

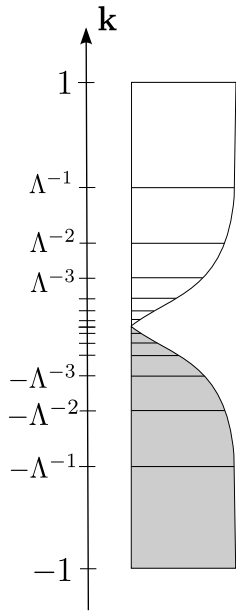


Figure C.1: Diagram showing the logarithmic discretization of the pseudogap conduction band, which runs in energy from $-D(k=-1)$ to $D(k=1)$. Since $\Lambda > 1$, the intervals become progressively smaller as the Fermi level energy (as $k \to 0$) is approached. In each logarithmic interval one state is retained, such that the conduction band is sampled on all energy scales.

C.2 Logarithmic discretization

The next step of the NRG procedure is to logarithmically discretize the conduction band controlled by the parameter $\Lambda > 1$ [11].[2] As shown in Fig. C.1 the conduction band is split up into logarithmic intervals such that the *nth* interval is defined by

$$\Lambda^{-(n+1)} < \pm k < \Lambda^{-n}. \tag{C.5}$$

A Fourier series for a complete set of states is constructed in each interval. In this basis, the conduction electrons couple to the impurity directly only through the symmetric combination of states in each interval (the other combinations couple indirectly and hence more weakly). Moreover, provided Λ is small,[3] it is a good approximation to neglect all other states in each interval [10]. A series of further transformations allow the Hamiltonian to be written in a linear-chain form. For further details of the Hamiltonian transformations for the pseudogap AIM, we refer the reader to refs [39, 43]. The linear-chain form of the Hamiltonian is given by

[2] The $\Lambda = 1$ case corresponds to the continuum limit where the band is not discretized.

[3] In practice, we set $\Lambda = 2$, in our calculations. Previous numerical calculations have shown that the NRG results are even valid for values of Λ up to ~ 9.

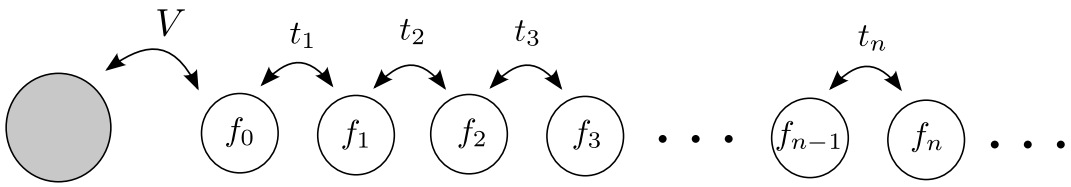


Figure C.2: Diagram of the linear-chain Hamiltonian (otherwise known as the Wilson chain) of eq. (C.6) for the AIM. The grey circle denotes the impurity coupled to the first orbital in the linear chain f_0 with strength $\sqrt{\Gamma} \sim V$. Successive orbitals are connected down the chain via the couplings t_n.

$$\frac{\hat{H}}{D} = \sum_{\sigma} \left[\frac{\varepsilon_\sigma}{D} d_\sigma^\dagger d_\sigma + \frac{U}{2D} \hat{n}_\sigma \hat{n}_{\sigma'} + \sum_{n=0}^{\infty} t_n \left[f_{n\sigma}^\dagger f_{n+1\sigma} + f_{n+1\sigma} f_{n\sigma} \right] \right. \\ \left. + \sqrt{\frac{\xi_0}{\pi}} \left[d_\sigma^\dagger f_{0\sigma} + f_{0\sigma}^\dagger d_\sigma \right] \right]. \tag{C.6}$$

where the dimensionless quantity, $\xi_0 = 2\Gamma/((r+1)D)$. The conduction band operators have been transformed into a new set of orthonormal operators $f_{N\sigma}$, $f_{N\sigma}^\dagger$, such that the impurity only couples to a single f_0 orbital. As shown in Fig. C.2, eq. (C.6), describes a semi-infinite linear chain of orbitals with one end coupled to the impurity, and successive orbitals connected via couplings, t_n. For the pseudogap model, the couplings take the form [39]:

$$t_n = \Lambda^{-n/2} \left[\frac{r+1}{r+2} \right] \left[\frac{1-\Lambda^{-(r+2)}}{1-\Lambda^{-(r+1)}} \right] \frac{[1-\Lambda^{-(n+r+1)}]}{[1-\Lambda^{-(2n+r+1)}]^{1/2} [1-\Lambda^{-(2n+r+3)}]^{1/2}} \tag{C.7a}$$

for even n and

$$t_n = \Lambda^{-(n+r)/2} \left[\frac{r+1}{r+2} \right] \left[\frac{1-\Lambda^{-(r+2)}}{1-\Lambda^{-(r+1)}} \right] \frac{[1-\Lambda^{-(n+1)}]}{[1-\Lambda^{-(2n+r+1)}]^{1/2} [1-\Lambda^{-(2n+r+3)}]^{1/2}} \tag{C.7b}$$

for odd n. In the limit that $n \to \infty$, these couplings reduce to

$$\lim_{n\to\infty} t_n \to \frac{r+1}{r+2} \frac{1-\Lambda^{-(r+2)}}{1-\Lambda^{-(r+1)}} \Lambda^{-n/2} \begin{cases} \times 1 & : n \text{ even} \\ \times \Lambda^{-r/2} & : n \text{ odd} \end{cases} \tag{C.7c}$$

The couplings t_n given via eq. (C.7) are proportional to $\Lambda^{-n/2}$ and thus decrease exponentially as the chain is traversed. This energy scale separation down the chain justifies the RG truncation scheme in which only the lowest N_k states are kept at each step.

C.3 Iterative diagonalisation

The linear chain Hamiltonian, eq. (C.6), can be diagonalized numerically, starting from the impurity itself, and successively coupling in extra sites of the Wilson chain at each step. For this purpose a rescaled chain Hamiltonian is defined of *finite length*, viz:

$$\hat{H}_N = \Lambda^{(N-1)/2}\left(\hat{H}_{\rm imp} + \sqrt{\frac{\xi_0}{\pi}}(d^\dagger_\sigma f_{0\sigma} + f^\dagger_{0\sigma} d_\sigma) + \sum_{\sigma,n=0}^{N-1} t_n (f^\dagger_{n\sigma} f_{n+1\sigma} + f^\dagger_{n+1\sigma} f_{n\sigma})\right) \tag{C.8}$$

such that the full (discretized) model is recovered on taking the limit $N \to \infty$,

$$\hat{H} = \lim_{N\to\infty} \Lambda^{-(N-1)/2} \hat{H}_N, \tag{C.9}$$

Two successive Hamiltonians are related by

$$\hat{H}_{N+1} = \sqrt{\Lambda}\hat{H}_N + \Lambda^{N/2} \sum_\sigma t_N (f^\dagger_{N\sigma} f_{N+1\sigma} + f^\dagger_{N+1\sigma} f_{N\sigma}), \tag{C.10}$$

which takes the form of an RG transformation,

$$\hat{H}_{N+1} = R(\hat{H}_N). \tag{C.11}$$

At each step, the N_k lowest energy (diagonal) eigenstates of $\hat{H}_N$ are used to construct $\hat{H}_{N+1}$. Higher lying states are discarded at each step - this is the central approximation within NRG. It is justified by the fact that hoppings down the chain decrease exponentially, which results in an energy scale separation.

C.4 Fixed points

Under the RG transformation, eq. (C.11), there are specific points in parameter space where the effective Hamiltonian, H^*, is left unchanged, i.e. $R(H^*) = H^*$. Furthermore, these 'fixed points' are classified as either being stable or unstable. Under a small perturbation, δH^*, the RG transformation becomes

$$R(H^* + \delta H^*) = R(H^*) + R(\delta H^*). \tag{C.12}$$

Whether the second term gets progressively bigger or smaller under this transformation determines the stability of the fixed point. For $R(\delta H^*)$, diminishing in size, the flows are attracted to the *stable* fixed point. In contrast, if $R(\delta H^*)$ gets larger in size, then the flows are repelled from the *unstable* fixed point. Moreover, a *critical*

fixed point is stable on a particular RG trajectory, but unstable on all others.

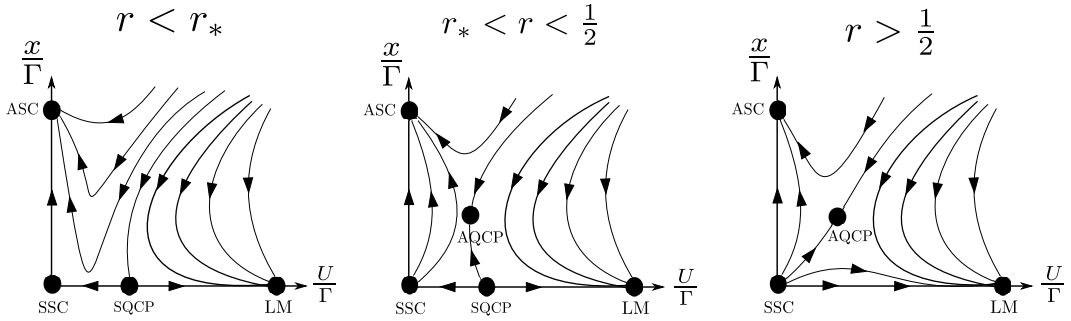


Figure C.3: Zero-field pseudogap AIM RG flows and fixed points in the $(U/\Gamma, x/\Gamma)$ plane. The LHS shows the situation for $r < r_*$ where only the SQCP exists, the middle shows the flows in the range $r_* < r < \frac{1}{2}$ where both critical fixed points coexist, and the RHS shows the scenario for $r > \frac{1}{2}$, where only the AQCP exists. Reproduced from ref [43].

Fig. C.3 shows the RG flows in the $(U/\Gamma, x/\Gamma)$ plane[4]) for the pseudogap Anderson model. The three panels show the three distinct cases known from ref [43] and discussed in Section 4.1. On the LHS, the scenario for $r < r_* \simeq \frac{3}{8}$ is shown, where the SQCP characterizes the phase transition. For $U > U_c$, the system flows to the LM fixed point, corresponding to effective parameters, $(U/\Gamma = \infty, x/\Gamma = 0)$. By contrast, for $U > U_c$, the system flows to either the SSC or ASC fixed points if $x/\Gamma = 0$ or $x/\Gamma \neq 0$ respectively.[5] We emphasize that the SSC fixed point is only stable specifically at $x = 0$, and unstable w.r.t any finite asymmetry. Precisely at $U = U_c$, the system flows to the critical fixed point of the SQCP. The middle panel shows the r range where both the AQCP and SQCP fixed points coexist. At $r = r_*$, the AQCP moves into the plane, whilst the SQCP stays on the U/Γ axis. Thus, for any finite ph asymmetry and $U = U_c(r)$, the system flows to the AQCP. By contrast, precisely at $x/\Gamma = 0$, the SQCP remains the critical fixed point. The RHS panel shows the third case where the SQCP has merged with the SSC, such that the system at ph symmetry always flows towards the LM fixed point for any U. For finite x, the RG picture is the same as the middle case.

C.5 Calculation of the dynamics

C.5.1 Anders-Schiller basis set

The Anders and Schiller (AS) basis set is a complete (but approximate) set of states made up of all the discarded states from all NRG iterations (with all the states of the

[4]The parameter $x = \varepsilon + \frac{U}{2}$ determines the ph asymmetry of the system. At $x = 0$, the system is invariant under a ph transformation - for details we refer the reader to Appendix B.

[5]Technically, there are a pair of ASC fixed points, positioned at $(U/\Gamma = 0, x/\Gamma = \pm\infty)$ plane, i.e. one for each $x > 0$, $x < 0$ - related via a ph transformation.

final iteration considered discarded) [115,116]. States of the AS basis are necessarily orthogonal, as illustrated in Fig. C.4.

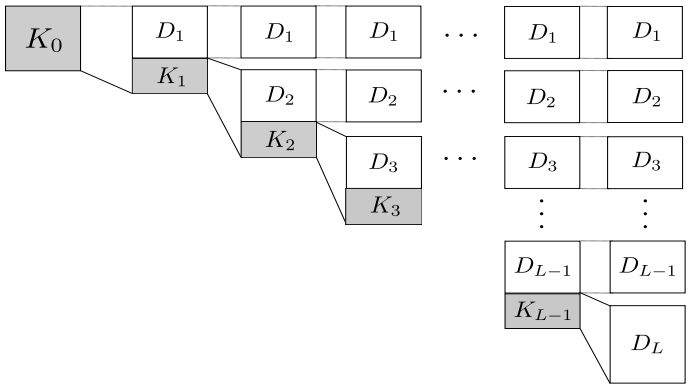


Figure C.4: Schematic of the Anders-Schiller basis set reproduced from ref [117]. The grey boxes show the kept states, K_N at a given iteration, N, whereas the white boxes show the discarded states, D_N. Combining all of the discarded states for the total number of iterations, L, forms the complete orthogonal Anders-Schiller basis set.

C.5.2 Full density matrix approach

Within the FDM approach, one considers the entire Wilson chain of total (finite) length N_{tot} from the outset. The hopping matrix elements, t_n, are then considered to be successively 'switched on' through the iterative process. At a given iteration N, we label states of the coupled N-orbital system comprising orbitals up to and including f_N as $|s\rangle$ (where s stands for 'system'). The remaining N_{tot}-N orbitals comprise the 'environment' denoted $|e\rangle$. An overall state is then given via the direct product of the system and environment states: $|se\rangle = |s\rangle \otimes |e\rangle$. The unity operator in the AS basis is written as [116]

$$\hat{1} = \sum_{N>N_0}^{N_{tot}} \sum_{se} |se\rangle_N^D {}^D\langle se|, \tag{C.13}$$

where $|se\rangle_N^D$ is a discarded state at iteration N, N_0 is the last iteration for which all states are retained and N_{tot} is the total number of iterations. Importantly, each state $|se\rangle_N$ is $4^{N_{tot}-N}$-fold degenerate by virtue of the environmental degrees of freedom.

The full density matrix $\hat{\rho} = \sum_N \hat{\rho}^N$, where $\hat{\rho}_{ij}^N = \delta_{ij} \mathrm{e}^{-\beta \hat{H}_N}$, is constructed (in the AS basis from discarded states) from each iteration of the NRG. Dynamics in the Lehmann representation, are then calculated via $\langle \ldots \rangle_T = \mathrm{Tr}\hat{\rho}\ldots$. The details of the FDM formulation are discussed in refs [101,102].

C.5.3 Spectral broadening

Due to the discretization of the bath in NRG - which is inherent to the method - calculation of dynamics are naturally also discrete, consisting of a finite set of poles. To recover the true spectrum, one broadens these poles, as, described in ref [101]. this is done by convolving the discrete data with a broadening kernel,

$$\delta(\omega - \omega_n) \to \frac{\mathrm{e}^{-b^2/4}}{b\omega_n\sqrt{\pi}} \exp\left[- \frac{(\ln\omega - \ln\omega_n)^2}{b^2} \right], \tag{C.14}$$

where b, known as the broadening parameter, controls the width of the Gaussian function, such that in the limit $b \to 0$ the pole is recovered. The broadening is done on a log-scale because the poles are distributed logarithmically due to the logarithmic discretization. Typically we use $b \approx 0.45 - 0.6$, for $\Lambda = 2$.

C.6 Self-energies

The local impurity self-energy, $\Sigma_{ii;\sigma}(\omega)$, may be calculated directly from NRG, as originally explained by Bulla *et al.* [98]. From the equations of motion methods [2] of Section 2.3, the local impurity Green function for the single-impurity Anderson model is given by

$$G_{ii;\sigma}(\omega) = [\omega^+ - \varepsilon_\sigma - \Gamma_{ii;\sigma}(\omega) - F_{ii;\sigma}(\omega)/G_{ii;\sigma}(\omega)]^{-1} \tag{C.15}$$

with $\omega^+ = \omega + i\eta$ for the retarded function, and $\varepsilon_\sigma = \varepsilon - \sigma h$. The correlation functions are given by $F_{ii;\sigma}(\omega) = U\langle\langle \hat{n}_{i-\sigma}\hat{c}_{i\sigma}; c^\dagger_{i\sigma}\rangle\rangle_\omega$, and $G_{ii\sigma}(\omega) = \langle\langle \hat{c}_{i\sigma}; c^\dagger_{i\sigma}\rangle\rangle_\omega$. On comparison of eq. (C.15) with the Dyson equation, eq. (2.50), we see that the self-energy, $\Sigma_{ii;\sigma}(\omega)$ is given by the ratio

$$\Sigma_{ii;\sigma}(\omega) = \frac{F_{ii;\sigma}(\omega)}{G_{ii;\sigma}(\omega)}. \tag{C.16}$$

Using FDM-NRG, $F_{ii}(\omega)$ and $G_{ii}(\omega)$ can be calculated directly, and $\Sigma_{ii}(\omega)$ follows by eq. (C.16), In fact the Lehmann representation in NRG yields the spectral functions ImF and ImG, and so Hilbert transformations are performed to yield the entire (complex) analytic functions for use in eq. (C.16). Furthermore, an "improved" Green function can be obtained by using the self-energy $\Sigma_{ii}(\omega)$, from eq. (C.16) in the Dyson equation, eq. (2.50).

APPENDIX D

Free energies and hyperscaling

In the first part of this appendix we show that the local magnetization, $m(h)$, and the local static spin susceptibility, χ_s, may be written as the first and second derivatives (w.r.t a local field, h) of the free energy of the system. In the second half of this appendix we consider a scaling ansatz for the singular part of the free energy as the QCP is approached (as a function of T, h and $|U-U_c|$). From this free energy form a number of 'hyperscaling' relations between the critical exponents may be deduced.[1] In the LM phase we explicitly consider the implications of the $T \to 0$, $h \to 0^{\pm}$ of the non-commuting limits on the critical exponents.

D.1 Free energy

In this section we show two important results for the local magnetization, $m(h)$, and local susceptibility, $\chi(T)$ at finite temperature in response to a magnetic field. First, with F denoting the free energy of the full system, and $h = \frac{1}{2}g\mu_B B$, a purely local magnetic field, we show that the local magnetization, $m(h)$ is given by the derivative

$$m(h) = 2\langle \hat{s}_z \rangle = -\frac{\partial F}{\partial h} \tag{D.1}$$

with $\hat{s}_z = \frac{1}{2}\sum_\sigma \sigma \hat{n}_\sigma$ referring to the local impurity spin and $\langle \ldots \rangle$ denoting an average in the presence of the field. Second, we show that the finite T static spin-susceptibility defined by

$$\chi_s(T) = \left(\frac{\partial \langle \hat{s}_z \rangle}{\partial h} \right)_{h=0}, \tag{D.2}$$

[1] The analysis of Section D.3 essentially yields the same results as that of ref [37] for the pseudogap Kondo model, but here we focus on the pseudogap Anderson model.

is given by

$$\chi_s(T) = 2\int_0^\beta \mathrm{d}\tau_1 \langle \delta\hat{s}_\mathrm{z}(\tau_1)\hat{s}_\mathrm{z}\rangle_0, \tag{D.3}$$

where $\beta = 1/T$, $\langle \ldots \rangle_0$ denotes an average in the absence of a field ($\hat{H}_0$ is the Hamiltonian of the system at $h = 0$). The imaginary-time ($\tau = it$) operator $\hat{s}_\mathrm{z}(\tau)$ is expressed in the interaction picture [62] as $\hat{s}_\mathrm{z}(\tau) = \mathrm{e}^{\tau\hat{H}_0}\hat{s}_\mathrm{z}\mathrm{e}^{-\tau\hat{H}_0}$ and $\delta\hat{s}_\mathrm{z} = \hat{s}_\mathrm{z} - \langle\hat{s}_\mathrm{z}\rangle_0$. In this appendix we consider finite T, such that the zero-field magnetization $m(h) = 2\langle\hat{s}_\mathrm{z}\rangle_0 = 0$, regardless of whether the zero-temperature phase is SC or LM. Therefore $\delta\hat{s}_\mathrm{z} \equiv \hat{s}_\mathrm{z}$ in all cases and the 'δ' is in effect redundant. Finally we show that

$$\chi_s(T) = -\frac{1}{2}\left(\frac{\partial^2 F}{\partial h^2}\right)_{h=0}, \tag{D.4}$$

which follows from eq. (D.2) provided eq. (D.1) holds.

In the presence of the local field the full Hamiltonian is given by

$$\hat{H} = \hat{H}_0 - 2h\hat{s}_\mathrm{z} \tag{D.5}$$

with corresponding free energy given by

$$F = -T\ln Z = -T\ln(\mathrm{Tr}\mathrm{e}^{-\beta[\hat{H}_0 - 2h\hat{s}_\mathrm{z}]}) \tag{D.6}$$

with Z the partition function (where we consider a canonical ensemble). If we had instead considered a uniform global field (applied to both the impurity and conduction band states), then the full Hamiltonian becomes $\hat{H} = \hat{H}_0 - 2h\hat{S}_\mathrm{z}$, with $\hat{S}_\mathrm{z}$ referring to the *entire* system. Since $\hat{S}_\mathrm{z}$ and $\hat{H}$ commute, by simply differentiating eq. (D.6) we obtain $2\langle\hat{S}_\mathrm{z}\rangle = -\partial F/\partial h$. However, for a purely local field, $\hat{s}_\mathrm{z}$ do not commute and showing eq. (D.1) is not quite so easy.

D.1.1 Results

By adapting the early parts of Luttinger and Ward's seminal work [59] (we refer to as LW), we may show the results above. The purpose of LW was to consider a Hamiltonian of the form $\hat{H} = \hat{H}_0 + \hat{H}'$, where $\hat{H}_0$ refers to the non-interacting system and $\hat{H}'$ is the interaction part. However, their original analysis in fact applies generally to *any* $\hat{H}$ of the form $\hat{H} = \hat{H}_0 + \hat{H}'$, and thus we make use of it here. Before proceeding we note that

$$\frac{Z}{Z_0} = \mathrm{e}^{-\beta(F-F_0)} = \langle\hat{U}(\beta)\rangle_0 \quad (= \tfrac{1}{Z_0}\mathrm{Tr}\mathrm{e}^{-\beta\hat{H}_0}\hat{U}(\beta)) \tag{D.7}$$

where $Z_0 = \mathrm{Tr} e^{-\beta \hat{H}_0}$ is the partition function for $\hat{H}_0$ and the operator $\hat{U}(\beta)$ is defined by $\hat{U}(\beta) = e^{\beta \hat{H}_0} e^{-\beta \hat{H}}$. The essential result from LW is that the operator $\hat{U}(\beta)$ may be expressed by

$$\hat{U}(\beta) = 1 + \sum_{n=1}^{\infty} \frac{(-1)^n}{n!} \int_0^\beta \mathrm{d}\tau_1 \ldots \int_0^\beta \mathrm{d}\tau_n T_\tau [\hat{H}'(\tau_1) \ldots \hat{H}'(\tau_n)], \tag{D.8}$$

where $\hat{H}'(\tau_i)$ is expressed in the interaction representation by $\hat{H}'(\tau_i) = e^{\tau_i \hat{H}_0} \hat{H}' e^{-\tau_i \hat{H}_0}$ and T_τ is a time-ordering operator that places operators acting earliest in time to the right.

In the present context, we consider $\hat{H}_0$ to be the Hamiltonian for the system in the absence of a field (itself an interacting Hamiltonian - eq. (1.1)), and $\hat{H}' = -2h\hat{s}_z$, the coupling to the local field. Inserting this form into eq. (D.8) we obtain specifically

$$\hat{U}(\beta) = 1 + \sum_{n=1}^{\infty} \frac{(2h)^n}{n!} \int_0^\beta \mathrm{d}\tau_1 \ldots \int_0^\beta \mathrm{d}\tau_n T_\tau [\hat{s}_z(\tau_1) \ldots \hat{s}_z(\tau_n)], \tag{D.9}$$

By inserting this operator into eq. (D.7) it follows that

$$\frac{Z}{Z_0} = e^{-\beta(F-F_0)} = 1 + \sum_{n=1}^{\infty} \frac{(2h)^n}{n!} \int_0^\beta \mathrm{d}\tau_1 \ldots \int_0^\beta \mathrm{d}\tau_n \langle T_\tau [\hat{s}_z(\tau_1) \ldots \hat{s}_z(\tau_n)] \rangle_0 \tag{D.10a}$$

$$= 1 + \lambda(h) \tag{D.10b}$$

and therefore $\lambda(h)$ is defined as a power series in h:

$$\lambda(h) = \sum_{n=1}^{\infty} \frac{(2h)^n}{n!} \lambda_n. \tag{D.11}$$

Thus, from eq. (D.10) we have: $F - F_0 = -T \ln(Z/Z_0) = -T \ln(1 + \lambda(h))$. Differentiating this equation, we obtain

$$-\frac{\partial F}{\partial h} = \frac{T}{(1+\lambda(h))} \frac{\partial \lambda(h)}{\partial h} \tag{D.12a}$$

$$= \frac{2T}{(1+\lambda(h))} \Big(\lambda_1 + \sum_{n=1}^{\infty} \frac{(2h)^n}{n!} \lambda_{n+1} \Big) \tag{D.12b}$$

and

$$-\frac{\partial^2 F}{\partial h^2} = \frac{-T}{(1+\lambda(h))^2} \left(\frac{\partial \lambda(h)}{\partial h} \right)^2 + \frac{T}{(1+\lambda(h))} \frac{\partial^2 \lambda(h)}{\partial h^2}. \tag{D.13}$$

Differentiating eq. (D.11) gives

$$\left(\frac{\partial\lambda(h)}{\partial h}\right)_{h=0} = 2\lambda_1 = 2\int_0^\beta \mathrm{d}\tau_1\langle\hat{s}_\mathrm{z}(\tau_1)\rangle_0 = 2\beta\langle\hat{s}_\mathrm{z}\rangle_0, \tag{D.14}$$

where $\langle\hat{s}_\mathrm{z}(\tau_1)\rangle_0 = \frac{1}{Z_0}\mathrm{Tr}\mathrm{e}^{-\beta\hat{H}_0}\mathrm{e}^{\tau_1\hat{H}_0}\hat{s}_\mathrm{z}\mathrm{e}^{-\tau_1\hat{H}_0} = \frac{1}{Z_0}\mathrm{Tr}\mathrm{e}^{-\beta\hat{H}_0}\hat{s}_\mathrm{z} = \langle\hat{s}_\mathrm{z}\rangle_0$ (using the cyclical invariance of the trace); and

$$\left(\frac{\partial^2\lambda(h)}{\partial h^2}\right)_{h=0} = 4\lambda_2 = 4\int_0^\beta \mathrm{d}\tau_1\int_0^\beta \mathrm{d}\tau_2\langle T_\tau[\hat{s}_\mathrm{z}(\tau_1)\hat{s}_\mathrm{z}(\tau_2)]\rangle_0. \tag{D.15}$$

Therefore, by virtue of the fact that eq. (D.11) gives $\lambda(h=0)=0$, inserting eq. (D.14) into eq. (D.12) we obtain

$$-\left(\frac{\partial F}{\partial h}\right)_{h=0} = T\left(\frac{\partial\lambda(h)}{\partial h}\right)_{h=0} = 2\langle\hat{s}_\mathrm{z}\rangle_0, \tag{D.16}$$

whilst eqs. (D.13, D.15) give

$$-\left(\frac{\partial^2 F}{\partial h^2}\right)_{h=0} = 4\left(T\lambda_2 - \frac{1}{T}\langle\hat{s}_\mathrm{z}\rangle_0^2\right), \tag{D.17}$$

and hence

$$-\frac{1}{2}\left(\frac{\partial^2 F}{\partial h^2}\right)_{h=0} = 2T\int_0^\beta \mathrm{d}\tau_1\int_0^\beta \mathrm{d}\tau_2\langle T_\tau[\delta\hat{s}_\mathrm{z}(\tau_1)\hat{s}_\mathrm{z}(\tau_2)]\rangle_0, \tag{D.18}$$

where $\delta\hat{s}_\mathrm{z}(\tau_1) = \hat{s}_\mathrm{z}(\tau_1) - \langle\hat{s}_\mathrm{z}\rangle_0$. Thus, eq. (D.17) confirms eq. (D.1) but for $h=0$ only — a point we return to below. Firstly however, let us obtain eq. (D.3) for $\chi_s(T)$. Using $\mathrm{e}^{-\beta\hat{H}} = \mathrm{e}^{-\beta\hat{H}_0}U(\beta)$, together with eq. (D.10), we obtain

$$\langle\hat{s}_\mathrm{z}\rangle = \frac{1}{Z}\mathrm{Tr}\mathrm{e}^{-\beta\hat{H}}\hat{s}_\mathrm{z} = \frac{Z_0}{Z}\frac{1}{Z_0}\mathrm{Tr}\mathrm{e}^{-\beta\hat{H}_0}U(\beta)\hat{s}_\mathrm{z} = \frac{1}{(1+\lambda(h))}\langle U(\beta)\hat{s}_\mathrm{z}\rangle_0. \tag{D.19}$$

Hence by using eq. (D.9) we find

$$\begin{aligned}\langle\hat{s}_\mathrm{z}\rangle =& \frac{1}{(1+\lambda(h))}\left(\langle\hat{s}_\mathrm{z}\rangle_0 + \sum_{n=1}^{\infty}\frac{(2h)^n}{n!}\int_0^\beta \mathrm{d}\tau_1\ldots\int_0^\beta \mathrm{d}\tau_n\langle T_\tau[\hat{s}_\mathrm{z}(\tau_1)\ldots\hat{s}_\mathrm{z}(\tau_n)]\hat{s}_\mathrm{z}\rangle_0\right)\\ =& \frac{1}{(1+\lambda(h))}\left(\langle\hat{s}_\mathrm{z}\rangle_0 + 2h\int_0^\beta \mathrm{d}\tau_1\langle\hat{s}_\mathrm{z}(\tau_1)\hat{s}_\mathrm{z}\rangle_0 + O(h^2)\right)\end{aligned} \tag{D.20}$$

Differentiating this equation we obtain

$$\chi_s(T) = \left(\frac{\partial\langle\hat{s}_z\rangle}{\partial h}\right)_{h=0} = -\left(\frac{\partial\lambda(h)}{\partial h}\right)_{h=0}\langle\hat{s}_z\rangle_0 + 2\int_0^\beta \mathrm{d}\tau_1\langle\hat{s}_z(\tau_1)\hat{s}_z\rangle_0 \tag{D.21a}$$

$$= -2\langle\hat{s}_z\rangle_0^2 + 2\int_0^\beta \mathrm{d}\tau_1\langle\hat{s}_z(\tau_1)\hat{s}_z\rangle_0 = 2\int_0^\beta \mathrm{d}\tau_1\langle\delta\hat{s}_z(\tau_1)\hat{s}_z\rangle_0, \tag{D.21b}$$

which is eq. (D.3) as sought. Finally on comparison of eq. (D.21b) with eq. (D.18) that $\chi_s(T) = -\frac{1}{2}\partial^2 F/\partial h^2$, eq. (D.4) provided that

$$\beta\int_0^\beta \mathrm{d}\tau_1\langle\hat{s}_z(\tau_1)\hat{s}_z\rangle_0 = \int_0^\beta \mathrm{d}\tau_1\int_0^\beta \mathrm{d}\tau_2\langle T_\tau[\hat{s}_z(\tau_1)\hat{s}_z(\tau_2)]\rangle_0, \tag{D.22a}$$

which may be explicitly shown by some lengthy algebra involving decomposing $f(\tau_1,\tau_2) \equiv f(\tau_1-\tau_2) = \langle T_\tau[\hat{s}_z(\tau_1)\hat{s}_z(\tau_2)]\rangle_0$ as a Fourier series. By inserting eqs. (D.14-D.15) into eq. (D.12) to obtain

$$-\frac{1}{2}\frac{\partial F}{\partial h} = \frac{1}{(1+\lambda(h))}\left(\langle\hat{s}_z\rangle_0 + 2hT\int_0^\beta \mathrm{d}\tau_1\int_0^\beta \mathrm{d}\tau_2\langle\hat{T}_\tau[\hat{s}_z(\tau_1)\hat{s}_z(\tau_2)]\rangle_0 + O(h^2)\right). \tag{D.23}$$

Comparison of this equation with eq. (D.20), we see that provided eq. (D.22a) holds then $-\frac{\partial F}{\partial h} = 2\langle\hat{s}_z\rangle$, explicitly confirming that eq. (D.1) holds beyond the $h = 0$ level of eq. (D.16).

D.2 Homogeneous functions

In this section we begin with a general discussion of homogeneous functions following the considerations of ref [118] page 433, before turning to hyperscaling (in Section D.3) in the context of the local quantum phase transitions of which we are interested.

A function $F(x)$ of a single variable is homogeneous if, for all values of a scale parameter λ

$$F(\lambda x) = g(\lambda)F(x) \tag{D.24}$$

(so that $g(\lambda = 1) = 1$). The general form of $g(\lambda)$ can be found as follows. We first note that

$$F(\mu\lambda x) = g(\lambda)F(\mu x) = g(\mu)g(\lambda)F(x) \tag{D.25a}$$

$$= g(\mu\lambda)F(x) \tag{D.25b}$$

and therefore $g(\lambda)g(\mu) = g(\lambda\mu)$. Differentiating we obtain

$$\frac{\partial g(\lambda)g(\mu)}{\partial \mu} = \lambda g'(\mu\lambda) = g'(\mu)g(\lambda) \tag{D.26}$$

where $g'(\mu) = dg(\mu)/d\mu$. We now set $\mu = 1$, thus defining p by: $g'(1) = p$, then $\lambda g'(\lambda) = pg(\lambda)$ which on integrating (and remembering that $g(1) = 1$), gives

$$g(\lambda) = \lambda^p. \tag{D.27}$$

Hence by inserting this equation into eq. (D.24), we obtain

$$F(\lambda x) = \lambda^p F(x) \tag{D.28}$$

and $F(x)$ is said to be a homogeneous function of degree p. If we let $\lambda = x^{-1}$ in eq. (D.28), then

$$F(x) = F(1)x^p \tag{D.29}$$

i.e. $F(x)$ has a power-law dependence on its argument.

We now generalize the result eq. (D.29) to functions of two or more variables. The generalization of the definition eq. (D.24) to a function of two variables $F(x, y)$ is that it is homogeneous if

$$F(\lambda x, \lambda^q y) = g(\lambda)F(x, y) \tag{D.30}$$

for all λ. Hence, proceeding in parallel to eq. (D.25)

$$F(\mu\lambda x, \mu^q\lambda^q y) = g(\mu)F(\lambda x, \lambda^q y) = g(\mu)g(\lambda)F(x, y) \tag{D.31a}$$

$$= g(\mu\lambda)F(x, y). \tag{D.31b}$$

Hence from the same argument as above, with $g(\lambda)g(\mu) = g(\lambda\mu)$ and $g(\lambda) = \lambda^p$ we obtain

$$F(\lambda x, \lambda^q y) = \lambda^p F(x, y) \tag{D.32}$$

which is the generalization of eq. (D.28) to two variables, holding for any λ. If for example we choose $\lambda x = 1$, then eq. (D.32) gives

$$F(x, y) = x^p F\left(1, \frac{y}{x^p}\right) \tag{D.33}$$

(so that $F(x, 0)$ is homogeneous of degree p in x); whilst if we instead choose $\lambda^q y = 1$,

then eq. (D.32) becomes

$$F(x,y) = y^{\frac{p}{q}} F\left(\tfrac{x}{y^{1/q}}, 1\right), \tag{D.34}$$

so that $F(0,y)$ is a homogeneous function of degree p/q in y. Alternatively, and move relevantly to the discussion below, we may consider $\lambda^p = \gamma^{-1}$, such that eq. (D.32) becomes

$$F(x,y) = \gamma F\left(\frac{x}{\gamma^{1/p}}, \frac{y}{\gamma^{q/p}}\right). \tag{D.35}$$

The generalization to functions of higher number of variables is obvious. For three variables which we explicitly consider below, the generalization of eq. (D.32) is

$$F(\lambda x, \lambda^q y, \lambda^r z) = \lambda^p F(x,y,z). \tag{D.36}$$

Once again, with $\lambda^p = \gamma^{-1}$, this equation becomes

$$F(x,y,z) = \gamma F\left(\frac{x}{\gamma^{1/p}}, \frac{y}{\gamma^{q/p}}, \frac{z}{\gamma^{r/p}}\right), \tag{D.37}$$

where of course writing $\lambda = \gamma^{-1/p}$ is nothing more than defining a new scale parameter.

The essential assumption now made is that the free energy of a quantum impurity system close to criticality, or more specifically the singular part of the free energy, is a homogeneous function of its physical parameters. In the case we consider the 3 distinct relevant quantities are 'distance from criticality' $|t| \equiv |U - U_c|$, local magnetic field h, and temperature, T. Eq. (D.37) then gives

$$F(|t|,h,T) = \gamma F\left(\frac{|t|}{\gamma^{1/p}}, \frac{h}{\gamma^{q/p}}, \frac{T}{\gamma^{r/p}}\right). \tag{D.38}$$

We are free to choose the scale parameter γ - we choose $\gamma^{\frac{r}{p}} = T$, and therefore

$$F(|t|,h,T) = T^{\frac{p}{r}} F\left(\frac{|t|}{T^{1/r}}, \frac{h}{T^{q/r}}, 1\right). \tag{D.39}$$

Now simply relabeling the exponents, $a = 1/r$, $b = q/r$, $c = 1 - p/r$, such that eq. (D.39) becomes

$$F(|t|,h,T) = T^{1-c} F\left(\frac{|t|}{T^a}, \frac{h}{T^b}, 1\right) \equiv T^{1-c} f\left(\frac{|t|}{T^a}, \frac{h}{T^b}\right), \tag{D.40}$$

thus defining $f(|t|/T^a, h/T^b)$. The scaling form of the free energy is therefore specified by three exponents a, b and c, one for each of the physical parameters. For the

type of QCP that we consider in this thesis we later show that the exponent $c = 0$, reflecting the fact that the LM phase has a non-zero entropy. As such, we consider explicitly the scaling form for the singular part of the free energy

$$F(|t|, h, T) = TF\left(\frac{|t|}{T^a}, \frac{h}{T^b}, 1\right) \equiv Tf\left(\frac{|t|}{T^a}, \frac{h}{T^b}\right). \tag{D.41}$$

This is the scaling ansatz employed by refs [37, 46, 48, 79]. In the next section we consider the hyperscaling that it leads to.

D.3 Hyperscaling

With $m(h) \equiv m = -\partial F/\partial h$ and $\chi_s = -\partial^2 F/\partial h^2$, eq. (D.41) gives

$$m \sim T^{1-b} f'\left(\frac{|t|}{T^a}, \frac{h}{T^b}\right), \tag{D.42a}$$

$$\chi_s \sim T^{1-2b} f''\left(\frac{|t|}{T^a}, \frac{h}{T^b}\right). \tag{D.42b}$$

where $f'(u, v) = \partial f(u, v)/\partial v$ and $f''(u, v) = \partial^2 f(u, v)/\partial v^2$. The critical exponents that we consider in the following are $\beta, \gamma, \gamma', \delta$ and y, defined by

$$m(U > U_c, T = 0, h \to 0) \sim (U - U_c)^{\beta} \tag{D.43a}$$

$$\chi_s(U \lessgtr U_c, T = 0, h \to 0) \sim |U - U_c|^{-\gamma} \tag{D.43b}$$

$$T\chi_s(U > U_c, T \to 0, h = 0) \sim (U - U_c)^{\gamma'} \tag{D.43c}$$

$$m(U = U_c, T = 0, h \to 0) \sim |h|^{\frac{1}{\delta}} \tag{D.43d}$$

$$\chi_s(U = U_c, T \to, h = 0) \sim T^{-y} \tag{D.43e}$$

such that β and γ' refer to the LM phase ($U > U_c$), and γ encompasses both phases; while δ and y refer to $U = U_c$ itself. Fig. D.1 shows the critical point located at $h, T, t = 0$. The critical exponents tell us how each of the physical quantities in eq. (D.43) behave as the QPT is approached along each of the three axes.

D.3.1 LM phase

$h \to 0$, $T = 0$

As discussed in Chapters 3,7 and shown in Fig. 7.1, in a LM phase the limits $h \to 0^{\pm}$ and $T \to 0$ do not commute. Here we first consider taking the limit $T \to 0$, followed by $h \to 0^{\pm}$; whence the ratio $v = h/T^b \to \pm\infty$ (according to the sign of h). In this case eq. (D.42a) becomes $m \sim T^{1-b} f'(\frac{|t|}{T^a}, \pm\infty)$. Now with $u = |t|/T^a$, we assume that $f'(u, \pm\infty) \overset{u\to\infty}{\sim} \mathrm{sgn}(h) u^x$ (where $\mathrm{sgn}(h) \equiv \mathrm{sgn}(v)$); and therefore

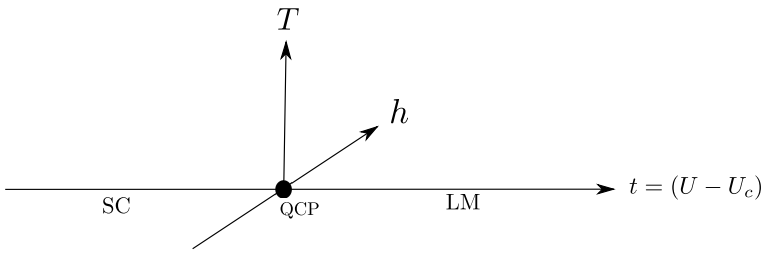


Figure D.1: Schematic showing the QPT in the (t, h, T) plane. The QPT is located at $T = 0$, $h = 0$, $t = 0$. For any finite, t, h, or T the 'pristine' QCP is destroyed.

$m \sim \mathrm{sgn}(h)(T^{1-b}/T^{ax})|t|^x$. The fact that in a LM phase, the $T = 0$ local moment m is finite requires that $ax = 1 - b$, or equivalently $x = (1 - b)/a$. Therefore the local moment becomes

$$|\tilde{\mu}| \equiv m(U > U_c, T = 0, h \to 0) \sim \mathrm{sgn}(h)(U - U_c)^{\beta} \qquad \beta = \frac{(1-b)}{a}, \tag{D.44}$$

thus relating β to a and b.

Now we consider the local susceptibility, χ_s. In eq. (D.42b) assume that $f''(u, \pm\infty) \overset{u\to\infty}{\sim} u^{x'}$, and therefore $\chi_s \sim (T^{1-2b}/T^{ax'})|t|^{x'}$. Once again, as for m, χ_s is finite in the $T = 0$ LM phase, which requires that $x' = 1 - 2b/a$. Therefore eq. (D.43b) becomes

$$\chi_s(U > U_c, T = 0, h \to 0) \sim |U - U_c|^{-\gamma} \qquad \gamma = \frac{(2b-1)}{a}, \tag{D.45}$$

relating γ to both a and b.

Before we proceeding we comment on the assumed form $f''(u, v) \sim u^{x'}$ as $u \to \infty$ and $v \to \pm\infty$. This dependence of the second derivative, means that the first derivative has the form

$$\frac{\partial f(u,v)}{\partial v} = f'(u, v) \sim u^{x'} v + \mathrm{sgn}(v) g(u) \qquad : u \to \infty, v \to \pm\infty \tag{D.46}$$

with $g(u)$ a function solely of $u = |t|/T^a$. The $\mathrm{sgn}(v)$ reflects the fact that the derivative w.r.t. v is of a different sign according to whether $v \to \infty$ $(h > 0)$ or $v \to -\infty$ $(h < 0)$, since the local moment $m \equiv m(h)$ is necessarily an odd function of field. Therefore by inserting eq. (D.46) into eq. (D.42a) we obtain

$$m \sim T^{1-b} \frac{|t|^{x'}}{T^{ax'}} \frac{h}{T^b} + T^{1-b}\,\mathrm{sgn}(v) g(u). \tag{D.47}$$

Moreover, since from above $ax' = 1 - 2b$ (and noting that $\mathrm{sgn}(h) = \mathrm{sgn}(v)$), this

becomes

$$m \sim 2\chi(U > U_c, T = 0, h \to 0)h + T^{1-b}\,\mathrm{sgn}(h)g(u). \tag{D.48}$$

Just as above, the function $g(u)$ is then assumed to be of the form $g(u) \sim u^x$ as $u \to \infty$ which leads to the result of eq. (D.44). Thus on differentiation of eq. (D.48) w.r.t. h, we obtain the correct form of $\chi_s = \frac{1}{2}(\partial m/\partial h)_{h\to 0^{\pm}}$, and all results are physically consistent. Moreover, we note that when the second term in eq. (D.48) is differentiated it gives rise to the singular $|\tilde{\mu}|\delta(h)$ contribution to $\frac{1}{2}(\partial m/\partial h)$ which we normally neglect from explicit consideration.

$h = 0$, $T \to 0$

Still focusing on the LM phase where $U > U_c$, we now consider the limits temperature and field limits in the opposite order, such that $h \to 0$ is taken first followed by $T \to 0$. In this case $v = h/T^b \to 0$, whereas $u = |t|/T^a \to \infty$. We know that when the limits are taken in this order the zero-field magnetization, $m(h = 0) = 0$, vanishes for all T. If we carry out the same procedure as above from eq. (D.42a) we obtain $m \sim T^{1-b}f'(u, 0)$, for $u \to \infty$ $f'(u, 0) \sim u^{\phi}$ with $a\phi = 1 - b$, such that $m \sim A|t|^{\phi}$, all we could conclude is that the coefficient $A = 0$. Therefore we focus on the $h = 0$ susceptibility given from eq. (D.42b) as $\chi_s \sim T^{1-2b}f''(u, 0)$. Now we assume that $f''(u, 0) \overset{u\to\infty}{\sim} u^{x''}$, such that $\chi_s \sim (T^{1-2b}/T^{ax''})|t|^{ax''}$. Furthermore, in a LM phase for $h \to 0$ then $T \to 0$ we know that it is $T\chi_s$ that tends to a constant, which requires that $ax'' = 2(1 - b)/a$, i.e. $x'' = 2(1 - b)/a$. Therefore

$$T\chi_s(U > U_c, T \to 0, h = 0) \sim (U - U_c)^{\gamma'}; \qquad : \gamma' = \frac{2(1-b)}{a}, \tag{D.49}$$

relating γ' to a and b.

D.3.2 SC phase

As the QCP is approached for $U \to U_c^-$ only the spin susceptibility $\chi_s(U < U_c, T, h)$ is critical, so only it need be considered. First considering taking the limit $T \to 0$, followed by $h \to 0^{\pm}$, so that $v \to \pm\infty$, and proceeding in direct parallel with eq. (D.45) above, we assume that $f''(u, \pm\infty) \overset{u\to\infty}{\sim} u^{\tilde{x}}$. Therefore from eq. (D.42b), $\chi_s \sim (T^{1-2b}/T^{a\tilde{x}})|t|^{\tilde{x}}$. Since χ_s is finite in the $T = 0$ SC phase, we require that $\tilde{x} = 1 - 2b/a$ and hence

$$\chi_s(U < U_c, T = 0, h \to 0) \sim (U - U_c)^{-\gamma}; \qquad : \gamma = \frac{(2b-1)}{a}, \tag{D.50}$$

which is the same result as eq. (D.45) above for $U > U_c$. Thus, the exponent, γ, for the divergence of χ_s in both phases should be the same as the QCP is approached.

Moreover, if we had considered taking $h \to 0^{\pm}$ first followed by $T \to 0$, we would have obtained precisely the same form for χ_s as eq. (D.49), reflecting the fact that in a SC phase the limits commute. This is in contrast to the LM phase considered above, where the result for χ_s depends on the order of the limits.

D.3.3 $U = U_c$

Finally we consider the case of $t = 0$, such that we sit precisely at the QCP and then consider taking the limits as T and h approach zero. Firstly we take $h \to 0$, and then $T \to 0$, such that both $v = h/T^b = 0$ and $u = |t|/T^a = 0$. eq. (D.42b) then gives $\chi_s \sim T^{1-2b} f''(0,0) \propto T^{1-2b}$, and hence

$$\chi_s(U = U_c, T \to 0, h = 0) \sim T^{-y}; \qquad : y = 2b - 1, \tag{D.51}$$

relating y to b.

Next we consider the exponent δ defined by eq. (D.43d), such that $t = 0$, $v = h/T^b \to \pm\infty$ and $u = |t|/T^a = 0$. In eq. (D.42a) we assume that $f'(0, \pm\infty) \sim \mathrm{sgn}(v) v^{x'''}$ as $|v| \to \infty$, such that $m \sim \mathrm{sgn}(h)(T^{1-b}/T^{bx'''})|h|^{x'''}$. For any finite-$h$, this form must be finite as $T \to 0$, which then requires that $x''' = (1-b)/b$. Therefore

$$m(U = U_c, T = 0, h \to 0) \sim \mathrm{sgn}(h)|h|^{\frac{1}{\delta}}; \qquad : \delta = \frac{b}{(1-b)}, \tag{D.52}$$

relating δ to b.

D.3.4 Hyperscaling relations

We now have that critical exponents β (eq. (D.44)), γ (eqs. (D.45, D.50)), γ' (eq. (D.49)), y (eq. (D.51)) and δ (eq. (D.52)) in terms of the initial exponents a and b:

$$\begin{aligned} &\beta = \frac{1-b}{a}, \qquad \gamma = \frac{2b-1}{a}, \qquad \gamma' = \frac{2(1-b)}{a}, \\ &y = 2b - 1, \qquad \delta = \frac{b}{1-b}. \end{aligned} \tag{D.53}$$

We may thus eliminate the exponents a and b to obtain the following hyperscaling relations:

$$\delta = \frac{1+y}{1-y}, \qquad \beta = \gamma\frac{1-y}{2y}, \qquad \gamma' = 2\beta, \qquad 2\beta + \gamma = \frac{1}{a} \equiv \nu. \tag{D.54}$$

The exponent $\nu = \frac{1}{a}$ is commonly employed [37, 79], such that the low-energy scale $\omega_* \propto |t|^{\nu} = |U - U_c|^{\nu}$.

We note here that the relation $\gamma' = 2\beta$ is derived on fully microscopic grounds

from the analysis of Section 7.3 by considering the Lehmann representation of $\chi_s(T,\omega)$, eq. (7.68d).

Finally, recall that in analysing the singular part of the free energy, we set the exponent $c = 0$ in eq. (D.41). We now show why this is correct. We could of course repeat the above analysis with the general form eq. (D.41). In doing this eq. (D.55) is replaced by

$$\begin{aligned} \beta &= \frac{(1-c)-b}{a}, \qquad \gamma = \frac{2b-(1-c)}{a}, \qquad \gamma' = \frac{2(1-b)-c}{a}, \\ y &= 2b-(1-c), \qquad \delta = \frac{b}{(1-c)-b}. \end{aligned} \tag{D.55}$$

from which it follows that $\gamma' = 2\beta + \frac{c}{a} = 2\beta + c\nu$. However from the arguments of Section 7.3, $\gamma' = 2\beta$ can be proven microscopically. Hence $c = 0$ is required since the exponent a cannot be infinite.

There is another way to see that the exponent c must vanish. Throughout the entire LM phase ($U > U_c$) the residual entropy goes to a finite constant: $S_{\rm imp}(T = 0, h = 0) = \ln 2$ [43]. (Also note that the entropy of the whole system $S(T) \equiv S_{\rm imp}(T)$ — as the entropy of the system in the absence of the impurity vanishes). From basic thermodynamics for $h = 0$, $dF = -SdT$, and as such $S = -\partial F/\partial T$. Hence, in the limit that $T \to 0$, by virtue of the fact that S goes to a finite constant, $F \propto T$. Now consider eq. (D.40), $F(U > U_c, T, h = 0) \sim T^{1-c} f(u, 0)$ with $u = |t|/T^a$ (and $v = h/T^b = 0$). As $T \to 0$ (or equivalently $u \to \infty$), assume that $f(u, 0) \sim u^\tau$, such that $F(U > U_c, T \to 0, h = 0) \sim (T^{1-c}/T^{a\tau})|t|^\tau$. For $F \propto T$ to arise from this form we require $a\tau = -c$, so $F(U > U_c, T \to 0, h = 0) \sim T|t|^{-c/a}$ and hence $S(T \to 0) = -\partial F/\partial T \sim A|t|^{-c/a} = A|t|^{-c\nu}$ (with A a constant coefficient). Therefore, in order for $S(T \to 0)$ to go to a constant value, $c = 0$ is required (a is not infinite).

APPENDIX E

Free spins

In order to illustrate some general points about the doubly-degenerate LM phases considered in this thesis, in this appendix we consider the very simple case of an ensemble of free spins.

The Hamiltonian for a free spin-$\frac{1}{2}$ object coupling to an applied magnetic field $h = \frac{1}{2}g\mu_B B$ is given by

$$\hat{H} = -2h\hat{S}_{\rm z}. \tag{E.1}$$

where the $(-)$ sign reflects that $\uparrow$ spins are favoured in energy over $\downarrow$ spins. The finite-temperature magnetization of the sample, $m(h)$, is then obtained by the thermal average of the operator, $\hat{S}_{\rm z} = \frac{1}{2}[\hat{n}_\uparrow - \hat{n}_\downarrow]$, viz.

$$m(h,T) = 2\langle\hat{S}_{\rm z}\rangle = 2\frac{{\rm Tr}\hat{S}_{\rm z}{\rm e}^{2\beta h\hat{S}_{\rm z}}}{{\rm Tr}{\rm e}^{2\beta h\hat{S}_{\rm z}}} = 2\frac{\sum_\sigma\langle\sigma|\hat{S}_{\rm z}{\rm e}^{2\beta h\hat{S}_{\rm z}}|\sigma\rangle}{\sum_\sigma\langle\sigma|{\rm e}^{2\beta h\hat{S}_{\rm z}}|\sigma\rangle}. \tag{E.2}$$

where $\sigma = \uparrow, \downarrow$ and $\beta = 1/T$ as usual. Now, using the fact that the spin states are eigenfunctions of the Hamiltonian i.e. $\hat{S}_{\rm z}|\sigma\rangle = \frac{\sigma}{2}|\sigma\rangle$, $m(h)$ is easily shown to be given by

$$m(h,T) = \tanh(\beta h). \tag{E.3}$$

(We note that the only non-zero magnetization arises along the z-axis - it is easily shown that both $\langle\hat{S}_x\rangle, \langle\hat{S}_y\rangle = 0$ by direct consideration). The corresponding spin-susceptibility is then obtained from taking the derivative of either eq. (E.2) or eq. (E.3)

$$\chi_s(h,T) = \frac{1}{2}\frac{\partial m(h,T)}{\partial h} = \frac{\beta}{2}[\langle\hat{S}_z^2\rangle - \langle\hat{S}_z\rangle^2] = \frac{\beta}{2}[1 - m^2(h,T)]. \tag{E.4}$$

where we have used $\langle\hat{S}_z^2\rangle = \frac{1}{4}$.

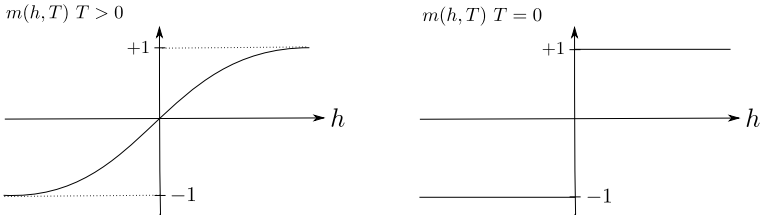


Figure E.1: Left: The finite-temperature magnetization, $m(h,T)$, as a function of h. Right: $m(h,T)$ as a function of the at $T=0$.

Now let us consider the two separate limiting processes $\lim_{T\to 0}\lim_{h\to 0^{\pm}}[m(h,T)]$ and $\lim_{h\to 0^{\pm}}\lim_{T\to 0}[m(h,T)]$. First, taking the limit $h\to 0^{\pm}$ for any finite T, yields the picture on the LHS of Fig. E.1, i.e. the magnetization is given by eq. (E.3) vanishing for $h\to 0$. The corresponding susceptibility is thus given from eq. (E.4) by

$$\chi_s(h,T)=\frac{1}{2T}\overset{T\to 0}{\sim}\infty. \tag{E.5}$$

with a characteristic $1/T$ Curie-law divergence as $T\to 0$. This is the natural result for a doubly degenerate state with the spin having equal probability of being up or down (with $\langle \hat{S}_z^2\rangle=\frac{1}{4}$). Alternatively, consider the RHS of Fig. E.1 which shows that $m(h,T=0)=-m(-h,T=0)$ is discontinuous across $h=0$ given simply by

$$m(h,T=0)=[\theta(h)-\theta(-h)], \tag{E.6}$$

which is obtained by simply taking the limit $\beta\to\infty$ in eq. (E.3). For $h\to 0^{+}$, $m(h,T=0)\to +1$, whereas for $h\to 0^{-}$, $m(h,T=0)\to -1$. This behaviour reflects the fact that for any $h>0$, the $|\uparrow\rangle$ pure state is 'picked out', whereas for $h<0$, the $|\downarrow\rangle$ pure state is the ground-state. Identically at $h=0$, $m(h=0,T=0)=0$, describes the point where the ground-state is doubly-degenerate and the $|\uparrow\rangle$, $|\downarrow\rangle$ pure states have precisely the same energy. The spin-susceptibility follows as

$$\chi_s(h,T=0)=\frac{1}{2}\frac{\partial m(h,T)}{\partial h}=\delta(h), \tag{E.7}$$

containing a delta function singularity at $h=0$ reflecting the discontinuity in the magnetization, $m(h)$, eq. (E.6).

We make two important points about the results obtained above. Firstly considering the magnetization, $m(h)$. From eq. (E.3) $m(h=0,T)\overset{T\to 0}{\sim}0$, whereas by contrast from eq. (E.6), $m(h,T=0)\overset{h\to 0^{\pm}}{\sim}\pm 1$. Thus, the two limiting processes do

not commute, i.e.

$$\lim_{T\to 0}\lim_{h\to 0}[m(h,T)] \neq \lim_{h\to 0}\lim_{T\to 0}[m(h,T)], \tag{E.8}$$

reflecting the fact that at finite temperature, the point $T = 0, h = 0$ is continuously accessed as a function of h, whereas for $T = 0$, $m(h, T = 0)$ is discontinuous. This underlying behaviour is of course also characteristic of the LM phases in quantum impurity systems that we consider in this thesis.

Secondly we note that eq. (E.7) is not what we would obtain by setting $T = 0$ in eq. (E.4) and then taking the limit $h \to 0^{\pm}$ (in that case we simply yield $\chi_s(h \to 0^{\pm}, T = 0) = 0$). The pole contribution of eq. (E.7) is thus not picked up by the form of eq. (E.4), reflecting the fact that we implicitly assumed that $m(h, T)$ was continuous when we took its derivative in going from eq. (E.3) to eq. (E.4). The eq. (E.4) does however give correctly $\chi_s(h \to 0^{\pm}, T = 0)$ - which for the case of free spins happens to be zero because the spins are by definition full saturated local moments. For h in the vicinity of 0, we can thus write

$$\chi_s(h, T = 0) = |\tilde{\mu}|\delta(h) + \chi_s(h \to 0^{\pm}, T = 0), \tag{E.9}$$

where $|\tilde{\mu}| = 1$ when the moments are fully saturated (as they are here), and where $\chi_s(h \to 0^{\pm}, T = 0)$ vanishes in this case. However, eq. (E.9) gives the general form for $\chi_s(h, T = 0)$ in a LM phase at zero temperature (c.f. eq. (7.6)).

Bibliography

[1] P. W. Anderson, Science **177**, 393 (1972).

[2] A. C. Hewson, *The Kondo Problem to Heavy Fermions* (Cambridge University Press, Cambridge, 1993).

[3] P. A. Lee, N. Nagaosa, and X.-G. Wen, Rev. Mod. Phys. **78**, 17 (2006).

[4] P. Coleman, in *Handbook of Magnetism and Advanced Magnetic Materials* (John Wiley, New York, 2007).

[5] Y. Zhang, Y. Tan, H. L. Stormer, and P. Kim, Nature **438**, 201 (2005).

[6] L. P. Kouwenhoven and L. I. Glazman, Phys. World **14**, 33 (2001).

[7] P. W. Anderson, Phys. Rev. **124**, 41 (1961).

[8] W. G. van der Wiel *et al.*, Science **289**, 2105 (2000).

[9] M. Pustilnik and L. I. Glazman, Phys. Rev. Lett. **87**, 216601 (2001).

[10] K. G. Wilson, Rev. Mod. Phys. **47**, 773 (1975).

[11] H. R. Krishnamurthy, J. W. Wilkins, and K. G. Wilson, Phys. Rev. B **21**, 1003 (1980).

[12] H. R. Krishnamurthy, J. W. Wilkins, and K. G. Wilson, Phys. Rev. B **21**, 1044 (1980).

[13] W. de Haas, J. de Boer, and G. van dn Berg, Physica **1**, 1115 (1934).

[14] J. Kondo, Prog. Theor. Phys **32**, 37 (1964).

[15] M. P. Sarachik, E. Corenzwit, and L. D. Longinotti, Phys. Rev. **135**, A1041 (1964).

[16] C. Zener, Phys. Rev. **81**, 440 (1951).

[17] J. R. Schrieffer and P. A. Wolff, Phys. Rev. **149**, 491 (1966).

[18] P. W. Anderson, J. Phys. C **3**, 2436 (1970).

[19] P. Nozières, J. Low Temp. Phys. **17**, 31 (1974).

[20] L. D. Landau, Sov. Phys. JETP **3**, 920 (1956).

[21] L. D. Landau, Sov. Phys. JETP **5**, 101 (1957).

[22] N. Andrei, K. Furuya, and J. H. Lowenstein, Rev. Mod. Phys. **55**, 331 (1983).

[23] A. M. Tsvelik and P. B. Wiegmann, Adv. Phys. **32**, 453 (1983).

[24] K. Yosida and K. Yamada, Prog. Theor. Phys. Supp. **46**, 244 (1970).

[25] K. Yamada, Prog. Theor. Phys **53**, 970 (1975).

[26] K. Yosida and K. Yamada, Prog. Theor. Phys **53**, 1286 (1975).

[27] K. Yamada, Prog. Theor. Phys **54**, 316 (1975).

[28] D. E. Logan, M. P. Eastwood, and M. A. Tusch, J. Phys.: Cond. Matt. **10**, 2673 (1998).

[29] N. L. Dickens and D. E. Logan, J. Phys.: Cond. Matt. **13**, 4505 (2001).

[30] M. T. Glossop and D. E. Logan, J. Phys.: Cond. Matt. **14**, 6737 (2002).

[31] P. Nozières and A. Blandin, J. Phys. France **41**, 193 (1980).

[32] D. L. Cox and A. Zawadowski, Advances in Physics **47**, 599 (1998).

[33] D. Withoff and E. Fradkin, Phys. Rev. Lett. **64**, 1835 (1990).

[34] M. T. Glossop and D. E. Logan, J. Phys.: Cond. Matt. **15**, 7519 (2003).

[35] M. Vojta and R. Bulla, Phys. Rev. B **65**, 014511 (2001).

[36] M. Vojta, R. Zitzler, R. Bulla, and T. Pruschke, Phys. Rev. B **66**, 134527 (2002).

[37] K. Ingersent and Q. Si, Phys. Rev. Lett. **89**, 076403 (2002).

[38] K. Chen and C. Jayaprakash, J. Phys. Cond. Matt **7**, L491 (1995).

[39] R. Bulla, T. Pruschke, and A. C. Hewson, J. Phys. Cond. Matt. **9**, 10463 (1997).

[40] K. Ingersent, Phys. Rev. B **54**, 11936 (1996).

[41] R. Bulla, M. T. Glossop, D. E. Logan, and Th. Pruschke, J. Phys.: Cond. Matt. **12**, 4899 (2000).

[42] J. H. Pixley, S. Kirchner, K. Ingersent, and Q. Si, Phys. Rev. Lett. **109**, 086403 (2012).

[43] C. Gonzalez-Buxton and K. Ingersent, Phys. Rev. B. **57**, 14254 (1998).

[44] D. E. Logan and M. T. Glossop, J. Phys.: Cond. Matt. **12**, 985 (2000).

[45] M. T. Glossop and D. E. Logan, Europhys. Lett. **61**, 810 (2003).

[46] L. Fritz and M. Vojta, Rev. Rev. B **70**, 214427 (2004).

[47] M. Vojta and M. Kircan, Phys. Rev. Lett. **90**, 157203 (2003).

[48] M. Kircan and M. Vojta, Phys. Rev. B **69**, 174421 (2003).

[49] L. Fritz, S. Florens, and M. Vojta, Phys. Rev. B **74**, 114410 (2006).

[50] K. Chen and C. Jayaprakash, Phys. Rev. B **57**, 5225 (1998).

[51] M. R. Galpin and D. E. Logan, Eur. Phys. J. B **62**, 129 (2008).

[52] M. R. Galpin and D. E. Logan, Phys. Rev. B **77**, 195108 (2008).

[53] C. P. Moca and A. Roman, Phys. Rev. B **81**, 235106 (2010).

[54] M. T. Glossop and K. Ingersent, Phys. Rev. Lett **95**, 067202 (2005).

[55] M. T. Glossop and K. Ingersent, Phys.Rev. B **75**, 104410 (2007).

[56] M. Cheng, M. T. Glossop, and K. Ingersent, Phys. Rev. B **80**, 165113 (2009).

[57] J. H. Pixley, S. Kirchner, K. Ingersent, and Q. Si, Phys. Rev. B **88**, 245111 (2013).

[58] W. Kohn and J. M. Luttinger, Phys. Rev. **118**, 41 (1960).

[59] J. M. Luttinger and J. C. Ward, Phys. Rev. **118**, 1417 (1960).

[60] J. M. Luttinger, Phys. Rev. **121**, 942 (1961).

[61] J. M. Luttinger and P. Nozières, Phys. Rev. **127**, 1431 (1962).

[62] A. L. Fetter and J. D. Walecka, *Quantum Theory of Many-Particle Systems* (McGraw-Hill, New York, 1971).

[63] R. D. Mattuck, *A Guide to Feynman Diagrams in the Many-Body Problem* (Dover, New York, 1992).

[64] D. E. Logan and M. T. Glossop, J. Phys.: Cond. Matt. **12**, 985 (1999).

[65] M. T. Glossop, G. E. Jones, and D. E. Logan, J. Phys. Chem. B **109**, 6564 (2005).

[66] G. Baym and L. P. Kadanoff, Phys. Rev. **124**, 287 (1961).

[67] G. Baym, Phys. Rev. **127**, 1391 (1962).

[68] D. C. Langreth, Phys. Rev. **150**, 516 (1966).

[69] N. E. Bickers and D. Scalapino, Ann. Phys. (N.Y.) **193**, 206 (1989).

[70] N. E. Bickers and D. Scalapino, Phys. Rev. B **43**, 8044 (1991).

[71] N. E. Bickers, D. Scalapino, and S. White, Phys. Rev. Lett. **62**, 961 (1989).

[72] J. A. White, Phys. Rev. B **45**, 1100 (1992).

[73] C. X. Chen, Q. Luo, and N. E. Bickers, J. Appl. Phys. **69**, 5469 (1991).

[74] M. Gell-Mann and F. Low, Phys. Rev. **84**, 350 (1951).

[75] G. C. Wick, Phys. Rev. **80**, 268 (1950).

[76] J. M. Luttinger, Phys. Rev. **119**, 1153 (1960).

[77] P. Nozières and J. M. Luttinger, Phys. Rev. **127**, 1423 (1962).

[78] C. Gonzalez-Buxton and K. Ingersent, Phys. Rev. B **54**, R15614 (1996).

[79] M. Vojta, Phil. Mag. **86**, 1807 (2006).

[80] M. Vojta, L. Fritz, and R. Bulla, Europhy. Lett. **90**, 27006 (2010).

[81] M. T. Glossop, S. Kirchner, J. Pixley, and Q. Si, Phys.Rev. B **107**, 076404 (2011).

[82] K. Takegahara, Y. Shimitzu, and O. Sakai, J. Phys. Soc. Jpn. **61**, 3443 (1992).

[83] M. Cheng and K. Ingersent, Phys. Rev. B **87**, 075145 (2013).

[84] E. M. Nica, K. Ingersent, J.-X. Zhu, and Q. Si, Phys. Rev. B **88**, 014414 (2013).

[85] F. Zamani *et al.*, physica status solidi (b) **250**, 547 (2013).

[86] M. R. Galpin, D. E. Logan, and H. R. Krishnamurthy, Phys. Rev. Lett. **94**, 186406 (2005).

[87] M. R. Galpin, D. E. Logan, and H. R. Krishnamurthy, J. Phys.: Cond. Matt. **18**, 6545 (2006).

[88] M. R. Galpin and D. E. Logan, J. Phys.: Cond. Matt. **17**, 6959 (2005).

[89] F. W. Jayatilaka, M. R. Galpin, and D. E. Logan, Phys. Rev. B **84**, 115111 (2011).

[90] S. J. Chorley *et al.*, Phys. Rev. Lett. **109**, 156804 (2012).

[91] T. Kuzmenko, K. Kikoin, and Y. Avishai, Phys. Rev. B **73**, 235310 (2006).

[92] W. Wang, Phys. Rev. B **76**, 115114 (2007).

[93] A. K. Mitchell, T. F. Jarrold, and D. E. Logan, Phys. Rev. B **79**, 085124 (2009).

[94] A. K. Mitchell, T. F. Jarrold, M. R. Galpin, and D. E. Logan, J. Phys. Chem. B **117**, 12777 (2013).

[95] P. P. Baruselli, R. Requist, M. Fabrizio, and E. Tosatti, Phys. Rev. Lett. **111**, 047201 (2013).

[96] D. E. Logan, C. J. Wright, and M. R. Galpin, Phys. Rev. B **80**, 125117 (2009).

[97] C. J. Wright, M. R. Galpin, and D. E. Logan, Phys. Rev. B **84**, 115308 (2011).

[98] R. Bulla, A. C. Hewson, and T. Pruschke, J. Phys.: Cond. Matt. **10**, 8365 (1998).

[99] D. N. Zubarev, Soviet Physics Uspekhi **3**, 320 (1960).

[100] M. T. Glossop and D. E. Logan, Eur. Phys. J. B **13**, 513 (2000).

[101] R. Peters, T. Pruschke, and F. B. Anders, Phys. Rev. B **74**, 245114 (2006).

[102] A. Weichselbaum and J. von Delft, Phys. Rev. Lett. **99**, 076402 (2007).

[103] D. E. Logan, A. P. Tucker, and M. R. Galpin, Phys. Rev. B **90**, 075150 (2014).

[104] G. B. Arfken and H. J. Weber, *Mathematical Methods for Physicists*, 4th ed. (Academic Press, London, 1995).

[105] V. Janis and P. Augustinsky, Phys. Rev. B **75**, 165108 (2007).

[106] Y. M. Vilk and A.-M. S. Tremblay, J. Phys. I **7**, 1309 (1997).

[107] V. Janis and P. Augustinsky, Phys. Rev. B **77**, 085106 (2008).

[108] A. P. Tucker, M. R. Galpin, and D. E. Logan, Conserving approximations for the pseudogap Anderson impurity model, (in preparation).

[109] D. J. Thouless, *The Quantum Mechanics of Many-Body Systems* (Academic Press, London, 1961).

[110] M. Hanl and A. Weichselbaum, Phys. Rev. B **89**, 075130 (2014).

[111] P. Nozières, *The Theory of Interacting Fermi Systems* (Westview Press, New York, 1997).

[112] G. D. Mahan, *Many-Particle Physics*, 3rd ed. (Klewer Academic / Plenum Publishers, New York, 2000).

[113] R. Bulla, T. A. Costi, and T. Pruschke, Rev. Mod. Phys. **80**, 395 (2008).

[114] R. Žitko and J. Bonča, Phys. Rev. B **74**, 045312 (2006).

[115] F. B. Anders and A. Schiller, Phys. Rev. Lett. **95**, 196801 (2005).

[116] F. B. Anders and A. Schiller, Phys. Rev. B **74**, 245113 (2006).

[117] C. J. Wright, Phd thesis, University of Oxford, 2011.

[118] L. E. Reichl, *A modern course in statistical physics* (John Wiley, New York, 1998).